Influencing Metal-organic Framework Catalysis through Nanoscale Structuralisation

A thesis presented to

The School of Physical Sciences

at

The University of Adelaide

in fulfilment of the requirements for

The Degree of

Doctor of Philosophy in Chemical Science

by

Oliver M. Linder-Patton

THE UNIVERSITY of ADELAIDE

Adelaide, Australia

February 2020

Contents

Declaration

I certify that this work contains no material which has been accepted for the award of any other degree or diploma in my name, in any university or other tertiary institution and, to the best of my knowledge and belief, contains no material previously published or written by another person, except where due reference has been made in the text. In addition, I certify that no part of this work will, in the future, be used in a submission in my name, for any other degree or diploma in any university or other tertiary institution without the prior approval of the University of Adelaide and where applicable, any partner institution responsible for the joint-award of this degree.

I acknowledge that copyright of published works contained within this thesis resides with the copyright holder(s) of those works.

I also give permission for the digital version of my thesis to be made available on the web, via the University's digital research repository, the Library Search and also through web search engines, unless permission has been granted by the University to restrict access for a period of time.

I acknowledge the support I have received for my research through the provision of an Australian Government Research Training Program Scholarship.

Oliver M. Linder-Patton

Acknowledgements

Foremost, I would like to express my sincere gratitude to my supervisors Prof. Christopher Sumby, Prof. Christian Doonan and Dr Kenji Sumida for their continuous support and advice throughout my candidature. I would like to specifically thank Chris and Christian for their guidance, insight, and immense knowledge base without which this thesis would not have eventuated.

It is my pleasure to acknowledge the roles of several individuals who were instrumental for the completion of my PhD research. Firstly, I would like to thank Assoc. Prof. Shuhei Furukawa for my two month placement within his lab in Kyoto. My time spent in his group shaped my methodology and provided much inspiration for the work detailed in this thesis. I would like to express my gratitude to Assoc. Prof Stephen Bell for his assistance with experimental planning, GC-MS training, and sarcastic reminders that I should be doing work. Thanks also to both Matthew Bull and Peter Apoefis as without their vast technical knowledge and assistance many of my catalytic experiments would never have come to fruition. In addition, I would like to thank the staff at Adelaide Microscopy, Ken Neubauer and Sarah Gilbert, for their support with instrumentation.

To all of the members of our extended research group, specifically past and present members of Johnson room 104; thank you for all of the good times, the many cakes and lab outings. I would like to acknowledge the mentorship of Dr Jesse Tao, Dr Campbell Coghlan and Dr Alexandre Burgun at various points of my candidature.

To my friends and family, I am grateful for all of the support and love you have given me. David, Simone, Anita, Peter, Nathaniel, Phoebe, Aaron and Tianyi, thank you for providing moments of much needed respite and countless free meals. I would like to express gratitude to Kate, Harley, Pat and Aimee for their enduring friendship, support, and for making this time so enjoyable.

And finally, I would like to thank my amazing partner Natasha, who has been my rock throughout the best and worst experiences of my PhD candidature. I could never have made it this far without you.

Abbreviations

AA	Acetic acid
AAS	Atomic absorption spectrometry
acac	Acetylacetonate
adc	Anthracenedicarboxylate
BA	Benzoic acid
BET	Brunauer-Emmett-Teller
bdc	1,4-benzenedicarboxylate
bpy	4,4'-bipyridine
Cetane	*n*-hexadecane
COD	Cyclooctadiene
CSD	Cambridge structural database
CS-MOF	Core-shell metal-organic framework
CTAB	Cetyltrimethylammonium bromide
DFT	Density functional theory
DMA	N,N-dimethylacetamide
DMBIM	5,6-dimethylbenzimidazole
DMF	N,N-dimethylformamide
DMSO	Dimethyl sulfoxide
DNA	Deoxyribonucleic acid
DUT	Dresden University of Technology
EDX	Energy-dispersive X-ray spectroscopy
EtOH	Ethanol
GC-MS	Gas chromatography-mass spectrometry

GC-FID	Gas chromatography-flame ionising detector
H_2bpdc	4,4’-biphenyl-dicaboxylic acid
H_2bpydc	2,2’-bipyridyl-5,5’-dicarboxylic acid
ICP-MS	Inductively coupled plasma mass spectrometry
IR	Infrared
Isocetane	2,4,4,6,8-heptamethylnonane
LAOs	Linear-α-olefins
MAO	Methylaluminoxane
Me_2bpydc	6,6’-dimethyl-(2,2’-bipyridine)-5,5’-dicarboxylic acid
MeCN	Acetonitrile
MeOH	Methanol
MIL	Matérial Institut Lavoisier
MMM	Mixed-matrix membrane
MOF	Metal-organic framework
MOP	Metal-organic polyhedra
NMR	Nuclear magnetic resonance
NU	Northwestern University
PCN	Porous coordination network
PCP	Porous coordination polymer
PPA	Phenylphosphinic acid
PSMet	Post-synthetic metalation
py	pyridine
PXRD	Powder X-ray diffraction
RGA	Residual gas analyser

SALE	Solvent-assisted-ligand-exchange
SBU	Secondary building unit
SE	Secondary electron
SEM	Scanning electron microscopy
SCXRD	Single-crystal X-ray diffraction
SLER	Surface ligand exchange reaction
STP	Standard temperature and pressure
TBAPy	1,3,6,8-tetrakis(p-benzoic acid)pyrene
TFA	Trifluoroacetic acid
THF	Tetrahydrofuran
TMB	3,3',5,5'-tetramethylbenzidine
TOF	Turn over frequency
TON	Turn over number
UiO	University of Oslo
ZIF	Zeolitic imidazolate framework
2-mIM	2-methylimidazole

Abstract

Metal-organic Frameworks (MOFs) are a class of porous crystalline materials formed from the self-assembly of organic and inorganic components. Due to the modular nature of their synthesis and reversibility of metal-ligand bonding, these materials can be tailored at the nanoscale and functionalised to suit specific applications including heterogeneous catalysis. However, in order to apply MOFs on an industrial scale they must be incorporated within existing technologies and to do so they must be synthesised with defined particle sizes with precise control over their nanoscale structure (i.e. size, morphology, and surface chemistry). The work presented in this thesis investigates the influence of nanoscale structuralisation on MOF catalysis.

The first chapter introduces MOFs as versatile materials for heterogeneous catalysis and discusses how their nanoscale structure can be altered to enable better integration within existing technologies. New materials phenomena have arisen from alterations to the particle size, morphology, and surface chemistry of MOFs, indicating the potential for the optimisation of MOF catalysts through nanoscale structuralisation.

Chapter 2 presents a systematic investigation of the influence of particle size and morphology on surface catalysis of a zinc-based MOF, Zeolitic Imidazolate Framework 8 (ZIF-8). Herein, ZIF-8 was synthesised at discrete particle sizes (50 nm to 100 μm) with three distinct crystal morphologies (rhombic dodecahedral, truncated rhombic dodecahedral and cubic) and the surface catalysed transesterification of hexanol with vinyl acetate was investigated.

Work in Chapter 3 explored the impact of surface to volume ratios on the activity and reaction selectivity of a rhodium(I) homogeneous catalyst site isolated post synthetically at vacant chelating sites within the zirconium framework UiO-67-bpydc (UiO = University of Oslo, bpydc = 2,2'-bipyridyl-5,5'-dicarboxylic acid). The particle size and ligand loading of UiO-67-bpydc was controlled through crystal engineering techniques of coordination modulation and mixed ligand synthesis, resulting in discrete particle sizes of 100 nm, 1 μm and 10 μm, and 0-100% bpydc incorporation. Particle size and pore confinement effects were shown to influence the reaction selectivity (hydroformylation/hydrogenation) and activity of the samples post-synthetically metalated with $[Rh(COD)(acetone)_2]BF_4$.

Chapter 4 extends the investigations initiated in Chapter 3 to gas phase catalysis of ethylene oligomerisation within a core-shell framework post-synthetically metalated with [PdMe(MeCN)]BF_4. Taking advantage of the reversibility of metal-ligand bonds within MOFs, diffuse core-shell framework composites were synthesised via slow diffusion solvent-assisted-ligand-exchange. The activity and selectivity of core-shell catalysts with active sites localised at the interior, exterior, and throughout framework were subsequently studied.

Finally, in Chapter 5, the attempted isolation of reactive intermediates was investigated with an isostructural zirconium-based framework, UiO-67-Me_2bpydc (Me_2bpydc = 6,6'-dimethyl-(2,2'-bipyridine)-5,5'-dicarboxylic acid). Using protocols developed in preceding chapters, the crystal engineering techniques of coordination modulation, modulator exchange, and "crystal healing" large X-ray quality crystals of UiO-67-Me_2bpydc were synthesised and an X-ray crystal structure could be obtained. Preliminary experiments demonstrated that small tetrahedral transition metal complexes, such as those formed when $CoCl_2$ and $ZnCl_2$ coordinate at the 2,2'-bipyridine site, could be isolated within the framework and their structures determined via single crystal X-ray diffraction (SCXRD). In this manner UiO-67-Me_2bpydc was used as a crystalline matrix to isolate transition metal complexes.

Chapter 1.

Introduction

Chapter 1. Introduction

1.1. Background

1.1.1. Supramolecular Chemistry

Supramolecular chemistry is the study of intermolecular bonding, investigating the extension of a molecules chemistry in terms of its interactions with other molecules, i.e. 'chemistry beyond the molecule'.[1] The field of supramolecular chemistry involves the design and construction of assemblies of higher complexity or 'supermolecules' from simple small molecular building blocks held together by non-covalent reversible interactions.[2] In general these interactions are weaker than typical covalent bonds and include van der Waals forces,[3] dipole-dipole interactions,[4] hydrogen bonding,[5] π-π interactions, halogen bonding,[6] and metal-ligand interactions amongst others.[7-9] Such intermolecular interactions are ubiquitous in the physical world and govern the formation of structures essential to life.

Supramolecular chemistry can be dissected into two broad domains: self-assembly and host-guest chemistry. Self-assembly is the spontaneous and reversible association of molecular building blocks to form complex assemblies.[10] The reversibility of the self-assembly process enables supramolecular systems to adapt to local changes and self-correct during formation.[4] One such fundamental example is the double stranded helical structure of DNA; in which two polymeric strands are held together through π-π interactions and hydrogen bonding between complimentary base pairs.[11-12] The bonding between the two complimentary strands is reversible, allowing for DNA replication and repair. On the other hand, host-guest chemistry refers to the molecular recognition of small guests within specific binding sites of a host molecule. Host-guest interactions are essential in many biological receptor systems and interfaces.[13-14] Substrate binding within enzymes, referred to as the induced fit mechanism, exemplifies the efficient and functional supramolecular assemblies derived from nature. Synthetic chemistry has since adopted these concepts in a variety of ways including, selective anion recognition by organic dyes and the self-assembly of block co-polymers,[15-16] which can be applied in molecular sensing and organic electronics respectively.

1.1.2. Metallosupramolecular Chemistry

The toolkit of supramolecular chemistry is by no means limited to organic systems and can be extended to inorganic systems. Metallosupramolecular chemistry refers to the self-assembly of complex architectures from organic and inorganic building blocks, directed by reversible non-covalent metal-ligand bonds. The strength of a metal-ligand bond can vary between that of hydrogen and weak covalent bonds, allowing for great control over the form and function of metallosupramolecular assemblies.[9] Since its inception, this field has expanded toward the construction of increasingly complex and intricate discrete structures such as helicates,[17] molecular knots,[18] squares,[19] tetrahedra,[20] coordination cages and metal-organic polyhedra (MOPs) (see Figure **1.1**).[9, 21-22] Such studies rely on the combination of convergent components to direct the construction of said discrete metallosupramolecular structures, conversely the use of divergent components results in the formation of infinite assemblies.[23]

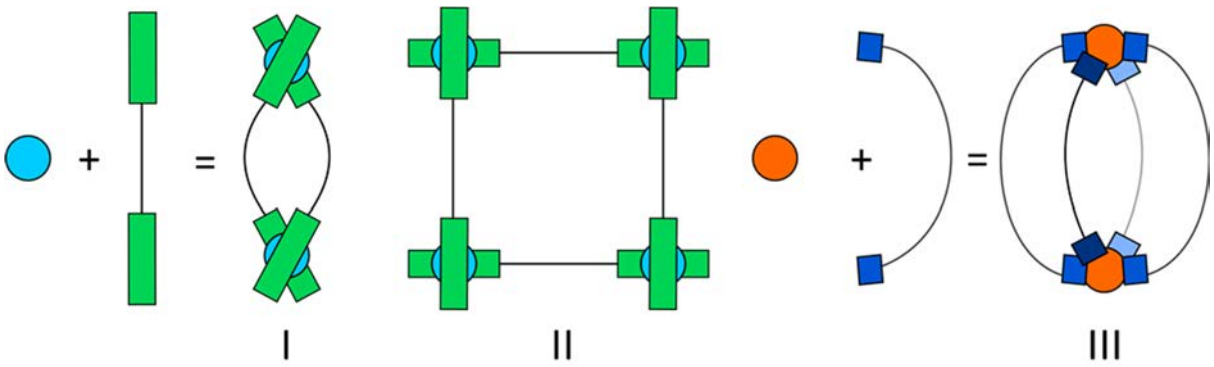

Figure **1.1**: Schematic representations of discrete metallosupramolecular structures including helicates (I), squares (II) and metal-organic polyhedra (III), synthesised from combinations of different di-topic linkers and metal nodes with varied geometries, octahedral metal ions (light blue) and square planar metal paddle wheel dimer (orange).

1.2. Metal-Organic Frameworks

1.2.1. Overview

A further extension of the principles of metallosupramolecular chemistry can be observed in the bourgeoning field of metal-organic frameworks (MOFs). These materials are a subclass of coordination polymers and have been the subject of intense study for the past 20 years, with over 2000 new papers published every year.[24] MOFs are crystalline highly porous extended materials formed from the self-assembly of divergent inorganic and organic subunits. The structure of MOFs can be controlled through judicious selection of inorganic metal nodes and organic ligands, enabling the formation of 1, 2 and 3 dimensional structures (see Figure **1.2**).[25] The multitude of potential metal and ligand combinations led to the discovery of a large library of new materials with a diverse range of properties including but not limited to high porosity, large internal surface areas and chemically mutable structures.[26] Consequently, MOFs are promising candidates for many industrially relevant applications, such as gas storage,[27-30] molecular separations,[31-34] heterogeneous catalysis,[35-39] and are poised for integration within biological,[40-43] medicinal,[44-46] and high precision sensing fields.[47-49]

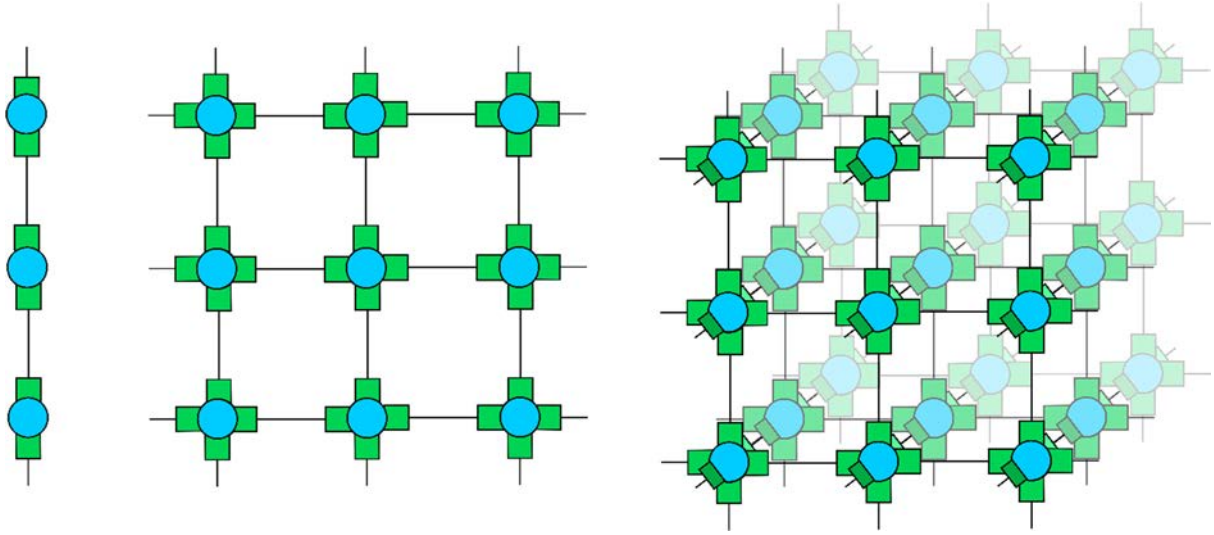

Figure **1.2**: Schematic representations of 1, 2, and 3-D frameworks (left to right) formed from the combination of metal nodes and organic ligands.

1.2.2. Synthesis and Characterisation of MOFs

The study of MOFs is an inter-disciplinary field bridging synthetic (organic and inorganic), physical and materials chemistry, requiring the utilisation of a wide range of techniques to prepare and properly analyse these materials. MOFs are highly ordered crystalline materials, as such elucidation of their structures is often performed via X-ray crystallographic techniques. Consequently, in the early years of the field the initial focus of MOF synthesis was to produce large, single crystals for ease of structural characterisation. The reversibility of metal-ligand bonds between subunits allows excellent control over MOF self-assembly, enabling the formation of thermodynamic products (extended frameworks) rather than the kinetic formation of discrete complexes. There are a wide range of reported synthetic conditions including variation in temperature, solvent composition, reagent ratios, reagent concentrations and reaction times. As such, the high through-put screening of synthesised materials via powder X-ray diffraction (PXRD), to probe their crystallinity/long range structural order, has been widely implemented to verify their quality.

1.2.3. Modulated Synthesis

Crystal engineering techniques, such as coordination modulation, have also been implemented to control the rate of MOF formation, thereby modulating crystal size and morphology. Coordination modulation involves the addition of monotopic non-bridging ligands, which can either influence the linker deprotonation equilibria or act as capping agents, reversibly competing with the bridging ligands at vacant coordination sites of the metal centre.[50] Monotopic ligands are able to impact the crystal size of MOFs by controlling rate of crystal nucleation and impart morphological control by preferentially binding to certain crystal facets, see Figure **1.3**.[51] The role that modulators play in regulating crystal shape, size and monodispersity is dictated by their pKa, steric profile and concentration.[52]

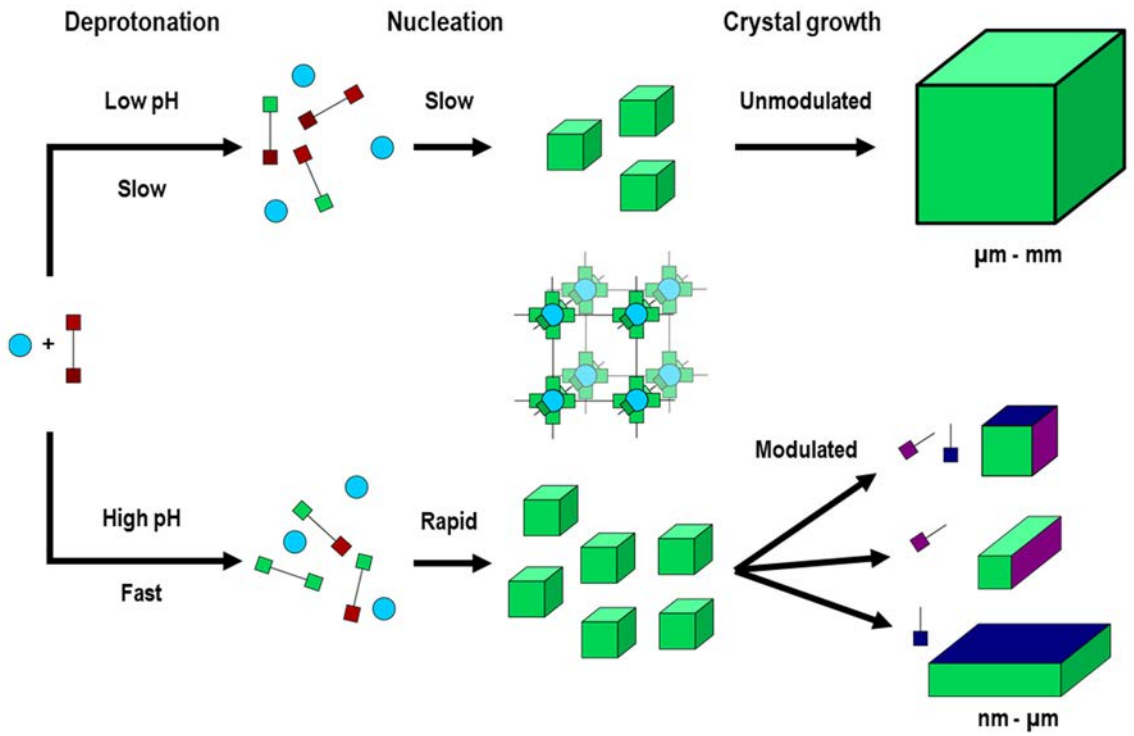

Figure **1.3**: Schematic of crystal size/morphological control of MOFs through variation in synthesis conditions including solution pH and the inclusion of monotopic modulators with affinities for different crystal facets in the structure.

Modulators have also been shown to improve the crystallinity of frameworks, most notably in the synthesis of zirconium-based MOFs such as the UiO (University of Oslo) and PCN (porous coordination network) families. The prototypical synthesis of these systems involves rapid nucleation and low reversibility of bond formation between oxophilic Zr^{4+} salts and di-/tetra-topic carboxylic acid linkers (commonly terephthalic acid, biphenyl-4,4'-dicarboxylic acid or tetrakis(4-carboxyphenyl)porphyrin for the UiO and PCN families respectively) which precludes control over crystal size or morphology.[50, 53-54] Monotopic modulators were subsequently introduced to slow the kinetics of the reaction, increasing the reversibility of ligand exchange which resulted in the synthesis of homogeneous highly crystalline Zr-based MOFs. The inclusion of monotopic ligands into the reaction mixture leads to the initial formation of Zr-modulator coordination complexes, and over time the modulators are replaced with the di-topic bridging ligand initiating framework formation.[53] This exchange equilibrium provides control over crystallization rates and enables control over product morphology, with certain groups being able to demonstrate the transformation from amorphous intergrown crystallites to highly crystalline monodispersed phases through the addition of monotopic modulators such as benzoic acid or acetic acid.[53] Additionally, the pKa of the

modulator can be leveraged to control porosity (defects),[55] surface charge and crystal size dispersity.[56]

1.2.4. Higher-Order Structuralisation of MOFs

In recent years, research in MOF chemistry has focussed on structural processing, in order to make these materials more suitable for integration in existing technologies. The higher-order structuralisation of MOFs refers to optimising the synthesis of these materials over a variety of length scales, as displayed in Figure **1.4**, in order to improve their processability. At the molecular scale (< nm), the modular approach to synthesis enables control over the generation of desired network structures based on precursor selection. This allows material properties such as pore size, chemical functionality, and stability to be highly tuneable. Additionally, molecular scale control over the spatial distribution of mixed ligand/node domains within the framework further increases the complexity of the materials which can be formed.[57] At the nanoscale (nm-μm), the features of individual crystals such as crystal size, morphology and surface chemistry can be manipulated. Individual crystals can be utilised as building blocks to construct larger structures at the mesoscale (μm-mm), leading to the formation of sophisticated architectures including thin films,[47-48, 58] hollow spheres,[59] and monolithic systems.[60-62] Higher-order structuralisation can be further extended to the macroscale (> mm), which is the external shaping of MOF systems into a desired macroscopic form e.g. pelletization.[63] Higher-order structuralisation provides the opportunity for the emergence of new properties, independent of the molecular composition and network structure of the MOF. In terms of adsorption-based applications (the storage and separation of gases), the adsorptive capacity,[64] molecular diffusion rates and dynamic properties (flexibility) of the framework have been shown to differ considerably for structuralised materials relative to those of the bulk form of the MOF (single crystals).[65-68] As such, a systematic understanding of how the structural processing of MOFs influences their physical properties is therefore paramount if these materials are to successfully transition from the laboratory to industrial applications. This thesis will focus on the first two length scales (molecular and nanoscale), which will be henceforth termed nanoscale structuralisation.

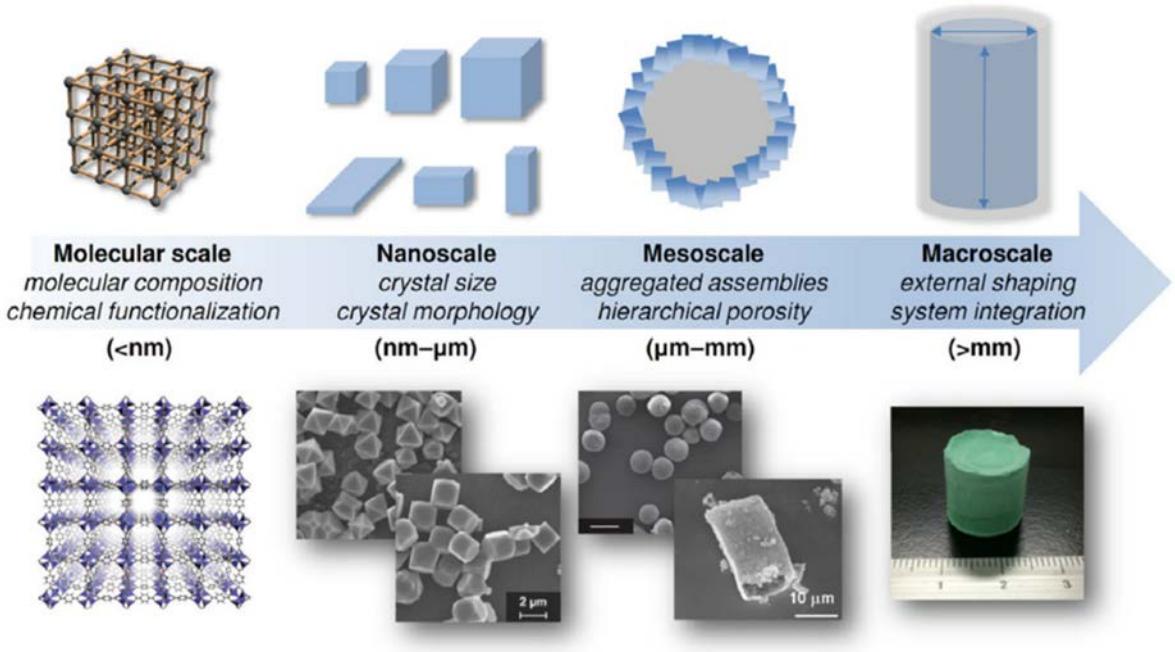

Figure **1.4**: Various length scales of MOF systems including; molecular-, nano-, meso- and macroscale.[69] Figure adapted from reference 69.

1.3. Nanoscale Structuralisation of MOFs

Control over the nanoscale structure of MOFs is essential for their integration within high-precision devices and for the fabrication of MOF-containing composites.[70] The nanoscale structuralisation of MOFs involves the manipulation of crystal size, morphology, and surface chemistry of these systems. Typically control of this nature can be achieved through variations in the reaction conditions, as discussed previously, to direct the self-assembly process towards crystals of the desired form. Although there have been advances towards the nanoscale structuralisation of MOFs, few studies have systematically probed the properties of the resulting materials. Further to this point, new materials phenomena have arisen from early studies in this area, suggesting this field could provide new pathways to optimise the performance of MOF materials.

1.3.1. Crystal Size

Changing the crystal size of MOFs has been shown to impart unique physical characteristics to the materials. Fundamentally, downsizing MOFs alters guest molecule diffusion rates and the surface to volume ratios (internal vs external surface area).[71] Changes in these two factors have resulted in alterations in the properties of MOF systems, including but not limited to: gas adsorption capacity,[72-73] framework flexibility,[68, 74] gate opening pressures,[75-77] structural reorganisation,[78] shape memory,[79] pressure amplification,[80] drug release rates,[81-82] and catalytic activity.[83-84] A broad range of MOFs can be readily prepared in a highly monodispersed fashion at different sizes, enabling the systematic evaluation of size effects. The following examples highlight a selection of these studies, emphasising the importance of analysing and understanding the impact of crystal size on the properties of MOFs.

One of the most well-studied MOF systems with respect to control of crystal size is Zeolitic Imidazolate Framework-8 (ZIF-8; $[Zn(2\text{-mIM})_2]$, 2-mIM$^-$ = 2-methylimidazole). ZIF-8 is a porous framework consisting of tetrahedral Zn^{2+} nodes bridged by 2-mIM$^-$ linkers in a sodalite topology and featuring cages within the structure with 3.4 Å apertures. These materials are well known for their structural flexibility upon guest incorporation, which arises from the rotation of imidazole linkers lining the pores as the pressure increases, enabling the accommodation of a greater density of guest molecules into the framework. [75, 85] This structural transition results in steps in the N_2 and Ar adsorption isotherms (77 and 87 K respectively).[68, 85-86] In one study the relationship between structural transitions within ZIF-8 and crystal size was probed over a range of sizes from 60 nm to 88 μm (synthesised from select conditions). A significant size dependence in the transition pressure was observed (see Figure **1.5**), with the onset pressure of the structural transition increasing as the crystal size of ZIF-8 was reduced. [86] The variation in structural flexibility is related to the change in surface to volume ratio of the crystals, which is large in smaller crystals. Since the pores of the framework which are close to the surface have lower adsorption enthalpies for Ar, higher pressures are necessary to achieve the degree of pore filling required for the structural transition of smaller crystals.[86]

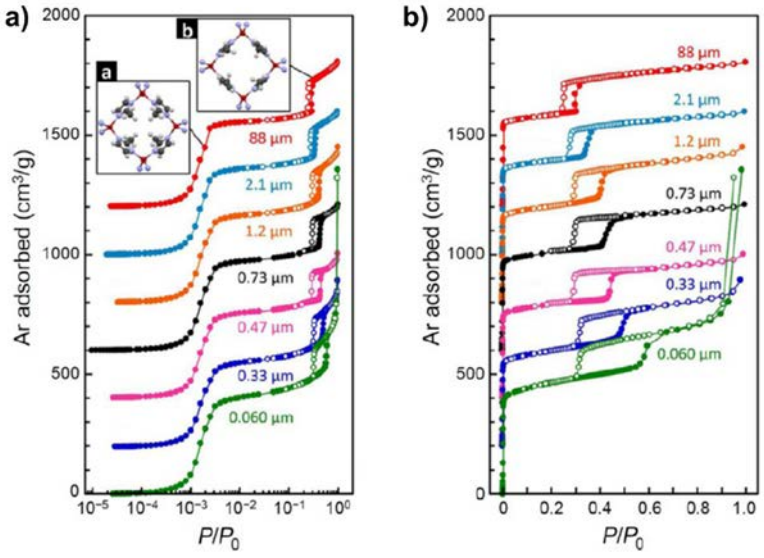

Figure **1.5**: Ar (87 K) adsorption isotherms of various sized crystals of ZIF-8, as plotted on a) a logarithmic and b) a linear pressure scale (x axis). The filled and open symbols represent the adsorption and desorption branches of the isotherm respectively, the isotherms are offset by 200 cm^3g^{-1} for clarity.[86] Figure adapted from reference 86.

In another salient study, the downsizing of crystals of the two fold interpenetrated MOF $[Cu_2(bdc)_2(bpy)]$ (bdc= 1,4-benzenedicarboxylate, bpy = 4,4'-bipyridine) produces a material with different physical properties to those of micrometre size crystals (see Figure **1.6**).[79] Here, the conventionally synthesised material demonstrates structural flexibility upon guest adsorption, reversibly transitioning between closed (guest free) and open (guest filled) forms. Upon reducing the crystal size to 50 nm, a third temporary open guest free phase is observed, and can be converted back to the closed form upon thermal treatment.[79] This novel structural flexibility is defined as a shape memory effect.[79] The emergence of this meta-stable state results from size dependent kinetic suppression of the phase transition, between meta-stable open and closed, and could be due to a decrease in the number of lattice defects. Larger crystals formed over a longer period would statistically contain fewer defects than smaller crystals, allowing for a larger kinetic suppression in defect rich crystals. [79] This insight is consistent with the premise that given time and energy, there is a degree of self-correction in the formation of PCP/MOFs afforded by the labile metal-ligand bonds. Similarly, gate opening upon downsizing has also been observed for other systems including DUT-8(Ni) (Dresden University of Technology) and the interdigitated Hoffman type framework $[Fe(py)_2[Pt(CN)_4]$ (py = pyridine), and is often attributed to the lowering of the potential energy barrier (to gate opening) with reduced crystal/film size.[76-77]

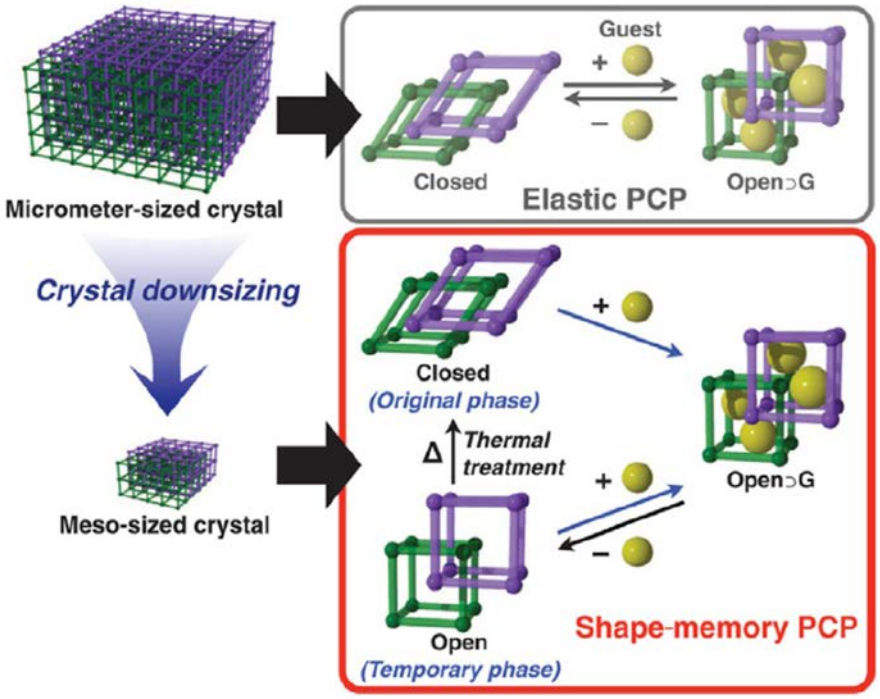

Figure **1.6**: A schematic diagram to show the influence of downsizing $[Cu_2(bdc)_2(bpy)]$ crystals to the nanometre, demonstrating the shape memory effect.[79] Figure adapted from reference 79.

1.3.2. Morphology

The morphology control of MOF crystals is important because for many systems, the different facets of the crystal surface will have intrinsically distinct chemical features.[87-88] Control over crystal morphology enables predictable exposure of certain crystal facets and allows control over surface reactivity, stability and diffusion kinetics.[88-89] There are several different routes to morphology control, but one of the most common is coordination modulation (as discussed previously).[90-93] The following examples highlight studies which investigate the shape dependence of MOF materials on their adsorptive and catalytic properties.

Introducing selective coordination modulators into a MOF system which contains two distinct coordination environments has been shown to allow considerable control over morphology for $[Cu_2(ndc)_2(dabco)]$.[89] This framework is isostructural to the $[Cu_2(bdc)_2(bpy)]$ framework, as discussed previously, consisting of square grid layers of di-nuclear copper-based paddlewheels bridged by ndc^{2-} ligands, pillared by dabco units. Due to the variation in ligand types in this framework (i.e. carboxylic acid groups and N-donor groups), anisotropy could be introduced into the crystallisation process through the addition of modulators containing similar oxygen- or nitrogen-based donating groups as the framework ligands. Three distinct morphologies were realised; nanocubes, nanosheets and nanorods, based on the ratio of

monotopic modulators (acetic acid and pyridine) added (see Figure **1.7**). The adsorption properties of each of the nano-morphologies was probed via N_2 and CO_2 adsorption isotherms (77 and 273 K respectively). All of the nano-crystalline morphologies displayed enhanced adsorption capacities for N_2, which was also observed in the higher Brunauer-Emmet-Teller (BET) surface areas of the nanocube (1040 m^2g^{-1}), nanosheet (1175 m^2g^{-1}), and nanorod (1180 m^2g^{-1}) samples relative to the conventionally synthesised bulk material (916 m^2g^{-1}).[89] Similarly, the nano-scale crystals exhibited higher CO_2 adsorption capacities relative to the bulk MOF. These enhanced adsorption properties are primarily attributed to the variations in the ratios of exposed surfaces, which are expected to have different chemical and electrostatic affinities towards guest molecules (based on the orientation of the two porous channels in the framework).[89, 94]

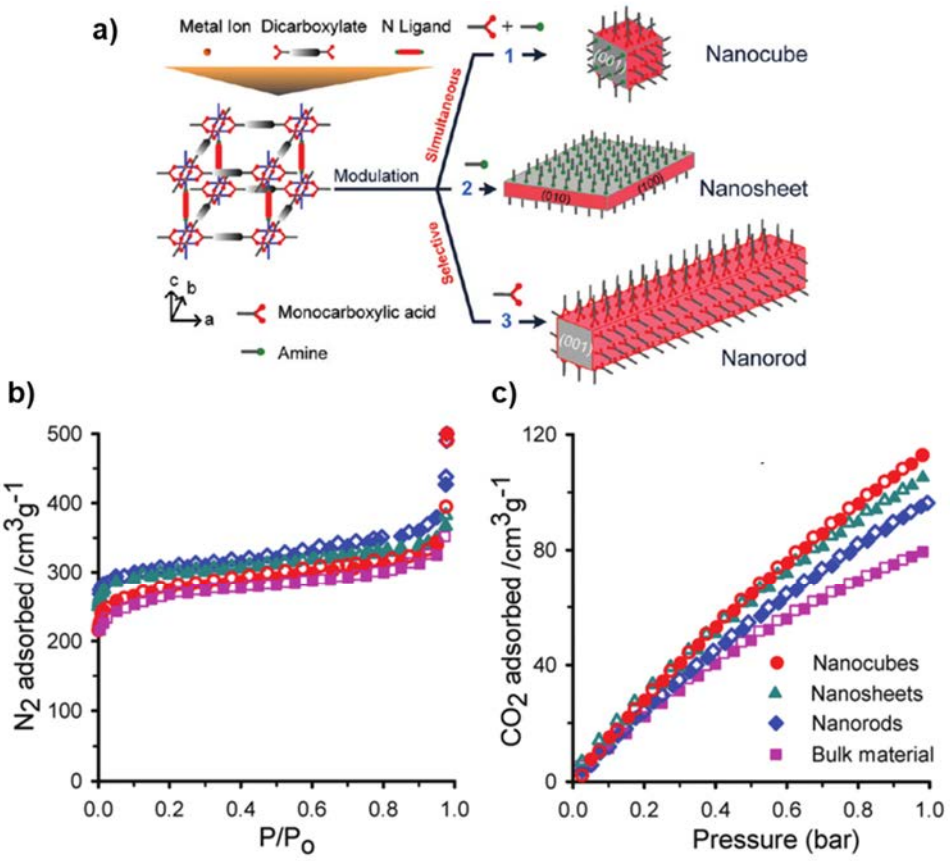

Figure **1.7**: a) A schematic diagram to show crystal growth modulation in the $[Cu_2(ndc)_2(dabco)]$ framework by addition of a monocarboxylic acid (acetic acid) and an amine (pyridine), and b,c) adsorption isotherms for N_2 at 77 K and CO_2 at 273 K, respectively, for the samples.[89] Figure adapted from reference 89.

Recently, the morphology dependence of MOF samples on their catalytic activity has been reported. Excellent intrinsic peroxidase-like activity has been reported for several iron-based MOFs including Fe-MIL-88NH_2 (MIL = Matérial Institut Lavoisier),[95] MIL-68 and MIL-100.[96-97] In order to systematically investigate the shape dependent activity of similar systems, three distinct morphologies, octahedron, bipyramidal hexagon and spindle, of an iron-bdc MOF (Fe-MIL-88) were synthesised (with the addition of modulators sodium acetate and glycerol), and the activity was analysed.[98] The oxidation of 3,3',5,5'-tetramethylbenzidine (TMB) was monitored by following the 650 nm absorption band of the oxidised product (ox-TMB). It was shown that the peroxidase-like activity of Fe-MIL-88 was related to crystal morphology, with the different morphologies displaying varied activity in the order of bipyramidal hexagonal>octahedron>spindle.[98] Highest activity observed was attributed to the cracking of the bipyramidal hexagonal crystals during catalysis, exposing more metal sites (specific surfaces). This crystal degradation was potentially due to the enhanced breathing effect of the bipyramidal hexagonal crystals relative to the other morphologies. Hence, the intrinsic catalytic activity of certain MOFs relates to the exposure of active sites, which can come from crystal degradation as well as morphological control, but due to the limited studies in this area, these phenomena are poorly understood.

1.3.3. Surface Chemistry

Given the lability of the metal-ligand bonds of MOFs, their exterior surfaces are well positioned for chemical functionalisation to better enable their integration within existing technologies. There are three categories of surface modifications with MOFs: during MOF synthesis via coordination modulation (as discussed previously), post-synthetic, and the epitaxial growth of MOF systems on the surface of other MOFs.[99] Surface modifications can enable control over the chemistry at the entrance to framework pores, terminating functional groups and porosity of the exterior framework. As such, subtle changes to MOF surface chemistry can enable a myriad of effects including surface passivation, adsorptive capacity, and selectivity. The following examples highlight how the external surface chemistry of MOFs can be influenced to alter or improve the properties of the framework.

Post-synthetic surface functionalisation often involves the exchange of terminating ligands with ones that can provide additional functions including but not limited to altering the hydrophobicity/hydrophilicity of the MOF. In one such example, the surface ligands of ZIF-8, 2-mIM were exchanged with the hydrophobic ligand 5,6-dimethylbenzimidazole (DMBIM)

via a surface ligand exchange reaction (SLER), see Figure **1.8**.[100] The composite material ZIF-8-DMBIM demonstrated enhanced stability towards hydrolysis under hydrothermal conditions, with the outer hydrophobic layer protecting the ZIF from attack by water. Additionally, the increased hydrophobicity afforded by the ZIF-8-DMBIM composite enabled direct integration within a mixed-matrix membrane (MMM), and this membrane exhibited improved selectivity for the recovery of isobutanol from water relative to one consisting of just ZIF-8. The improved selectivity was attributed to the increased hydrophobicity, decreased threshold pressure for isobutanol adsorption and enhanced transport diffusivity of the composite post SLER. This example indicates that modifications to the surface chemistry of MOFs can have a significant impact on the host-guest chemistry of the framework, due to changes in the chemical environment at pore openings.[99] Ligand exchange has been shown with other MOF systems,[101-102] but controlling the location of such exchange is non-trivial, being directed by a number of factors including ligand solubility, steric bulk and diffusion amongst others.[103-104]

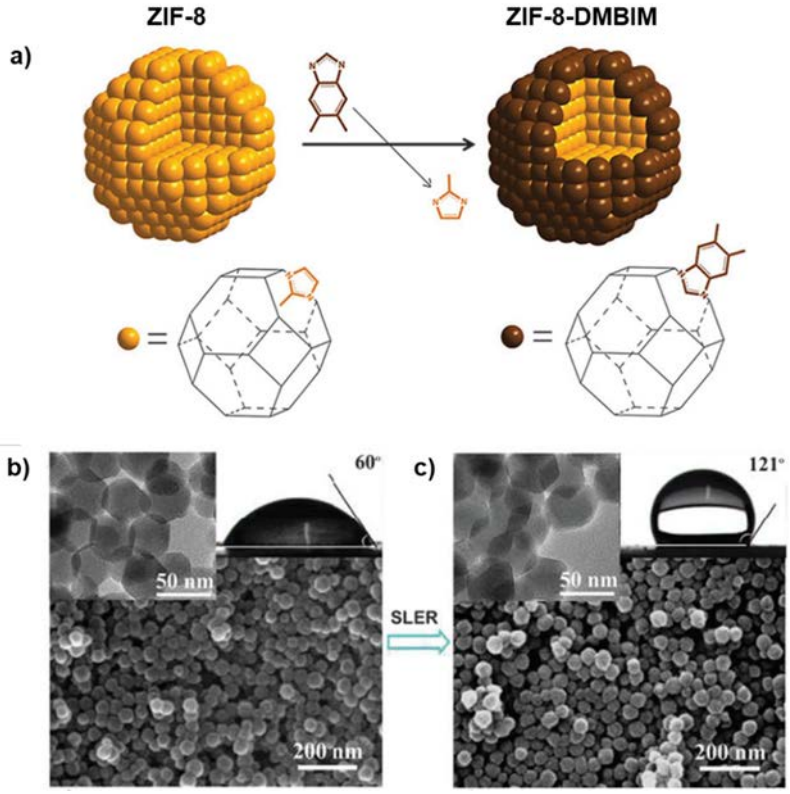

Figure **1.8**: a) A schematic representation of the shell-ligand-exchange-reaction (SLER) process of ZIF-8 to form the ZIF-8-DMBIM composite, and SEM images of b) ZIF-8 and c) ZIF-8-DMBIM with inserts of the corresponding TEM images and contact angle images of water droplets.[100] Figure adapted from reference 100.

Epitaxial growth of MOFs on the surface of other MOFs enables access to hybrid systems with properties that cannot be achieved by either unfunctionalized MOF alone. Core-shell MOF formation can be achieved via epitaxial growth and there are several examples where the shell MOF differs from the core through variation of the shell ligand,[105] metal node or a combination of the two.[57] These complex architectures have been examined through the formation of MOF-5@IR-MOF-3 and IR-MOF-3@MOF-5 composites which were formed from sequential growth from seed crystallites (see Figure **1.9**). In that study a templating effect was observed, whereby the growth of MOF-5 on the seed crystal of IR-MOF-3 produced non-interpenetrated MOF-5 under conditions which would typically result in the formation of phase impure material (interpenetrated and non-interpenetrated). Core-shell structures have also been shown to demonstrate unique bulk properties, as seen with the hybrid structure comprised of a $[Zn_2(1,4\text{-bdc})_2(dabco)]_n$ core coated with a $[Zn_2(9,10\text{-adc})_2(dabco)]_n$ shell (adc = anthracenedicarboxylate).[106] The outer framework, $[Zn_2(9,10\text{-adc})_2(dabco)]_n$, was shown to selectively absorb cetane (*n*-hexadecane) over isocetane (2,4,4,6,8-heptamethylnonane) due to the steric bulk of the 9,10-adc linker and smaller pore openings. Conversely, the inner framework, $[Zn_2(1,4\text{-bdc})_2(dabco)]_n$, displayed appreciably higher storage capacities, due to its larger pore volume, but displayed poor selectivity for the absorption of the two isomers. The core-shell hybrid however combined the selectivity of the outer framework with the increased storage capacity of the inner framework to display enhanced selective uptake of cetane over isocetane (see Figure **1.9**). As such, surface modification of a MOF system, by increasing its complexity via epitaxial growth, can produce a hybrid material with properties that are inaccessible without modification.

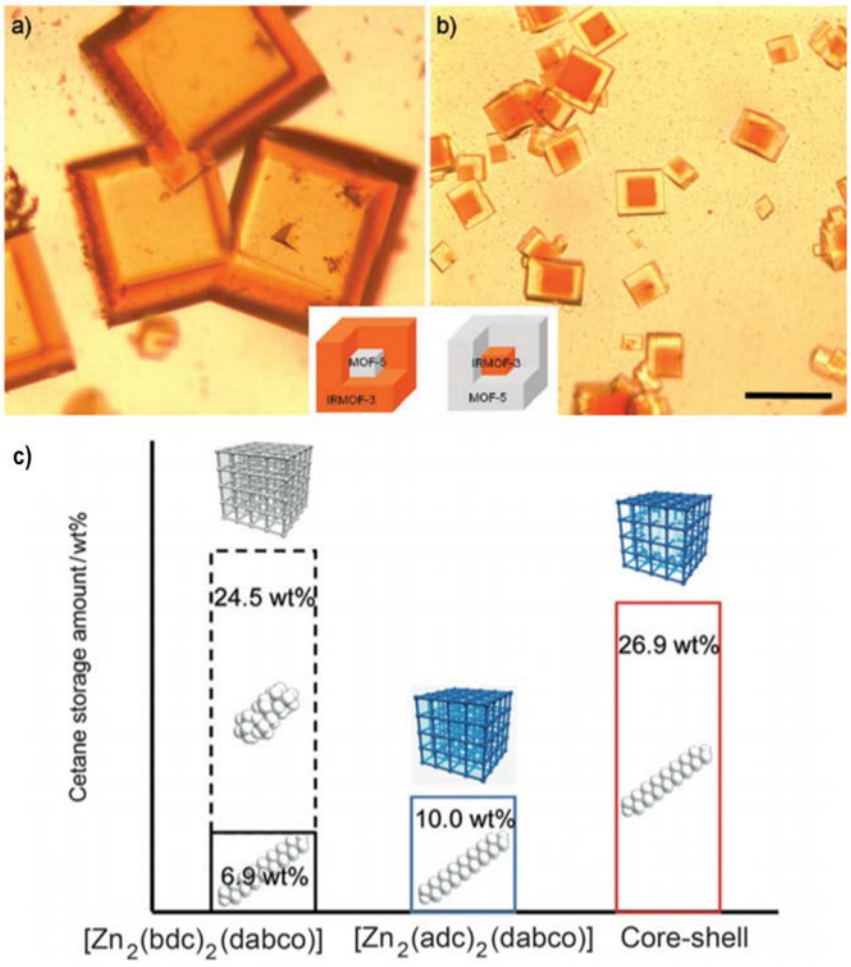

Figure **1.9**: Microscope images of core-shell MOFs a) IRMOF-3@MOF-5 and b) MOF-5@IRMOF-3 (scale bar = 0.2 mm).[105] c) Cetane storage of $[Zn_2(9,10\text{-bdc})_2(dabco)]_n$, $[Zn_2(9,10\text{-adc})_2(dabco)]_n$ and the core-shell composite which demonstrates increased storage capacity and selectivity for linear cetane over isocetane.[106] Figure adapted from references 105 and 106.

1.4. MOFs as Heterogeneous Catalysts

1.4.1. Origins of Catalytic Activity

One of the cornerstone applications of MOFs is in heterogeneous catalysis; this field was first explored in 1994 and has since grown dramatically over the past 26 years.[107] There are a great number of reactions catalysed by homogeneous catalysts, but the recovery/reusability of these catalysts is limited because they exist in the same phase as the reactants and products. These catalysts can be heterogenized by grafting them onto solid supports to improve their recoverability and applicability in industrial catalysis. More recently heterogeneous catalysts have been developed based on MOFs, where the intrinsic catalytic activity originates from two places: coordinatively unsaturated metal sites (Lewis acid sites) and pendent acid/base sites from the organic ligands of the framework. Due to the chemically mutable nature of MOFs, both the metal and ligand active sites can be modified pre- or post-synthetically, enabling incorporation of different functional groups or active sites for catalysis (see Figure **1.10**).[108]

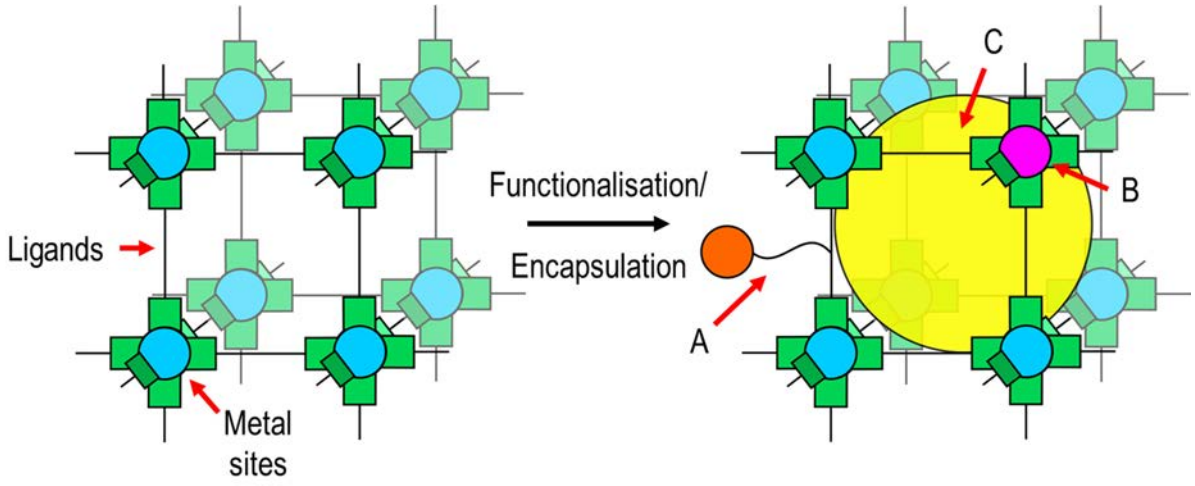

Figure **1.10**: Schematic representation of the catalytic active site origins within MOFs, on the left active sites within pristine MOFs are localised at metal nodes/organic ligand, frameworks can be further functionalised through by grafting sites on ligands (A), at metal nodes (B), or through the encapsulation of molecular catalysts/enzymes (C).

As porous materials MOFs can also act as scaffolds to encapsulate and heterogenize a great diversity of active species, such as metal nanoparticles,[109] molecular catalysts and biomacromolecule catalysts (enzymes), (see Figure **1.10**).[110-111] This encapsulation can enhance the stability and reusability of the previously homogeneous active species. As such, MOFs are able to combine the favourable qualities of both homogeneous and heterogeneous

catalysts including, excellent selectivity, high activity, and ease of recovery. MOFs have subsequently been utilised to catalyse a broad range of reactions, including CO_2 reduction,[112] hydroboration,[113] hydrogenation,[114] transesterification,[115] oligomerization,[116] Friedel-Crafts and coupling reactions.[102, 117]

1.4.2. Challenges with MOF Catalysis

MOF catalysis is reliant on mass transport of substrates/products to and from active sites within/on the framework. To date there is minimal understanding about the synergistic relationship between reactants and MOFs during catalysis, which active sites are targeted and with what frequency. As such, these materials have not been optimised despite the tools to do so being readily available. One such example is that of ethylene dimerization catalysed by site isolated molecular nickel catalysts in the pores of NU-1000. In this study Hupp *et al*. reported excellent activity and selectivity for solution phase catalysis, but poor activity for gas phase catalysis until the crystals were manually crushed (downsized).[118] The increased activity observed was purported to be a result of the reduced crystal size increasing catalyst site accessibility, but no systematic investigations were undertaken to confirm this observation or to determine whether the accessible active sites were on the interior or exterior of the crystals. Additionally, there are a selection of examples where reaction mechanisms with site isolated transition metal catalysts within MOFs have been followed via SCXRD, but these studies often follow relatively slow reactions which progress via the stepwise addition of guests.[119] Whilst enabling the elucidation of reaction mechanisms, such studies do not provide information about which active sites within the framework are preferred and must be performed on large, pristine single crystals for structural analysis.

If MOF catalysts are to be implemented on a more widely and/or integrated within existing technologies, the particle size at which they are produced must change. To do so different length scales of MOFs must be considered, most notably the nanoscale. As discussed in section 1.3, the nanoscale structuralisation of MOFs has the capacity to dramatically alter the physical properties of MOFs including diffusion rates, adsorptive capacity, and substrate selectivity, through precise control over the particle size, morphology, and surface chemistry. In the context of heterogeneous catalysis, control of this nature could enable optimisation of MOF catalysts to suit desired applications and allows for fundamental questions within the field to be explored.

In this thesis a systematic investigation of nanoscale structuralisation effects on catalysis with MOFs will be undertaken. Control over particle size, morphology, and surface chemistry of MOF catalysts will be covered, which will also include the subsequent testing of the activity/selectivity of these catalysts. The questions that this work aims to investigate include: determining which active sites are primarily accessed in frameworks during catalysis (internal vs external) and how this can be influenced by altering the ratio of exposed facets, the surface to volume ratios (particle size/morphology), or surface chemistry of MOFs. Elucidating of fundamental concepts in this area will inform future investigations into heterogeneous catalysis with MOFs, in the context of optimising these materials for applications outside of lab-scale use. Additionally, this work will also provide a perspective on the necessity of such studies within the MOF field.

1.5. Thesis Coverage

This thesis presents a study of nanoscale structuralisation effects on catalysis with MOFs, with a specific focus on the control and characterisation of crystal size, morphology, and surface chemistry. This thesis is composed of a mixture of standard chapters and manuscripts that form the introduction and the subsequent chapters of research and discussion. All of the manuscripts were completed during the doctorial candidature. Chapters 1 and 6 are introduction and conclusion chapters, respectively. The first chapter has provided background information on MOFs, their applications, and how nanoscale structuralisation has been shown to impact the properties of these materials. Additionally, parts of Chapter 1 have been adapted from a review published in a peer reviewed, international journal.[69] The final chapter gives a brief conclusion and discusses the future directions of the presented work. Both aim to provide context and understanding for the overall direction of the work presented in this thesis.

The work presented in Chapters 2, 3 and 4 sought to target the overall aims of this thesis. Chapters 2 and 3 focussed on particle size effects on catalysis with MOFs; in 2 catalysis was localised at the exterior of the crystals whereas in 3 catalysis could occur within the pores of the framework, allowing for an investigation of pore confinement effects. Chapter 4 investigated the impact of surface chemistry modification, in the formation of core-shell frameworks and further investigated internal catalysis.

Chapter 2 details the systematic study of nanoscale structuralisation effects on the ZIF-8 surface catalysed transesterification of hexanol with vinyl acetate. This chapter aims to simplify the nanoscale structuralisation study to just external crystal surface catalysis with ZIF-8. Described in this chapter is the synthesis and characterisation of ZIF-8 at a range of different particle sizes and crystal morphologies. The activity of ZIF-8 samples with different sized and morphologies was examined, with smaller particle sizes exhibiting nominally higher surface activity, although at the cost of increased structural instability. This work highlights the importance of fundamental characterisation of MOF catalysts prior to their integration within existing technologies, specifically demonstrating crystal size-induced surface instability to reaction conditions. Chapter 2 has been adapted from a peer reviewed, international journal.[120]

Chapter 3 presents the investigation of particle size effects on ethylene hydroformylation by a rhodium(I) catalyst embedded within UiO-67-bpydc. Building upon the work detailed in Chapter 2, the work presented in this chapter seeks to explore how the crystal size of the MOF support impacts the activity and reaction selectivity of a coordinated

rhodium(I) catalyst. In this case catalysis can occur at exterior and interior sites of the MOF crystals, as such this study additionally probes pore confinement effects on catalyst selectivity. Initially, the synthesis and characterisation of three different particle sizes of UiO-67-bpydc with different ligand loadings and their subsequent post-synthetic metalation with rhodium(I) species was investigated. The activity/selectivity for the gas phase hydroformylation/hydrogenation of ethylene were examined for each of the sizes. In this work, control of catalyst reaction selectivity for hydroformylation over hydrogenation was observed by increasing the particle size of the MOF scaffold supporting the homogeneous catalyst.

Chapter 4 sought to extend the observations of pore confinement mediated selectivity by focusing on internal catalysis through the synthesis of core-shell MOFs. The synthesis of core-shell MOF architectures was explored through a detailed study involving slow diffusion solvent-assisted-ligand-exchange (SALE) of the exterior ligands (as discussed above) of UiO-67-bpydc with a ligand which cannot chelate metal species. The most promising candidate was subsequently metalated with [Pd(COD)(Me)MeCN)]BF_4 and analysed for activity/selectivity for gas phase ethylene oligomerisation. Samples with active sites localised at the interior, exterior and throughout the crystal were examined, and it was determined that catalyst longevity was improved by localising active sites within the crystal. Unfortunately, catalyst deactivation through pore blockage was observed in all instances, but this work provided insight on catalyst stabilisation within the framework.

The work presented in Chapter 5 built upon the synthetic protocols developed in Chapter 4 and applying them to the synthesis of large single crystals of UiO-67-Me_2bpydc. This MOF was then used to isolate reactive transition metal species and characterise their structure via single crystal X-ray crystallography (SCXRD). The investigations described within Chapter 5 highlight the challenges of collecting and solving structures which undergo single-crystal to single-crystal phase transformations from high to low symmetry upon post-synthetic metalation.

1.6. References

1. Lehn, J. M., Supramolecular Chemistry—Scope and Perspectives Molecules, Supermolecules, and Molecular Devices (Nobel Lecture). *Angew Chem Int Ed Engl* **1988,** *27* (1), 89-112.

2. Savyasachi, A. J.; Kotova, O.; Shanmugaraju, S.; Bradberry, S. J.; Ó'Máille, G. M.; Gunnlaugsson, T., Supramolecular Chemistry: A Toolkit for Soft Functional Materials and Organic Particles. *Chem* **2017,** *3* (5), 764-811.

3. Atwood, J. L.; Barbour, L. J.; Jerga, A., Storage of Methane and Freon by Interstitial van der Waals Confinement. *Science* **2002,** *296* (5577), 2367-2369.

4. Holliday, B. J.; Mirkin, C. A., Strategies for the Construction of Supramolecular Compounds through Coordination Chemistry. *Angew Chem Int Ed* **2001,** *40* (11), 2022-2043.

5. Slater, A. G.; Perdigão, L. M. A.; Beton, P. H.; Champness, N. R., Surface-Based Supramolecular Chemistry Using Hydrogen Bonds. *Acc Chem Res* **2014,** *47* (12), 3417-3427.

6. Metrangolo, P.; Meyer, F.; Pilati, T.; Resnati, G.; Terraneo, G., Halogen Bonding in Supramolecular Chemistry. *Angew Chem Int Ed* **2008,** *47* (33), 6114-6127.

7. Ye, B.-H.; Tong, M.-L.; Chen, X.-M., Metal-Organic Molecular Architectures With 2,2′-Bipyridyl-Like and Carboxylate Ligands. *Coord Chem Rev* **2005,** *249* (5), 545-565.

8. Schneider, H.-J., Binding Mechanisms in Supramolecular Complexes. *Angew Chem Int Ed* **2009,** *48* (22), 3924-3977.

9. Stang, P. J.; Olenyuk, B., Self-Assembly, Symmetry, and Molecular Architecture: Coordination as the Motif in the Rational Design of Supramolecular Metallacyclic Polygons and Polyhedra. *Acc Chem Res* **1997,** *30* (12), 502-518.

10. Ariga, K.; Nishikawa, M.; Mori, T.; Takeya, J.; Shrestha, L. K.; Hill, J. P., Self-Assembly as a Key Player for Materials Nanoarchitectonics. *Sci Technol Adv Mater* **2019,** *20* (1), 51-95.

11. Fonseca Guerra, C.; Bickelhaupt, F. M.; Snijders, J. G.; Baerends, E. J., Hydrogen Bonding in DNA Base Pairs: Reconciliation of Theory and Experiment. *J Am Chem Soc* **2000,** *122* (17), 4117-4128.

12. Watson, J. D.; Crick, F. H. C., Molecular Structure of Nucleic Acids: A Structure for Deoxyribose Nucleic Acid. *Nature* **1953,** *171* (4356), 737-738.

13. Fish, R. H.; Jaouen, G., Bioorganometallic Chemistry: Structural Diversity of Organometallic Complexes with Bioligands and Molecular Recognition Studies of Several Supramolecular Hosts with Biomolecules, Alkali-Metal Ions, and Organometallic Pharmaceuticals. *Organometallics* **2003,** *22* (11), 2166-2177.

14. Yang, H.; Yuan, B.; Zhang, X.; Scherman, O. A., Supramolecular Chemistry at Interfaces: Host–Guest Interactions for Fabricating Multifunctional Biointerfaces. *Acc Chem Res* **2014,** *47* (7), 2106-2115.

15. Görl, D.; Zhang, X.; Stepanenko, V.; Würthner, F., Supramolecular Block Copolymers by Kinetically Controlled Co-Self-Assembly of Planar and Core-Twisted Perylene Bisimides. *Nat Commun* **2015,** *6* (1), 7009.

16. Busschaert, N.; Caltagirone, C.; Van Rossom, W.; Gale, P. A., Applications of Supramolecular Anion Recognition. *Chem Rev* **2015,** *115* (15), 8038-8155.

17. Piguet, C.; Bernardinelli, G.; Hopfgartner, G., Helicates as Versatile Supramolecular Complexes. *Chem Rev* **1997,** *97* (6), 2005-2062.

18. Forgan, R. S.; Sauvage, J.-P.; Stoddart, J. F., Chemical Topology: Complex Molecular Knots, Links, and Entanglements. *Chem Rev* **2011,** *111* (9), 5434-5464.

19. Würthner, F.; You, C.-C.; Saha-Möller, C. R., Metallosupramolecular Squares: from Structure to Function. *Chem Soc Rev* **2004,** *33* (3), 133-146.

20. Albrecht, M.; Janser, I.; Meyer, S.; Weis, P.; Fröhlich, R., A Metallosupramolecular Tetrahedron with a Huge Internal Cavity. *Chem Commun* **2003,** (23), 2854-2855.

21. Ahmedova, A., Biomedical Applications of Metallosupramolecular Assemblies—Structural Aspects of the Anticancer Activity. *Front Chem* **2018,** *6* (620).

22. Vardhan, H.; Yusubov, M.; Verpoort, F., Self-Assembled Metal–Organic Polyhedra: An Overview Of Various Applications. *Coord Chem Rev* **2016,** *306*, 171-194.

23. Cook, T. R.; Zheng, Y.-R.; Stang, P. J., Metal–Organic Frameworks and Self-Assembled Supramolecular Coordination Complexes: Comparing and Contrasting the Design, Synthesis, and Functionality of Metal–Organic Materials. *Chem Rev* **2013,** *113* (1), 734-777.

24. Chang, Z.; Yang, D.-H.; Xu, J.; Hu, T.-L.; Bu, X.-H., Flexible Metal-Organic Frameworks: Recent Advances and Potential Applications. *Adv Mat* **2015,** *27* (36), 5432-5441.

25. He, H.; Collins, D.; Dai, F.; Zhao, X.; Zhang, G.; Ma, H.; Sun, D., Construction of Metal−Organic Frameworks with 1D Chain, 2D Grid, and 3D Porous Framework Based on a Flexible Imidazole Ligand and Rigid Benzenedicarboxylates. *Cryst Growth Des* **2010,** *10* (2), 895-902.

26. Rowsell, J. L. C.; Yaghi, O. M., Metal–Organic Frameworks: a New Class of Porous Materials. *Micropor Mesopor Mater* **2004,** *73* (1-2), 3-14.

27. Suh, M. P.; Park, H. J.; Prasad, T. K.; Lim, D.-W., Hydrogen Storage in Metal–Organic Frameworks. *Chem Rev* **2012,** *112* (2), 782-835.

28. Getman, R. B.; Bae, Y.-S.; Wilmer, C. E.; Snurr, R. Q., Review and Analysis of Molecular Simulations of Methane, Hydrogen, and Acetylene Storage in Metal–Organic Frameworks. *Chem Rev* **2012,** *112* (2), 703-723.

29. Mason, J. A.; Veenstra, M.; Long, J. R., Evaluating Metal–Organic Frameworks for Natural Gas Storage. *Chem Sci* **2014,** *5* (1), 32-51.

30. He, Y.; Zhou, W.; Qian, G.; Chen, B., Methane Storage in Metal–Organic Frameworks. *Chem Soc Rev* **2014,** *43* (16), 5657-5678.

31. Li, J.-R.; Sculley, J.; Zhou, H.-C., Metal–Organic Frameworks for Separations. *Chem Rev* **2012,** *112* (2), 869-932.

32. Sumida, K.; Rogow, D. L.; Mason, J. A.; McDonald, T. M.; Bloch, E. D.; Herm, Z. R.; Bae, T.-H.; Long, J. R., Carbon Dioxide Capture in Metal–Organic Frameworks. *Chem Rev* **2012,** *112* (2), 724-781.

33. Barea, E.; Montoro, C.; Navarro, J. A. R., Toxic Gas Removal – Metal–Organic Frameworks for the Capture and Degradation of Toxic Gases and Vapours. *Chem Soc Rev* **2014,** *43* (16), 5419-5430.

34. Herm, Z. R.; Bloch, E. D.; Long, J. R., Hydrocarbon Separations in Metal–Organic Frameworks. *Chem Mater* **2014,** *26* (1), 323-338.

35. Yoon, M.; Srirambalaji, R.; Kim, K., Homochiral Metal–Organic Frameworks for Asymmetric Heterogeneous Catalysis. *Chem Rev* **2012,** *112* (2), 1196-1231.

36. Dhakshinamoorthy, A.; Asiri, A. M.; Garcia, H., Catalysis by Metal–Organic Frameworks in Water. *Chem Commun* **2014,** *50* (85), 12800-12814.

37. Gascon, J.; Corma, A.; Kapteijn, F.; Llabrés i Xamena, F. X., Metal Organic Framework Catalysis: Quo vadis? *ACS Catal* **2014,** *4* (2), 361-378.

38. Liu, J.; Chen, L.; Cui, H.; Zhang, J.; Zhang, L.; Su, C.-Y., Applications of Metal–Organic Frameworks in Heterogeneous Supramolecular Catalysis. *Chem Soc Rev* **2014,** *43* (16), 6011-6061.

39. Chughtai, A. H.; Ahmad, N.; Younus, H. A.; Laypkov, A.; Verpoort, F., Metal–Organic Frameworks: Versatile Heterogeneous Catalysts for Efficient Catalytic Organic Transformations. *Chem Soc Rev* **2015,** *44* (19), 6804-6849.

40. Diring, S.; Wang, D. O.; Kim, C.; Kondo, M.; Chen, Y.; Kitagawa, S.; Kamei, K.-i.; Furukawa, S., Localized Cell Stimulation by Nitric Oxide using a Photoactive Porous Coordination Polymer Platform. *Nat Commun* **2013,** *4* (1), 2684.

41. Lyu, F.; Zhang, Y.; Zare, R. N.; Ge, J.; Liu, Z., One-Pot Synthesis of Protein-Embedded Metal–Organic Frameworks with Enhanced Biological Activities. *Nano Lett* **2014,** *14* (10), 5761-5765.

42. Doonan, C.; Riccò, R.; Liang, K.; Bradshaw, D.; Falcaro, P., Metal–Organic Frameworks at the Biointerface: Synthetic Strategies and Applications. *Acc Chem Res* **2017,** *50* (6), 1423-1432.

43. Maddigan, N. K.; Tarzia, A.; Huang, D. M.; Sumby, C. J.; Bell, S. G.; Falcaro, P.; Doonan, C. J., Protein Surface Functionalisation as a General Strategy for Facilitating Biomimetic Mineralisation of ZIF-8. *Chem Sci* **2018,** *9* (18), 4217-4223.

44. Lu, K.; He, C.; Lin, W., A Chlorin-Based Nanoscale Metal–Organic Framework for Photodynamic Therapy of Colon Cancers. *J Am Chem Soc* **2015,** *137* (24), 7600-7603.

45. Peller, M.; Böll, K.; Zimpel, A.; Wuttke, S., Metal–Organic Framework Nanoparticles for Magnetic Resonance Imaging. *Inorg Chem Front* **2018,** *5* (8), 1760-1779.

46. Rojas, S.; Carmona, F. J.; Maldonado, C. R.; Horcajada, P.; Hidalgo, T.; Serre, C.; Navarro, J. A. R.; Barea, E., Nanoscaled Zinc Pyrazolate Metal–Organic Frameworks as Drug-Delivery Systems. *Inorg Chem* **2016,** *55* (5), 2650-2663.

47. Bradshaw, D.; Garai, A.; Huo, J., Metal–Organic Framework Growth at Functional Interfaces: Thin Films and Composites for Diverse Applications. *Chem Soc Rev* **2012,** *41* (6), 2344-2381.

48. Falcaro, P.; Ricco, R.; Doherty, C. M.; Liang, K.; Hill, A. J.; Styles, M. J., MOF Positioning Technology and Device Fabrication. *Chem Soc Rev* **2014,** *43* (16), 5513-5560.

49. Stavila, V.; Talin, A. A.; Allendorf, M. D., MOF-Based Electronic And Opto-Electronic Devices. *Chem Soc Rev* **2014,** *43* (16), 5994-6010.

50. Wang, S.; McGuirk, C. M.; d'Aquino, A.; Mason, J. A.; Mirkin, C. A., Metal–Organic Framework Nanoparticles. *Adv Mater* **2018,** *30* (37), 1800202.

51. Tsuruoka, T.; Furukawa, S.; Takashima, Y.; Yoshida, K.; Isoda, S.; Kitagawa, S., Nanoporous Nanorods Fabricated by Coordination Modulation and Oriented Attachment Growth. *Angew Chem Int Ed* **2009,** *48* (26), 4739-4743.

52. Seoane, B.; Dikhtiarenko, A.; Mayoral, A.; Tellez, C.; Coronas, J.; Kapteijn, F.; Gascon, J., Metal Organic Framework Synthesis in the Presence of Surfactants: Towards Hierarchical MOFs? *CrystEngComm* **2015,** *17* (7), 1693-1700.

53. Schaate, A.; Roy, P.; Godt, A.; Lippke, J.; Waltz, F.; Wiebcke, M.; Behrens, P., Modulated Synthesis of Zr-Based Metal–Organic Frameworks: From Nano to Single Crystals. *Chem Eur J* **2011,** *17* (24), 6643-6651.

54. Feng, D.; Gu, Z.-Y.; Li, J.-R.; Jiang, H.-L.; Wei, Z.; Zhou, H.-C., Zirconium-Metalloporphyrin PCN-222: Mesoporous Metal–Organic Frameworks with Ultrahigh Stability as Biomimetic Catalysts. *Angew Chem Int Ed* **2012,** *51* (41), 10307-10310.

55. Shearer, G. C.; Chavan, S.; Bordiga, S.; Svelle, S.; Olsbye, U.; Lillerud, K. P., Defect Engineering: Tuning the Porosity and Composition of the Metal–Organic Framework UiO-66 via Modulated Synthesis. *Chem Mater* **2016,** *28* (11), 3749-3761.

56. Morris, W.; Wang, S.; Cho, D.; Auyeung, E.; Li, P.; Farha, O. K.; Mirkin, C. A., Role of Modulators in Controlling the Colloidal Stability and Polydispersity of the UiO-66 Metal–Organic Framework. *ACS Appl Mater Inter* **2017,** *9* (39), 33413-33418.

57. Luo, T.-Y.; Liu, C.; Gan, X. Y.; Muldoon, P. F.; Diemler, N. A.; Millstone, J. E.; Rosi, N. L., Multivariate Stratified Metal-Organic Frameworks: Diversification Using Domain Building Blocks. *J Am Chem Soc* **2019**.

58. Heinke, L.; Tu, M.; Wannapaiboon, S.; Fischer, R. A.; Wöll, C., Surface-Mounted Metal-Organic Frameworks for Applications in Sensing and Separation. *Micropor Mesopor Mater* **2015,** *216*, 200-215.

59. Ameloot, R.; Vermoortele, F.; Vanhove, W.; Roeffaers, M. B. J.; Sels, B. F.; De Vos, D. E., Interfacial Synthesis of Hollow Metal–Organic Framework Capsules Demonstrating Selective Permeability. *Nat Chem* **2011,** *3* (5), 382-387.

60. Reboul, J.; Furukawa, S.; Horike, N.; Tsotsalas, M.; Hirai, K.; Uehara, H.; Kondo, M.; Louvain, N.; Sakata, O.; Kitagawa, S., Mesoscopic Architectures of Porous Coordination Polymers Fabricated by Pseudomorphic Replication. *Nat Mater* **2012,** *11* (8), 717-723.

61. Stassen, I.; Campagnol, N.; Fransaer, J.; Vereecken, P.; De Vos, D.; Ameloot, R., Solvent-free Synthesis of Supported ZIF-8 Films and Patterns through Transformation of Deposited Zinc Oxide Precursors. *CrystEngComm* **2013,** *15* (45), 9308-9311.

62. Moitra, N.; Fukumoto, S.; Reboul, J.; Sumida, K.; Zhu, Y.; Nakanishi, K.; Furukawa, S.; Kitagawa, S.; Kanamori, K., Mechanically Stable, Hierarchically Porous Cu3(Btc)2 (HKUST-1) Monoliths via Direct Conversion of Copper(II) Hydroxide-Based Monoliths. *Chem Commun* **2015,** *51* (17), 3511-3514.

63. Sumida, K.; Hu, M.; Furukawa, S.; Kitagawa, S., Structuralization of Ca^{2+}-Based Metal–Organic Frameworks Prepared via Coordination Replication of Calcium Carbonate. *Inorg Chem* **2016,** *55* (7), 3700-3705.

64. Hirai, K.; Reboul, J.; Morone, N.; Heuser, J. E.; Furukawa, S.; Kitagawa, S., Diffusion-Coupled Molecular Assembly: Structuring of Coordination Polymers Across Multiple Length Scales. *J Am Chem Soc* **2014,** *136* (42), 14966-14973.

65. Tovar, T. M.; Zhao, J.; Nunn, W. T.; Barton, H. F.; Peterson, G. W.; Parsons, G. N.; LeVan, M. D., Diffusion of CO2 in Large Crystals of Cu-BTC MOF. *J Am Chem Soc* **2016,** *138* (36), 11449-11452.

66. Fairen-Jimenez, D.; Moggach, S. A.; Wharmby, M. T.; Wright, P. A.; Parsons, S.; Düren, T., Opening the Gate: Framework Flexibility in ZIF-8 Explored by Experiments and Simulations. *J Am Chem Soc* **2011,** *133* (23), 8900-8902.

67. Springuel-Huet, M.-A.; Nossov, A.; Guenneau, F.; Gédéon, A., Flexibility of ZIF-8 Materials Studied Using 129Xe NMR. *Chem Commun* **2013,** *49* (67), 7403-7405.

68. Zhang, C.; Gee, J. A.; Sholl, D. S.; Lively, R. P., Crystal-Size-Dependent Structural Transitions in Nanoporous Crystals: Adsorption-Induced Transitions in ZIF-8. *J Phys Chem C* **2014,** *118* (35), 20727-20733.

69. Linder-Patton, O. M.; Rogers, B. T.; Sumida, K., Impact of Higher-Order Structuralization on the Adsorptive Properties of Metal–Organic Frameworks. *Chem Asian J* **2018,** *13* (16), 1979-1991.

70. Stassen, I.; Burtch, N.; Talin, A.; Falcaro, P.; Allendorf, M.; Ameloot, R., An Updated Roadmap for the Integration of Metal–Organic Frameworks with Electronic Devices and Chemical Sensors. *Chem Soc Rev* **2017,** *46* (11), 3185-3241.

71. Uehara, H.; Diring, S.; Furukawa, S.; Kalay, Z.; Tsotsalas, M.; Nakahama, M.; Hirai, K.; Kondo, M.; Sakata, O.; Kitagawa, S., Porous Coordination Polymer Hybrid Device with Quartz Oscillator: Effect of Crystal Size on Sorption Kinetics. *J Am Chem Soc* **2011,** *133* (31), 11932-5.

72. Kim, Y. K.; Hyun, S.-m.; Lee, J. H.; Kim, T. K.; Moon, D.; Moon, H. R., Crystal-Size Effects on Carbon Dioxide Capture of a Covalently Alkylamine-Tethered Metal-Organic Framework Constructed by a One-Step Self-Assembly. *Sci Rep* **2016,** *6* (1), 19337.

73. Ren, J.; Langmi, H. W.; North, B. C.; Mathe, M., Review on Processing of Metal–Organic Framework (MOF) Materials Towards System Integration for Hydrogen Storage. *Int J Energy Res* **2015,** *39* (5), 607-620.

74. Hijikata, Y.; Horike, S.; Tanaka, D.; Groll, J.; Mizuno, M.; Kim, J.; Takata, M.; Kitagawa, S., Differences of Crystal Structure and Dynamics Between a Soft Porous Nanocrystal and a Bulk Crystal. *Chem Commun* **2011,** *47* (27), 7632-4.

75. Fairen-Jimenez, D.; Moggach, S. A.; Wharmby, M. T.; Wright, P. A.; Parsons, S.; Duren, T., Opening the Gate: Framework Flexibility in ZIF-8 Explored by Experiments and Simulations. *J Am Chem Soc* **2011,** *133* (23), 8900-2.

76. Sakaida, S.; Otsubo, K.; Sakata, O.; Song, C.; Fujiwara, A.; Takata, M.; Kitagawa, H., Crystalline Coordination Framework Endowed with Dynamic Gate-Opening Behaviour by being Downsized to a Thin Film. *Nat Chem* **2016,** *8* (4), 377-383.

77. Miura, H.; Bon, V.; Senkovska, I.; Ehrling, S.; Watanabe, S.; Ohba, M.; Kaskel, S., Tuning the Gate-Opening Pressure and Particle Size Distribution of the Switchable Metal-Organic Framework DUT-8(Ni) by Controlled Nucleation in a Micromixer. *Dalton Trans* **2017,** *46* (40), 14002-14011.

78. Linder-Patton, O. M.; Bloch, W. M.; Coghlan, C. J.; Sumida, K.; Kitagawa, S.; Furukawa, S.; Doonan, C. J.; Sumby, C. J., Particle Size Effects in the Kinetic Trapping of a Structurally-Locked Form of a Flexible MOF. *CrystEngComm* **2016,** *18* (22), 4172-4179.

79. Sakata, Y.; Furukawa, S.; Kondo, M.; Hirai, K.; Horike, N.; Takashima, Y.; Uehara, H.; Louvain, N.; Meilikho, M.; Tsuruoka, T.; Isoda, S.; Kosaka, W.; Sakata, O.; Kitagawa, S., Shape-Memory Nanopores Induced in Coordination Frameworks by Crystal Downsizing. *Science* **2013,** *339*, 193-196.

80. Krause, S.; Bon, V.; Senkovska, I.; Többens, D. M.; Wallacher, D.; Pillai, R. S.; Maurin, G.; Kaskel, S., The Effect of Crystallite Size on Pressure Amplification in Switchable Porous Solids. *Nat Commun* **2018,** *9* (1), 1573.

81. Duan, D.; Liu, H.; Xu, M.; Chen, M.; Han, Y.; Shi, Y.; Liu, Z., Size-Controlled Synthesis of Drug-Loaded Zeolitic Imidazolate Framework in Aqueous Solution and Size Effect on Their Cancer Theranostics in Vivo. *ACS Appl Mater Inter* **2018,** *10* (49), 42165-42174.

82. Carrillo-Carrión, C., Nanoscale Metal–Organic Frameworks as Key Players in the Context of Drug Delivery: Evolution Toward Theranostic Platforms. *Anal Bioanal Chem* **2020,** *412*, 37-54.

83. Wang, Q.; Astruc, D., State of the Art and Prospects in Metal–Organic Framework (MOF)-Based and MOF-Derived Nanocatalysis. *Chem Rev* **2020,** *120* (2), 1438-1511.

84. Guo, F.; Yang, S.; Liu, Y.; Wang, P.; Huang, J.; Sun, W.-Y., Size Engineering of Metal–Organic Framework MIL-101(Cr)–Ag Hybrids for Photocatalytic CO_2 Reduction. *ACS Catalysis* **2019,** *9* (9), 8464-8470.

85. Moggach, S. A.; Bennett, T. D.; Cheetham, A. K., The Effect of Pressure on ZIF-8: Increasing Pore Size with Pressure and the Formation of a High-Pressure Phase at 1.47 GPa. *Angew Chem Int Ed Engl* **2009,** *48* (38), 7087-9.

86. Tanaka, S.; Fujita, K.; Miyake, Y.; Miyamoto, M.; Hasegawa, Y.; Makino, T.; Van der Perre, S.; Cousin Saint Remi, J.; Van Assche, T.; Baron, G. V.; Denayer, J. F. M., Adsorption

and Diffusion Phenomena in Crystal Size Engineered ZIF-8 MOF. *J Phys Chem C* **2015,** *119* (51), 28430-28439.

87. Biemmi, E.; Scherb, C.; Bein, T., Oriented Growth of the Metal Organic Framework Cu3(BTC)2(H2O)3,xH2O Tunable with Functionalized Self-Assembled Monolayers. *J Am Chem Soc* **2007,** *129* (26), 8054-8055.

88. Avci, C.; Arinez-Soriano, J.; Carne-Sanchez, A.; Guillerm, V.; Carbonell, C.; Imaz, I.; Maspoch, D., Post-Synthetic Anisotropic Wet-Chemical Etching of Colloidal Sodalite ZIF Crystals. *Angew Chem Int Ed Engl* **2015,** *54* (48), 14417-21.

89. Pham, M.-H.; Vuong, G.-T.; Fontaine, F.-G.; Do, T.-O., Rational Synthesis of Metal–Organic Framework Nanocubes and Nanosheets Using Selective Modulators and Their Morphology-Dependent Gas-Sorption Properties. *Cryst Growth Des* **2012,** *12* (6), 3091-3095.

90. Wang, F.; Guo, H.; Chai, Y.; Li, Y.; Liu, C., The Controlled Regulation of Morphology and Size of HKUST-1 by "Coordination Modulation Method". *Micropor Mesopor Mater* **2013,** *173*, 181-188.

91. Umemura, A.; Diring, S.; Furukawa, S.; Uehara, H.; Tsuruoka, T.; Kitagawa, S., Morphology Design of Porous Coordination Polymer Crystals by Coordination Modulation. *J Am Chem Soc* **2011,** *133* (39), 15506-13.

92. Guo, H.; Zhu, Y.; Wang, S.; Su, S.; Zhou, L.; Zhang, H., Combining Coordination Modulation with Acid–Base Adjustment for the Control over Size of Metal–Organic Frameworks. *Chem Mater* **2012,** *24* (3), 444-450.

93. Tsuruoka, T.; Furukawa, S.; Takashima, Y.; Yoshida, K.; Isoda, S.; Kitagawa, S., Nanoporous Nanorods Fabricated by Coordination Modulation and Oriented Attachment Growth. *Angew Chem Int Ed Engl* **2009,** *48* (26), 4739-43.

94. Lee, C. Y.; Bae, Y. S.; Jeong, N. C.; Farha, O. K.; Sarjeant, A. A.; Stern, C. L.; Nickias, P.; Snurr, R. Q.; Hupp, J. T.; Nguyen, S. T., Kinetic Separation of Propene and Propane in Metal-Organic Frameworks: Controlling Diffusion Rates in Plate-Shaped Crystals via Tuning of Pore Apertures and Crystallite Aspect Ratios. *J Am Chem Soc* **2011,** *133* (14), 5228-31.

95. Liu, Y. L.; Zhao, X. J.; Yang, X. X.; Li, Y. F., A Nanosized Metal–Organic Framework of Fe-MIL-88NH2 as a Novel Peroxidase Mimic used for Colorimetric Detection of Glucose. *Analyst* **2013,** *138* (16), 4526-4531.

96. Zhang, J.-W.; Zhang, H.-T.; Du, Z.-Y.; Wang, X.; Yu, S.-H.; Jiang, H.-L., Water-Stable Metal–Organic Frameworks with Intrinsic Peroxidase-Like Catalytic Activity as a Colorimetric Biosensing Platform. *Chem Commun* **2014,** *50* (9), 1092-1094.

97. Liu, S.; Lu, F.; Xing, R.; Zhu, J.-J., Structural Effects of Fe_3O_4 Nanocrystals on Peroxidase-Like Activity. *Chem Eur J* **2011,** *17* (2), 620-625.

98. Liu, Y.; Gao, P.; Huang, C.; Li, Y., Shape- and Size-Dependent Catalysis Activities of Iron-Terephthalic Acid Metal-Organic Frameworks. *Sci China Chem* **2015,** *58* (10), 1553-1560.

99. McGuire, C. V.; Forgan, R. S., The Surface Chemistry of Metal–Organic Frameworks. *Chem Commun* **2015,** *51* (25), 5199-5217.

100. Liu, X.; Li, Y.; Ban, Y.; Peng, Y.; Jin, H.; Bux, H.; Xu, L.; Caro, J.; Yang, W., Improvement of Hydrothermal Stability of Zeolitic Imidazolate Frameworks. *Chem Commun* **2013,** *49* (80), 9140-9142.

101. Karagiaridi, O.; Bury, W.; Mondloch, J. E.; Hupp, J. T.; Farha, O. K., Solvent-Assisted Linker Exchange: an Alternative to the de novo Synthesis of Unattainable Metal-Organic Frameworks. *Angew Chem Int Ed Engl* **2014,** *53* (18), 4530-40.

102. Fei, H.; Cohen, S. M., A Robust, Catalytic Metal-Organic Framework with Open 2,2'-Bipyridine Sites. *Chem Commun* **2014,** *50* (37), 4810-2.

103. Boissonnault, J. A.; Wong-Foy, A. G.; Matzger, A. J., Core-Shell Structures Arise Naturally During Ligand Exchange in Metal-Organic Frameworks. *J Am Chem Soc* **2017,** *139* (42), 14841-14844.

104. Liu, C.; Zeng, C.; Luo, T.-Y.; Merg, A. D.; Jin, R.; Rosi, N. L., Establishing Porosity Gradients within Metal–Organic Frameworks Using Partial Postsynthetic Ligand Exchange. *J Am Chem Soc* **2016,** *138* (37), 12045-12048.

105. Koh, K.; Wong-Foy, A. G.; Matzger, A. J., MOF@MOF: Microporous Core–Shell Architectures. *Chem Commun* **2009,** (41), 6162-6164.

106. Hirai, K.; Furukawa, S.; Kondo, M.; Uehara, H.; Sakata, O.; Kitagawa, S., Sequential Functionalization of Porous Coordination Polymer Crystals. *Angew Chem Int Ed* **2011,** *50* (35), 8057-8061.

107. Fujita, M.; Kwon, Y. J.; Washizu, S.; Ogura, K., Preparation, Clathration Ability, and Catalysis of a Two-Dimensional Square Network Material Composed of Cadmium(II) and 4,4'-Bipyridine. *J Am Chem Soc* **1994,** *116* (3), 1151-1152.

108. Li, D.; Xu, H.-Q.; Jiao, L.; Jiang, H.-L., Metal-Organic Frameworks for Catalysis: State of the Art, Challenges, and Opportunities. *EnergyChem* **2019,** *1* (1), 100005.

109. Yang, Q.; Xu, Q.; Jiang, H.-L., Metal–organic Frameworks Meet Metal Nanoparticles: Synergistic Effect for Enhanced Catalysis. *Chem Soc Rev* **2017,** *46* (15), 4774-4808.

110. Wu, C.-D.; Zhao, M., Incorporation of Molecular Catalysts in Metal–Organic Frameworks for Highly Efficient Heterogeneous Catalysis. *Adv Mater* **2017,** *29* (14), 1605446.

111. Drout, R. J.; Robison, L.; Farha, O. K., Catalytic Applications of Enzymes Encapsulated in metal–Organic Frameworks. *Coord Chem Rev* **2019,** *381*, 151-160.

112. Sun, D.; Fu, Y.; Liu, W.; Ye, L.; Wang, D.; Yang, L.; Fu, X.; Li, Z., Studies on Photocatalytic CO_2 Reduction over NH_2-UiO-66(Zr) and Its Derivatives: Towards a Better Understanding of Photocatalysis on Metal–Organic Frameworks. *Chem Euro J* **2013,** *19* (42), 14279-14285.

113. Ji, P.; Sawano, T.; Lin, Z.; Urban, A.; Boures, D.; Lin, W., Cerium-Hydride Secondary Building Units in a Porous Metal–Organic Framework for Catalytic Hydroboration and Hydrophosphination. *J Am Chem Soc* **2016,** *138* (45), 14860-14863.

114. Li, Z.; Schweitzer, N. M.; League, A. B.; Bernales, V.; Peters, A. W.; Getsoian, A. B.; Wang, T. C.; Miller, J. T.; Vjunov, A.; Fulton, J. L.; Lercher, J. A.; Cramer, C. J.; Gagliardi, L.; Hupp, J. T.; Farha, O. K., Sintering-Resistant Single-Site Nickel Catalyst Supported by Metal–Organic Framework. *J Am Chem Soc* **2016,** *138* (6), 1977-1982.

115. Chizallet, C.; Lazare, S.; Bazer-Bachi, D.; Bonnier, F.; Lecocq, V.; Soyer, E.; Quoineaud, A.-A.; Bats, N., Catalysis of Transesterification by a Nonfunctionalized Metal−Organic Framework: Acido-Basicity at the External Surface of ZIF-8 Probed by FTIR and ab Initio Calculations. *J Am Chem Soc* **2010,** *132* (35), 12365-12377.

116. Canivet, J.; Aguado, S.; Schuurman, Y.; Farrusseng, D., MOF-Supported Selective Ethylene Dimerization Single-Site Catalysts through One-Pot Postsynthetic Modification. *J Am Chem Soc* **2013,** *135* (11), 4195-8.

117. Horcajada, P.; Surblé, S.; Serre, C.; Hong, D.-Y.; Seo, Y.-K.; Chang, J.-S.; Grenèche, J.-M.; Margiolaki, I.; Férey, G., Synthesis and Catalytic Properties of MIL-100(Fe), an Iron(Iii) Carboxylate with Large Pores. *Chem Commun* **2007,** (27), 2820-2822.

118. Madrahimov, S. T.; Gallagher, J. R.; Zhang, G.; Meinhart, Z.; Garibay, S. J.; Delferro, M.; Miller, J. T.; Farha, O. K.; Hupp, J. T.; Nguyen, S. T., Gas-Phase Dimerization of Ethylene under Mild Conditions Catalyzed by MOF Materials Containing (bpy)NiIIComplexes. *ACS Catal* **2015,** *5* (11), 6713-6718.

119. Burgun, A.; Coghlan, C. J.; Huang, D. M.; Chen, W.; Horike, S.; Kitagawa, S.; Alvino, J. F.; Metha, G. F.; Sumby, C. J.; Doonan, C. J., Mapping-Out Catalytic Processes in a Metal–Organic Framework with Single-Crystal X-ray Crystallography. *Angew Chem* **2017,** *129* (29), 8532-8536.

120. Linder-Patton, O. M.; de Prinse, T. J.; Furukawa, S.; Bell, S. G.; Sumida, K.; Doonan, C. J.; Sumby, C. J., Influence of Nanoscale Structuralisation on the Catalytic Performance of ZIF-8: a Cautionary Surface Catalysis Study. *CrystEngComm* **2018,** *20* (34), 4926-4934.

Chapter 2.

Influence of Nanoscale Structuralisation on Surface Catalysis with ZIF-8

This work appears in the following publication:

Linder-Patton, O. M.; de Prinse, T. J.; Furukawa, S.; Bell, S. G.; Sumida, K.; Doonan, C. J.; Sumby, C. J., Influence of Nanoscale Structuralisation on the Catalytic Performance of ZIF-8: a Cautionary Surface Catalysis Study. *CrystEngComm* **2018,** *20* (34), 4926-4934.

Statement of Authorship

Title of Paper	Influence of nanoscale structuralisation on the catalytic performance of ZIF-8: a cautionary surface catalysis study.
Publication Status	☑ Published ☐ Accepted for Publication ☐ Submitted for Publication ☐ Unpublished and Unsubmitted work written in manuscript style
Publication Details	**Linder-Patton, O. M.**; de Prinse, T. J.; Furukawa, S.; Bell, S. G.; Sumida, K.; Doonan, C. J.; Sumby, C. J., Influence of nanoscale structuralisation on the catalytic performance of ZIF-8: a cautionary surface catalysis study. *CrystEngComm* **2018,** *20* (34), 4926-4934.

Principal Author

Name of Principal Author (Candidate)	Oliver Linder-Patton		
Contribution to the Paper	Experimental work, analysing results/interpretation, manuscript conception, manuscript writing and editing.		
Overall percentage (%)	85%		
Certification:	This paper reports on original research I conducted during the period of my Higher Degree by Research candidature and is not subject to any obligations or contractual agreements with a third party that would constrain its inclusion in this thesis. I am the primary author of this paper.		
Signature		Date	24/02/2020

Co-Author Contributions

By signing the Statement of Authorship, each author certifies that:

i. the candidate's stated contribution to the publication is accurate (as detailed above);
ii. permission is granted for the candidate in include the publication in the thesis; and
iii. the sum of all co-author contributions is equal to 100% less the candidate's stated contribution.

Name of Co-Author	Thomas de Prinse		
Contribution to the Paper	Initial experimental screening		
Signature		Date	27/02/2020

Name of Co-Author	Shuhei Furukawa		
Contribution to the Paper	Manuscript conception and drafting.		
Signature		Date	27/02/2020

Name of Co-Author	Stephen Bell
Contribution to the Paper	Aided in experimental method development, interpretation of results and manuscript drafting.
Signature	Date 25/2/20

Name of Co-Author	Kenji Sumida
Contribution to the Paper	Aided in manuscript drafting. Signing on behalf of Kenji Sumida
Signature	Date 28/2/20

Name of Co-Author	Christian Doonan
Contribution to the Paper	Assisted in manuscript conception, experimental design, and manuscript drafting.
Signature	Date 25/2/20

Name of Co-Author	Christopher Sumby
Contribution to the Paper	Assisted in manuscript conception, experimental design, interpretation of results and manuscript drafting and acted as corresponding author.
Signature	Date 25/2/20

Chapter 2. Influence of Nanoscale Structuralisation on Surface Catalysis with ZIF-8

2.1. Abstract

Although metal-organic frameworks (MOFs) have been shown to catalyse a wide range of reactions, understanding the influence of nanoscale structuralisation (*e.g.* crystal size and morphology) on their performance is a difficult challenge. Here, we have prepared Zn(2-mIM)$_2$ (ZIF-8; 2-mIM$^-$ = 2-methylimidazolate) crystals of varied size and morphology, and studied the catalytic properties of these samples in the context of the transesterification of vinyl acetate with hexanol. ZIF-8 has previously been shown to catalyse reactions at Lewis acidic sites at the crystal surface and at defect sites. The substrates were selected as they are significantly larger than the pore apertures, allowing the reaction to be confined to the surface of the crystals and providing the best opportunity to understand the influence of the structuralisation on the observed properties. In this case, the rate of hexyl acetate production increased as the crystal size was reduced; however, the effect of crystal morphology on the rate of reaction was not appreciable due to the instability of ZIF-8 under catalytic conditions. It was clearly observed that the surface of ZIF-8 was unstable in catalytic conditions featuring hydrophobic reagents with polar functional groups, with scanning electron microscopy (SEM) revealing indiscriminate etching of all crystal surfaces. Atomic adsorption spectrometry (AAS) analyses confirmed the etching led to significant leaching of Zn^{2+}, which was observed to contribute considerably to the catalytic activity of ZIF-8. Our results highlight the need for fundamental characterisation of MOF catalysts to enable their deployment under a wider variety of catalytic conditions.

2.2. Introduction

The catalytic properties of metal-organic frameworks (MOFs) have attracted increased attention in recent years.[1-3] The modular synthesis of MOFs, from a combination of organic linkers and metal nodes,[4] imbues these materials with features that are highly desired for catalysis including; large surface areas, high substrate adsorption capacity and chemical tunability with respect to their internal pore environment.[4-5] As such, MOFs can act as heterogeneous catalysts *via* an intrinsic activity stemming directly from the metal nodes/organic ligands, or by supporting catalytic moieties that resemble their homogeneous counterparts.[5-10] MOFs have been shown to catalyse a broad range of reactions. Both the Knoevenagel condensation[11] and Suzuki coupling reactions have been catalysed by MOFs for fine chemical synthesis,[12-13] while industrially relevant reactions such as esterification,[14] transesterification,[7] and ethylene oligomerization reactions have also been explored.[15-16]

Crystal size and morphology have been shown to impact the physical properties of MOFs.[17] Crystal size can affect the framework flexibility,[18-20] and even the rate at which a "structurally-locked" framework recovers its flexibility.[21] Meanwhile, modulators used to control crystal morphology, and which remain bound to crystal surfaces, can alter guest adsorption throughout the pores and at the crystal surface.[22-23] In the context of heterogeneous catalysis, control over the crystal size is expected to be crucial for optimising the diffusion path lengths for both reactant and product molecules and for varying ratio between external and internal surface areas.[24] Additionally, tuning the crystal morphology can alter the ratios between exposed crystal facets, which could potentially enhance catalytic performance by increasing the density of active sites at the surface of the MOF.[25] Despite its potential to greatly enhance the catalytic performance of MOFs, the effect of nanoscale structuralisation of this type is not well-understood. Therefore, studies that probe the effects of such modifications on the catalytic properties of MOFs are urgently needed.

The characterisation of MOFs as catalysts is complicated by the fact that the chemical environment available on the crystal surface and within the inner pores is often distinct. As a first step in analysing the influence of crystal size and morphology a system where the catalytic reaction is restricted to the surface is desirable. For example, the $Zn(2\text{-mIM})_2$ framework (ZIF-8; 2- mIM^- = 2-methylimidazolate), which comprises tetrahedral Zn^{2+} nodes bridged by 2-mIM^- linkers to form a sodalite-like structure, has been shown to catalyse a variety of reactions at Lewis acidic sites on its crystal surface, including the transesterification of triglycerides and Knoevenagel condensation reactions.[7, 11, 26-29] Since the crystallographically measured pore aperture of ZIF-8 is 3.4 Å, in order to probe surface catalysis, a catalytic reaction involving molecules with dimensions significantly larger than this value were used.[30] Further, the well-established synthetic protocols for ZIF-8 allow a variety of crystal sizes and morphologies to be obtained while maintaining a high level of crystallinity.[18-19, 31]

Herein, we report an investigation into ZIF-8 surface catalysis in the context of model a transesterification reaction, as a function of both crystal size and morphology. Building on established protocols, ZIF-8 was synthesised with a precise control over the crystal size and morphology. Six crystal sizes of ZIF-8 ranging from 50 nm to 100 μm were synthesised. The effect of the crystal morphology was examined specifically at the 500 nm (rhombic dodecahedra and cubic) and 100 μm size regimes (rhombic dodecahedra and truncated rhombic dodecahedron). The catalytic performance of each of the ZIF-8 samples was examined for the transesterification of hexanol and vinyl acetate using two representative experimental protocols

(stirred and agitated using a plate shaker/incubator). Interestingly, an increase in the rate of hexyl acetate production was observed with a reduction in crystal size, but the magnitude of the rate increase was smaller than expected based on the difference in external surface areas. This prompted closer examination of the ZIF-8 crystals before and after catalysis, which revealed indiscriminate etching of all of surfaces of the crystal. Furthermore, atomic absorption spectroscopy (AAS) confirmed Zn^{2+} leaching, with smaller crystal sizes being more susceptible to Zn^{2+} release than larger crystals. The amount of Zn^{2+} leached correlated to the catalytic activity of each ZIF-8 particle size regime, with a significant proportion of the catalytic activity being attributed to Zn^{2+} in solution rather than at the surface of ZIF-8 (Figure **1.1**). Surface etching and Zn^{2+} leaching was also observed for ZIF-8 under conditions in which the Knoevenagel condensation reaction can be catalysed by ZIF-8. In all, these observations indicate that while MOF crystal size and morphology can have considerable influence on the catalyst performance, the characterisation of the activity can be complicated by issues pertaining to stability, transition metal leaching and mechanical degradation. As such, this current study highlights that significant care is required in the characterisation of MOFs as heterogeneous catalysts.

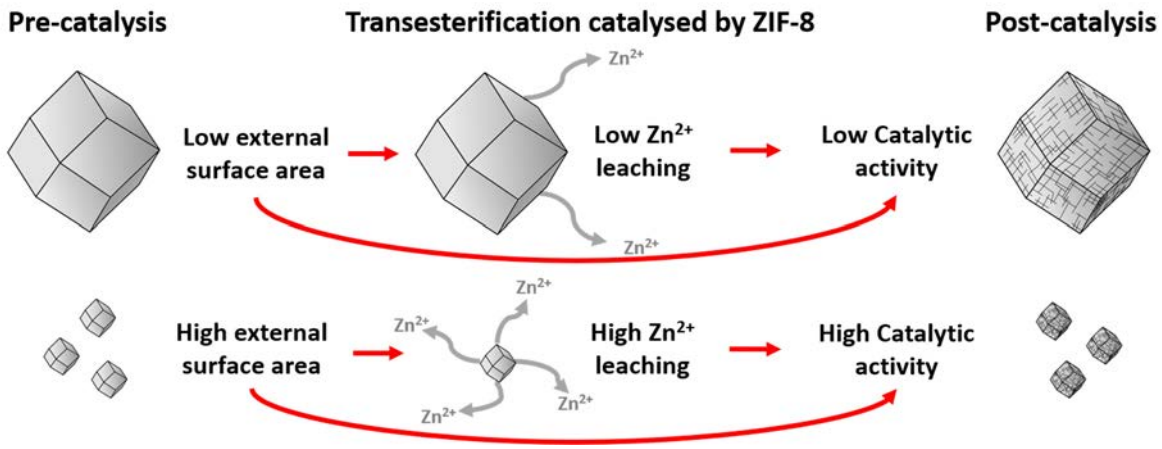

Figure **1.1**: Schematic showing the relationship between particle size and catalytic activity of ZIF-8, with larger crystals having a low external surface area, with fewer active/defect sites for leaching/catalysis to occur, which results in minimal Zn^{2+} leaching and low catalytic activity. Smaller crystals have a correspondingly higher external surface area, with more active/defect sites for leaching/catalysis to occur resulting in higher Zn^{2+} leaching and higher catalytic activity.

2.3. Experimental

2.3.1. General Considerations

All materials were purchased commercially unless otherwise stated. The procedures for synthesis of different crystal sizes and crystal morphologies of ZIF-8 were adapted from literature methods with appropriate modifications, see Table **2.1** and Appendix **2.9.1**.[18,32-33] Scanning electron microscopy (SEM) images were collected on a Philips XL30 scanning electron microscope at Adelaide Microscopy. Samples were dry-loaded onto adhesive carbon tabs on aluminium stubs and coated with a 5 nm carbon coating. N_2 (UHP grade, 99.999%) adsorption isotherm measurements were performed on a 3Flex physisorption analyser. The temperature was maintained at 77 K via a Helium cryostat. Powder X-ray diffraction data was collected on a Bruker D8 Advance X-ray powder diffractometer (parallel X-ray, capillary loaded) using a Cu Kα (λ =1.5418 Å) radiation source. Samples were mounted in 0.5 mm glass capillaries and data collected for between 2θ of 2° to 52.94° with Phi rotation at 20 rotations/min (1 second exposure per step, 5001 steps). The data were then converted into xye format and background subtracted using WinPlotr 2000 software.[34] Simulated powder X-ray diffraction patterns were generated from the single crystal X-ray data using Mercury 3.9.[35-36] Atomic adsorption spectroscopy (AAS) measurements were conducted on SpectrAA 250 Phase using a Zinc lamp (λ = 213.9 nm, slit width 1.0 nm and lamp current 5 mA) with air/acetylene flame fuel source. Gas chromatography mass spectrometry (GC-MS) analyses were carried out on a Shimadzu GC-2010 coupled to a GCMS-QP2010S detector equipped with a DB-5 MS fused silica column (30 m x 0.25 mm, 0.25 μm) using helium as the carrier gas. The oven temperature was held at 50 °C for 2 minutes, then increased at 4 °C min^{-1} to 100 °C and held for 2 minutes, then raised at 30 °C min^{-1} to 220 °C and maintained for 1 minute. The injector and interface temperature were 250 °C and 280 °C respectively.

2.3.2. Catalysis Testing: Transesterification (Stirred)

The transesterification reaction between hexanol and vinyl acetate, using various crystal sizes and morphologies of ZIF-8 as a catalyst, was carried out in a magnetically stirred round-bottom flask under a N_2 atmosphere. Dried ZIF-8 (20.0 mg, 0.088 mmol, 0.25 wt % relative to vinyl acetate) was dispersed in hexanol (20.0 mL) and heated at 65 °C for 1 h. Vinyl acetate (3.3 mL, 35.79 mmol) was added to the reaction mixture, which was then heated at 65 °C for 6 h. The reaction was monitored by withdrawing 50 μl aliquots from the reaction mixture at different time intervals, these aliquots were centrifuged at 10,000 rpm for 1 minute to separate the ZIF-8 catalyst. An aliquot of the supernatant (15 μL) was transferred to a 2 mL

GC-MS vial, the internal standard propyl propionate (16.3 µL, 760 mM in ethyl acetate) was added and the solution was subsequently diluted to 1.5 mL with ethyl acetate. The solution was then analysed via GC-MS. Catalytic controls including; blank (hexanol + vinyl acetate), 2-mIM, zinc nitrate and mixed controls (2-mIM and zinc nitrate) were conducted (see Appendix **2.9.2**).

2.3.3. Catalysis Testing: Transesterification (Agitated)

A modified procedure for the transesterification reaction was conducted in 50 mL sealed conical flasks in a plate shaker/incubator. Dried ZIF-8 (10.0 mg, 0.044 mmol, 0.25 wt % relative to vinyl acetate) was dispersed in hexanol (10.0 mL) and heated at 60 °C for 1 h, agitated at 165 rpm. Vinyl acetate (1.65 mL, 17.89 mmol) was added to the reaction mixture, which was then heated at 60 °C for 6 h. The reaction was monitored via GC-MS in the same manner as described for the stirred reaction above. After the 6 h reaction a 1.5 mL aliquot of the reaction mixture was collected, centrifuged at 10,000 rpm for 1 min. Catalytic controls as detailed above were conducted (see Appendix **2.9.2**).

2.3.4. Catalysis Testing: Knoevenagel Condensation (Agitated)

Knoevenagel condensation reactions between benzaldehyde and malononitrile using ZIF-8 as the catalyst were carried out in sealed 50 mL conical flasks in a plate shaker/incubator.[11] Dried 100 µm ZIF-8 (20.0 mg, 0.088 mmol, 2.5 wt %), benzaldehyde (0.4 mL, 3.8 mmol) were dispersed in a 50 mL conical flask containing toluene (5 mL). A solution of malononitrile (0.5 g, 7.6 mmol) in toluene (5 mL) was then added and the resultant mixture was agitated at room temperature for 6 h at 165 rpm. The ZIF-8 sample was recovered by washing the crystals with toluene and methanol, and the sample was dried under vacuum before SEM analysis. Additionally, controls with neat toluene, benzaldehyde and malononitrile were conducted with **ZIF-8 100 µm** for etching analysis.

2.3.4. Sample Preparation for AAS

Aliquots of the transesterification reaction mixture (0.4 mL) from each stirred reaction were diluted to 20 mL with HNO_3 (3%) and left overnight to extract the zinc into the aqueous layer. The diluted sample was analysed via AAS. Aliquots of the Knoevenagel condensation reaction mixture (0.2 mL) from each stirred reaction were diluted to 20 mL with HNO_3 (3%) and left overnight to extract the zinc into the aqueous layer. The diluted sample was analysed via AAS.

2.4. Results and Discussion

The catalytic activity of ZIF-8 arises from Lewis acidic sites on the surface of the crystal and at defect sites.[7] This was recently confirmed via super-resolution fluorescence microscopy, which showed that the acid-base hydrolysis of fluorescein diacetate occurred only on the outer surface of ZIF-8 crystals or at defect sites on the surface.[37] Lewis acidic sites on the surface of ZIF-8 are localised on crystal facets that contain metal-ligand linkages at the immediate surface, and their concentration is significantly influenced by the crystal morphology. In this context, the facets representing the [100] and [211] planes are expected to enhance the catalytic reaction via a higher concentration of Lewis acidic sites (Figure **2.2**).[33] The crystal size can also be manipulated for ZIF-8, allowing the ratio of Lewis acid sites to total crystal surface area to be fine-tuned. For example, a greater proportion of Lewis acid sites can be exposed in smaller crystals of ZIF-8, which should result in a dramatic acceleration in the reaction rate.[18-19, 31] However, while ZIF-8 is broadly considered to be a chemically stable framework (its hydrophobicity conferring reasonable water stability),[26, 30] changes in the crystal size are likely to impact its chemical stability, particularly under catalytic conditions (see below).

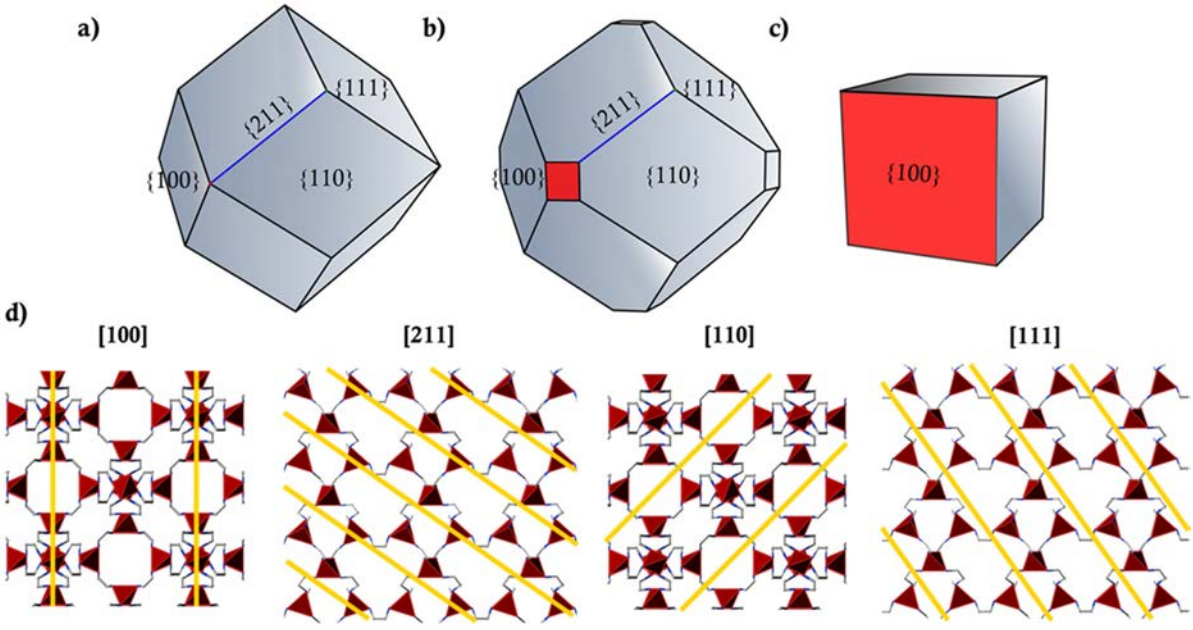

Figure **2.2**: Different morphologies of ZIF-8; a) rhombic dodecahedra, b) truncated rhombic dodecahedra, c) cubic and d) the Miller planes associated with the crystals of ZIF-8. The [100] and [211] planes contain highest density of Zn-2-mIM linkages, indicating that at surfaces corresponding to these Miller planes there will be a high density of Zn(II) centres. The tetrahedral zinc nodes are highlighted in red and the Miller planes are displayed as yellow lines intersecting the crystal lattice.

2.4.1. Controlling Crystal Size and Morphology in Preparation for ZIF-8 Surface Catalysis

A systematic investigation of the effect of crystal size and crystal morphology on catalytic activity required the development of robust synthetic protocols for ZIF-8 with control over both attributes. Accordingly, we synthesized ZIF-8 over six discrete crystal sizes ranging from 50 nm to 100 µm with rhombic dodecahedral morphology and at two additional morphologies at 500 nm and 100 µm sizes, as shown in Figure **2.3** and summarised in Table **2.1**. Crystal size control was achieved through controlled nucleation by varying the Zn^{2+}:2-mIM^{-} molar ratio, the concentration of the modulator,[18, 31] the counterion in the Zn^{2+} source,[32] the reaction solvent, and the temperature.[31] The crystal size distributions of the ZIF-8 samples were determined via scanning electron microscopy (SEM) (Figure **2.3** and Figure **2.A.1**). Note that the synthetic yields for each of the protocols differ significantly, which conceivably is a parameter requiring optimisation prior to scale-up to industrially relevant quantities (grams to kilograms). For instance, the highest yielding synthesis (**ZIF-8 50 nm**, 76%) was achieved under basic conditions (without modulator) and the lowest yielding protocol (**ZIF-8 10 µm**, 6%) utilised sodium formate as a modulator. The crystallinity and phase purity of the samples was confirmed via PXRD (Figure **2.A.2**).

2.4.2. Transesterification Catalysis

Transesterification is a reversible reaction that can be catalysed under both acidic and basic conditions.[38-39] In order to push the equilibrium in favour of the product an excess of the alcohol is typically used in the presence of a catalyst.[38] For the purposes of this study, the transesterification of vinyl acetate was selected because it is effectively a terminating transesterification reaction (Schematic **2.1**). The by-product of the reaction, vinyl alcohol (4), rapidly undergoes tautomerisation to acetaldehyde (5), which reacts with the excess alcohol to form a hemiacetal (6), (see Scheme **2.1** and Appendix **2.9.3**). The effect of crystal size and morphology of ZIF-8 on the surface catalysis of transesterification reactions was analysed by following the reaction between vinyl acetate and hexanol (Scheme **2.1**). Initial testing was conducted at 65 °C with the solution agitated via stirring for 6 h (Figure **2.4a**), and the reaction progress was monitored via GC-MS (Figures **2.A.5** and **2.A.6**).

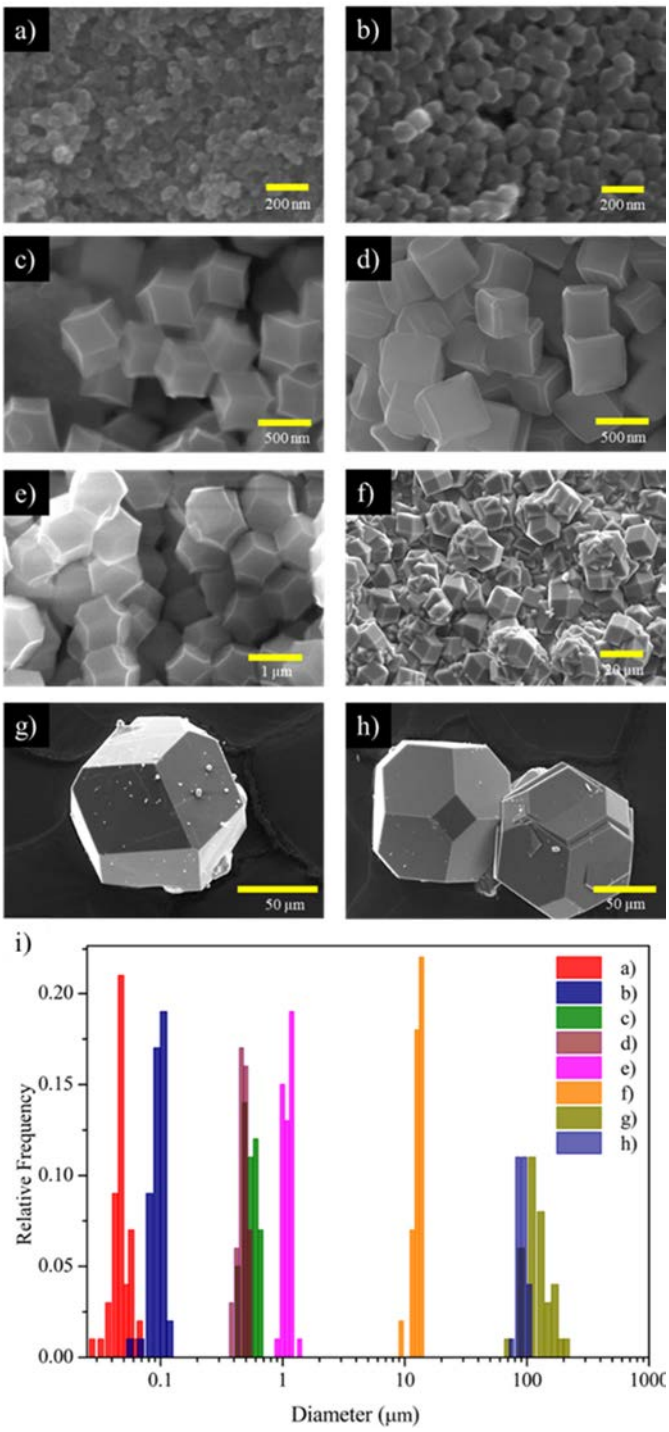

Figure **2.3**: SEM images showing the crystal size and morphology control achieved for ZIF-8 with the corresponding crystal size distributions, all rhombic dodecahedra unless otherwise specified, a) **ZIF-8 50 nm**, b) **ZIF-8 100 nm**, c) **ZIF-8 500 nm**, d) **ZIF-8 500 nm cubic**, e) **ZIF-8 1 µm**, f) **ZIF-8 10 µm**, g) **ZIF-8 100 µm,** h) **ZIF-8 100 µm truncated rhombic dodecahedra** and i) crystal size distributions.

Table **2.1**: Detailed synthetic parameters (Zn source, solvent, 2-methylimidazole:Zn ratio, modulator concentration, and temperature), including yields, and morphological characteristics and crystal diameters for all ZIF-8 size regimes.

ZIF-8 sample	Zn source	Solvent (mL)	2-mIM/Zn	Additive/2-mIM (conc.)	Temp. (°C)	Yield (%)	Crystal diameter (µm)[a]	Crystal Morphology	Figure 2.3 entry
50 nm	$Zn(NO_3)_2$	MeOH (8 mL)	4	0.745 (0.073 M, NaOH)	25	76	0.049 ± 0.001	Rhombic Dodecahedra[d]	a
100 nm	$Zn(NO_3)_2$	MeOH (8 mL)	4	-	25	23	0.093 ± 0.002	Rhombic Dodecahedra	b
500 nm	$ZnBr_2$	MeOH (8 mL)	8	-	25	9	0.544 ± 0.009	Rhombic Dodecahedra	c
500 nm cubic	$Zn(NO_3)_2$	H_2O (10 mL)	56	0.0001 (0.098 mM, CTAB[b])	50	73	0.476 ± 0.006	Cubic[e]	d
1 µm	$Zn(NO_3)_2$	MeOH (8 mL)	4	1.000 (0.098 M, 1-mIM[c])	25	7	1.057 ± 0.013	Rhombic Dodecahedra	e
10 µm	$Zn(NO_3)_2$	MeOH (8 mL)	2	1.000 (0.148 M, HCOONa)	50	10	12.633 ± 0.142	Rhombic Dodecahedra	f
100 µm	$Zn(NO_3)_2$	DMF (8 mL)	0.9	-	140	50	129.945 ± 5.205	Rhombic Dodecahedra	g
100 µm trd	$Zn(NO_3)_2$	MeOH (8 mL)	2	1.122 (0.332 M, HCOONa)	100	6	89.601 ± 1.194	Truncated Rhombic Dodecahedra[f]	h

[a.] Average crystal size determined from SEM observations. [b.] Cetyltrimethylammonium bromide. [c.] 1-Methylimidazole. [d.] Rhombic dodecahedra: 12 faces. [e.] Cubic: 6 faces. [f.] Truncated rhombic dodecahedra (trd): 18 faces.

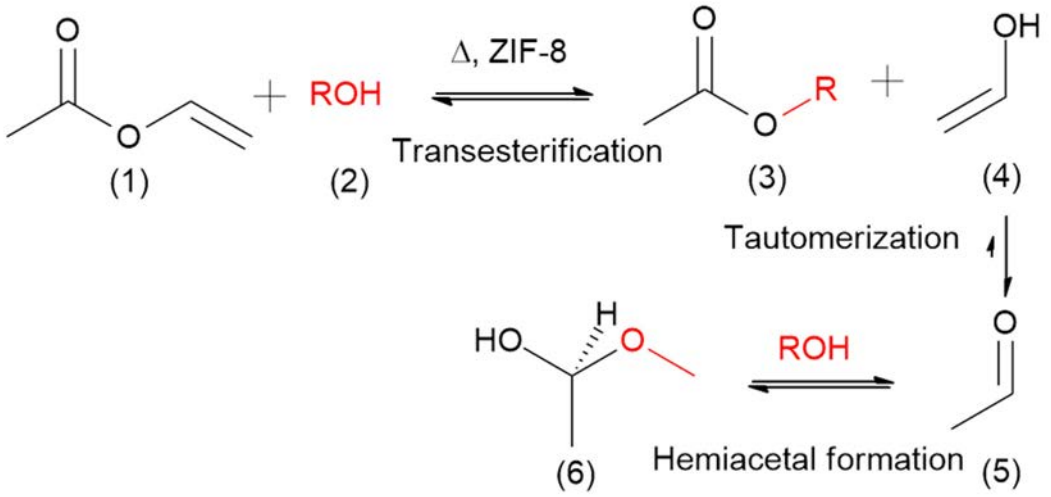

Schematic **2.1**: Transesterification of vinyl acetate (1) with an alcohol (2), catalysed by ZIF-8, forming an ester (3) and vinyl alcohol (4), the latter of which rapidly tautomerises to acetaldehyde (5) and goes on to react with excess alcohol forming a hemiacetal (6).

Firstly, it was observed that there is an inverse relationship between crystal size and hexyl acetate production, with **ZIF-8 50 nm** and **ZIF-8 100 µm** generating 154 and 82 mM respectively after 6 h. Under these deliberately chosen, mild catalytic conditions modest conversion (10%) is achieved for the best catalyst (**ZIF-8 50 nm**). In comparison, other studies have achieved almost 100% conversion by utilising higher temperatures, up to 200 °C, and shorter length primary alcohols, such as methanol and ethanol.[7] Secondly, it was found that crystal morphology had no noticeable impact on catalytic activity, with hexyl acetate production for both morphologies of **ZIF-8 500 nm** and **ZIF-8 100 µm** displaying almost identical production, see Appendix Figure **2.A.7**. Given that this reaction occurs at Lewis acidic sites on the surface of ZIF-8 (Figure **2.2**),[33] a much more dramatic difference in catalytic activity would be expected based on both crystal size and morphology. In fact, there is an inverse power law relationship between crystal size and catalytically active external surface area for ZIF-8; assuming a uniform rhombic dodecahedral morphology (see Appendix **2.9.4** Figure **2.A.8** and Table **2.A.2**). For example, considering two size regimes of ZIF-8, namely 100 µm and 50 nm, we estimate a 4-million-fold increase in catalytically active external surface area; however, only observe a 2-fold increase in hexyl acetate (mM) produced after a 6 h reaction.

To understand the difference between the predicted and actual catalytic performance, SEM was used to analyse ZIF-8 samples post-catalysis. SEM of **ZIF 100 µm** post catalysis

revealed that there was mechanical degradation of the crystals resulting from the method of agitation (stirring) (Figure **2.4a**, Appendix **2.9.5** Figure **2.A.9**), despite crystallinity being retained (Figure **2.A.10**). The observed fragmentation of ZIF-8 crystals likely increased the amount of catalytically active surface external area available, which corresponded with larger than expected hexyl acetate production for the larger crystal sizes. Additionally, no meaningful contrast between the different morphologies of ZIF-8 could be made because of the crystal degradation under the stirred experimental setup.

To avoid mechanical fragmentation of ZIF-8 crystals, an alternate experimental setup was utilised, with reaction mixture agitated by a plate shaker/incubator (heating at 60 °C, agitated at 165 rpm). Under the modified protocol there was a moderate decrease in catalytic activity across all crystal sizes, attributed to the lower reaction temperature, but the inverse relationship between crystal size and hexyl acetate production was still observed (Figure **2.4b**). As expected, there was a noticeable increase in hexyl acetate production for smaller crystal sizes relative to the **ZIF-8 10 µm** and **ZIF-8 100 µm** samples. This outcome indicated that the impact of mechanical degradation of the crystals on the rate of reaction during the catalysis experiments had been minimised. Again, there was no significant difference in hexyl acetate production for the two distinct morphologies of **ZIF-8 500 nm** and **ZIF 100 µm** (see Appendix **2.9.5** Figure **2.A.11**). SEM analysis of **ZIF 100 µm** post-catalysis (agitated) confirmed that no crystal fragmentation had occurred, but instead revealed prominent indiscriminate etching of all facets of the crystal (Figures **2.4g** and **2.A.12**). Interestingly, partial etching also occurred in the presence of hexanol at 60 °C, although under catalytic conditions the etching was more severe (Figure **2.4g** and **2.A.12**). Exposing defects on the surface of ZIF-8 crystals increases the number of Lewis acidic sites available for surface catalysis,[37] again accounting for the higher than expected activity of **ZIF-8 10 µm** and **ZIF-8 100 µm**. 77 K N_2 adsorption isotherms were performed on activated samples of as-synthesised, hexanol treated, and post-catalysis **ZIF-8 100 µm**, to assess their permanent porosity, (Figure **2.A.13** and Table **2.A.3**) and possible etching-induced macroporosity. Pore size analysis at 77 K with N_2 revealed that there was no notable change in microporosity between the **ZIF-8 100 µm** samples, nor were macropores identified, indicating that the etching only occurred at the surface of the crystal and no large channels had formed throughout the crystal (Figure **2.A.14**). The pattern of the crystal surface etching may result from nanometre scale defects on the surface of the crystals, which has been previously observed via *in situ* atomic force microscopy whilst analysing the growth processes of ZIF-8.[40]

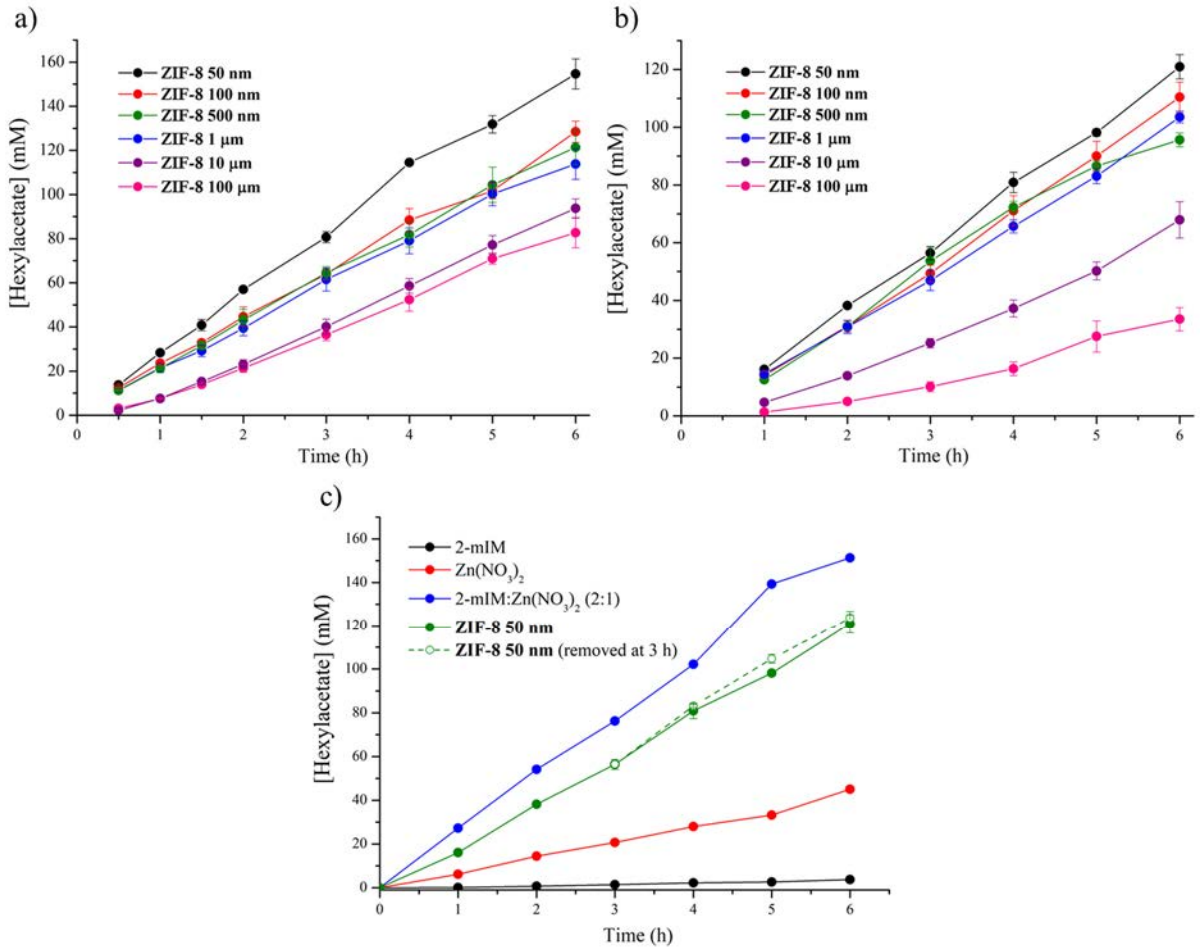

Figure **2.4 (a-c)**: Hexyl acetate production (mM) over a 6 h transesterification reaction between hexanol and vinyl acetate, analysed via GC-MS, catalysed by different crystal sizes of **ZIF-8**; a) reactions heated at 65 °C with stirring agitation, b) reactions heated at 60 °C with shaking agitation and c) catalytic controls including 2-mIM, $Zn(NO_3)_2$ and 2-mIM: $Zn(NO_3)_2$ (2:1) compared to **ZIF-8 50 nm** (both a 6 h reaction and after 3 h where ZIF-8 has been removed from solution). (Modified from Figure 4).

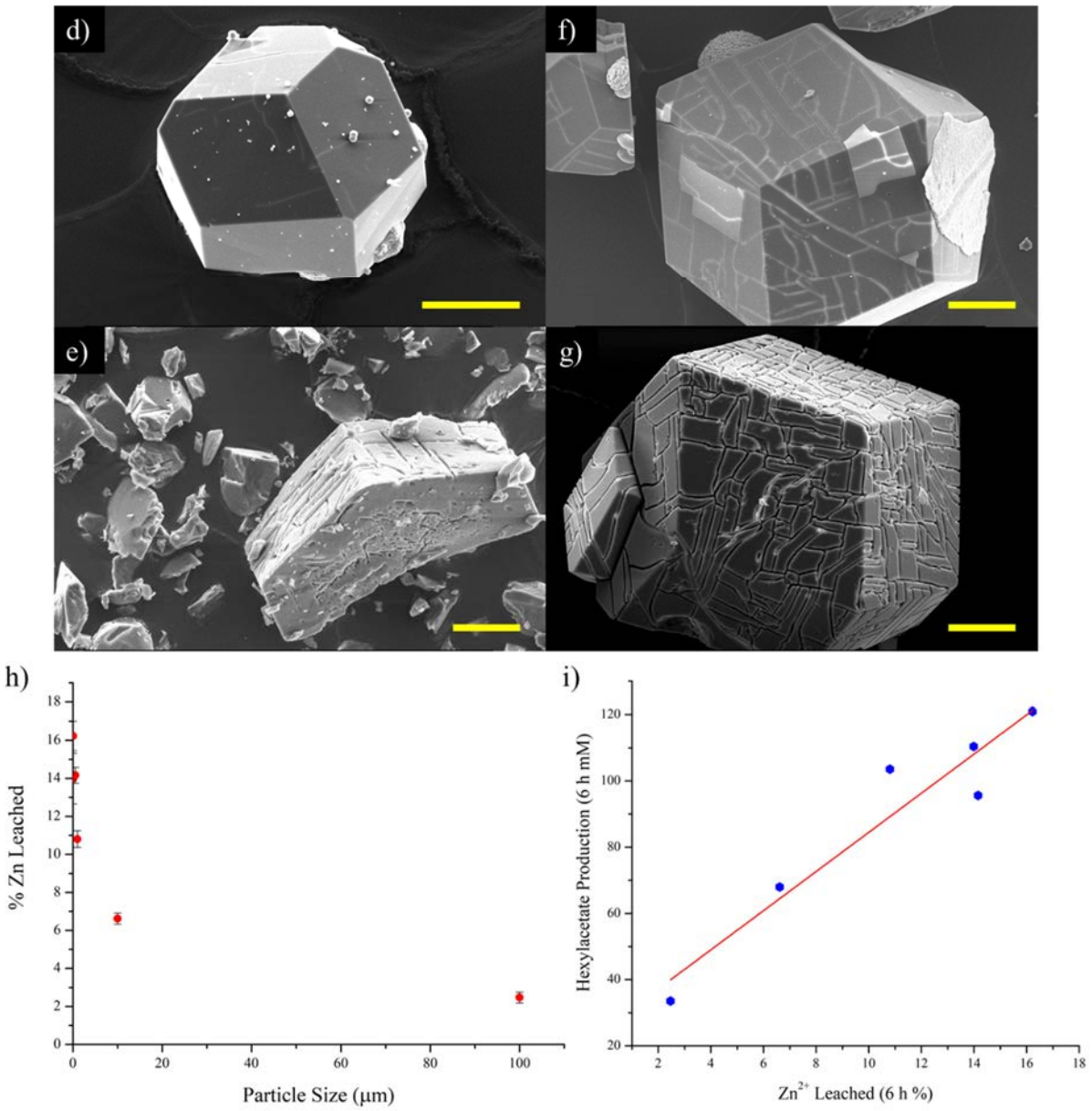

Figure **2.4 (d-i)**: SEM images of **ZIF-8 100 µm** d) as-synthesised, e) post-catalysis (stirred), f) agitated in hexanol at 60 °C and g) post-catalysis (agitated). All scale bars represent 50 µm for the SEM images. h) AAS Zn leaching analysis (as a percentage of Zn present in 10 mg of ZIF-8) post 6 h of catalysing the transesterification of hexanol with vinyl acetate for all particle sizes. i) A comparison of hexyl acetate production (mM) and % Zn leached post 6 h of catalysing the transesterification of hexanol with vinyl acetate for all particle sizes. (Modified from Figure 4).

Given that etching of the crystal surface may lead to Zn^{2+} release, we probed the release of Zn^{2+} post-catalysis by Atomic Absorption Spectroscopy (AAS). By AAS it was found that there was considerable Zn^{2+} leaching for smaller crystal sizes, 16% for **ZIF-8 50 nm**, relative to larger crystal sizes, 2% for **ZIF-8 100 µm** (Figure **2.4h**). The extent of Zn^{2+} leaching is proportional to the external surface area of the ZIF-8 crystals. Since etching of the surface leads to the release of Zn^{2+} and 2-mIM into solution, catalytic controls were conducted with $Zn(NO_3)_2$, 2-mIM and a mixture (1:2, $Zn(NO_3)_2$:2-mIM). These controls demonstrated that Zn^{2+} and a mixture of Zn^{2+} and 2-mIM catalyse the transesterification reaction (Figure **2.4c**). It is notable that a stoichiometric mixture of Zn^{2+} and 2-mIM (relative to 10 mg of ZIF-8) demonstrates significantly higher catalytic activity than Zn^{2+} or 2-mIM alone, indicating a synergistic effect between Zn^{2+} and 2-mIM or some low coordinate Zn(2-mIM) complex forming in solution to catalyse this reaction. In fact, the Zn^{2+}/2-mIM mixture is more active than **ZIF-8 50 nm**, although this may in part be attributed to poor dispersion under shaking agitation. To determine whether the liberated Zn^{2+} could contribute the observed catalytic activity of ZIF-8, an experiment was conducted whereby **ZIF-8 50 nm** was removed (by centrifugation) after 3 h and the progress of the reaction without the solid phase catalyst was followed via GC-MS (Figure **2.4c**). It was observed that the residual Zn^{2+} in solution had equivalent catalytic activity to **ZIF-8 50 nm** after 6 h (Figure 4c). The amount of Zn^{2+} leached at 3 h, was similar to the amount leached after 6 h with ZIF-8 in solution (15 and 16% respectively as determined by AAS), indicating that the majority of Zn^{2+} leached within the first 3 h of the reaction. Additionally, an interesting relationship was observed between hexyl acetate production and the percentage Zn^{2+} leached after a 6 h reaction, with hexyl acetate production increasing linearly as percentage Zn^{2+} leached increased (Figure **2.4i**). Decreasing particle size increases the available external surface area which can be etched, releasing increased amounts of Zn^{2+} into solution propagating the catalysis of transesterification reactions. A further ^{1}H NMR study was conducted to determine whether Zn^{2+} could be released by a smaller chain alcohol such as methanol and be catalytically active (See Appendix **2.9.3** and Table **2.A.1**). In this experiment the progress of the transesterification of vinyl acetate with d_4MeOH at 60 °C was monitored via ^{1}HNMR. 67 – 70% conversion of vinyl acetate to methyl acetate was observed at 3 h and there was 90% conversion at 6 h with ZIF-8 present. When the solid catalyst was removed after 3 h there was 81% conversion at 6 h, indicating homogeneous catalysis had occurred post-solid catalyst removal (likely resulting from leached Zn^{2+} in solution). Combined these results indicate that (under the conditions used) the catalytic activity

of ZIF-8 is mainly attributed to homogeneous catalysis by release of Zn^{2+} and not to heterogeneous catalysis by active sites on the surface of ZIF-8.

Given that the liberated Zn^{2+}/2-mIM^- contribute significantly to the catalysis of the transesterification of vinyl acetate with hexanol, it is thus challenging to draw concrete conclusions as to the direct impact of crystal size and morphology on surface catalysis with ZIF-8, although crystal size directly appears to impact the stability of ZIF-8. Importantly, this investigation has highlighted that MOF catalysts, such as ZIF-8 which are typically thought to be 'robust', are susceptible to surface etching and degradation under liquid phase catalytic conditions.

Surface etching of ZIF-8, both anisotropic and indiscriminate, have been reported previously.[33, 37] In one example, ZIF-8 crystals were exposed to oleic acid as a means to introduce more defect sites at the surface of the crystals and improve the hydrolysis of fluorescein diacetate.[37] Oleic acid is a long chain carboxylic acid with a hydrophobic tail, which likely has high affinity for the hydrophobic surface of ZIF-8. The carboxylic acid group of oleic acid could then bind Zn(II) nodes, potentially liberating Zn^{2+}, 2-mIM^- and etch the surface of ZIF-8. Hexanol also has a hydrophobic chain, although much shorter than oleic acid, and so the mechanism of etching observed here is presumably similar. Since etching has been observed under catalytic conditions using reagents that have functional groups with an affinity for Zn(II) but are primarily hydrophobic, it would be expected that other reactions with similar reagents might also etch the surface of ZIF-8 and release Zn^{2+}/2-mIM^-. For example, a well-known reaction, catalysed at the surface of ZIF-8, that would be expected to engender surface etching is the Knoevenagel condensation of benzaldehyde and malononitrile.[11]

2.4.3. Knoevenagel catalytic condition induced surface etching of ZIF-8

The Knoevenagel condensation of benzaldehyde and malononitrile was investigated to determine whether the surface of ZIF-8 was susceptible to etching under other reaction conditions. Given that this is a well-studied reaction for ZIF-8 catalysis,[11, 26-29] and that the focus of the investigation was to indicate the susceptibility of ZIF-8 to surface etching, a full catalytic study was not undertaken. As such, **ZIF-8 100 µm** samples were studied by SEM to determine whether surface degradation occurred during the Knoevenagel condensation of benzaldehyde with malononitrile.[11] The only modification made to the previously used protocol was to avoid mechanical crushing that would occur from stirring; hence the reaction solution was agitated via a plate shaker/incubator at 165 rpm at 25 °C. SEM analysis revealed

that **ZIF-8 100 µm** etching occurred when samples were suspended in toluene, or mixtures of toluene/benzaldehyde and toluene/malononitrile, and under catalytic conditions for Knoevenagel condensation (Figure **2.5**). Indiscriminate surface etching was observed in toluene, in the presence of malononitrile and under catalytic conditions, but etching was most severe in the presence of benzaldehyde, with all surfaces appearing noticeably rougher at high magnification than before. Benzaldehyde is hydrophobic and contains a polar functional group (aldehyde), similar to hexanol and oleic acid, which could be expected to etch the surface of ZIF-8 and release Zn^{2+} in a similar manner.

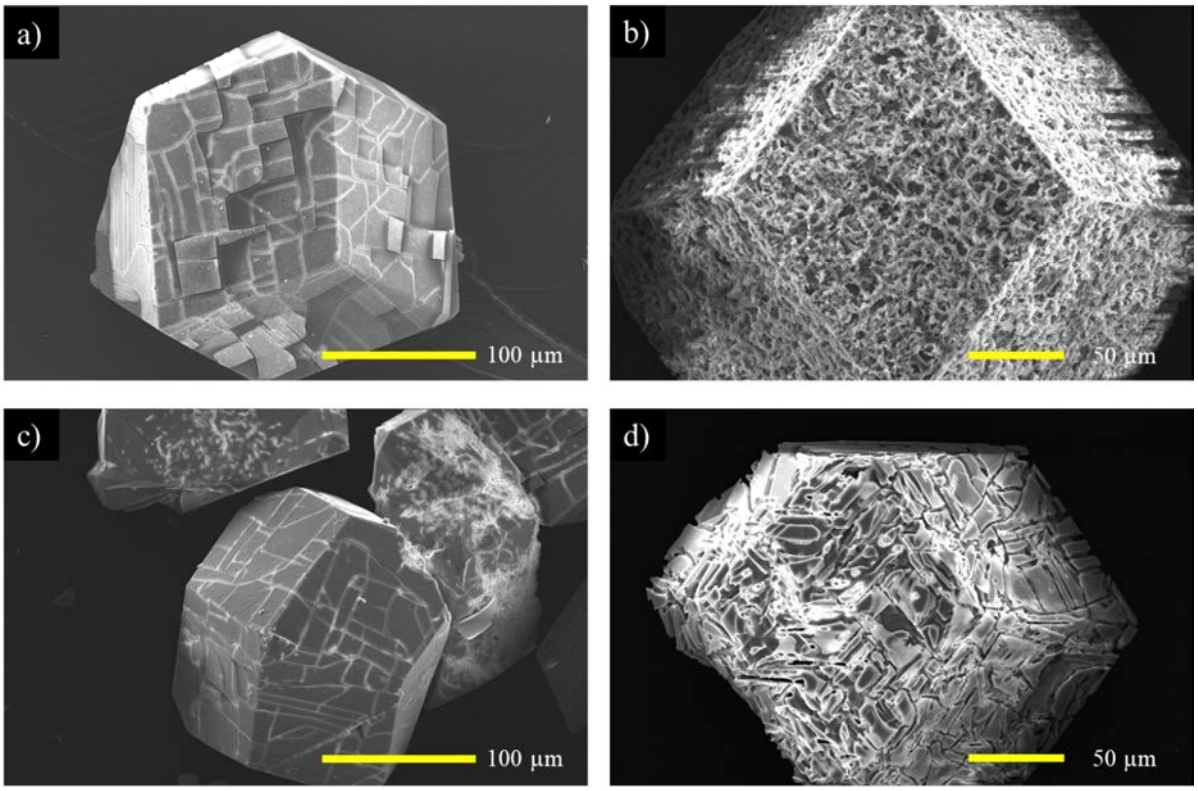

Figure **2.5**: SEM images of **ZIF-8 100 µm** in a) toluene for 6 h, b) benzaldehyde and toluene for 6 h, c) malononitrile and toluene for 6 h and d) under Knoevenagel condensation conditions with malononitrile, benzaldehyde and toluene. All reactions were agitated with a plate shaker/incubator to avoid mechanical degradation of the crystals. (Modified from Figure 5).

AAS analysis of the samples after 6 h revealed that for toluene and toluene/malononitrile free Zn^{2+} could not be detected. However, for the samples treated with benzaldehyde in toluene and under catalytic conditions, a significant amount of Zn^{2+} was detected in solution: 11.16 ± 0.07 ppm (2% relative to total Zn in 20 mg ZIF-8) and 92.14 ± 0.29 ppm (16%) respectively. PXRD analysis confirmed that the sodalite topology of ZIF-8 was retained post-Knoevenagel condensation catalysis conditions, see Appendix **2.9.5** Figure **2.A.15**. While the crystalline structure of ZIF-8 was retained, it has been shown again that the surface of ZIF-8 is not stable under catalytic conditions that feature a hydrophobic reagent with a polar functional group.

2.4.4. Challenges for MOF Catalysis

Throughout this investigation we have observed that crystal size has an adverse effect on the stability of ZIF-8 under catalytic conditions (transesterification with hexanol/methanol and Knoevenagel condensation with benzaldehyde), resulting in etching of the crystal surface and leaching of Zn^{2+} and 2-mIM. The etching/Zn^{2+} leaching of ZIF-8 correlates with the amount of the external surface area per crystallite and therefore number of active sites/defects. This trend has also been noted, in part, for the cyclodimerization of epichlorohydrin catalysed at defect sites on ZIF-8, with significant degradation of the crystal surface and a decrease in crystallinity being observed upon recycling the catalyst.[41] We have also recently reported the effects of crystal size on the rate of structural reorganisation of a "kinetically trapped" phase of a flexible MOF, and noted that the stability of the "kinetically trapped" phase decreased with reduced crystal size.[21] As well as phase/framework instability under certain conditions, MOFs have been reported to leach transition metals during catalysis (both metals integral to the structure and those appended post-synthetically to a ligand or a defect binding site).[42-43] Thus, crystal size likely affects MOF stability during catalysis for other systems as well. As such, appropriate consideration of the catalytic conditions and crystal size regime of candidate MOFs must be given, particularly for materials that are expected to be susceptible to etching/leaching.

2.5. Conclusions and Future Outlook

This work examined the catalytic activity of ZIF-8 crystal surfaces for a model transesterification reaction and the crystal surface stability under Knoevenagel condensation reaction conditions. While, as anticipated, improved catalytic performance was observed with decreasing crystal size, the interpretation of this data was complicated by the fact that the ZIF-8 crystal surfaces were indiscriminately etched during catalysis. AAS analysis further confirmed that crystal surface etching is associated with leaching of Zn^{2+}, with the best performing and smallest crystal size regime (50 nm) being most susceptible to this phenomenon. Further analysis revealed that the catalytic activity of ZIF-8 was primarily due to Zn^{2+} leached in solution during catalysis. Similar surface instability was also confirmed for ZIF-8 under catalytic conditions for the Knoevenagel condensation reaction, with significant etching and Zn^{2+} leaching observed. Crystal size appears to have a direct impact on the surface stability of ZIF-8 under catalytic conditions due to the increased external surface of the smaller crystals leading to a proportionally larger number defects/coordination sites being available. For both the surface-based transesterification and Knoevenagel condensation reactions it was observed that ZIF-8 was susceptible to etching by hydrophobic reagents with polar functional groups such as hexanol and benzaldehyde. Although smaller crystals sizes are theoretically more active for surface-based catalysis our observations indicate that crystal size has a greater impact on catalyst stability (and hence reusability). Another outcome of this study is that when investigating MOF catalysis in solution the susceptibility of crystals to undergo changes in their nanoscale structuralisation over time must be carefully considered when assessing catalytic performance.

2.6. Conflicts of Interest

There are no conflicts to declare.

2.7. Acknowledgements

OMLP thanks Matthew Bull for assistance with the Atomic Adsorption Spectrometry measurements, Adelaide Microscopy for access to the XL30 SEM and the Australian Federal Government for a Research Training Program Scholarship. CJS, CJD and KS thank the Australian Research Council for funding (KS: DE160100306; CJD & CJS: DP160103234).

2.8. References

1. Zhu, L.; Liu, X. Q.; Jiang, H. L.; Sun, L. B., Metal-Organic Frameworks for Heterogeneous Basic Catalysis. *Chem Rev* **2017,** *117* (12), 8129-8176.

2. Liang, J.; Liang, Z.; Zou, R.; Zhao, Y., Heterogeneous Catalysis in Zeolites, Mesoporous Silica, and Metal-Organic Frameworks. *Adv Mater* **2017,** *29* (30).

3. Zhao, M.; Yuan, K.; Wang, Y.; Li, G.; Guo, J.; Gu, L.; Hu, W.; Zhao, H.; Tang, Z., Metal-Organic Frameworks as Selectivity Regulators for Hydrogenation Reactions. *Nature* **2016,** *539* (7627), 76-80.

4. Dhakshinamoorthy, A.; Alvaro, M.; Garcia, H., Commercial Metal-Organic Frameworks as Heterogeneous Catalysts. *Chem Commun* **2012,** *48* (92), 11275-88.

5. García-García, P.; Müller, M.; Corma, A., MOF Catalysis in Relation to their Homogeneous Counterparts and Conventional Solid Catalysts. *Chem Sci* **2014,** *5* (8), 2979.

6. Liu, J.; Chen, L.; Cui, H.; Zhang, J.; Zhang, L.; Su, C. Y., Applications of Metal-Organic Frameworks in Heterogeneous Supramolecular Catalysis. *Chem Soc Rev* **2014,** *43* (16), 6011-61.

7. Chizallet, C. l.; Lazare, S.; Bazer-Bachi, D.; Bonnier, F.; Lecocq, V.; Soyer, E.; Quoineaud, A.-A.; Bats, N., Catalysis of Transesterification by a Nonfunctionalized Metal-Organic Framework: Acido-Basicity at the External Surface of ZIF-8 Probed by FTIR and ab Initio Calculations. *J Am Chem Soc* **2010,** *132*, 12365-12377.

8. Huxley, M. T.; Coghlan, C. J.; Bloch, W. M.; Burgun, A.; Doonan, C. J.; Sumby, C. J., X-ray Crystallographic Insights into Post-Synthetic Metalation Products in a Metal-Organic Framework. *Philos Trans A Math Phys Eng Sci* **2017,** *375* (2084).

9. Evans, J. D.; Sumby, C. J.; Doonan, C. J., Post-Synthetic Metalation of Metal-Organic Frameworks. *Chem Soc Rev* **2014,** *43* (16), 5933-51.

10. Gonzalez, M. I.; Bloch, E. D.; Mason, J. A.; Teat, S. J.; Long, J. R., Single-Crystal-to-Single-Crystal Metalation of a Metal-Organic Framework: a Route Toward Structurally Well-Defined Catalysts. *Inorg Chem* **2015,** *54* (6), 2995-3005.

11. Tran, U. P. N.; Le, K. K. A.; Phan, N. T. S., Expanding Applications of Metal−Organic Frameworks: Zeolite Imidazolate Framework ZIF-8 as an Efficient Heterogeneous Catalyst for the Knoevenagel Reaction. *ACS Catal* **2011,** *1* (2), 120-127.

12. Fei, H.; Cohen, S. M., A Robust, Catalytic Metal-Organic Framework with Open 2,2'-Bipyridine Sites. *Chem Commun* **2014,** *50* (37), 4810-2.

13. Li, X.; Van Zeeland, R.; Maligal-Ganesh, R. V.; Pei, Y.; Power, G.; Stanley, L.; Huang, W., Impact of Linker Engineering on the Catalytic Activity of Metal–Organic Frameworks Containing Pd(II)–Bipyridine Complexes. *ACS Catal* **2016,** *6* (9), 6324-6328.

14. Kiyonaga, T.; Higuchi, M.; Kajiwara, T.; Takashima, Y.; Duan, J.; Nagashima, K.; Kitagawa, S., Dependence of Crystal Size on the Catalytic Performance of a Porous Coordination Polymer. *Chem Commun* **2015,** *51* (13), 2728-30.

15. Gonzalez, M.; Oktawiec, J.; Long, J. R., Ethylene Oligomerization in Metal–Organic Frameworks Bearing Nickel(II) 2,2′-Bipyridine Complexes. *Faraday Discuss* **2017**.

16. Canivet, J.; Aguado, S.; Schuurman, Y.; Farrusseng, D., MOF-Supported Selective Ethylene Dimerization Single-Site Catalysts through One-Pot Postsynthetic Modification. *J Am Chem Soc* **2013,** *135* (11), 4195-8.

17. Furukawa, S.; Reboul, J.; Diring, S.; Sumida, K.; Kitagawa, S., Structuring of Metal-Organic Frameworks at the Mesoscopic/Macroscopic Scale. *Chem Soc Rev* **2014,** *43* (16), 5700-34.

18. Zhang, C.; Gee, J. A.; Sholl, D. S.; Lively, R. P., Crystal-Size-Dependent Structural Transitions in Nanoporous Crystals: Adsorption-Induced Transitions in ZIF-8. *J Phys Chem C* **2014,** *118* (35), 20727-20733.

19. Tanaka, S.; Fujita, K.; Miyake, Y.; Miyamoto, M.; Hasegawa, Y.; Makino, T.; Van der Perre, S.; Cousin Saint Remi, J.; Van Assche, T.; Baron, G. V.; Denayer, J. F. M., Adsorption and Diffusion Phenomena in Crystal Size Engineered ZIF-8 MOF. *J Phys Chem C* **2015,** *119* (51), 28430-28439.

20. Sakata, Y.; Furukawa, S.; Kondo, M.; Hirai, K.; Horike, N.; Takashima, Y.; Uehara, H.; Louvain, N.; Meilikho, M.; Tsuruoka, T.; Isoda, S.; Kosaka, W.; Sakata, O.; Kitagawa, S., Shape-Memory Nanopores Induced in Coordination Frameworks by Crystal Downsizing. *Science* **2013,** *339*, 193-196.

21. Linder-Patton, O. M.; Bloch, W. M.; Coghlan, C. J.; Sumida, K.; Kitagawa, S.; Furukawa, S.; Doonan, C. J.; Sumby, C. J., Particle Size Effects in the Kinetic Trapping of a Structurally-Locked Form of a Flexible MOF. *CrystEngComm* **2016,** *18* (22), 4172-4179.

22. Lee, H. J.; Cho, W.; Jung, S.; Oh, M., Morphology-Selective Formation and Morphology-Dependent Gas-Adsorption Properties of Coordination Polymer Particles. *Adv Mater* **2009,** *21* (6), 674-677.

23. Pham, M.-H.; Vuong, G.-T.; Fontaine, F.-G.; Do, T.-O., Rational Synthesis of Metal–Organic Framework Nanocubes and Nanosheets Using Selective Modulators and Their Morphology-Dependent Gas-Sorption Properties. *Cryst Growth Des* **2012,** *12* (6), 3091-3095.

24. Uehara, H.; Diring, S.; Furukawa, S.; Kalay, Z.; Tsotsalas, M.; Nakahama, M.; Hirai, K.; Kondo, M.; Sakata, O.; Kitagawa, S., Porous Coordination Polymer Hybrid Device with Quartz Oscillator: Effect of Crystal Size on Sorption Kinetics. *J Am Chem Soc* **2011,** *133* (31), 11932-5.

25. Biemmi, E.; Scherb, C.; Bein, T., Oriented Growth of the Metal Organic Framework Cu3(BTC)2(H2O)3,xH2O Tunable with Functionalized Self-Assembled Monolayers. *J Am Chem Soc* **2007,** *129* (26), 8054-8055.

26. Lei, Z.; Deng, Y.; Wang, C., Multiphase Surface Growth of Hydrophobic ZIF-8 on Melamine Sponge for Excellent Oil/Water Separation and Effective Catalysis in a Knoevenagel Reaction. *J Mater Chem A* **2018**.

27. Tsai, C.-W.; Langner, E. H. G., The Effect of Synthesis Temperature on the Particle Size of Nano-ZIF-8. *Micropor Mesopor Mater* **2016,** *221*, 8-13.

28. Lee, Y.-R.; Jang, M.-S.; Cho, H.-Y.; Kwon, H.-J.; Kim, S.; Ahn, W.-S., ZIF-8: A comparison of synthesis methods. *Chem Eng J* **2015,** *271*, 276-280.

29. Zhao, X.; Fang, X.; Wu, B.; Zheng, L.; Zheng, N., Facile synthesis of Size-Tunable ZIF-8 Nanocrystals using Reverse Micelles as Nanoreactors. *Sci China Chem* **2013,** *57* (1), 141-146.

30. Zhang, K.; Lively, R. P.; Zhang, C.; Chance, R. R.; Koros, W. J.; Sholl, D. S.; Nair, S., Exploring the Framework Hydrophobicity and Flexibility of ZIF-8: From Biofuel Recovery to Hydrocarbon Separations. *J Phys Chem Lett* **2013,** *4* (21), 3618-3622.

31. Pan, Y.; Heryadi, D.; Zhou, F.; Zhao, L.; Lestari, G.; Su, H.; Lai, Z., Tuning the Crystal Morphology and Size of Zeolitic Imidazolate Framework-8 in Aqueous Solution by Surfactants. *CrystEngComm* **2011,** *13* (23), 6937.

32. Schejn, A.; Balan, L.; Falk, V.; Aranda, L.; Medjahdi, G.; Schneider, R., Controlling ZIF-8 Nano- and Microcrystal Formation and Reactivity through Zinc Salt Variations. *CrystEngComm* **2014,** *16* (21), 4493.

33. Avci, C.; Arinez-Soriano, J.; Carne-Sanchez, A.; Guillerm, V.; Carbonell, C.; Imaz, I.; Maspoch, D., Post-Synthetic Anisotropic Wet-Chemical Etching of Colloidal Sodalite ZIF Crystals. *Angew Chem Int Ed Engl* **2015,** *54* (48), 14417-21.

34. Rosinel, T.; Rodriguez-Carvajal, J., WinPLOTR. *Proceedings of the Seventh European Powder Diffraction Conference (EPDIC 7)* **2000**, 118-123.

35. Macrae, C. F.; Edgington, P. R.; P. McCabe, E. P.; Shields, G. P.; Taylor, R.; Towler, M.; Streek, J. v. d., Mercury. *J. Appl. Cryst.* **2006,** *39*, 453-457.

36. Macrae, C. F.; Bruno, I. J.; Chisholm, J. A.; Edgington, P. R.; P. McCabe, E. P.; Rodriguez-Monge, L.; Taylor, R.; Streek, J. v. d.; Wood, P. A., Mercury CSD 2.0. *J. Appl. Cryst.* **2008,** *41*, 466-470.

37. Kubarev, A.; Roeffaers, M. B. J., Surface Acid-Base Catalytic Activity of ZIF-8 Revealed by Super-Resolution Fluorescence Microscopy. *CrystEngComm* **2017**.

38. Ataya, F.; Dube, M. A.; Ternan, M., Acid-Catalyzed Transesterificaion of Canola Oil to Biodiesel under Single- and Two-Phase Reaction Conditions. *Energ Fuel* **2007,** *21*, 2450-2459.

39. Jain, S.; Sharma, M. P.; Rajvanshi, S., Acid Base Catalyzed Transesterification Kinetics of Waste Cooking Oil. *Fuel Process Technol* **2011,** *92* (1), 32-38.

40. Moh, P. Y.; Cubillas, P.; Anderson, M. W.; Attfield, M. P., Revelation of the Molecular Assembly of the Nanoporous Metal Organic Framework ZIF-8. *J Am Chem Soc* **2011,** *133* (34), 13304-7.

41. Mousavi, B.; Luo, Z.; Phatanasri, S.; Su, W.; Wang, T.; Chaemchuen, S.; Verpoort, F., One-Step Synthesis of 2,5-Bis(chloromethyl)-1,4-dioxane from Epichlorohydrin Using ZIF-8, Taking Advantage of Structural Defects. *Eur J Inorg Chem* **2017,** (42), 4947-4954.

42. Gascon, J.; Corma, A.; Kapteijn, F.; Llabrés i Xamena, F. X., Metal Organic Framework Catalysis:Quo vadis? *ACS Catal* **2014,** *4* (2), 361-378.

43. Burgun, A.; Crees, R. S.; Cole, M. L.; Doonan, C. J.; Sumby, C. J., A 3-D Diamondoid MOF Catalyst Based on in situ Generated [Cu(L)$_2$] N-heterocyclic Carbene (NHC) Linkers: Hydroboration of CO2. *Chem Commun* **2014,** (50), 11760-11763.

2.9. Appendix

2.9.1. Synthetic Protocols for ZIF-8

ZIF-8 50 nm: Zinc nitrate hexahydrate ($Zn(NO_3)_2 \cdot 6H_2O$, 58.8 mg, 0.197 mmol) was dissolved in methanol (4 mL) and in a separate vial 2-methylimidazole (2-mIM, 64.8 mg, 0.787 mmol) was dissolved in methanol (4 mL) with NaOH (2 M, 0.295 mL, 0.591 mmol). Both solutions were sonicated until the solids dissolved, the zinc nitrate solution added to the solution of 2-mIM, and the mixture was left at room temperature (25 °C) for 24 h in a 20 mL screw cap vial. The resultant white suspension was washed with methanol (5×10 mL) then dried resulting in a colourless micro-crystalline powder (34.4 mg, 76%).

ZIF-8 100 nm: $Zn(NO_3)_2 \cdot 6H_2O$ (58.8 mg, 0.197 mmol) was dissolved in methanol (4 mL) and in a separate vial 2-mIM (64.8 mg, 0.787 mmol) was dissolved in methanol (4 mL). Both solutions were sonicated until the solids dissolved, the zinc nitrate solution added to the solution of 2-mIM and the mixture was left at room temperature (25 °C) for 24 h in a 20 mL screw cap vial. The resultant white suspension was washed with methanol (5×10 mL) then dried resulting in a colourless micro-crystalline powder (10.5 mg, 23%).

ZIF-8 500 nm: Zinc bromide ($ZrBr_2$, 44.4 mg, 0.197 mmol), was dissolved in methanol (4 mL). In a separate vial 2-mIM (64.8 mg, 0.787 mmol) was dissolved in methanol (4 mL). Both solutions were sonicated until the solids dissolved. The solutions were combined, and the mixture was left at room temperature (25 °C) for 24 h in a 20 mL screw cap vial. The resultant white suspension was washed with methanol (5×10 mL) then dried resulting in a colourless micro-crystalline powder (4.2 mg, 9%).

ZIF-8 500 nm cubic: $Zn(NO_3)_2 \cdot 6H_2O$ (29.0 mg, 0.097 mmol) was dissolved in MilliQ water (4 mL). In a separate vial 2-mIM (454.0 mg, 5.530 mmol) was dissolved in MilliQ water (4 mL) and cetyltrimethylammonium bromide (CTAB, 79 µl, 0.01 M). Both solutions were sonicated until the solids were dissolved. The zinc nitrate solution was added to the solution of 2-mIM and CTAB and the mixture was heated at 100 °C for 24 h in a 20 mL screw cap vial. The resultant white suspension was washed with methanol (5×10 mL) then dried resulting in a colourless micro-crystalline powder (16.2 mg, 73%).

ZIF-8 1 µm: $Zn(NO_3)_2 \cdot 6H_2O$ (58.8 mg, 0.197 mmol) was dissolved in methanol (4 mL) while in a separate vial 2-mIM (64.8 mg, 0.787 mmol) and 1-methylimidazole (1-mIM, 64.8 µl, 0.787 mmol) were dissolved in methanol (4 mL). Both solutions were sonicated until the solids dissolved. The zinc nitrate solution was added to the solution of 2-mIM and the

mixture was left at room temperature (25 °C) for 24 h in a 20 mL screw cap vial. The resultant white suspension was washed with methanol (5×10 mL) then dried resulting in a colourless crystalline powder (3.1 mg, 7%).

ZIF-8 10 µm: $Zn(NO_3)_2 \cdot 6H_2O$ (176.4 mg, 0.593 mmol) was dissolved in methanol (4 mL) and in a separate vial 2-mIM (97.2 mg, 1.184 mmol) and sodium formate (HCOONa, 80.7 mg, 0.789 mmol) were dissolved in methanol (4 mL). Both solutions were sonicated until the solids dissolved, the zinc nitrate solution added to the solution of 2-mIM in a 20 mL screw cap vial, and the mixture was heated at 50 °C for 24 h. The resultant clear crystals were washed with methanol (5×10 mL) then dried resulting in a colourless crystalline powder (14.8 mg, 11%).

ZIF-8 100 µm: $Zn(NO_3)_2 \cdot 6H_2O$ (134.0 mg, 0.450 mmol) was dissolved in DMF (5 mL). In a separate vial 2-mIM (33.4 mg, 0.407 mmol) was also dissolved in DMF (5 mL). Both solutions were sonicated until the solids dissolved, the zinc nitrate solution added to the solution of 2-mIM in a 20 mL screw cap vial and the mixture was heated at 140 °C for 24 h. The resultant clear crystals were washed with DMF (2×10 mL) methanol (5×10 mL) then dried resulting in a colourless crystalline powder (46.9 mg, 50%). PXRD indicated a small amount of ZnO contaminant.

ZIF-8 100 µm truncated rhombic dodecahedron (trd): $Zn(NO_2)_3 \cdot 6H_2O$ (352.8 mg, 1.186 mmol) was dissolved in methanol (4 mL) and in a separate vial 2-mIM (194.4 mg, 2.368 mmol) and sodium formate (180.7 mg, 2.657 mmol) were dissolved in methanol (4 mL). Both solutions were sonicated until the solids dissolved. The solutions were combined in a 20 mL screw cap vial and the mixture was heated at 50 °C for 24 h. The colourless crystals were washed with methanol (5×10 mL) then dried resulting in a colourless crystalline powder (17.3 mg, 6%).

Activation procedure: The as-synthesised samples were washed with methanol (×5), dried under a nitrogen flow, and stored under vacuum in a desiccator for 1 h prior to use. For gas adsorption activation the “dried” sample was then heated under a high vacuum at 100 °C for 3 h. Activation yielded colourless microcrystalline powders.

2.9.2. Transesterification Catalytic Control Experiments

Stirred Agitation

2-mIM (14.42 mg, 0.176 mmol) was dissolved in hexanol (20 ml), the solution was stirred under an atmosphere of nitrogen for 1 h at 65 °C. Vinyl acetate (3.3 ml, 35.79 mmol) was added to the reaction mixture, which was then heated at 65 °C for 6 h. The progress of the reaction was followed via GC-MS, as outlined in the experimental.

A blank was run with just hexanol and vinyl acetate, a zinc control was run with a molar equivalent of $Zn(NO_3)_2$ to ZIF-8 (26.14 mg, 0.088 mmol) in place of 2-mIM and a mixed control of $Zn(NO_3)_2$ (26.14 mg, 0.088 mmol) and 2-mIM (14.42 mg, 0.175 mmol) was also done. All reagents were fully dissolved in hexanol prior to heating or addition of vinylacetate.

Shaking Agitation

2-mIM (7.21 mg, 0.088 mmol) was dissolved in hexanol (10 ml), the solution was dispersed via shaking at 165 rpm for 1 h at 60 °C. Vinyl acetate (1.65 ml, 17.89 mmol) was added to the reaction mixture, which was then heated at 60 °C for 6 h. The progress of the reaction was followed via GC-MS, as outlined in the experimental.

A blank was run with just hexanol and vinyl acetate, a zinc control was run with a molar equivalent of $Zn(NO_3)_2$ to ZIF-8 (13.07 mg, 0.044 mmol) in place of 2-mIM and a mixed control of $Zn(NO_3)_2$ (13.07 mg, 0.044 mmol) and 2-mIM (7.21 mg, 0.088 mmol) was also done. All reagents were fully dissolved in hexanol prior to heating or addition of vinylacetate.

An additional control was run to assess the activity of leached Zn^{2+} in solution, whereby a standard reaction was set up with **ZIF-8 50 nm** (10 mg, 0.044 mmol) dispersed in hexanol (10 ml) via shaking at 165 rpm for 1 h at 60 °C. Vinyl acetate (1.65 ml, 17.89 mmol) was added to the reaction mixture, which was then heated at 60 °C for 6 h. At the 3 h time point the ZIF-8 catalyst was removed by centrifugation at 10000 rpm and the supernatant was then heated for a further 3 h. The progress of the reaction was followed via GC-MS, as outlined in the experimental. See Figure 3c for GC-MS results for catalytic controls.

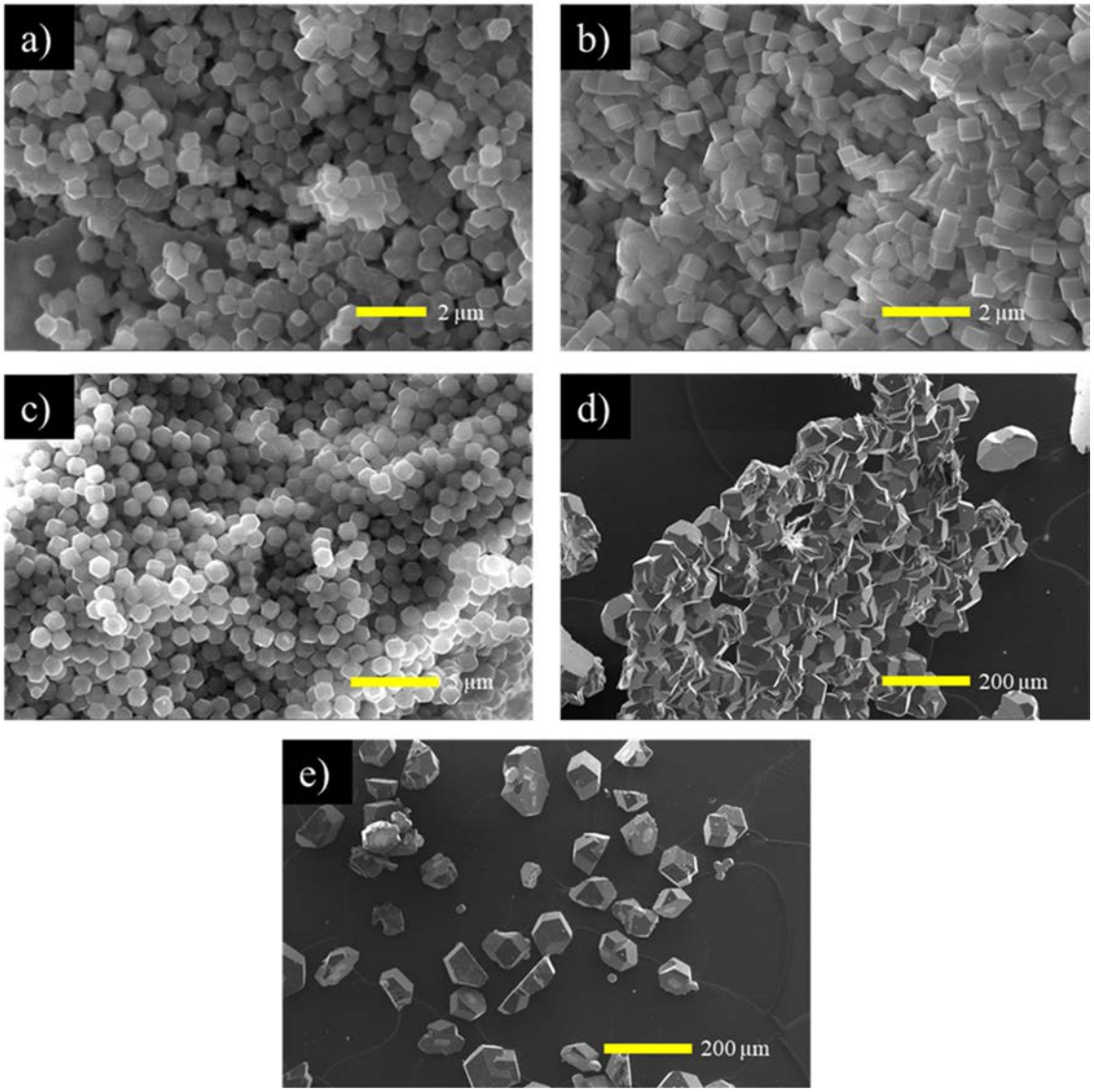

Figure **2.A.1**: Scanning electron microscope images of ZIF-8 samples for particle size distribution analysis for a) **ZIF-8 500 nm**, b) **ZIF-8 500 nm Cubic**, c) **ZIF-8 1 µm**, d) **ZIF-8 100 µm**, e) **ZIF-8 100 µm Truncated Rhombic Dodecahedra**.

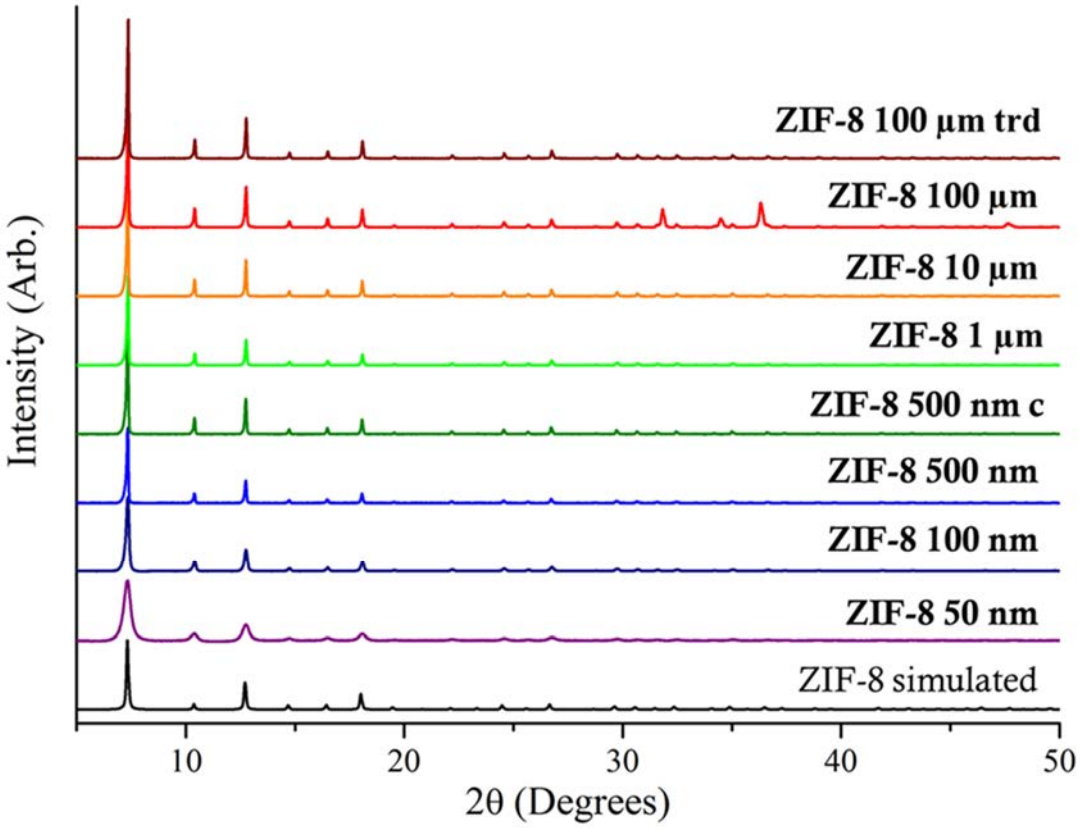

Figure **2.A.2**: Powder X-ray diffraction patterns of ZIF-8 samples; simulated, **ZIF-8 50 nm**, **ZIF-8 100 nm**, **ZIF-8 500 nm**, **ZIF-8 500 nm c** (cubic), **ZIF-8 1 µm**, **ZIF-8 10 µm**, **ZIF-8 100 µm**, **ZIF-8 100 µm trd** (truncated rhombic dodecahedra). Note all morphologies of ZIF-8 were rhombic dodecahedra unless otherwise specified. The conditions used to form **ZIF-8 100 µm** led to the formation of ZnO, seen in the PXRD trace.

2.9.3. Development of Catalysis Testing Conditions

Preliminary testing showed that the progress of the reaction between vinylacetate and MeOH-d_4, catalysed by ZIF-8, could be followed by ^{1}H NMR spectroscopy, with an increased production of methyl acetate observed with increasing temperature from 25 to 55 °C, (See Appendix **2.9.3**, Figure **2.A.3**). PXRD analysis demonstrated that the crystallinity of the ZIF-8 catalyst was retained post catalysis after 24 h (Figure **2.A.4**). To facilitate analysis by GC-MS methods, hexanol was used in place of methanol to ensure accurate product quantification (hexyl-acetate is easily distinguished from hexanol and the chosen internal standard propyl-propionate), see Figures **2.A.5** & **2.A.6**.

^{1}H NMR Analysis of the Transesterification of Vinyl acetate with d_4MeOH

Dried **ZIF-8 1 µm** (5 mg, 0.022 mmol) was dispersed in d_4MeOH (1 ml) at room temperature into 4 identical 2.5 ml vials. To these solutions vinyl acetate (82.5 µl, 0.895 mmol) was added and the solution was heated at 25, 35, 45 and 55 °C for 24 h. The solutions were then centrifuged at 10,000 rpm, the ZIF-8 catalyst was separated from the supernatant which was then analysed via ^{1}H NMR (see Figure **2.A.3**). The ^{1}H NMR signals corresponding to methyl acetate, vinyl acetate, acetaldehyde and the hemiacetal, that were detected after the reaction in d_4MeOH, were as follows: methyl acetate ^{1}H NMR (500 MHz/d_4MeOH): δ 2.03 (3H, s, CH_3); vinyl acetate ^{1}H NMR (500 MHz/d_4MeOH): δ 2.12 (s, 3H, CH_3), 4.58 (dd, J = 6.3, 1.5 Hz, 1H), 4.87 (dd, J = 14.0, 1.5 Hz, 1H), 7.27 (dd, J = 14, 6.3 Hz, 1H); acetaldehyde ^{1}H NMR (500 MHz/d_4MeOH): δ 9.71 (m, 3H); hemiacetal ^{1}H NMR (500 MHz/d_4MeOH): δ 1.26 (m), 4.69 (t, 3H), 4.79 (s, 1H).

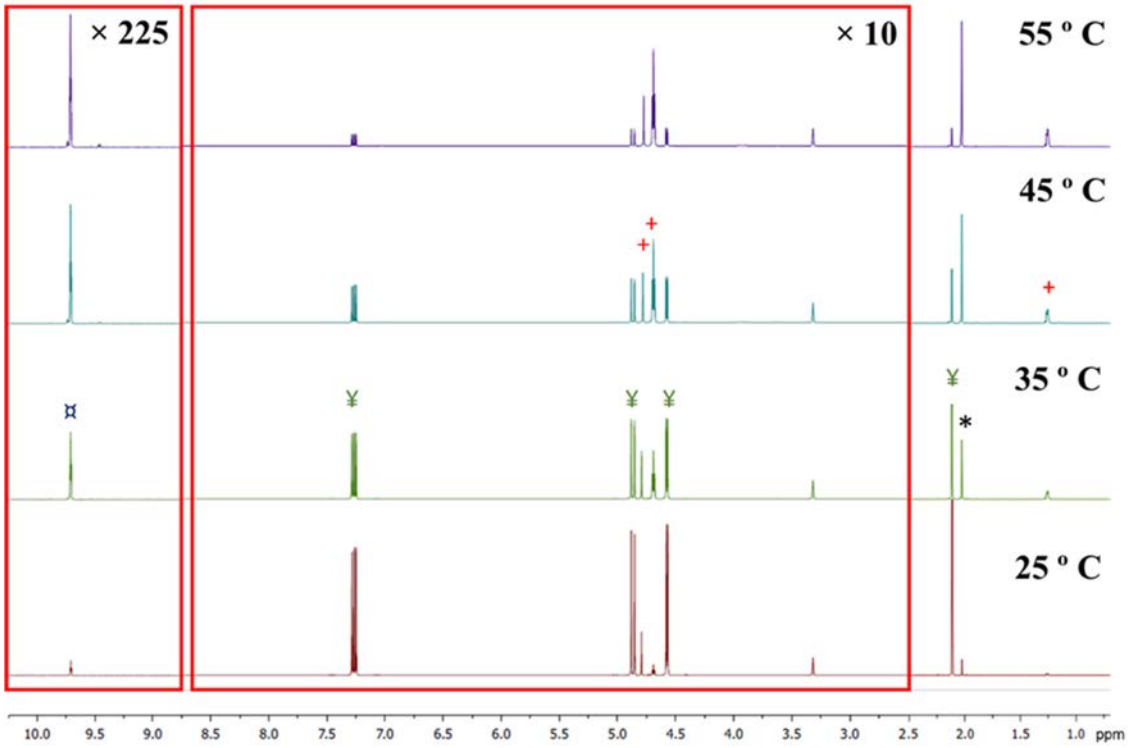

Figure **2.A.3**: ^{1}H NMR spectra of the transesterification reaction between d_4MeOH and vinyl acetate catalysed by **ZIF-8 1 µm**, where *, ¥, + and ¤ correspond to peaks associated with methyl acetate, vinyl acetate, the hemiacetal and acetaldehyde, respectively. For clarity, the sections between 2.5-8.75 ppm and 8.75-10.25 ppm are displayed at ×10 and × 225 magnification, respectively.

60 ºC ^{1}H NMR control reaction with catalyst removal at 3 h

Dried **ZIF-8 50 nm** (5 mg, 0.022 mmol) was dispersed in d$_4$MeOH (1 ml) at room temperature into 2 identical 2.5 ml vials. To these solutions vinyl acetate (82.5 µl, 0.895 mmol) was added and the solution was heated at 60 °C for 6 h. For one vial at the 3 and 6 h time points 50 µl aliquot of each solution was taken and centrifuged at 10,000 rpm, the ZIF-8 catalyst was separated from the supernatant which was then analysed via ^{1}H NMR in 0.65 ml d$_4$MeOH. For the other vial at the 3 h time point, after the 50 µl aliquot was taken, the ZIF-8 catalyst was separated from the supernatant by centrifugation and the supernatant was heated for a further 3 h at which point the supernatant was analysed via ^{1}HNMR. The ^{1}H NMR signals corresponding to methyl acetate, vinyl acetate, acetaldehyde and the hemiacetal, that were detected after the reaction in d$_4$MeOH were as follows: methyl acetate ^{1}H NMR (500 MHz/d$_4$MeOH): δ 2.03 (3H, s, CH_3); vinyl acetate ^{1}H NMR (500 MHz/d$_4$MeOH): δ 2.12 (s, 3H, CH_3), 4.58 (dd, J = 6.3, 1.5 Hz, 1H), 4.87 (dd, J = 14.0, 1.5 Hz, 1H), 7.27 (dd, J = 14, 6.3 Hz, 1H); acetaldehyde ^{1}H NMR (500 MHz/d$_4$MeOH): δ 9.71 (m, 3H); hemiacetal ^{1}H NMR (500 MHz/d$_4$MeOH): δ 1.26 (m), 4.69 (t, 3H), 4.79 (s, 1H).

Table **2.A.1**: ^{1}H NMR analysis of controls for the transesterification of vinyl acetate with d$_4$MeOH catalysed by **ZIF-8 50 nm**.

Sample	Integration of vinyl acetate CH_3 (δ 2.12)	Integration of methyl acetate CH_3 (δ 2.03)	Conversion (%)
3 h with ZIF-8 50 nm (1)	1	2.43	70
3 h with ZIF-8 50 nm (2)	1	2.08	67
6 h with ZIF-8 50 nm (1)	1	9.60	90
6 h with ZIF-8 50 nm removed at 3 h (2)	1	4.34	81

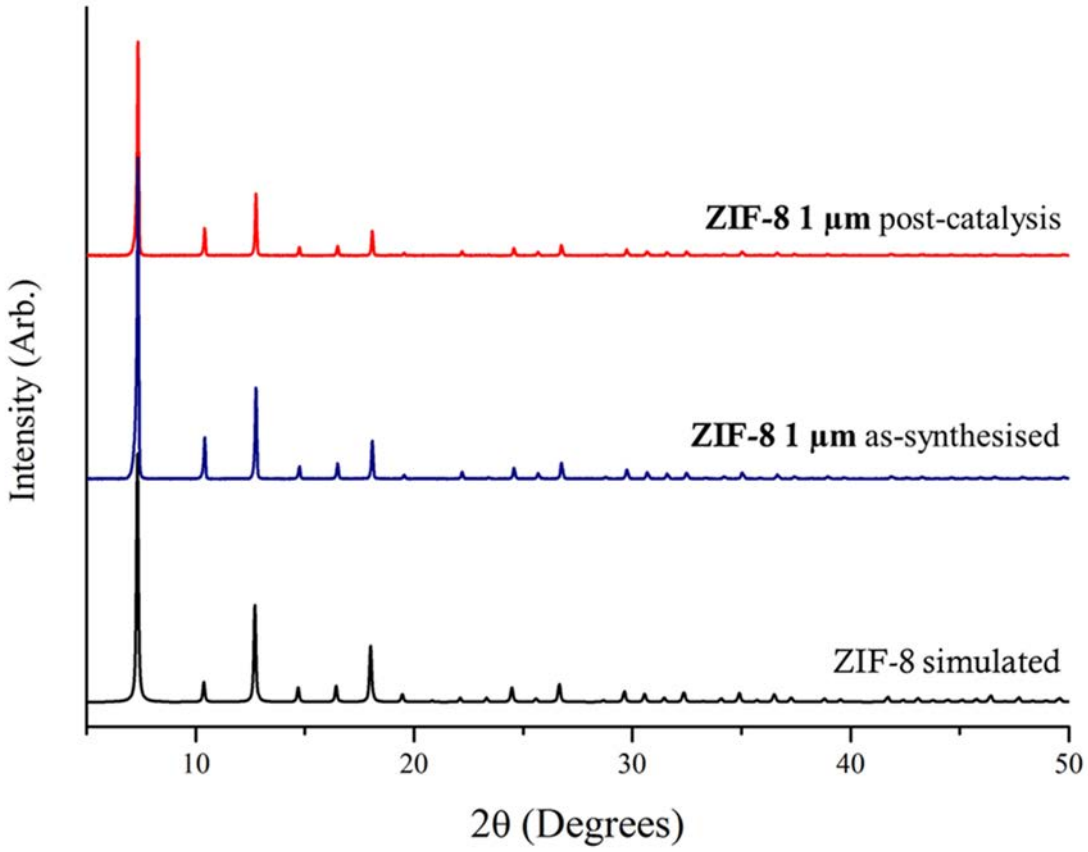

Figure **2.A.4**: Powder X-ray Diffraction patterns of ZIF-8; simulated, **ZIF-8 1 µm** as-synthesised and **ZIF-8 1 µm** post-catalysis at 55 °C in methanol, catalysing the transesterification of vinyl acetate with d_4MeOH.

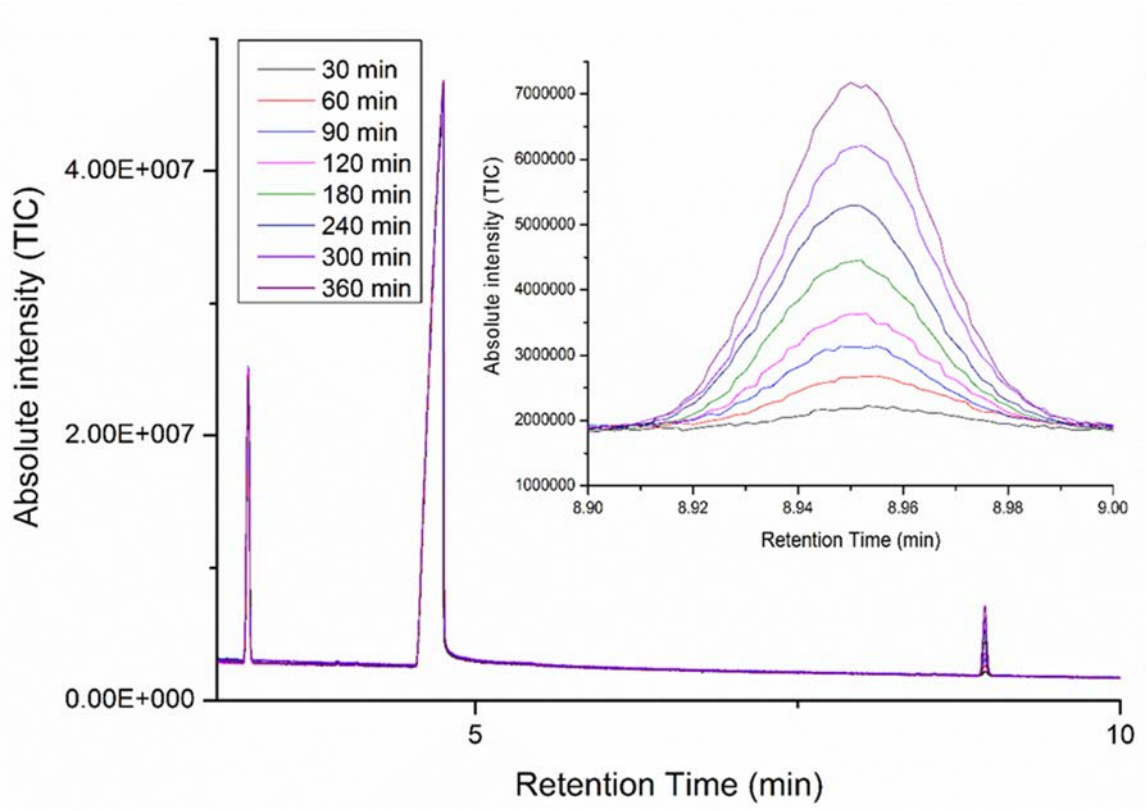

Figure **2.A.5**: GC-MS traces for the transesterification of hexanol with vinyl acetate, catalysed at 65 °C by **ZIF-8 1 µm** agitated by stirring, with peaks at retention times 3.10, 4.81 and 8.95 min corresponding to propyl propionate, hexanol and hexyl acetate respectively. The inset is an expansion of the hexyl acetate peak at 8.95 min.

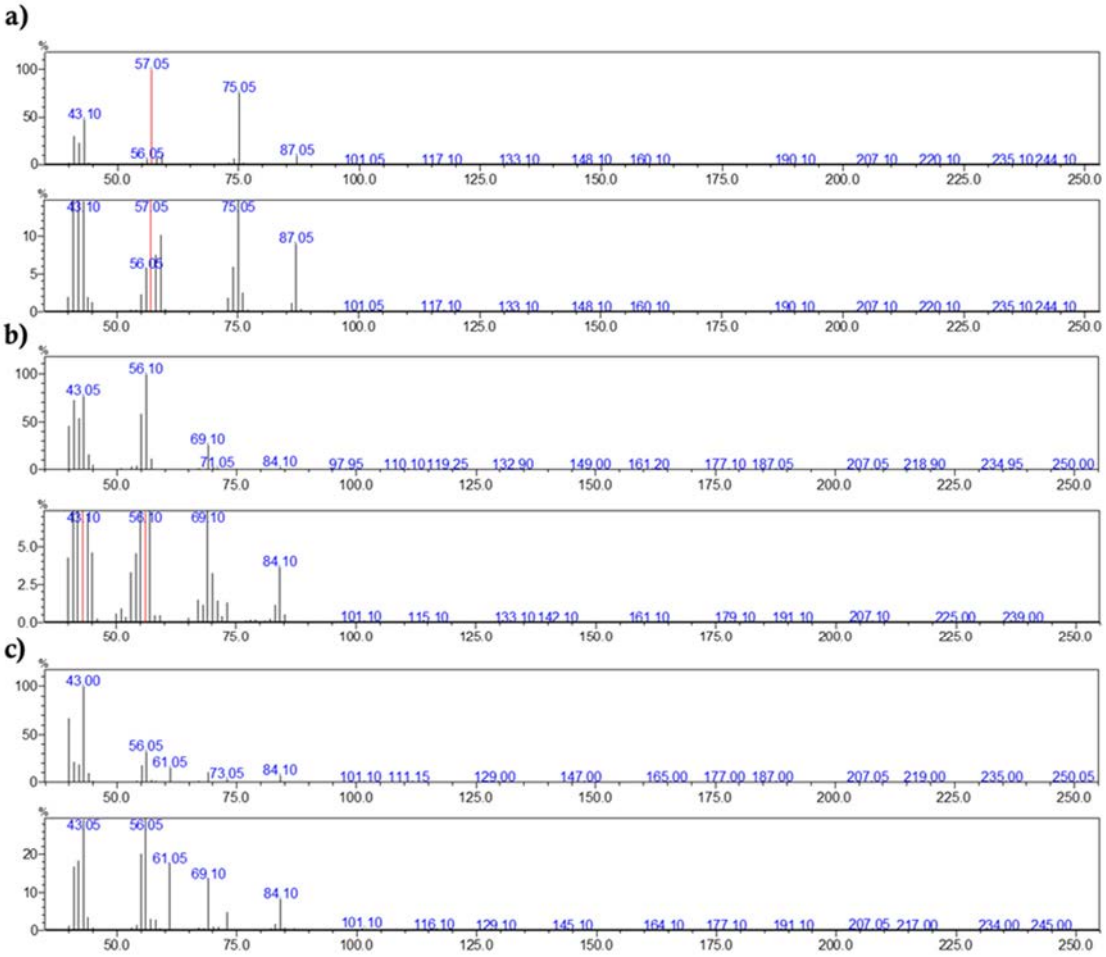

Figure **2.A.6**: Mass Spectra corresponding to peaks in the GC-MS trace in Figure S5 for a) propyl propionate, b) hexanol and c) hexyl acetate, which correspond to mass spectra in the NIST data base.[1]

2.9.4. Transesterification catalytic activity and crystal degradation analyses

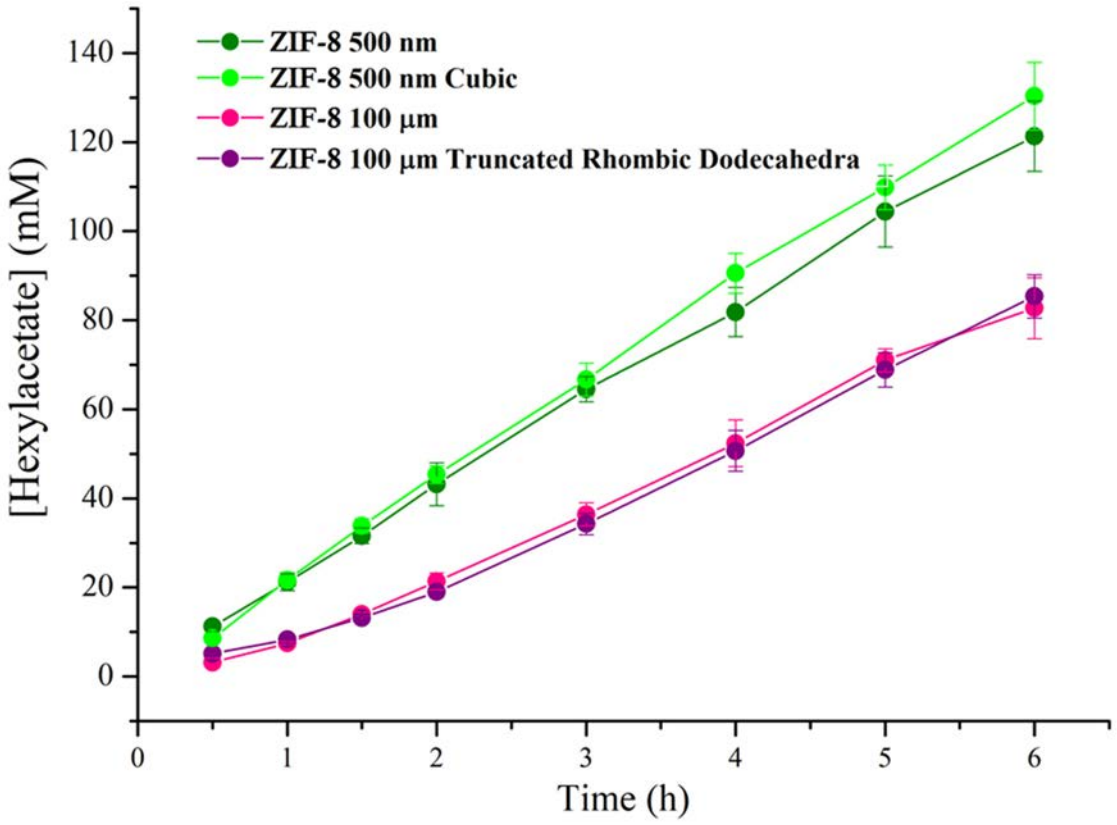

Figure **2.A.7**: Comparison of hexyl acetate production from the transesterification of hexanol with vinyl acetate catalysed by ZIF-8 samples of different morphology under stirring agitation.

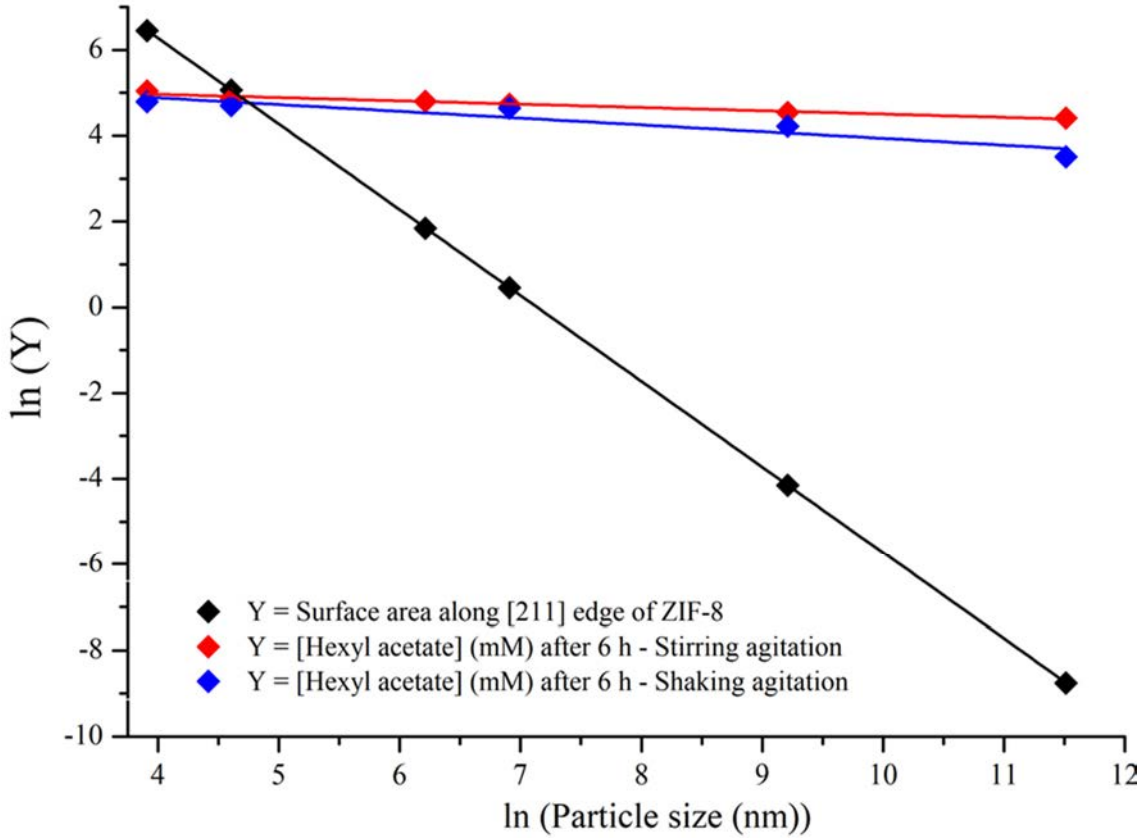

Figure **2.A.8**: Ln/Ln plots of Ln (Y) vs Ln (Particle size (nm)), where Y = the surface area along the [211] edge (assuming a width of 0.1 nm) of rhombic dodecahedra ZIF-8 (black) (these values were calculated as shown in Appendix **2.9.5**), Y = [Hexyl acetate] (mM) after 6 h with stirring agitation (red) and Y = [Hexyl acetate] (mM) after 6 h with shaking agitation (blue).

Table **2.A.2**: Values for the line of best fit plots for Figure **2.A.8** to the equation $y = a + b \times x$ for the ln/ln plot.

Y	Intercept (a)	Std. Error in Intercept	Slope (b)	Std. Error in slope	R^2
Surface area	14.2752	1.73027E-14	-2.0000	2.29776E-15	1.00000
[Hexyl acetate] mM: Stirring	5.2728	0.0593	-0.0768	0.0079	0.94941
[Hexyl acetate] mM: Shaking	5.5144	0.2482	-0.1577	0.0319	0.85381

*2.9.5. Calculations for Figure **2.A.8***

The catalytically active surface area for 20 mg of ZIF-8 (along the [211] edge, assuming an edge thickness of 0.1 nm) was calculated as follows. The crystal size was assigned as the midsphere of the rhombic dodecahedra crystals (d) and the radius of the midsphere ($r = d/2$) was then used to determine the side length of the crystal (l, where $l = \frac{\left(\frac{3r}{2}\right)}{2\sqrt{2}}$). The surface area along the edges corresponding to the [211] plane in one crystal of ZIF-8 assuming a thickness of 0.1 nm (SA_{edge}) was determined by multiplying the edge length (l) by 0.1 nm. Rhombic dodecahedra have 24 edges that correspond to the [211] plane, therefore SA_{edge} was multiplied by 24 to give the catalytically active surface area for 1 crystal ($SA_{all\ edges}$). The mass of one crystallite was calculated by multiplying the volume of one crystal (given by $\frac{16\sqrt{3}}{9}l^3$) by the bulk density of ZIF-8 (0.35 g/cm^3). The number of crystallites in a 20 mg sample of ZIF-8 (N) was determined by dividing 20 mg by the mass of one crystallite. The catalytically active surface area for a 20 mg sample of ZIF-8 (SA_{active}) could then be determined by multiplying N by $SA_{all\ edges}$. Figure S8 was then generated by plotting ln (SA_{active} (cm^2)) vs ln (Particle size (nm)).

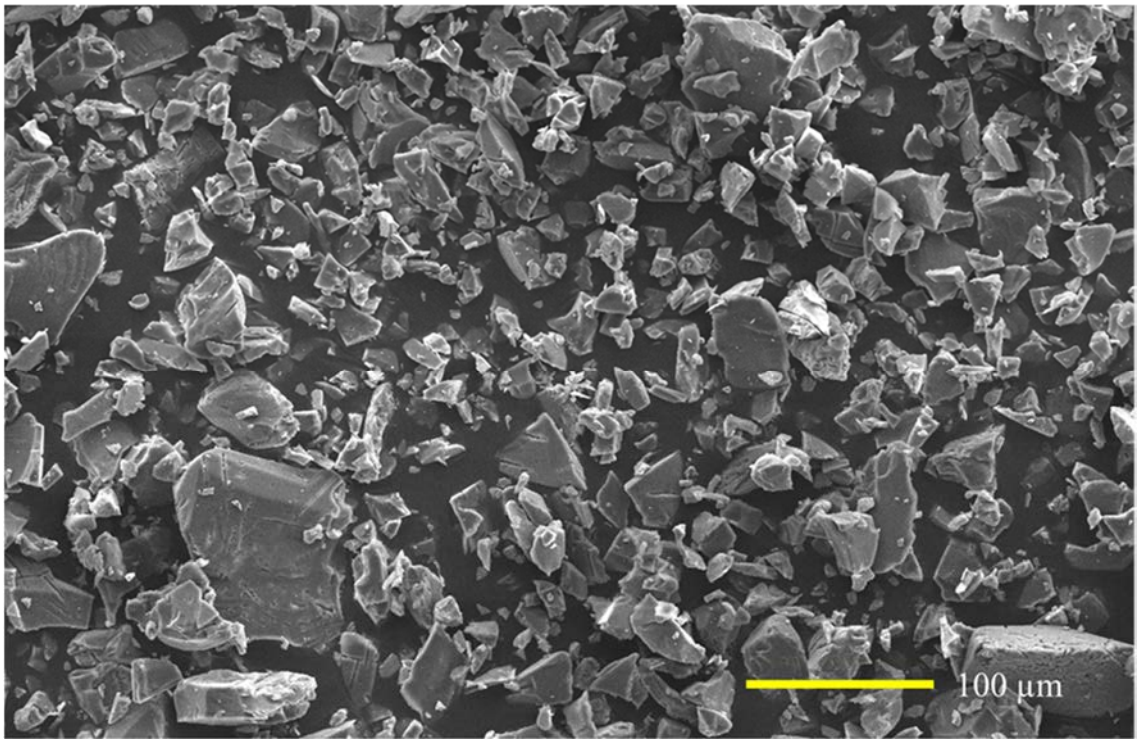

Figure **2.A.9**: SEM image of **ZIF-8 100 µm** post-catalysis for the transesterification of hexanol with vinylacetate at 65 °C, demonstrating mechanical degradation of crystals arising from stirring.

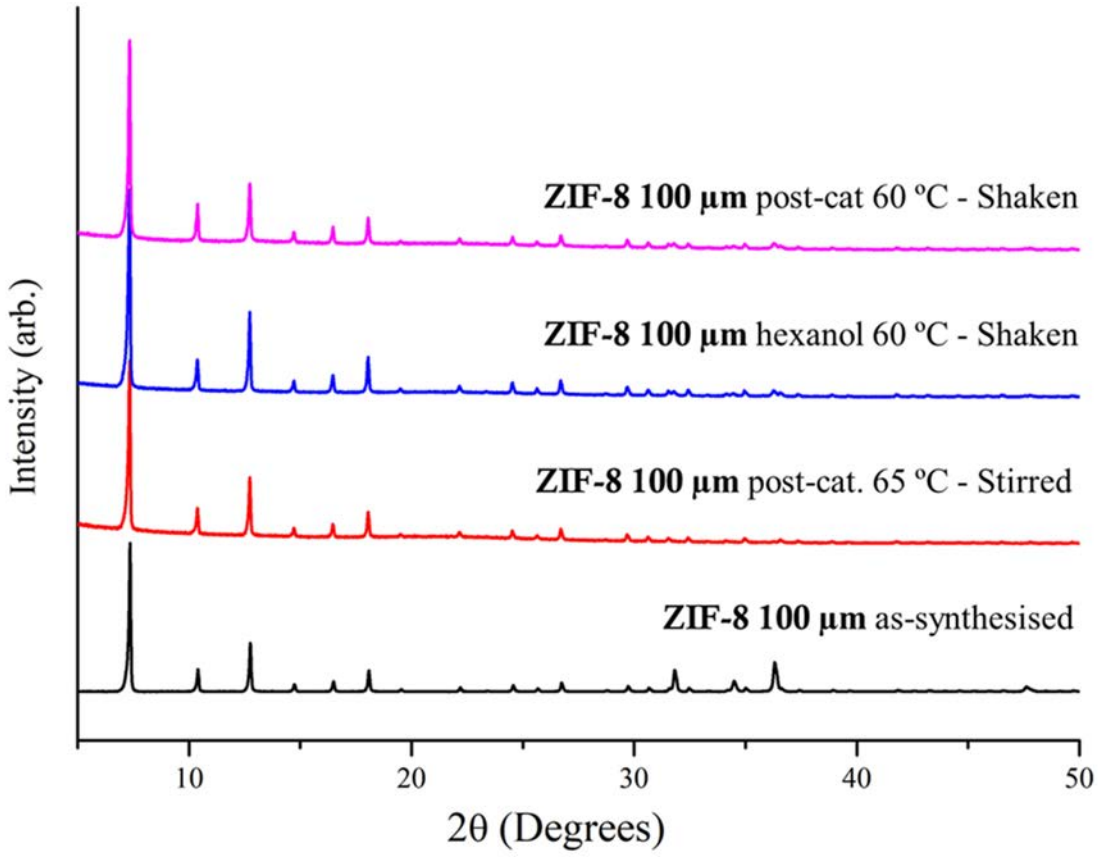

Figure **2.A.10**: Powder X-ray diffraction patterns of **ZIF-8 100 µm**; as-synthesised, post-catalysis at 65 °C with stirring agitation, hexanol soaked at 60 °C with shaking agitation and post-catalysis at 60 °C with shaking agitation.

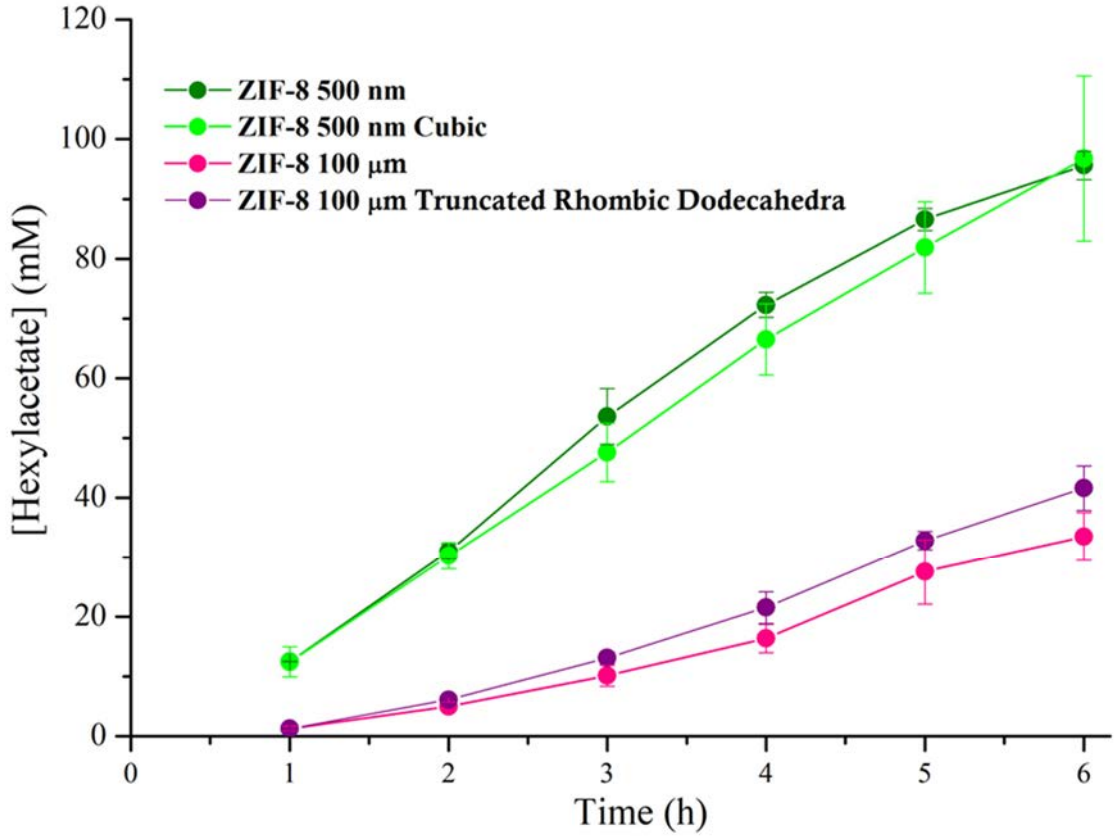

Figure **2.A.11**: Comparison of hexyl acetate production from the transesterification of hexanol with vinyl acetate catalysed by ZIF-8 samples of different morphology under shaking agitation.

2.9.5. Surface etching investigation with SEM, N_2 77 K adsorption, pore size analysis and PXRD analysis of ZIF-8 crystallinity under Knoevenagel condensation conditions.

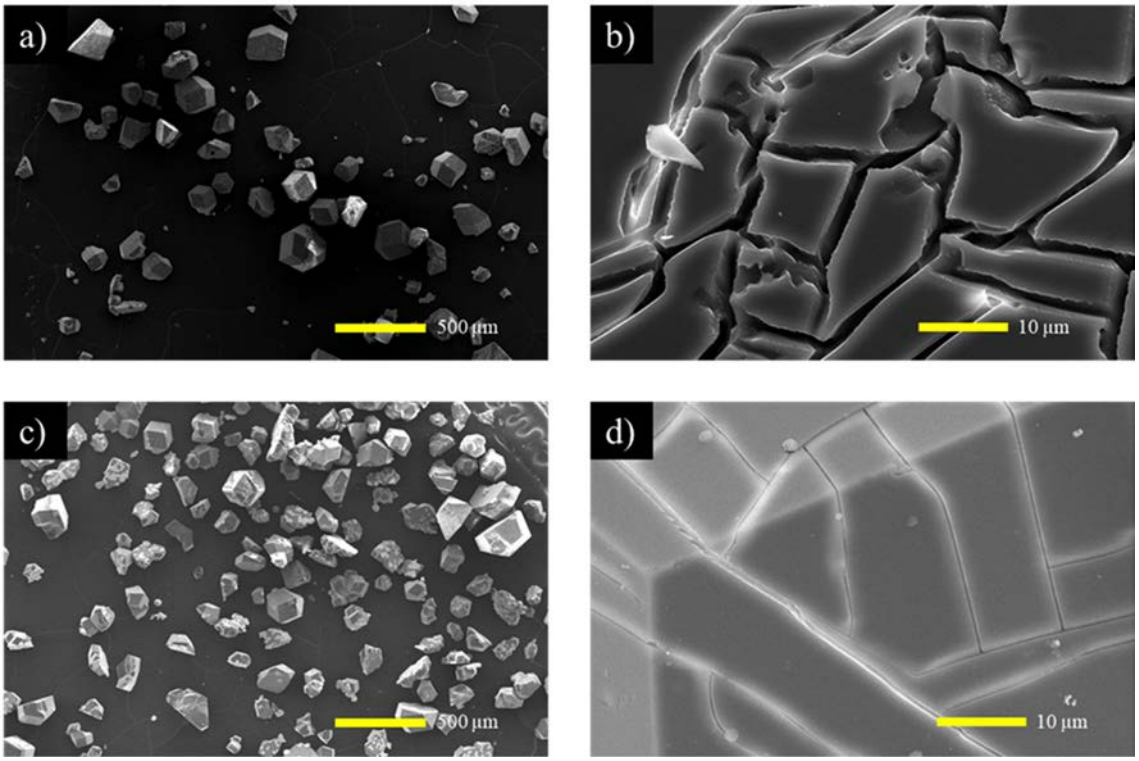

Figure **2.A.12**: SEM images of **ZIF-8 100 µm**, a) & b) post-catalysis at 60 °C with shaking agitation, c) & d) hexanol at 60 °C with shaking agitation, demonstrating increased etching under catalytic conditions.

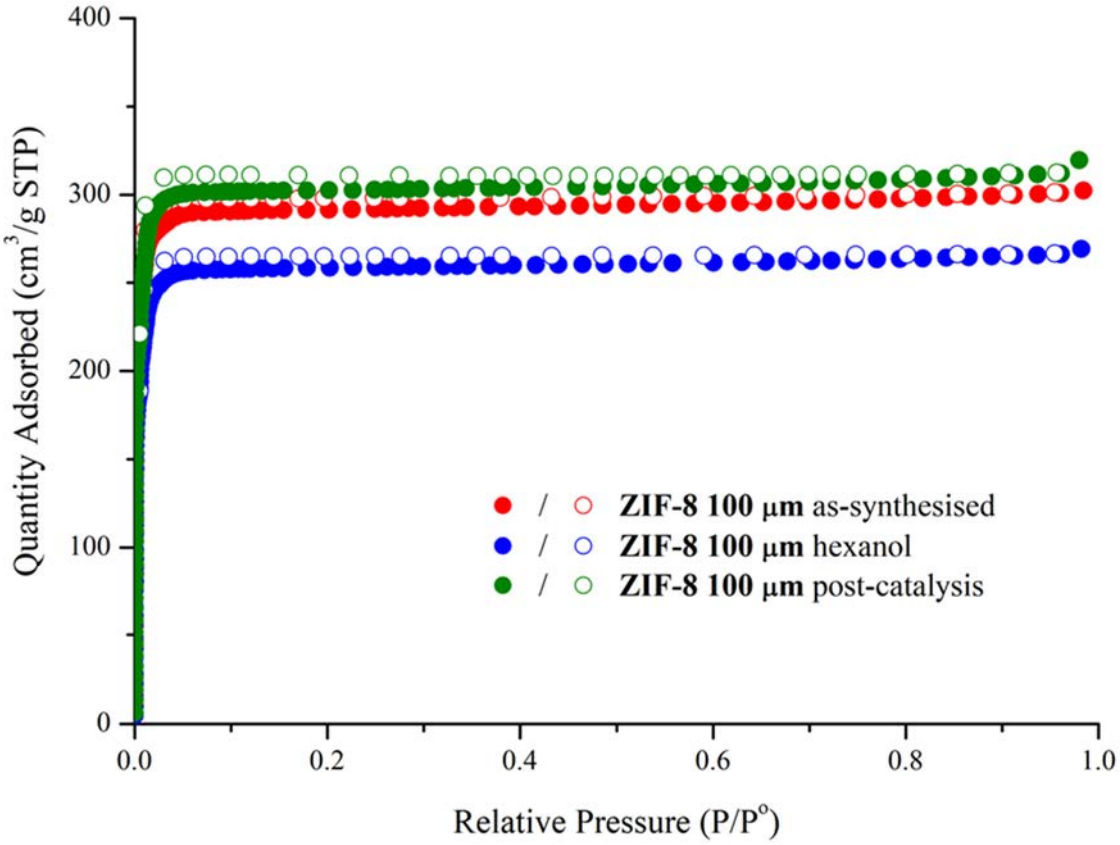

Figure **2.A.13**: N_2 77 K isotherms of **ZIF-8 100 µm** as-synthesised (red), heated in hexanol for 6 h (blue) and post-catalysis (green).

Table **2.A.3**: Brunauer-Emmett-Teller (BET) surface areas of **ZIF-8 100 µm**.

Sample	**BET (m^2/g)**
ZIF-8 100 µm as-synthesised	1164.1143 ± 17.5396
ZIF-8 100 µm hexanol	881.9513 ± 5.7647
ZIF-8 100 µm post-catalysis	1036.0673 ± 8.2199

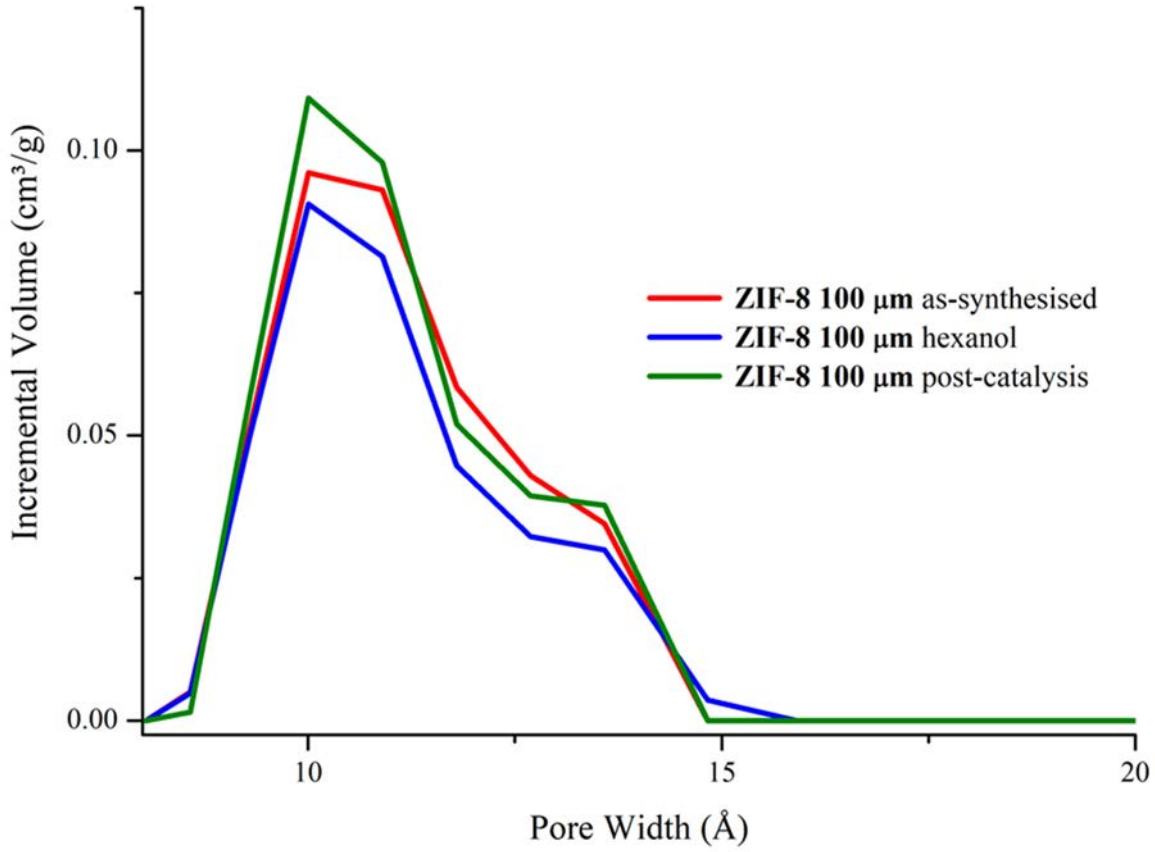

Figure **2.A.14**: Pore size distributions of **ZIF-8 100 µm** as-synthesised (red), heated in hexanol for 6 h (blue) and post-catalysis (green).

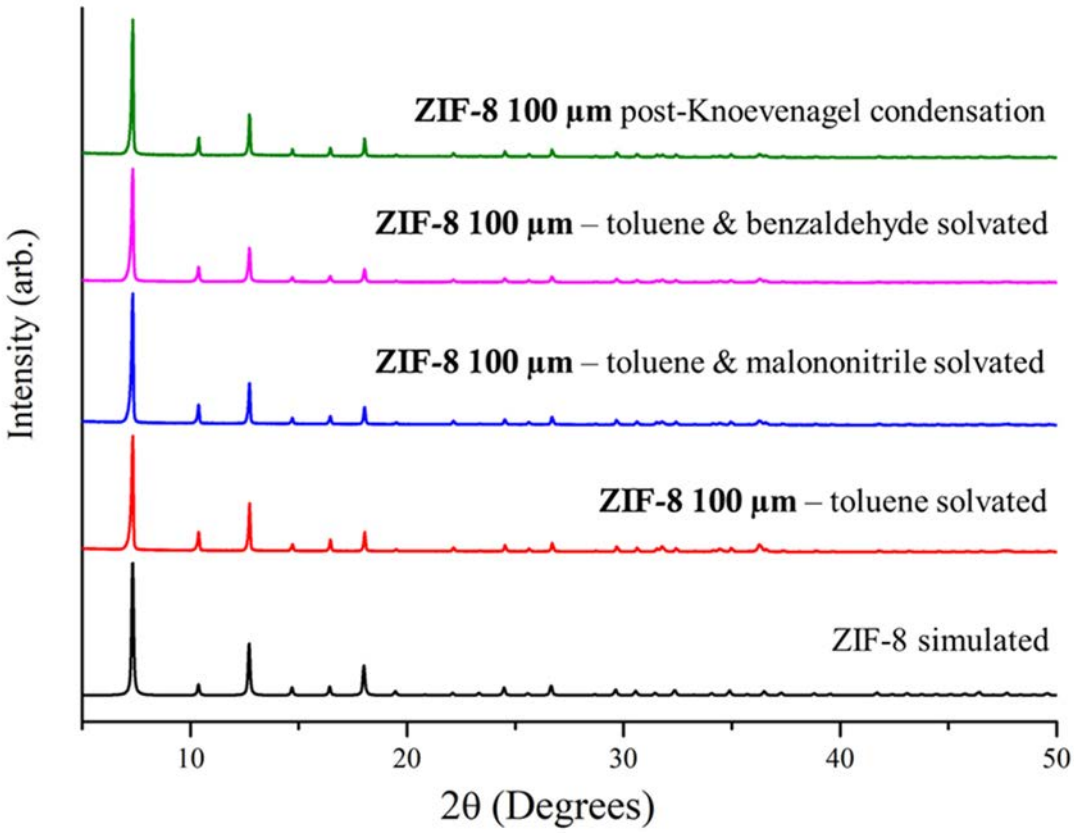

Figure **2.A.15**: Powder X-ray diffraction patterns of **ZIF-8 100 µm**; simulated, toluene solvated 6 h, toluene & malononitrile solvated 6 h, toluene & benzaldehyde solvated 6 h and post-Knoevenagel condensation conditions 6 h.

Appendix 2.9. References

1. Linstrom, P. J.; Mallard, W. G., *NIST Chemistry WebBook*. National Institute of Standards and Technology: Gaithersburg MD, Vol. 20899.

Chapter 3.

Particle Size Effects on Ethylene Hydroformylation with UiO-67-bpydc

Chapter 3. Particle Size Effects on Ethylene Hydroformylation with UiO-67-bpydc

3.1. Introduction

In heterogeneous catalysis, particle shape and size are key features which dictate the activity of a catalyst.[1] From bulk to metal nanocluster catalysts, size impacts catalytic performance, as the surface area increases as particles get smaller,[2] and below certain size regimes quantum effects begin to play an important role.[1, 3-4] Nanoscale structuralisation has also been shown to impact the catalytic performance and stability of surface catalysis with MOFs, specifically ZIF-8, as discussed in Chapter 2.[5] Increasing the surface area of a heterogeneous catalyst, or rather the number of active sites, results in an increased activity, consistent with collision theory.[6] Since MOFs are highly porous materials, reactions can be catalysed at active sites within the MOF crystals as well as at their exterior surfaces.[7] As such, the catalytic performance of MOFs, upon reducing the particle size, is a consequence of several factors working in tandem including; the ratio of internal to external surface area, the path length to the active site and the diffusion rate of guests, as summarised in Figure **3.1**.[5, 8-9] The diffusion path lengths of reactants/products is directly impacted by MOF crystal size, whereby the diffusion rates will not significantly change with particle downsizing, but the diffusion paths will decrease dramatically.[9] Since MOFs can be synthesised with a high degree of control over particle size and internal pore environment,[10-11] the performance of MOF catalysts could be further enhanced through nanoscale structuralisation. As discussed in Chapter 2, despite this potential enhancement of activity, the impact of particle size and active site concentration within MOFs is not well understood, especially with frameworks which feature both internal and external active sites.

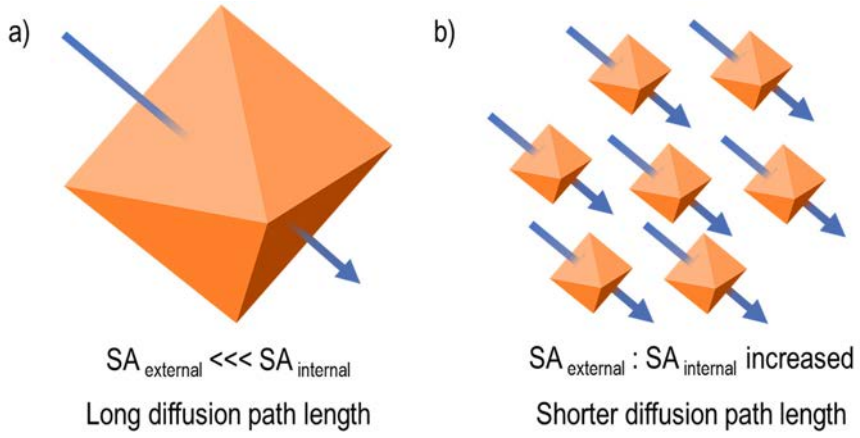

Figure **3.1**: Schematic showing the effect size on external : internal surface area ratio and diffusion pathlength through the framework.

To be utilised in the study on the impact of size/active site concentration on catalytic activity, the MOF candidates must fulfil several criteria:

1. Frameworks must be sufficiently stable to a wide range of reaction conditions (high temperature/ varied solvents).
2. The density/ accessibility of MOF active sites must be easily modulated.
3. The candidate MOF must be synthesisable over a range of crystal sizes, with a high degree of control over the size distribution and crystallinity.

The stability of MOFs lies in both the strength of the metal-ligand bonds between the metal containing secondary building unit (SBU) and organic ligands, and in the connectivity of the framework. SBUs containing high oxidation state transition metals (Zr^{4+} versus Zn^{2+}) have high charge densities at the metal centre and experience significant ligand field stabilization (from the splitting of d-orbitals) upon ligation.[12] These factors make such SBUs less vulnerable to ligand substitution from the resultant increased bond strength. Additionally, higher nuclearity in the metal containing SBU increases the stability of the MOF, as the framework will suffer disproportionally less disconnection if substitution were to occur.[13] As such, MOFs containing highly connected Zr-oxo SBUs, for example UiO-66 (University of Oslo MOF-66), UiO-67 and NU-1000 (Northwestern University MOF-1000), have shown excellent thermal, organic/aqueous solvent, and acid stability.[14-16] All three MOFs are comprised of the 12 connected $Zr_6O_4(OH)_4$ SBU and their respective ligands; 1,4'-benzene dicarboxylic acid (bdc, UiO-66), 4,4'-biphenyl dicarboxylic acid (bpdc, UiO-67) and the larger tetracarboxylic acid,[17] 1,3,6,8-tetrakis(*p*-benzoic acid)pyrene, (TBAPy, NU-1000) see Figure **3.2**.[14]

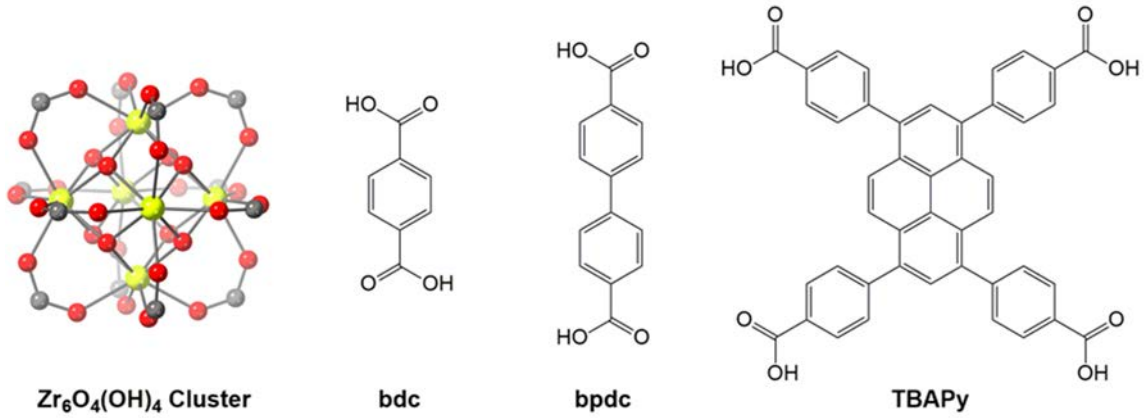

Figure **3.2**: Representations of the Zr-oxo SBU with 12 connected ligands and the ligands of UiO-66 (bdc), UiO-67 (bpdc) and NU-1000 (TBAPy).

Framework stability to catalytic conditions can also be attributed to the location of active sites and needs to be controlled, not only to provide a stable platform, but also to prevent interference from adventitious catalytic sites. Active sites situated at co-ordinately unsaturated sites of the metal SBU, either intrinsic to the framework (e.g. NU-1000),[14] or resulting from ligand defects/terminating coordination environments at the exterior of the MOF crystal (e.g. ZIF-8), could induce ligand substitution and destabilise the framework, see Chapter 2.[5] As such, the MOF selected for this study needs to contain no adventitious active sites for the desired reaction, and should instead be capable of being appended with site isolated molecular catalysts at desired positions throughout the framework, without destabilising the MOF support. To facilitate direct incorporation of molecular catalysts in this manner, the functionality of linker units needs to be able to be altered to allow the MOF to act as a scaffold. For example, the 4,4'-biphenyl dicarboxylic acid (bpdc) UiO-67 linker can be replaced with a bipyridine analogue (2,2'-bipyridyl-5,5'-dicarboxylic acid, bpydc) during MOF synthesis to produce UiO-67-bpydc, which is {, #929} to UiO-67 except it contains sites that are readily metalated.[18] Metalation of a MOF, such as UiO-67-bpydc, can be achieved either pre- or post MOF synthesis to impregnate the framework with molecular catalysts.[19-20] Typically, however, UiO-67-bpydc can chelate transition metals once the MOF scaffold has been formed; this process is described as post-synthetic metalation (PSMet).[19] Metalated MOFs have shown promise as recyclable heterogeneous catalysts, with a wide range of transition metal catalysts available for metalation and consequently allowing access to a broad range of catalytic reactions.[18, 21-23]

The candidate framework UiO-67-bpydc has been investigated previously for a range of liquid phase catalysis reactions, catalysed at site isolated molecular catalysts appended to the framework. Long *et al*. reported single-crystal-to-single-crystal (SC-SC) metalation of UiO-67-bpydc with a range of transition metal complexes including; $CuCl_2$, CuCl, $CoCl_2$, $FeBr_2$, $Cr(CO)_4$ and $[Ir(COD)_2]BF_4$, the latter of which was investigated for catalytic activity in C-H borylation.[21] The density of active sites within UiO-67-bpydc can be controlled through the dilution of the chelating bipyridine ligand (bpydc) with bpdc either during MOF synthesis or post synthetically via solvent-assisted-ligand-exchange (SALE).[18] Cohen *et al.* were able to metalate UiO-67-bpydc with $PdCl_2$ and use the material to catalyse the Suzuki coupling of para-bromotoluene and phenyl-boronic acid, demonstrating that a 50% loading of bpydc into UiO-67 afforded the fastest reaction rates, equivalent to molecular $PdCl_2$ catalysts in solution.[18] Reactant diffusion through the framework is essential for an efficient MOF catalyst, if all the

bipyridyl sites are metalated in UiO-67-bpydc it is possible that pore blockage may occur, stopping larger reactants from passing through the framework. Modular control of active site density within the framework affords control over solvent and reagent diffusion, potentially reducing pore blockage upon PSMet.[18] As such, UiO-67-bpydc is an ideal platform to investigate catalytic reactions which are diffusion reliant.

In addition, the highly modulated synthesis of Zr-MOFs, such as UiO-67-bpydc, enables excellent control over the size, morphology and quality of crystals.[24-25] UiO-67-bpydc has been synthesised over a variety of size regimes through the use of additives such as acetic and benzoic acid, with high ratios of modulators being necessary to produce high quality, mono-dispersed crystals.[17, 26] Diring *et al*. were able to incorporate photoactive moieties ($MnBr(bpydc)(CO)_3$) into UiO-67-bpydc and tune the release of CO, post UV irradiation, by controlling the crystal size from between 260 nm to 1.2 μm of the material.[27] Additionally, synthetic pathways to larger single crystals have been reported, but mono-dispersity is challenging during the synthesis of larger crystals and a microcrystalline powder often co-crystallises.[28] As such, UiO-67-bpydc fits the three aforementioned criteria and was subsequently selected as the framework for the study of particle effects on catalysis with MOFs in this chapter.

The objective of the work described in Chapter 3 was to investigate the impact of crystal size and ligand concentration on catalysis of hydroformylation in the gas phase using UiO-67-bpydc metalated with different reactive rhodium(I) species. This was achieved by synthesising UiO-67-bpydc in a range of different particle sizes and analysing the activity/product distributions for the gas phase hydroformylation reactions catalysed by the MOF materials. The synthesis and characterisation of suitable size regimes of UiO-67-bpydc will be described in the first half of this chapter. The PSMet of these samples with a selection of rhodium(I) catalysts and subsequent hydroformylation reactions will be further discussed in the second half of this chapter.

3.2. Size Control of UiO-67-bpydc

In order to achieve the overall aims of this project it was necessary to first synthesise UiO-67-bpydc over a few discrete size ranges. Ideally, each size regime would differ by one order of magnitude, so that size effects on MOFs catalysis could be more readily observed. As such, the three size ranges around 100 nm, 1 μm and 10 μm were selected as targets for the size control of UiO-67-bpydc. To ensure that the particle size distribution and crystal quality (morphology etc.) of crystals prepared from each of the synthetic conditions were similar, the

samples were examined via scanning electron microscopy (SEM). Once candidates with a narrow particle size distribution and uniform crystal morphology for each of the desired crystal sizes had been identified, the crystallinity was examined via Powder X-ray Diffraction (PXRD) and compared to a simulated pattern of UiO-67-bpydc. The following discussion outlines the screening of synthetic conditions for UiO-67-bpydc at 100 nm, 1 μm and 10 μm and the analysis of candidate samples via SEM and PXRD.

Alkaline conditions have been applied for the synthesis of nano-MOFs (< 1 μm),[29] but have not been widely reported for the synthesis of Zr-MOFs such as UiO-67-bpydc. Adding base to the reaction mixture for MOF synthesis has been shown to deprotonate the carboxylic acid groups, such as those of H_2bpydc, initiating the rapid precipitation of MOFs.[30] The bases examined for the synthesis of nano-scale UiO-67-bpydc included; sodium formate, sodium acetate, sodium hydroxide, triethylamine, n-butylamine and tert-butylamine. These additives were added to a solution of $ZrCl_4$ and H_2bpydc in DMF at room temperature and the reactions were stirred overnight, see experimental section **3.8.2** for further details. The basic additives were added to the solution at a 1:1 ratio of base to ligand, resulting in a 2:1 ratio of carboxylic acid to base, meaning only partial deprotonation could occur. The samples were washed with DMF (× 2) and tetrahydrofuran (×4), and then dried in a desiccator prior to analysis via SEM. Sub-micron crystals formed under all of the trialled basic conditions, but unfortunately none of the conditions yielded uniform crystals in discrete size ranges, see Appendix **3.10.1** Figure **3.A.1**. The rapid nucleation of precipitate under basic conditions resulted in varied particle sizes and inconsistent crystal morphologies, hence none of the conditions tested were suitable for further analysis.

Zr-MOFs are more typically synthesised using acidic additives, which modulate crystal growth by competing at the metal SBU with the ligand in a process described as coordination modulation.[31-32] High equivalents of acidic additives are necessary for the synthesis of high quality crystals of UiO-67-bpydc.[15, 17] It has also been shown that acid modulators are essential in the synthesis of the Zr-oxo cluster, with some Zr-MOFs requiring the pre-formation of the zirconium SBU prior to the addition of the ligand for successful MOF synthesis (NU-1000).[33-35] As mentioned previously, Diring *et al*. demonstrated the synthesis of UiO-67-bpydc at two discrete size regimes using varying equivalents of acetic acid as the modulator, with average particle sizes of 260 nm and 1.2 μm for 30 and 90 equivalents of additive respectively.[27] As such, the solvothermal synthesis of UiO-67-bpydc was examined with acidic additives, glacial acetic acid and benzoic acid, in collaboration with the Furukawa research group in Kyoto.

UiO-67-bpydc was synthesised using 30 equivalents of acetic acid (AA) and benzoic acid (BA), separately, at 120 ºC for 1-4 days to modulate the crystal growth, see experimental section **3.8.2** for further details. The as-synthesised samples were solvent exchanged with DMF (× 2) and tetrahydrofuran (×4, THF), dried and then examined via SEM and PXRD. Synthesis with 30 equivalents of BA produced uniformly distributed octahedral crystals with an average diameter of 1.41 ± 0.05 μm after 1 day, (see Appendix **3.10.1**, Figure **3.A.2**). Longer reaction times resulted in an increase in the average crystal diameter and broader size distributions; 1.79 ± 0.11, 1.85 ± 0.11 and 1.85 ± 0.10 μm for 2, 3 and 4 days respectively, (see Appendix **3.10.1**, Figure **3.A.2**). A similar trend was observed for crystals synthesised using 30 equivalents of AA, although at a smaller size regime. After 1 day rough octahedral crystals with a narrow size distribution of 0.33 ± 0.01 μm were synthesised and again, the average crystal diameter/size distribution increased to 0.38 ± 0.01, 0.51 ± 0.05 and 0.54 ± 0.04 μm after 2, 3 and 4 days respectively, (see Appendix **3.10.1**, Figure **3.A.3**). It must be noted that the quality of crystals was improved over 2-4 days, with the crystal edges becoming more defined. The trends observed indicated initial nucleation within 1 day of synthesis with 30 equivalents of BA/AA, and crystal ripening over longer reaction times. BA has a lower pKa than AA (4.20 and 4.76 respectively) and so competes at the Zr-oxo centre more readily enabling the growth of larger crystals.[36] All of the as-synthesised samples were crystalline and phase pure via PXRD, matching the simulated pattern of UiO-67-bpydc (Appendix **3.10.1**, Figure **3.A.4**). The 1 day synthesis with 30 equivalents of BA satisfied the intermediate size range of approximately 1 μm and will be henceforth denoted $\mathbf{1}_{1\mu m}$. Size modulation with AA was promising, producing narrow size distributions, but did not fit into the target size regime of approximately 100 nm; hence, further screening was attempted at a higher modulator to ligand ratio and under more dilute conditions.

Controlling crystal growth, via coordination modulation, can be further refined by altering the concentration of reagents, thereby reducing the rate of crystal nucleation. The synthesis of UiO-67-bpydc with was attempted by increasing the modulator to ligand ratio by a factor of 4, in tandem with a 3.5 fold reduction in reagent concentration, (see experimental section **3.8.2** for more details). These modifications to the aforementioned AA modulator conditions (1 d, 120 ºC) resulted in the formation of homogeneously dispersed crystals with an average diameter of 47.2 ± 1.1 nm, as examined via SEM (see Appendix **3.10.1**, Figure **3.A.5**). The reproducibility of these reaction conditions was examined by altering the reaction vessel from a Teflon lined vial to a glass Wheaton vial, which resulted in an increase in average crystal

diameter to 124.7 ± 7.5 nm, (see Appendix **3.10.1**, Figure **3.A.6**). The crystals synthesised in glass vials had better definition of crystal edges, and these conditions were easily reproducible. MOF samples synthesised with 120 eq. of AA for 1 day, were highly crystalline, matching the simulated powder pattern of UiO-67-bpydc (see Appendix **3.10.1**, Figure **3.A.7**). As such, crystals synthesised under these conditions were ideal as the smallest size regime (approximately 100 nm) and will be denoted $\mathbf{1}_{100\ nm}$.

Ligand solubility can directly impact the rate of MOF formation.[37] The better the MOF components are solubilised, the better the quality of MOF crystals, because there are fewer sites of nucleation in solution and hence crystals can grow slower and bigger. In collaboration with the Furukawa group, conditions to synthesize larger UiO-67-bpydc crystals were investigated using a better solvent for H_2bpydc; dimethylacetamide (DMA). Since 30 eq. of BA was shown to yield highly crystalline MOF crystals at 1-2 μm crystal diameters, BA was selected to modulate MOF synthesis in DMA. The conditions initially tested included variations from $\mathbf{1}_{1\mu m}$; a two-fold increase in component concentration and, increasing the reaction temperature and time to 140 ºC and 72 hours respectively (see experimental section **3.8.2** for further details). These conditions yielded large octahedral crystals on the sides of the glass vials and a mixture of polycrystalline material at the bottom of the vial. The polycrystalline material was removed from the vial before the octahedral crystals were washed from the sides of the glass vials. These crystals were handled in a similar manner as $\mathbf{1}_{100nm}$ and $\mathbf{1}_{1\mu m}$ prior to analysis via SEM and PXRD, being washed with DMA (× 2) and THF (× 4) and then dried. SEM analysis of the sample revealed an average crystal diameter of 11.9 ± 0.4 μm for the large octahedral crystals and the presence of a smaller co-precipitate, which could be removed through successive washing steps, as discussed above (see Appendix **3.10.1**, Figure **3.A.8**). The crystallinity of the sample was examined by PXRD and, was found to match the simulated powder pattern of UiO-67-bpydc (see Appendix **3.10.1**, Figure **3.A.9**). The modified synthetic conditions of $\mathbf{1}_{1\mu m}$ afforded crystals with a diameter > 10 μm, satisfying the largest desired size regime and henceforth will be denoted as $\mathbf{1}_{10\mu m}$. The three size regimes $\mathbf{1}_{100nm}$, $\mathbf{1}_{1\mu m}$ and $\mathbf{1}_{10\mu m}$, as seen in Figure **3.3**, were utilised to investigate the impact of crystal size on gas phase catalysis with MOFs.

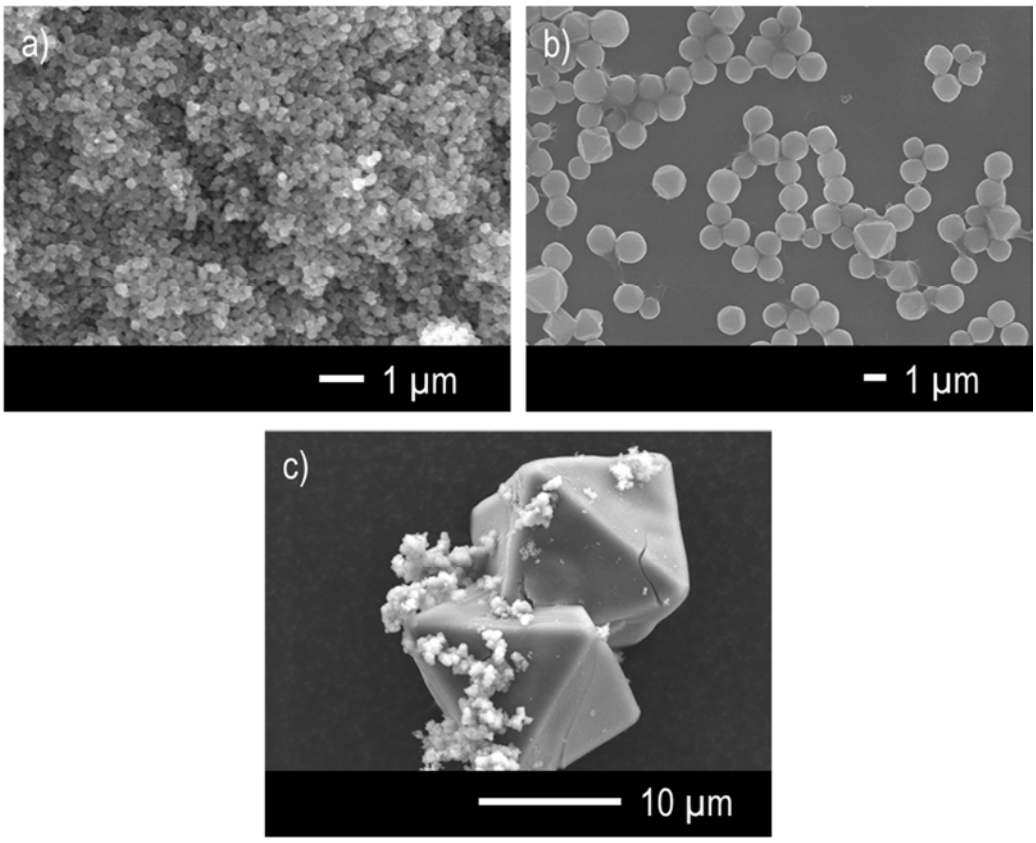

Figure **3.3**: SEM images of a) $\mathbf{1}_{100nm}$, b) $\mathbf{1}_{1\mu m}$ and c) $\mathbf{1}_{10\mu m}$ which have average crystal diameters of 124.7 ± 7.5 nm, 1.41 ± 0.05 µm and 11.9 ± 0.4 µm, respectively.

The porosity and internal surface areas of $\mathbf{1}_{100nm}$, $\mathbf{1}_{1\mu m}$ and $\mathbf{1}_{10\mu m}$ were examined prior to metalation/catalysis, to determine whether the crystal size of UiO-67-bpydc would influence the permanent porosity of the MOF. N_2 77 K adsorption isotherms were collected on all three samples, post-activation from THF (see experimental section **3.8**). The isotherms for all three samples exhibited Type 1 characteristics, demonstrating high N_2 uptake at low partial pressures which is indicative of microporosity (see Figure **3.4**).[38] The total uptake of N_2 increased slightly from $\mathbf{1}_{100nm}$ to $\mathbf{1}_{1\mu m}$, while $\mathbf{1}_{10\mu m}$ remained similar to $\mathbf{1}_{1\mu m}$, with the corresponding Brunauer-Emmett-Teller (BET) surface areas of 2490 ± 37, 2641 ± 3 and 2593 ± 7 m^2/g (see Figure **3.4**). Similarly, the pore-size distribution (calculated via DFT N_2 model) did not vary significantly for the different crystal sizes in Figure **3.4**, indicating that permanent porosity and pore structure is retained for UiO-67-bpydc when synthesised at 100 nm, 1 µm and 10 µm size regimes.

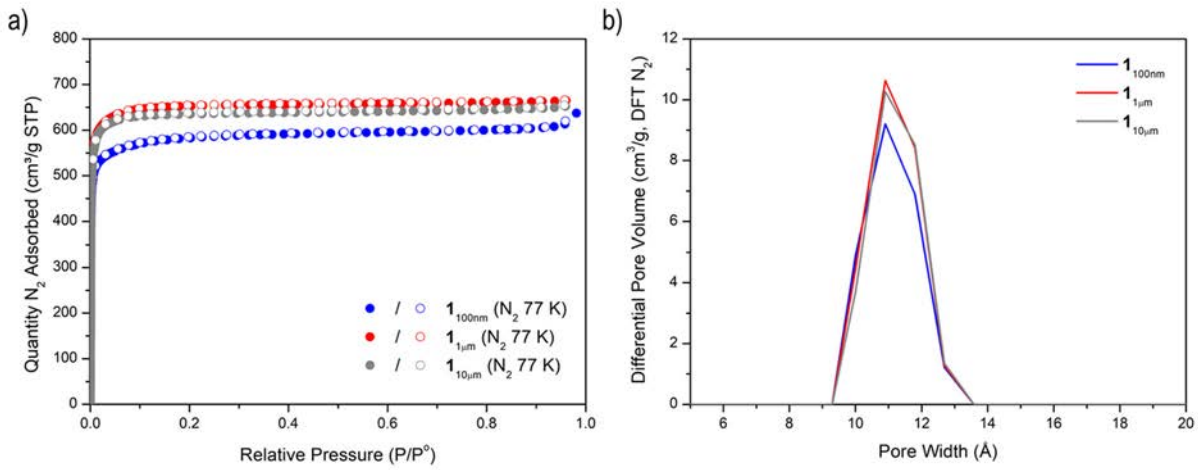

Figure **3.4**: a) N_2 77 K sorption isotherms and b) pore-size distributions for $\mathbf{1}_{100nm}$, $\mathbf{1}_{1\mu m}$ and $\mathbf{1}_{10\mu m}$ plotted in red, blue, and grey, respectively.

3.3. Mixed Linker Synthesis of UiO-67

Non-metalated UiO-67-bpydc has an average pore diameter of 11.5 Å, but metalation of the N-donor sites of the ligand can significantly reduce the porosity of the metalated material and can lead to limited substrate diffusion during catalysis.[18] Additionally, over metalation could further reduce available pore space, as shown by Gonzalez *et al.*, who recently reported the formation of metal halide sheets within the pores of UiO-67-bpydc, albeit, under extended metalation times of 1 month.[39] Hence, it was necessary to find a crystal engineering solution to minimise potential pore blockage upon post-synthetic metalation (PSMet) of $\mathbf{1}_{100nm}$, $\mathbf{1}_{1\mu m}$, and $\mathbf{1}_{10\mu m}$ with the desired metal catalyst. UiO-67 can be synthesised using a mixture of ligands to control the concentration of H_2bpydc by diluting it within the framework with a non-chelating ligand H_2bpdc. Control over the concentration of chelating sites affords direct control over the extent of metalation and consequently enables modulation of active site concentration and the capacity to minimise pore-blockage upon PSMet. Cohen *et al*. demonstrated excellent control over the concentration of H_2bpydc within UiO-67 by varying the ratio of H_2bpydc to H_2bpdc in the precursor solutions used for direct solvothermal MOF synthesis.[18] Overall, ligand concentration was examined via ^{1}H NMR spectroscopy post-acid digestion in DMSO (hydrofluoric acid, HF), which revealed that Cohen *et al.* were able to synthesise UiO-67 with H_2bpydc loadings of 0, 25, 50, 75 and 100 % without a reduction in crystallinity.[18] Using the protocols developed by Cohen *et al.* mixed linker synthesis of UiO-67 was attempted for $\mathbf{1}_{100nm}$, $\mathbf{1}_{1\mu m}$ and $\mathbf{1}_{10\mu m}$ in order to minimise potential pore blockage upon PSMet.

Direct solvothermal mixed ligand synthesis of UiO-67-bpydc$_x$-bpdc$_{6-x}$ has the potential to impact the crystal size under the previously optimised conditions for **1**$_{100nm}$, **1**$_{1\mu m}$ and **1**$_{10\mu m}$, because the two ligands have different solubilities in DMF and DMA. H$_2$bpdc is significantly more soluble than H$_2$bpydc in both DMF and DMA, which could result in the formation of larger crystals at high loading of H$_2$bpdc in the precursor solution. The size distribution of all samples synthesised via mixed ligand synthesis was checked using SEM. The crystallinity of all samples was monitored via PXRD and the ligand incorporation was determined via ^{1}H NMR spectroscopy. Prior to analysis by ^{1}H NMR spectroscopy analysis samples needed to be digested under acidic conditions, HF is commonly used acid for such digestions, but due to its toxicity and safety concerns, alternate acidic conditions were pursued. In our research group acidic digestion conditions using DCl/DMSO$_{d6}$ had been shown to effectively digest Zr-based MOFs such as NU-1000 and UiO-67 enabling defect analysis via ^{1}H NMR spectroscopy, and were subsequently adopted for this work, (see experimental **3.8** for more details).[40-41] SEM, PXRD and ^{1}H NMR spectroscopic techniques were used in tandem to determine the quality of samples of **1**$_{100nm}$, **1**$_{1\mu m}$ and **1**$_{10\mu m}$ synthesised via mixed ligand synthesis. The notation for H$_2$bpydc inclusion into **1**$_{100nm}$, **1**$_{1\mu m}$ and **1**$_{10\mu m}$ will be based on the feed percentage within the sample, i.e. **1**$_{100nm}$-50% and **1**$_{100nm}$-100% would indicate samples synthesised using the conditions for **1**$_{100nm}$ using feed stocks featuring 1:1 and 1:0 ratios of H$_2$bpydc to H$_2$bpdc.

Mixed ligand synthesis of UiO-67 under the aforementioned solvothermal conditions for the synthesis of **1**$_{100nm}$, **1**$_{1\mu m}$ and **1**$_{10\mu m}$, was attempted by altering the feed stock ligand ratio (H$_2$bpydc:H$_2$bpdc). Other than the ligand ratio, the reaction conditions were not altered in any other way; 25, 50, 75 and 100 % H$_2$bpydc reaction mixtures were used tested for **1**$_{100nm}$ and **1**$_{1\mu m}$, and 50/100% H$_2$bpydc reaction mixtures were used for **1**$_{10\mu m}$. The ligand loading in the synthesised samples was determined, as a percentage relative to H$_2$bpdc in the digested sample, via ^{1}H NMR spectroscopy, (see Table **3.1**). Exemplar ^{1}H NMR spectra for **1**$_{100nm}$-25% to **1**$_{100nm}$-100%, are displayed in Figure **3.5** and demonstrate the incorporation of H$_2$bpydc into the framework. The ligand loading for **1**$_{1\mu m}$ and **1**$_{10\mu m}$ samples are summarised in Table **3.1**, and the corresponding spectra are plotted in Figure **3.A.10**, Appendix **3.10.2**. The ligand loading correlates to the H$_2$bpydc % in the reaction mixture for all samples except **1**$_{100nm}$-25% and **1**$_{100nm}$-75%, which had loadings of 36.5 and 88.8% respectively. As such, for PSMet/catalysis only samples of 50/100% H$_2$bpydc loadings will be tested for all three size regimes, additionally PSMet of **1**$_{1\mu m}$-25% to **1**$_{1\mu m}$-100% will be analysed due to the excellent ligand loading control achieved.

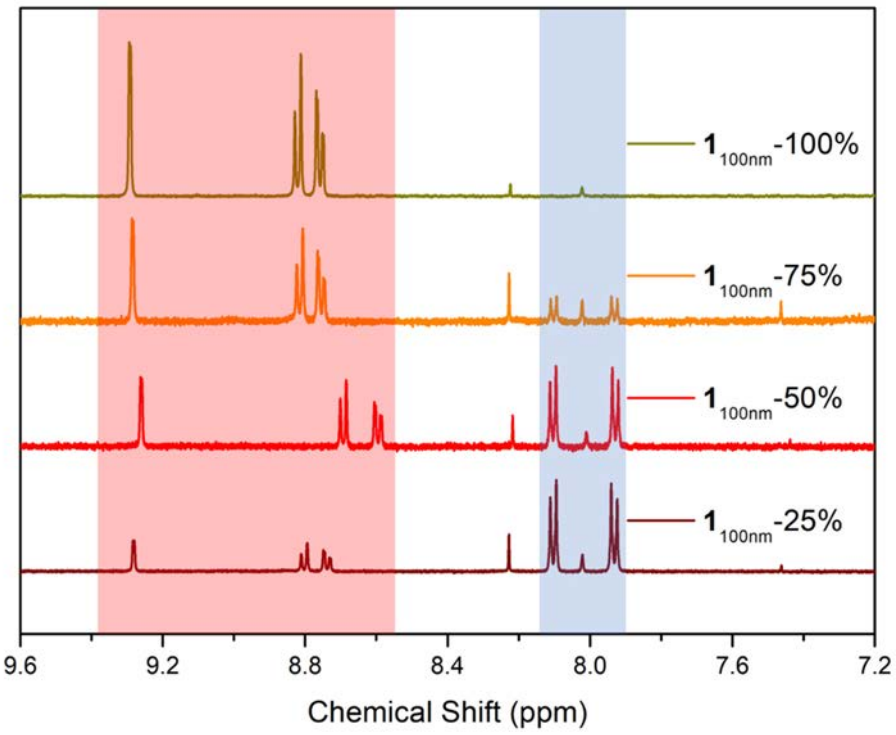

Figure **3.5**: ^{1}H NMR spectra of DCl/DMSO$_{d6}$ digested samples of UiO-67 with varied H$_2$bpydc loadings synthesised under solvothermal conditions (**1**$_{100nm}$); 25%, 50%, 75% and 100%. The chemical shifts for ligands H$_2$bpydc and H$_2$bpdc are highlighted in red and blue, respectively. Note the chemical shifts of proton signals of H$_2$bpydc subtly change with acid concentration due to the protonation of the pyridyl nitrogens in the ligand during the DCl/DMSO$_{d6}$ digestion.

Table **3.1**: Ligand incorporation data (^{1}H NMR H_2bpydc:H_2bpdc ratio) and SEM size distribution data for the mixed ligand synthesis of UiO-67 under solvothermal conditions $\mathbf{1}_{100nm}$, $\mathbf{1}_{1\mu m}$ and $\mathbf{1}_{10\mu m}$.

Sample	**% H_2bpydc (reaction mixture)**	**% H_2bpydc (loading in sample; ^{1}H NMR digest)**	**Average Crystal Diameter (SEM)**
$\mathbf{1}_{100nm}$-25%	25	36.5	53.1 ± 2.5 nm
$\mathbf{1}_{100nm}$-50%	50	58.8	65.9 ± 3.6 nm
$\mathbf{1}_{100nm}$-75%	75	88.8	75.3 ± 6.8 nm
$\mathbf{1}_{100nm}$-100%	100	100	124.7 ± 7.5 nm
$\mathbf{1}_{1\mu m}$-25%	25	27.3	1.28 ± 0.06 µm
$\mathbf{1}_{1\mu m}$-50%	50	51.1	1.07 ± 0.04 µm
$\mathbf{1}_{1\mu m}$-75%	75	77.3	0.81 ± 0.02 µm
$\mathbf{1}_{1\mu m}$-100%	100	100	0.73 ± 0.02 µm
$\mathbf{1}_{10\mu m}$-50%	50	55.4	21.8 ± 0.5 µm
$\mathbf{1}_{10\mu m}$-100%	100	100	11.9 ± 0.4 µm

The average crystal size and morphology of mixed ligand samples of $\mathbf{1}_{100nm}$, $\mathbf{1}_{1\mu m}$ and $\mathbf{1}_{10\mu m}$ were analysed by SEM, as summarised in Table **3.1**. The varied ligand loading impacted the average crystal diameter in interesting ways depending upon the synthesis conditions (see Table **3.1**, Figures **3.6**, **3.A.11** and **3.A.12**). When AA was used as a modulator (1_{100nm}) the average crystal size increased with a higher loading of H_2bpydc (see Table **3.1** and Figure **3.6**), whereas under synthetic conditions where BA was utilised ($1_{1\mu m}$ and $1_{10\mu m}$) the average crystal diameter decreased with high H_2bpydc loadings. Note that all of the reactions were conducted in identical 20 ml glass Wheaton vials, as such the average crystal diameter of $1_{1\mu m}$-100% is smaller than previously discussed because the previous sample was synthesised in a Teflon-lined vial. The trends in crystal size are due to two competing factors, ligand solubility and

solution concentration. H_2bpdc is much more soluble than H_2bpydc in both DMF and DMA, hence the nucleation of crystals is dictated by the loading of H_2bpydc in relatively high ligand concentration synthesis conditions, 10.5 and 20 μM for $1_{1\mu m}$ and $1_{10\mu m}$ respectively. Poor ligand solubility leads to faster crystal nucleation as undissolved ligand in the reaction mixture acts as nucleation sites, leading the more rapid growth of crystals and hence smaller crystals on average. As such, reducing the loading of H_2bpydc in solution leads to the formation of larger crystals (25-75% loading vs. 100% loading). Interestingly, the same trend is not observed for 1_{100nm} which is synthesised under much more dilute conditions, with a lower overall ligand concentration of 3 μM. At this low concentration both ligands dissolve completely in DMF, and so the rate of MOF formation is dictated by the acid dissociation constants of the ligands. The pKa_1/pKa_2 values of the carboxylic acid groups of H_2bpydc and H_2bpdc are 4.25/9.5 and 3.91/9.02 respectively.[42-43] Since H_2bpdc is more acidic than H_2bpydc, initial MOF formation occurs faster at low loadings of H_2bpydc leading to rapid nucleation of MOF crystals and lower average crystal sizes. PXRD analysis of the mixed ligand samples of $\mathbf{1}_{100nm}$, $\mathbf{1}_{1\mu m}$ and $\mathbf{1}_{10\mu m}$ confirmed their phase purity as they all matched the simulated pattern of UiO-67-bpydc (see Figures **3.7**, **3.A.13** and **3.A.14**).

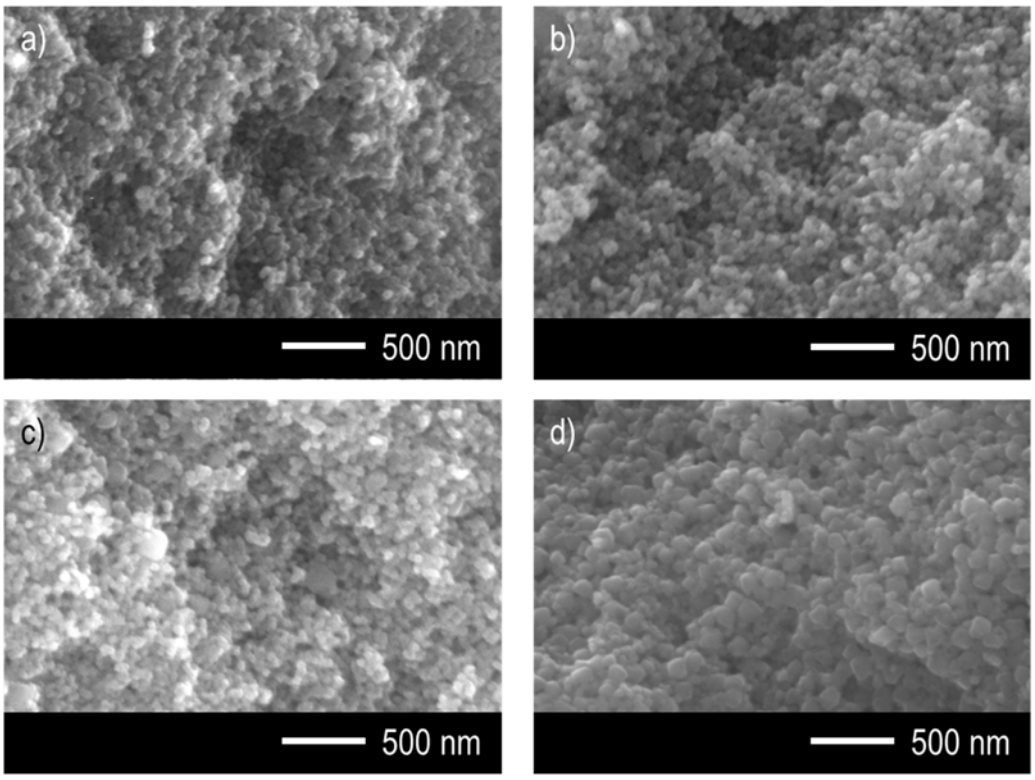

Figure **3.6**: SEM images of a) $\mathbf{1}_{100nm}$-25%, b) $\mathbf{1}_{100nm}$-50%, c) $\mathbf{1}_{100nm}$-75% and d) $\mathbf{1}_{100nm}$-100%.

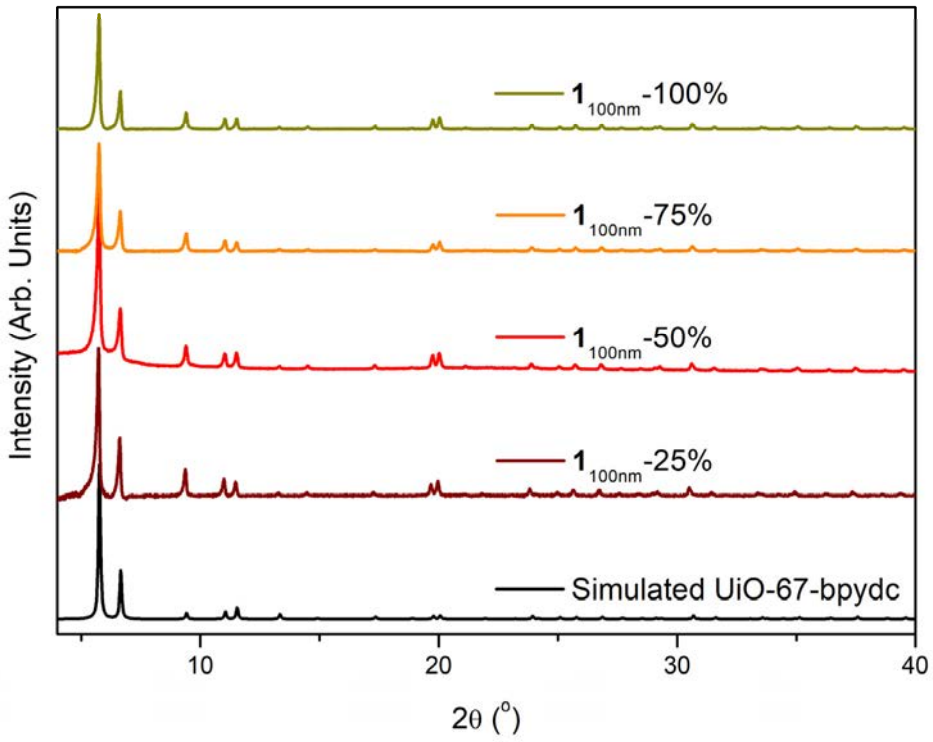

Figure **3.7**: PXRD patterns of UiO-67-bpydc; simulated (black), **1**$_{100nm}$-25% (dark red), **1**$_{100nm}$-50% (red), **1**$_{100nm}$-75% (orange) and **1**$_{100nm}$-100% (dark yellow).

In this section the synthesis and characterisation of UiO-67-bpydc at three different size regimes, **1**$_{100nm}$, **1**$_{1\mu m}$ and **1**$_{10\mu m}$, was discussed. Additionally, the synthesis of mixed ligand UiO-67 with varied loading of H_2bpydc for each size regime was described, with these samples enabling control over active site concentration - but not location - within the MOF samples. As such, samples synthesised at the three size regimes, with varied ligand loadings, were used to investigate the impact of crystal size/active site dilution on the catalytic activity of catalysts for gas phase hydroformylation of ethylene.

3.4. Background on Hydroformylation Catalysis

In order to evaluate the impact of particle size on the catalytic activity of MOFs without pore blockage, a simple small molecule reaction needed to be investigated. Solid-gas phase reactions present an opportunity to study heterogeneous catalysis of small molecule reactions with MOFs.[44] Hydroformylation is one such reaction which is widely used in the petrochemical, fragrance, and food industries.[45-46] The hydroformylation reaction involves the addition of a formyl group to an alkene moiety, which is typically a metal catalysed addition of CO and H_2 to an alkene (see Scheme **3.1**).[46] The conversion of olefins to aldehydes opens

the door to further chemistry, enabling the synthesis of alcohols, esters, hemiacetals, acetals, and carboxylic acids, cementing the importance of the hydroformylation reaction for fine chemical synthesis on an industrial scale.[46] Under hydroformylation reaction conditions, it is possible to form a range of side products; since hydrogen is always present alkenes/aldehydes can be hydrogenated forming alkanes and alcohols (see Scheme **3.1**).[47] Alkene hydrogenation is the more thermodynamically favoured reaction, as such hydroformylation reactions are typically conducted with kinetic control.[47] This kinetic control is commonly achieved by varying the reaction conditions such as, pressure, temperature, increasing reagent concentrations and varying the ratio of reagents ($CO:H_2$ ratio), to promote the kinetic reaction (hydroformylation over hydrogenation),[48-49] which will be further discussed in section **3.6**. Additionally, the alkene substrate can isomerise under catalytic conditions, leading to the production of a mixture of terminal and branched alkenes/aldehydes from tandem isomerisation-hydroformylation.[47, 50] As this reaction can be performed in the gas phase, using volatile alkenes such as ethylene or 1-propene, it represents an ideal reaction to use to investigate solid-gas catalysis with MOFs.

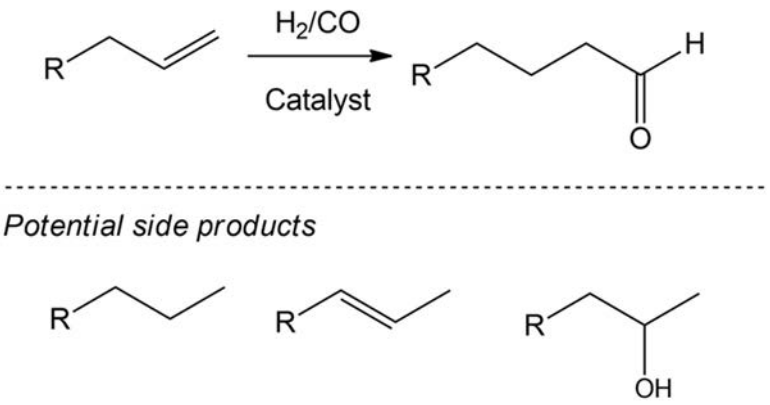

Scheme **3.1**: General reaction scheme of the hydroformylation reaction, converting alkenes into aldehydes, and potential side products (alkanes, isomerisation, and alcohols).

The mechanism for the hydroformylation reaction was originally proposed by Heck and Breslow,[51] and has since undergone refinement since its initial proposal.[52-53] The general mechanism, as displayed in Scheme **3.2**, begins with a rhodium(I)hydride complex (**I**) which is typically formed in situ from a rhodium(I)carbonyl complex upon exposure to hydrogen. Ethylene coordinates at the vacant site of (**I**) to form the common intermediate (**II**), the hydride then migrates to one of the carbon atoms of the coordinated ethylene molecule (**IIa**) leading to the rhodium alkyl species (**III**). Note, migratory hydride insertion on the non-terminal carbon of longer alkenes than ethylene leads to the formation of branched products. CO coordination

(**IV**) and subsequent migration of the alkyl group to the CO (carbonylation), leads to formation of the rhodium acyl species **V**. Oxidative addition of hydrogen can then occur (**VI**) which is followed by reductive elimination to form the aldehyde product and regenerate the catalyst (**I**). It is important to note that all of the steps in this reaction, besides the final step, are equilibria and consequently the regio- and enantioselectivity could be determined by the hydride migration step from intermediate **IIa**.[47] Additionally, oxidative addition of hydrogen to the rhodium alkyl species (**IIIa**) provides an alternate pathway to the formation of alkanes via reductive elimination regenerating the catalyst (**I**) in the process.[49] CO coordination to **III** disfavours paraffin production, hence the catalyst selectivity between the hydrogenation/hydroformylation can be controlled by varying the CO:H_2 ratio.[49] Ethylene was selected as the alkene for this study, in order to conduct the reaction in the gas phase, simplify the possible products formed and remove the possibility of branched products from forming.

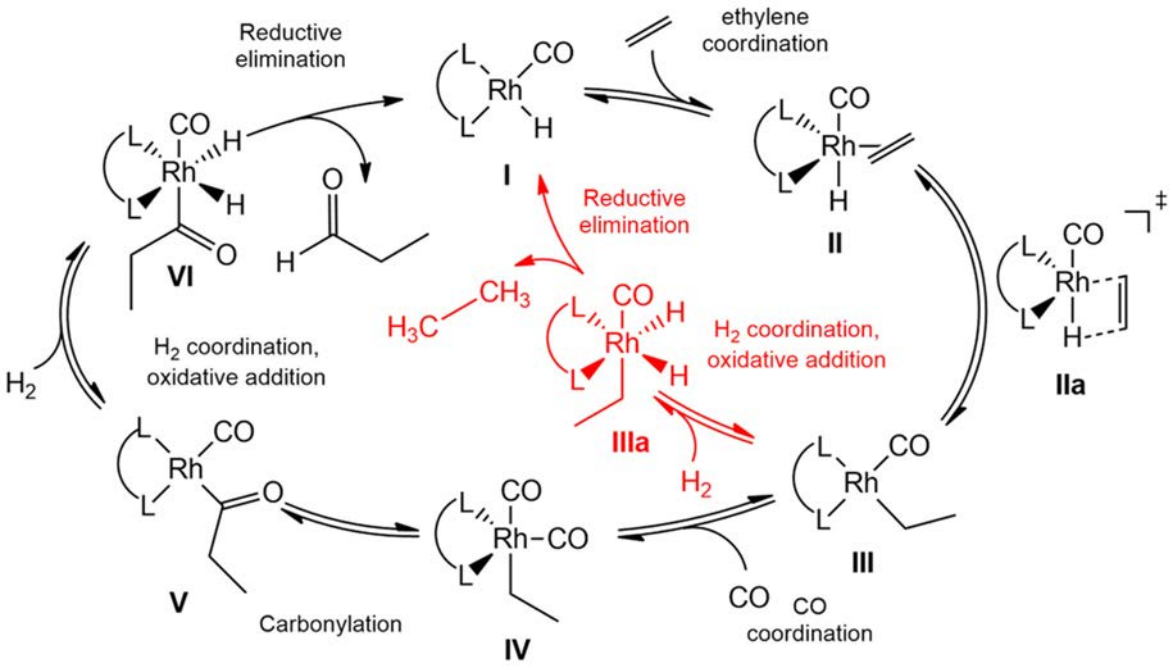

Scheme **3.2**: Mechanism of rhodium-catalysed hydroformylation of ethylene, with the proposed competing hydrogenation reaction highlighted in red.[49]

The hydroformylation reaction is typically catalysed by a homogeneous rhodium complex in industry, but as with most homogeneous reactions this process suffers from poor catalyst recovery.[54] There have been many examples of the heterogenization of these homogeneous catalysts through immobilisation onto a solid support such as alumina,[55] silica,[56-57] micro and meso-porous materials such as zeolites[58-59] and also activated carbons.[60-61] However, the heterogenization is challenging and much of the activity is lost upon

immobilisation.[62] Hence, dispersing the catalyst in a site isolated manner within a porous MOF may improve the activity of the immobilised catalyst, because the high porosity and large pore apertures enable fast mass transport through the framework. Rhodium complexes/nanoparticles have been adsorbed onto MOFs including: MOF-5, IR-MOF-3 and ZIF-8 and subsequently used to catalyse hydroformylation reactions.[54, 63-64] However, in these studies the adsorption of rhodium complexes/nanoparticles onto a MOF scaffold lacked the precision or control over the location/dispersion of active sites that this study necessitates. Homogeneous rhodium catalysts can alternatively be heterogenized with MOFs through their coordination at vacant chelating N-donor bipyridine moieties on the ligands of frameworks, for example with UiO-67-bpydc. Gas phase hydroformylation reactions and the heterogenization of typical homogeneous rhodium catalysts will be further discussed in the next section.

3.5. Metalation of UiO-67-bpydc with Rhodium(I) Species

A general method of preparing a homogeneous rhodium catalyst for hydroformylation reaction involves chelating a rhodium(I)carbonyl complex with an electron donating P-donor ligand, typically triphenylphosphine (PPh_3), under syngas conditions.[45] The stability of the catalyst is improved markedly through the use of a bulky bi-dentate P-donor ligand, but the pre-catalysts are often difficult to isolate and are required to be synthesised under inert atmospheres.[65] There are limited reports of bidentate N-donor ligands being used to stabilise rhodium(I) complexes for hydroformylation reactions simply because P-donor ligands are more electron donating, resulting in a more active catalyst and are ubiquitously used in the aforementioned industries.[66] As such, this study will also involve screening the PSMet of UiO-67-bpydc with several different rhodium(I) precursors prior to catalysis testing. The rhodium(I) species that were screened are summarised in Figure **3.7**.

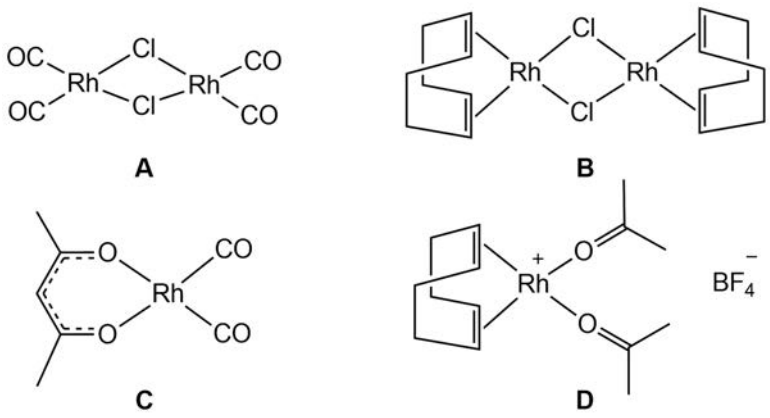

Figure **3.7**: Structures of the rhodium(I) complexes screened for PSMet including $[Rh(CO)_2Cl]_2$ (A), $[RhCODCl]_2$ (B), $[RhCOD(acetone)_2]BF_4$ (C) and $Rh(CO)_2(acac)$ (D).

Initial PSMet studies were conducted with **1**$_{1\mu m}$ and its varied ligand loading variants because **1**$_{1\mu m}$ was the easiest to synthesize reproducibly on a large scale. The rhodium(I) dimer $[Rh(CO)_2Cl]_2$, as seen in Figure **3.7**, was used to probe the accessibility of the chelating sites to simple rhodium(I) dimers. **1**$_{1\mu m}$-25% to **1**$_{1\mu m}$-100% were metalated with $[Rh(CO)_2Cl]_2$ in distilled acetonitrile (MeCN) under an inert atmosphere overnight (see experimental section **3.8**). The maroon coloured micro-crystalline powders were washed with freshly distilled MeCN (×7). The metalated samples were then analysed via SEM/EDX to determine the occupation of the chelating bipyridine moieties within the framework. Since the molecular formula of UiO-67-bpydc is $Zr_6O_4(OH)_4(bpydc)_6$, there is a 1:1 ratio of Zr to bipyridine sites within the framework, at lower ligand loadings this ratio changes accordingly, i.e. **1**$_{1\mu m}$-25% has a 3:1 ratio of Zr to bipyridine sites. Hence, the occupation of bipyridine sites can be determined indirectly by analysing the Rh:Zr ratio via EDX, see Figure **3.8**. In order to maintain charge balance, the rhodium(I) complex likely chelates with the bipyridine units to form a rhodium(I) carbonyl cation, charge balanced with an anionic $[Rh(CO)_2Cl_2]^-$ complex, as proposed in Scheme **3.3**, which is consistent with literature examples with bidentate N-donor ligands.[66-67] Hence, there should be two rhodium atoms per H_2bpydc ligand in UiO-67-bpydc upon PSMet with $[Rh(CO)_2Cl]_2$. At low ligand loadings (27.3 and 51.1%) quantitative metalation occurs, with slightly higher than 200% occupation of the ligand by the rhodium complex, indicating there is space for $[Rh(CO)_2Cl_2]^-$ to sit in the pores of the framework. At higher H_2bpydc ligand loadings (77.2 and 100%) less than quantitative metalation occurs with the % Rh loading dropping to 146 and 163% respectively. The reduction in rhodium incorporation at high ligand loadings in the MOF is indicative of pore blocking, which results in less than quantitative metalation. PSMet with $[Rh(CO)_2Cl]_2$ resulted in no reduction in crystallinity or changes to crystal morphology, as shown by PXRD and SEM analysis (see Appendix **3.10.3**, Figures **3.A.15** and **3.A.16**).

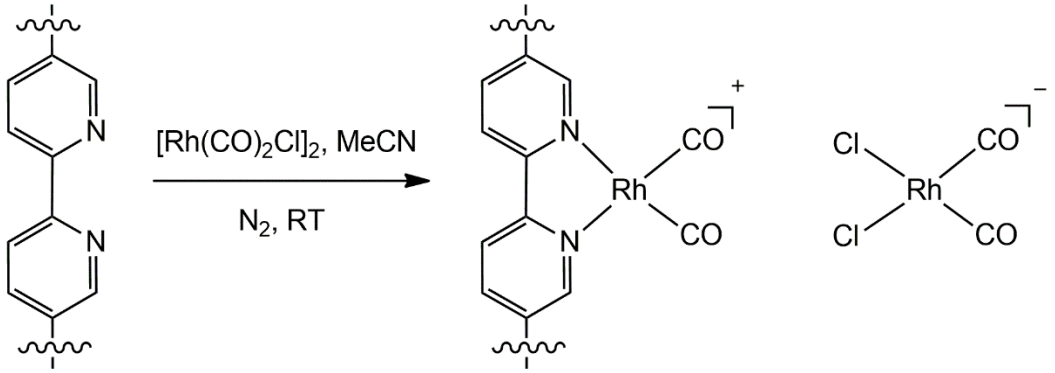

Scheme **3.3**: Reaction of H_2bpydc with $[Rh(CO)_2Cl]_2$ forming $[Rh(bpydc)(CO)_2][Rh(CO)_2Cl_2]$.

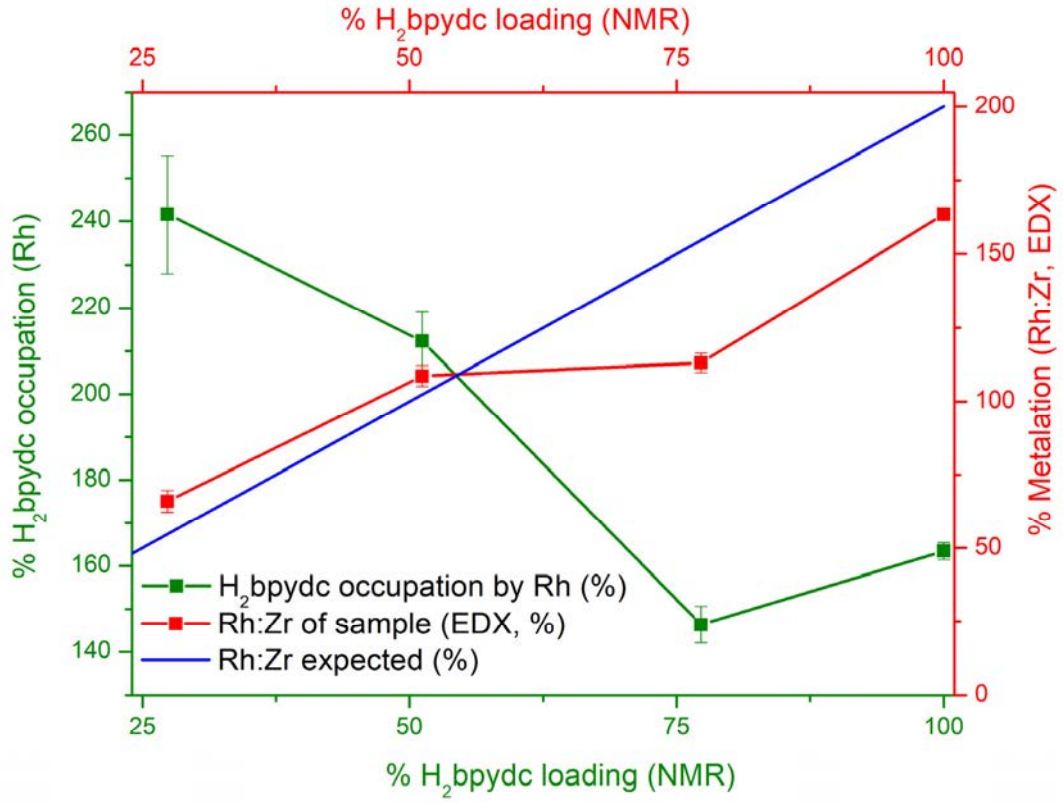

Figure **3.8**: Comparison of the % H_2bpydc loading of $\mathbf{1}_{1\mu m}$ (as determined by ^{1}H NMR, post DCl/$DMSO_{d6}$ digestion) versus the Rh:Zr ratio plotted as % metalation via EDX (red), the % H_2bpydc occupation by rhodium (green). Additionally, the expected Rh:Zr ratio (assuming 200% ligand occupation) is plotted as a blue line.

The structure of the rhodium complex within the framework was further analysed via infrared spectroscopy, see Figure **3.9**. UiO-67-bpydc (MeCN washed) displays no stretches for CO or MeCN, bound or free in the framework, indicating the sample had been appropriately

dried prior to analysis. Samples of **1**$_{1\mu m}$ demonstrated stretches corresponding to coordinated CO, the four characteristic CO stretches are 2099, 2066, 2041 and 1991 cm^{-1}, with higher ligand loadings corresponding to increased intensity of these stretches.[68] Interestingly, at higher ligand loadings there is an increased presence of MeCN, both coordinated and within the pores of the framework. As such, the rhodium complex coordinated to the framework may be more complicated than described in Schematic **3.3**, with either the cationic or anionic rhodium species coordinating MeCN and either becoming five-coordinate or remaining square planar from CO displacement by MeCN. In order to determine the structure of the rhodium complexes single crystal X-ray diffraction (SCXRD) analysis of the material could be conducted. However, at 100% H$_2$bpydc loading, the ligand was not fully occupied with the Rh dimer due to limited pore space for the counter ion, and hence there would likely be significant challenges in solving (and refining) the structure of the metalated framework (see Chapter 5 for a full discussion on the challenges associated with crystallographic analysis of high symmetry structures). As such, no attempt was made to obtain a single crystal X-ray structure of UiO-67-bpydc metalated with [Rh(CO)$_2$Cl]$_2$.

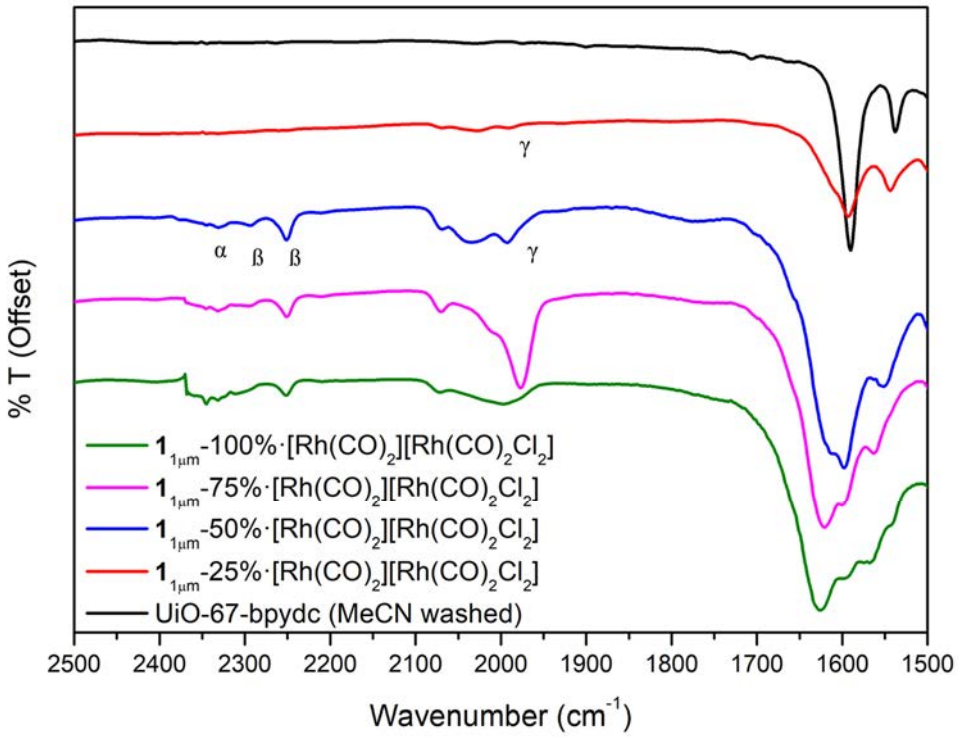

Figure **3.9**: Infrared spectra of UiO-67-bpydc (black), **1**$_{1\mu m}$-25%·[Rh(CO)$_2$][Rh(CO)$_2$Cl$_2$] (red), **1**$_{1\mu m}$-50%·[Rh(CO)$_2$][Rh(CO)$_2$Cl$_2$] (blue), **1**$_{1\mu m}$-75%·[Rh(CO)$_2$][Rh(CO)$_2$Cl$_2$] (pink) and **1**$_{1\mu m}$-100%·[Rh(CO)$_2$][Rh(CO)$_2$Cl$_2$] (green). IR stretches: α) coordinated MeCN, ß) free MeCN and γ) coordinated CO.

Attempts were made to negate the observed pore blockage upon metalation with $[Rh(CO)_2Cl]_2$ by exchanging the rhodium(I) anion with a smaller counter-ion, BF_4^-, and through the use of a bulky rhodium(I) dimer $[Rh(COD)Cl]_2$ (cyclooctadiene: COD). $\mathbf{1}_{1\mu m}$-50% was used for these metalation studies, because quantitative metalation would yield a Rh:Zr ratio of 0.5 (100% ligand occupation), but dimer formation within the pores would result in a Rh:Zr ratio of 1 ("200% ligand occupation"). PSMet of $\mathbf{1}_{1\mu m}$-50% with the rhodium(I) complexes was conducted at room temperature, under an inert atmosphere in distilled MeCN overnight. A 1:4 ratio of $[Rh(CO)_2Cl]_2$ to $NaBF_4$ was used to ensure full anion exchange upon PSMet and $[Rh(COD)Cl]_2$ was used in excess, see experimental section **3.8.2** for more details. The PSMet samples, $\mathbf{1}_{1\mu m}$-50%·$[Rh(CO)_2]BF_4$ and $\mathbf{1}_{1\mu m}$-50%·[Rh(COD)Cl] were washed with distilled MeCN (×7) and the Rh:Zr and Cl:Rh ratios were analysed via SEM/EDX and plotted as a percentage in Figure **3.10** (multiplying the ratio by 100). Additionally, the Rh:Zr ratio was analysed via inductively coupled plasma mass spectrometry (ICP-MS) post acid digest in HNO_3 (see experimental section **3.8.2**). In comparison to $\mathbf{1}_{1\mu m}$-50%·$[Rh(CO)_2][Rh(CO)_2Cl_2]$, $\mathbf{1}_{1\mu m}$-50%·$[Rh(CO)_2]BF_4$ and $\mathbf{1}_{1\mu m}$-50%·[Rh(COD)Cl] demonstrated lower Rh:Zr ratios (EDX); 103.2 ± 4.3, 52.0 ± 2.0 and 51.5 ± 1.4 respectively, with ICP-MS Rh:Zr ratios following a similar trend. The Cl:Rh ratios indicate the presence of a small percentage of the rhodium counter ion persisting for $\mathbf{1}_{1\mu m}$-50%·$[Rh(CO)_2]BF_4$ despite anion exchange with $NaBF_4$. Since this rhodium(I) species was challenging to unambiguously characterise, $\mathbf{1}_{1\mu m}$-50%·$[Rh(CO)_2]BF_4$ was not utilised for catalytic studies. The bulky complex $[Rh(COD)Cl]_2$ demonstrated quantitative metalation of bipyridine sites within $\mathbf{1}_{1\mu m}$-50% and the Cl:Rh ratio (0.93) indicates that the coordinated complex is likely a charge neutral [Rh(bpydc)(COD)Cl] species. The steric bulk of COD directs PSMet with $[Rh(COD)Cl]_2$, disfavouring the formation of the possible $[Rh(bpydc)COD]^+$ $[Rh(COD)Cl_2]^-$ dimer.

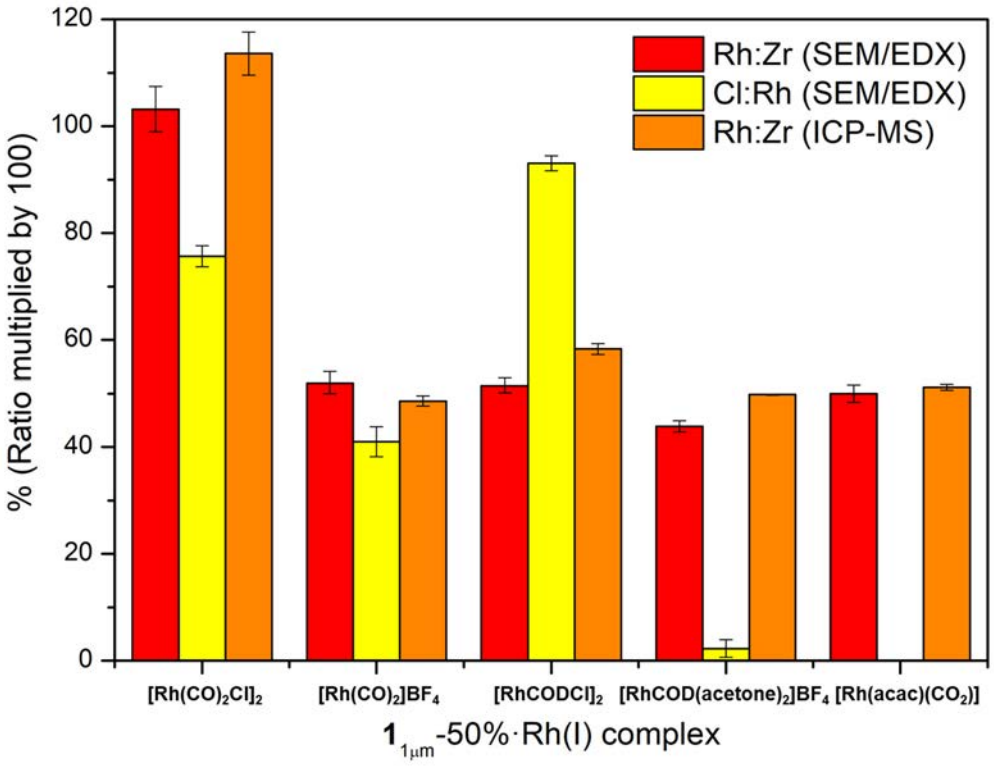

Figure **3.10**: Rh:Zr (SEM/EDX), Cl:Rh (SEM/EDX) and Rh:Zr (ICP-MS) ratios (%, multiplied by 100) of **1**$_{1\mu m}$-50% metalated with rhodium(I) complexes; $[Rh(CO)_2Cl]_2$, $[Rh(CO)_2]BF_4$, $[RhCODCl]_2$, $[RhCOD(acetone)_2]BF_4$ and $[Rh(acac)(CO_2)]$.

The crystallinity of the PSMet samples **1**$_{1\mu m}$-50%·$[Rh(CO)_2]BF_4$ and **1**$_{1\mu m}$-50%·[Rh(COD)Cl] was analysed via PXRD, see Appendix **3.10.3** Figure **3.A.17**. The powder pattern of **1**$_{1\mu m}$-50%·$[Rh(CO)_2]BF_4$ matches the simulated pattern of UiO-67-bpydc indicating retention of long range order upon PSMet. However, the crystallinity of **1**$_{1\mu m}$-50% is significantly reduced upon PSMet with $[Rh(COD)Cl]_2$, with a reduction in peak intensity, peak broadening, and the presence of an amorphous phase. This reduction in long range order could originate from rotational disorder of the ligand and/or from disorder around the rhodium(I) centre potentially resulting from ligand dissociation. COD is a weakly bound ligand of rhodium(I) and could be coordinated in a range of different conformations resulting in a mixture of rhodium(I) species within the framework, thereby reducing long range order. COD lability was examined by bubbling CO through a solvated sample of **1**$_{1\mu m}$-50%·[Rh(COD)Cl] in MeCN and analysing the IR spectra of the resultant complex 10 min, 1 h and 24 h post CO exposure (see Figure **3.11**). Upon exposure to CO the **1**$_{1\mu m}$-50%·[Rh(COD)Cl] darkened in colour, indicative of a change in the rhodium coordination environment and the IR spectra demonstrated the presence of characteristic CO stretches (as discussed earlier). After 1 h of

MeCN solvation, the samples colour lightened and the characteristic CO stretches in the IR spectra were less prevalent and, were absent after 24 h solvation. There appears to be MeCN in the solvated samples, but no coordinated MeCN, indicating the coordination sites of rhodium(I) are already occupied by another species, possibly COD. This experiment demonstrated that the COD co-ligand within **1**$_{1\mu m}$-50%·[Rh(COD)Cl] is weakly bound but can be displaced by CO temporarily, enabling the formation of a transient rhodium(I)carbonyl species, which could be utilised for to catalyse hydroformylation reactions.

In order to broaden the range of catalysts which could be tested, PSMet of **1**$_{1\mu m}$-50% with other rhodium(I) hydroformylation catalyst precursors, [RhCOD(acetone)$_2$]BF$_4$ and [Rh(acac)(CO)$_2$], were also investigated. [RhCOD(acetone)$_2$]BF$_4$ was synthesised from the reaction between [Rh(COD)Cl]$_2$ and AgBF$_4$, which were combined in a 1:2 ratio in acetone at room temperature. Ag(I) abstracts Cl^- from the rhodium dimer and a precipitate of AgCl is formed which must be removed prior to metalation. PSMet of **1**$_{1\mu m}$-50% is then conducted in acetone with the as-synthesised [RhCOD(acetone)$_2$]BF$_4$ at room temperature (see experimental **3.8.2**). PSMet with [Rh(acac)(CO)$_2$] was conducted in dried DCM, (see experimental **3.8.2**). The PSMet samples were subsequently washed with their respective metalation solvents (×7), dried and analysed via SEM/EDX, PXRD and ICP-MS (post acid digestion). **1**$_{1\mu m}$-50%·[RhCOD(acetone)$_2$]BF$_4$ and **1**$_{1\mu m}$-50%·[Rh(acac)(CO)$_2$] both demonstrated quantitative metalation of Rh into the framework, with approximately 100% occupation of H$_2$bpydc, as determined by the EDX and ICP-MS Rh:Zr ratios (see Figure **3.10**). The Cl:Rh ratio for **1**$_{1\mu m}$-50%·[RhCOD(acetone)$_2$]BF$_4$ is very low, 2.3 ± 1.6 %, indicating successful halide abstraction prior to metalation. Both **1**$_{1\mu m}$-50%·[RhCOD(acetone)$_2$]BF$_4$ and **1**$_{1\mu m}$-50%·[Rh(acac)(CO)$_2$] are highly crystalline, matching the powder pattern of UiO-67-bpydc, (see Appendix **3.10.3**, Figure **3.A.17**). The sharpness of the diffraction peaks of **1**$_{1\mu m}$-50%·[RhCOD(acetone)$_2$]BF$_4$ indicate minimal COD dissociation related disorder, meaning COD is more tightly coordinated to the rhodium(I) than in **1**$_{1\mu m}$-50%·[Rh(COD)Cl]. SEM analysis of all of the PSMet samples revealed no surface deposition of rhodium and not alterations to the crystal morphology of **1**$_{1\mu m}$-50% upon PSMet (see Appendix **3.10.3**, Figure **3.A.18**). Hence, **1**$_{1\mu m}$-50%·[Rh(COD)Cl], **1**$_{1\mu m}$-50%·[RhCOD(acetone)$_2$]BF$_4$ and **1**$_{1\mu m}$-50%·[Rh(acac)(CO)$_2$] were used to screen for the most active rhodium(I) catalyst for gas phase hydroformylation of ethylene to 1-propanal.

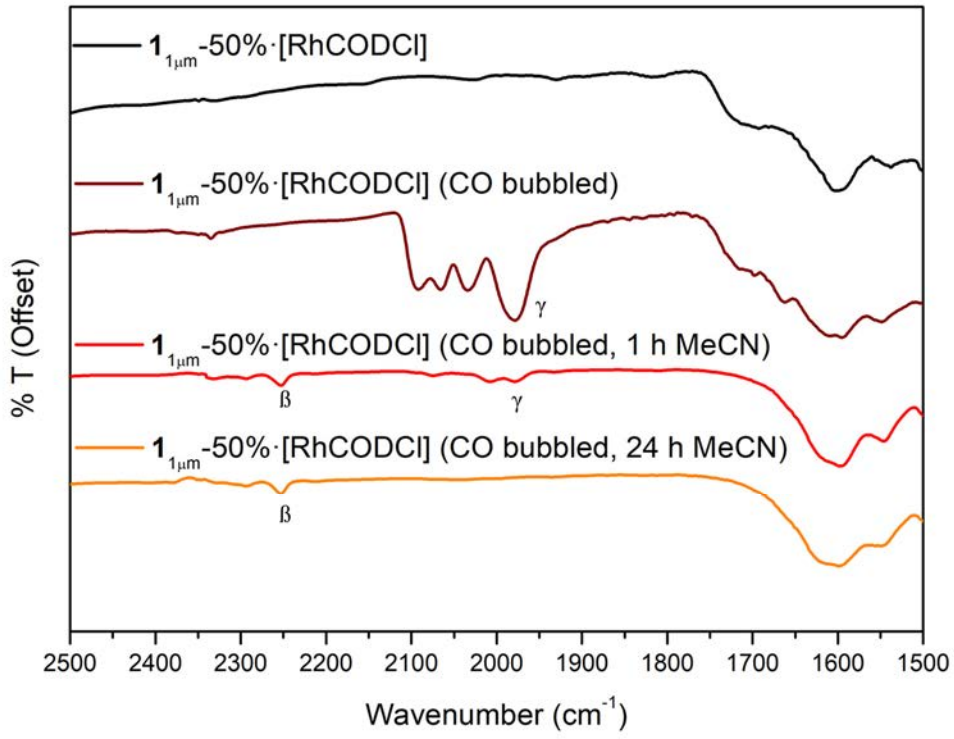

Figure **3.11**: Infrared spectra of **1**$_{1\mu m}$-50%·[Rh(COD)Cl]; as-synthesised (black) and post CO bubbling, 10 min (dark red), 1 h (red) and 24 h (orange). IR stretches: ß) free MeCN and γ) coordinated CO.

3.6. Gas Phase Hydroformylation Catalysis

Typical rhodium-catalysed hydroformylation reactions involve high pressures (10 to 40 bar) and varied temperatures (dependent on the selectivity/ activity of the chosen catalyst).[47, 69-70] Since most homogeneous rhodium(I) catalysts reported contain electron donating P-based ligands, catalyst activity is relatively high, enabling the use of modest reaction temperatures (75-120ºC).[44, 69] Ligand design for homogeneous rhodium(I) catalysts has also been used to tune the selectivity of the catalyst, allowing for control over isomerisation during hydroformylation and to disfavour hydrogenation.[47] Reactions are also typically conducted under kinetic control, as mentioned previously, which is achieved under the conditions of high pressure and moderate reaction temperature, favouring alkene hydroformylation over the more thermodynamically favoured reaction, hydrogenation. The shift in equilibria results from increased CO insertion, which occurs more readily at higher pressures and suppresses alkene hydrogenation.[47, 49] Additionally, most reactions are conducted in a bi-phasic system, and the homogeneous catalyst dispersed in an organic solvent (toluene) with the reaction vessel pressurised with CO/H_2 prior to heating.[70] As such, conditions were screened to maximise the

activity of the catalyst within the MOF for the solid/gas phase reaction within the limitations of the home-built catalytic set up.

The catalytic reactor set up used for all of the solid/gas phase hydroformylation reactions was a high pressure stainless steel batch reactor, see Figure **3.A.19** for a schematic representation of the batch reactor. The batch reactor is a small volume (3.26 cm^3) stainless steel vessel connected to a manifold (CO, H_2, Ar and ethylene), a high pressure manometer (0-20 bar), a vacuum pump, a pulse nozzle coupled to a residual gas analyser (RGA) and a gas chromatograph coupled to flame ionising detector (GC-FID). The batch reactor has a working temperature range between 25 – 200 ºC. The batch reactor set up enables real time analysis of the reaction progression via the RGA as a small portion of the reaction mixture is pulsed into the RGA at low pressure (2×10^{-6} Torr) throughout the duration of the reaction. The RGA gives information about the reaction profile in terms of product/substrate fragmentation in the gas mixture. Since the volume of the reaction vessel is held constant and the pressure/temperature of the reaction are monitored, the collected RGA data is therefore quantitative. Unfortunately, a number of reagents and products have overlapping fragmentation patterns (CO/ethylene/ethane), hence the RGA cannot provide quantitative information about reagent consumption. The reaction mixture can however be analysed once per reaction via GC-FID, which can quantitatively determine the reagent consumption (ethylene) and production of ethane/1-propanal. The GC-FID has a low pressure working range (< 1 bar), as such analysis via GC-FID can only occur once per reaction at the end of the reaction after the majority of the gas mixture has been evacuated prior to an injection onto the column of the GC-FID. Hence, the working range of the batch reactor is 0-20 bar, 25-200 ºC, analysed via the RGA throughout the reaction and post the reaction via the GC-FID.

Initial gas phase hydroformylation reactions were screened with $\mathbf{1}_{1\mu m}$-50%·[Rh(COD)Cl] to determine the activity of the catalyst at a different temperatures. $\mathbf{1}_{1\mu m}$-50%·[Rh(COD)Cl] was activated under vacuum on the batch reactor at 100 ºC overnight to remove residual solvent and moisture from the pores of the MOF. The batch reactor was then cooled to 25 ºC and the catalyst was exposed to ethylene (1 bar), H_2 (6 bar) and CO (12 bar) in a 1:5:6 molar ratio for 1 h, while the reaction was monitored via the RGA. The reaction chamber was then heated to 80 ºC and held at constant temperature for 3 h before increasing the temperature to 120 ºC and holding at 120 ºC for a further 14 h. The production of 1-propanal and release of COD were followed by monitoring the mass fragments 58 and 54 respectively via the RGA, (see Figure **3.12**). There was no production/release of 1-propanal or COD at 25

or 80 ºC, however there was noticeable production/release after the reaction temperature was increased to 120 ºC. COD evolution occurred immediately after the reaction temperature reached 120 ºC, followed by the gradual 1-propanal production, indicating for that COD must be first released from the pore of the framework before the reaction can progress. 1-Propanal production was modest, with the formation of 3.29 µmol after 14 h at 120 ºC, equivalent to a turn over number (TON = [mol (1-propanal produced)]/ [mol (catalyst)]) of 0.25. GC-FID data for this reaction was collected but the file was corrupted and so the reaction was repeated under the optimised reaction conditions (120 ºC) to enable quantification of other possible side reactions, such as hydrogenation.

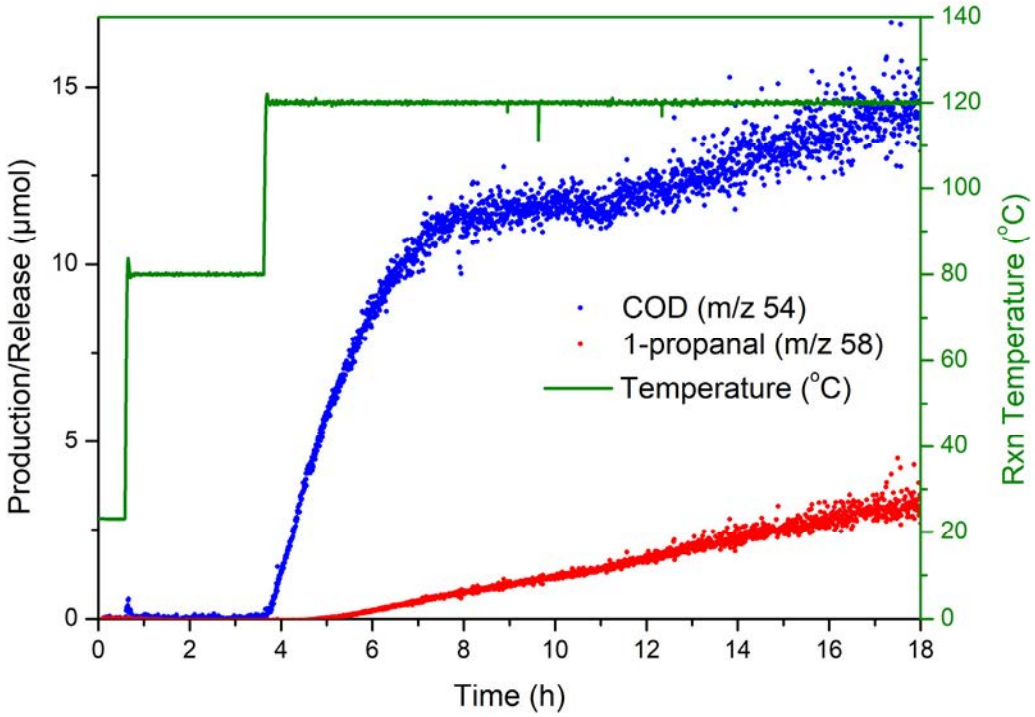

Figure **3.12**: RGA data for the first trial ethylene hydroformylation reaction catalysed by **1**$_{1\mu m}$-50%·[Rh(COD)Cl] on the batch reactor, with 1-propanal (m/z 58, red) production and COD (m/z 54, blue) release and the reaction temperature (green) shown.

Data for the repeat of the gas phase hydroformylation of ethylene by **1**$_{1\mu m}$-50%·[Rh(COD)Cl] at 120 ºC on the batch reactor is shown in Figure **3.13**. The RGA data demonstrates a similar production of 1-propanal to the first trial, producing 3.10 µmol with a TON of 0.21, however there is a marked reduction in COD release. This could be due to hydrogenation or hydroformylation of either or both alkene groups of COD producing a number of side products such as; cyclooctane (m/z 55, 56), cyclooctene (m/z 54, 67),

cyclooctane-carboxaldehyde (m/z 55, 69), or cyclooctane-methanol (m/z 55, 69), see Schematic **3.4**.[36] Since all of these by-products have overlapping primary mass fragments, their production could not be quantified, however their presence in the gas mixture is indicated by an increase in the partial pressure for mass fragments 55 and 56 in the RGA (see Appendix **3.10.4**, Figure **3.A.20**). Mass fragments 55 and 56 have higher partial pressures in the RGA in comparison to 54 (the primary fragment of COD), but the sensitivity of the RGA to these mass fragments has not been calibrated, and hence the presence of these mass fragments is only a qualitative measure of the hydroformylation/hydrogenation of COD.

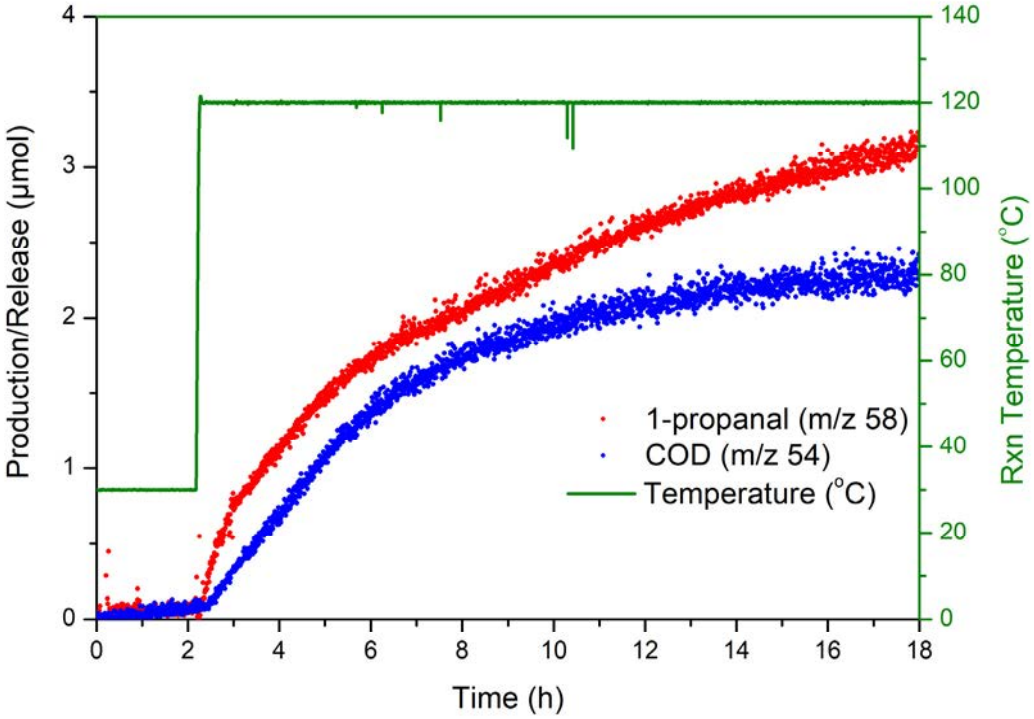

Figure **3.13**: RGA data for the second ethylene hydroformylation reaction catalysed by **1**$_{1\mu m}$-50%·[Rh(COD)Cl] on the batch reactor, with 1-propanal (m/z 58, red) production and COD (m/z 54, blue) release and the reaction temperature (green) shown

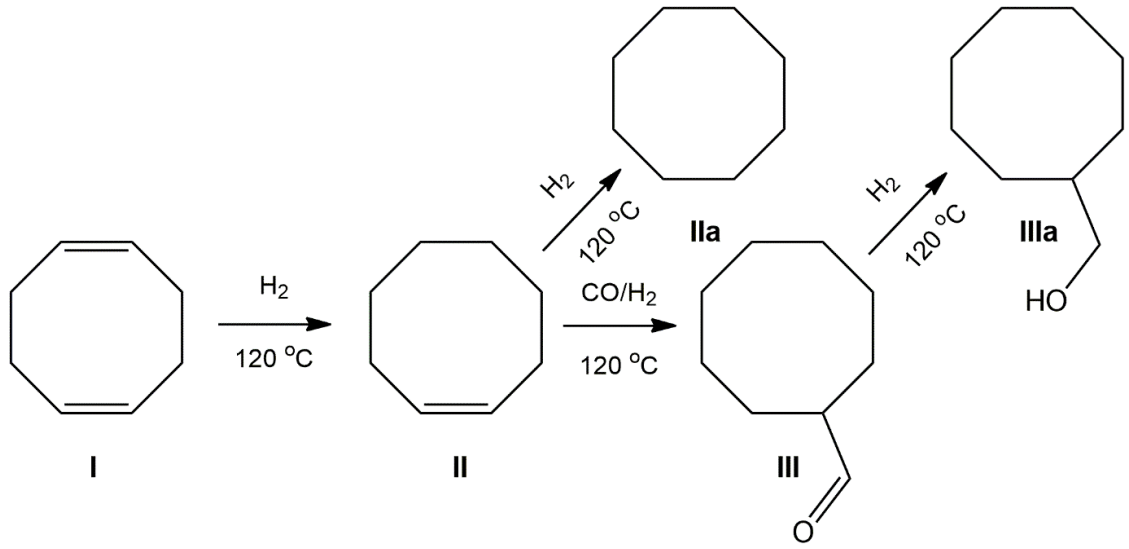

Scheme **3.4**: Proposed side reactions of 1,5'cyclooctadiene (I) under ethylene hydroformylation reaction conditions, catalysed by **1**$_{1\mu m}$-50%·[Rh(COD)Cl] forming cyclooctene (II), cyclooctane (IIa), cyclooctane-carboxaldehyde (III) and cyclooctane-methanol (IIIb).

The product distribution of the second ethylene hydroformylation reaction catalysed by **1**$_{1\mu m}$-50%·[Rh(COD)Cl] was quantified by GC-FID after the 18 h reaction. Note, hydrogen and CO were not quantified by GC-FID, and hence further discussions will relate to ethylene conversion because ethylene was the limiting reagent in the hydroformylation reaction. Ethylene, ethane and 1-propanal were detected in the GC-FID and quantified as 30.5, 1.8 and 1.0 µmol respectively. This indicates that hydrogenation of ethylene had occurred, and that the catalyst is not particularly active for the hydroformylation of ethylene. Additionally, there is a discrepancy between the amount of 1-propanal detected in the RGA vs GC-FID (by a factor of 3.11) and in the number of ethylene equivalent molecules in the gas mixture (33.4 µmol) relative to the starting amount of ethylene (130.3 µmol). This discrepancy could be caused by substrate and product adsorption within the porous framework at low pressures, prior to injection of the gas mixture onto the column of the GC-FID, which would lower the observed concentrations of the reagents/products. UiO-67 has previously been shown to have a high affinity for ethane and propane, with adsorption capacities of 3.00 and 8.18 mmol/g respectively at STP.[38] Ethylene, ethane and 1-propanal would likely have different affinities to the metalated framework, and ethylene/1-propanal can coordinate to vacant rhodium(I) sites within the framework, further complicating the quantification of the ethylene conversion via GC-FID.

To test this hypothesis, a qualitative desorption study was undertaken, whereby the reaction mixture vessel was evacuated to 10^{-7} bar briefly, dosed with a positive pressure of argon (1 bar) and then the gas mixture was analysed via RGA at 120 and 150 ºC, see Figure **3.14**. At 120 ºC there is a pronounced release of molecules corresponding to m/z 28 (ethylene/ethane/CO), m/z 54 (COD) and m/z 58 (1-propanal), indicating release of guest molecules from within the framework of **1**$_{1\mu m}$-50%·[Rh(COD)Cl] post catalysis. When the temperature was raised to 150 ºC, further evolution of ethylene/ethane/CO and COD was observed, but the amount of 1-propanal in the gas mixture gradually reduced over an hour at 150 ºC. These results, while qualitative, confirm that gases in the reaction mixture are adsorbed by the MOF catalyst prior to GC-FID analysis. Hence, analysis of the product distribution of ethylene hydroformylation catalysed by a rhodium catalyst appended to UiO-67-bpydc is qualitative via GC-FID. As such, products ethane and 1-propanal will be henceforth discussed as percent contribution to the products in the gas mixture and the percent conversion of ethylene will be reported for all reactions.

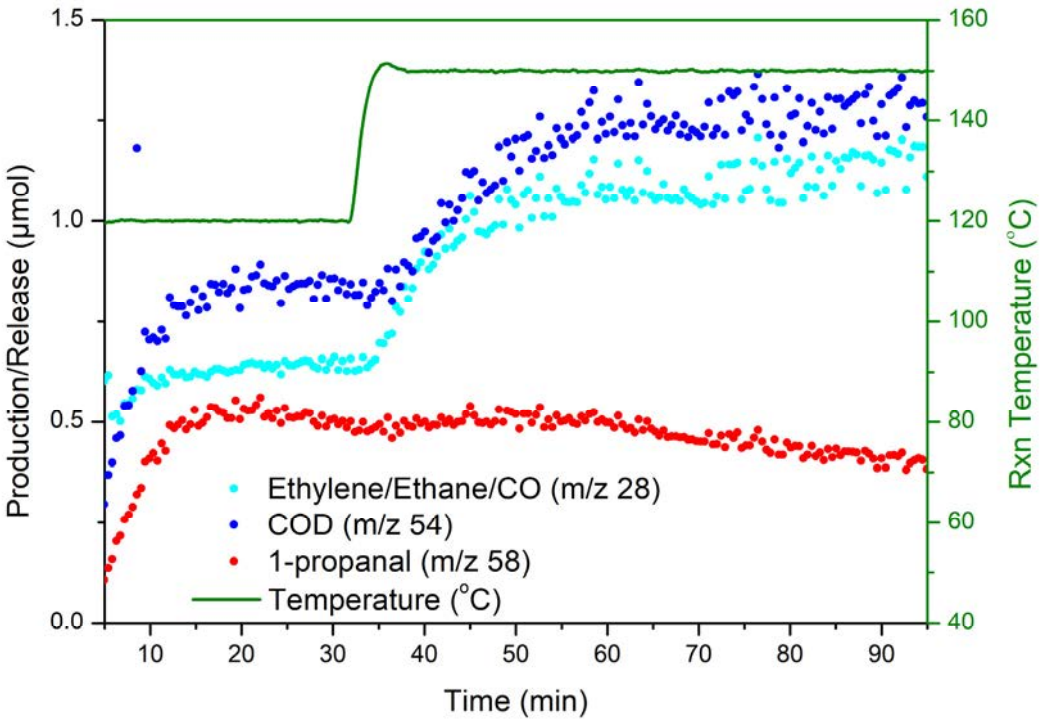

Figure **3.14**: Qualitative desorption study of **1**$_{1\mu m}$-50%·[Rh(COD)Cl] post-catalysis on the batch reactor, following the release of ethylene/ethane/CO (m/z 28), COD (m/z 54) and 1-propanal (m/z 58), with the reaction temperature shown in green.

Prior to investigating the impact of particle size of the chosen MOF catalyst on the activity of ethylene hydroformylation, the activity of the other rhodium-appended MOF catalysts was tested. The progression of gas phase ethylene hydroformylation reactions catalysed by **1**$_{1\mu m}$-50%·[RhCOD(acetone)$_2$]BF$_4$ and **1**$_{1\mu m}$-50%·[Rh(acac)(CO)$_2$] on the batch reactor were followed by RGA, see Appendix **3.10.4**, Figure **3.A.21**. For direct comparison to the activity of **1**$_{1\mu m}$-50%·[Rh(COD)Cl], the 1-propanal production was normalised relative to the amount of rhodium in each catalyst as displayed in Figure **3.15** (see Appendix **3.10.5**, Table **3.A.1** for details about the calculations). **1**$_{1\mu m}$-50%·[RhCOD(acetone)$_2$]BF$_4$ was the most active catalyst for ethylene hydroformylation, with **1**$_{1\mu m}$-50%·[Rh(acac)(CO)$_2$] and **1**$_{1\mu m}$-50%·[Rh(COD)Cl] demonstrating similar, but lower, initial activity for 1-propanal production, see Table **3.2**. The initial activity is the turn over frequency (TOF = [mol (1-propanal produced)]/[mol (catalyst)] h^{-1}) for the production of 1-propanal over the first 2 hours of activity. Qualitative GC-FID analysis of the gas mixtures from each reaction demonstrates that all of the catalysts favour the hydrogenation of ethylene over hydroformylation, with the thermodynamic product, ethane, produced in excess in all instances. Additionally, **1**$_{1\mu m}$-50%·[Rh(acac)(CO)$_2$] converted the most ethylene (60.8%) followed by **1**$_{1\mu m}$-50%·[RhCOD(acetone)$_2$]BF$_4$ (59.9%) and **1**$_{1\mu m}$-50%·[Rh(COD)Cl] (8.9%), see Table **3.2**. Post-hydroformylation, the catalysts were shown to retain crystallinity and SEM analysis revealed no surface defects for each of the samples (see Appendix **3.10.4**, Figure **4.A.22**). Since the most active catalyst for the hydroformylation of ethylene to 1-propanal was **1**$_{1\mu m}$-50%·[RhCOD(acetone)$_2$]BF$_4$, [RhCOD(acetone)$_2$]BF$_4$ was selected for the size effect investigation.

Table **3.2**: Summary of GC-FID data for ethylene hydroformylation catalysed by **1**$_{1\mu m}$-50%; [Rh(COD)Cl], [RhCOD(acetone)$_2$]BF$_4$ and [Rh(acac)(CO)$_2$].

Catalyst	**Ethylene Conversion (GC-FID, %)**	**Contribution to products in gas mixture (GC-FID, %)**		**TOF (1-propanal, h^{-1})**
		Ethane	1-propanal	
1$_{1\mu m}$-50%·[RhCODCl]	8.3	63.9	36.1	0.03
1$_{1\mu m}$-50%·[RhCOD(acetone)$_2$]BF$_4$	59.9	71.9	28.1	0.22
1$_{1\mu m}$-50%·[Rh(acac)(CO)$_2$]	60.8	97.3	2.7	0.03

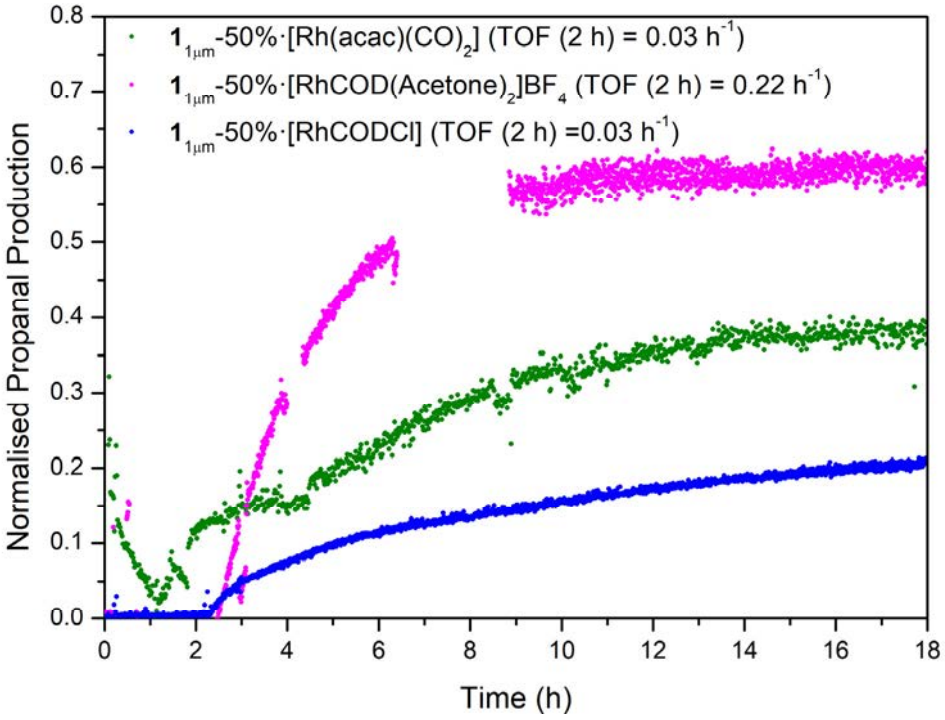

Figure **3.15**: Normalised 1-propanal production for each of the rhodium catalysts appended to $\mathbf{1}_{1\mu m}$-50%; [Rh(COD)Cl] (blue), [RhCOD(acetone)$_2$]BF$_4$ (magenta) and [Rh(acac)(CO)$_2$] (green). Note, gaps in data for $\mathbf{1}_{1\mu m}$-50%·[RhCOD(acetone)$_2$]BF$_4$ arose from a communication issue between the RGA software and the RGA, the experiment was not affected by this issue, but no data was collected for short periods of time.

The effect of particle size of the UiO-67-bpydc support on ethylene hydroformylation with the optimal [RhCOD(acetone)$_2$]BF$_4$ catalyst was investigated by comparing the activity under optimised batch reactor conditions. The MOF supports used were $\mathbf{1}_{100nm}$-50%, $\mathbf{1}_{1\mu m}$-50% and $\mathbf{1}_{10\mu m}$-50% metalated with [RhCOD(acetone)$_2$]BF$_4$ and will be henceforth denoted **Rh**·$\mathbf{1}_{100nm}$-50%, **Rh**·$\mathbf{1}_{1\mu m}$-50% and **Rh**·$\mathbf{1}_{10\mu m}$-50% respectively. The metalation and rhodium content for each sample is tabulated in Appendix **3.10.5** Table **3.A.1**, with each sample shown to have quantitative metalation with [RhCOD(acetone)$_2$]BF$_4$ via SEM/EDX analyses. The activity of each sample was directly compared, under the aforementioned optimised batch reactor conditions (Appendix **3.10.6**, Figure **3.A.23)**. The normalised 1-propanal production for each of the catalysts is displayed in Figure **3.16**. All of the different sized MOF catalysts displayed similar TOFs for 1-propanal, with the activity differing by only 0.07 h^{-1} between the most and least active samples, **Rh**·$\mathbf{1}_{1\mu m}$-50% and **Rh**·$\mathbf{1}_{10\mu m}$-50% respectively. Additionally, a sample of crushed **Rh**·$\mathbf{1}_{10\mu m}$-50% was also used for ethylene hydroformylation and displayed near identical 1-propanal production as **Rh**·$\mathbf{1}_{10\mu m}$-50%. These results indicate that the rate of 1-propanal production is seemingly independent from the particle size of the MOF catalyst.

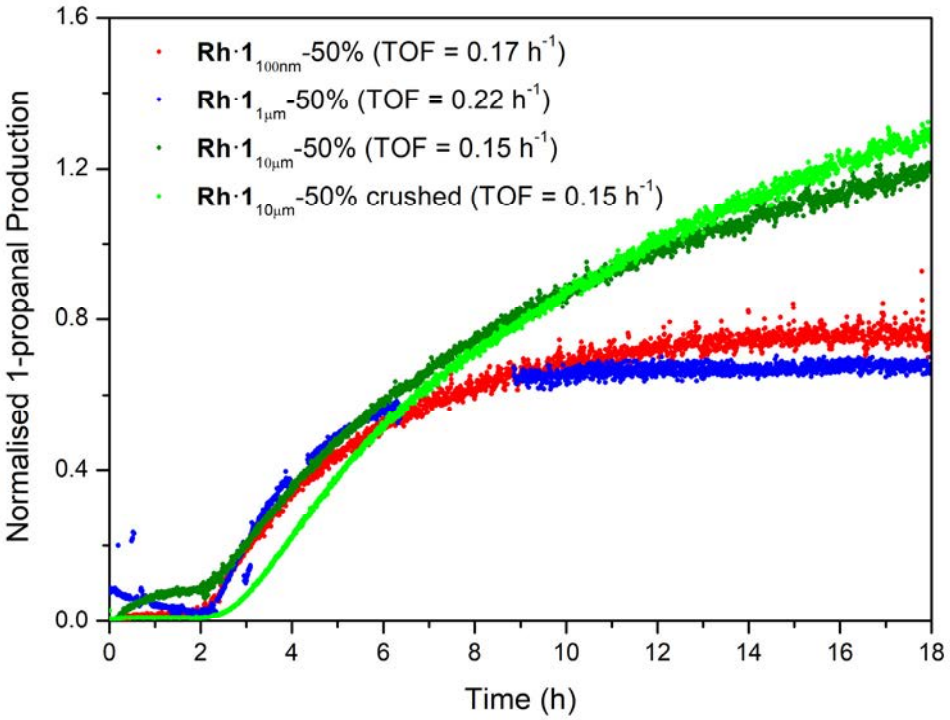

Figure **3.16**: Normalised 1-propanal production from gas phase ethylene hydroformylation reactions catalysed by **Rh·1**$_{100nm}$-50% (red), **Rh·1**$_{1\mu m}$-50% (blue), **Rh·1**$_{10\mu m}$-50% (dark green) and crushed **Rh·1**$_{10\mu m}$-50% (light green).

The product distributions of the gas mixtures of all of the samples was also analysed via GC-FID after the reactions had been completed and the data displayed in Table **3.3**. Interestingly, particle size has a dramatic impact on catalyst activity and product distribution upon analysis of the GC-FID results. There is an inverse relationship between particle size and percent ethylene conversion, with **Rh·1**$_{100nm}$-50% demonstrating the most conversion followed by **Rh·1**$_{1\mu m}$-50% and **Rh·1**$_{10\mu m}$-50%; 75.0, 59.9 and 20.8% respectively. This relationship is likely related to the availability of active sites. At smaller particle sizes there is a greater proportion of readily available surface active sites, which results in higher overall ethylene consumption. Whereas with increased particle size, there is a greater proportion of internal active site, to which access is diffusion dependent, resulting in proportionally reduced ethylene consumption. The trend observed matches the predicted impact of decreasing particle size, i.e. increased overall activity through greater access to active sites, as discussed in the introduction. Additionally, the selectivity of the catalyst for hydroformylation vs hydrogenation of ethylene is seemingly also affected by catalyst size.

Degradation was not observed for any of the catalyst samples used upon examination of the long range order (crystallinity) and the crystal surface (morphology). Post-catalysis no reduction in crystallinity was observed for **Rh·1**$_{100nm}$-50%, **Rh·1**$_{1\mu m}$-50% and **Rh·1**$_{10\mu m}$-50% with their respective PXRD patterns matching the powder pattern of simulated UiO-67-bpydc (Appendix **3.10.6**, Figure **3.A.24**). Similarly, no alterations to crystal morphology were observed post-catalysis for any of the samples by SEM (Appendix **3.10.6**, Figure **3.A.25**). The robust nature of these catalysts results from the stability of the scaffold UiO-67-bpydc to the reaction conditions. As such, this study underlines the capacity of MOFs to stabilise and heterogenize molecular catalysts for reactions such as hydroformylation/hydrogenation.

Table **3.3**: Summary of GC-FID data for ethylene hydroformylation catalysed by **Rh·1**$_{100nm}$-50%, **Rh·1**$_{1\mu m}$-50% and **Rh·1**$_{10\mu m}$-50%.

Catalyst **Rh** = $[RhCOD(acetone)_2]BF_4$	**Ethylene Conversion (GC-FID, %)**	**Contribution to products in gas mixture (GC-FID, %)**		**TOF (1-Propanal, h^{-1})**
		Ethane	1-Propanal	
Rh·1$_{100nm}$-50%	75.0	75.5	24.5	0.17
Rh·1$_{1\mu m}$-50%	59.9	71.9	28.1	0.22
Rh·1$_{10\mu m}$-50%	20.8	42.7	57.3	0.15

The selectivity of the rhodium(I) catalyst varied with framework particle size, as displayed in Table **3.3**. Decreasing particle size resulted in the catalyst favouring ethylene hydrogenation over hydroformylation, with the inverse trend was observed at larger particle sizes. As mentioned previously, the selectivity of rhodium(I) catalysts can be tuned through control of reaction conditions, with typically higher pressures, moderate reaction temperatures and high reactant concentrations favouring hydroformylation over hydrogenation. More specifically, high CO concentration at the active site disfavours hydrogenation, see Scheme **3.2**. This is described as kinetic control because hydroformylation is the kinetically favoured reaction. The reaction conditions for each experiment were identical in regard to reagent ratios, reaction temperature and initial pressure. The independent variable in these experiments was the MOF catalyst particle size. As stated above, varying particle size changes two factors; the surface to volume ratio (availability of surface to internal active sites) and the diffusion time through the framework. Larger particle sizes will have proportionally more internal than

external catalytically active sites and longer diffusion times than for smaller particles sizes. Hence, the activity could be influenced more significantly by pore-confinement effects such as the pre-concentration of reactants at internal active sites for larger particle sizes.

In order to quantify the internal surface areas of each of the particle sizes N_2 77 K adsorption isotherms were collected on all three samples, post activation from acetone (see experimental section **3.8**). The isotherms for all three samples exhibited Type 1 characteristics, with high N_2 uptake at low partial pressures, indicative of microporosity (see Figure **3.A.26**). [38] The total uptake of N_2 was lower for **Rh·1**$_{100nm}$-50% in comparison to **Rh·1**$_{1\mu m}$-50% and **Rh·1**$_{10\mu m}$-50%, with the corresponding BET surface areas of 603 ± 3, 1060 ± 4 and 1124 ± 4 m^2/g (see Table **3.4**). The pore-size distribution (calculated via DFT N_2 model) of the metalated samples was very similar, but was there was a shift to smaller pore sizes relative to the bare framework due to the rhodium(I) catalyst occupying space within the pores of the crystals (see Figures **3.4** and **3.A.26**). Hence, the metalated samples retained permanent porosity, and guest molecules can likely access active sites within the crystals. The geometric external surface area of each size regime (m^2/g) was also calculated (see Appendix **3.10.7**) and the ratio of internal to external surface areas are displayed in Table **3.4**. This data indicates that there is a significantly higher proportion of internal surface area to external surface area for larger crystals relative to smaller crystals, in fact there is a 617 fold difference in the ratio of internal to external surface area between **Rh·1**$_{100nm}$-50% and **Rh·1**$_{10\mu m}$-50%.

Table **3.4**: Internal (BET from Figure **3.A.26**) and external (calculated in Appendix **3.10.7**) surface areas for **Rh·1**$_{100nm}$-50%, **Rh·1**$_{1\mu m}$-50%, and **Rh·1**$_{10\mu m}$-50%.

Catalyst	Internal Surface Area (BET, m^2/g)	External Surface Area (calculated, m^2/g)	Internal : External Surface Area
Rh·1$_{100nm}$-50%	603 ± 3	892.0	0.678
Rh·1$_{1\mu m}$-50%	1060 ± 4	54.9	19.29
Rh·1$_{10\mu m}$-50%	1124 ± 4	2.7	416.91

Pre-concentration, or differential absorption, is a well-known phenomenon within micro-porous materials, whereby the selective adsorption of guests/reactants increases their local concentration (within the MOF pores) relative to the surrounding environment. Increasing the local concentration of guests/reactants has been shown to enhance the activity of MOF catalysts and their sensitivity as selective sensors.[71-73] UiO-67 has previously shown high affinity for short chain hydrocarbons (C_1-C_3),[38, 74] the capacity for high pressure storage of hydrogen gas,[75] and particle size controlled release of CO.[27] Whilst adsorption studies for H_2, CO and ethylene have not been explicitly studied under the specific catalytic conditions used, as described above, there is however precedence to suggest that the metalated framework could adsorb and pre-concentrate these reactants. If this indeed occurs, it may explain the observed selectivity trends, whereby increasing the local concentration of reactants at active sites within the pores of the MOF potentially affords kinetic control favouring hydroformylation over hydrogenation for larger particle sizes. In this circumstance, larger crystals, having more internal active sites available than external ones, could have a greater proportion of internal catalysis occur than smaller particle sizes. As such, pore confinement effects may play a larger role in dictating reaction selectivity for larger particle sizes than smaller ones. Unfortunately, it is difficult to deconvolute internal and external catalysis for the catalytic system used, and as such any discussion is somewhat speculative without further experiments. Indeed, this prompted further studies as outlined in Chapter 4, aiming to investigate the impact of active site location within MOFs on catalyst selectivity and stability.

3.7. Summary

In summary, the impact of the particle size of a robust MOF catalyst on the activity/selectivity for the gas phase hydroformylation of ethylene to 1-propanal has been examined. In this study, crystal engineering techniques, such as coordination modulation, were used to synthesise Zr-MOF UiO-67-bpydc at discrete size regimes 100 nm, 1 μm and 10 μm and ligand loadings (25-100%). The PSMet of **1**$_{1\mu m}$-50% was subsequently investigated with rhodium complexes including: $[Rh(CO)_2Cl]_2$, $[Rh(CO)_2Cl]BF_4$, $[RhCODCl]_2$, $[RhCOD(acetone)_2]BF_4$ and $[Rh(acac)(CO)_2]$. The catalytic activity of the latter three complexes embedded within the MOF supports was examined, and the most active catalyst for 1-propanal production, **[**$RhCOD(acetone)_2]BF_4$, was selected for the size dependent activity study. In terms of hydroformylation, there was no significant difference in 1-propanal production between the three different sized MOF supports. However, MOF particle size was shown to greatly influence the selectivity of the appended catalyst for hydrogenation versus hydroformylation. Smaller particles sizes displayed high ethylene conversion (75%) and favoured hydrogenation over hydroformylation, with the inverse observed for larger particle sizes. Active site location, reactant diffusion and pore confinement effects must therefore play an important role in the selectivity of MOF catalysis. This study highlights how control over the particle size of MOF catalysts can be used to tune to their activity/selectivity for certain reactions and emphasises that catalyst isolation within the pores of the framework can lead to unique reaction selectivity resulting from pore-confinement of reactants.

This work could be extended to further study pore-confinement effects for hydroformylation reactions by using longer chain alkenes. The selectivity for hydroformylation of different isomers could therefore be examined. To reliably investigate this, MOF scaffolds with greater control over active site location (at the interior/exterior of the crystals) would need to be synthesized, since this study would necessitate isolation of the catalytic activity within the pores of the framework (and not at the surface). The impact of active site location with MOF catalysts was specifically investigated in Chapter 4.

3.8. Experimental

3.8.1. Materials and Measurements

Unless otherwise stated, all chemicals were obtained from commercial sources and used as received. MeCN was distilled over CaH_2 under N_2 and degassed with Ar prior to use. NMR spectra were recorded on a Varian 500 MHz spectrometer at 23 ºC using a 5 mm probe. MOF samples (5 – 10 mg) were digested in DCl/*d*$_6$-DMSO (2 drops of DCl/ 600 µl *d*$_6$-DMSO) at 85 °C, stirred at 500 rpm for 30 min – 1 h, or until fully dissolved, prior to NMR analysis. Infrared spectra were collected on a Perkin-Elmer Spectrum 100 using a UATR sampling accessory (cm^{-1} = 750 – 4000), with dry samples loaded on NaCl disks in Paratone-N oil. Powder X-ray diffraction data were collected on a Bruker Advanced D8 diffractometer (capillary stage) using Cu Kα radiation (λ = 1.54056 Å, 40 kW/ 40 mA, 2θ = 2 – 52.94°, Phi rotation = 20 rotation/min at 1 sec exposure per step, with 5001 steps using 0.5 mm glass capillaries). Scanning Electron Microscope (SEM) images were collected on a Phillips XL30 scanning electron microscope in secondary electron mode, (spot size 3 and 10 KeV). Electron Dispersive X-ray Analysis was collected with an Oxford Instruments Ultim Max 170 EDX attachment on the Phillips XL30/Quanta 450 (spot size 4, 15 KeV). Samples for SEM analysis were dry loaded onto adhesive carbon tabs on aluminium stubs and carbon coated (5 nm) prior to analysis.

3.8.2. Synthetic Methods

2,2'-Bipyridine-5,5'-dicarboxylic acid (bpydc)

This compound was prepared according to a literature procedure with minor alterations.[76] 5,5'-Dimethyl-2,2'-bipyridine (5.00 g, 16.60 mmol) and $KMnO_4$ (21.01 g, 133.04 mmol, 8 eq.) were added to 200 mL of water. The resulting mixture was heated at 100 ºC for 24 h. The reaction was cooled to room temperature then filtered over Celite to remove excess brown precipitate and the filtrate was extracted with diethyl ether (3 × 50 mL). The aqueous layer was then acidified to pH 2 with HCl (1 M) whilst stirring. The greenish white precipitate was collected by vacuum filtration and washed with diethyl ether (100 mL) and dried to give crude 2,2'-bipyridine-5,5'-dicarboxylic acid. The crude product was dispersed in 50 % HNO_3 (140 mL) and the solution was heated at 130 ºC for 1-2 h. The reaction mixture was cooled to room temperature then poured over approximately 50 – 70 g ice and stirred for 20 min. The white precipitate was collected by vacuum filtration and washed with diethyl ether (100 mL) and oven dried (100 ºC for 1 h) to give pure 2,2'-bipyridine-5,5'-dicarboxylic acid (3.73 g, 15.29 mmol, 92 %). ^{1}HNMR data was consistent with previous reports.[76] ^{1}HNMR (500 MHz,

d_6-DMSO): δ = 8.45 (dd, J = 8.3, 2.2 Hz, 2H), 8.57 (d, J = 8.3 Hz, 2H) and 9.20 ppm (d, J = 2.2 Hz, 2H).

UiO-67-bpydc synthetic protocols:

MOF synthesis with basic additives

Zirconium chloride ($ZrCl_4$, 24.5 mg, 0.105 mmol), 2,2'bipyridyl 5,5'-dicarboxylic acid (bpydc, 26 mg, 0.105 mmol, 1 eq.) were added to a 20 ml screw cap Wheaton vial (Teflon capped), DMF (5 ml) was added and the solution was sonicated for 10 mins or until fully dispersed. The solution was then stirred at 6000 rpm at room temperature and a basic additive (1 eq., 0.105 mmol, see below) was added to the solution, which was left to stir for a further 16 h. The resultant suspensions were cooled to room temperature and the white precipitates were collected via centrifugation at 14,000 rpm, washed with DMF (2×10 ml) and THF(4×10 ml) and dried in a vacuum desiccator for 1 h prior to SEM analysis.

The basic additives used included: sodium formate (7.14 mg), sodium acetate (8.61 mg), sodium hydroxide (0.05 ml, 2M), triethylamine (14.0 µl), n-butylamine (10.3 µl) and tert-butylamine (11 µl). All of the bases were added as 1 equivalent relative to the ligand i.e. 0.105 mmol.

MOF synthesis with acidic additives

$ZrCl_4$ (24.5 mg, 0.105 mmol), bpydc (26 mg, 0.105 mmol) and 30 equivalents of acid modulator (glacial acetic acid or benzoic acid, 0.2 ml and 384.7 mg respectively, 3.15 mmol, 30 eq.) were added to a 20 ml screw cap Wheaton vial (Telfon capped), DMF (10 ml) was added and the solution was sonicated until dissolved/fully dispersed (10 - 30 min sonication). The solutions were then heated in a preheated oven for 24 h at 120 ºC. The resulting white suspension was allowed to cool to room temperature, then it was centrifuged at 14,000 rpm then washed with DMF (2×10 ml) and THF (4×10 ml) resulting in a white microcrystalline powder.

1$_{100nm}$

$ZrCl_4$ (21 mg, 0.09 mmol) and bpydc (22 mg, 0.09 mmol) were dissolved in DMF (30 ml) and sonicated for 10 minutes or until fully dissolved. Glacial acetic acid (618 µl, 10.8 mmol, 120 eq.) was then added to this solution which was then separated into three 20 ml screw cap Wheaton vials (Teflon capped, 10 ml in each) and then heated in an oven for 24 h at 120 ºC. The resulting white suspension was allowed to cool to room temperature, then it was

centrifuged at 14,000 rpm then washed with DMF (2×10 ml) and THF(4×10 ml) resulting in a white microcrystalline powder.

1$_{1\mu m}$

$ZrCl_4$ (24.5 mg, 0.105 mmol), bpydc (26 mg, 0.105 mmol) and benzoic acid (384.7 mg 3.15 mmol, 30 eq.) were added to a 20 ml screw cap wheaton vial (Teflon capped), DMF (10 ml) was added and the solution was sonicated until dissolved/fully dispersed (10 - 30 min sonication). The solution was heated in a pre-heated oven for exactly 24 h at 120 ºC. The resulting white suspension was allowed to cool to room temperature, then it was centrifuged at 9,000 rpm then washed with DMF (2×10 ml) and THF (4×10 ml) resulting in a white microcrystalline powder.

1$_{10\mu m}$

$ZrCl_4$ (46.5 mg, 0.200 mmol), bpydc (48 mg, 0.200 mmol) and benzoic acid (750 mg, 6.14 mmol, 30 eq.) were dissolved in dimethylacetamide (DMA, 10 ml), in a 20 ml screw cap wheaton vial (Teflon capped), and the solution was heated in an oven for 72 h at 140 ºC. The resulting crystals on the sides of the container were washed DMA (2×10 ml) and THF (4×10 ml) resulting in pure single crystals of UiO-67-bpydc.

Variations to these synthetic conditions include changing the reaction vessels to 30 ml Teflon lined vials housed in a stainless steel autoclave.

UiO-67-bpydc$_X$-bpdc$_{6-X}$ synthetic protocols:

Mixed ligand solvothermal synthesis of UiO-67 with bpydc and bpdc using protocols **1**$_{100nm}$, **1**$_{1\mu m}$ and **1**$_{10\mu m}$ was achieved by simply varying the molar ratio of the two ligands for each protocol, whilst maintaining the same total molar amount of ligand (as stipulated above). For example, in order to synthesise **1**$_{1\mu m}$-50% a 1:1 ratio of bpydc to bpdc was used i.e. 52.5 µmol of each ligand to reach a total of 0.105 mmol for the reaction. The same process was applied to all the synthesis of all mixed ligand samples in this chapter for their respective protocols.

PSMet with Rhodium Complexes:

$[RhCOCl]_2$

$[RhCOCl]_2$ (32.0 mg, 82.3 μmol) was dissolved in freshly distilled MeCN (4 ml) and the solution was degassed with N_2 for 5 minutes prior to the addition of a dried sample of UiO-67-bpydc (10-30 mg, solvent exchanged from distilled MeCN and dried under vacuum for 1 h). The vial was degassed for a further 5 min with N_2 and stored in darkness at room temperature overnight. The solution was removed, and the maroon coloured MOF crystals were solvent exchanged with distilled MeCN (×7) and stored at room temperature until ready for analysis.

$[RhCOCl]BF_4$

$[RhCOCl]_2$ (32.0 mg, 82.3 μmol, 1 eq.) and $NaBF_4$ (36.1 mg, 0.33 mmol, 4 eq.) were dissolved in freshly distilled MeCN (4 ml), and the solution was degassed with N_2 for 5 minutes prior to the addition of a dried sample of UiO-67-bpydc (10-30 mg, solvent exchanged from distilled MeCN and dried under vacuum for 1 h). The vial was degassed for a further 5 min with N_2 and stored in darkness at room temperature overnight. The solution was removed, and the yellow/orange coloured MOF crystals were solvent exchanged with distilled MeCN (×7) and stored at room temperature until ready for analysis.

$[RhCODCl]_2$

$[RhCODCl]_2$ (41.7 mg, 84.6 μmol) was dissolved in freshly distilled MeCN (4 ml) and the solution was degassed with N_2 for 5 minutes prior to the addition of a dried sample of UiO-67-bpydc (10-30 mg, solvent exchanged from distilled MeCN and dried under vacuum for 1 h). The vial was degassed for a further 5 min with N_2 and stored in darkness at room temperature overnight. The solution was removed, and the orange/red coloured MOF crystals were solvent exchanged with distilled MeCN (×7) and stored at room temperature until ready for analysis.

$[RhCOD(acetone)_2]BF_4$

$[RhCODCl]_2$ (36.4 mg, 73.8 μmol, 1 eq.) was dissolved in acetone (10 ml) and the solution was degassed with Ar for 5 min. To this solution $AgBF_4$ (29.1 mg, 147.2 μmol, 2 eq.) was added, and the solution was stirred 2 h under an atmosphere of Ar in darkness. The solution was filtered via a canula with a cotton wool plug and filter-paper into a separate vial with positive Ar pressure, then degassed with Ar and stored under Ar at 3 ºC until the solution was

used for metalation. A dried sample of UiO-67-bpydc (10-30 mg, solvent exchanged from distilled acetone and dried under vacuum for 1 h) was added to the $[RhCOD(acetone)_2]BF_4$ solution (4 ml). The vial was stored under darkness overnight. The solution was removed, and the red MOF crystals were solvent exchanged with acetone (×7) and stored at room temperature until ready for analysis.

$[Rh(acac)(CO)_2]$

$[Rh(acac)(CO)_2]$ (21.8 mg, 84.6 μmol) was dissolved in dry DCM (4 ml) and the solution was degassed with N_2 for 5 minutes prior to the addition of a dried sample of UiO-67-bpydc (10-30 mg, solvent exchanged from dry DCM and dried under vacuum for 1 h). The vial was degassed for a further 5 min with N_2 and stored in darkness at room temperature overnight. The solution was removed, and the orange/red coloured MOF crystals were solvent exchanged with dry DCM (×7) and stored at room temperature until ready for analysis.

Samples were analysed via SEM/EDX and via ICP-MS post HNO_3 digestion to analyse the Rh:Zr ratio. Additionally, the samples which were analysed via IR spectroscopy were dried under reduced pressure in a desiccator for 1 h, then crushed and placed between NaCl disks with Nujol for analysis.

CO Bubbling experiments

A sample of $\mathbf{1}_{1\mu m}$-50% metalated with $[RhCODCl]_2$ (approximately 15 mg, dried) were solvated in distilled MeCN (4 ml) in a 5 ml glass screw-cap vial. CO was bubbled through the solution for 1 h (all CO bubbling experiments were conducted in the fume hood), after which the vial was sealed and stored in darkness. An aliquot of the CO bubbled sample was removed (approximately 1/3 of the sample) at increments of 10 min, 1 and 24 h post CO exposure, and centrifuged at 14,000 rpm. The solution was then removed, and the sample was dried under reduced pressure in a desiccator for 1 h prior to IR analysis (see above).

3.8.3. Inductively coupled plasma mass spectrometry

Inductively coupled plasma mass spectrometry was performed on a Solution 7500CS ICPMS spectrometer at Adelaide microscopy on samples in a 5% HNO_3 matrix in MilliQ water. Samples of were digested in a triplicate in analytical grade 70% HNO_3 in MilliQ water (2 ml) at 65 ºC for 16 h in 5 ml polyethylene capped polypropylene vials. The solution was then cooled to room temperature and the yellow/orange solutions were opened under a fume-hood to remove the volatile and toxic NO_x by-products. The solution was diluted with MilliQ

water (2 ml) and filtered through a 0.45 µm cellulose acetate filter and 50 µl further diluted in 5 ml of MilliQ and analysed via ICPMS.

3.8.4. Gas Adsorption Analysis

Activation Protocol:

In a typical activation procedure, crystals of UiO-67-bpydc were solvent exchanged with DMF (10 ml × 5) over a 1-day period and the distilled MeCN (10 ml × 5) over a 1-day period. The samples were then dried in a desiccator for 1 h then transferred into sorption analysis tubes. The samples were then dried under a vacuum at 150 ºC for 3 h to yield activated samples.

Gas Adsorption Measurements:

Gas adsorption isotherms were measured using volumetric methods on a micromeritics 3-Flex analyser (Micromeritics Instrument Corporation, Norcross, GA, USA) at 77 K (using a cryo-cooler circulator). Brunauer-Emmett-Teller (BET) surface areas were calculated using experimental points at relative pressure of P/P_0 = 0.05-0.25. Pore size distributions were calculated from N_2 using DFT modelling software on a Micromeritics 3-Flex analyser. UHP grade (99.999 %) N_2 was used for all measurements.

3.8.5. Catalysis Experiments

Batch Instrumentation:

Batch gas phase catalytic experiments were carried out using a custom-built high temperature and high-pressure pulse-gas sampling equipment coupled with a mass spectrometer for real-time analysis of the reaction mixture.[77] The batch reaction cell has an internal volume of 3.26 mL and is in direct contact with a copper block containing a 100 W heater cartridge controlled by a proportional-integral derivative (PID) temperature controller (CAL Controls, Cal 3300) and K-type thermocouple attached to the side of the cell. The pressure in the batch reaction cell is monitored by a piezoresistive manometer (Keller, Leo Record series, 30 bar range). The cell is connected to a pulsed nozzle (Parker, Series 9 Pulse Valve) which is used to pulse controlled amounts of gas from the reaction cell via a 1/16" stainless steel tube into the vacuum system, comprised of a residual gas analyser (RGA) for sampling of the gas mixture (vide infra). The pulsed nozzle is driven by a custom-built pulsed nozzle driver connected to the acquisition computer and controlled by LabVIEW software. Typical pulse rates range from 0.3 to 20 Hz with a pulse width of 29 to 34 ms and is controlled

in real-time via a PID software controller in the LabVIEW code. This controller allows precise regulation of the amount of gas being delivered, while maintaining a constant pressure level in the vacuum system (typically 2.00×10−6 Torr) to allow for reliable operation of the RGA at calibrated pressures. The gas phase reaction mixture can also be analysed using a gas chromatograph (SRI-8610C model) which is directly connected to the reaction cell.

RGA:

Gas mixtures are analysed by an RGA (Stanford Research Systems, RGA200) which is housed in a vacuum chamber with an electron multiplier, controlled via Stanford Research Systems RGA software for data collection. Pressure is measured by a Bayard-Alpert ionisation gauge with a tungsten filament (Duniway, T-CFF-275) monitored via a combined ion and thermocouple controller (Agilent Technologies, XGS-600). The system is pumped via an oil-free turbo-pump (Agilent TwisTorr 84FS) backed by a rotary vane pump (Edwards, E2M8) with an oil trap (Duniway IFT-NW25-4).

Calibrations:

The m/z 58 peak used to quantify the production of 1-propanal was calibrated using a CO_2/1-propanal mixture of 0.32 bar 1-butene and 9.68 bar CO_2 with a total pressure of 10.00 bar in the reaction cell. The m/z 54 peak used to quantify the production of COD was calibrated using a COD/N_2 mixture of 0.023 bar of COD and 3.635 bar of N_2 with a total pressure of 3.658 bar in the reaction cell.

Gas Chromatography:

Gas chromatography analyses were carried out with an SRI-8610C (MG#3) instrument with FID detector with methaniser. The first chromatographic column was a S.S. molecular sieve 13X packed column (6' length, 1/8" O.D.) followed by a S.S. Haye Sep D packed column (6' length, 1/8" O.D.) with argon as the carrier gas. Initial oven temperature was 50 °C held for 5 minutes, followed by a ramp at 20 °C/min to 250 °C and held for 6 minutes. Injection port temperature was 60 °C, and methaniser was 300 °C. Pressure of was initially held at 3 PSI for 0.03 min, increased to 20 PSI and held for 2 min, then further increased to 40 PSI and held for 3.8 min and subsequently decreased to 0 PSI and held for 18 min.

Hydroformylation reaction conditions:

Dried **Rh·1**$_{1\mu m}$-50% (1μm-UiO-67-bpydc$_{0.5}$bpdc$_{0.5}$·[Rh(COD)(acetone)$_2$]BF$_4$, 11.4 mg, 9.6 μmol Rh) was loaded into a stainless-steel sample holder capped by a VCR gasket with a 0.5 μm filter and placed in the batch reactor cell. After sealing the reaction cell, the sample was evacuated for 1 h under high vacuum, then the sample was activated by heating to 100 °C under high vacuum for 24 h. Once the reaction cell cooled to room temperature (25 °C) ethylene was introduced into the reaction cell (1 bar), followed by H_2 (6 bar) and CO (12 bar). The reaction was continuously monitored immediately after the gasses were introduced by pulsing a small amount of gas (2.00×10−6 Torr) into the vacuum chamber. The reaction was left at room temperature for 2 h, then heated at 120 °C for 16 h. The reaction was then stopped, and the gaseous reaction mixture was analysed via gas chromatography.

This experimental procedure was repeated with the other catalysts, the sample mass and rhodium loading are listed in Table **3.A.1** in Appendix **3.10.5**.

3.9. References

1. Yang, X.-F.; Wang, A.; Qiao, B.; Li, J.; Liu, J.; Zhang, T., Single-Atom Catalysts: A New Frontier in Heterogeneous Catalysis. *Acc Chem Res* **2013,** *46* (8), 1740-1748.

2. Li, J.; Li, B.; Shao, H.; Li, W.; Lin, H., Catalysis and Downsizing in Mg-Based Hydrogen Storage Materials. *Catalysts* **2018,** *8* (2).

3. Valden, M.; Lai, X.; Goodman, D. W., Onset of Catalytic Activity of Gold Clusters on Titania with the Appearance of Nonmetallic Properties. *Science* **1998,** *281* (5383), 1647.

4. Li, J.; Li, X.; Zhai, H.-J.; Wang, L.-S., Au₂₀: A Tetrahedral Cluster. *Science* **2003,** *299* (5608), 864.

5. Linder-Patton, O. M.; de Prinse, T. J.; Furukawa, S.; Bell, S. G.; Sumida, K.; Doonan, C. J.; Sumby, C. J., Influence of Nanoscale Structuralisation on the Catalytic Performance of ZIF-8: a Cautionary Surface Catalysis Study. *CrystEngComm* **2018,** *20* (34), 4926-4934.

6. Grajciar, L.; Heard, C. J.; Bondarenko, A. A.; Polynski, M. V.; Meeprasert, J.; Pidko, E. A.; Nachtigall, P., Towards Operando Computational Modeling in Heterogeneous Catalysis. *Chem Soc Rev* **2018,** *47* (22), 8307-8348.

7. Pascanu, V.; González Miera, G.; Inge, A. K.; Martín-Matute, B., Metal–Organic Frameworks as Catalysts for Organic Synthesis: A Critical Perspective. *J Am Chem Soc* **2019,** *141* (18), 7223-7234.

8. Li, L.; He, J.; Wang, Y.; Lv, X.; Gu, X.; Dai, P.; Liu, D.; Zhao, X., Metal–Organic Frameworks: a Promising Platform for Constructing Non-Noble Electrocatalysts for the Oxygen-Reduction Reaction. *J Mater Chem A* **2019,** *7* (5), 1964-1988.

9. Uehara, H.; Diring, S.; Furukawa, S.; Kalay, Z.; Tsotsalas, M.; Nakahama, M.; Hirai, K.; Kondo, M.; Sakata, O.; Kitagawa, S., Porous Coordination Polymer Hybrid Device with Quartz Oscillator: Effect of Crystal Size on Sorption Kinetics. *J Am Chem Soc* **2011,** *133* (31), 11932-5.

10. Dhakshinamoorthy, A.; Alvaro, M.; Garcia, H., Commercial Metal-Organic Frameworks as Heterogeneous Catalysts. *Chem Commun* **2012,** *48* (92), 11275-88.

11. García-García, P.; Müller, M.; Corma, A., MOF Catalysis in Relation to their Homogeneous Counterparts and Conventional Solid Catalysts. *Chem Sci* **2014,** *5* (8), 2979.

12. Bosch, M.; Zhang, M.; Zhou, H.-C., Increasing the Stability of Metal-Organic Frameworks. *Advances in Chemistry* **2014,** *2014*, 8.

13. Valenzano, L.; Civalleri, B.; Chavan, S.; Bordiga, S.; Nilsen, M. H.; Jakobsen, S.; Lillerud, K. P.; Lamberti, C., Disclosing the Complex Structure of UiO-66 Metal Organic Framework: A Synergic Combination of Experiment and Theory. *Chem Mater* **2011,** *23* (7), 1700-1718.

14. Bai, Y.; Dou, Y.; Xie, L. H.; Rutledge, W.; Li, J. R.; Zhou, H. C., Zr-Based Metal-Organic Frameworks: Design, Synthesis, Structure, and Applications. *Chem Soc Rev* **2016,** *45* (8), 2327-67.

15. Mondloch, J. E.; Katz, M. J.; Planas, N.; Semrouni, D.; Gagliardi, L.; Hupp, J. T.; Farha, O. K., Are Zr(6)-Based Mofs Water Stable? Linker Hydrolysis vs. Capillary-Force-Driven Channel Collapse. *Chem Commun* **2014,** *50* (64), 8944-6.

16. Kim, M.; Cohen, S. M., Discovery, Development, and Functionalization of Zr(IV)-Based Metal–Organic Frameworks. *CrystEngComm* **2012,** *14* (12), 4096-4104.

17. Katz, M. J.; Brown, Z. J.; Colon, Y. J.; Siu, P. W.; Scheidt, K. A.; Snurr, R. Q.; Hupp, J. T.; Farha, O. K., A Facile Synthesis of UiO-66, UiO-67 and their Derivatives. *Chem Commun (Camb)* **2013,** *49* (82), 9449-51.

18. Fei, H.; Cohen, S. M., A robust, catalytic metal-organic framework with open 2,2'-bipyridine sites. *Chem Commun (Camb)* **2014,** *50* (37), 4810-2.

19. Evans, J. D.; Sumby, C. J.; Doonan, C. J., Post-Synthetic Metalation of Metal-Organic Frameworks. *Chem Soc Rev* **2014,** *43* (16), 5933-51.

20. Bloch, W. M.; Burgun, A.; Doonan, C. J.; Sumby, C. J., Probing Post-Synthetic Metallation in Metal-Organic Frameworks: Insights from X-ray Crystallography. *Chem Commun* **2015,** *51* (25), 5486-9.

21. Gonzalez, M. I.; Bloch, E. D.; Mason, J. A.; Teat, S. J.; Long, J. R., Single-Crystal-to-Single-Crystal Metalation of a Metal-Organic Framework: a Route Toward Structurally Well-Defined Catalysts. *Inorg Chem* **2015,** *54* (6), 2995-3005.

22. Horcajada, P.; Surblé, S.; Serre, C.; Hong, D.-Y.; Seo, Y.-K.; Chang, J.-S.; Grenèche, J.-M.; Margiolaki, I.; Férey, G., Synthesis and Catalytic Properties of MIL-100(Fe), an Iron(III) Carboxylate with Large Pores. *Chem Commun* **2007,** (27), 2820-2822.

23. Canivet, J.; Aguado, S.; Schuurman, Y.; Farrusseng, D., MOF-Supported Selective Ethylene Dimerization Single-Site Catalysts through One-Pot Postsynthetic Modification. *J Am Chem Soc* **2013,** *135* (11), 4195-8.

24. Ren, J.; Langmi, H. W.; North, B. C.; Mathe, M.; Bessarabov, D., Modulated Synthesis of Zirconium-Metal Organic Framework (Zr-MOF) for Hydrogen Storage Applications. *Int J Hydrogen Energ* **2014,** *39* (2), 890-895.

25. Schrimpf, W.; Jiang, J.; Ji, Z.; Hirschle, P.; Lamb, D. C.; Yaghi, O. M.; Wuttke, S., Chemical Diversity in a Metal-Organic Framework Revealed by Fluorescence Lifetime Imaging. *Nat Commun* **2018,** *9* (1), 1647-1647.

26. Schaate, A.; Roy, P.; Godt, A.; Lippke, J.; Waltz, F.; Wiebcke, M.; Behrens, P., Modulated Synthesis of Zr-Based Metal–Organic Frameworks: From Nano to Single Crystals. *Chem Eur J* **2011,** *17* (24), 6643-6651.

27. Diring, S.; Carné-Sánchez, A.; Zhang, J.; Ikemura, S.; Kim, C.; Inaba, H.; Kitagawa, S.; Furukawa, S., Light Responsive Metal–Organic Frameworks as Controllable CO-Releasing Cell Culture Substrates. *Chem Sci* **2017,** *8* (3), 2381-2386.

28. Øien, S.; Wragg, D.; Reinsch, H.; Svelle, S.; Bordiga, S.; Lamberti, C.; Lillerud, K. P., Detailed Structure Analysis of Atomic Positions and Defects in Zirconium Metal–Organic Frameworks. *Cryst Growth Des* **2014,** *14* (11), 5370-5372.

29. Guo, H.; Zhu, Y.; Wang, S.; Su, S.; Zhou, L.; Zhang, H., Combining Coordination Modulation with Acid–Base Adjustment for the Control over Size of Metal–Organic Frameworks. *Chem Mater* **2012,** *24* (3), 444-450.

30. Linder-Patton, O. M.; Bloch, W. M.; Coghlan, C. J.; Sumida, K.; Kitagawa, S.; Furukawa, S.; Doonan, C. J.; Sumby, C. J., Particle Size Effects in the Kinetic Trapping of a Structurally-Locked Form of a Flexible MOF. *CrystEngComm* **2016,** *18* (22), 4172-4179.

31. Bunzen, H.; Grzywa, M.; Hambach, M.; Spirkl, S.; Volkmer, D., From Micro to Nano: A Toolbox for Tuning Crystal Size and Morphology of Benzotriazolate-Based Metal–Organic Frameworks. *Cryst Growth Des* **2016,** *16* (6), 3190-3197.

32. Zhang, R.-Z.; Huang, Y.-q.; Zhang, W.; Yang, J.-M., Effect of Particle Size Distribution of UiO-67 Nano/Microcrystals on the Adsorption of Organic Dyes from Aqueous Solution. *CrystEngComm* **2018,** *20* (38), 5672-5676.

33. Wang, T. C.; Vermeulen, N. A.; Kim, I. S.; Martinson, A. B.; Stoddart, J. F.; Hupp, J. T.; Farha, O. K., Scalable Synthesis and Post-Modification of a Mesoporous Metal-Organic Framework called NU-1000. *Nat Protoc* **2016,** *11* (1), 149-62.

34. Yang, D.; Odoh, S. O.; Wang, T. C.; Farha, O. K.; Hupp, J. T.; Cramer, C. J.; Gagliardi, L.; Gates, B. C., Metal-Organic Framework Nodes as Nearly Ideal Supports for Molecular Catalysts: NU-1000- and UiO-66-Supported Iridium Complexes. *J Am Chem Soc* **2015,** *137* (23), 7391-6.

35. Deria, P.; Mondloch, J. E.; Tylianakis, E.; Ghosh, P.; Bury, W.; Snurr, R. Q.; Hupp, J. T.; Farha, O. K., Perfluoroalkane functionalization of NU-1000 via Solvent-Assisted Ligand Incorporation: Synthesis and CO2 Adsorption Studies. *J Am Chem Soc* **2013,** *135* (45), 16801-4.

36. Linstrom, P. J.; Mallard, W. G., *NIST Chemistry WebBook*. National Institute of Standards and Technology: Gaithersburg MD, Vol. 20899.

37. Seetharaj, R.; Vandana, P. V.; Arya, P.; Mathew, S., Dependence of Solvents, pH, Molar Ratio and Temperature in Tuning Metal Organic Framework Architecture. *Arab J Chem* **2019,** *12* (3), 295-315.

38. Zhang, Y.; Xiao, H.; Zhou, X.; Wang, X.; Li, Z., Selective Adsorption Performances of UiO-67 for Separation of Light Hydrocarbons C1, C2, and C3. *Ind Eng Chem Res* **2017,** *56* (30), 8689-8696.

39. Gonzalez, M. I.; Turkiewicz, A. B.; Darago, L. E.; Oktawiec, J.; Bustillo, K.; Grandjean, F.; Long, G. J.; Long, J. R., Confinement of Atomically Defined Metal Halide Sheets in a Metal–Organic Framework. *Nature* **2020,** *557*, (7788), 64-68.

40. Capon, P. K.; Burgun, A.; Coghlan, C. J.; Crees, R. S.; Doonan, C. J.; Sumby, C. J., Hydrogen Adsorption in Azolium and Metalated N-heterocyclic Carbene Containing MOFs. *CrystEngComm* **2016,** *18* (37), 7003-7010.

41. Flint, K. Honours Thesis. The University of Adelaide, 2016.

42. James, B. R.; Williams, R. J. P., 383. The Oxidation–Reduction Potentials of some Copper Complexes. *J Chem Soc* **1961,** (0), 2007-2019.

43. Lu, P.; Wu, Y.; Kang, H.; Wei, H.; Liu, H.; Fang, M., What can pKa and NBO Charges of the Ligands Tell us About the Water and Thermal Stability of Metal Organic Frameworks? *J Mater Chem A* **2014,** *2* (38), 16250-16267.

44. Wang, C.; An, B.; Lin, W., Metal–Organic Frameworks in Solid–Gas Phase Catalysis. *ACS Catalysis* **2019,** *9* (1), 130-146.

45. Franke, R.; Selent, D.; Börner, A., Applied Hydroformylation. *Chem Rev* **2012,** *112* (11), 5675-5732.

46. Gusevskaya, E. V.; Jiménez-Pinto, J.; Börner, A., Hydroformylation in the Realm of Scents. *ChemCatChem* **2014,** *6* (2), 382-411.

47. Nurttila, S. S.; Linnebank, P. R.; Krachko, T.; Reek, J. N. H., Supramolecular Approaches To Control Activity and Selectivity in Hydroformylation Catalysis. *ACS Catal* **2018,** *8* (4), 3469-3488.

48. Statham, G., The Manipulation of Chemical Reactions: Probing the Limits of Interventionism. *Synthese* **2017,** *194* (12), 4815-4838.

49. Arai, H., Hydroformylation, Hydrogenation, and Isomerization of Olefins over Polymer-Immobilized Rhodium Complexes. *J Catal* **1978,** *51* (2), 135-142.

50. Yuki, Y.; Takahashi, K.; Tanaka, Y.; Nozaki, K., Tandem Isomerization/Hydroformylation/Hydrogenation of Internal Alkenes to n-Alcohols Using Rh/Ru Dual- or Ternary-Catalyst Systems. *J Am Chem Soc* **2013,** *135* (46), 17393-17400.

51. Heck, R. F.; Breslow, D. S., The Reaction of Cobalt Hydrotetracarbonyl with Olefins. *J Am Chem Soc* **1961,** *83* (19), 4023-4027.

52. Heck, R. F., Addition Reactions of Transition Metal Compounds. *Acc Chem Res* **1969,** *2* (1), 10-16.

53. Decker, S. A.; Cundari, T. R., DFT Study of the Ethylene Hydroformylation Catalytic Cycle Employing a $HRh(PH_3)_2(CO)$ Model Catalyst. *Organometallics* **2001,** *20* (13), 2827-2841.

54. Vu, T. V.; Kosslick, H.; Schulz, A.; Harloff, J.; Paetzold, E.; Lund, H.; Kragl, U.; Schneider, M.; Fulda, G., Influence of the Textural Properties of Rh/MOF-5 on the Catalytic Properties in the Hydroformylation of Olefins. *Micropor Mesopor Mat* **2012,** *154*, 100-106.

55. Wrzyszcz, J.; Zawadzki, M.; Trzeciak, A. M.; Ziółkowski, J. J., Rhodium Complexes Supported on Zinc Aluminate Spinel as Catalysts for Hydroformylation and Hydrogenation: Preparation and Activity. *J Mol Catal A: Chem* **2002,** *189* (2), 203-210.

56. Song, K.-C.; Baek, J. Y.; Bae, J. A.; Yim, J.-H.; Ko, Y. S.; Kim, D. H.; Park, Y.-K.; Jeon, J.-K., Octene Hydroformylation by Using Rhodium Complexes Tethered onto Selectively Functionalized Mesoporous Silica and in situ High Pressure IR Study. *Catal Today* **2011,** *164* (1), 561-565.

57. Cauzzi, D.; Lanfranchi, M.; Marzolini, G.; Predieri, G.; Tiripicchio, A.; Costa, M.; Zanoni, R., Anchoring Rhodium(I) on Benzoylthiourea-Functionalized Silica Xerogels. Production of Recyclable Hydroformylation Catalysts and the Crystal Structure of the Model Compound [Rh(COD)(Hbztu)Cl]. *J Organomet Chem* **1995,** *488* (1), 115-125.

58. Shannon, R. D.; Vedrine, J. C.; Naccache, C.; Lefebvre, F., Rhodium Exchange in Zeolites. *J Catal* **1984,** *88* (2), 431-447.

59. Mukhopadhyay, K.; Chaudhari, R. V., Heterogenized $HRh(CO)(PPh_3)_3$ on Zeolite Y using Phosphotungstic Acid as Tethering Agent: a Novel Hydroformylation Catalyst. *J Catal* **2003,** *213* (1), 73-77.

60. Zhang, Y.; Zhang, H.-B.; Lin, G.-D.; Chen, P.; Yuan, Y.-Z.; Tsai, K. R., Preparation, Characterization and Catalytic Hydroformylation Properties of Carbon Nanotubes-Supported Rh–Phosphine Catalyst. *Appl Catal A Gen* **1999,** *187* (2), 213-224.

61. Zeelie, T. A.; Root, A.; Krause, A. O. I., Rh/Fibre Catalyst for Ethene Hydroformylation: Catalytic Activity and Characterisation. *Appl Catal A Gen* **2005,** *285* (1), 96-109.

62. Sharma, S. K.; Parikh, P. A.; Jasra, R. V., Hydroformylation of Alkenes using Heterogeneous Catalyst Prepared by Intercalation of $HRh(CO)(TPPTS)_3$ Complex in Hydrotalcite. *J Mol Catal A: Chem* **2010,** *316* (1), 153-162.

63. Van Vu, T.; Kosslick, H.; Schulz, A.; Harloff, J.; Paetzold, E.; Schneider, M.; Radnik, J.; Steinfeldt, N.; Fulda, G.; Kragl, U., Selective Hydroformylation of Olefins over the Rhodium Supported Large Porous Metal–Organic Framework MIL-101. *Appl Catal A Gen* **2013,** *468*, 410-417.

64. Hou, C.; Zhao, G.; Ji, Y.; Niu, Z.; Wang, D.; Li, Y., Hydroformylation of Alkenes over Rhodium Supported on the Metal-Organic Framework ZIF-8. *Nano Research* **2014,** *7* (9), 1364-1369.

65. Matsumoto, M.; Tamura, M., Reinvestigation of Atmospheric Hydroformylation of 1-Octene Catalyzed by a Rhodium Complex. Some Advantages given by Added α,ω-Bis(Diphenylphosphino)Alkane. *J Mol Catal* **1982,** *16* (2), 209-216.

66. Kim, J. J.; Alper, H., Ionic Diamine Rhodium(I) Complexes—Highly Active Catalysts for the Hydroformylation of Olefins. *Chem Commun* **2005,** (24), 3059-3061.

67. Haarman, H. F.; Ernsting, J. M.; Kranenburg, M.; Kooijman, H.; Veldman, N.; Spek, A. L.; van Leeuwen, P. W. N. M.; Vrieze, K., Oxidative Addition of Carbon−Chloride Bonds to Rhodium(I) Complexes Containing Terdentate Nitrogen Ligands. X-ray Analyses of Rhodium(I) Chloride and Rhodium(III) Chloromethyl Complexes. *Organometallics* **1997,** *16* (5), 887-900.

68. Burgun, A.; Coghlan, C. J.; Huang, D. M.; Chen, W.; Horike, S.; Kitagawa, S.; Alvino, J. F.; Metha, G. F.; Sumby, C. J.; Doonan, C. J., Mapping-Out Catalytic Processes in a Metal–Organic Framework with Single-Crystal X-ray Crystallography. *Angew Chem* **2017,** *129* (29), 8532-8536.

69. Gorbunov, D.; Safronova, D.; Kardasheva, Y.; Maximov, A.; Rosenberg, E.; Karakhanov, E., New Heterogeneous Rh-Containing Catalysts Immobilized on a Hybrid Organic–Inorganic Surface for Hydroformylation of Unsaturated Compounds. *ACS Appl Mater Inter* **2018,** *10* (31), 26566-26575.

70. van der Slot, S. C.; Duran, J.; Luten, J.; Kamer, P. C. J.; van Leeuwen, P. W. N. M., Rhodium-Catalyzed Hydroformylation and Deuterioformylation with Pyrrolyl-Based Phosphorus Amidite Ligands: Influence of Electronic Ligand Properties. *Organometallics* **2002,** *21* (19), 3873-3883.

71. Roy, S.; George, C. B.; Ratner, M. A., Catalysis by a Zinc-Porphyrin-Based Metal–Organic Framework: From Theory to Computational Design. *J Phys Chem C* **2012,** *116* (44), 23494-23502.

72. Fang, X.; Zong, B.; Mao, S., Metal–Organic Framework-Based Sensors for Environmental Contaminant Sensing. *Nano-Micro Letters* **2018,** *10* (4), 64.

73. Li, C.-Y.; Liu, J.-M.; Wang, Z.-H.; Lv, S.-W.; Zhao, N.; Wang, S., Integration of Fe3O4@UiO-66-NH2@MON Core-Shell Structured Adsorbents for Specific Preconcentration and Sensitive Determination of Aflatoxins Against Complex Sample Matrix. *J Hazard Mater* **2020,** *384*, 121348.

74. Wang, X.; Li, L.; Wang, Y.; Li, J.-R.; Li, J., Exploiting the Pore Size and Functionalization Effects in UiO Topology Structures for the Separation of Light Hydrocarbons. *CrystEngComm* **2017,** *19* (13), 1729-1737.

75. Chavan, S.; Vitillo, J. G.; Gianolio, D.; Zavorotynska, O.; Civalleri, B.; Jakobsen, S.; Nilsen, M. H.; Valenzano, L.; Lamberti, C.; Lillerud, K. P.; Bordiga, S., H_2 storage in Isostructural UiO-67 and UiO-66 MOFs. *PCCP* **2012,** *14* (5), 1614-1626.

76. Li, X.; Van Zeeland, R.; Maligal-Ganesh, R. V.; Pei, Y.; Power, G.; Stanley, L.; Huang, W., Impact of Linker Engineering on the Catalytic Activity of Metal–Organic Frameworks Containing Pd(II)–Bipyridine Complexes. *ACS Catalysis* **2016,** *6* (9), 6324-6328.

77. Alvino, J. F.; Bennett, T.; Kler, R.; Hudson, R. J.; Aupoil, J.; Nann, T.; Golovko, V. B.; Andersson, G. G.; Metha, G. F., Apparatus for the Investigation of High-Temperature, High-Pressure Gas-Phase Heterogeneous Catalytic and Photo-Catalytic Materials. *Rev Sci Instrum* **2017,** *88* (5), 054101.

3.10. Appendix

3.10.1. Crystal Size Analysis of Single UiO-67-bpydc Crystals

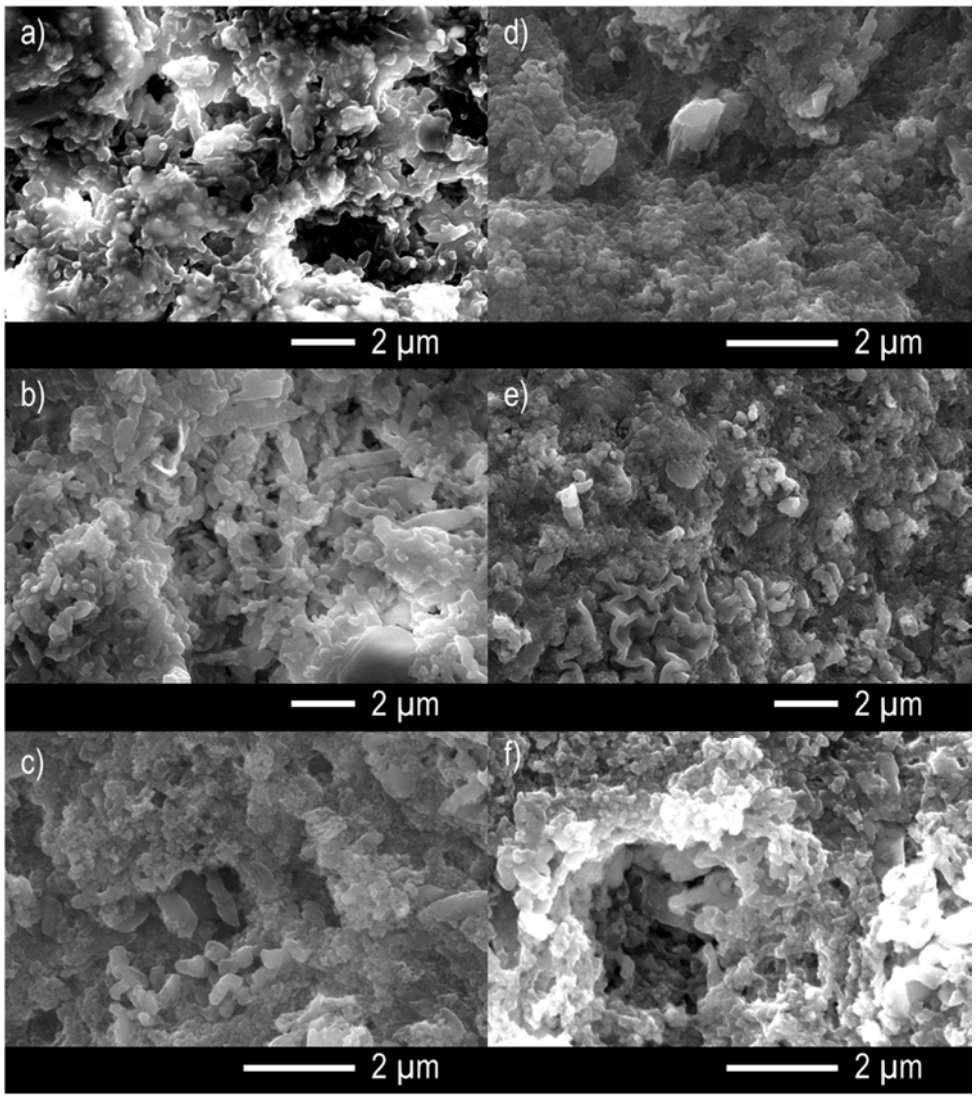

Figure **3.A.1**: SEM images of UiO-67-bpydc synthesised at room temperature with a ligand to base ratio of 1:1 using basic additives a) sodium formate, b) sodium acetate, c) sodium hydroxide, d) triethylamine, e) n-butylamine and f) tert-butylamine.

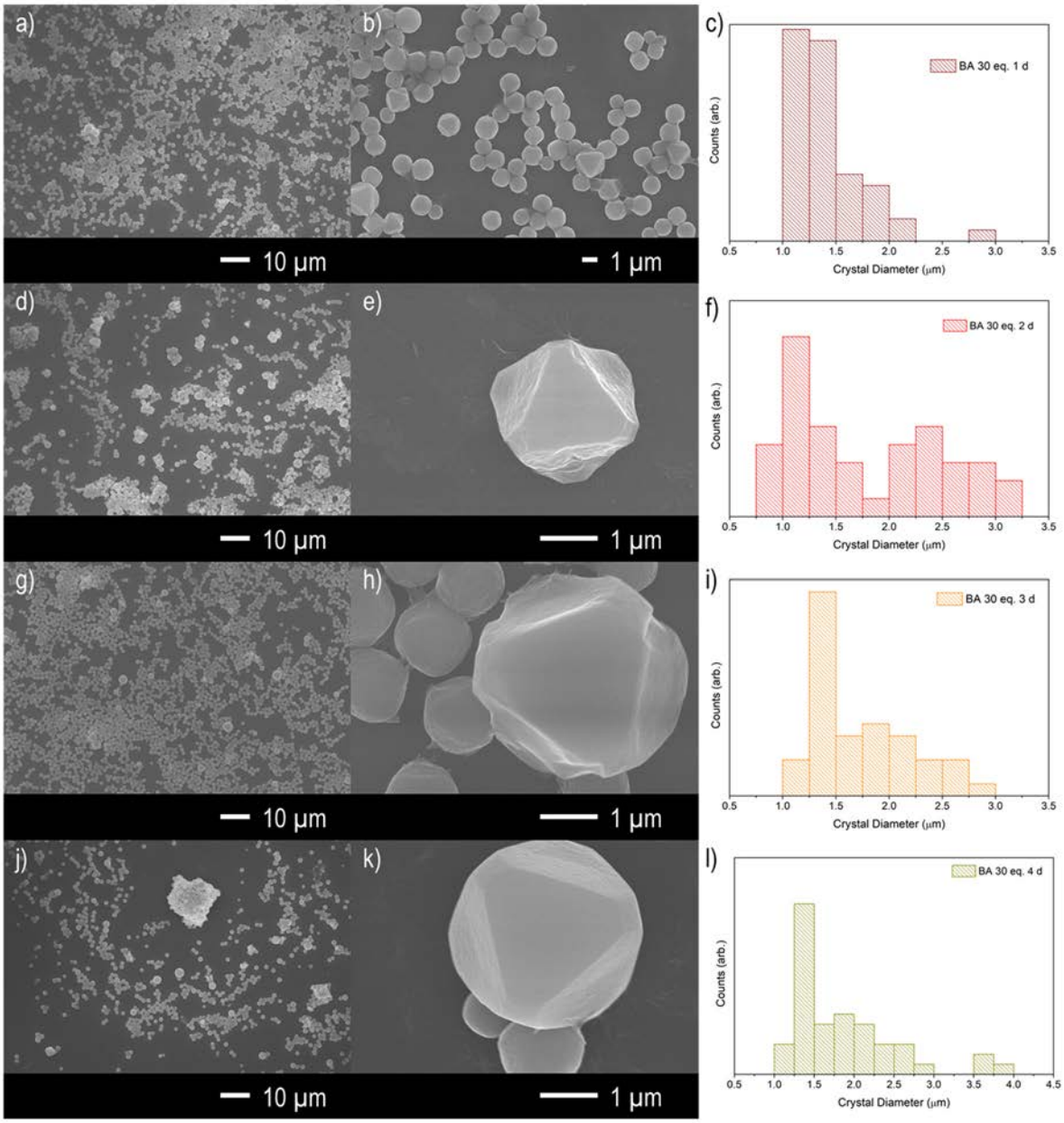

Figure **3.A.2**: SEM images of UiO-67-bpydc synthesised with 30 equivalents of benzoic acid at 120 ºC for a)-b) 1, d)-e) 2, g)-h) 3 and j)-k) 4 days, with size distributions of the crystal diameter for c) 1, f) 2, i) 3 and l) 4 days, respectively.

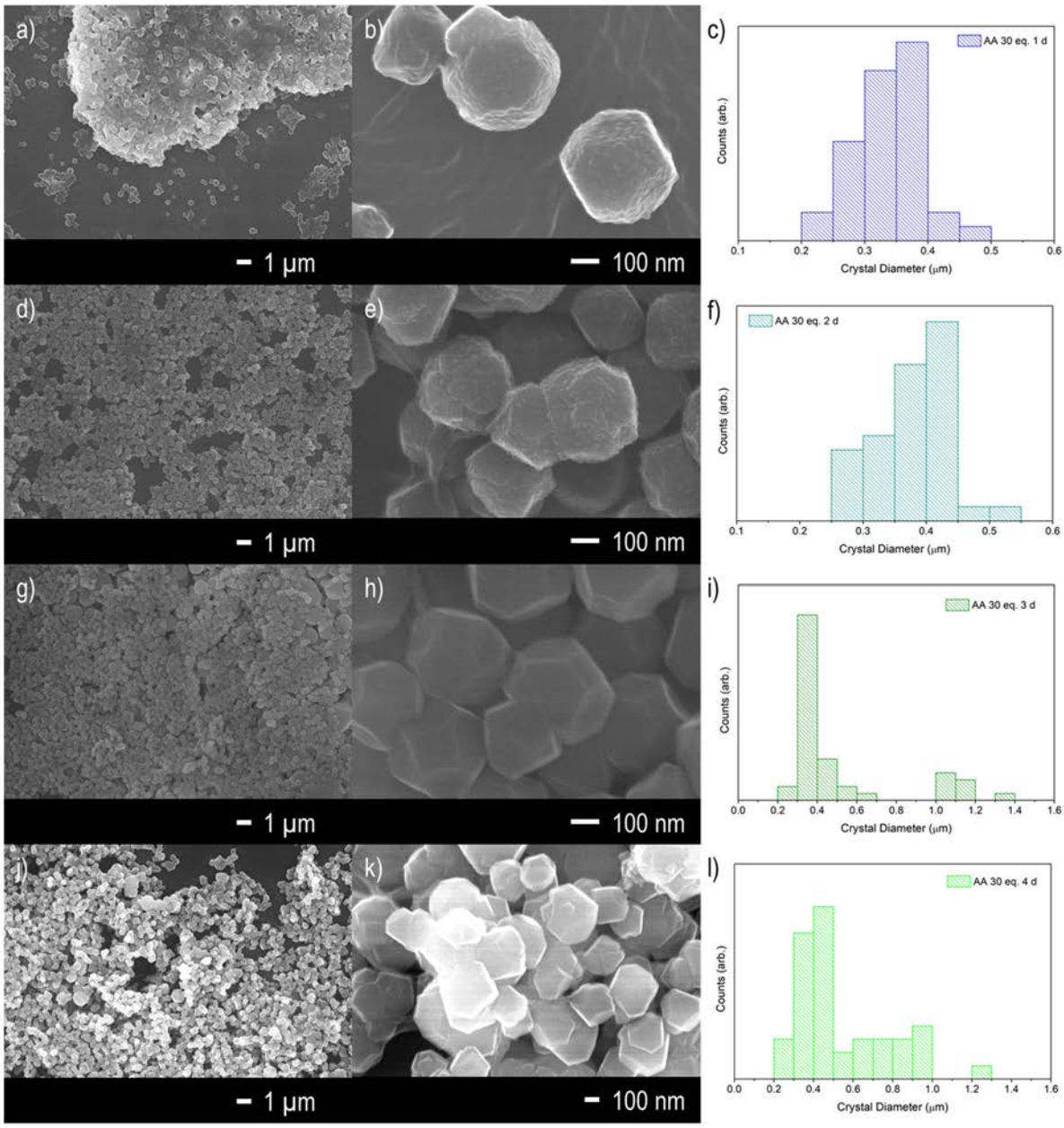

Figure **3.A.3**: SEM images of UiO-67-bpydc synthesised with 30 equivalents of glacial acetic acid at 120 ºC for a)-b) 1, d)-e) 2, g)-h) 3 and j)-k) 4 days, with size distributions of the crystal diameter for c) 1, f) 2, i) 3 and l) 4 days, respectively.

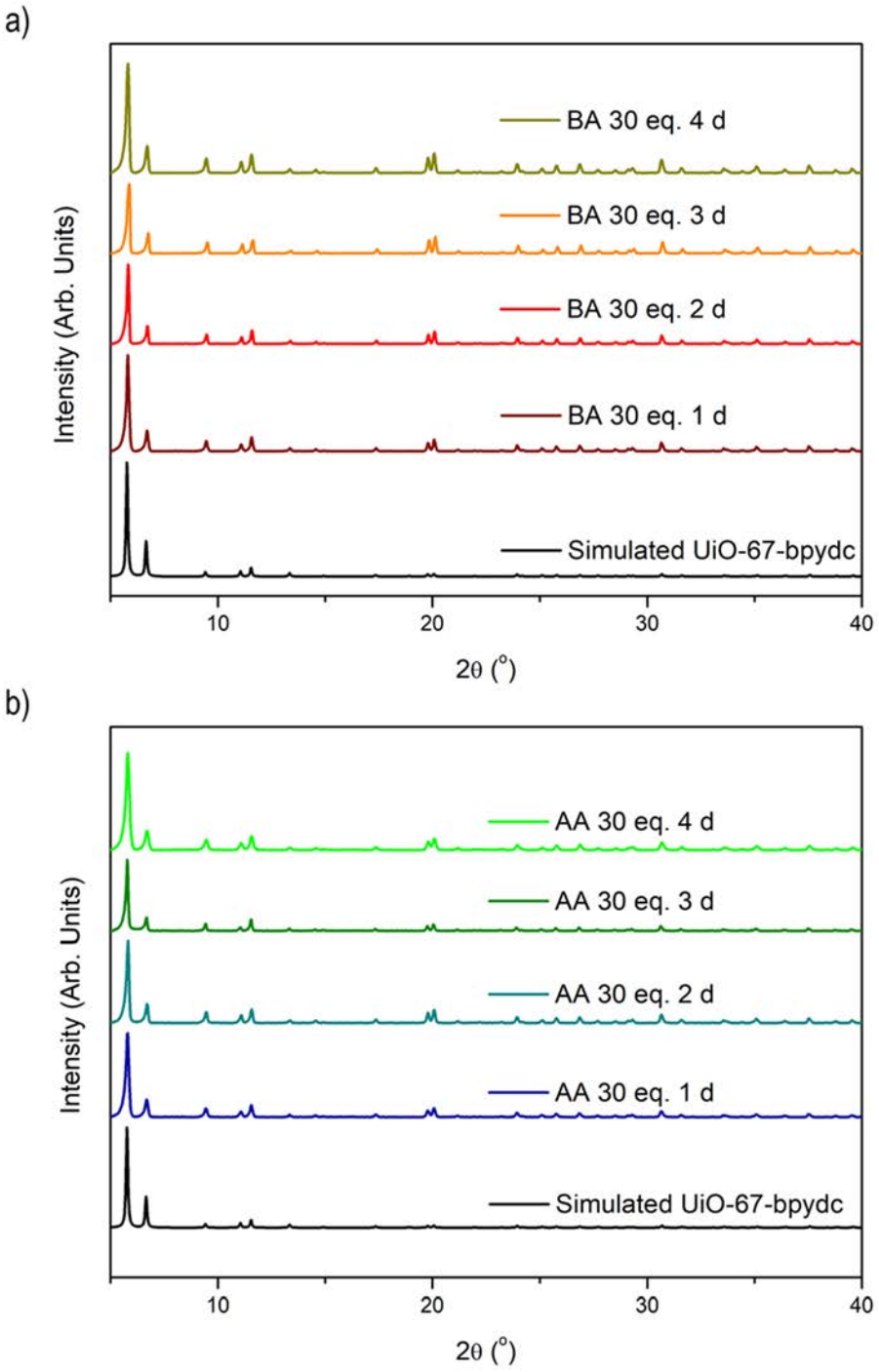

Figure **3.A.4**: PXRD patterns of UiO-67-bpydc synthesised with 30 equivalents of a) benzoic acid (BA) and b) acetic acid (AA) over 1-4 days, plotted in comparison to a simulated pattern of UiO-67-bpydc (black).

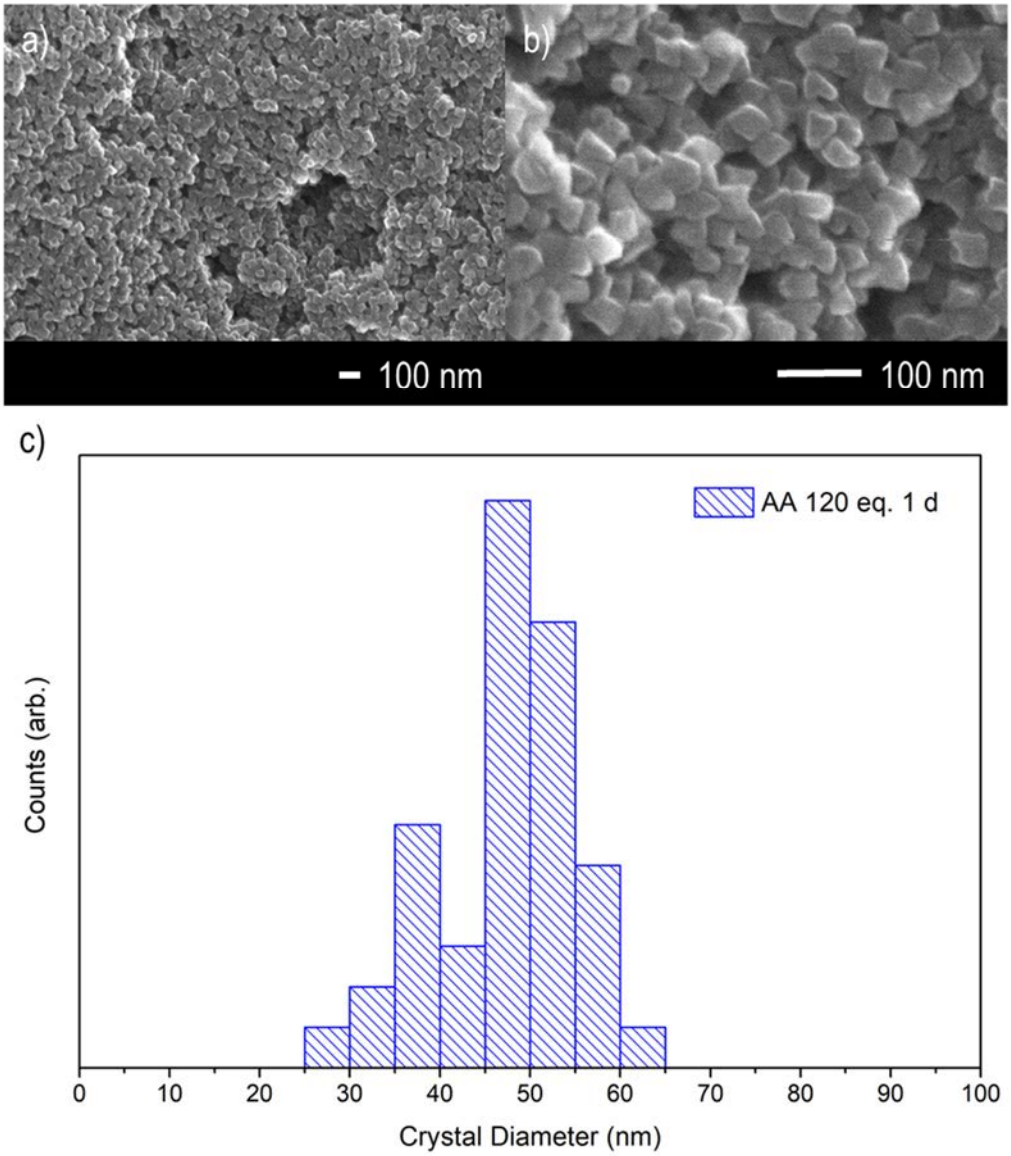

Figure **3.A.5**: a)-b) SEM images of UiO-67-bpydc synthesised with 120 equivalents of glacial acetic acid at 120 ºC for 1 day in Teflon lined vials and c) the corresponding size distribution of crystal diameter.

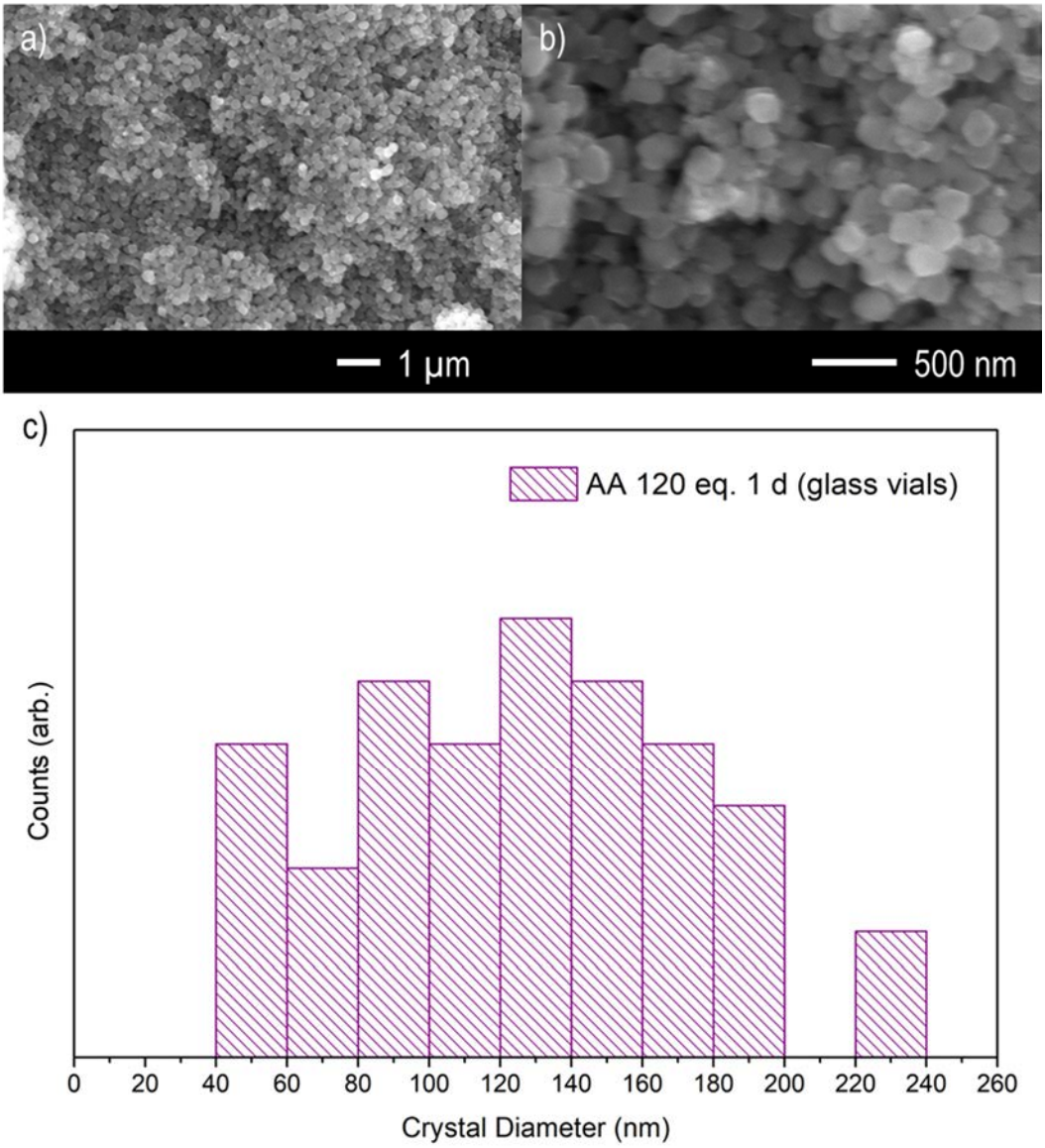

Figure **3.A.6**: a)-b) SEM images of UiO-67-bpydc synthesised with 120 equivalents of glacial acetic acid at 120 ºC for 1 day in glass vials and c) the corresponding size distribution of crystal diameter.

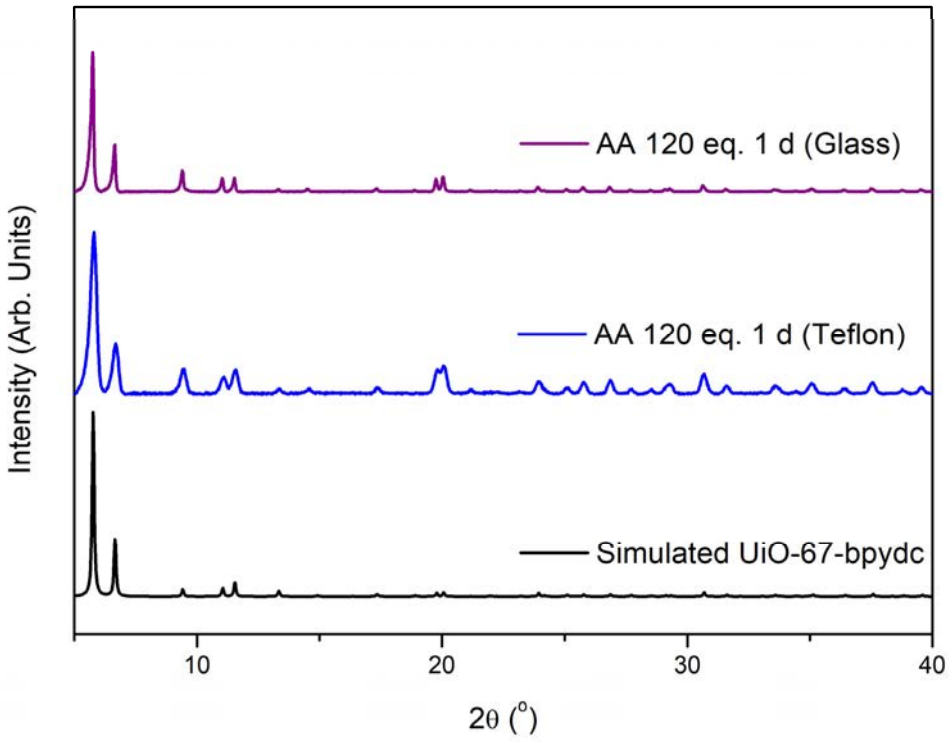

Figure **3.A.7**: PXRD patterns of UiO-67-bpydc synthesised with 120 equivalents of acetic acid (AA) in Teflon lined vials (blue) and glass vials (purple), plotted in comparison to a simulated pattern of UiO-67-bpydc (black).

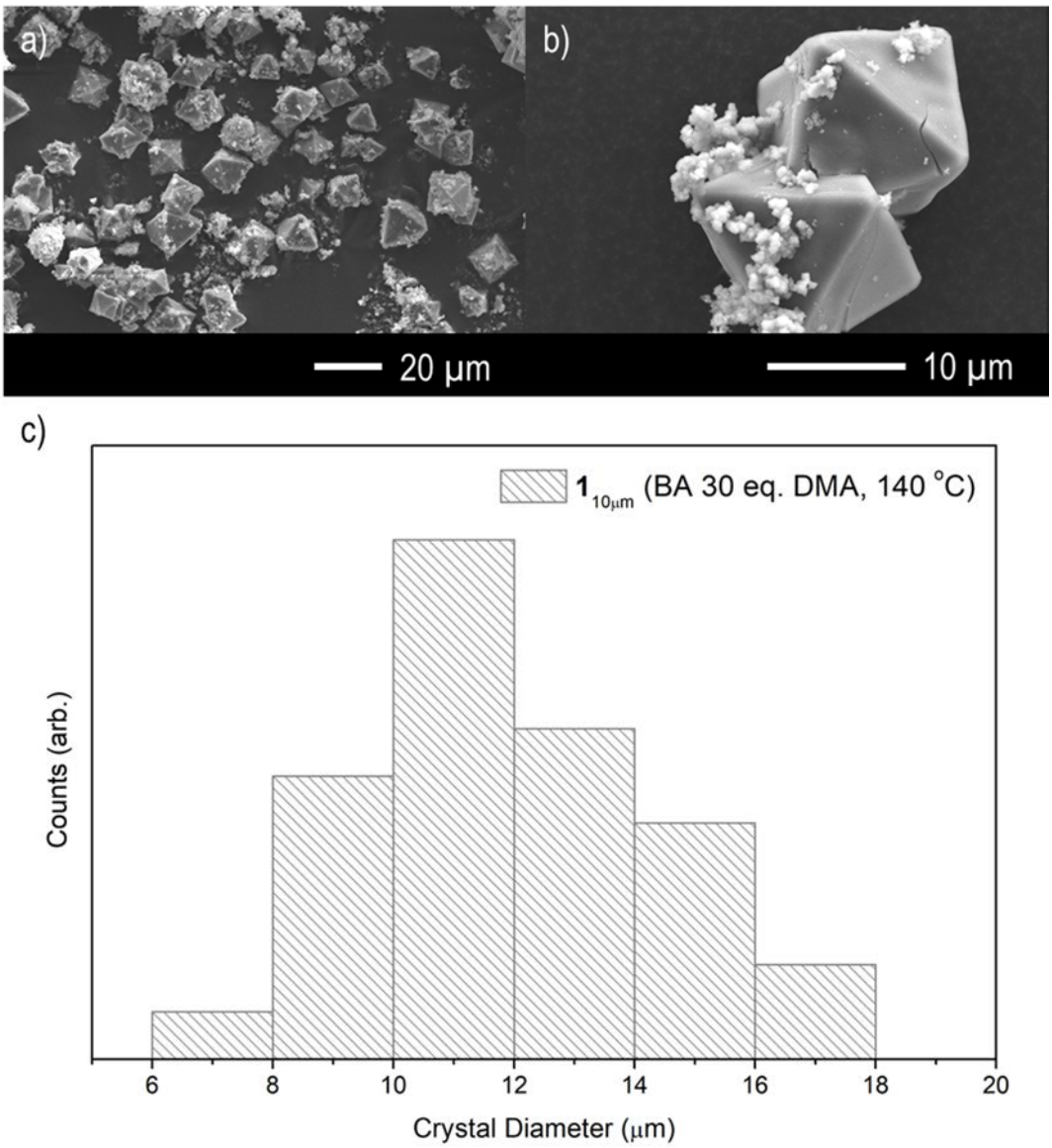

Figure **3.A.8**: a)-b) SEM images of UiO-67-bpydc synthesised 30 equivalents of benzoic acid (BA), in DMA at 140 ºC for 3 days (**1**$_{10\mu m}$) and c) the corresponding size distribution of crystal diameter.

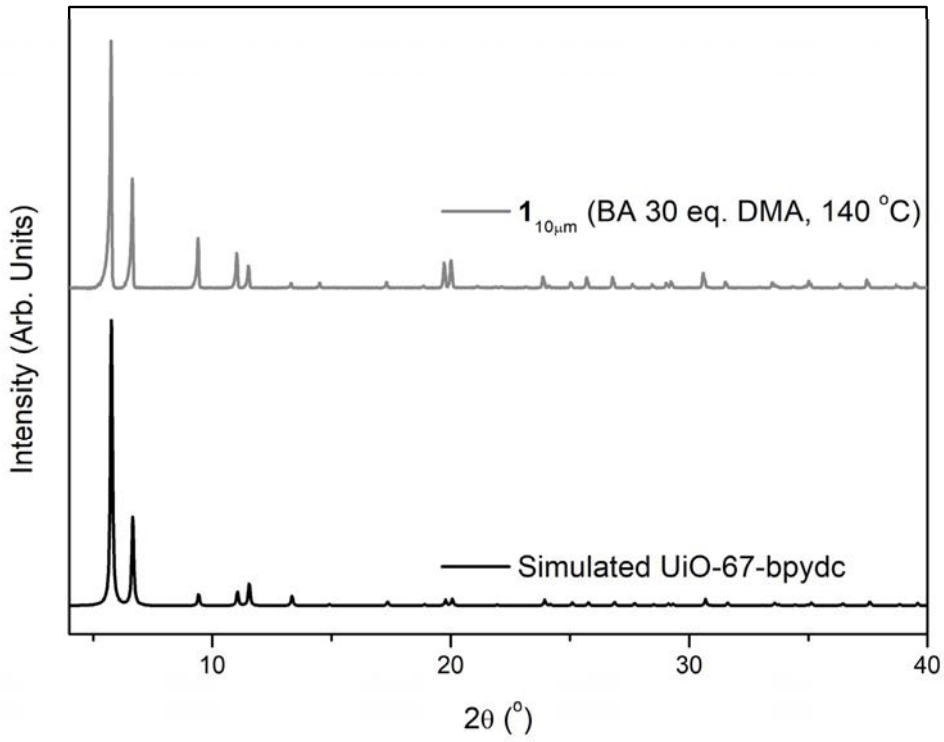

Figure **3.A.9**: PXRD pattern of UiO-67-bpydc synthesised with 30 equivalents of benzoic acid (BA), in DMA at 140 ºC for 3 days (**1**$_{10\mu m}$, grey), plotted in comparison to a simulated pattern of UiO-67-bpydc (black).

3.10.2. Characterisation of Ligand dilution for $\mathbf{1}_{100nm}$, $\mathbf{1}_{1\mu m}$ *and* $\mathbf{1}_{10\mu m}$

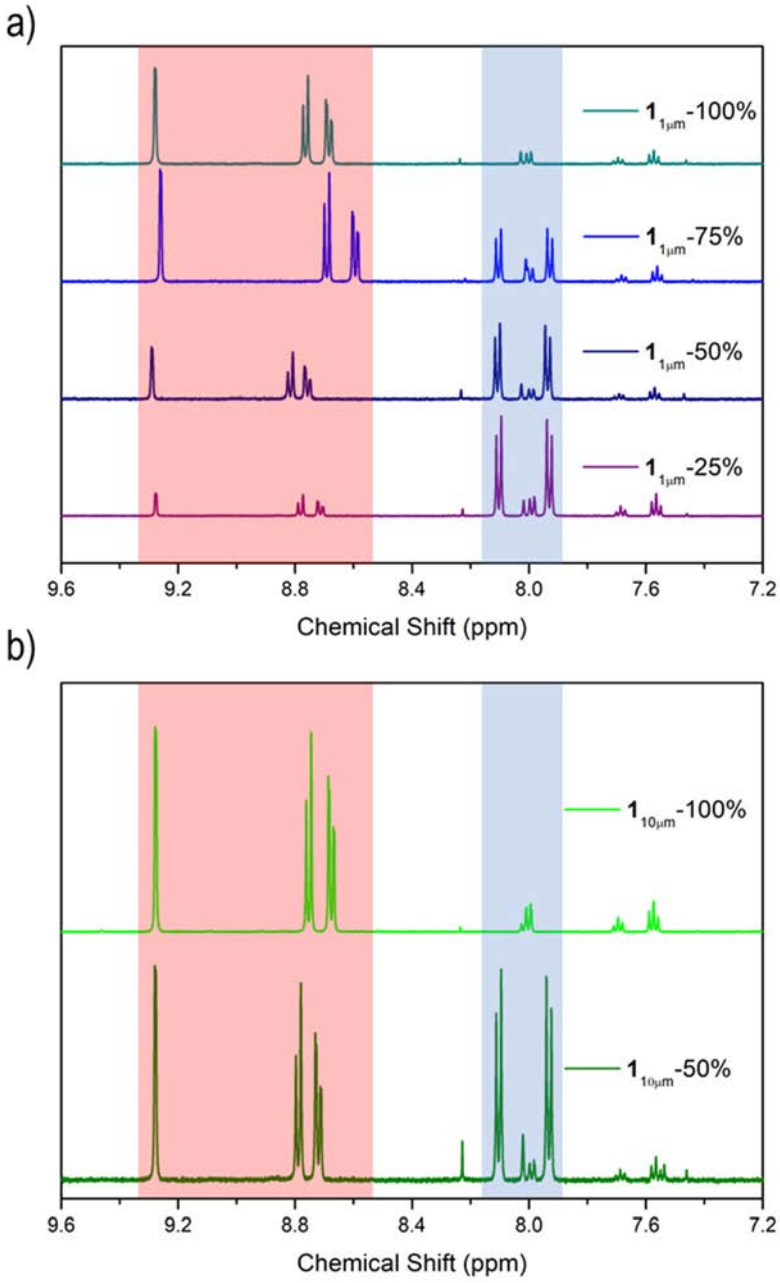

Figure **3.A.10**: ^{1}H NMR spectra of DCl/DMSO$_{d6}$ digested samples of UiO-67 with varied H$_2$bpydc loadings synthesised under solvothermal conditions $\mathbf{1}_{1\mu m}$ (a) and $\mathbf{1}_{10\mu m}$ (b); 25%, 50%, 75% and 100%. The chemical shifts for ligands H$_2$bpydc and H$_2$bpdc are highlighted in red and blue, respectively. Note the chemical shifts of proton signals of H$_2$bpydc subtly change with acid concentration due to the protonation of the pyridyl nitrogens in the ligand during the DCl/DMSO$_{d6}$ digestion.

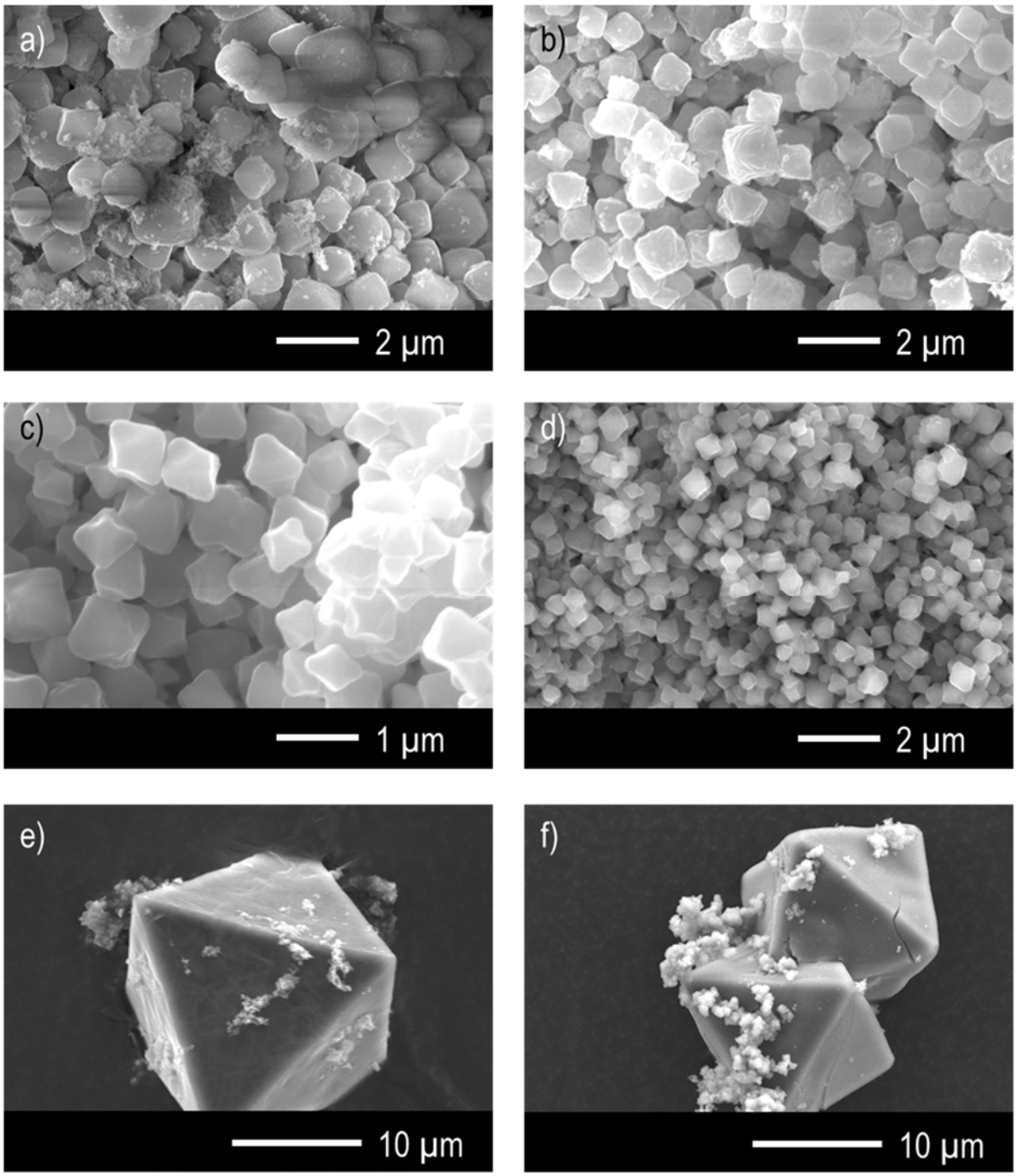

Figure **3.A.11**: SEM images a) **1**$_{1\mu m}$-25%, b) **1**$_{1\mu m}$-50%, c) **1**$_{1\mu m}$-75%, d) **1**$_{1\mu m}$-100%, e) **1**$_{10\mu m}$-50% and f) **1**$_{10\mu m}$-100%.

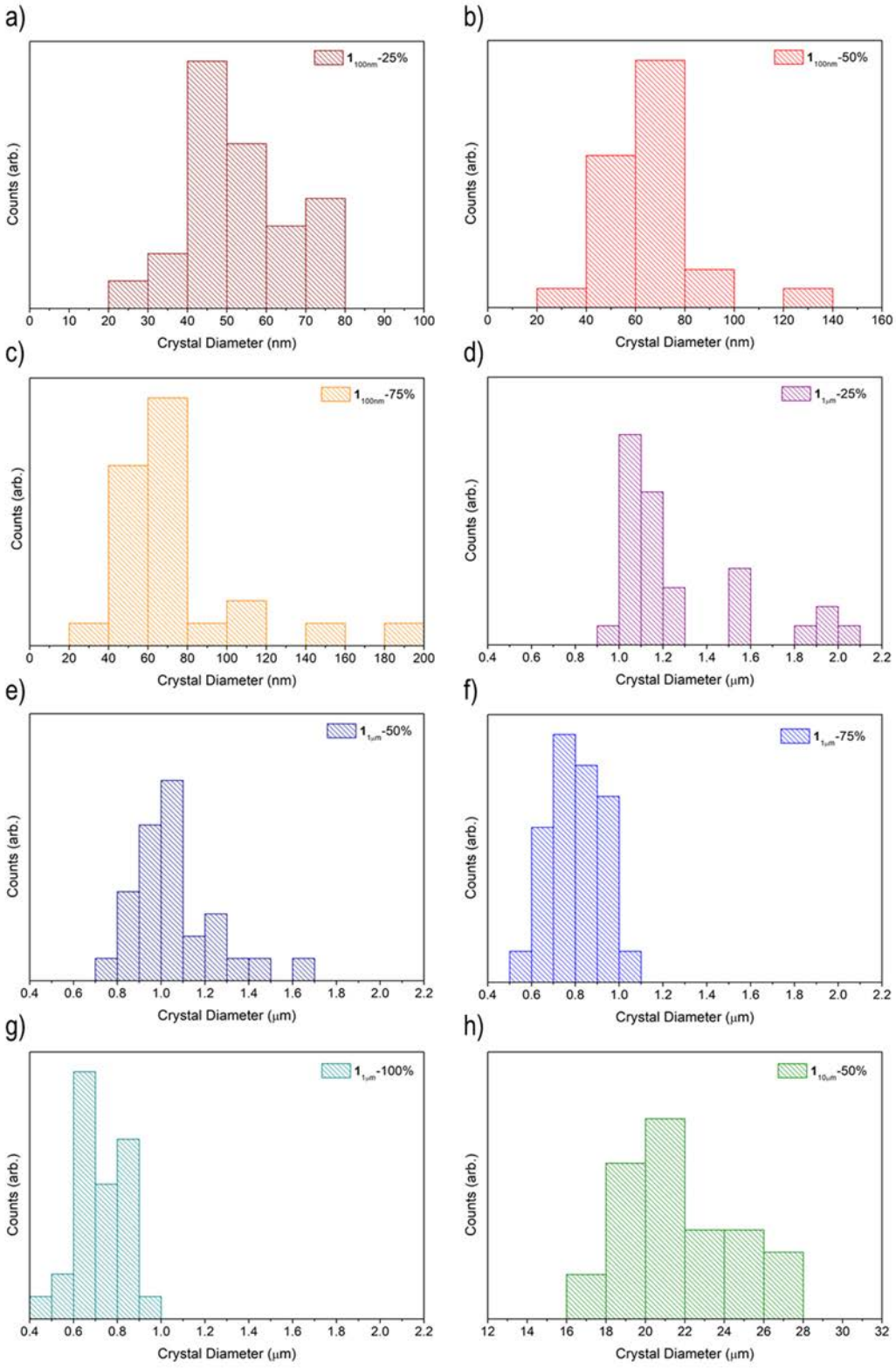

Figure **3.A.12**: Crystal diameter distributions for a) $\mathbf{1}_{100nm}$-25%, b) $\mathbf{1}_{100nm}$-50%, c) $\mathbf{1}_{100nm}$-75%, d) $\mathbf{1}_{1\mu m}$-25%, e) $\mathbf{1}_{1\mu m}$-50%, f) $\mathbf{1}_{1\mu m}$-75%, g) $\mathbf{1}_{1\mu m}$-100% and h) $\mathbf{1}_{10\mu m}$-50%. Crystal size distributions for $\mathbf{1}_{100nm}$-100% and $\mathbf{1}_{10\mu m}$-100% can be found in Figures **3.A.6** and **3.A.8** respectively.

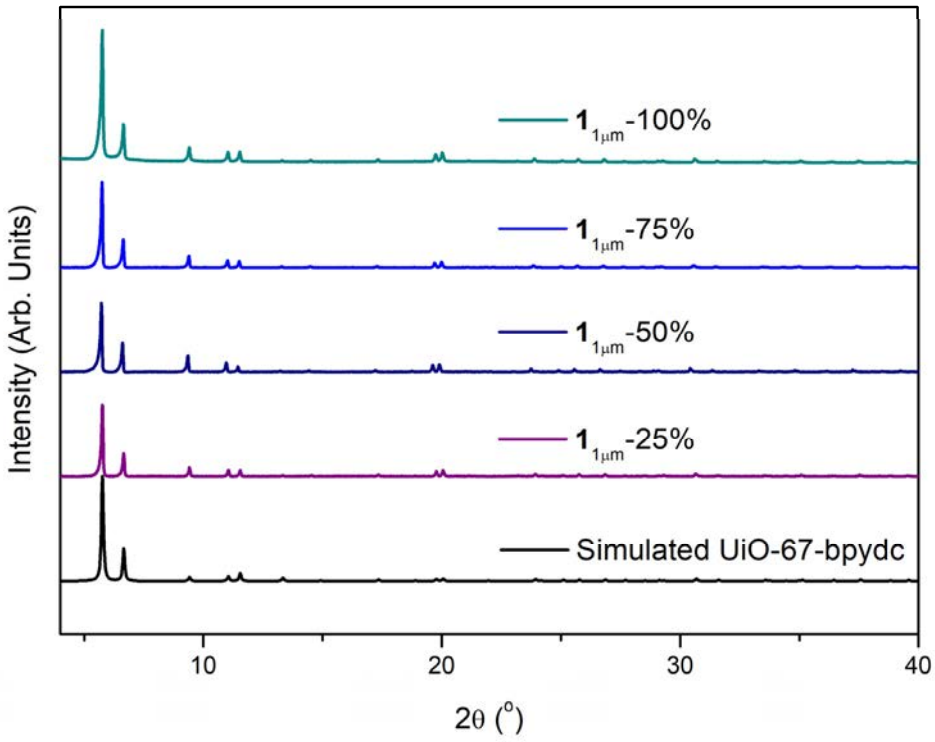

Figure **3.A.13**: PXRD patterns of UiO-67-bpydc; simulated (black), **1**$_{1\mu m}$-25% (purple), **1**$_{1\mu m}$-50% (dark blue), **1**$_{1\mu m}$-75% (blue) and **1**$_{1\mu m}$-100% (dark cyan).

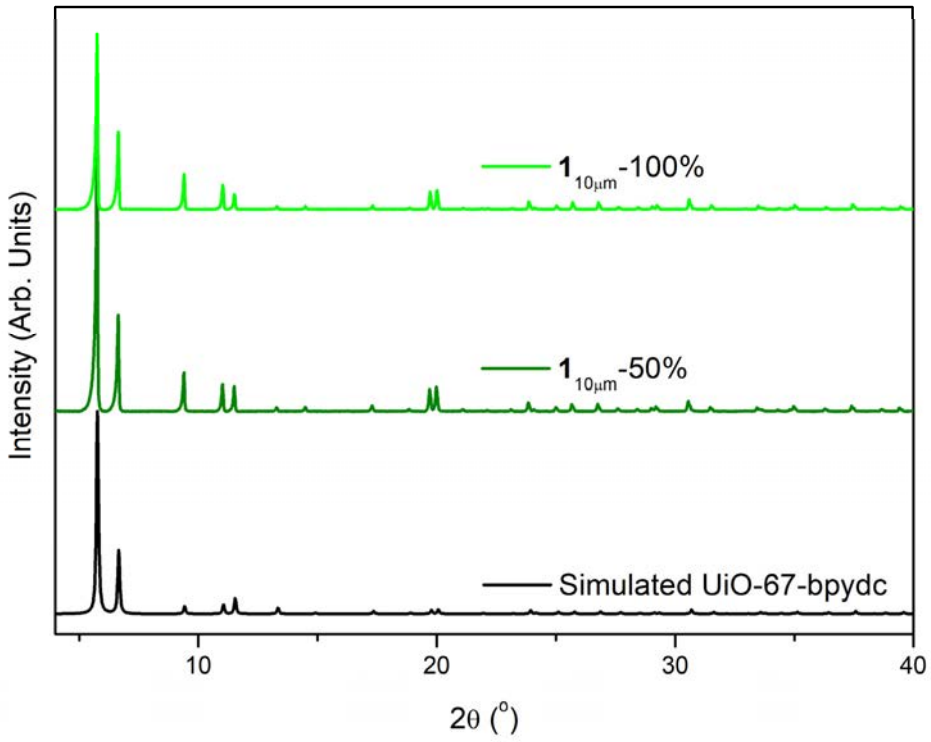

Figure **3.A.14**: PXRD patterns of UiO-67-bpydc; simulated (black), **1**$_{10\mu m}$-50% (dark green) and **1**$_{10\mu m}$-100% (light green).

3.10.3. Characterisation PSMet UiO-67-bpydc

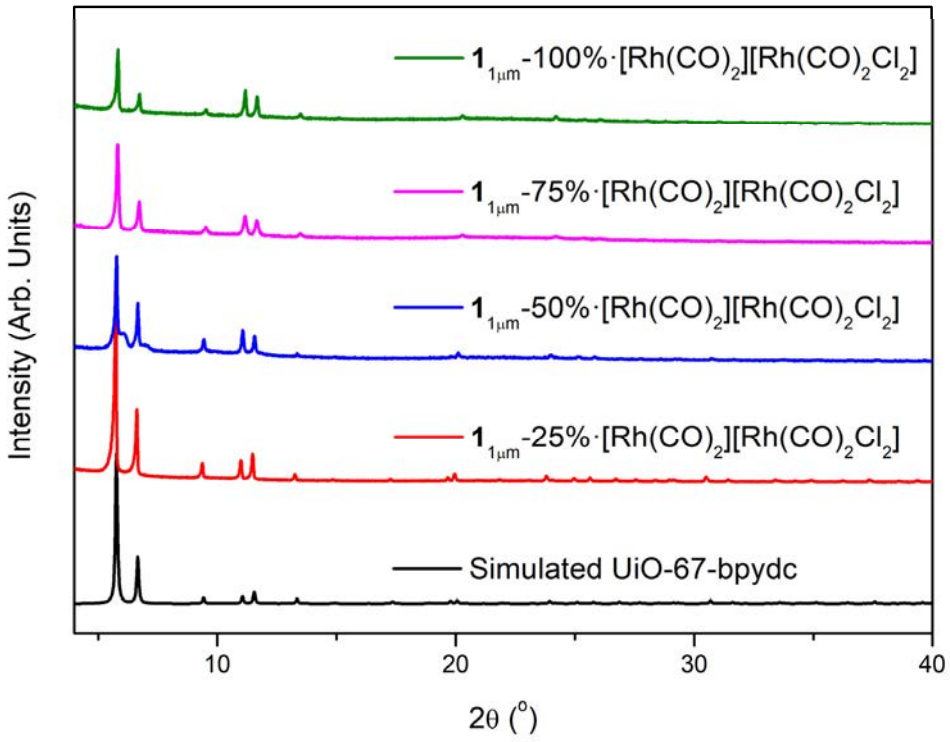

Figure **3.A.15**: PXRD patterns of simulated UiO-67-bpydc (black) and samples of **1**$_{1\mu m}$-25%, **1**$_{1\mu m}$-50%, **1**$_{1\mu m}$-75% and **1**$_{1\mu m}$-100% metalated with $[Rh(CO)_2Cl]_2$ which forms the complex $[Rh(bpydc)(CO)_2][Rh(CO)_2Cl_2]$ within the MOF.

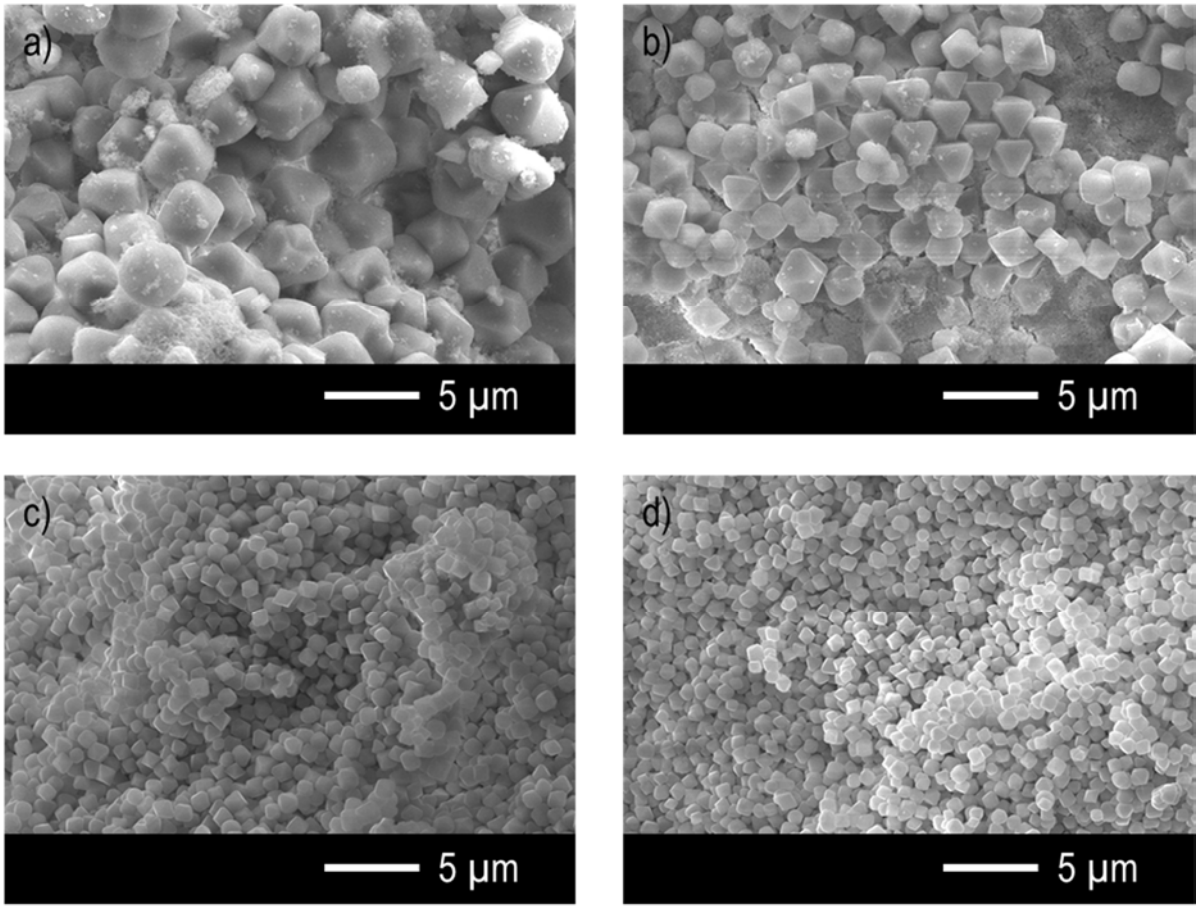

Figure **3.A.16**: SEM images of a) $\mathbf{1}_{1\mu m}$-25%·$[Rh(CO)_2][Rh(CO)_2Cl_2]$, b) $\mathbf{1}_{1\mu m}$-50%·$[Rh(CO)_2][Rh(CO)_2Cl_2]$, c) $\mathbf{1}_{1\mu m}$-75%·$[Rh(CO)_2][Rh(CO)_2Cl_2]$ and d) $\mathbf{1}_{1\mu m}$-100%·$[Rh(CO)_2][Rh(CO)_2Cl_2]$.

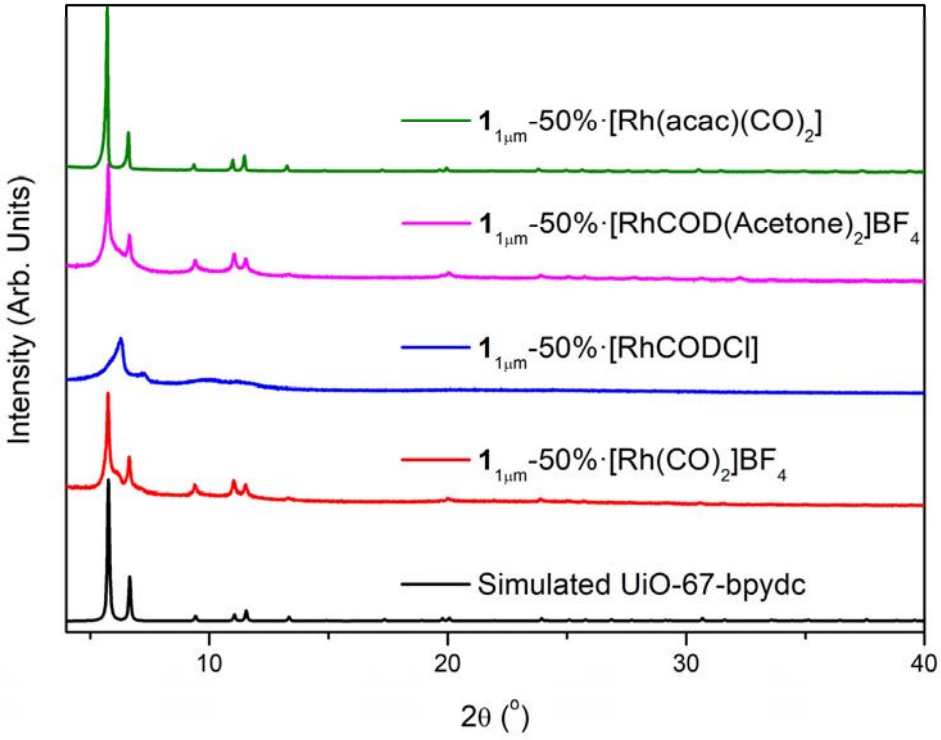

Figure **3.A.17**: PXRD patterns of simulated UiO-67-bpydc (black) and samples of **1**$_{1\mu m}$-50% metalated with $[Rh(CO)_2]BF_4$ (red), [RhCODCl] (blue), $[RhCOD(Acetone)_2]BF_4$ (purple) and $[Rh(acac)(CO)_2]$ (green).

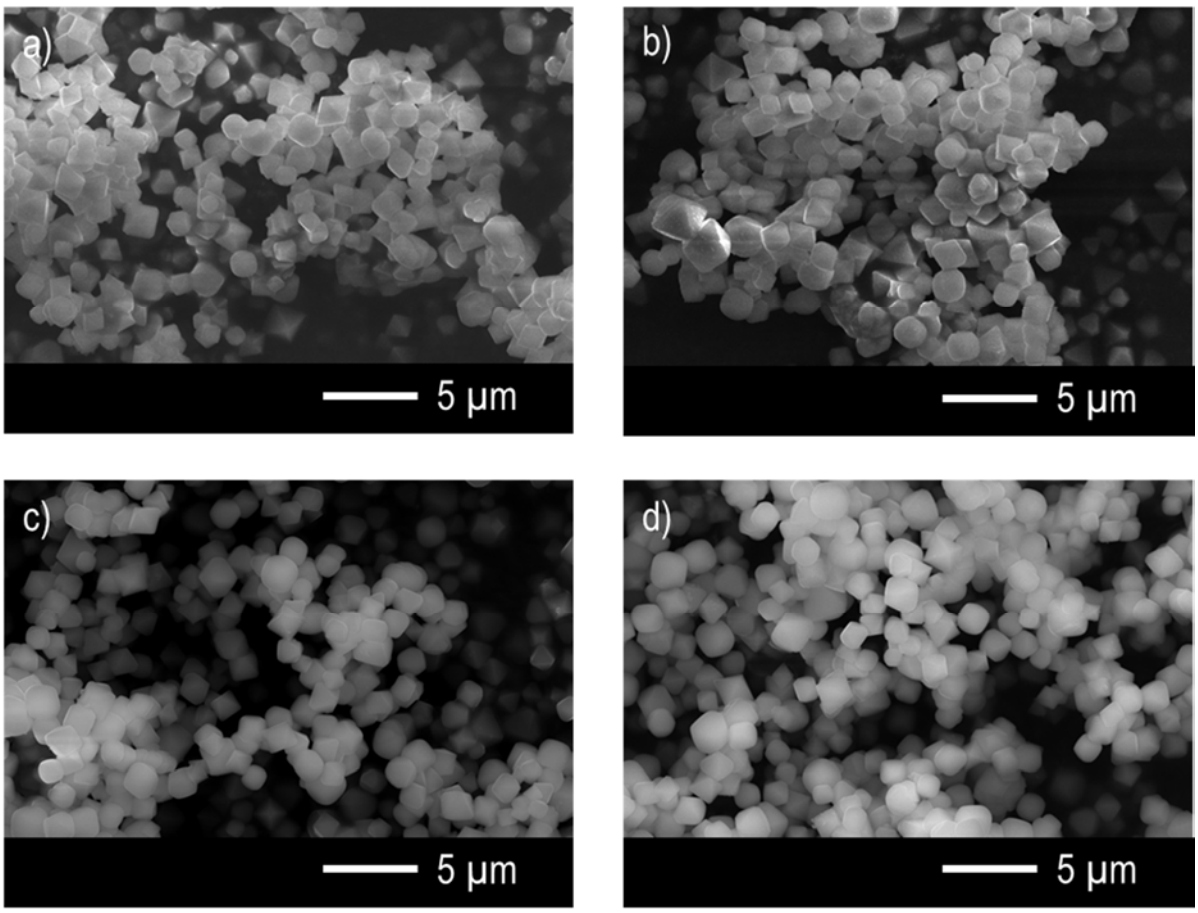

Figure **3.A.18**: SEM images of a) **1**$_{1\mu m}$-50%·[Rh(CO)$_2$]BF$_4$, b) **1**$_{1\mu m}$-50%·[RhCODCl], c) **1**$_{1\mu m}$-50%·[RhCOD(acetone)$_2$]BF$_4$ and d) **1**$_{1\mu m}$-50%·[Rh(acac)(CO)$_2$].

3.10.4. Screening Rhodium Ethylene Hydroformylation Catalysts

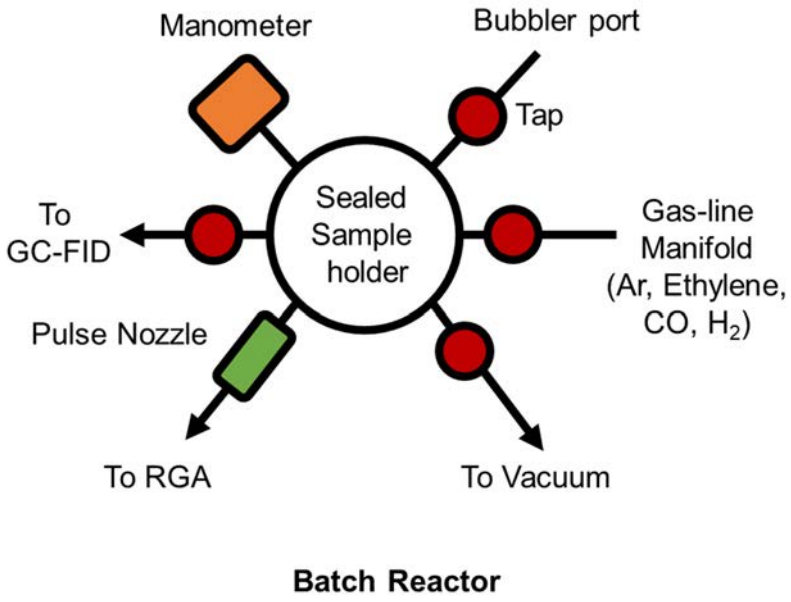

Figure **3.A.19**: Schematic representation of the batch reactor used during catalytic testing.

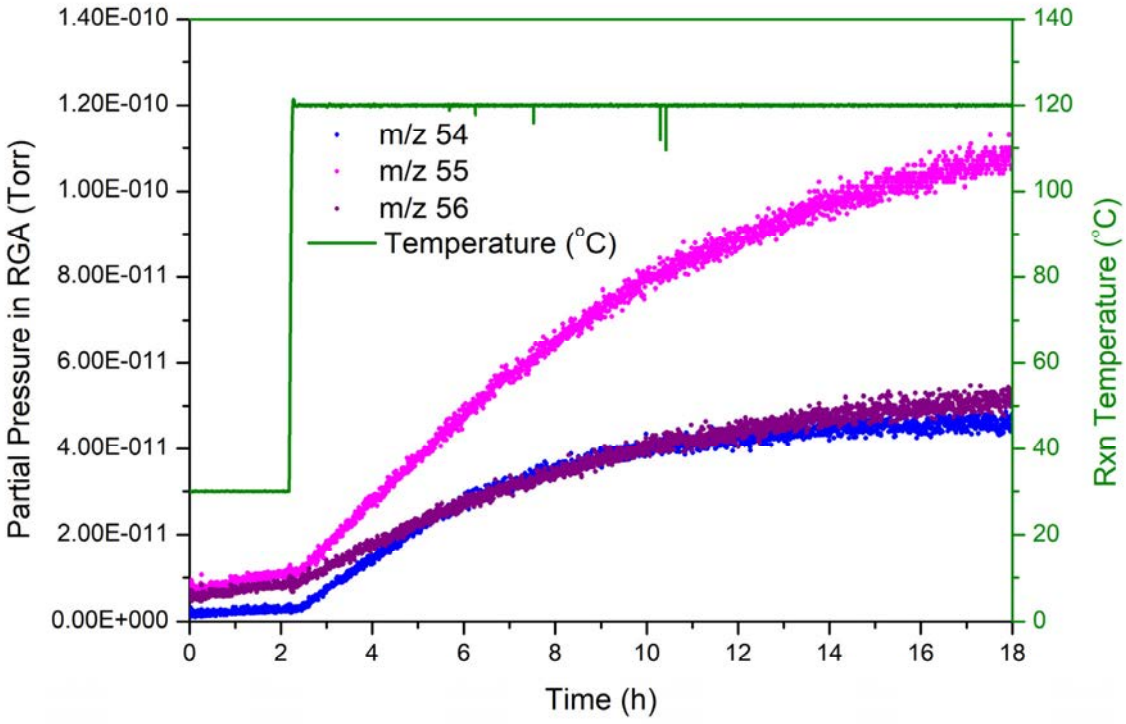

Figure **3.A.20**: RGA partial pressures (Torr) of mass fragments 54, 55 and 56 for the second ethylene hydroformylation reaction catalysed by **1**$_{1\mu m}$-50%·[Rh(COD)Cl]. Indicating the hydroformylation and hydrogenation of COD under reaction conditions.

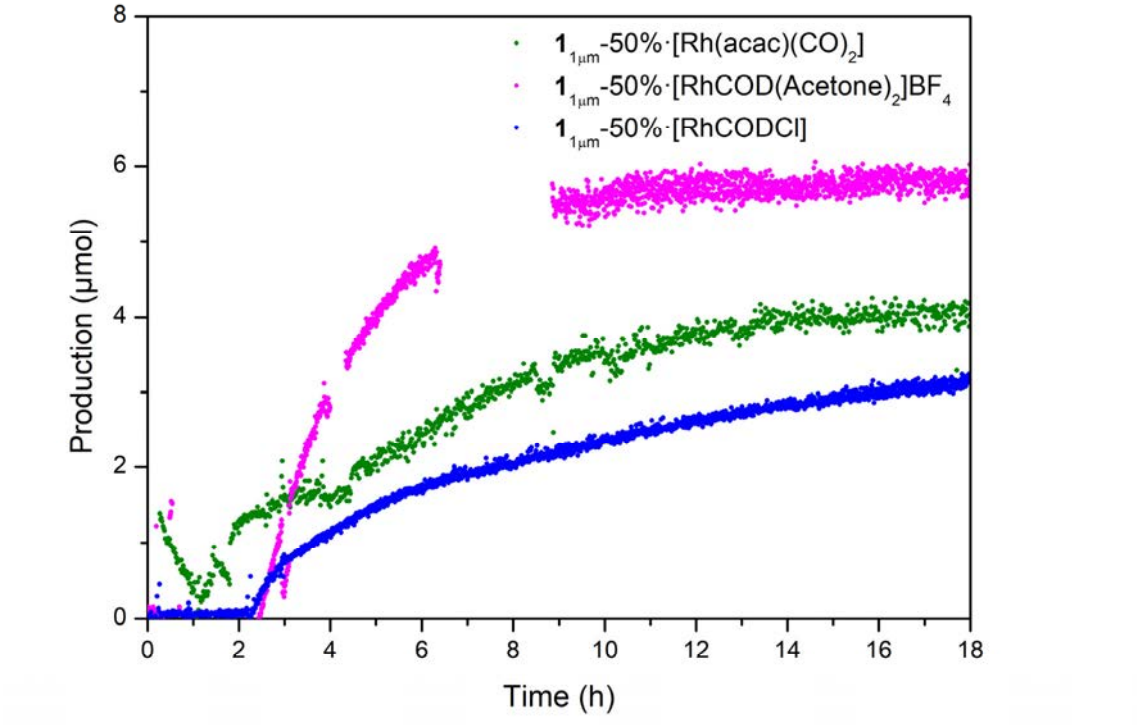

Figure **3.A.21**: 1-Propanal production for each of the rhodium catalysts appended to $\mathbf{1}_{1\mu m}$-50%; [Rh(COD)Cl] (blue), [RhCOD(acetone)$_2$]BF$_4$ (magenta) and [Rh(acac)(CO)$_2$] (green). Note, gaps in data for $\mathbf{1}_{1\mu m}$-50%·[RhCOD(acetone)$_2$]BF$_4$ arose from a communication issue between the RGA software and the RGA, the experiment was not affected by this issue, but no data was collected for short periods of time.

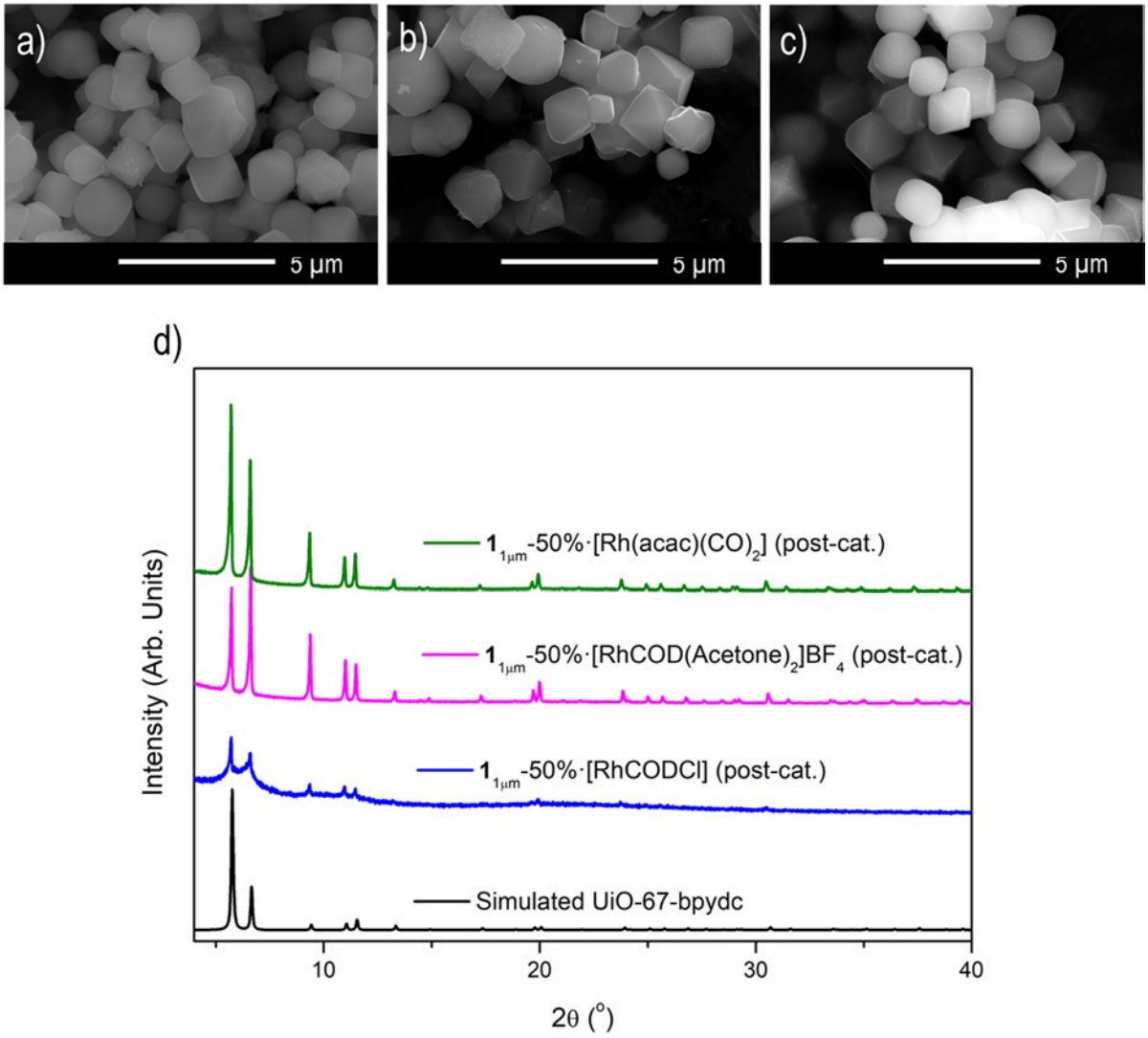

Figure **3.A.22**: SEM of images of a) **1**$_{1\mu m}$-50%·[Rh(COD)Cl], b) **1**$_{1\mu m}$-50%·[RhCOD(acetone)$_2$]BF$_4$ and c) **1**$_{1\mu m}$-50%·[Rh(acac)(CO)$_2$] post-catalysis, and d) the corresponding PXRD patterns compared to the simulated pattern of UiO-67-bpydc.

3.10.5. Calculations of Rhodium Content

The molecular formula for each sample is determined by combining ^{1}H NMR spectroscopy data with elemental analysis of Rh:Zr ratio via EDX. ^{1}H NMR spectroscopy data provides the H_2bpydc:H_2bpdc ratio of the sample in the bulk, enabling assignment of x and y in the molecular formula $Zr_6(OH)_4O_4(bpydc)_x(bpdc)_y$, x + y = 6 because there are 6 ligands per Zr node in the framework. Elemental analysis of the MOF samples gives the Rh:Zr ratio (Rh_{ratio}), hence the amount of Rh associated with the formula equals Rh_{ratio} × 6 as there are 6 Zr atoms in the formula. The molecular weight (MW) for the repeating unit of the metalated MOF can be calculated ($MW_{PS\text{-}met}$) by adding the MW of the bare framework with Rh_{ratio} × 6 × MW(Rh complex). The number of milli-moles of the repeating unit per mg of sample can be calculated by dividing 1 by $MW_{PS\text{-}met}$ and this can be converted to μmol (repeating unit)/mg (sample) by multiplying by 1000. The number of moles of the rhodium catalyst per mg of sample can be calculated by multiplying this value by Rh_{ratio} × 6. And subsequently the moles of rhodium catalyst in each sample is calculated by further multiplying by the mass of the sample used. A summary of the μmol of rhodium catalyst in each of the samples reported in Chapter 3 is outlined in Table **3.A.1**.

Table **3.A.1:** Summary of Rh content in catalysts used for hydroformylation reactions.

Catalyst	Rh : Zr (SEM/EDX, %)	Sample Mass (mg)	Rh catalyst in sample (μmol)
1$_{1\mu m}$-50%·[RhCODCl]	47.0 ± 0.3	15.2	15.2
1$_{1\mu m}$-50%·[RhCOD(acetone)$_2$]BF_4	45.4 ± 0.5	11.4	9.6
1$_{1\mu m}$-50%·[Rh(acac)(CO)$_2$]	30.0 ± 0.5	14.9	10.6
Rh·1$_{100nm}$-50%	43.8 ± 0.5	10.4	8.5
Rh·1$_{1\mu m}$-50%	45.4 ± 0.5	11.4	9.6
Rh·**1**$_{10\mu m}$-50%	44.5 ± 1.1	5.0	4.2

3.10.6. Size Effects on Ethylene Hydroformylation Catalysis

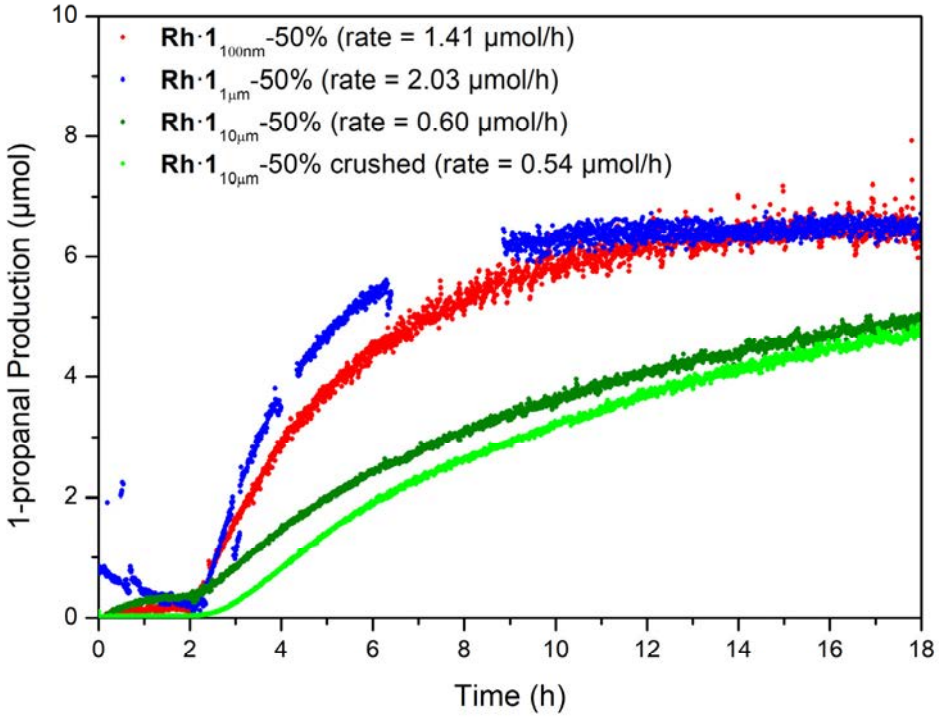

Figure **3.A.23**: 1-propanal production from gas phase ethylene hydroformylation reactions catalysed by **Rh**·**1**$_{100nm}$-50% (red), **Rh**·**1**$_{1\mu m}$-50% (blue), **Rh**·**1**$_{10\mu m}$-50% (dark green) and crushed **Rh**·**1**$_{10\mu m}$-50% (light green). The displayed rates were calculated from the first 2 hours of 1-propanal production for each catalyst.

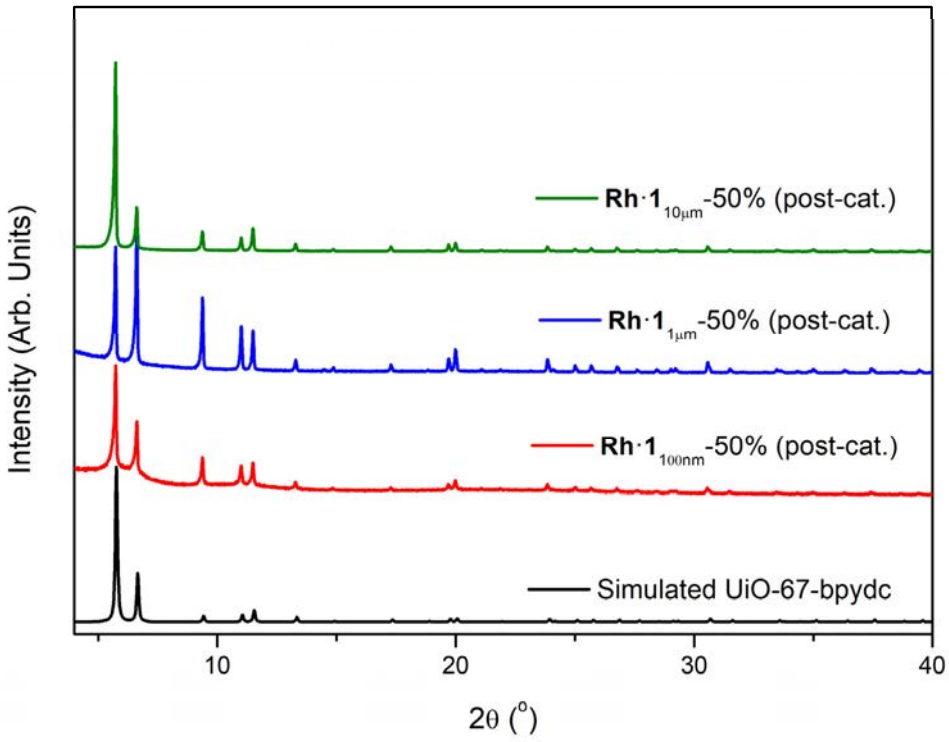

Figure **3.A.24**: PXRD patterns of simulated UiO-67-bpydc (black), **Rh·1**$_{100nm}$-50% (red), **Rh·1**$_{1\mu m}$-50% (blue) and **Rh·1**$_{10\mu m}$-50% (dark green), post-catalysis.

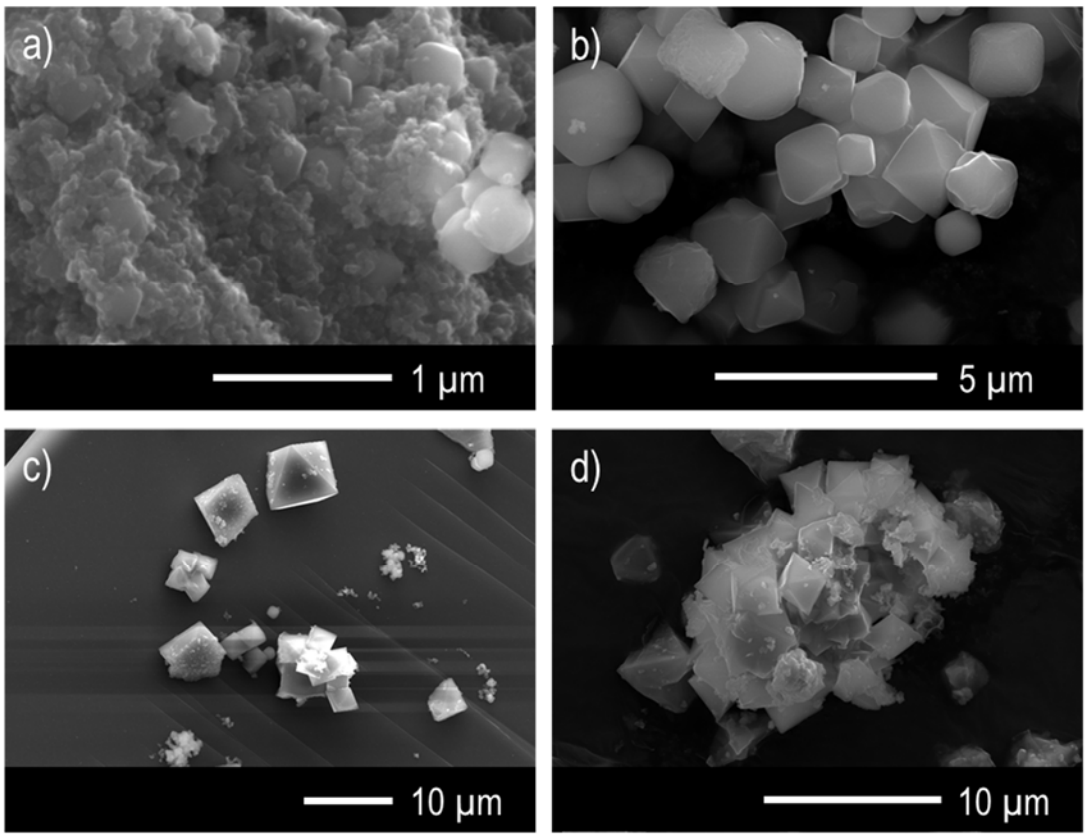

Figure **3.A.25**: SEM images of a) **Rh**·**1**$_{100nm}$-50%, b) **Rh**·**1**$_{1µm}$-50%, c) **Rh**·**1**$_{10µm}$-50% and d) crushed **Rh**·**1**$_{10µm}$-50%, post-catalysis.

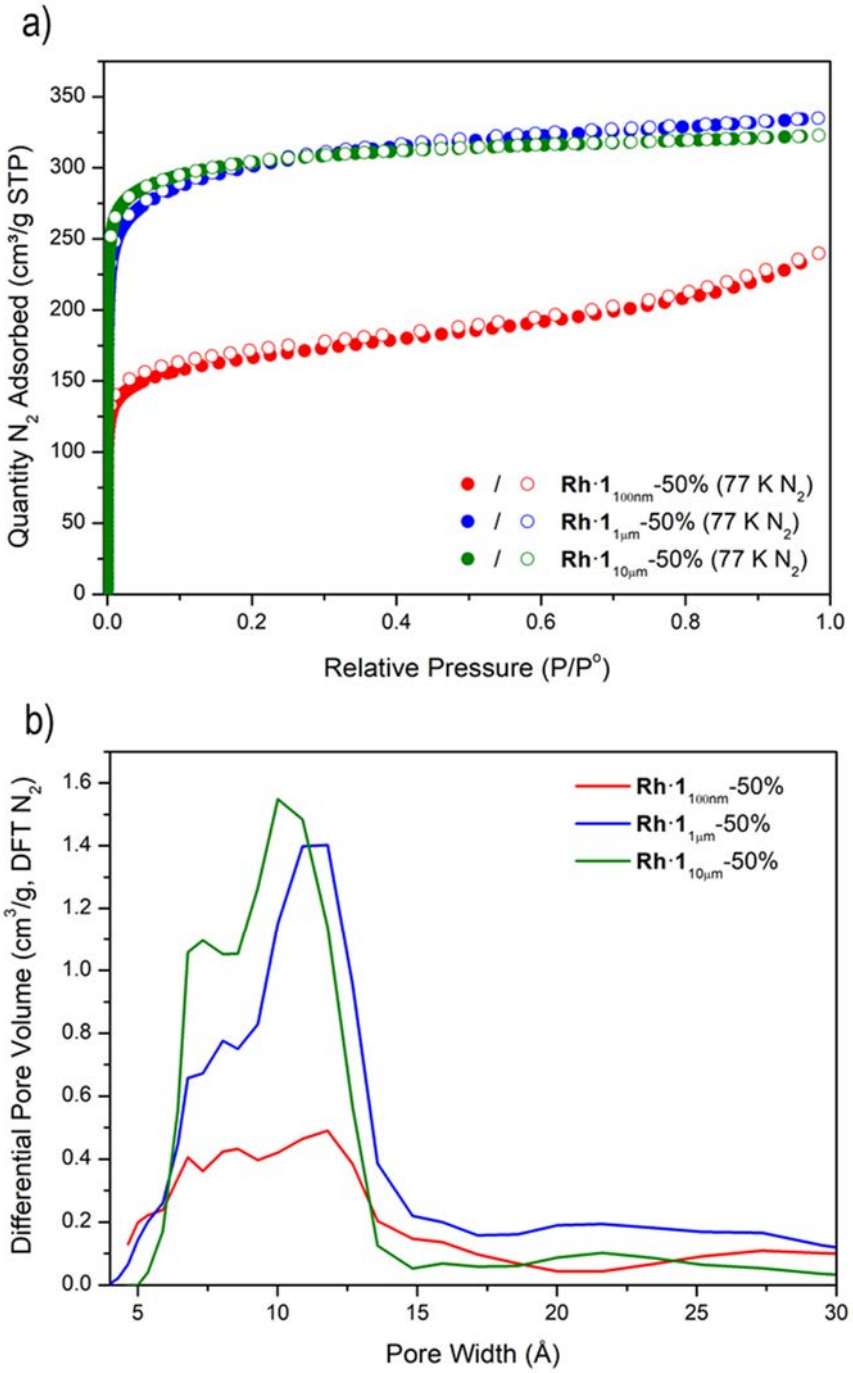

Figure **3.A.26**: a) 77 K N_2 isotherms and b) pore-size distributions of **Rh·1**$_{100nm}$-50%, **Rh·1**$_{1\mu m}$-50%, and **Rh·1**$_{10\mu m}$-50%.

3.10.7. Calculations of Ratio of Internal vs External Surface Area

The geometric external surface area per gram of each different sized UiO-67-bpydc sample was calculated as follows. The crystal size was assigned as the mid-sphere diameter of the octahedral crystals (*d*, as determined by SEM) and the side edge length ($l = d/2$) was used to calculate the external surface area of one crystal ($A = 2 \times l^2 \times \sqrt{3}$). The mass of one crystallite was calculated by multiplying the volume of one crystal (given by $V = \frac{l^3}{3} \times \sqrt{2}$) by the bulk density of UiO-67-bpydc (0.25 g/cm^3). The number of crystallites in a 1 g sample of UiO-67-bpydc (*N*) was determined by dividing 1 g by the mass of one crystallite. The external surface area per 1 g sample of UiO-67-bpydc could then be determined by multiplying *N* by *A* and is displayed in Table **3.4**.

Chapter 4.

Core-Shell Catalysis of Ethylene Oligomerisation with UiO-67-bpydc

Chapter 4. Core-Shell Catalysis of Ethylene Oligomerisation with UiO-67-bpydc

4.1. Introduction

One of biggest the challenges in understanding the activity of MOF catalysts is identifying the location of the catalytic activity, either within or on the framework. The active sites of MOFs can be categorised as accessible at the exterior surface of the MOF crystals and/or within the interior, lining the MOF pores. This categorisation applies for all forms of active sites, whether they be intrinsically active at metal nodes/organic ligands or from supported catalytic moieties,[1-3] because they can be found at both the exterior surface as the terminating group and within the crystal interior, accessible via the pores or through defects in the framework.[4] It is necessary to distinguish MOF catalytic activity as external/internal because the activity and product distribution of those sites is reliant on different factors. External catalysis, as discussed in Chapter 2, is highly dependent on the amount of catalytically active surface area exposed, i.e. crystal size and morphologically dependent, and is not contingent on the diffusion of reagents.[5-7] Conversely, internal catalysis is reliant on the diffusion of reagents into the MOF framework and hence is dependent on the kinetic diameter of reagents/products,[5, 8] the pore size and chemical environment, as well as crystal size effects on diffusion.[9] Pore confinement effects are also important for internal catalysis, potentially enabling control over the product distribution for certain reactions relative to their homogeneous molecular counterparts.[7] In the context of heterogeneous catalysis with MOFs, control over the location of catalytic activity is paramount in enhancing the catalytic performance of MOFs without altering the chemistry of the active sites in the framework.

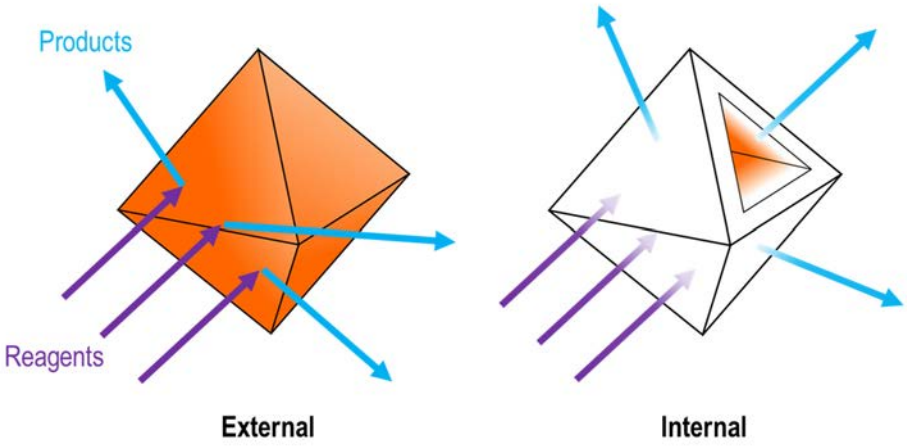

Figure **4.1**: Schematic of the catalytically active sites in MOFs (highlighted in orange) with external surface catalysis (left) and internal catalysis (right).

Most of the reported catalytic activity of MOFs stems from a combination internal and external active sites and deconvoluting the activity information is difficult. The best way to identify the location of activity for MOFs would be to conduct control experiments for external and internal catalysis and then compare observed activity/product distribution to those controls. Isolating the catalytic activity of MOFs to the exterior crystal surface has been reported, predominantly through the use of reagents that have kinetic diameters that discriminate diffusion into the MOF pore.[1, 5, 10-11] This strategy is often used to prove the catalytic activity occurs within the pores of the MOF rather than at the crystal surface.[11-12] Alternatively, surface active sites can also be poisoned through the use of tightly coordinating ligands such as bisphosphines or triphenylphosphine, which block surface active sites without diffusing into the pores of the framework.[13] The aforementioned strategies fundamentally rely on either blocking surface active sites or comparing the activity of reagents with varied steric bulk and hence different diffusion characteristics to discern the location of catalytic activity. As such, these strategies do not provide a true representation of the location of catalytic activity because either they do not utilise the same reagents to directly compare internal and external activity, or they rely on altering the chemistry of active sites. A true control study would involve comparing the activity of a MOF which contained active sites exclusively located at either the exterior or interior of the MOF crystal.

Tuning the precise location of active sites within a MOF is a crystal engineering challenge which can be partially solved through the synthesis of core-shell MOF composites. Core-shell MOFs (CS-MOFs) are comprised of at least two layers, a core and a shell, which are chemically distinct due to MOF components used in their synthesis i.e. metal nodes and organic ligands. CS-MOFs have been synthesised with the core/shell being comprised of frameworks with the same topology but with varied ligands/metal nodes (MOF-A⊂MOF-A),[14-16] and with the core/shell being made up frameworks with entirely different topologies (MOF-A⊂MOF-B).[17-19] Coating one framework with another that has a different topology will result in variance in the diffusion characteristics of guests due to porosity differences within the CS-MOF, whereas a CS-MOF where the core/shell frameworks have the same topology will not suffer from this variance to the same extent.[20] Ideally the CS-MOF of choice for this work can be engineered in a way that allows for control over the location of active sites (either in the core or shell layer) and minimal influence on diffusion of guest molecules.

MOF-A⊂MOF-A type CS-MOFs can be synthesised in two general ways: epitaxial growth on a core crystal or through solvent-assisted-ligand-exchange (SALE) of the ligand of

a core crystal. Epitaxial growth involves exposing crystals to a solution of MOF precursors containing, either a different ligand or metal node, and controlling the growth of the shell layer from the original crystal surface. This can be achieved by varying the synthetic conditions such as time, temperature, metal source, ligand, additives used and reaction concentration.[16] It has been shown that a defined boundary can be formed between the strata of the core and the shell when there is a significant difference between the steric bulk of the ligands which make up the framework of each domain.[16] For ligands with similar steric bulk the boundary between the core and shell is less well defined, this is because ligand exchange can occur when the shell ligand is able to diffuse into the framework of the core crystals.[16] Additionally, when synthesising CS-MOFs via epitaxial growth it is also possible to get co-precipitation of the shell framework independent of the core crystals, (see Figure **4.2**).[16] Conversely, synthesising CS-MOFs via SALE avoids the issue of co-precipitation as no metal-node precursors are used. SALE is a post-synthetic crystal engineering tool which can be used to incorporate a new ligand into the parent framework by soaking the parent framework in a concentrated solution of the new ligand. The outcome of a successful SALE reaction is a material that features the ligand from the solution incorporated into a framework which possesses the topology of the parent material (see Figure **4.2**).[21] Controlling the diffusion of the shell ligand has been shown to produce a material with a defined core-shell boundary with the shell ligand being localised to only the exterior of the crystal.[20, 22] Slow diffusion SALE is the most promising technique to use in order to synthesise a CS-MOF, with no porosity gradients or co-precipitation, for catalytic testing.

The location of catalytic activity in MOFs was investigated through the synthesis of CS-MOFs with active sites localised exclusively at the exterior/interior, UiO-67 was chosen as the framework for this work. As previously discussed in Chapter 3, UiO-67 can be synthesised with the ligand H_2bpydc with excellent control over the ligand concentration in the framework and the crystal size distribution.[23-24] In fact, UiO-67 is an ideal candidate for the synthesis of CS-MOFs because controlling the localisation of H_2bpydc during the synthesis of the CS-MOF affords direct control over the catalytically active sites because the bipyridine N-donors of H_2bpydc can coordinate to transition metal catalysts.[24-26] UiO-67 is typically synthesised with H_2bpdc, which provides similar pore characteristics as H_2bpydc due to its similar steric bulk. Additionally, UiO-67 has already been shown to be amenable to SALE using these two ligands, with the composite able to be metalated with $PdCl_2$ and shown to be catalytically active for the coupling of 4-bromotoluene and phenylboronic acid.[24]

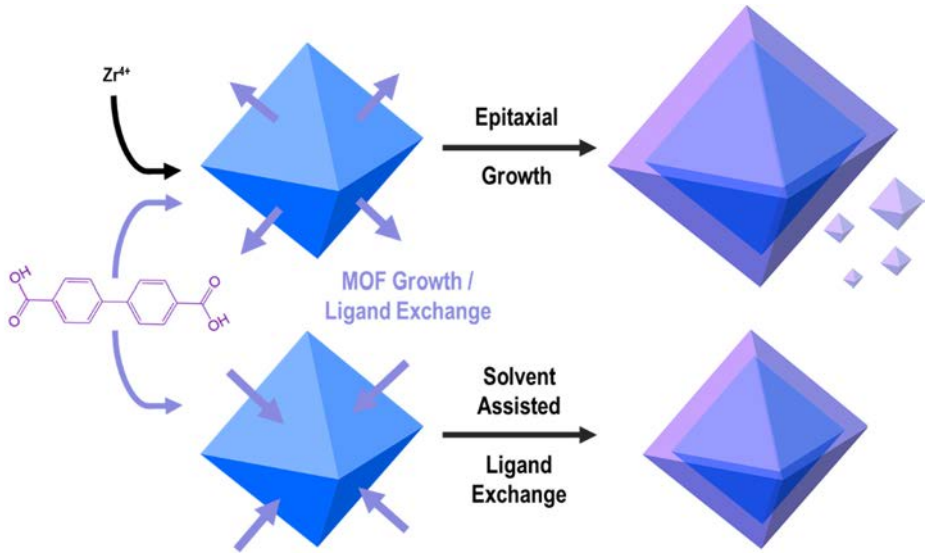

Figure **4.2**: Schematic of epitaxial growth vs SALE for the formation of a CS-MOF, with epitaxial growth increasing the size of the CS-MOF whilst forming a co-precipitate of varied size and SALE resulting in no change to the size/topology of the crystals.

For this project, the ideal CS-MOF would feature a UiO-67-bpydc core with the shell being synthesised via slow diffusion SALE to give a catalytically inert shell of UiO-67-bpdc. CS-MOFs obtained this way could be metalated with a transition metal catalyst of choice and the composite could be used for catalysis. The overall objective in Chapter 4 is to compare internal and external catalysis with MOFs. This will be achieved by synthesising CS-MOF materials and analysing the activity/product distribution for gas phase ethylene oligomerisation reactions catalysed by core-shell and non-core-shell MOF materials. The catalyst will be further discussed in the second half of this chapter with the first half focusing on the synthesis and characterisation of CS-MOFs with UiO-67-bpydc.

4.2. Considerations for the Synthesis and Analysis of Core-Shell Candidates

The key consideration when synthesising a CS-MOF architecture via solvent-assisted linker exchange (SALE) is controlling the diffusion of the shell ligand throughout the framework. The ideal circumstance would have minimal diffusion of the incoming ligand into the MOF structure so that all of the linker exchange occurs at the external surface of the MOF crystals, creating a well-defined core-shell boundary. Guest molecule diffusion can be controlled through "hard" controls such as crystal engineering, by varying either the steric bulk of the framework ligand or by altering the crystal size;[16, 22, 27] however, these require changes to the MOF structure. As previously mentioned in Chapters 2 and 3, increasing crystal size with MOFs increases the distance guest molecules have to travel through the framework whilst

still diffusing at the same rate. Consequently, screening slow diffusion SALE conditions with larger crystals is beneficial because the diffusion of guest molecules can be further controlled through judicious selection of "soft" controls including temperature, diffusion/reaction time, guest molecule concentration and the solvent system.[22]

Considerations must also be made in regard to the analysis of any core-shell candidates and the limitations of potential analytic techniques may have. The most important requirement to characterising core-shell candidates is the ability to analyse the spatial distribution of the two ligands used in order to characterise the core-shell boundary. There is a minimum resolution in Raman microscopy of approximately 0.1 μm, which therefore necessitates the use of large MOF crystals.[22] Similarly, higher through-put screening is much easier on samples larger than 10 μm via SEM/EDX analysis of core-shell candidates, due to the depth of the electron 'droplet' that EDX analysis actually analyses (1-5 μm from the surface). The depth that EDX analysis can sample can vary significantly, for materials comprised of low atomic number atoms the interaction volume is large, whereas for materials with high atomic number this volume is much smaller. Transmission electron microscopy (TEM) could be utilised for samples smaller than 1 μm with higher EDX resolution than SEM, but analysis via TEM is low-throughput and time intensive. Bulk analysis of core-shell candidates ligand and metal composition can be done via NMR spectroscopy of the digested MOF sample and ICP-MS or SEM/EDX respectively; all three are relatively high throughput techniques, but there needs to be a focus on analysing the spatial arrangement of the ligands/metals in core-shell candidates. Due to these considerations, this work focussed on the synthesis and analysis of core-shell candidates using large core crystals (> 10 μm) of UiO-67-bpydc.

4.3. Synthesis and Characterisation of Large UiO-67-bpydc Core Crystals

UiO-67-bpydc with crystal sizes larger than 10 μm were prepared by screening conditions which built upon the protocols established in Chapter 3 and on recently published work used by Yang *et. al.* to prepare hybrid core-shell Zr-MOF materials in one step.[19] Yang *et. al.* outlined the synthesis of composite materials which relied on the kinetics of MOF growth for two different ligands, with PCN-222 (formed from a tetratopic linker) crystallizing homogeneously in solution after 1 day and UiO-67 (formed from bpydc) forming after 7 days.[19] Their conditions outlined the use of trifluoroacetic acid in 80 eq. relative to the linkers/Zr^{4+} which acted as a modulator slowing crystal growth significantly more than the conditions previously screened and used in Chapter 3. Thus, the synthetic conditions used were modified from the protocols used by Yang *et. al.*, removing the ligand used for PCN-222 synthesis and

scaling the reaction down to a 10 ml reaction (see experimental section **4.11**). The chosen reaction conditions; $ZrCl_4$ (0.273 mmol), H_2bpydc (0.277 mmol), trifluoroacetic acid (TFA, 21.69 mmol, 80 equivalents) and DMF (10 ml) with heating at 120 ºC for 7 days, afforded large single crystals of UiO-67-bpydc on the sides of the vials (see reaction scheme in Figure **4.3**). Of note with these synthetic conditions, washing the crystals with DMF (4 × 10 ml) was essential to remove any excess unreacted ligand, metal salts, TFA and degraded DMF from the MOF pores. The MOF crystals were stable to DMF solvation for 12 months without reduction in crystallinity. Additionally, single crystals only formed on the sides of the vial with the material on the bottom being a mixture of intergrown microcrystalline material; for the purposes of this work single crystals were essential so the microcrystalline material was removed during the washing steps before the single crystals were collected. Unfortunately, the necessity for high quality single crystals reduced the yield of MOF per batch to approximately 5-10 mg of single crystals. As previously discussed in Chapter 3, all UiO-67-bpydc samples must be solvent exchanged with volatile solvents such as THF or MeCN 3-5 times and dried prior to analysis, in order to reduce solvent related disorder/reduction in crystallinity. Powder X-ray Diffraction (PXRD) analysis of single crystals, as-synthesised and solvated in DMF for 12 months (both THF washed prior to analysis), confirmed phase purity of the samples as they matched the simulated pattern of UiO-67-bpydc (Figure **4.4**).

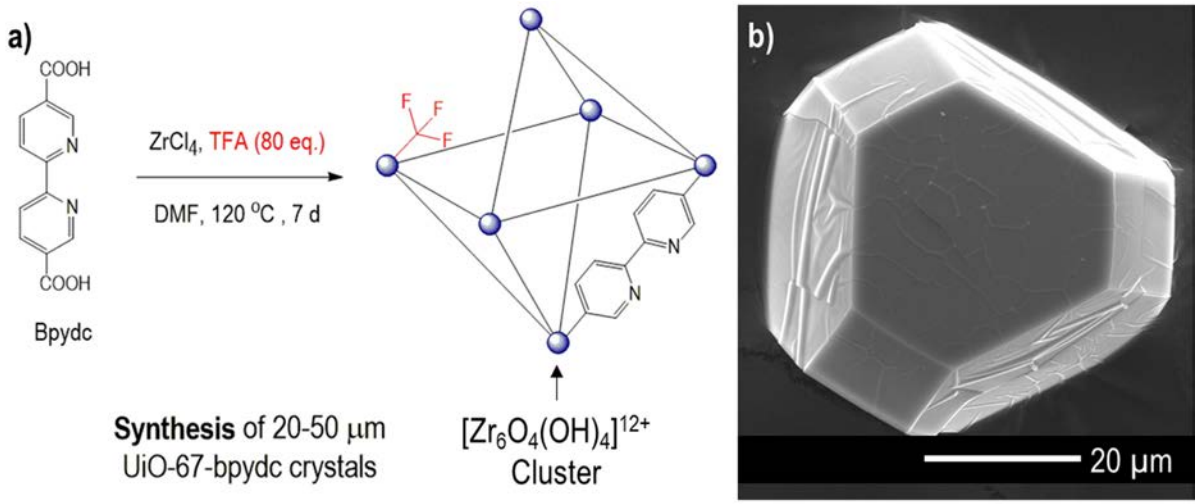

Figure **4.3**: a) Reaction scheme for the synthesis of 20-50 µm crystals of UiO-67-bpydc, with a cartoon representation of the MOF structure identifying 3 key features; the zirconium-oxo cluster $[Zr_6O_6(OH)_{4+}]^{12+}$, the bpydc ligand coordinated to two different clusters and a trifluoroacetate (TFA) coordinating to one cluster causing a ligand defect and b) an SEM image of a single crystal of UiO-67-bpydc synthesised using these conditions.

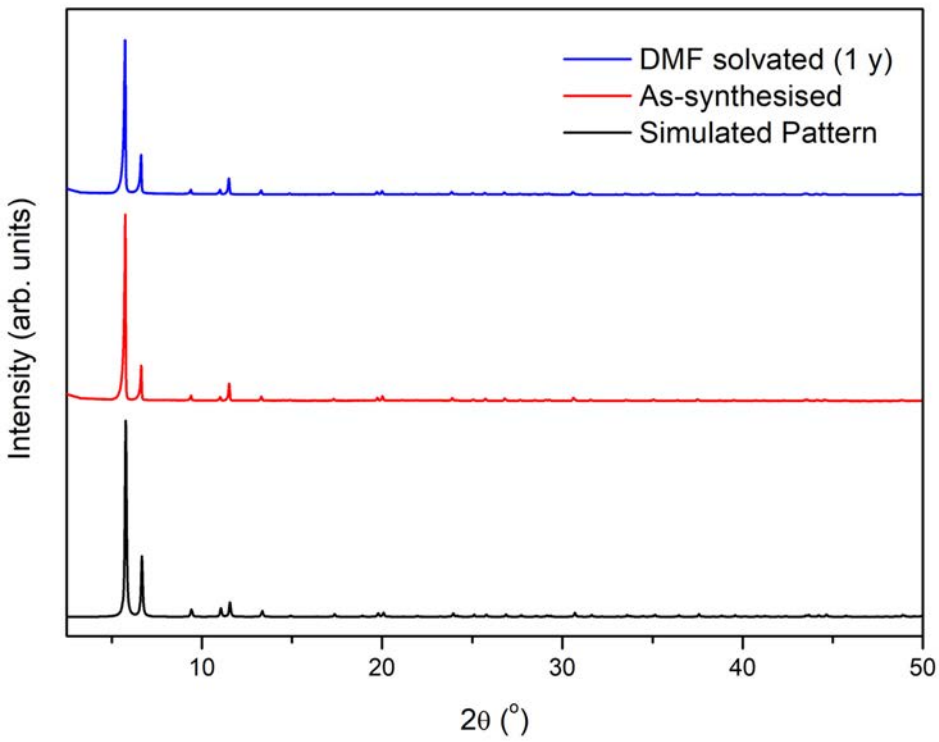

Figure **4.4**: PXRD patterns of large crystals of UiO-67-bpydc, including a simulated pattern (black), as-synthesised via TFA prep (7 days 120 deg and THF washed, red) and solvated in DMF for 1 year (THF washed, blue).

The size and morphology of the single crystals of UiO-67-bpydc were analysed via scanning electron microscopy (Figure **4.3** and **4.5**). The single crystals of UiO-67-bpydc had an average diameter of 46.3 ± 8.8 μm and are morphologically distinct from previously synthesised UiO-67 crystals being truncated octahedra rather than the more common octahedral morphology (see Figure **4.5b** for size distribution data).[9] The change in morphology is likely due to the modulator TFA, which can act as a capping agent coordinating preferentially to a chemical environment associated with the Miller plane which would make up the vertices of the octahedron UiO-67 crystals.[28] The faces of octahedral UiO-67 crystals have been previously been determined correspond to the [111] plane,[28] where-as the vertices have not been directly characterised, but for octahedral metal nano particles the vertices correspond to the [100] Miller plane.[29]

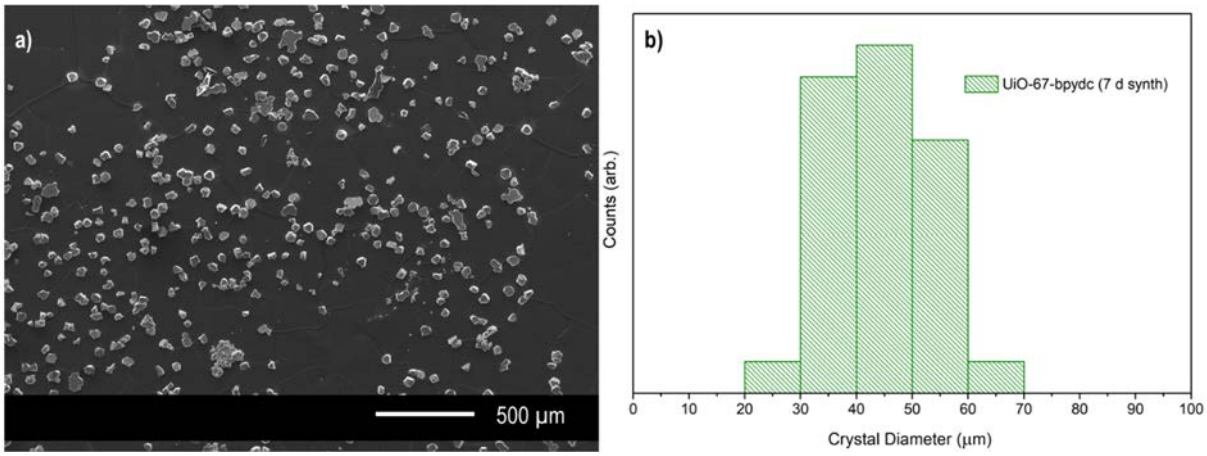

Figure **4.5**: a) SEM image of UiO-67-bpydc 50 µm crystals and b) crystal size distribution analysis of crystals in a).

Modulators such as TFA have been shown to introduce defects in framework of UiO-67, which can arise as missing ligand and/or node defects.[30-31] These defects can offer new avenues for guest molecules diffusion and hence increase the rate of guest diffusion through the framework. A detailed defect analysis is necessary to understand the type of defects and how they might be minimised in order to control diffusion of guest molecules during the synthesis of CS-MOF candidates via slow diffusion SALE. The defect analysis was conducted on the as-synthesised single crystals, which were digested with $DMSO_{d6}$/DCl in accordance with previously established protocols (see experimental sections **4.11** and **3.8**). The digested sample was analysed via ^{1}H and ^{19}F NMR spectroscopy and the presence of the ligand H_2bpydc and TFA were observed (Figure. **4.6**). In order to quantify the number of ligand defects present in the framework TFA must be exchanged with another ligand which can be quantified via ^{1}H NMR spectroscopy. An additional requirement is that the incoming ligand does not replace bpydc in the framework, there by introducing more ligand defects than were initially present. Benzoic acid (BA) and phenylphosphinic acid (PPA) were chosen as candidate replacement ligands for TFA to determine the impact of ligand pKa (4.20, 2.1 and 0.23 respectively for BA, PPA and TFA) on ligand exchange for both TFA and bpydc.[32] Exchange reactions with BA (8%, 0.65 M) and PPA (0.01 M) in DMF were incubated for 24 h at 85 ºC, the supernatant and the solvent exchanged/digested MOF samples were analysed via ^{1}H and ^{19}F NMR spectroscopy in $DMSO_{d6}$ (see experimental **4.11** and Figure **4.6**). As seen in Figure **4.6**, H_2bpydc and TFA were shown to be present in the as-synthesised digest sample via ^{1}H and ^{19}F NMR spectroscopy respectively. Following post-synthetic exchange with BA, both H_2bpydc and BA are present in the ^{1}H NMR spectra of the digested solids, but only BA was present in the solution.

Additionally, TFA is not seen in the ^{19}F NMR spectra of the BA-exchanged digested MOF but is present in the solution, indicating BA replaces TFA at defect sites without removing H_2bpydc (see Figure **4.6**). Interestingly PPA, which has a much lower pKa than BA and hence is more acidic, also replaces TFA at defect sites in the MOF but also exchanges with H_2bpydc, clearly binding tightly with the Zr-oxo cluster of UiO-67. Quantitative defect analysis with BA and PPA is summarised in Table **4.1** following the calculation of ligand defects via ^1H NMR spectroscopy (see Figure **4.7**) outlined by Gutov *et. al.* (see Appendix **4.1** for the related calculations).[30] BA and PPA exchanged samples demonstrated 14 and 32 % ligand defects respectively via NMR (see Table **4.1**), this difference relates to the displacement of H_2bpydc by PPA and hence analysis via PPA exchange is not a realistic measure of defects.

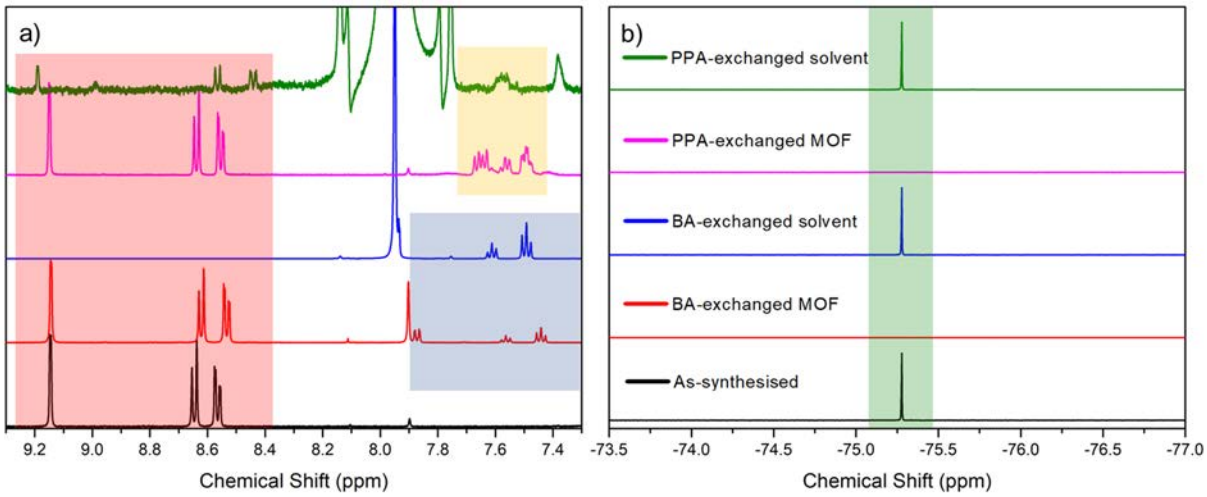

Figure **4.6**: Stacked ^1H (a) and ^{19}F NMR spectra (b) of as-synthesised, benzoic acid and phenylphosphinic acid exchanged MOF showing the appearance and disappearance of ligand modulators and the removal of TFA. H_2bpydc, benzoic acid, phenylphosphinic acid and trifluoroacetic acid NMR chemical shifts are highlighted by red, blue, orange, and green shaded regions respectively.

Ligand defects in UiO-67 can be controlled through choice of modulator in synthesis conditions or post-synthetically removed through ligand exchange. Reducing the number of ligand defects in the UiO-67-bpydc core crystals is essential when attempting to control the rate of diffusion of guests for the synthesis of CS-MOFs via slow diffusion SALE. As such, an attempt was made to "heal" the ligand defects using SALE to install H_2bpydc into the ligand defect sites in place of the coordinated modulator (see proposed schematic Figure **4.7**).

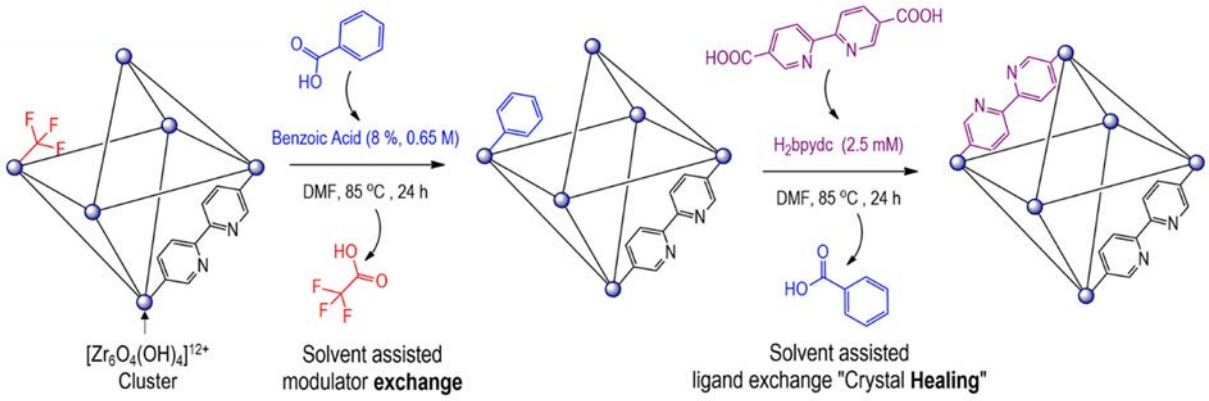

Figure **4.7**: Schematic of modulator exchange and "crystal healing" protocols for UiO-67-bpydc to minimise ligand defects, with BA used as an exemplar modulator used to replace TFA at the ligand defect site.

Following protocols adapted from Gutov *et al.* an attempt at "healing" ligand defects was undertaken by reintroducing H_2bpydc back into the framework via SALE to displace the BA or PPA modulators.[30] The BA and PPA exchanged samples were soaked in a 2.5 mM H_2bpydc solution in DMF at 85 ºC for 24 hr and the subsequently solvent exchanged and dried samples were digested and analysed via NMR spectroscopy (see Figure **4.8** , Table **4.1** and Appendix **4.13.1** for calculations). It was found that the more labile BA modulator could be entirely removed using this "healing" protocol, whereas PPA was still bound to the framework which now had approximately half the ligand defects post "healing". This difference is likely due to the strength of the acids, with PPA having a much lower pKa than BA, meaning BA is more labile and thus more susceptible to removal via SALE to be replaced by H_2bpydc. The "healing" ligand exchange process favours the incoming H_2bpydc ligand for two reasons. Firstly, H_2bpydc coordinates to two zirconium-oxo clusters so once it is bound four bonds need to be broken for its removal rather than the two bonds for either BA or PPA. Secondly, when H_2bpydc coordinates to the framework it displaces two acid modulators, which is entropically favourable. This rationale explains why PPA can be partially exchanged by H_2bpydc even though it is a much weaker acid than PPA. BA was used for all further ligand exchange and "healing" protocols because the ligand exchange incorporation was reproducible, BA exchange did not release H_2bpydc from the framework and BA is labile enough to be exchanged for H_2bpydc for "crystal healing". The crystallinity of BA and PPA exchanged samples was confirmed by PXRD, matching the pattern of as-synthesised UiO-67-bpydc (see Fig **4.9**). The PXRD patterns of the BA and PPA exchanged samples show no additional peaks at low angle

indicating that there has not been the introduction nor the presence of a phase change to a more node defect rich material.

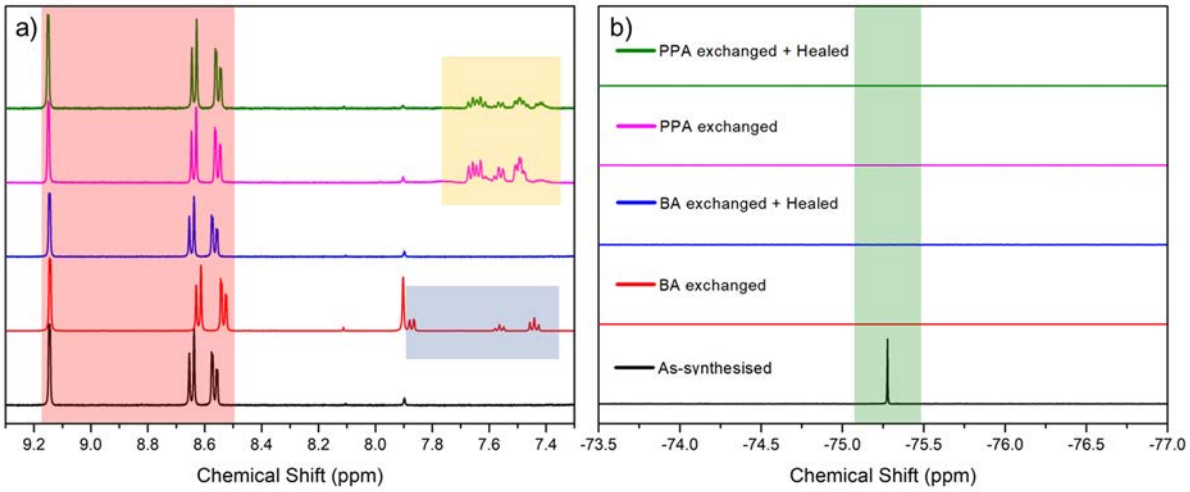

Figure **4.8**: a) ^{1}H and b) ^{19}F NMR spectra of BA and PP exchanged samples of as-synthesised and "healed" UiO-67-bpydc to demonstrate the extent of modulator removal post healing. H_2bpydc, benzoic acid, phenylphosphinic acid and trifluoroacetic acid NMR chemical shifts are highlighted by red, blue, orange, and green shaded regions, respectively.

Table **4.1**: Defect analysis of BA and PP exchanged samples of as-synthesised and "healed" UiO-67-bpydc from ^{1}H NMR data.

Sample	Acid:H_2bpydc (by integration)	#Acid molecules in formula	#H_2bpydc molecules in formula	H_2bpydc:Zr	% Ligand defects
BA exchanged	0.33	1.72	5.14	0.86	14
PPA exchanged	0.95	3.87	4.06	0.68	32
BA exchanged + H_2bpydc healed	0.00	0.00	6.00	1.00	0
PPA exchanged + H_2bpydc healed	0.38	1.90	5.04	0.84	16

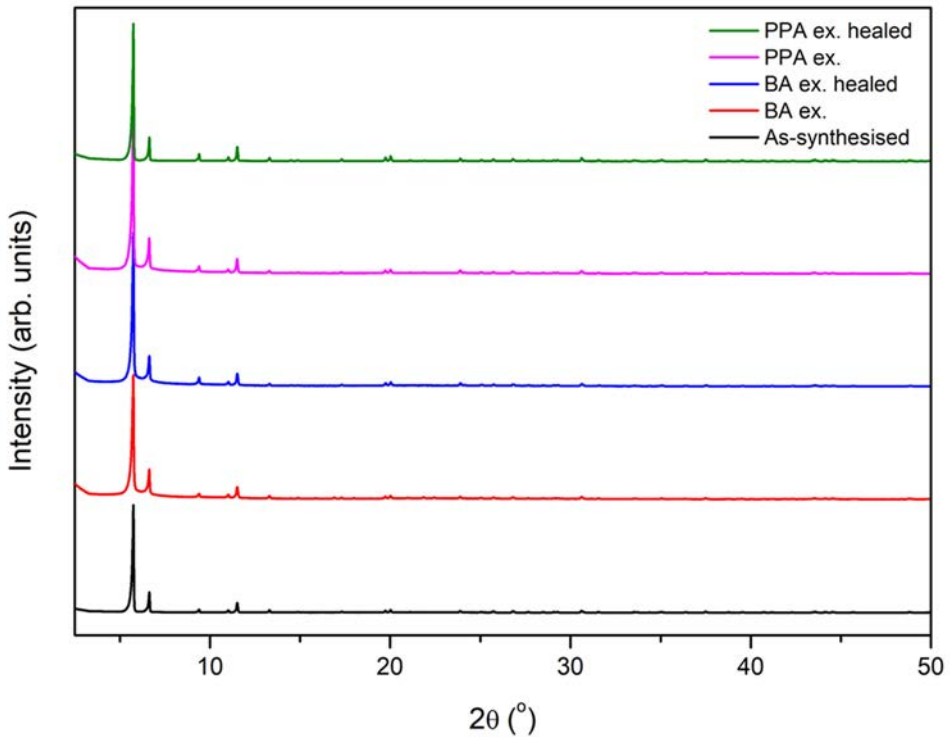

Figure **4.9:** PXRD patterns of BA and PPA exchanged samples of as-synthesised and "healed" UiO-67-bpydc demonstrating retention of long-range order and phase purity of the samples.

Controlling the diffusion of shell ligands through MOF crystals is vital for directing where ligand exchange can occur, thereby enabling the formation of complex CS-MOF architectures. The impact of modulator exchange and "crystal healing" via SALE with H_2bpydc to remove ligand defects in UiO-67-bpydc was followed by measuring the BET and pore-size distributions at each stage in the exchange and healing protocols. N_2 77 K adsorption isotherms for as-synthesised, BA-exchanged and "healed" single crystal samples of UiO-67-bpydc were collected post-activation from acetonitrile (see experimental section **4.11**). The N_2 77 K isotherms for all samples exhibited Type 1 characteristics with high uptake at low pressure, indicating that all of the samples are microporous (see Figure **4.10**).[33] The total uptake of N_2 increased going from the as-synthesised, BA-exchanged and "healed" samples of UiO-67-bpydc, with corresponding BET surface areas of 2190 ± 15, 2671 ± 12 and 2620 ± 10 m^2/g (see Figure **4.10**). Additionally, the pore size distribution (calculated via DFT N_2 model) in Figure **4.10** shows that with each step in the ligand exchange and "crystal healing" process the average pore size distribution decreases. These results indicate that the exchange of TFA for BA and subsequently "healing" the framework with H_2bpydc increases the internal surface area of the sample by connecting Zr-oxo nodes, previously disconnected due to ligand defects in the framework. Consequently, ligand defect free UiO-67-bpydc should demonstrate slower

diffusion of guest molecules than as-synthesised defect rich UiO-67-bpydc and will be a better candidate for slow-diffusion core-shell synthesis.

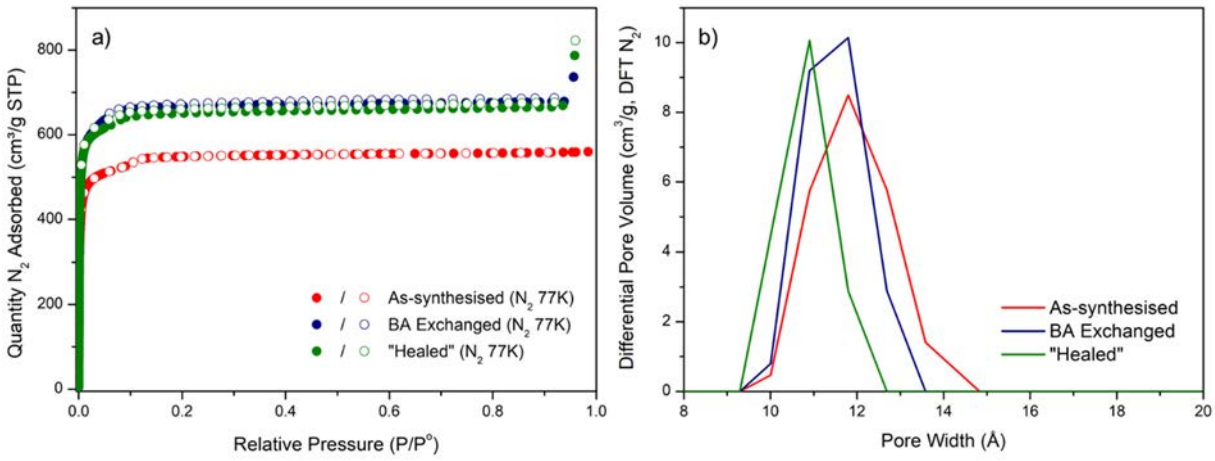

Figure **4.10**: a) 77 K N_2 sorption isotherms and b) pore-size distributions of UiO-67-bpydc as-synthesised, BA exchanged and "healed" with H_2bpydc.

4.4. Synthesis and Characterisation CS-MOF candidates

Core-shell candidate samples needed to be screened by two complementary techniques to determine the bulk composition and localisation of the core ligand (H_2bpydc) relative to the shell ligand (H_2bpdc). ^{1}H NMR spectroscopy was used to directly compare the bulk composition of the two ligands by digesting a small portion of dried sample in $DMSO_{d6}$/DCl. The spatial distribution of the two ligands was more challenging to discern requiring a technique with high resolution and a method to better distinguish the two ligands. Since the core ligand H_2bpydc has a vacant bidentate N-donor chelating site, a transition metal could be introduced to the core-shell material post-synthetically and it would bind selectively to the core ligand over the shell ligand; therefore the presence or absence of the introduced transition metal would indicate the relative spatial distribution of the two ligands. $[RhCODCl]_2$ was chosen as the indicator transition metal complex because previous work has shown that a RhCODCl species will quantitatively coordinate to bpydc sites in UiO-67-bpydc (see section **3.5**). The spatial distribution of [Rh(bpydc)(COD)Cl] entities within the core-shell candidates was followed by SEM/EDX and the atomic ratio Rh:Zr was analysed. There is one ligand per Zr atom in the UiO-67-bpydc chemical formula, so 100% occupation of bpydc sites by RhCODCl would be registered by the measurement of Rh:Zr = 1. SEM/EDX is a surface analysis technique, but the depth of penetration of electrons (interaction volume) into a particle is dependent on the composition (average atomic number and density of atomic packing) as such,

the area of analysis of X-rays which are emitted from the sample for EDX analysis includes a depth between 1-5 μm of the sample.[34] Since UiO-67-bpydc is comprised of both low and high atomic number atoms and contains a significant proportion of void space, it is challenging to quantify the interaction volume and hence the depth from the surface that EDX analysis samples. Screening core-shell candidates involved directly comparing the ^{1}H NMR HH_2bpdc of the bulk sample to the "surface" ratio of Rh:Zr via SEM/EDX. If the "surface" Rh:Zr ratio equals the bulk H_2bpydc:H_2bpdc ratio then **homogeneous** SALE has occurred and the shell ligand has been equally dispersed throughout the crystals evenly. If the surface Rh:Zr ratio is less than the H_2bpydc:H_2bpdc ratio then this indicates **non-homogeneous** SALE, and the shell ligand has preferentially exchanged closer to the external surface.

Initial screening of CS-MOF synthesis conditions via slow-diffusion SALE were initially conducted with non-healed core-crystals to determine whether the ligand defects would affect the diffusion of H_2bpdc into the framework. The non-healed UiO-67-bpydc 50 μm crystal samples were shown previously to have 15% ligand defects. Under varied conditions (ligand concentration, temperature, time, and solvent system used) it was found that the synthesised samples contained a comparable Rh:Zr ratio to the overall ligand content of both the reaction mixture and MOF (see Appendix **4.13.2**). The homogeneous SALE observed in preliminary screening studies resulted from the measured larger pore size distributions of defect rich MOF crystals, which enabled fast diffusion of H_2bpdc into the framework and subsequent ligand exchange. Further slow diffusion SALE experiments utilised ligand defect-free core crystals, prepared as discussed previously (Section **4.3**), which should limit diffusion of guest molecules into the MOF. Additionally, the initial screening was conducted on 0.5-1 mg of MOF per reaction, which was sufficient for high throughput SEM/EDX analysis, but not enough sample remained for an NMR digest. As such, the original results only gave rise to a qualitative understanding of the composition of the samples i.e. a comparing the surface SEM/EDX Rh:Zr ratio to the total ligand composition of the reaction mixture H_2bpydc (in the MOF) : H_2bpdc (in the solution). Hence, further experiments were conducted with a larger amount of core-crystals to enable a quantitative analysis of the composition of CS-MOF candidates via SEM/EDX and NMR spectroscopy on digested samples.

Slow diffusion SALE conditions were screened using the "healed" ligand defect free 20-50 µm UiO-67-bpydc core and candidate core shell samples were analysed quantitatively by directly comparing the bulk H_2bpydc:H_2bpdc ratio of digested samples via NMR spectroscopy and the 'surface' ratio of Rh:Zr via SEM/EDX. A control experiment was undertaken to demonstrate the quantitative uptake of rhodium, whereby a portion of "healed" core MOF was metalated with $[RhCODCl]_2$ and subsequently analysed via NMR and EDX (see Figure **4.11**). The control sample indicated a Rh:Zr of 96 ± 3% whilst NMR digestion analysis indicated only the presence of H_2bpydc in the MOF sample. Slow diffusion SALE conditions were screened with a 2.5 mM H_2bpdc solution in DMF with varied temperatures (25, 50, 80 and 120 °C) and reaction times (0.5 h to 1 h), the results are displayed in Figure **4.11**. SEM images of all of the samples indicate that there was no noticeable degradation of the crystals under SALE conditions (see Appendix **4.13.3**, Figure **4.A.3**). In Figure **4.11** the dashed red line represents the point at which ratio of Rh to Zr at the surface equals the digested bulk H_2bpydc:H_2bpdc ratio. Samples below the red dotted line have undergone **non-homogeneous SALE**, having more H_2bpdc at the surface than H_2bpydc, indicating the increased likelihood that slow diffusion SALE has occurred and resulted in a shell or diffuse shell of H_2bpdc around the core of H_2bpydc in the sample. Samples with a surface Rh:Zr ratio much lower than the measured H_2bpydc:H_2bpdc bulk composition should therefore have a much more distinct H_2bpdc shell. It can be seen that with short reaction times and high temperatures a series of candidates emerge, with the most promising being 0.5 h at 120 °C; Rh:Zr = 58 % and H_2bpydc:H_2bpdc = 88 % (see Figure **4.11**). All candidates which were heated above 25 °C demonstrated a shift towards increased H_2bpdc uptake and homogeneous SALE going from 0.5 to 1 h of heating, indicating that over a longer time scale the system would tend towards a statistical distribution of the two ligands throughout the crystals. These observations prompted further experiments at 120 °C, with shorter time scales (10, 20 and 30 mins), varied ligand concentrations (2.5 mM and 5 mM) and with pre-heated and not pre-heated ligand solutions.

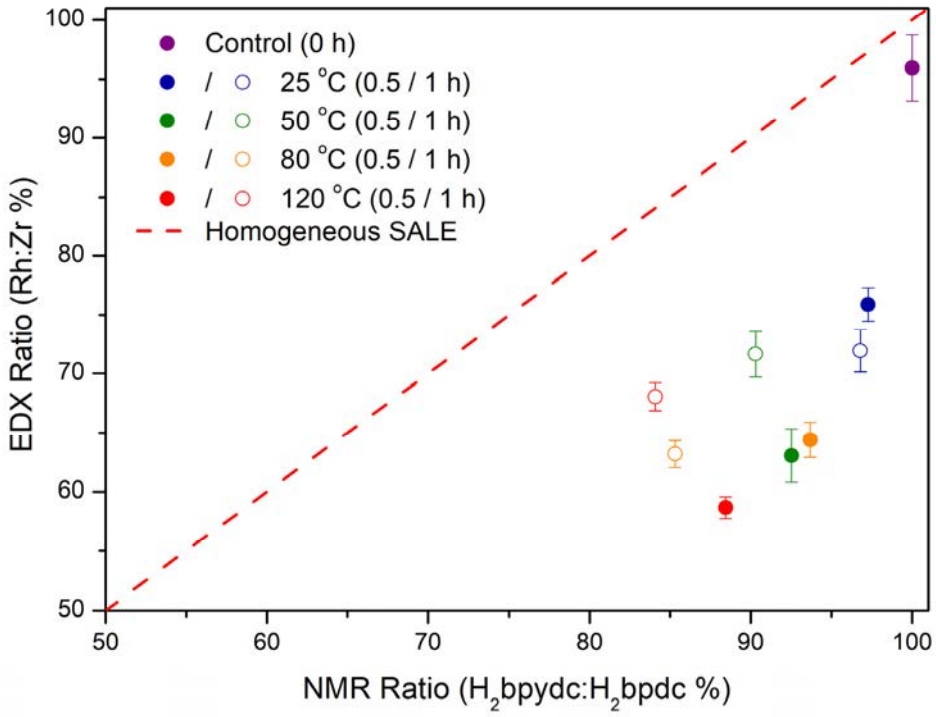

Figure **4.11:** Initial screening of NMR (bulk) and EDX (surface) ratios of core-shell candidates at varied temperature and time.

The importance of temperature for the slow diffusion SALE reaction was investigated by comparing samples synthesised at shorter time scales (10-30 min), varied H_2bpdc ligand concentrations (2.5 mM and 5 mM) and with and without pre-heated solutions. All MOF samples were quantitatively analysed via NMR digestion and SEM/EDX with the results displayed in Figure **4.12**. Pre-heating the H_2bpdc solution to 120 ºC enabled analysis of a constant temperature profile i.e. instantly bringing the reaction mixture up to 120 ºC and holding that temperature for 10-30 minutes. Pre-heating the H_2bpdc ligand solutions resulted in homogeneous SALE at all timescales and ligand concentrations analysed. The observed homogeneous SALE was likely caused by immediately providing enough energy to exchange ligands and enabled fast diffusion of H_2bpdc through the MOF framework. In comparison, the samples synthesised without pre-heated ligand solutions were exposed to a temperature gradient, with the system starting at room temperature and being placed in the 120 ºC oven at T = 0. Varying the end time point of the experiment (10-30 min) affects both diffusion into the crystals and the rate of exchange of H_2bpdc with H_2bpydc. As such, the samples without pre-heated ligand solutions all appeared to demonstrate non-homogeneous SALE, where the

shorter time scale (10 min) and lower shell ligand concentration (2.5 mM) conditions looked the most promising. The short time scale SALE experiments indicate limiting the time taken for the diffusion to occur and for the reaction solution to get up to temperature results in SALE occurring primarily at the surface of the MOF crystals. The longer that heating time 10-30 mins, the more significant the H_2bpdc incorporation into the framework. Another factor to consider was the reaction volume, increasing or decreasing the volume would result in a different temperature gradient, with the reaction mixture taking more or less time to heat up respectively. The screening experiments were conducted using 1-5 mg of single crystals, meaning only 1-2 ml of ligand solution was needed to be heated for slow diffusion SALE, as such that heating time needed to be adjusted for larger scale samples because the volume of the ligand solution is larger. For MOF samples with masses less than 15 mg (less than 4.5 ml) a heating time of 10 min was used and for samples with masses larger than 15 mg (greater than 4.5 ml) a heating time of 20 min was needed.

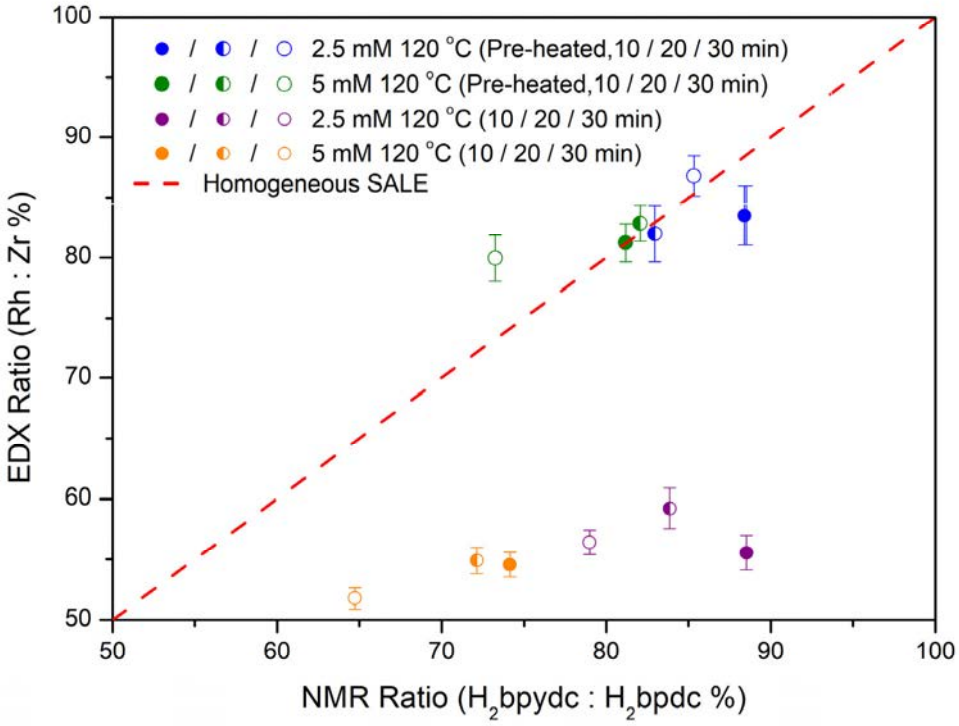

Figure **4.12**: Slow diffusion SALE experiments at 120 ºC with and without pre-heated solutions at varied ligand concentration of the H_2bpdc solution for 10, 20 and 30 minutes.

Spatial analysis of the two ligands was attempted using confocal Raman spectroscopy on a promising CS-MOF candidate, synthesised under the optimised conditions of slow diffusion SALE (2.5 mM H_2bpdc, 20 min at 120 °C). Analysis via Raman spectroscopy is possible because both ligands are Raman active in the UiO-67 framework when excited with a 532 nm laser, see Figure **4.13**. Three samples were analysed via Raman spectroscopy; UiO-67-bpdc, UiO-67-bpydc$_{0.5}$-bpdc$_{0.5}$ and UiO-67-bpydc, there is a distinct difference between the spectra, with characteristic peaks for UiO-67-bpydc and UiO-67-bpdc appearing at 1590 and 1612 cm^{-1} respectively. The characteristic peaks were resolvable in the spectra of UiO-67-bpydc$_{0.5}$-bpdc$_{0.5}$ prompting spatial analysis of the aforementioned core-shell candidate via confocal Raman spectroscopy.

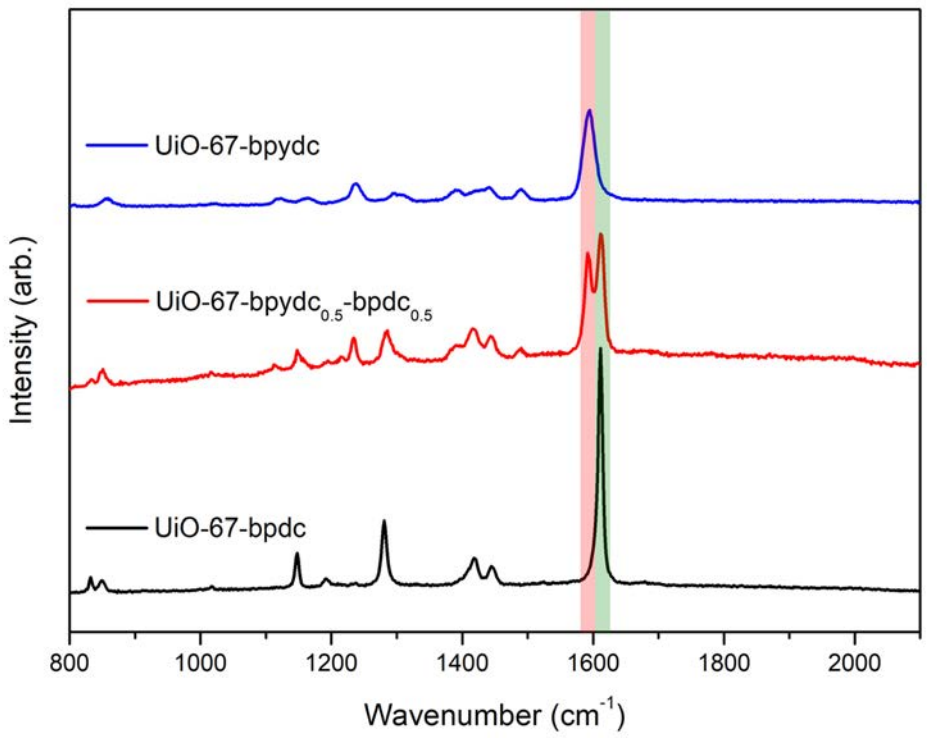

Figure **4.13**: Raman spectra of UiO-67-bpdc (black), UiO-67-bpydc$_{0.5}$-bpdc$_{0.5}$ (red) and UiO-67-bpydc (blue) with characteristic peaks highlighted in red and green for UiO-67-bpydc and UiO-67-bpdc, respectively.

Spectra at varied confocal depths of a single crystal were collected, scanning for the characteristic peaks for both ligands across the crystal. Figure **4.14** shows one such spectrum at an optical depth of approximately 4 µm from the crystals surface, which contained the largest contribution of the shell ligand. The shell ligand is isolated at the exterior of the crystal, with

no Raman signals detected at the centre of the crystal for H_2bpdc. The H_2bpdc:H_2bpydc ratio at the exterior is 0.04, which indicates (assuming a thin pure shell) that the shell thickness is approximately 160 nm. These results confirm the localisation of the shell ligand to the exterior of the crystal, but that the shell thickness is likely to be fairly thin or diffuse (consistent with prior analysis). Correspondingly, attempts were made to increase the shell thickness by exposing the core-shell candidate crystal to multiple cycles of slow diffusion SALE.

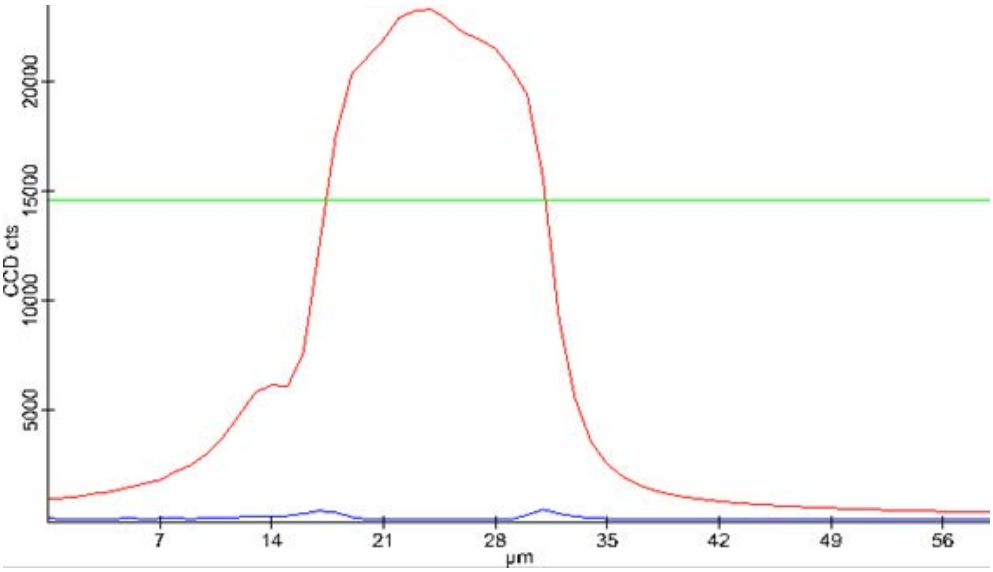

Figure **4.14**: Confocal Raman spectrum of a core-shell candidate at an optical depth of 4 µm from the crystals surface scanning across the crystal. The core and shell ligands (H_2bpydc and H_2bpdc) are shown as the red and blue traces, respectively.

Stepwise shell growth was investigated by cycling a large batch of "healed" core single crystals through three successive slow diffusion SALE cycles. In this set of experiments a large sample of "healed" core UiO-67-bpydc single crystals were used for three slow diffusion SALE cycles (2.5 mM H_2bpdc, 20 min at 120 °C). Aliquots of the crystalline sample were taken after each cycle and solvent exchanged with DMF and MeCN prior to analysis (see experimental **4.11** for further details). The ligand and metal ratios were analysed after each successive cycle with the data displayed in Figure **4.15**. It can be seen that, with successive cycles of slow diffusion SALE, bulk analysis indicates more H_2bpdc is incorporated into the framework and that there is less Rh detected at the surface (relative to Zr). There are two possible rationales for these results, which could be occurring exclusively or in tandem; successive cycles of slow diffusion SALE experiments could potentially increase the thickness of the H_2bpdc shell and/or further dilute H_2bpydc at the exterior of the crystal.

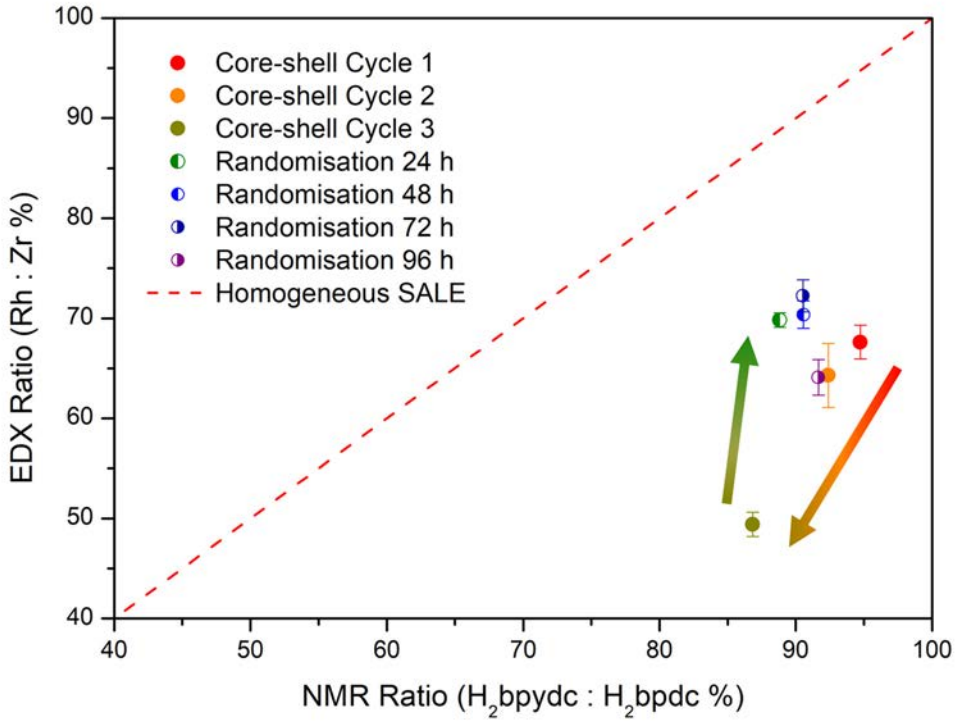

Figure **4.15**: Bulk NMR and surface EDX analysis of slow diffusion SALE experiments for the stepwise growth of a shell through three core-shell cycles and ligand randomisation experiments for crystals solvated in DMF at 120 °C for varied times (24, 48, 72 and 96 h).

To garner a better understanding of the mechanics of SALE and the lability of coordinated ligands in the UiO-67 framework, a ligand scrambling experiment was undertaken. MOFs are not static crystalline materials, there is ligand rotation, solvent incorporation,[35] ligands can be exchanged,[36] transition metals coordinate to the framework,[37] and many different post-synthetic processes can be undertaken.[38] The ligand randomisation study involved heating a core-shell candidate sample, in this case a sample synthesised via three successive core-shell cycles (CS×3), in DMF at 120 °C for extended periods of time (24, 48, 72 and 96 h). These samples were then analysed, following solvent, exchange via EDX/SEM (post $[RhCODCl]_2$ metalation) and NMR digestion and compared to the starting material (see experimental section **4.11** and Figure **4.15**). As seen in Figure **4.15**, there is an initial increase in surface Rh from 50% to 70% in the first 24 h, but over time the ratio of Rh:Zr at the surface doesn't tend towards the bulk H_2bpydc:H_2bpdc ratio instead plateauing around 70% for the 48, 72 h time points. Additionally, at 96 h the Rh:Zr ratio decreases slightly to 65%. It is worth noting that there is a slight increase in the H_2bpydc:H_2bpdc ratio of about 5%, potentially due

to the loss of the least soluble ligand H_2bpydc, this also is within the error when integrating low concentration substrates for ^{1}H NMR analysis. Considering these results, it would seem that full rearrangement of the structure to one having homogeneous ligand distribution is not possible. As shown, earlier under similar heating conditions but with the presence of an additional ligand, a statistical ligand incorporation is possible i.e. homogeneous SALE. Therefore, without both factors (heat and additional ligand) the composition of core-shell UiO-67 composites remain relatively unaltered.

Prior to catalysis testing it was necessary to confirm that the overall composition of Rh:Zr of the core and core-shell samples matches the ligand composition. This data was used to confirm where catalytically active species (introduced below) will be located. This was achieved through ICP-MS analysis of the overall Rh:Zr ratio of core-shell candidates (post HNO_3 digestion, see experimental section **4.11**). The analysis of Rh:Zr ratio, via ICP-MS, provides data concerning the following points; whether, in the core sample, the EDX Rh:Zr ratio is indicative of the bulk H_2bpydc:H_2bpdc ratio determined by NMR spectroscopy and, whether there is a similar difference between the "surface" EDX Rh:Zr and the bulk Rh:Zr (ICP-MS)/ligand ratio (NMR) in the core-shell samples. Three candidate samples were analysed (all of which were later used for catalytic experiments), the "healed" core and core-shell samples synthesised from one and three cycles of slow diffusion SALE. The NMR, ICP-MS and EDX analyses of these three samples is graphed in Figure **4.16**. Analysis of the core sample revealed quantitative uptake of $[RhCODCl]_2$ by both ICP-MS and EDX indicating that Rh was dispersed quantitatively throughout the framework at a similar ratio to H_2bpydc and hence is coordinated at every chelating site available in the structure. Both core-shell candidate samples have a lower "surface" ratio of Rh:Zr in comparison to the bulk, with the latter matching trend of the overall ligand ratio. This result indicates that there was less H_2bpydc at the surface of the MOF crystals than H_2bpdc and that the ligands at the core of the samples are coordinating RhCODCl entities almost quantitatively. Overall, the ICP-MS analysis validates the screening of core-shell candidates via comparing the ligand ratio in the bulk by NMR analysis and the Rh:Zr ratio at the surface via SEM/EDX.

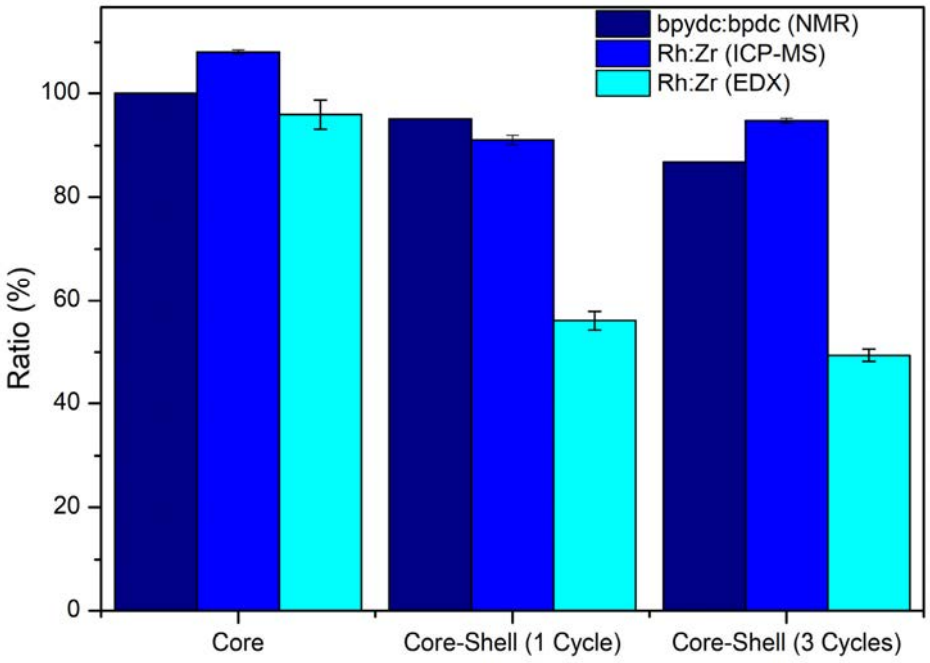

Figure **4.16**: Comparison of bulk and surface analysis of a Core sample, and two Core-Shell candidates synthesised from 1 and 3 successive cycles of slow-diffusion SALE (1 and 3 cycles respectively) samples via ^{1} NMR (H_2bpydc:H_2bpdc), SEM/EDX and ICP-MS (Rh:Zr).

Core-shell candidates were also examined via PXRD and N_2 77 K isotherms to ensure that synthetic conditions had not negatively impacted the crystallinity or porosity of the samples relative to the "healed" core crystals. For the studies of internal vs external catalytic activity, it is essential that there are no significant differences to the porosity of the catalysts supports; if there are then the diffusion of guest molecules will be altered. The core and core-shell (3 cycles) samples were confirmed to be isomorphous via PXRD, with both patterns matching the simulated pattern for UiO-67-bpydc (see Appendix **4.13.4**, Figure **4.A.4**). This indicates that there is no change in topology during the slow diffusion SALE synthesis of core-shell candidates. Sorption analysis of the two samples with N_2 at 77 K revealed that the core-shell sample had a slightly higher uptake of N_2 and a correspondingly larger BET surface area in comparison to the "healed" core, 2860 ± 3 and 2620 ± 11 m^2/g respectively (see Figure **4.17**). Additionally, the pore-size distribution analysis of these samples demonstrated a shift to slightly larger average pore-size upon core-shell synthesis. These porosity changes might impact the diffusion rates of guest molecules throughout the framework, but this is not indicative of the porosity during catalysis because neither sample was metalated. Metalation will decrease the porosity of the samples, hence pre-catalysis the core and core-shell samples were analysed in the same manner, (see section **4.8** for discussion of results).

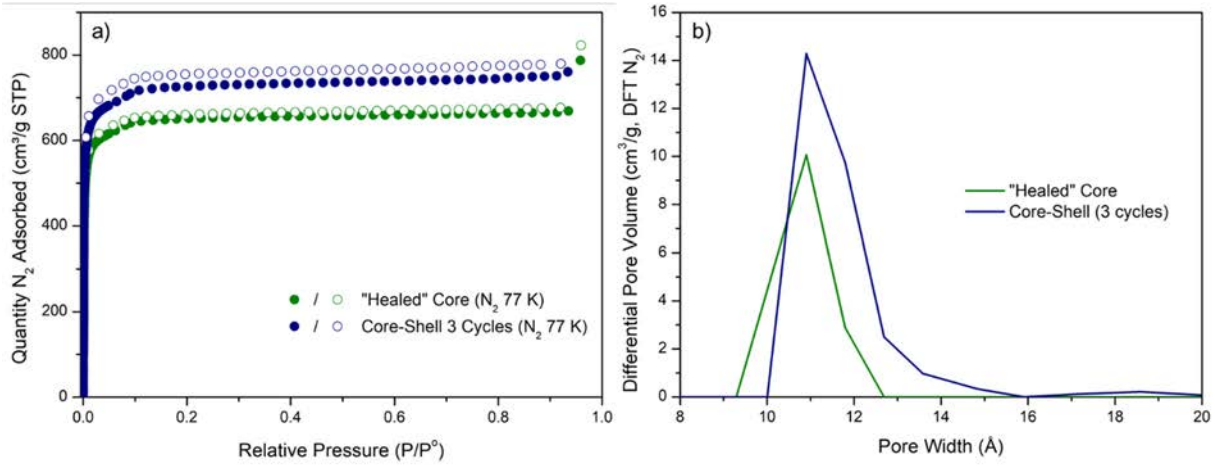

Figure **4.17**: a) 77K N_2 sorption isotherms and b) pore-size distributions of UiO-67-bpydc "healed" Core and Core-Shell (synthesised from 3 successive cycles of slow diffusion SALE) samples.

As proof of concept a sample of reverse CS UiO-67-bpdc with a bpydc shell (UiO-67-bpdc⊂UiO-67-bpydc) was synthesised from a healed core of UiO-67-bpdc. The core UiO-67-bpdc crystals were synthesised with the same protocol as core UiO-67-bpydc crystals (80 eq. TFA, DMF, 120 ºC for 7 d, see experimental **4.11**). SEM analysis of the as-synthesised core UiO-67-bpdc crystals revealed that the crystals were larger than its core UiO-67-bpydc counterpart, being approximately 100 μm in size, (see Appendix **4.13.5** Figure **4.A.5**). The ligand defects were removed from the core UiO-67-bpdc crystals following the previously outlined protocols of exchange with BA and "healing" with excess H_2bpdc (see experimental section **4.11**). The healing process was followed by ^{1}H and ^{19}F NMR spectroscopy to ensure TFA and BA were removed from the "healed" core UiO-67-bpdc crystals (see Appendix **4.13.5**, Figure **4.7**). The reverse CS UiO-67-bpdc⊂UiO-67-bpydc sample was synthesised via slow diffusion SALE incorporating H_2bpydc into the exterior of the core crystals under optimised conditions (2.5 mM H_2bpydc in DMF at 120 ºC for 20 min). ^{1}H NMR spectroscopy of the digested sample indicated a H_2bpydc:H_2bpdc of 4.4 % (see Appendix **4.13.5**, Figure **4.A.7**). SEM/EDX analysis of the reverse CS UiO-67-bpdc⊂UiO-67-bpydc sample metalated with RhCODCl revealed a 'surface' Rh:Zr of 11.5 ± 0.9 %, indicating that there are more [Rh(bpydc)(COD)Cl] entities at the surface of the composite than H_2bpydc in the bulk of the sample. These results indicate that H_2bpydc is localised at the surface of crystals and as such the reverse CS UiO-67-bpdc⊂UiO-67-bpydc composite has a diffuse H_2bpydc shell. All of the samples discussed were phase pure via PXRD, matching the powder pattern of UiO-67-bpdc

(see Appendix **4.13.5**, Figure **4.6**). The reverse CS UiO-67-bpdc⊂UiO-67-bpydc sample was used as a control catalyst where all of the active sites are localised at the exterior surface.

In this section the synthesis and characterisation of CS UiO-67-bpydc⊂UiO-67-bpdc and UiO-67-bpdc⊂UiO-67-bpydc samples was described. Along with the "healed" core UiO-67-bpydc sample, these samples represent three different localisations of active sites throughout the MOF crystals, at the exterior, throughout the crystal and at the core of the crystal. Whilst there are no defined core-shell boundaries for these samples, the distribution of active sites is different enough between samples that catalytic testing with them will enable an investigation into the dependence of catalytic site localisation on the activity and selectivity of catalysts for ethylene oligomerisation.

4.5. Background to Ethylene Oligomerisation Catalysis

Ethylene oligomerisation is a catalytic process by which ethylene monomers are converted to form longer chain oligomers. The oligomerisation of ethylene is an important catalytic process for the synthesis of a range of molecular weight olefins, which are used in the production of low-density polyethylene (linear C_4–C_8),[39] and as intermediates for the production of plasticizers (C_6-C_{10}), lubricants (C_{10}-C_{12}) and detergents (C_{12}-C_{16}).[40-44] Ethylene oligomerisation is predominantly carried out in industry through the use of transition metal (Ni and Cr) and Al catalysts,[40, 42] which produce either a geometric or full-range distribution of linear-α-olefins (LAOs), such as a Schulz-Flory distribution from Ni catalysts (SHOP) and a Poisson distribution from alkyl aluminium (alfen or ethyl process).[45-46] These distributions stem from varied mechanisms of chain growth. The first general mechanism is that of linear coordination-migratory insertion (the Cossee mechanism) which results in chain growth and a broad distribution of varied chain length polymers (see Figure **4.18**).[47] The second general mechanism for the selective production of shorter chain LAOs occurs via metallacycle intermediates.[48-49] This mechanism involves oxidative coupling of two ethylene units (coordinated to the metal) forming a metallocyclopentane, further insertion of ethylene units can produce larger metallocycles and, decomposition of the metallocycle at any point will produce LAOs.[45] The stability of the different sized metallocycles dictates the selectivity of a given LAO, and this can be controlled by the transition metal catalyst and the corresponding surrounding chemical environment.

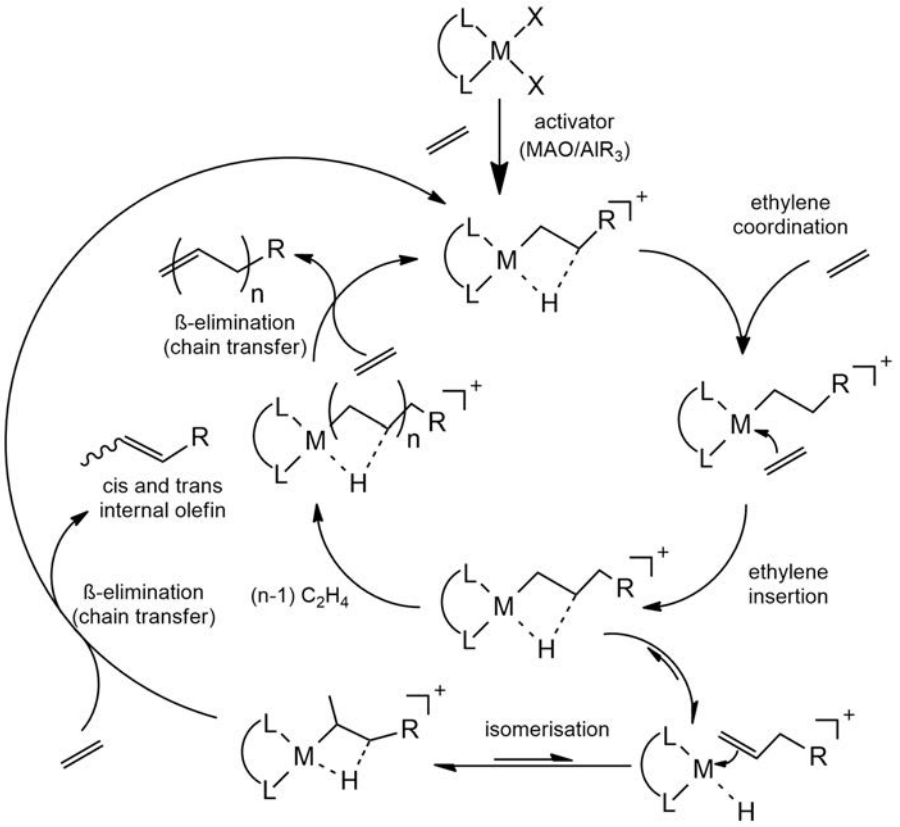

Figure **4.18**: A general reaction schematic for the Cossee mechanism of chain growth during ethylene oligomerization using a transition metal catalyst MX_2 and an activating agent (MAO/AlR_3).

Common transition metals used for ethylene oligomerisation include Ni, Pd, Fe, Cr and Co.[45] Typically a transition metal catalyst for ethylene oligomerisation features a metal halide coordinated to a chelating electron donating ligand, and these catalysts typically need to be activated with a co-catalyst in the form of methylaluminoxane (MAO) or AlR_3 *in situ*.[50-51] The steric bulk and functional groups appended to the chelating ligand of the complex has been shown to tune the activity of the catalyst. Most of these catalysts are reported as homogeneous catalysts; in fact the dimerization of ethylene to form α-butene, in industry, is almost entirely performed via large scale homogeneous catalytic reactions.[45] Common reaction conditions for ethylene oligomerisation include a solvent to solubilise the homogeneous transition metal catalyst (i.e. cyclohexane) and reaction products, > 100 equivalents of activating agent, high pressure (10 - 60 bar) and moderate temperatures depending on the catalyst (25 – 80 °C).[42, 50-53] Varying the temperature/pressure of reaction has been shown to influence the product distribution of the reaction (catalyst dependent), as the rate of chain transfer relative to chain isomerization increases with ethylene concentration at the active site (see Figure **4.18**).[51] Increasing the ethylene concentration in the reaction vessel (i.e. increasing the temperature and

hence ethylene solubility in cyclohexane or increasing the pressure of the reaction) has been shown to produce primarily LAOs.[51]

A benefit of using MOFs for ethylene oligomerisation over solid state or homogeneous catalysts is that they are porous and hence pore confinement of reagents can occur. Pore confinement could affect the product distribution more prominently than the ligand or mechanism of action by impacting the rate of insertion of ethylene and hence the percent isomerisation of LAOs. Several different MOF systems have been utilised for ethylene oligomerisation including Ni@(Fe)MIL-101,[54] NU-1000-bpy-$NiCl_2$,[55] UiO-67-bpydc-$NiBr_2$ and Ni-MFU-4*l*.[53, 56] In all cases a nickel complex is coordinated to the framework at a chelating site post-synthetically, whilst retaining most of the porosity of the parent framework. These systems boasted excellent selectivity for short chain LAOs due to pore-confinement effects. The most active and selective catalyst was the Ni-MFU-4*l* system, consuming ethylene at a rate of 41,500 mol per mol Ni per hour with 96.2 % selectivity for 1-butene.[56] All of these systems are biphasic, with the exception of NU-1000-bpydc-$NiCl_2$, with the catalyst and activating agent (>100 equivalents) in the solution (typically toluene) and the system pressurised with ethylene at high pressure. Additionally, the activities of the catalysts discussed are somewhat dependent on the amount of MAO/AlR_3 co-catalyst used, hence NiX_2 (X = Cl, Br) is not the optimum catalyst for a study of internal vs external catalysis.

Ethylene oligomerization can be catalysed by a Pd catalyst without the need for MAO/AlR_3, and hence is a better candidate for studying the impact of active site location on the activity/selectivity for a MOF catalyst. A palladium diphosphine complex, reported by Brookhart *et al.,* was shown to catalyse the oligomerization of ethylene without a co-catalyst, with the catalyst demonstrating a temperature dependent formation of branched / linear chain products.[57] The active catalyst is [PdMe(MeCN)]BAr^F coordinated to a diphosphine chelating ligand, which is generated in situ from reacting [PdMe(COD)]Cl with $NaBAr^F$ (where $NaBAr^F$ is sodium tetrakis[3,5-bis(trifluoromethyl)phenyl]borate).[57] The catalyst was shown to be active at pressures between 200 and 600 psig (13.8 – 41.3 bar) and was selective to branched polymers at low temperatures (22 ºC) and linear polymers at high temperatures (75 ºC).[57] It is worth noting that the experiments that were conducted by Brookhart *et al.* required toluene to solubilise their catalyst and their reactions were done in a bi-phasic system with high pressure ethylene added in a sealed batch reactor.

Catalysis of ethylene oligomerization in gas phase is an attractive prospect because it negates solvent use and hence speeds up product recovery/separation. Additionally, in the case of using a MOF-based catalyst in the gas phase, analysis of active site accessibility due to guest molecule diffusion is possible. Gas phase ethylene oligomerisation has been shown with MOF-based catalytic systems including NU-1000-bpydc-$NiCl_2$ and (Ru)HKUST-1.[55, 58] In the case of NU-1000-bpy-$NiCl_2$ crystal size and hence active site accessibility was shown to be a significant factor effecting the intrinsic activity (IA) of the catalyst. In this study NU-1000-bpy-$NiCl_2$ was compared to mechanically downsized batch of the catalyst; the crushed sample demonstrated a dramatic increase in IA due to the exposure of more surface-active sites with increased external surface area from downsizing.[55] The as-synthesised composite was also tested under conventional the bi-phasic conditions in heptane showing significantly higher IA than in the gas phase until the sample was crushed and then the IA was comparable.[55] These results highlight the necessity to further understand the location of activity within MOFs.

The overall aim of the work outlined in this section was to incorporate the catalyst synthesised by Brookhart *et al.* into the UiO-67-bpydc framework and use the composite to catalyse the gas phase oligomerisation of ethylene. In doing so an investigation of internal vs external catalysis and hence pore-confinement effects on product distribution would be undertaken by comparing the activity and product distribution of the CS UiO-67-bpydc⊂UiO-67-bpdc, UiO-67-bpdc⊂UiO-67-bpydc and core UiO-67-bpydc samples.

4.6. Preparation and Metalation of the MOF with [PdMe(MeCN)]$^+$

In order to incorporate the active catalyst $[PdMe(MeCN)]^+$ into UiO-67-bpydc composites the counterion was exchanged a less sterically demanding anion. The original counterion $NaBAr^F$ is too large to fit within the pores of UiO-67-bpydc, so during the synthesis of the catalyst precursor the counterion was exchanged with $AgBF_4$. $AgBF_4$ abstracts Cl^- from the pre-catalyst and AgCl forms as a precipitate during the halide abstraction and which was removed via filtration prior to metalation. The synthesis of $[(COD)PdMe(MeCN)]BF_4$ is outlined in the experimental section **4.11.2**, and involved treating the pre-catalyst [PdMe(COD)]Cl with > 1 eq. $AgBF_4$ in dry MeCN, see Scheme **4.1**.[57] A sample of MOF was then added to the filtered catalyst solution under Ar and left to react at 3 °C for 3 d. $[PdMe(MeCN)]BF_4$ coordinates to the N-donor sites in H_2bpydc in the MOF framework.

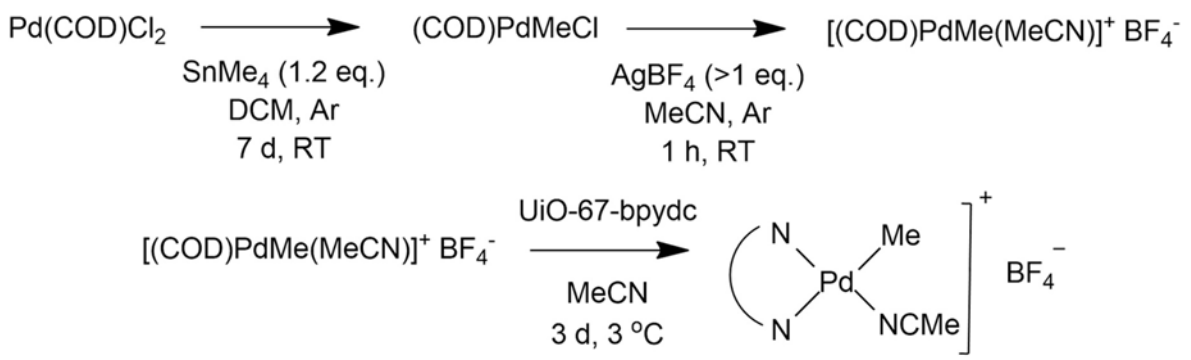

Scheme **4.1**: Synthesis of [(COD)PdMe(MeCN)]BF_4 from $PdCODCl_2$ and subsequent UiO-67-bpydc metalation with [(bpydc)PdMe(MeCN)]BF_4.[59]

Preliminary metalation studies were performed with 1 μm UiO-67-$bpydc_{0.5}bpdc_{0.5}$ (50 % bpydc UiO-67), which was prepared and characterised, as discussed previously in Chapter **3**, and chosen because it was easy to synthesise and characterise. EDX analysis of samples obtained from initial metalation experiments showed some Cl^- was still present in the metalated MOF sample, suggesting that not all of the Pd coordinated to the framework would be the active catalyst [PdMe(MeCN)]BF_4. This is due to an older sample of $AgBF_4$ being employed where some of the Ag(I) had reduced to Ag (0), and hence > 1.5 eq. $AgBF_4$ was necessary to abstract the majority of the Cl from [PdMe(COD)]Cl (see EDX results in Table **4.2**). Elemental analysis of the Pd:Zr ratio by SEM/EDX demonstrated that for the 50% bpydc 1 μm MOF sample near quantitative metalation of bpydc sites in the framework was achieved (< 92% occupation of bpydc sites). The SEM/EDX analysis on the sample prepared with 2 eq. $AgBF_4$ confirmed that the Pd complex coordinated to the framework is the BF_4^- salt of $[PdMe(MeCN)]^+$ as the F:Pd ratio is equal to 393.3 ± 8.9 %. It is worth noting that quantitative determination of low atomic weight elements is challenging, hence the presence of boron was not quantified via EDX. From these results 2 eq. of $AgBF_4$ was used for all subsequent reactions.

Table **4.2**: Screening $AgBF_4$ equivalents for optimised metalation of UiO-67-bpydc with $[PdMe(MeCN)]BF_4$.

Eq. $AgBF_4$ relative to Pd / sample name	H_2bpydc : H_2bpdc (post-NMR digest)	Pd : Zr (Atomic %) (SEM/EDX)	Cl : Pd (Atomic %) (SEM/EDX)	F : Pd (Atomic %) (SEM/EDX)
1.5 eq.	46	42.9 ± 0.9	54.2 ± 0.8	142.3 ± 26.7
2 eq.	46	41.7 ± 0.9	8.8 ± 0.9	393.9 ± 8.9
3 eq.	46	42.3 ± 0.4	7.19 ± 0.9	340.9 ± 32.8
Pd·1 (2 eq)	46	36.3 ± 0.9	2.4 ± 0.7	290.6 ± 34.4

Preliminary catalytic testing was conducted with 50% bpydc UiO-67 1 µm metalated with the Pd catalyst $[PdMe(MeCN)]^+BF_4^-$ (**Pd·1**) in order to develop a reproducible and reliable ethylene oligomerisation protocol. The crystallinity of **Pd·1** was confirmed via PXRD, with the powder pattern matching that of phase pure UiO-67-bpydc (see Figure **4.19**). SEM/EDX analysis of **Pd·1** revealed no change to the morphology of the crystals (see Figure **4.19**), with no deposition of Pd or Ag on the surface of the crystals and a Pd:Zr of 36% (summarised in Table **4.2**).

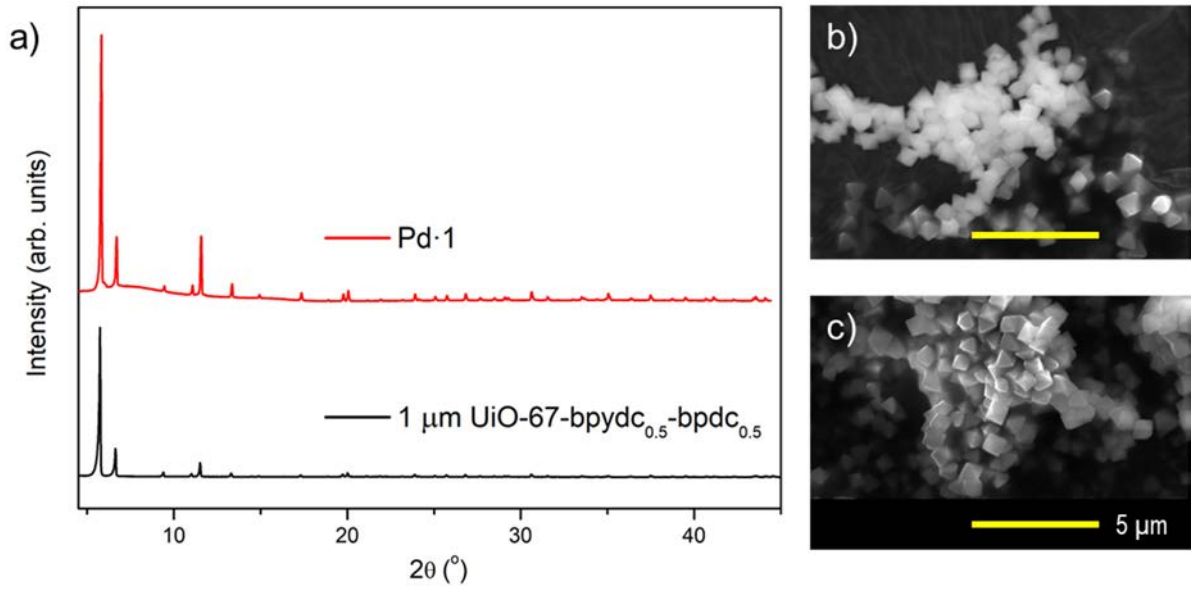

Figure **4.19**: a) PXRD patterns and SEM images of 1 µm UiO-67-bpydc$_{0.5}$bpdc$_{0.5}$ b) as-synthesised (black) and c) post-$[PdMe(MeCN)]BF_4$ metalation (**Pd·1**, red).

4.7. Gas-phase Catalytic Reactor Setup

Two gas phase reactor setups were available for following the progress of ethylene oligomerisation, a batch reactor capable of high pressures and a flow reactor capable of high flow rates. The progress of the reaction can be followed in real-time by using a residual gas analyser (RGA) which is a low-pressure mass-spectrometer. Schematic representations of the batch and flow reactor setups are shown in Figure **4.20**. When using a flow reactor, the RGA data is qualitative because the volume of the reaction cell varies (due to amount of glass wool used during sample preparation, see Appendix **4.13.6**, Figure **4.A.8**), but when using the batch reactor RGA data is quantitative. Furthermore, the RGA gives information about the reaction profile in terms of the fragmentation of reactants/products in the gas mixture; however, unfortunately isomers of key products such as 1-butene and 2-butene/isobutylene have identical fragmentation patterns, so the RGA cannot give information about isomer formation. The reaction gas mixture can also be analysed via gas chromatography coupled to a flame-ionising detector (GC-FID), which can quantitatively determine the product distribution and distinguish between isomers of certain products. The limitation of the GC-FID is that you can only inject gas mixtures at $\leq$ 1 bar onto the column otherwise it is saturated with ethylene. Thus, when using the batch reactor this can only be done once per reaction, where the majority of the gas mixture must be evacuated to almost 1 bar before injection into the GC-FID. In the flow reactor set up the residual gas mixture (output from the exhaust of the back-pressure regulator) can be constantly passed into the injection chamber of the GC-FID at a pressure of 1 bar and, multiple GC-traces can be taken across the course of the reaction. Considering the advantages and limitations of both the batch reactor and the flow reactor set up, initially ethylene oligomerisation reactions were tested in the batch reactor, with the progress of the reaction followed by RGA and the product distribution quantified after 1 h via GC-FID.

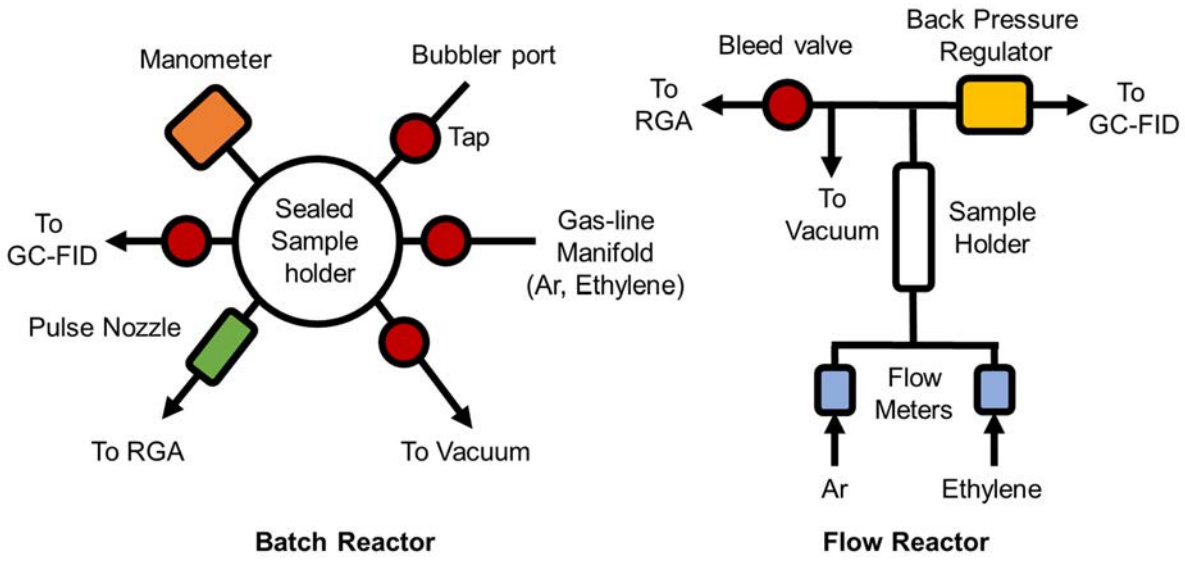

Figure **4.20**: Schematic representations of the batch and flow reactors used during catalytic testing.

4.8. Catalysis Experiments

Initial gas phase catalysis screening under batch reactor conditions was conducted with **Pd·1** to confirm the activity of the catalyst under reaction conditions similar to those reported in the literature in liquid/gas phase reactors. The related palladium complex, with a different chelating phosphine ligand rather than UiO-67-bpydc, had previously been reported to catalyse the oligomerisation at between 200 - 600 psi (13.7 – 41.3 bar) and 22 – 75 °C.[57] It was shown by Brookhart *et al.* that at high pressure and temperature their Pd catalyst produced primarily LAOs; hence, similar conditions were chosen for preliminary testing. Due to reaction cell limitations reaction pressures > 20 bar could not be maintained for safety reasons. **Pd·1** was activated under vacuum on the batch reactor at 50 °C overnight to remove excess solvent from the MOF pores. The batch reactor was cooled to 25 °C and **Pd·1** was exposed to ethylene 16.7 bar for 0.5 h, while the progress of the reaction was monitored via the RGA. The batch reactor was heated to 75 °C and the reaction temperature was held constant for 1 h, then the final pressure was noted (13.7 bar) and the reaction cell was evacuated to 1 bar and the gas mixture was injected into the GC-FID.

The pressure and temperature profile of the reaction were followed (see Figure **4.21**), showing there is constant reduction in ethylene pressure even at room temperature, indicating the catalyst was consuming ethylene to produce longer oligomers. At 75 °C the rate of consumption of ethylene is increased and the RGA was able to detect an increase in production of m/z fragments 41 and 56. The 1° fragments of 1-butene and 1-hexene are m/z 41 and 56

respectively, but there will be contribution to both m/z 41 and 56 from 1-butene, 1-hexene and longer chain volatile oligomers.[32] Since there is convolution in detected mass fragments via RGA the presence of 1-butene will be discussed as the evolution of m/z 41 and 56, 1-hexene is represented by m/z 69 and 84 and 1-octene corresponds to m/z 112 (the highest mass fragments for each oligomer).[32] Unfortunately, this complication means that RGA data analysis is qualitative because there is no real-time way to distinguish between the contribution to different m/z values from the presence of different chain length oligomers. The RGA data in Figure **4.21** demonstrates that the catalyst is active in producing ethylene oligomers which fragment to m/z 41 and 56 (1-butene and 1-hexene at least). The activity is fairly linear for the production of m/z 41 and 56 over the course of 1 h of heating, with no apparent drop off in activity over a short time scale in the batch reactor.

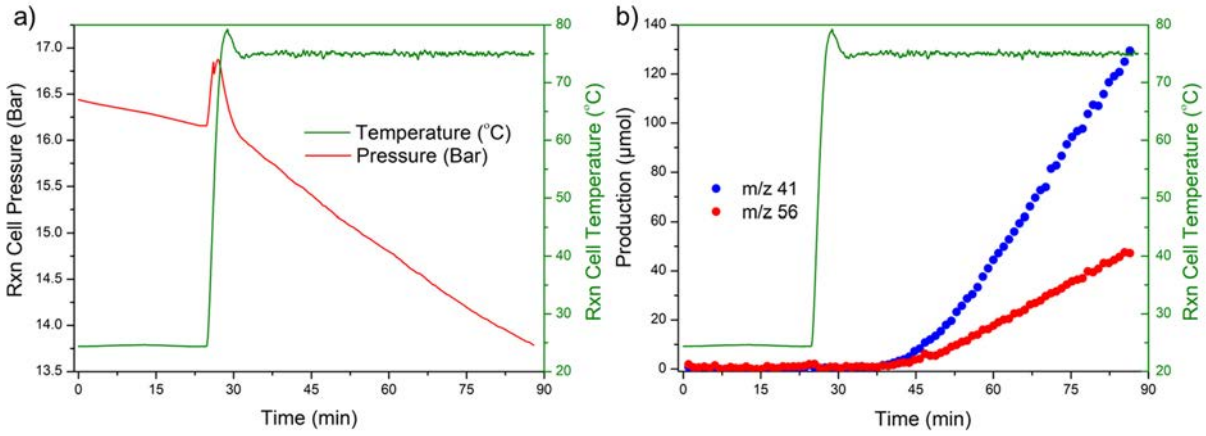

Figure **4.21**: a) Reaction cell temperature, pressure, and b) production data for 1-butene (m/z 41 and 56) for the first trial reaction for ethylene oligomerisation with **Pd·1** in the batch reactor.

The product distribution of the first ethylene oligomerisation reaction catalysed by **Pd·1** was quantified via GC-FID after 1 h of heating at 75 °C, see Figure **4.22**. There is a considerable excess of ethylene in the gas mixture (78.9 %) followed by 1-butene (0.8 %), 1-butene isomers (9.6 %) and 1-hexene (10.6 %). The turn-over frequency (TOF = [mol (ethylene consumed)]/[mol (catalyst)] h^{-1}) for this test reaction was 106.4 h^{-1} which is 90% of the equivalent homogeneous catalyst activity in comparable conditions in a gas/liquid phase reactor.[57] The product distribution displayed in Figure **4.22** shows that 1-hexene was the primary product observed via GC-FID but there is a considerable contribution from 1-butene isomers. The possible isomers which can form are cis/trans 2-butene and isobutylene. Isomerisation occurs when the rate of chain transfer is slow (insertion of ethylene into the Pd

complex in the MOF), see schematic in Figure **4.18**. In the reaction catalysed by **Pd·1** the ethylene concentration around the active sites is low enough for isomerisation of 1-butene to occur readily with a small proportion of linear 1-butene formed relative to other isomers. Additionally, there is a discrepancy of 388 µmol of ethylene equivalent molecules between the starting quantity of ethylene (2169 µmol) and the number of ethylene equivalent molecules detected via GC-FID (1781 µmol), where 1-butene and 1-hexene are equivalent to 2 and 3 molecules of ethylene respectively. This discrepancy is likely due to the formation of longer oligomers of ethylene such as 1-octene and 1-decene which are not particularly volatile at 75 °C, their boiling points are 121 and 170 °C respectively,[32] and hence cannot be readily detected via gas-phase analytic techniques (GC-FID/RGA).

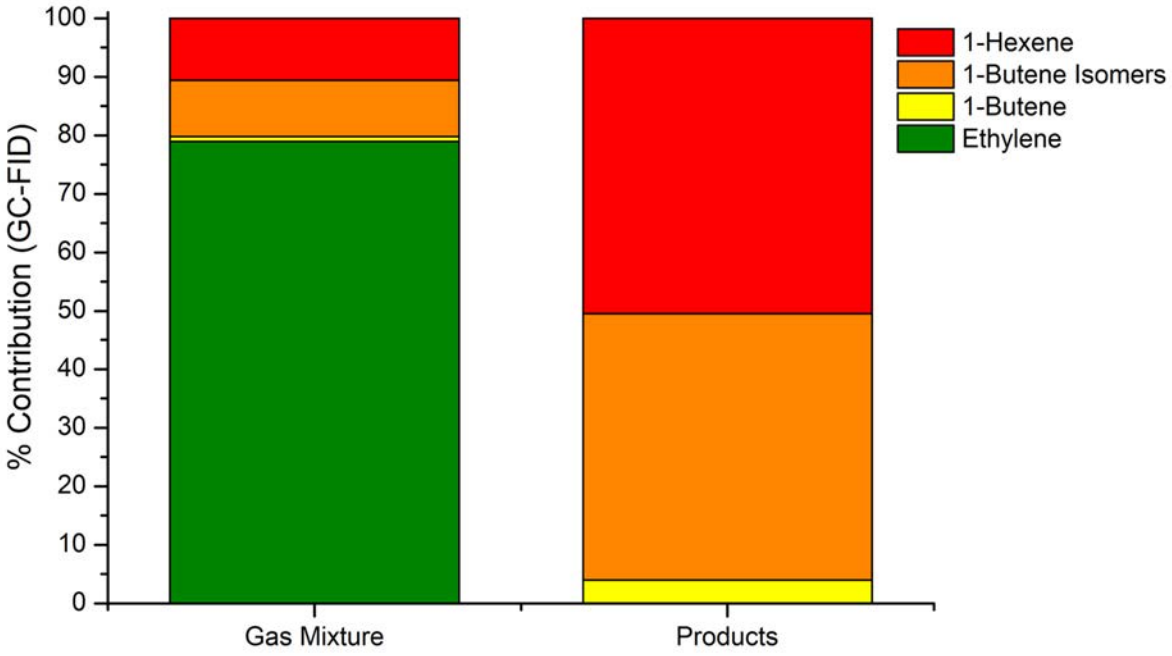

Figure **4.22**: GC-FID data of an ethylene oligomerisation reaction catalysed by **Pd·1** on the batch reactor, displaying the % contribution to the gas mixture as a whole and for the products.

Post-catalysis, **Pd·1** was examined via PXRD and SEM to determine if deposition of longer chain polymers had occurred. PXRD of **Pd·1**$_{\text{post batch cat}}$ (**Pd·1** post-catalysis) demonstrated a reduction in crystallinity with a masking of some of the primary reflections of UiO-67 with an amorphous phase and the presence of two primary reflections corresponding to crystalline polyethylene (see Figure **4.23**). SEM analysis of **Pd·1**$_{\text{post batch cat}}$ revealed that there is a surface coating on the MOF crystals which collected surface charge under the electron beam, indicating the presence of a non-conductive substance in SEM. It can be seen in Figure **4.23** that although there are 1 µm MOF crystals present, they are surrounded by a polymer

coating, with visible strands extending between MOF crystals. SEM and PXRD analysis of **Pd·1**$_{\textbf{post batch cat}}$ establish that the MOF catalyst becomes coated in polyethylene during the process of catalysing the oligomerisation of ethylene. Whilst this does not necessarily indicate that the catalyst is deactivated by the polyethylene coating, it does confirm the synthesis of long chain non-volatile ethylene oligomers (at 75 °C).

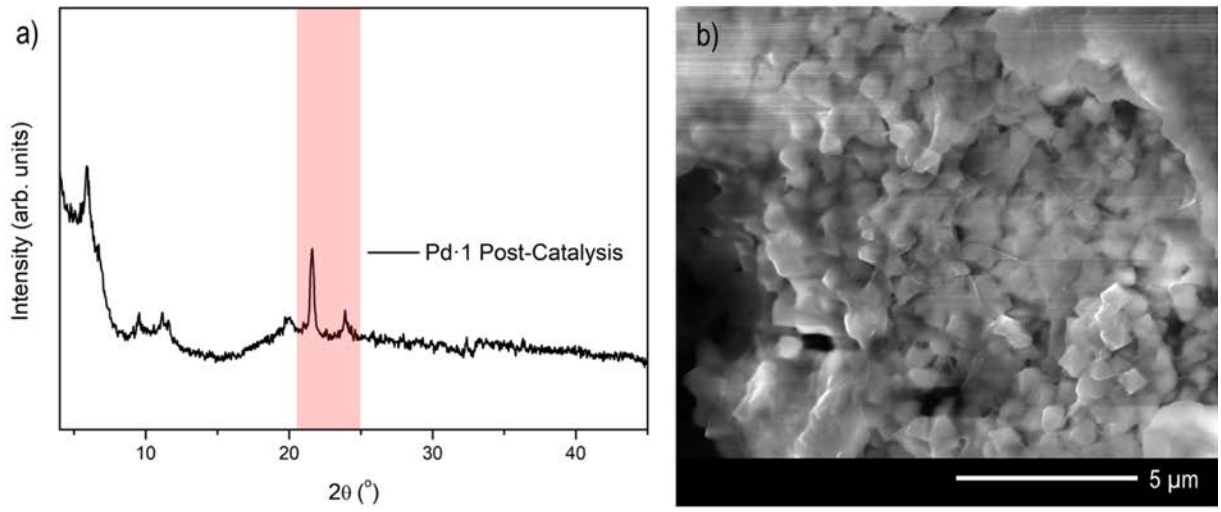

Figure **4.23**: a) PXRD of **Pd·1**$_{\textbf{post batch cat}}$ demonstrating the presence of crystalline polyethylene at highlighted in by the red shaded box at 21.5º and b) an SEM image of polymer coating on the crystals of **Pd·1**$_{\textbf{post batch cat}}$, surface charging is indicative of an insulator present on the surface of the sample (polyethylene).

The activity of **Pd·1** was also analysed on the flow reactor set up to better observe the profile of activity in real time. The major point of concern for the flow set up was controlling to pressure of the gas mixture which is fed into the RGA. Unlike the batch reactor set up this is controlled manually with a needle-valve and hence there is a lot more variability of pressure in the RGA, see schematic in Figure **4.18**. A portion of **Pd·1** (10 - 60 mg) was activated under a flow of Ar (50 ml/min) at 50 ºC for 1 h, with the pressure held at 6 bar via a back-pressure regulator, prior to catalytic testing. The activity of **Pd·1** examined under 3, 6 and 12 bar of ethylene at a flow rate of 50 ml/min, at 30 ºC for 1 h and then at 75 ºC for 1 h. 3 bar of ethylene was not sufficient to observe conversion to longer oligomers at either temperature. With 6 bar of ethylene, products could be detected via both the RGA and on the GC-FID at 30 and 75 ºC (see Figure **4.24**), and the pressure to the RGA could be regulated easily via the bleed-valve. When operating at a 12 bar back-pressure there were two problems; specifically, the pressure was very hard to regulate to the RGA resulting in no meaningful data collection and the catalyst was so active that a significant portion of pure polyethylene was formed and passed through

the 0.5 µm filter seal on the catalyst mount (see Appendix **4.13.6** for schematic details for the experimental set up). From these trial experiments the ideal reaction back pressure was determined to be 6 bar, ensuring modest catalytic activity which enabled the detection of products via RGA and GC-FID and easy regulation of pressure to the RGA.

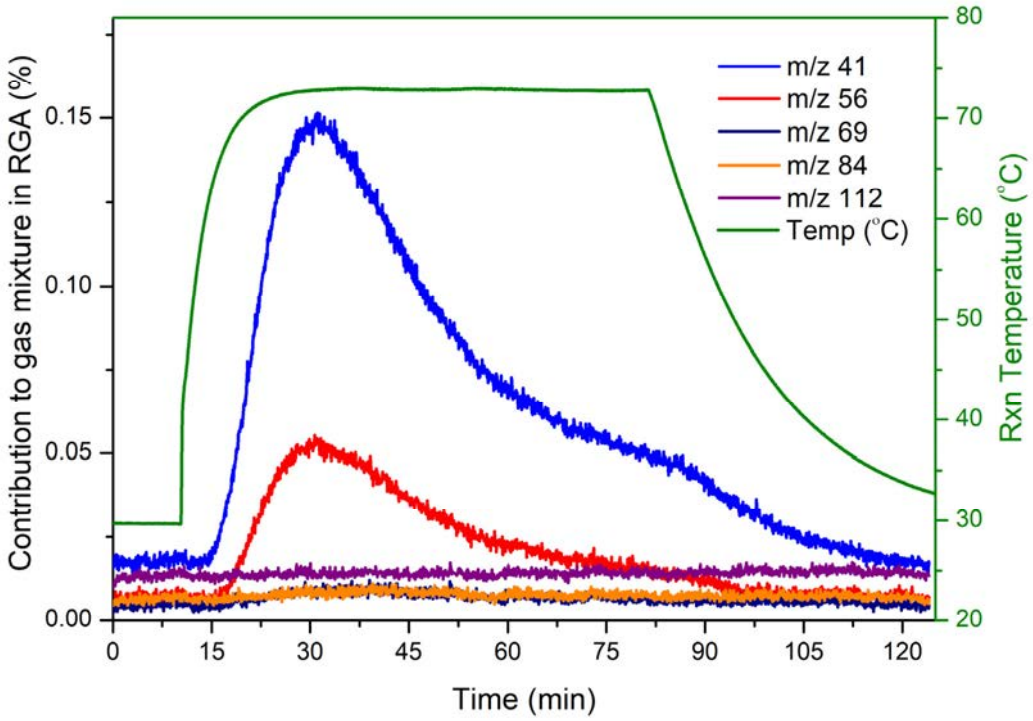

Figure **4.24**: Reaction profile of ethylene oligomerisation catalysed by **Pd·1** (50 ml/min, 6 bar back pressure) on the flow reactor. The reaction profile is displayed as the contribution to the total pressure in the RGA (%) for 1-butene (m/z 41 and 56), 1-hexene (m/z 69 and 84) and 1-octene (m/z 112).

The reaction profile of ethylene oligomerisation catalysed by **Pd·1** under flow conditions reveals some interesting details about the activity of the catalyst. Upon heating the system to 75 ºC there is an increase in production of 1-butene (m/z 41 and 56 detected by the RGA) with maximum production occurring 20 minutes after heating began. While the reaction temperature was held constant, the production of 1-butene decreases without a significant increase in 1-hexene production (see Figure **4.24**). This reaction profile indicates a possible deactivation of the catalyst after a period of rapid activity and/or the production of longer chain oligomers that are not volatile at 75 ºC, as discussed earlier. The flow reaction gas mixture was also analysed via GC-FID after 1 h of heating at 75 ºC, see Figure **4.25**. There is considerably more ethylene (92.2 %) present in comparison to 1-butene (1.4 %), 1-butene isomers (4.4 %) and 1-hexene (2 %). Additionally, the product distribution at the lower pressure in the flow is

significantly different to that of the batch reaction, with more 1-butene/1-butene isomers produced relative to 1-hexene. It is also notable that at lower pressures more isomerisation of 1-butene has occurred, with 1-butene isomers contributing more to the products (as detected via GC-FID) 56.5 % versus 45.5 % respectively for 6 and 13 bar, respectively. This is likely due to displacement of 1-butene/1-butene isomers from the active site by higher concentrations of ethylene at higher pressures.

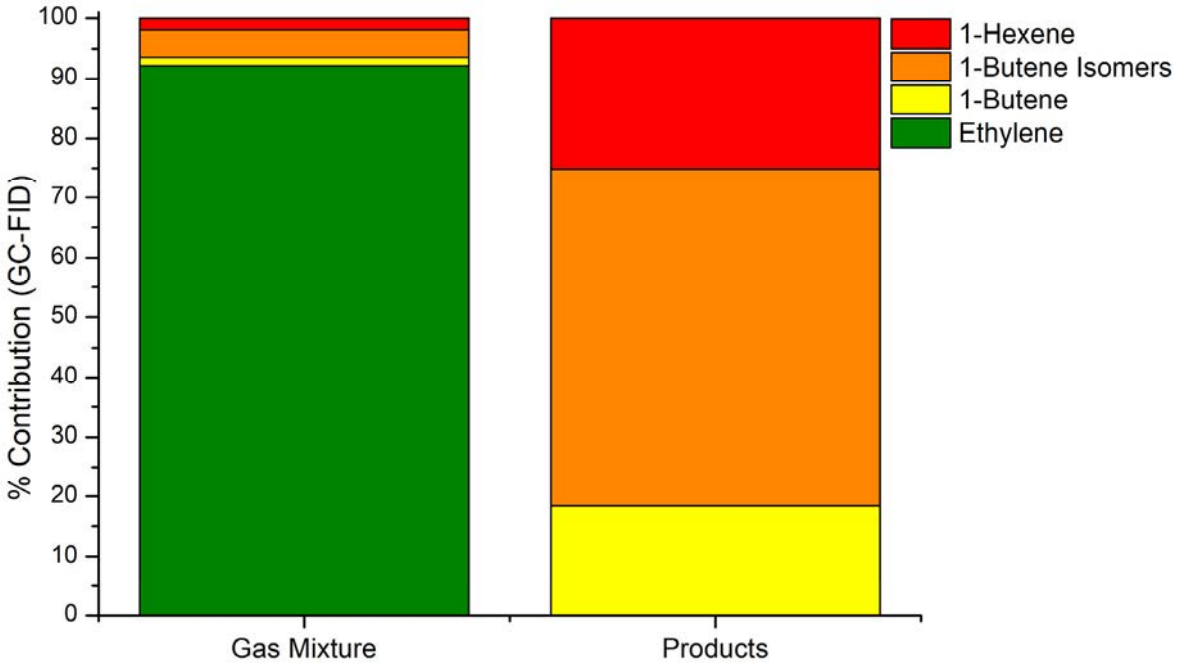

Figure **4.25**: GC-FID data of an ethylene oligomerisation reaction catalysed by **Pd·1** on the flow reactor (50 ml/min ethylene at 6 bar), displaying the % contribution to the gas mixture as a whole and for the products.

Again, the used catalyst **Pd·1** (**Pd·1**$_{\textbf{post flow cat}}$) was examined via PXRD and SEM to determine whether long chain oligomers had formed. PXRD analysis of **Pd·1**$_{\textbf{post flow cat}}$ again revealed a reduction in crystallinity and the presence of crystalline polyethylene (see Appendix **4.13.7**, Figure **4.A.9**). Visual inspection of **Pd·1**$_{\textbf{post flow cat}}$ and SEM analysis revealed that **Pd·1** had agglomerated and coated with a thick coating of polymer. Prior to catalysis **Pd·1** is an off-white microcrystalline powder. Figure **4.26** shows the polymer coating covering the surface of the crystals. Coupled with the reaction profile data in Figure **4.24**, the deactivation seen can be directly attributed to formation of long chain non-volatile ethylene oligomers which stick to the surface of the crystals and, either blocks access of ethylene to active sites in the MOF or stops the diffusion of products out of the catalyst. The location of catalytic activity within the

crystals of **Pd·1** is unknown (either internal/external) hence, long chain oligomers could be forming from internal-active sites, thereby blocking the pores as well as forming at external surface-active sites. This observation underpins the importance of understanding the difference between surface and internal catalysis with MOFs.

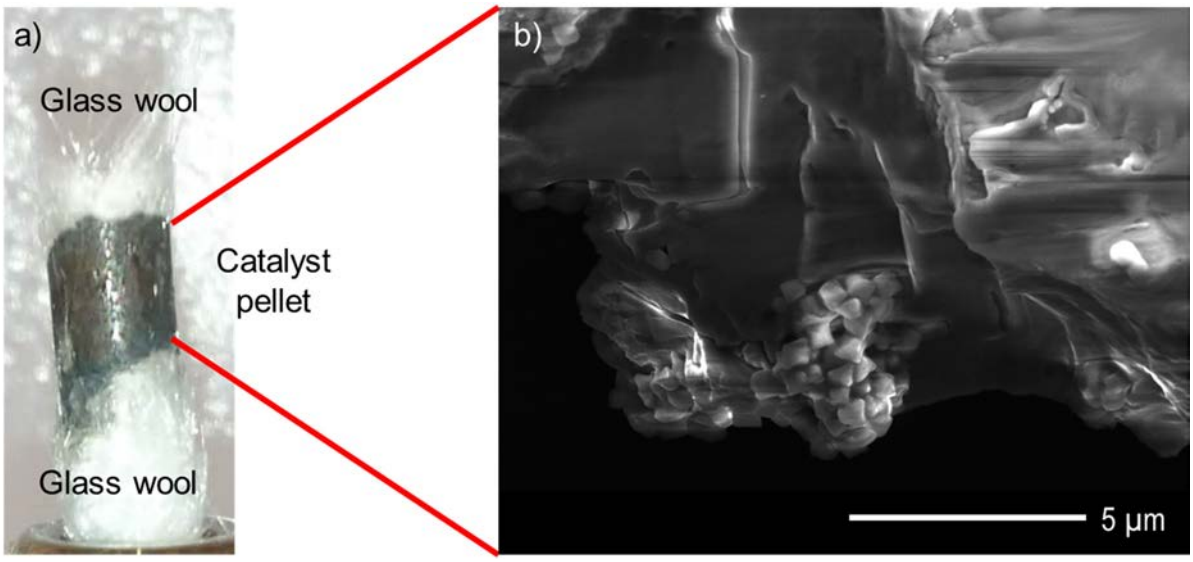

Figure **4.26**: a) A photo of the catalyst pellet of **Pd·1** post-flow reaction, with the catalyst held in place by glass wool (top and bottom) and the crystals pellet comprising of **Pd·1** and a polymer coating and b) an SEM image of the catalyst pellet.

4.9. Core and Core-Shell Catalysis Experiments

The impact of catalytic site localisation in UiO-67-bpydc for the catalysis of ethylene oligomerisation with a Pd catalyst was investigated by comparing the reaction activity profiles of core and core-shell samples under flow conditions. The samples used were core-UiO-67-bpydc, core-shell UiO-67-bpydc⊂UiO-67-bpdc (1 and 3 cycles), reverse core-shell UiO-67-bpdc⊂UiO-67-bpydc metalated with $[PdMe(MeCN)]^{+}BF_4^{-}$, henceforth denoted as **Pd·2**$_{\textbf{core}}$, **Pd·2**$_{\textbf{core-shell-1}}$, **Pd·2**$_{\textbf{core-shell-3}}$ and **Pd·2**$_{\textbf{rev-core-shell}}$ respectively. The metalation for each of these samples is displayed in Figure **4.27**; for the large crystals of UiO-67-bpydc there is low uptake of Pd as detected via ICP-MS and SEM/EDX. The Pd:Zr ratios match the expected trends relative to the distribution of ligand in the composites: **Pd·2**$_{\textbf{core}}$ has an equivalent metalation in the bulk as at the surface, **Pd·2**$_{\textbf{core-shell-1}}$ and **Pd·2**$_{\textbf{core-shell-3}}$ have lower Pd:Zr at the surface than in the bulk (within error) and, **Pd·2**$_{\textbf{rev-core-shell}}$ has a higher surface ratio than in the bulk. The ICP-MS Pd:Zr ratio was subsequently used to calculate the mols of catalyst for each sample (see Appendix **4.13.8**). Finally, the crystallinity for all samples was analysed via PXRD, with

all samples retaining long range order post metalation with [PdMe(MeCN)]BF_4 and being topologically identical to UiO-67-bpydc (see Appendix **4.13.9**, Figure **4.A.9**).

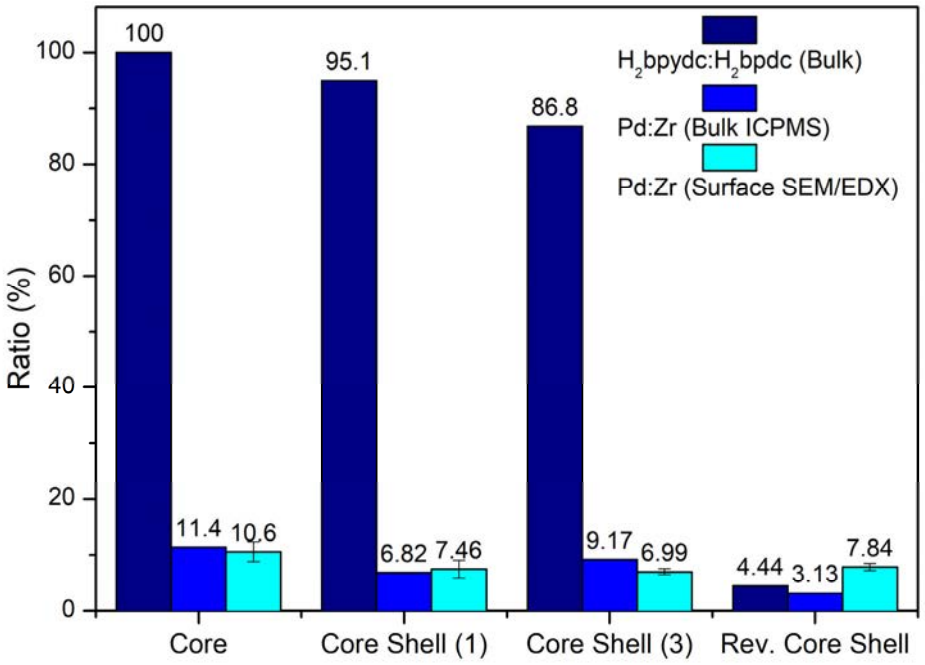

Figure **4.27**: A comparison of the bulk and surface composition of metalated **Pd·2** samples including the bulk H_2bpydc:H_2bpdc (^{1}H NMR, dark blue), the bulk Pd:Zr (ICP-MS, blue) and surface Pd:Zr (SEM/EDX, light blue).

The activity profiles for **Pd·2$_{core}$** and **Pd·2$_{core\text{-}shell\text{-}1}$** for the catalysis of ethylene oligomerisation were directly compared, under the aforementioned flow conditions. The activity profiles are displayed in Figure **4.28** for both reactions. The reaction profile for **Pd·2$_{core}$** is similar to **Pd·1**, characterised by rapid initial production of 1-butene (m/z 41 and 56) peaking within 15 min of heating to 75 ºC, followed by a relatively fast decline in activity. Both **Pd·2$_{core}$** and **Pd·1** have surface active sites, hence the deactivation of the catalysts could be a result of poisoning the surface catalyst sites by the production of polyethylene. **Pd·2$_{core\text{-}shell\text{-}1}$** has a very different activity profile to **Pd·2$_{core}$**, initial activity starts later in the heating cycle (approximately 15 mins) and the peak in activity is much broader, with a slower decline in activity. Quantitatively, the core-shell sample **Pd·2$_{core\text{-}shell\text{-}1}$** demonstrates only a 25% reduction in production of m/z 41 (1-butene) 25 minutes after peak activity, in comparison to 55% reduction for **Pd·2$_{core}$**.

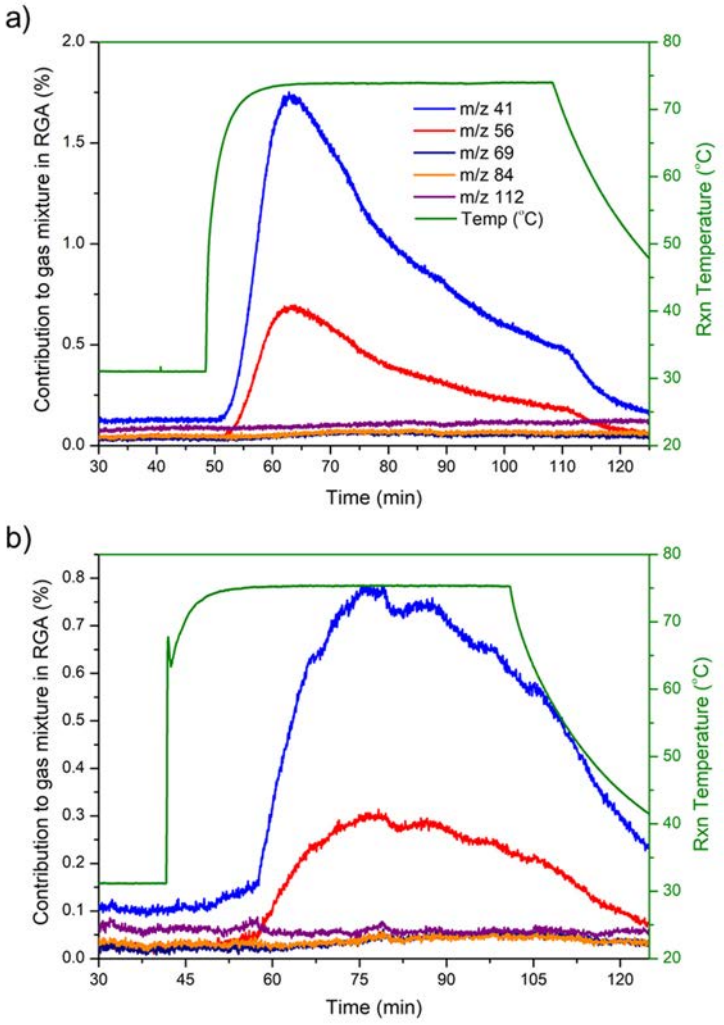

Figure **4.28**: Reaction profiles of ethylene oligomerisation catalysed by a) **Pd·2**$_{\textbf{core}}$ and b) **Pd·2**$_{\textbf{core-shell-1}}$, displayed as the contribution to the total pressure in the RGA (%) for 1-butene (m/z 41 and 56), 1-hexene (m/z 69 and 84) and 1-octene (m/z 112).

The product distribution of the gas mixture was analysed via GC-FID, after 1 h of heating at 75 ºC, for both samples (see Appendix **4.13.10**, Figure **4.A.11**). **Pd·2**$_{\textbf{core}}$ produces a significant proportion of 1-butene (18%) and 1-butene isomers (64%) and some 1-hexene (18%), whereas **Pd·2**$_{\textbf{core-shell-1}}$ favours the production of longer chain LAOs producing more 1-hexene (30%) than 1-butene (11%) but approximately the same proportion of 1-butene isomers (59%). The only difference between **Pd·2**$_{\textbf{core}}$ and **Pd·2**$_{\textbf{core-shell-1}}$ is the location of active sites within the framework, localised throughout the framework and primarily towards the interior, respectively. The diffuse shell of **Pd·2**$_{\textbf{core-shell-1}}$ seemingly prolongs the catalytic activity and mildly alters the product distribution, shifting to longer LAOs. Longer LAOs may be favoured due to higher local concentrations of ethylene within the pore of the MOF, but since there is a

significant proportion of 1-butene isomers the concentration of ethylene must not be high enough to minimise 1-butene isomerisation.

The activity of **Pd·2$_{\text{core-shell-1}}$** was further analysed by conducting three successive catalytic experiments with the same catalyst and observing any variation in activity and product distribution. A portion of **Pd·2$_{\text{core-shell-1}}$** was used to catalyse the oligomerisation of ethylene under flow conditions, after each active cycle the catalyst was outgassed with Ar (50 ml/min at 6 bar) for 1 h and subsequently evacuated overnight. The three successive catalytic cycles and the corresponding GC-FID product distributions are displayed in Figure **4.29**. The reaction profiles for each cycle demonstrate a plateau in activity when held at 75 ºC with production of 1-butene decreasing only when the reaction temperature is decreased. With each successive cycle there is, however, an overall reduction in percent contribution of 1-butene production to the gas mixture in the RGA, indicating a potential deactivation of the catalyst. The product distributions for all three cycles were identical, indicating that the catalyst retains the same selectivity despite overall activity appearing to decrease with successive cycles.

In order to elucidate the source of deactivation of **Pd·2$_{\text{core}}$** and **Pd·2$_{\text{core-shell-1}}$**, the catalysts were analysed via PXRD and SEM post-catalysis. **Pd·2$_{\text{core}}$** and **Pd·2$_{\text{core-shell-1}}$** were crystalline post-catalysis with PXRD analysis revealing the retention of long-range order and the presence of crystalline polyethylene for **Pd·2$_{\text{core}}$** and **Pd·2$_{\text{core-shell-1}}$** after 3 cycles (see Appendix **4.13.11**, Figure **4.A.12**). There was no crystalline polyethylene present in the PXRD pattern for **Pd·2$_{\text{core-shell-1}}$** after 1 cycle of catalysis. Additionally, SEM analysis revealed visible polymer on the surface of crystals of **Pd·2$_{\text{core}}$** and **Pd·2$_{\text{core-shell-1}}$** after 3 cycles, but not a significant amount after only 1 catalytic cycle, (see Appendix **4.13.11**, Figure **4.A.13**). Hence, the production of long chain oligomers must occur over a longer period of time for samples with few surface-active sites such as **Pd·2$_{\text{core-shell-1}}$**. To test this hypothesis the reaction needed to be followed for a longer period of time with a core-shell candidate with the fewest surface-active sites, **Pd·2$_{\text{core-shell-3}}$**.

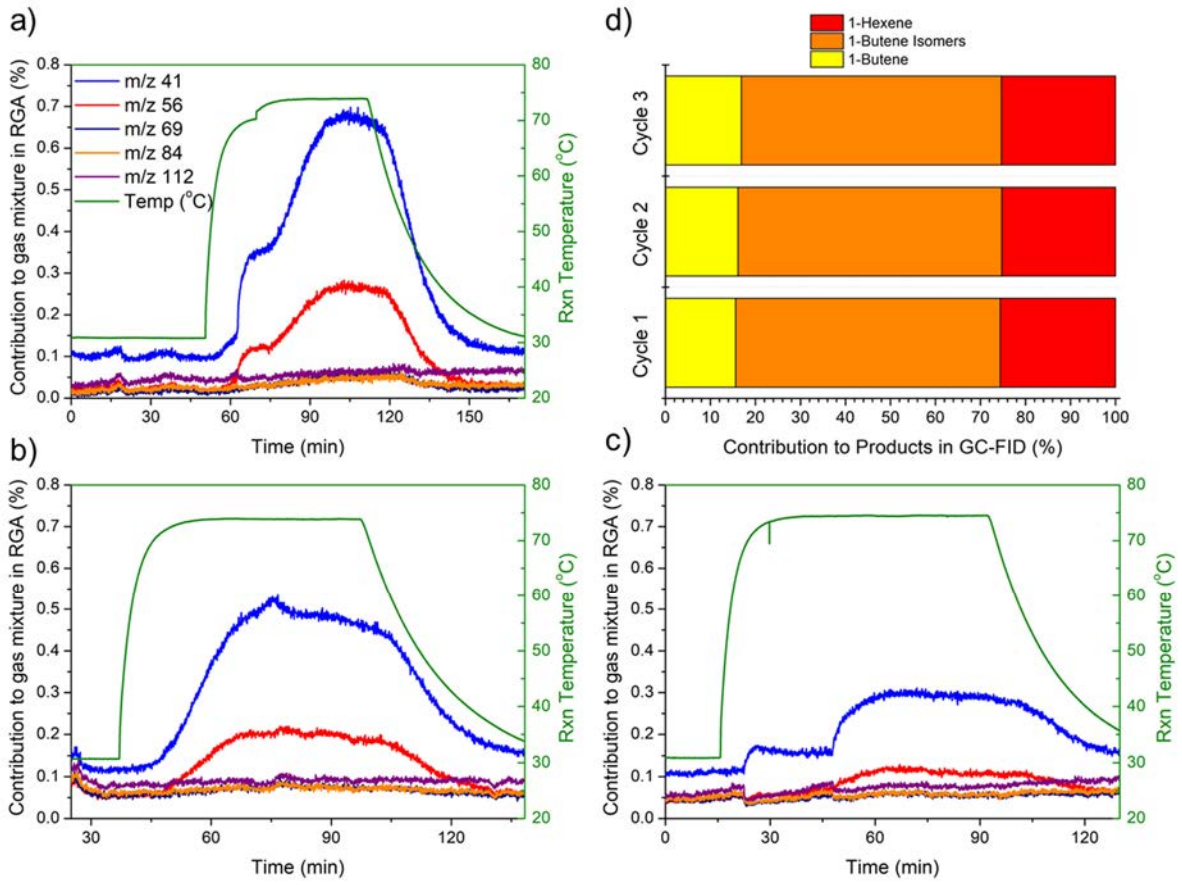

Figure **4.29**: Reaction profiles for three successive cycles of ethylene oligomerisation catalysed by **Pd·2**$_{\text{core-shell-1}}$, displayed as the contribution to the total pressure in the RGA (%) a) cycle 1, b) cycle 2, c) cycle 3, and d) GC-FID product distribution for each cycle 1 h into the reaction at 75 ºC.

The catalytic activity of **Pd·2**$_{\text{core-shell-3}}$ was followed over 3 h at 75 ºC in order to gauge whether catalysis of ethylene oligomerisation within the pores of the framework would lead to catalyst deactivation over time. As shown in Figure **4.30**, **Pd·2**$_{\text{core-shell-3}}$ remains active at peak 1-butene production for 30 minutes, decreasing only by 20 %, but over a longer time scale this activity reduces to almost background levels (that of room temperature). GC-FID analysis of the gas mixture after 1, 2 and 3 h of heating showed that the product distribution remained the same, whilst the overall production of volatile oligomers decreased as seen in the RGA (see Appendix **4.13.12**, Figure **4.A.14**). While selectivity is retained and there is an increase in catalytic longevity by moving active sites away from the surface of MOF crystals, the activity of **Pd·2**$_{\text{core-shell-3}}$ decreased over time, indicating deactivation of the catalyst still occurs. PXRD analysis of **Pd·2**$_{\text{core-shell-3}}$ post-catalysis revealed the presence of crystalline polyethylene, but via SEM very little polymer could be identified on the surfaces of the crystals (see Appendix

4.13.11, Figures **4.A.12** and **4.A.13**). Long chain polymers may not be detectable via SEM or PXRD if they form within the pores of the framework and, are not regularly ordered. To examine this, gas adsorption experiments were conducted.

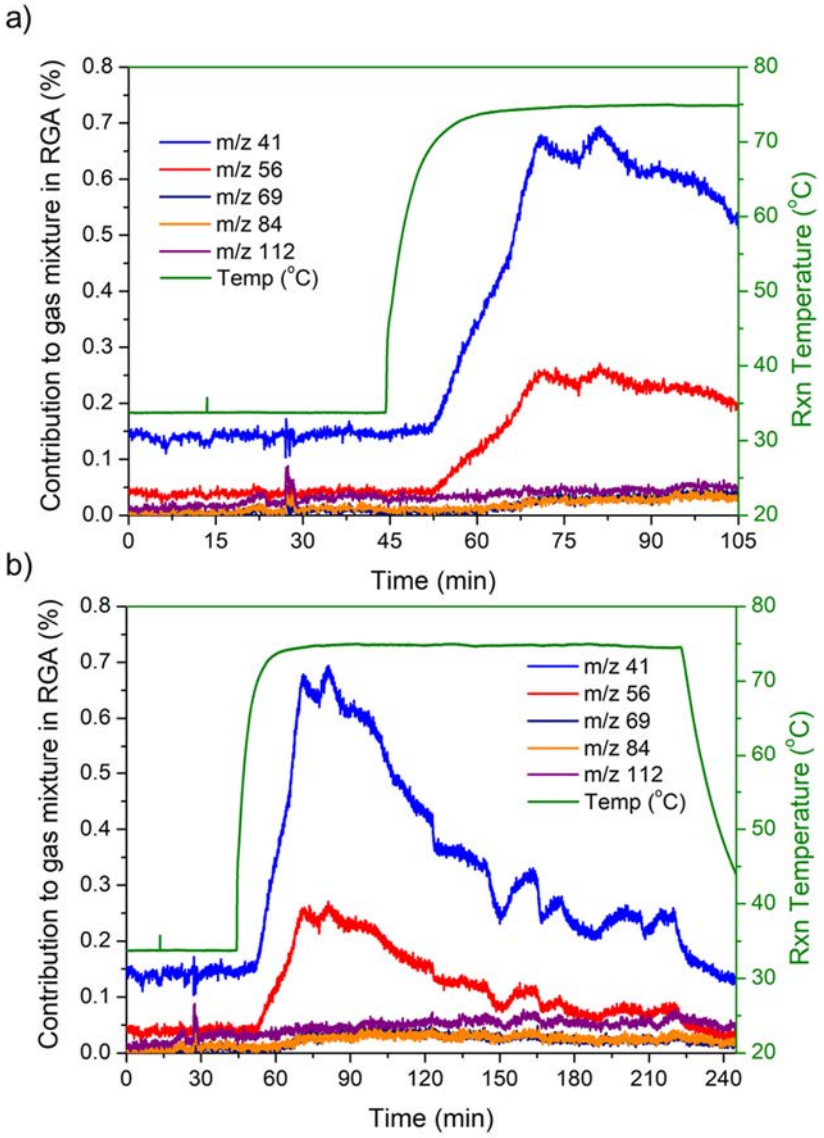

Figure **4.30**: Reaction profile of ethylene oligomerisation catalysed by **Pd·2**$_{\textbf{core-shell-3}}$, displayed as the contribution to the total pressure in the RGA (%) for a) 1 h and b) 3 h of heating at 75 °C.

Sorption analysis of **Pd·2**$_{\textbf{core}}$ and **Pd·2**$_{\textbf{core-shell-3}}$ post catalysis was performed with N_2 (77 K) and CO_2 (195 and 273 K) to ascertain whether porosity was retained despite apparent deactivation of the catalysts. Pre-catalysis both **Pd·2**$_{\textbf{core}}$ and **Pd·2**$_{\textbf{core-shell-3}}$ are porous to N_2 at 77 K and CO_2 at 195 and 273 K, as shown in Figure **4.31** and in Appendix **4.13.13** Figure **4.A.15**. **Pd·2**$_{\textbf{core}}$ and **Pd·2**$_{\textbf{core-shell-3}}$ both display Type 1 isotherms with no hysteresis with N_2 at

77 K, with maximum N_2 uptake of 693 and 625 cm^3/g respectively.[33] The BET surface areas of **Pd·2$_{core}$** and **Pd·2$_{core\text{-}shell\text{-}3}$** pre-catalysis are slightly lower than their pre-metalation counterparts; 2571 ± 3 and 2146 ± 3 m^2/g, due to metalation with Pd. Neither the core or core-shell samples retain porosity post-catalysis, with **Pd·2$_{core}$** and **Pd·2$_{core\text{-}shell\text{-}3}$** being non-porous to N_2 (77 K) and CO_2 (195 and 273 K) post-catalysis. Hence, the surface areas of the two samples, post-catalysis, could not be determined. The lack of porosity coupled with the retention of long-range structural order (via PXRD) indicates that the pores of the framework in **Pd·2$_{core}$** and **Pd·2$_{core\text{-}shell\text{-}3}$** are being blocked during catalysis. Pore blockage is therefore responsible for the deactivation of the catalysts, as previously observed.

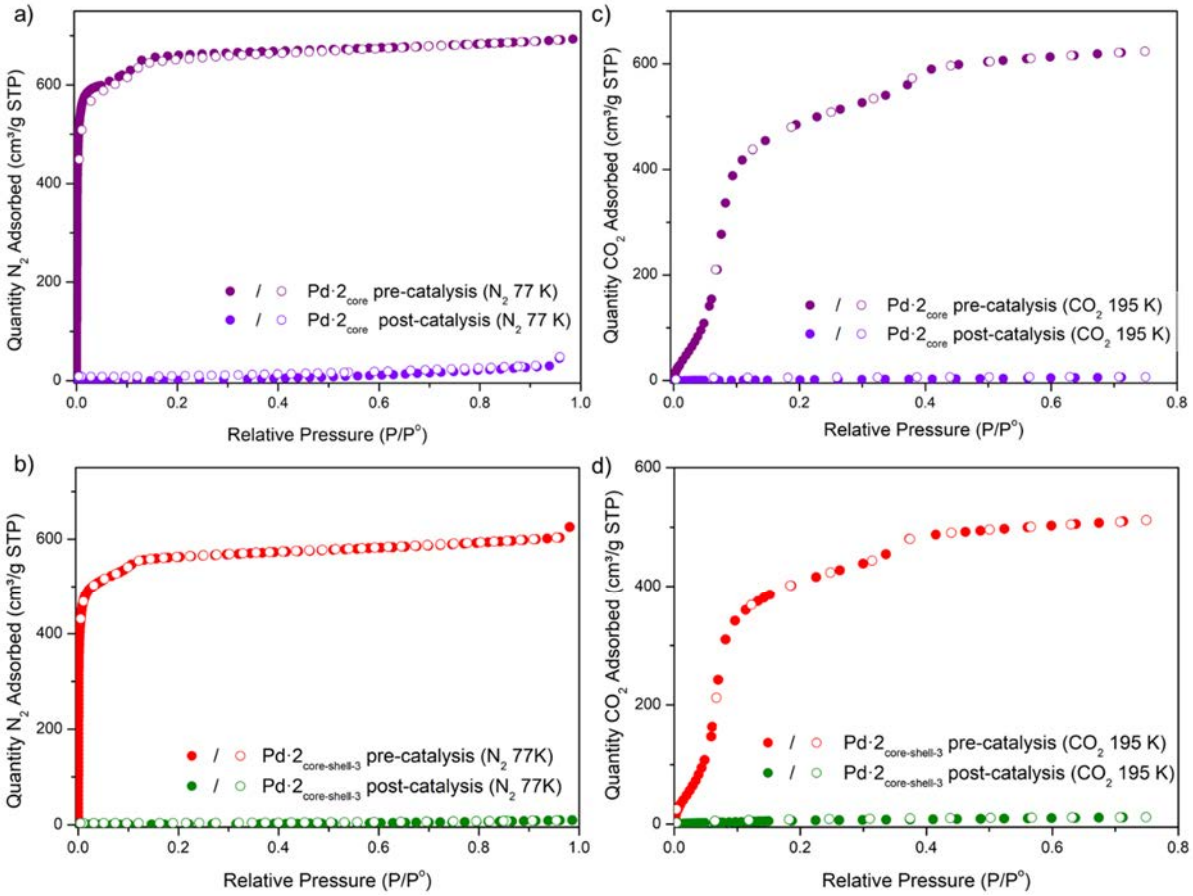

Figure **4.31**: N_2 77 K isotherms of a) **Pd·2$_{core}$** and b) **Pd·2$_{core\text{-}shell\text{-}3}$** and CO_2 195 K isotherms of c) **Pd·2$_{core}$** and d) **Pd·2$_{core\text{-}shell\text{-}3}$** both pre- and post-catalysis.

Deactivation occurred faster for **Pd·2$_{core}$** than **Pd·2$_{core\text{-}shell\text{-}3}$** and hence the location of active sites must play an important role in the formation of polyethylene and catalyst poisoning. The pore blockage with polymer must occur faster for catalysts with surface-active sites, enabling the formation of polyethylene which coats the exterior of the crystals. However, for catalysts with active sites within the crystals, the formation of the polymer is slower and so

activity is retained for a longer period of time. To test this hypothesis a flow reaction was performed with a sample which had only surface-active catalytic sites, **Pd·2** $_{\text{rev-core-shell}}$ (reverse core-shell UiO-67-bpdc⊂UiO-67-bpydc metalated with [PdMe(MeCN)]BF_4). The reaction profile for ethylene oligomerisation catalysed on the surface of **Pd·2** $_{\text{rev-core-shell}}$ is shown in Appendix **4.13.14**, Figure **4.A.16**. The drop off in activity of **Pd·2** $_{\text{rev-core-shell}}$ is similar to that of **Pd·2**$_{\text{core}}$ with a 49 % reduction in activity from max production after 30 min relative to 64 %. PXRD and SEM analysis confirmed that the deactivation observed for **Pd·2** $_{\text{rev-core-shell}}$ was due to the formation of polyethylene, with polymer visible on the surface of the crystals (see Appendix **4.13.11**, Figures **4.A.12** and **4.A.13**). For ease of comparison, deactivation data (flow conditions) is summarised in Figure **4.32**.

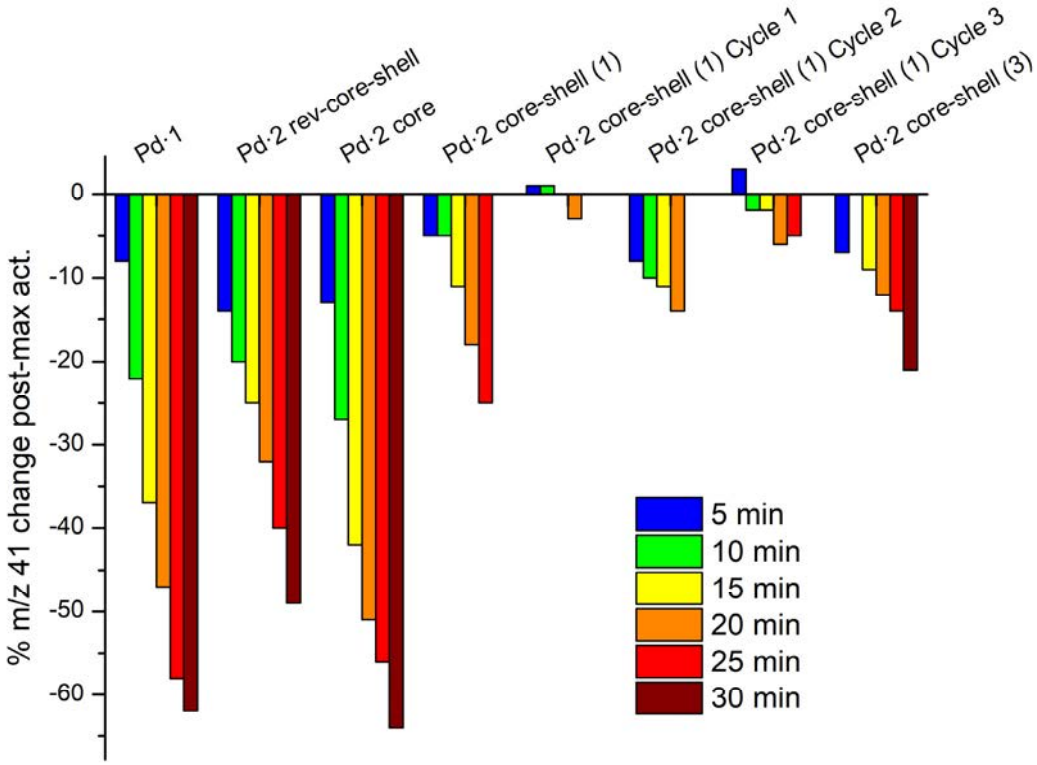

Figure **4.32**: Percent change in m/z 41 (1-butene) production for 5 – 30 min post-max activity under flow reaction conditions for **Pd·1**, **Pd·2** $_{\text{rev-core-shell}}$, **Pd·2**$_{\text{core}}$, **Pd·2**$_{\text{core-shell (1)}}$, **Pd·2** $_{\text{core-shell (1)}}$ (1-3 cycles) and, **Pd·2**$_{\text{core-shell (3)}}$.

The localisation of active catalytic sites directly impacts the rate of deactivation of the catalyst for the gas-phase oligomerisation of ethylene. Samples with external active sites (**Pd·1**, **Pd·2** $_{\text{rev-core-shell}}$ and **Pd·2**$_{\text{core}}$) demonstrate rapid deactivation, with a $\geq$ 50% reduction in 1-butene (m/z 41) production after 30 minutes. Conversely, for samples where the surface-active sites have been significantly diluted by forming a diffuse CS-MOF with an inert shell (**Pd·2**$_{\text{core-}}$

shell (1), **Pd·2 core-shell (1)** (1-3 cycles) and **Pd·2core-shell (3)**) deactivation is much less significant after 30 minutes (decreasing by less than 25 %). As shown by **Pd·2core-shell (3)**, the deactivation occurs over a prolonged period of time, returning to baseline levels after 3 h after peak activity. Hence, for the gas phase oligomerisation of ethylene by [PdMe(MeCN)]BF_4 dispersed throughout the UiO-67-bpydc framework, catalyst poisoning will occur due to the formation of polyethylene which blocks access to active sites, but the rate of catalyst poisoning can be reduced through precise control of the spatial distribution of active sites. In the gas phase there is no way to remove long chain oligomers, which coat the crystal surfaces/block the pores, from the catalyst because the reaction is only held at 75 ºC and long chain oligomers are not particularly volatile at this temperature. Conducting a similar reaction with the MOF catalyst suspended in a solvent might prolong catalyst activity further, by solubilising long chain oligomers, but there would be no easy way to follow the real-time activity profile of the reaction.

Surface passivation of catalyst with polymer coatings of polymethyl acrylate, polystyrene and polyimide was also attempted, but ultimately this was unsuccessful. The polymer coatings offered no protection from the aforementioned deactivation pathways during catalysis, i.e. polyethylene formation in the pores and at the surface of the MOF, hence this work was not discussed in detail in this chapter but is summarised in Appendix **4.13.15**.

4.10. Summary

In summary, the impact of catalyst site location of MOFs on the activity and product distribution for gas phase ethylene oligomerisation was investigated using bespoke core-shell MOF catalysts. The core-shell UiO-67-bpydc⊂UiO-67-bpdc frameworks were synthesised via crystal engineering techniques, such as coordination modulation and SALE; which enabled the synthesis of large 50 μm crystals, the removal of ligand defects and the installation of H_2bpdc primarily at the exterior of the crystal surface. The homogeneous catalyst $[PdMe(MeCN)]^+$, initially reported by Brookhart *et al*., was incorporated into the CS-MOFs as its BF_4^- salt.[57] The palladium catalyst was the first of its kind to be incorporated into a MOF which did not require an activator such as MAO or AlR_3 to catalyse the oligomerisation of ethylene. The palladium catalyst coordinated to the framework demonstrated 90% of its homogeneous counterparts' activity, under similar reaction conditions (albeit in a solid-gas phase reaction).[57] Catalysis testing revealed catalyst deactivation from the production of non-volatile long chain ethylene oligomers, with catalyst longevity being shown to be improved by diluting the number of surface active sites through the implementation of core-shell catalysts.

A limitation of CS-MOF synthesis via slow diffusion SALE was the formation of a diffuse shell rather than a well-defined core-shell boundary. Alternate techniques such as epitaxial growth of a shell could be implemented, with the steric bulk of the shell ligand defining the quality of the core-shell boundary.[16] Using an epitaxial growth strategy the synthesis of a range of CS-MOFs with a UiO-67-bpydc core and a shell of varied steric bulk could be undertaken and the impact of guest diffusion and pore confinement effects could be further probed. Additionally, the catalyst used, while active and interesting in its own right, might not be the best catalyst to investigate pore confinement effects in the framework or catalyst stability. The ideal reaction to probe this would have product distributions directly affected by access to the active site by reagents/deactivating agents; such reactions include 2-butene isomerisation and hydroformylation, as discussed in Chapter 3.[60-61]

4.11. Experimental

4.11.1. Materials and Measurements

Unless otherwise stated, all chemicals were obtained from commercial sources and used as received. MeCN was distilled over CaH_2 under N_2 and degassed with Ar prior to use. NMR spectra were recorded on a Varian 500 MHz spectrometer at 23 ºC using a 5 mm probe. MOF samples (1 – 5 mg) were digested in DCl/d_6-DMSO (2 drops of DCl/ 600 µl d_6-DMSO) at 85 °C, stirred at 500 rpm for 30 min – 1 h, or until fully dissolved, prior to NMR analysis. Powder X-ray diffraction data were collected on a Bruker Advanced D8 diffractometer (capillary stage) using Cu Kα radiation (λ = 1.54056 Å, 40 kW/ 40 mA, 2θ = 2 – 52.94°, Phi rotation = 20 rotation/min at 1 sec exposure per step, with 5001 steps using 0.5 mm glass capillaries). Scanning Electron Microscope (SEM) images were collected on a Phillips XL30 scanning electron microscope in secondary electron mode, (spot size 3 and 10 KeV). Some SEM images were collected on a Quanta450 scanning electron microscope with the same settings as the XL-30. Electron Dispersive X-ray Analysis was collected with an Oxford Instruments Ultim Max 170 EDX attachment on the Phillips XL30/Quanta 450 (spot size 4, 15 KeV). Samples for SEM analysis were dry loaded onto adhesive carbon tabs on aluminium stubs and carbon coated (5 nm) prior to analysis. Inductively coupled plasma mass spectrometry was performed on a Solution 7500CS ICPMS spectrometer at Adelaide microscopy on samples digested in 5% HNO_3 in MilliQ water at 65 ºC as outlined in Chapter 3. Infrared spectra were collected were collected on a Perkin-Elmer Spectrum 100 using a UATR sampling accessory with dry samples loaded on NaCl disks in Paratone-N oil. Raman spectra were collected using a delta-Nu

Advantage 200A Raman spectrophotometer, using a 532nm laser for excitation, ×50 objective lens, acquisition time 1 s, RTD 1, Acc 1 with the grating set at 600 gr/nm.

4.11.2. Synthetic Methods

2,2'-bipyridine-5,5'-dicarboxylic acid (H_2bpydc)

H_2bpydc was prepared according to a literature procedure with minor alterations, as outlined in the experimental section 3.8.2.[62]

UiO-67-bpydc Truncated Octahedron 50 µm crystals:

$ZrCl_4$ (63.54 mg, 0.273 mmol), bpydc (66.6 mg, 0.277 mmol) and trifluoroacetic acid (1.66 ml, 21.69 mmol, 80 equivalents) were dissolved in DMF (10 ml) in a 20 ml Teflon capped Wheaton vial and sonicated for 1 h until fully dissolved. The solution was heated in an oven for 7 days at 120 ºC. The resulting crystals on the sides of the container were collected and washed DMF (3×10 ml) and MeCN (3×10 ml) resulting in pure single crystals of UiO-67-bpydc.

UiO-67-bpydc$_{0.5}$bpdc$_{0.5}$:

UiO-67-bpydc$_{0.5}$bpdc$_{0.5}$ was synthesised as outlined in experimental section **3.8.2**.

[PdMe(COD)]Cl:

[PdMe(COD)]Cl was prepared according to literature protocol.[59, 63] In a 100 ml Schlenk tube $PdCl_2$ (0.50 g, 1.75 mmol) was dissolved in DCM (12.50 ml) and the solution was degassed with Ar for 5 minutes. $SnMe_4$ (0.29 ml, 2.10 mmol, 1.20 eq.) was added to the reaction vessel and the solution was further degassed for 5 min with Ar. The reaction was stirred at room temperature for 4-7 days in darkness until the solution lost its yellow colouration. The pale-yellow solution was filtered over Celite and the solvent was removed under reduced pressure at 0 ºC. The off-white powder was washed with diethyl-ether (1-5 ml) to remove the bi-product $SnMe_3Cl$. [PdMe(COD)]Cl was then crystallised from chloroform as an off-white powder (216 mg, 0.81 mmol, 46 %). ^{1}H NMR was consistent with previous reports.[63] ^{1}H NMR (500 MHz, $CDCl_3$) δ = 5.93 (m, 2H), 5.16 (m, 2H), 2.53 (m, 8H) and 1.20 (3H, s).

[(COD)PdMe(MeCN)]BF_4:

[(COD)PdMe(MeCN)]BF_4 was prepared according to literature protocols with small alterations, no characterisation of the intermediate was performed as this species was immediately coordinated to UiO-67-bpydc species.[57] [PdMe(COD)]Cl (18.77 mg, 70.6 µmol) was dissolved in distilled MeCN (10 ml) in a 50 ml Schlenk tube and the solution was degassed

with Ar for 5 minutes. $AgBF_4$ (27.62 mg, 141.2 μmol, 2 eq.) was added to the stirring solution and the solution was stirred for a further 2 h under an atmosphere of Ar in darkness. The solution was filtered via a canula with a cotton wool plug and filter-paper into a separate vial with positive Ar pressure, then degassed with Ar and stored under Ar at 3 ºC until the solution was used for metalation.

Metalation of UiO-67-bpydc with [(COD)PdMe(MeCN)]BF_4:

A sample of UiO-67-bpydc (10 mg, solvent exchanged from distilled MeCN, 10 ml × 3) was added to the solution of [(COD)PdMe(MeCN)]BF_4 in MeCN (10 ml, 70.6 μmol). The vial was degassed with Ar for 5 min, then sealed and stored in darkness at 3 ºC for 3 days. The solution was removed, and the off-white/yellowish MOF crystals were solvent exchanged with distilled MeCN (10 ml × 7) and stored at 3 ºC in MeCN in darkness until ready for catalytic experiments. Samples were analysed via SEM/EDX and via ICP-MS post HNO_3 digestion to analyse the Zr:Pd.

Metalation of UiO-67-bpydc with [Rh(COD)Cl]:

Samples of UiO-67-bpydc were metalated with $[Rh(COD)Cl]_2$ following protocols outlined in experimental section **3.8.2**.

Ligand Modulator Exchange (benzoic acid):

Single crystals of UiO-67-bpydc (10-30 mg dried from distilled MeCN) were dispersed in a solution of benzoic acid (8%, 0.65 M, 20 ml) in DMF in a 20 ml screw capped (Teflon cap) Wheaton vial. The solution was heated in an oven at 85 ºC overnight without agitation. The solution was cooled to room temperature and then the MOF crystals were solvent exchanged with DMF (10 ml × 5). Prior to NMR analysis samples were solvent exchanged with distilled MeCN (10 ml × 5) then dried under vacuum in a desiccator.

Ligand Modulator Exchange (phenylphosphinic acid):

Single crystals of UiO-67-bpydc (10-30 mg dried from distilled MeCN) were dispersed in a solution of phenylphosphinic acid (0.01 M, 20 ml) in DMF in a 20 ml screw capped (Teflon cap) Wheaton vial. The solution was heated in an oven at 85 ºC overnight without agitation. The solution was cooled to room temperature and then the MOF crystals were solvent exchanged with DMF (10 ml × 5). Prior to NMR analysis samples were solvent exchanged with distilled MeCN (10 ml × 5) then dried under vacuum in a desiccator.

Healing Protocol with H_2bpydc:

Modulator exchanged single crystals of UiO-67-bpydc (10-30 mg) were soaked in a solution of H_2bpydc (2.5 mM, 20 ml) in DMF in a 20 ml screw capped (Teflon cap) Wheaton vial. The solution was heated in an oven at 85 ºC overnight without agitation. The solution was cooled to room temperature and then the MOF crystals were solvent exchanged with DMF (10 ml × 5). Prior to NMR analysis samples were solvent exchanged with distilled MeCN (10 ml × 5) then dried under vacuum in a desiccator.

Slow diffusion solvent assisted linker exchange of "healed" UiO-67-bpydc with H_2bpdc:

Dry healed single crystals of UiO-67-bpydc (dried from distilled MeCN in a desiccator) were transferred to a 20 ml screw capped (Teflon cap) Wheaton vial. A room temperature solution of H_2bpdc (2.5 or 5 mM) in DMF was added to this vial (1 ml per 3.42 mg of dried MOF to achieve the desired ligand ratios of 2:1 of 4:1, H_2bpydc:H_2bpdc, in the reaction mixture). The reaction mixture was held at varied temperatures (25, 50, 80, 120 ºC) in an oven for a variety of different time scales (10 - 30 mins and 1 – 24 h) before the reaction was halted by cooling the solution on ice for 5 minutes and solvent exchanging the MOF crystals with DMF (10 ml × 5). Prior to NMR analysis samples were solvent exchanged with distilled MeCN (10 ml × 5) then dried under vacuum in a desiccator. Unless otherwise stated, ligand solutions were added to the MOF crystals at room temperature.

Polymer Coating of UiO-67-bpydc$_{0.5}$bpdc$_{0.5}$:

Polymer coating of UiO-67-bpydc$_{0.5}$bpdc$_{0.5}$ with PMA poly(methyl acrylate) and PS (polystyrene) was done by collaborators Tao Li *et. al*. following protocols outline in literature.[64] This coating was done prior to metalation with [(COD)PdMe(MeCN)]BF_4 in MeCN, the samples were prepared by Tao Li *et.al.* and resolvated with MeCN prior to metalation.

Polyimide (PI) coating of UiO-67-bpydc$_{0.5}$bpdc$_{0.5}$ was done post metalation with [(COD)PdMe(MeCN)]BF_4. A sample of metalated UiO-67-bpydc$_{0.5}$bpdc$_{0.5}$ (60 mg) was dispersed in chloroform (15 ml, dried over $MgSO_4$) containing polyimide (7.5 mg), the solution was stirred at room temperature. The MOF-polymer composite was precipitated out of solution with addition of petroleum ether (15 ml) while stirring the solution. The composite was centrifuged and washed with 1-pentane (× 5) then dried in an oven at 60 ºC. The sample was analysed via SEM and PXRD to confirm crystallinity and morphology retention.

4.11.3. Gas Adsorption Analysis

Activation Protocol:

In a typical activation procedure, crystals of UiO-67-bpydc were solvent exchanged with DMF (10 ml × 5) over a 1-day period and the distilled MeCN (10 ml × 5) over a 1-day period. The samples were then dried in a desiccator for 1 h then transferred into sorption analysis tubes. The samples were then dried under a vacuum at 150 ºC for 3 h to yield activated samples.

Gas Adsorption Measurements:

Gas adsorption isotherms were measured using volumetric methods on a micromeritics 3-Flex analyser (Micromeritics Instrument Corporation, Norcross, GA, USA) at 77, 195 and 273 K (using a cryo-cooler circulator). Brunauer-Emmett-Teller (BET) surface areas were calculated using experimental points at relative pressure of P/P_0 = 0.05-0.25. Pore size distributions were calculated from N_2 using DFT modelling software on a Micromeritics 3-Flex analyser. UHP grade (99.999 %) N_2 and (99.999 %) CO_2 was used for all measurements.

4.11.4. Catalysis Experiments

Batch Instrumentation:

Batch gas phase catalytic experiments were carried out using a custom-built high temperature and high-pressure pulse-gas sampling equipment coupled with a mass spectrometer for real-time analysis of the reaction mixture.[65] The batch reaction cell has an internal volume of 3.26 mL and is in direct contact with a copper block containing a 100 W heater cartridge controlled by a proportional-integral derivative (PID) temperature controller (CAL Controls, Cal 3300) and K-type thermocouple attached to the side of the cell. The pressure in the batch reaction cell is monitored by a piezoresistive manometer (Keller, Leo Record series, 30 bar range). The cell is connected to a pulsed nozzle (Parker, Series 9 Pulse Valve) which is used to pulse controlled amounts of gas from the reaction cell via a 1/16" stainless steel tube into the vacuum system, comprised of a residual gas analyser (RGA) for sampling of the gas mixture (vide infra). The pulsed nozzle is driven by a custom-built pulsed nozzle driver connected to the acquisition computer and controlled by LabVIEW software. Typical pulse rates range from 0.3 to 20 Hz with a pulse width of 29 to 34 ms and is controlled in real-time via a PID software controller in the LabVIEW code. This controller allows precise regulation of the amount of gas being delivered, while maintaining a constant pressure level in the vacuum system (typically 2.00×10−6 Torr) to allow for reliable operation of the RGA at

calibrated pressures. The gas phase reaction mixture can also be analysed using a gas chromatograph (SRI-8610C MG#3 model) which is directly connected to the reaction cell.

Flow Instrumentation:

Flow gas phase catalytic experiments were carried out using a custom-built flow reactor coupled to a mass spectrometer for real-time analysis of the reaction mixture. The flow reactor is a brass 1/4" tube fitting with two male connectors at either end, capped with a 1/4" stainless steel VCR silver plated snubber gasket with a 0.5 μm mesh. Inside the flow reactor the sample is suspended between packed glass wool. The temperature of the flow reactor was controlled by a PID temperature controller (CAL Controls, Cal 3300) and K-type thermocouple attached to the side of the cell. As shown in in Figure **4.20**, the flow reactor is connected to two mass flow controllers (Anri Instruments and Control Ltd, FG-201CV-AAD-88-V-DA-A1V) by 1/8" stainless steel tube. The mass flow controllers are controlled by setting the pressure in/outlet for ethylene and argon gasses using the FlowTune V2.08 program (Bronkhorst), the outlet pressures were set at 6 bar and inlet pressures set at 7 and 10 bar for argon and ethylene respectively. The flow rate of gasses was controlled using the FlowView V.123 software with flow rates set between 0 and 75 ml/min. The pressure of the flow system was set via a N_2 pressurised back pressure regulator set at 6 bar, which was directly connected to the exhaust via the GC-FID. The flow reactor is also connected to the RGA via a silica capillary (100 μm × 363 μm fused silica tubing, SGE Analytical Science), held at 120 ºC, which reduces the pressure to < 1 mbar. The reaction mixture is pulled through the silica capillary by a rotary pump, with a portion of the gas mixture being siphoned off via a needle valve to regulate the amount of gas being delivered to the RGA vacuum system (typically 2.00×10^{-6} Torr) to allow for reliable operation of the RGA.

RGA:

Gas mixtures are analysed by an RGA (Stanford Research Systems, RGA200) which is housed in a vacuum chamber with an electron multiplier, controlled via Stanford Research Systems RGA software for data collection. Pressure is measured by a Bayard-Alpert ionisation gauge with a tungsten filament (Duniway, T-CFF-275) monitored via a combined ion and thermocouple controller (Agilent Technologies, XGS-600). The system is pumped via an oil-free turbo-pump (Agilent TwisTorr 84FS) backed by a rotary vane pump (Edwards, E2M8) with an oil trap (Duniway IFT-NW25-4).

The m/z 41 peak used to quantify the production of 1-butene was calibrated using a CO_2/1-butene mixture of 1.68 bar 1-butene and 1.94 bar CO_2 with a total pressure of 3.63 bar in the reaction cell. Note this calibration is only valid for batch reaction analysis.

Gas Chromatography:

Gas chromatography analyses were carried out with an SRI-8610C (MG#3) instrument with FID detector with methaniser. The first chromatographic column was a S.S. molecular sieve 13X packed column (6' length, 1/8" O.D.) followed by a S.S. Haye Sep D packed column (6' length, 1/8" O.D.) with argon as the carrier gas. Initial oven temperature was 50 °C held for 5 minutes, followed by a ramp at 20 °C/min to 150 °C and held for 15 minutes, the temperature was then ramped at 10 °C/min to 250 °C and held for a further 10 minutes. Injection port temperature was 60 °C, and methaniser was 300 °C. Pressure of was initially held at 3 PSI for 0.03 min, increased to 20 PSI and held for 2 min, then further increased to 40 PSI and held for 3.8 min and subsequently decreased to 0 PSI and held for 42 min.

Experimental details (Batch reactor):

Pd·1 (UiO-67-bpydc$_{0.5}$bpdc$_{0.5}$·[PdMe(MeCN)]$^{+}$BF$_4^{-}$, 12.5 mg, 10.3 μmol Pd) was loaded into a stainless-steel sample holder capped by a VCR gasket with a 0.5 μm filter and placed in the batch reactor cell. After sealing the reaction cell, the sample was evacuated for 1 h under high vacuum, then the sample was activated by heating to 50 °C under high vacuum for 24 h. Once the reaction cell cooled to room temperature (25 °C) ethylene was introduced into the reaction cell (16.7 bar). The reaction was continuously monitored immediately after the ethylene was introduced by pulsing a small amount of gas (2.00×10−6 Torr) into the vacuum chamber. The reaction was left at room temperature for 0.5 h, then heated at 75 °C for 1 h. The reaction was then stopped, and the gaseous reaction mixture was analysed via gas chromatography.

Experimental details (Flow reactor):

Dried palladium metalated samples of UiO-67-bpydc (see below for masses and Pd loadings) were suspended between two pieces of glass wool in the flow reactor cell. The cell was attached to the flow rig set up, capped by two silver plated VCR gaskets with 0.5 μm filters on either end. After sealing the cell, Ar was flowed over the sample (50 ml/min at 6 bar) at 50 ºC for 1 h. The reactor was cooled to 30 ºC and ethylene was introduced into the reactor (50 ml/min at 6 bar). The reaction was continuously monitored after ethylene introduction with the pressure to the vacuum chamber controlled by a needle valve to maintain a constant pressure

for the RGA (2.00×10−6 Torr). The reaction was left at 30 ºC for 1 h, then the cell was heated to 75 ºC for between 1-3 h then cooled to 30 ºC. The gas mixture was analysed at 1 h intervals via gas chromatography after introduction of ethylene to the reactor for the duration of the reaction.

Cycling experiments followed the experimental procedure as described above, but after 1 h of heating the sample was exposed to Ar (50 ml/min at 6 bar) for 1 h at 30 ºC and then left under high vacuum overnight before the next cycle.

Palladium Content in Catalysts:

Table **4.11.1:** Summary of Pd content in catalysts used for batch and flow reactions.

Sample	Reactor Used	Pd : Zr ([a]SEM/EDX, [b]ICP-MS, %)	Sample Mass (mg)	Pd catalyst in sample (µmol)
Pd·1	Batch	41.7 ± 0.9 [a]	12.5	10.3
Pd·1	Flow	41.7 ± 0.9 [a]	63.9	52.5
Pd·1$_{PMA}$	Flow	65.8 ± 7.9 [a]	16.5	20.9
Pd·1$_{PS}$	Flow	3.1 ± 1.3 [a]	19.2	0.2
Pd·1$_{PI}$	Flow	35.5 ± 0.7 [a]	31.4	25.2
Pd·2$_{core}$	Flow	11.4 ± 0.0 [b]	27.6	8.2
Pd·2$_{core\text{-}shell\ (1)}$	Flow	7.0 ± 0.1 [b]	30.7	5.8
Pd·2$_{core\text{-}shell\ (3)}$	Flow	9.2 ± 0.1 [b]	40.1	9.8
Pd·2$_{core\text{-}shell\text{-}rev}$	Flow	3.1 ± 0.0 [b]	26.7	2.2

4.12. References

1. Gascon, J.; Corma, A.; Kapteijn, F.; Llabrés i Xamena, F. X., Metal Organic Framework Catalysis:Quo vadis? *ACS Catalysis* **2014,** *4* (2), 361-378.

2. Dhakshinamoorthy, A.; Li, Z.; Garcia, H., Catalysis and Photocatalysis by Metal Organic Frameworks. *Chem Soc Rev* **2018,** *47* (22), 8134-8172.

3. Huang, Y. B.; Liang, J.; Wang, X. S.; Cao, R., Multifunctional Metal-Organic Framework Catalysts: Synergistic Catalysis and Tandem Reactions. *Chem Soc Rev* **2017,** *46* (1), 126-157.

4. Ranocchiari, M.; van Bokhoven, J. A., Catalysis by Metal-Organic Frameworks: Fundamentals and Opportunities. *Phys Chem Chem Phys* **2011,** *13* (14), 6388-96.

5. Linder-Patton, O. M.; de Prinse, T. J.; Furukawa, S.; Bell, S. G.; Sumida, K.; Doonan, C. J.; Sumby, C. J., Influence of Nanoscale Structuralisation on the Catalytic Performance of ZIF-8: a Cautionary Surface Catalysis Study. *CrystEngComm* **2018,** *20* (34), 4926-4934.

6. Liu, Y.; Gao, P.; Huang, C.; Li, Y., Shape- and Size-Dependent Catalysis Activities of Iron-Terephthalic Acid Metal-Organic Frameworks. *Sci China Chem* **2015,** *58* (10), 1553-1560.

7. García-García, P.; Müller, M.; Corma, A., MOF Catalysis in Relation to their Homogeneous Counterparts and Conventional Solid Catalysts. *Chem Sci* **2014,** *5* (8), 2979.

8. Gu, J. M.; Kim, W. S.; Huh, S., Size-dependent Catalysis by DABCO-Functionalized Zn-MOF with One-Dimensional Channels. *Dalton Trans* **2011,** *40* (41), 10826-9.

9. Zhang, R.-Z.; Huang, Y.-q.; Zhang, W.; Yang, J.-M., Effect of Particle Size Distribution of UiO-67 Nano/Microcrystals on the Adsorption of Organic Dyes from Aqueous Solution. *CrystEngComm* **2018,** *20* (38), 5672-5676.

10. Chizallet, C. l.; Lazare, S.; Bazer-Bachi, D.; Bonnier, F.; Lecocq, V.; Soyer, E.; Quoineaud, A.-A.; Bats, N., Catalysis of Transesterification by a Nonfunctionalized Metal-Organic Framework: Acido-Basicity at the External Surface of ZIF-8 Probed by FTIR and ab Initio Calculations. *J Am Chem Soc* **2010,** *132*, 12365-12377.

11. Saha, D.; Sen, R.; Maity, T.; Koner, S., Anchoring of Palladium onto Surface of Porous Metal–Organic Framework through Post-Synthesis Modification and Studies on Suzuki and Stille Coupling Reactions under Heterogeneous Condition. *Langmuir* **2013,** *29* (9), 3140-3151.

12. Shi, D.; He, C.; Qi, B.; Chen, C.; Niu, J.; Duan, C., Merging of the Photocatalysis and Copper Catalysis in Metal–Organic Frameworks for Oxidative C–C Bond Formation. *Chem. Sci.* **2015,** *6* (2), 1035-1042.

13. Pascanu, V.; González Miera, G.; Inge, A. K.; Martín-Matute, B., Metal–Organic Frameworks as Catalysts for Organic Synthesis: A Critical Perspective. *J Am Chem Soc* **2019,** *141* (18), 7223-7234.

14. Koh, K.; Wong-Foy, A. G.; Matzger, A. J., MOF@MOF: Microporous Core-Shell Architectures. *Chem Commun* **2009,** (41), 6162-4.

15. Li, T.; Sullivan, J. E.; Rosi, N. L., Design and preparation of a core-shell metal-organic framework for selective CO2 capture. *J Am Chem Soc* **2013,** *135* (27), 9984-7.

16. Luo, T.-Y.; Liu, C.; Gan, X. Y.; Muldoon, P. F.; Diemler, N. A.; Millstone, J. E.; Rosi, N. L., Multivariate Stratified Metal-Organic Frameworks: Diversification Using Domain Building Blocks. *J Am Chem Soc* **2019,** *141* (5), 2161-2168.

17. Song, Z.; Qiu, F.; Zaia, E. W.; Wang, Z.; Kunz, M.; Guo, J.; Brady, M.; Mi, B.; Urban, J. J., Dual-Channel, Molecular-Sieving Core/Shell ZIF@MOF Architectures as Engineered Fillers in Hybrid Membranes for Highly Selective CO2 Separation. *Nano Lett* **2017,** *17* (11), 6752-6758.

18. Zhuang, J.; Chou, L. Y.; Sneed, B. T.; Cao, Y.; Hu, P.; Feng, L.; Tsung, C. K., Surfactant-Mediated Conformal Overgrowth of Core-Shell Metal-Organic Framework Materials with Mismatched Topologies. *Small* **2015,** *11* (41), 5551-5.

19. Yang, X.; Yuan, S.; Zou, L.; Drake, H.; Zhang, Y.; Qin, J.; Alsalme, A.; Zhou, H.-C., One-Step Synthesis of Hybrid Core–Shell Metal–Organic Frameworks. *Angew Chem Int Ed* **2018,** *57* (15), 3927-3932.

20. Liu, C.; Zeng, C.; Luo, T.-Y.; Merg, A. D.; Jin, R.; Rosi, N. L., Establishing Porosity Gradients within Metal–Organic Frameworks Using Partial Postsynthetic Ligand Exchange. *J Am Chem Soc* **2016,** *138* (37), 12045-12048.

21. Karagiaridi, O.; Bury, W.; Mondloch, J. E.; Hupp, J. T.; Farha, O. K., Solvent-Assisted Linker Exchange: an Alternative to the de Novo Synthesis of Unattainable Metal-Organic Frameworks. *Angew Chem Int Ed Engl* **2014,** *53* (18), 4530-40.

22. Boissonnault, J. A.; Wong-Foy, A. G.; Matzger, A. J., Core-Shell Structures Arise Naturally During Ligand Exchange in Metal-Organic Frameworks. *J Am Chem Soc* **2017,** *139* (42), 14841-14844.

23. Katz, M. J.; Brown, Z. J.; Colon, Y. J.; Siu, P. W.; Scheidt, K. A.; Snurr, R. Q.; Hupp, J. T.; Farha, O. K., A Facile Synthesis of UiO-66, UiO-67 and their Derivatives. *Chem Commun* **2013,** *49* (82), 9449-51.

24. Fei, H.; Cohen, S. M., A Robust, Catalytic Metal-Organic Framework with Open 2,2'-Bipyridine Sites. *Chem Commun* **2014,** *50* (37), 4810-2.

25. Braglia, L.; Borfecchia, E.; Maddalena, L.; Øien, S.; Lomachenko, K. A.; Bugaev, A. L.; Bordiga, S.; Soldatov, A. V.; Lillerud, K. P.; Lamberti, C., Exploring Structure and Reactivity of Cu Sites in Functionalized UiO-67 MOFs. *Catal Today* **2017,** *283*, 89-103.

26. Øien, S.; Agostini, G.; Svelle, S.; Borfecchia, E.; Lomachenko, K. A.; Mino, L.; Gallo, E.; Bordiga, S.; Olsbye, U.; Lillerud, K. P.; Lamberti, C., Probing Reactive Platinum Sites in UiO-67 Zirconium Metal–Organic Frameworks. *Chem Mater* **2015,** *27* (3), 1042-1056.

27. Feng, L.; Yuan, S.; Li, J.-L.; Wang, K.-Y.; Day, G. S.; Zhang, P.; Wang, Y.; Zhou, H.-C., Uncovering Two Principles of Multivariate Hierarchical Metal–Organic Framework Synthesis via Retrosynthetic Design. *ACS Cent Sci* **2018,** *4* (12), 1719-1726.

28. Hobday, C. L.; Marshall, R. J.; Murphie, C. F.; Sotelo, J.; Richards, T.; Allan, D. R.; Düren, T.; Coudert, F.-X.; Forgan, R. S.; Morrison, C. A.; Moggach, S. A.; Bennett, T. D., A Computational and Experimental Approach Linking Disorder, High-Pressure Behavior, and Mechanical Properties in UiO Frameworks. *Angew Chem Int Ed Engl* **2016,** *55* (7), 2401-2405.

29. Xia, Y.; Xia, X.; Peng, H.-C., Shape-Controlled Synthesis of Colloidal Metal Nanocrystals: Thermodynamic versus Kinetic Products. *J Am Chem Soc* **2015,** *137* (25), 7947-7966.

30. Gutov, O. V.; Gonzalez Hevia, M.; Escudero-Adan, E. C.; Shafir, A., Metal-Organic Framework (MOF) Defects under Control: Insights into the Missing Linker Sites and Their Implication in the Reactivity of Zirconium-Based Frameworks. *Inorg Chem* **2015,** *54* (17), 8396-400.

31. Fang, Z.; Bueken, B.; De Vos, D. E.; Fischer, R. A., Defect-Engineered Metal-Organic Frameworks. *Angew Chem Int Ed Engl* **2015,** *54* (25), 7234-54.

32. Linstrom, P. J.; Mallard, W. G., *NIST Chemistry WebBook*. National Institute of Standards and Technology: Gaithersburg MD, Vol. 20899.

33. Zhang, Y.; Xiao, H.; Zhou, X.; Wang, X.; Li, Z., Selective Adsorption Performances of UiO-67 for Separation of Light Hydrocarbons C1, C2, and C3. *Ind Eng Chem Res* **2017,** *56* (30), 8689-8696.

34. Etxeberria-Benavides, M.; David, O.; Johnson, T.; Łozińska, M. M.; Orsi, A.; Wright, P. A.; Mastel, S.; Hillenbrand, R.; Kapteijn, F.; Gascon, J., High Performance Mixed Matrix Membranes (MMMs) Composed of ZIF-94 Filler and 6FDA-DAM Polymer. *J Membr Sci* **2018,** *550*, 198-207.

35. Kirchon, A.; Feng, L.; Drake, H. F.; Joseph, E. A.; Zhou, H.-C., From Fundamentals to Applications: a Toolbox for Robust and Multifunctional MOF Materials. *Chem Soc Rev* **2018,** *47* (23), 8611-8638.

36. Li, T.; Kozlowski, M. T.; Doud, E. A.; Blakely, M. N.; Rosi, N. L., Stepwise Ligand Exchange for the Preparation of a Family of Mesoporous MOFs. *J Am Chem Soc* **2013,** *135* (32), 11688-11691.

37. Evans, J. D.; Sumby, C. J.; Doonan, C. J., Post-Synthetic Metalation of Metal–Organic Frameworks. *Chem Soc Rev* **2014,** *43* (16), 5933-5951.

38. Cohen, S. M., Postsynthetic Methods for the Functionalization of Metal–Organic Frameworks. *Chem Rev* **2012,** *112* (2), 970-1000.

39. Forestière, A.; Olivier-Bourbigou, H.; Saussine, L., Oligomerization of Monoolefins by Homogeneous Catalysts. *Oil Gas Sci Technol* **2009,** *64* (6), 649-667.

40. Belov, G. P.; Matkovsky, P. E., Processes for the Production of Higher Linear α-olefins. *Pet Chem* **2010,** *50* (4), 283-289.

41. van Leeuwen, P. W. N. M.; Clément, N. D.; Tschan, M. J. L., New Processes for the Selective Production of 1-Octene. *Coord Chem Rev* **2011,** *255* (13), 1499-1517.

42. Finiels, A.; Fajula, F.; Hulea, V., Nickel-Based Solid Catalysts for Ethylene Oligomerization – A Review. *Cat Sci* **2014,** *4* (8), 2412-2426.

43. Raspolli Galletti, A. M.; Geri, G.; Sbrana, G.; Marchionna, M.; Ferrarini, P., Striking Different Behavior in the Activation of α-olefins by Homogeneous and Heterogenized Catalysts Based on η5-Cyclopentadienyl Nickel Derivatives. *J Mol Catal A: Chem* **1996,** *111* (3), 273-280.

44. Braca, G.; Raspolli Galletti, A. M.; Di Girolamo, M.; Sbrana, G.; Silla, R.; Ferrarini, P., Organometallic Nickel Catalysts Anchored on Polymeric Matrices in the Oligomerization and/or Polymerization Of Olefins. Part II. Effect and Role of the Components of the Catalytic System. *J Mol Catal A: Chem* **1995,** *96* (3), 203-213.

45. McGuinness, D. S., Olefin Oligomerization via Metallacycles: Dimerization, Trimerization, Tetramerization, and Beyond. *Chem Rev* **2011,** *111* (3), 2321-41.

46. Skupinska, J., Oligomerization of α-olefins to Higher Oligomers. *Chem Rev* **1991,** *91* (4), 613-648.

47. van Leeuwen, P. W. N. M.; Roobeek, K. F., The Cossee Mechanism: Migratory Insertion Reactions in Palladium Phosphine-Phosphinite Complexes. *Recl Trav Chim Pays-Bas* **1995,** *114* (2), 73-75.

48. Chappell, S. D.; Cole-Hamilton, D. J., The Preparation and Properties of Metallacyclic Compounds of the Transition Elements. *Polyhedron* **1982,** *1* (11), 739-777.

49. Yasuda, H.; Nakamura, A., Diene, Alkyne, Alkene, and Alkyl Complexes of Early Transition Metals: Structures and Synthetic Applications in Organic and Polymer Chemistry. *Angew Chem Int Ed Engl* **1987,** *26* (8), 723-742.

50. Kurokawa, H.; Miura, K.; Yamamoto, K.; Sakuragi, T.; Sugiyama, T.; Ohshima, M.-a.; Miura, H., Oligomerization of Ethylene to Produce Linear α-Olefins Using Heterogeneous Catalyst Prepared by Immobilization of α-Diiminenickel(II) Complex into Fluorotetrasilicic Mica Interlayer. *Catalysts* **2013,** *3* (1), 125-136.

51. Speiser, F.; Braunstein, P.; Saussine, L., Catalytic Ethylene Dimerization and Oligomerization: Recent Developments with Nickel Complexes Containing P,N-Chelating Ligands. *Acc Chem Res* **2005,** *38* (10), 784-793.

52. Liu, Y., Catalytic Ethylene Oligomerization over Ni/Al-HMS: A Key Step in Conversion of Bio-Ethanol to Higher Olefins. *Catalysts* **2018,** *8* (11), 537.

53. Gonzalez, M.; Oktawiec, J.; Long, J. R., Ethylene Oligomerization in Metal–Organic Frameworks Bearing Nickel(II) 2,2′-Bipyridine Complexes. *Faraday Discuss* **2017**.

54. Canivet, J.; Aguado, S.; Schuurman, Y.; Farrusseng, D., MOF-Supported Selective Ethylene Dimerization Single-Site Catalysts through One-Pot Postsynthetic Modification. *J Am Chem Soc* **2013,** *135* (11), 4195-8.

55. Madrahimov, S. T.; Gallagher, J. R.; Zhang, G.; Meinhart, Z.; Garibay, S. J.; Delferro, M.; Miller, J. T.; Farha, O. K.; Hupp, J. T.; Nguyen, S. T., Gas-Phase Dimerization of Ethylene under Mild Conditions Catalyzed by MOF Materials Containing (bpy)NiIIComplexes. *ACS Catalysis* **2015,** *5* (11), 6713-6718.

56. Metzger, E. D.; Brozek, C. K.; Comito, R. J.; Dinca, M., Selective Dimerization of Ethylene to 1-Butene with a Porous Catalyst. *ACS Cent Sci* **2016,** *2* (3), 148-53.

57. Bézier, D.; Daugulis, O.; Brookhart, M., Oligomerization of Ethylene Using a Diphosphine Palladium Catalyst. *Organometallics* **2017,** *36* (2), 443-447.

58. Agirrezabal-Telleria, I.; Luz, I.; Ortuño, M. A.; Oregui-Bengoechea, M.; Gandarias, I.; López, N.; Lail, M. A.; Soukri, M., Gas Reactions under Intrapore Condensation Regime within Tailored Metal–Organic Framework Catalysts. *Nat Commun* **2019,** *10* (1), 2076.

59. Rulke, R. E.; Ernsting, J. M.; Spek, A. L.; Elsevier, C. J.; van Leeuwen, P. W. N. M.; Vrieze, K., NMR Study on the coordination behavior of Dissymmetric Terdentate Trinitrogen Ligands on Methylpalladium(II) Compounds. *Inorg Chem* **1993,** *32* (25), 5769-5778.

60. Boronat, M.; Viruela, P.; Corma, A., Theoretical Study of the Mechanism of Zeolite-Catalyzed Isomerization Reactions of Linear Butenes. *J Phys Chem A* **1998,** *102* (6), 982-989.

61. Torres, G. M.; Frauenlob, R.; Franke, R.; Börner, A., Production of Alcohols via Hydroformylation. *Catal Sci* **2015,** *5* (1), 34-54.

62. Li, X.; Van Zeeland, R.; Maligal-Ganesh, R. V.; Pei, Y.; Power, G.; Stanley, L.; Huang, W., Impact of Linker Engineering on the Catalytic Activity of Metal–Organic Frameworks Containing Pd(II)–Bipyridine Complexes. *ACS Catalysis* **2016,** *6* (9), 6324-6328.

63. Rudler-Chauvin, M.; Rudler, H., Chimie Organometallique: VII. Nouvelle Methode de Preparation de $CODPdMe_2$. *J Organomet Chem* **1977,** *134* (1), 115-119.

64. He, S.; Wang, H.; Zhang, C.; Zhang, S.; Yu, Y.; Lee, Y.; Li, T., A Generalizable Method for the Construction of MOF@Polymer Functional Composites through Surface-Initiated Atom Transfer Radical Polymerization. *Chem Sci* **2019,** *10* (6), 1816-1822.

65. Alvino, J. F.; Bennett, T.; Kler, R.; Hudson, R. J.; Aupoil, J.; Nann, T.; Golovko, V. B.; Andersson, G. G.; Metha, G. F., Apparatus for the Investigation of High-Temperature, High-Pressure Gas-Phase Heterogeneous Catalytic and Photo-Catalytic Materials. *Rev Sci Instrum* **2017,** *88* (5), 054101.

4.13. Appendix

4.13.1. Calculations for the defect analysis of displayed in Table 4.1

The number of ligand (H_2bpydc) and acid (BA or PPA) molecules and hence the percentage ligand defects per Zr-oxo node were calculated as follows from the ^{1}H NMR spectra of digested samples. The normalised integration ($I_{norm\,(x)}$) for the acid and ligand was calculated by integrating all of the peaks corresponding to the ligand and the acid and dividing them by the total number of protons for each molecule respectively, ($I_{norm\,(acid)} = \frac{I_{total\,(acid)}}{Number\ of\ protons}$). The ratio between the normalised integration of the acid and the ligand was then determined (R, where $R = I_{norm\,(acid)}:I_{norm\,(ligand)}$). The number of acid molecules (X) per Zr-oxo node can then be calculated using this ratio (given by $X = \frac{6R}{(1+0.5R)}$). Consequently, the number of ligand molecules per Zr-oxo node can be calculated (given by $6\text{-}0.5R$). The calculations satisfy the general equation for the empirical formula of UiO-67 which is given by $Zr_6O_4(OH)_4L_{(6+0.5X)}A_x$ where L and A correspond to the ligand and acid modulator, respectively. The percentage defects per Zr-oxo node could then be calculated by dividing the number of ligand molecules (L) by the number of Zr atoms (6) per Zr-oxo node, subtracting this value from 1 and multiplying by 100. The calculated values for the acid to ligand, the number of acid molecules and the ligand molecules in the formula, the ligand to Zr ratio and the % ligand defects per Zr-oxo node are displayed in Table **4.1**.

4.13.2. Initial screening of CS-MOF synthesis conditions

Initial slow diffusion SALE conditions were screened with non-healed core crystals by varying the time, temperature, solvent, and concentration of the shell ligand. These initial tests were conducted with non-healed core crystals with a H_2bpdc solution (5 mM in DMF, 1 ml per 3.42 mg of MOF) held at 25, 50 and 85 °C for 1, 4 and 24 h time periods, (refer to experimental section 4.11.2 for more detailed set up). There is 9.5 μmol of H_2bpydc in 3.42 mg of UiO-67-bpydc and in 1 ml of a 5 mM solution of H_2bpdc in DMF there is 4.75 μmol H_2bpdc, meaning that between ratio of H_2bpydc (in the MOF) to H_2bpdc (in the solution) is 66.6%. SEM/EDX analysis of these initial tests revealed that the Rh:Zr was tended to 66% for all samples after 24 h of exchange, (see Figure **4.A.1**). The more energy given to the sample solution the faster the Rh:Zr tended towards an equilibrium of 66.6% within a margin of error (mass of MOF sample used and error in EDX analysis). Since the H_2bpydc:H_2bpdc (overall) is equal to the Rh:Zr it can be concluded that the conditions used for slow diffusion SALE have resulted in **homogeneous** SALE over time. These results indicate that SALE will occur even at room temperature and that small timescale exposure to the solution will likely limit diffusion and the possibility of statistical rearrangement of component ligands. DMF is a good solvent for H_2bpydc, which might be why homogeneous SALE was favoured even at room temperature.

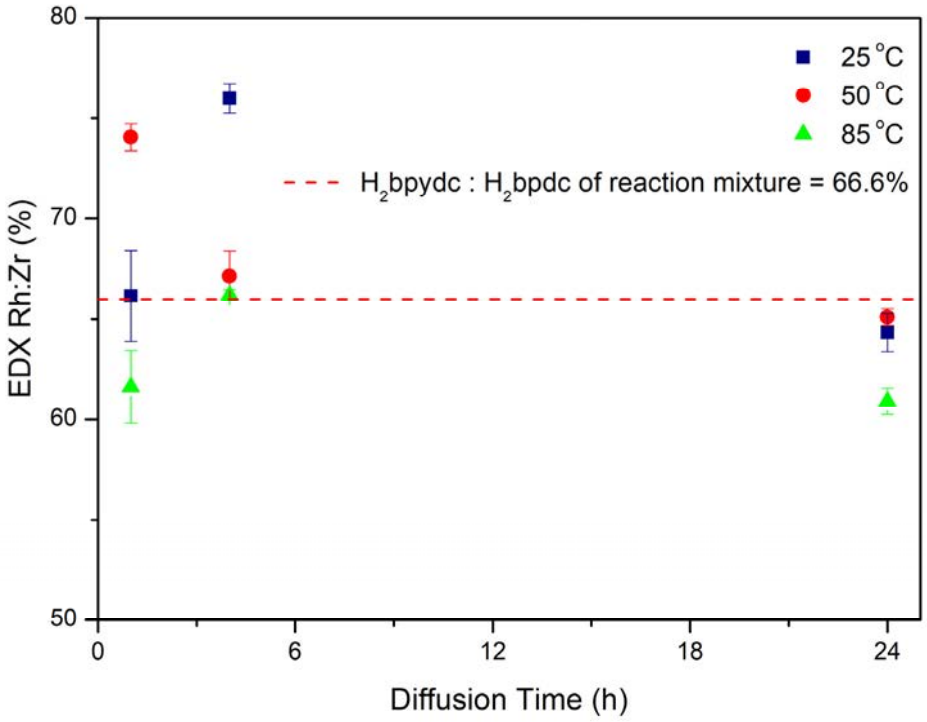

Figure **4.A.1**: Time and temperature impact on slow diffusion SALE experiments with DMF in UiO-67, following the Rh:Zr via SEM/EDX of solvent exchanged and dried samples at 1, 4 and 24 h timepoints for solutions heated at 25, 50 and 85 °C. The dotted red line indicates the overall ratio of H_2bpydc:H_2bpdc for the H_2bpydc in initially in the MOF framework and H_2bpdc in the solvent mixture = 66.6%.

In order to investigate the impact of solvent on slow diffusion SALE as well as ligand concentration other solvents and lower ligand concentrations were used (because the H_2bpdc is relatively insoluble in most solvents besides DMF). Solvents with a poorer solubility for H_2bpdc were tested at a shorter time scale (0.5 h), lower ligand concentration (2.5 mM H_2bpdc) and at room temperature to further favour slow diffusion of H_2bpdc into the framework, (see Figure **4.A.2**). After 0.5 h for all solvent systems used the Rh:Zr approximately matches the H_2bpydc:H_2bpdc (overall) which is 0.8 or 80 % (represented as the red dotted line on Figure **4.A.2**). These results indicate that even under favourable conditions for slow diffusion SALE, H_2bpdc is diffuses into the MOF and exchanges homogeneously throughout the framework.

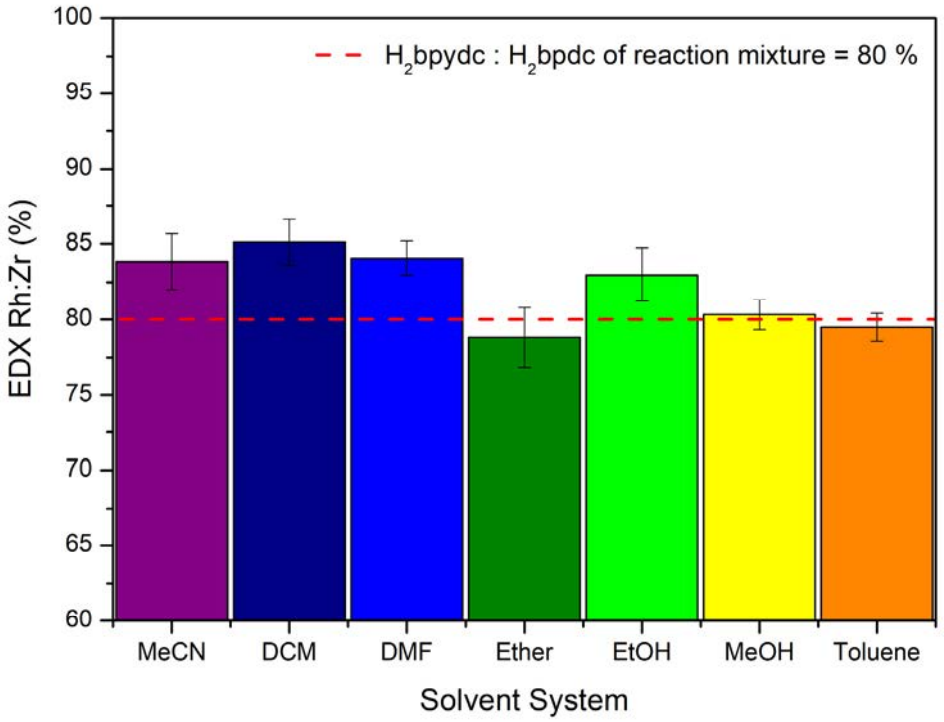

Figure **4.A.2**: Solvent effects on slow diffusion SALE at lower ligand concentrations and shorter time scale. The dotted red line indicates the overall ratio of H_2bpydc:H_2bpdc for the H_2bpydc in initially in the MOF framework and H_2bpdc in the solvent mixture = 80%.

4.13.3. SEM images of CS-MOF candidates synthesised via slow-diffusion SALE

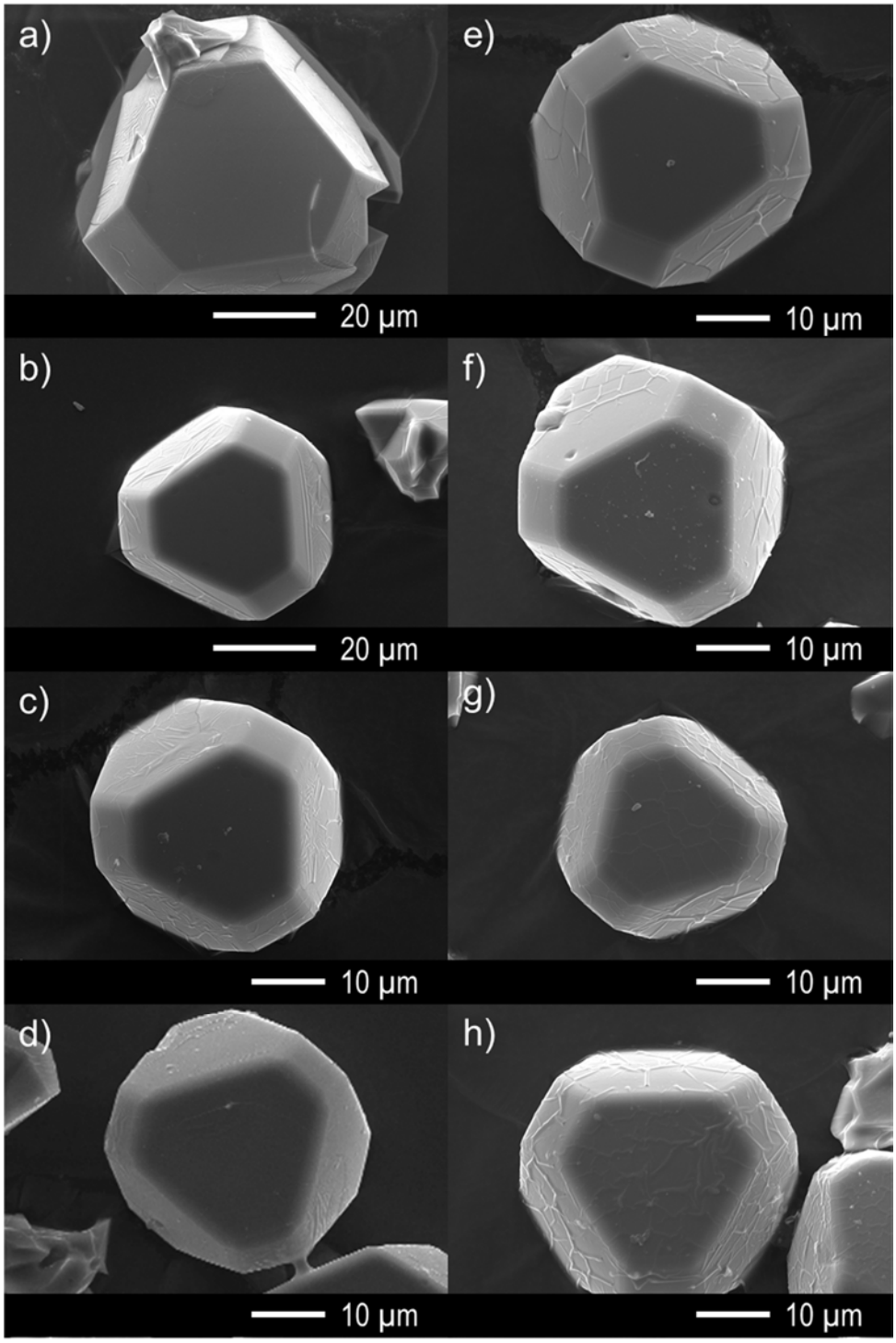

Figure **4.A.3**: SEM images of UiO-67-bpydc after slow diffusion SALE with 2.5 mM H_2bpydc in DMF at a)/e) 25, b)/f) 50, c)/g) 80 and d)/h) 120 ºC for 0.5 and 1 h respectively.

4.13.4. PXRD analysis of core and core-shell samples

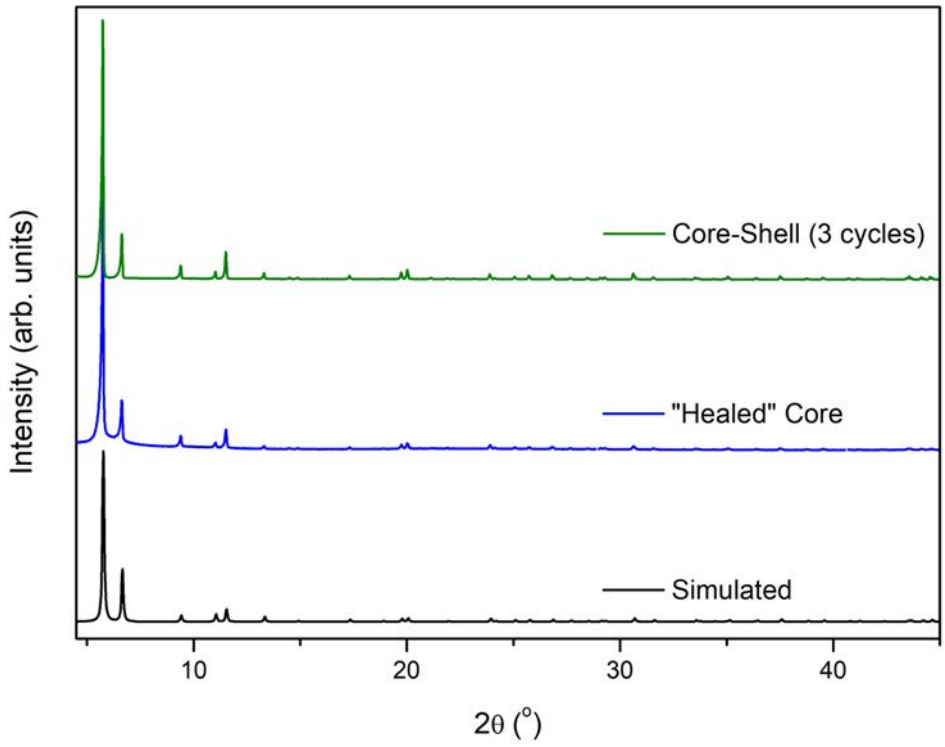

Figure **4.A.4**: PXRD patterns of simulated (black), "healed" core (blue) and core-shell (synthesised from 3 successive cycles of slow diffusion SALE, green) UiO-67-bpydc samples.

4.13.5. Characterisation of reverse CS UiO-67-bpdc⊂UiO-67-bpydc

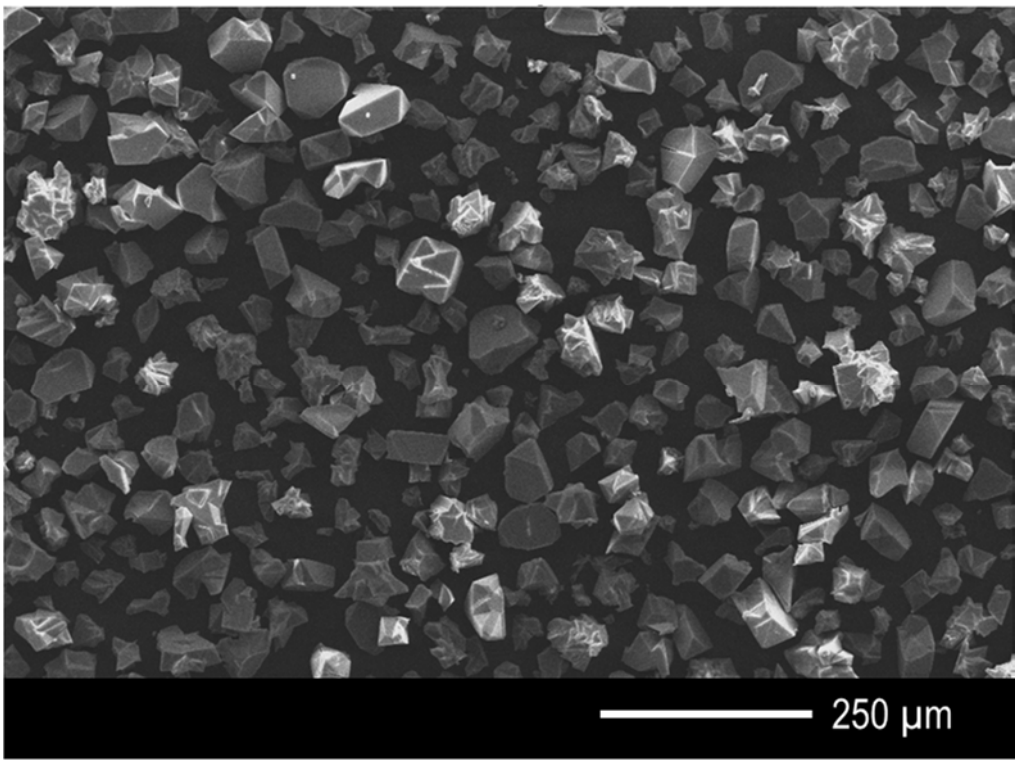

Figure **4.A.5**: SEM image of a sample of UiO-67-bpdc, synthesised with 80 eq. TFA at 120 °C for 7 d, the as-synthesised single crystals are approximately 100 µm in size.

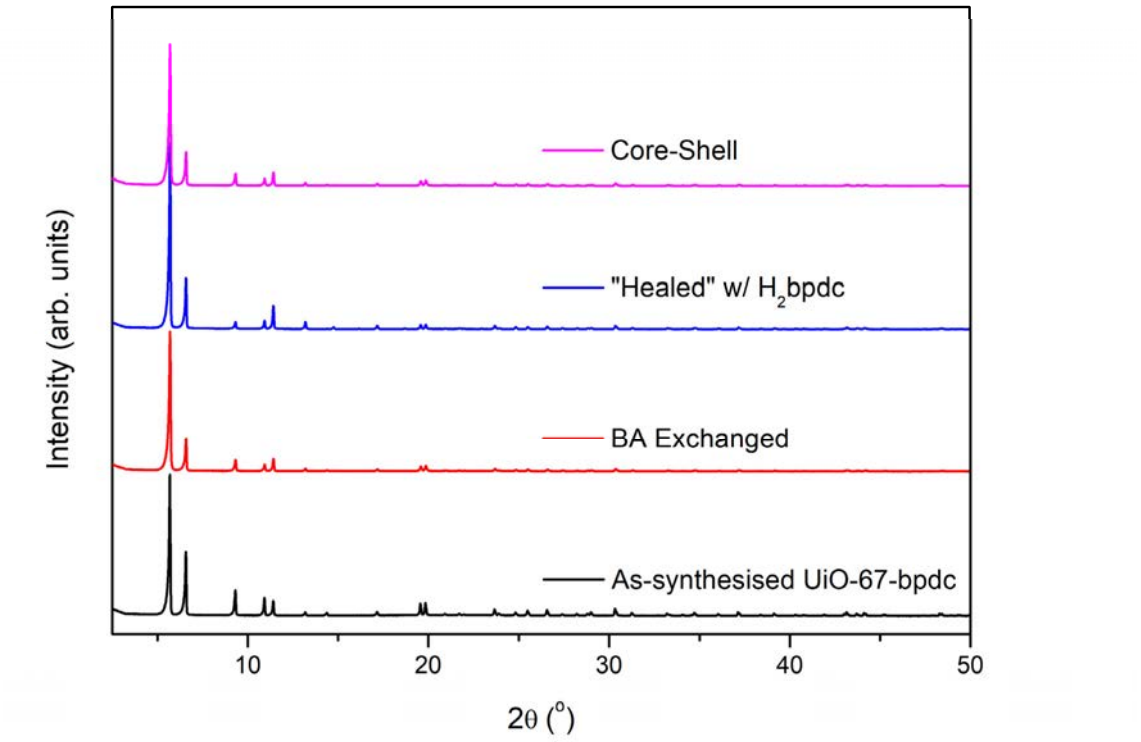

Figure **4.A.6**: PXRD patterns of samples of 100 µm UiO-67-bpdc, as-synthesised (black), exchanged with benzoic acid (BA, 0.65 M in DMF at 85 °C for 24 h, red), "healed" with ligand exchange with H_2bpdc (2.5 mM, in DMF at 85 °C for 24 h. blue) and a core-shell sample synthesised via slow diffusion SALE with H_2bpydc as the shell ligand (2.5 mM 20 min at 120 °C, pink).

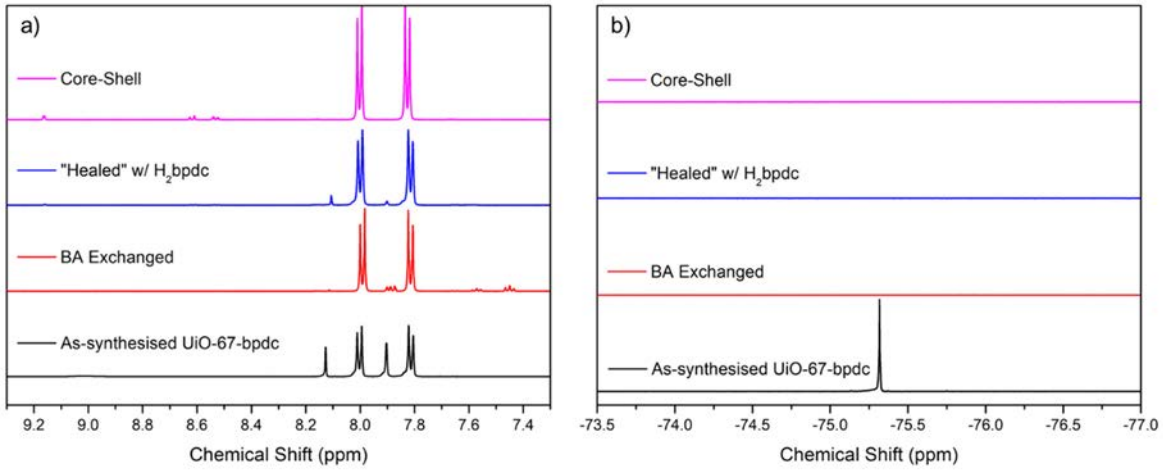

Figure **4.A.7**: a) ^{1}H and b) ^{19}F NMR spectra of $DMSO_{d6}$/DCl digested samples of UiO-67-bpdc, as-synthesised (black), benzoic acid exchanged (red), "healed" with H_2bpydc (blue) and Core-Shell (pink). These spectra demonstrate that with subsequent exchange and healing steps TFA and BA modulators are removed leaving a ligand defect free framework, additionally a core-shell composite was synthesised via slow diffusion SALE with H_2bpydc as the shell ligand.

4.13.6. Schematic of Flow Reactor Sample Holder

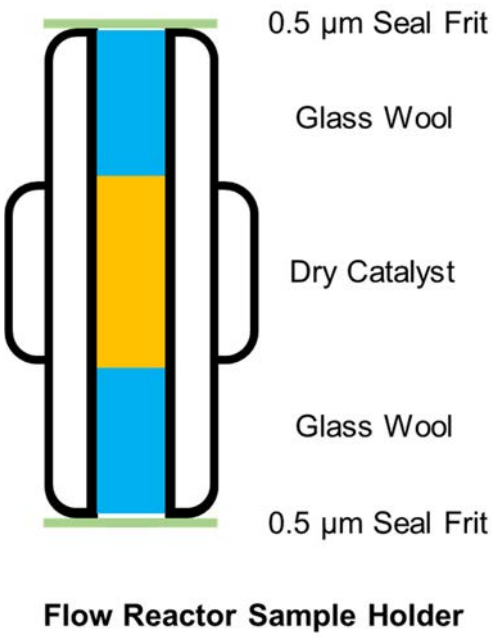

Figure **4.A.8**: Schematic of the flow reactor sample holder, where the catalyst packed in place between two pieces of glass wool (above and below). The sample holder is screwed into on the flow reactor with seal frits (with a 0.5 µm mesh filter) in place at either end of the sample holder.

*4.13.7. PXRD analysis of post-flow reaction **Pd·1***

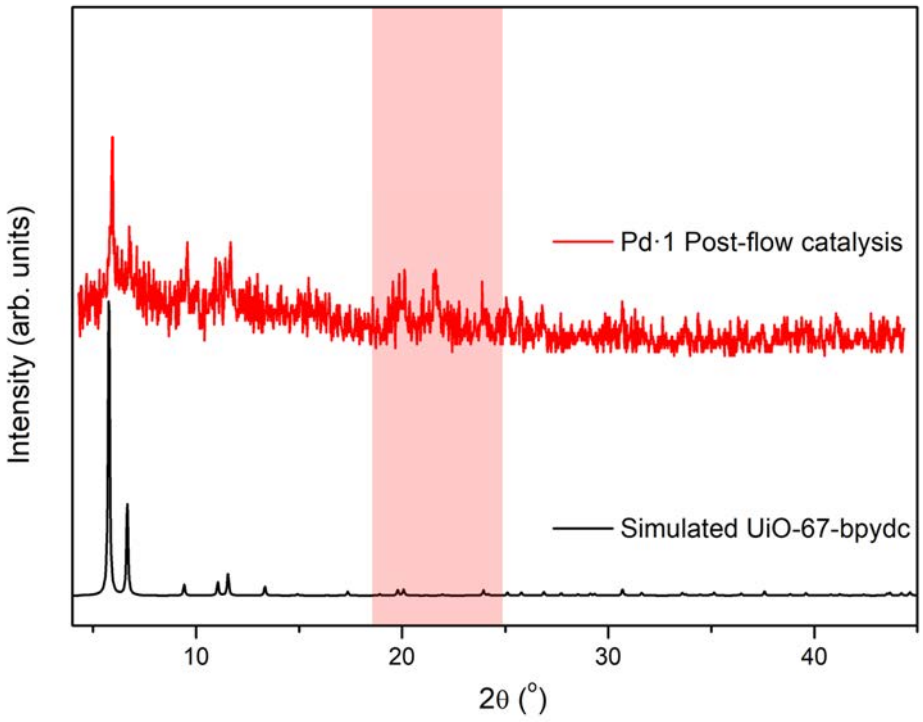

Figure **4.A.9**: PXRD patterns of simulated UiO-67-bpydc (black) and **Pd·1** post flow catalysis (red) with the peaks associated with crystalline polyethylene highlighted in the red shaded box at 21.5º.

*4.13.8. ICP-MS Analysis of **Pd·2** samples*

The molecular formula for each sample is determined by combining ^{1}H NMR spectroscopy data with elemental analysis of Pd:Zr ratio via either ICP-MS or EDX. ^{1}H NMR spectroscopy data provides the H_2bpydc:H_2bpdc ratio of the sample in the bulk, enabling assignment of x and y in the molecular formula $Zr_6(OH)_4O_4(bpydc)_x(bpdc)_y$, x + y = 6 because there are 6 ligands per Zr node in the framework. Elemental analysis of the MOF samples gives the Pd:Zr ratio (Pd_{ratio}), hence the amount of Pd associated with the formula equals $Pd_{ratio} \times 6$ as there are 6 Zr atoms in the formula. The molecular weight (MW) for the repeating unit of the metalated MOF can be calculated ($MW_{PS\text{-}met}$) by adding the MW of the bare framework with $Pd_{ratio} \times 6 \times$ MW([Pd(MeCN)Me]BF_4). The number of milli-moles of the repeating unit per mg of sample can be calculated by dividing 1 by $MW_{PS\text{-}met}$ and this can be converted to μmol (repeating unit)/mg (sample) by multiplying by 1000. The number of moles of the palladium catalyst per mg of sample can be calculated by multiplying this value by $Pd_{ratio} \times 6$. And subsequently the moles of palladium catalyst in each sample is calculated by further multiplying by the mass of the sample used. A summary of the μmol of palladium catalyst in each of the samples reported in Chapter 4 is outlined in Table **4.11.1** in the Experimental section.

*4.13.9. PXRD Analysis of **Pd·2** samples pre-catalysis*

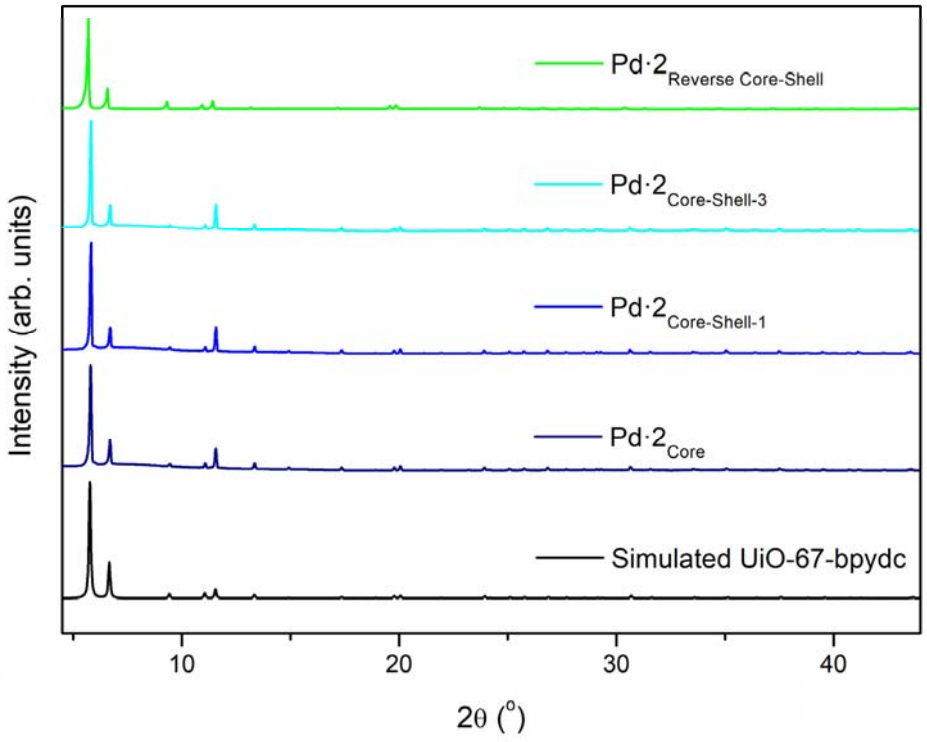

Figure **4.A.10**: PXRD patterns of simulated UiO-67-bpydc (black), and samples metalated with $[PdMe(MeCN)]^{+}BF_4^{-}$ (pre-catalysis) including; **Pd·2$_{core}$** (navy blue), **Pd·2$_{core\text{-}shell\text{-}1}$** (blue), **Pd·2$_{core\text{-}shell\text{-}3}$** (cyan), and **Pd·2$_{rev\text{-}core\text{-}shell}$** (green).

*4.13.10. GC-FID analysis of **Pd·2** samples*

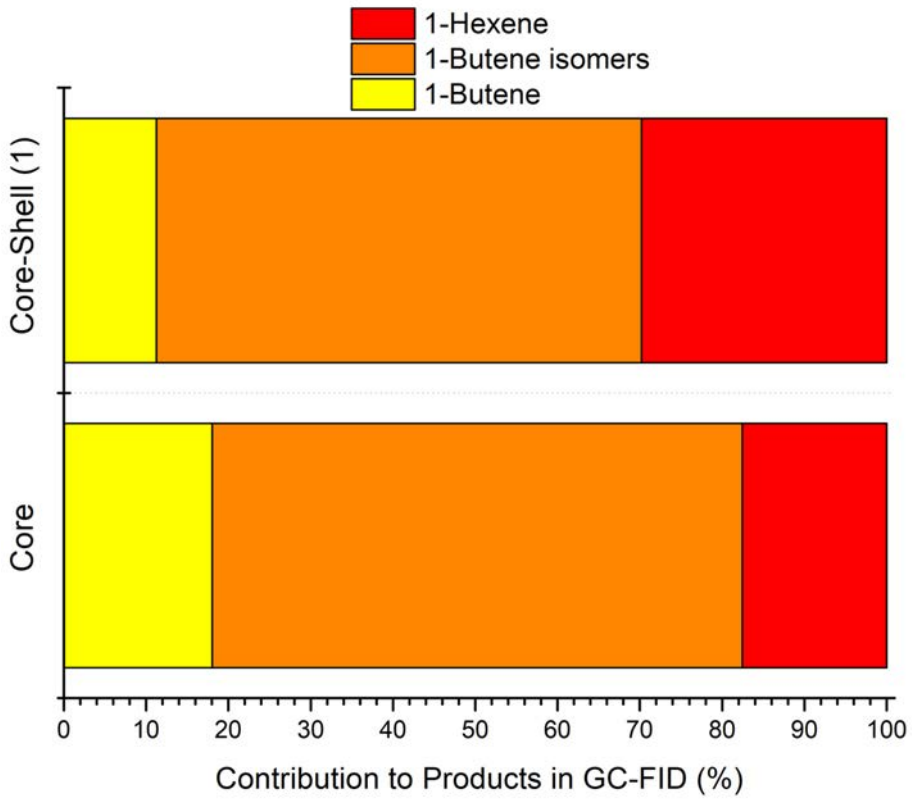

Figure **4.A.11**: GC-FID analysis of gas mixture 1 h into ethylene oligomerisation reaction catalysed by **Pd·2**$_{\mathbf{core}}$ and **Pd·2**$_{\mathbf{core\text{-}shell\text{-}1}}$, showing the contribution of products (%) of 1-butene, 1-butene isomers and 1-hexene.

*4.13.11. PXRD and SEM Analysis of **Pd·2** samples pre- and post-catalysis*

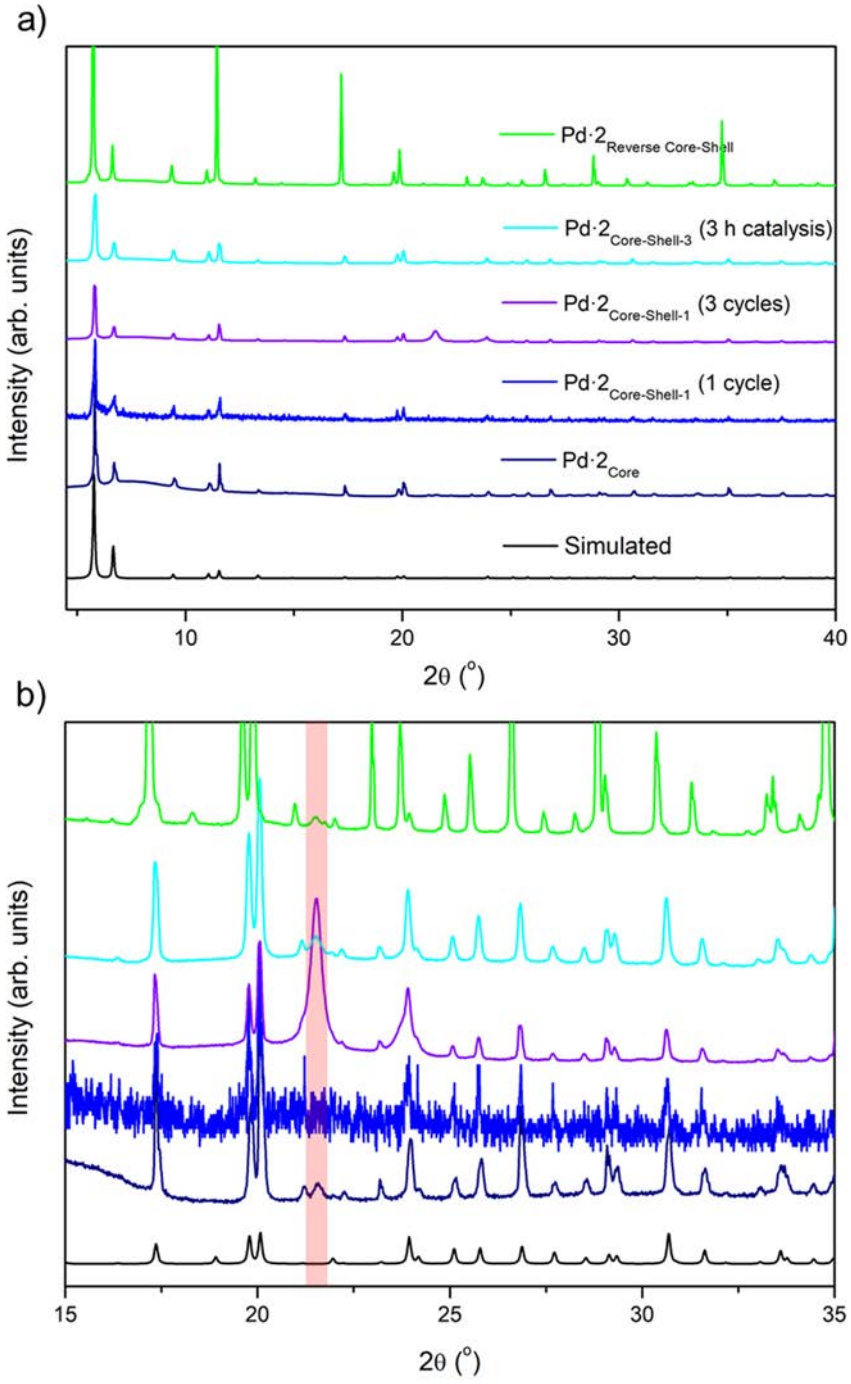

Figure **4.A.12**: a) PXRD patterns of simulated UiO-67-bpydc (black), and post-catalysis samples including; **Pd·2$_{core}$**, **Pd·2$_{core-shell-1}$** (1st cycle), **Pd·2$_{core-shell-1}$** (3rd cycle), **Pd·2$_{core-shell-3}$** (3 h), and **Pd·2$_{rev-core-shell}$**. Increased magnification of a) in b) highlights the 21.5 º peak for crystalline polyethylene present in some of the samples post-catalysis (highlighted in the shaded red box).

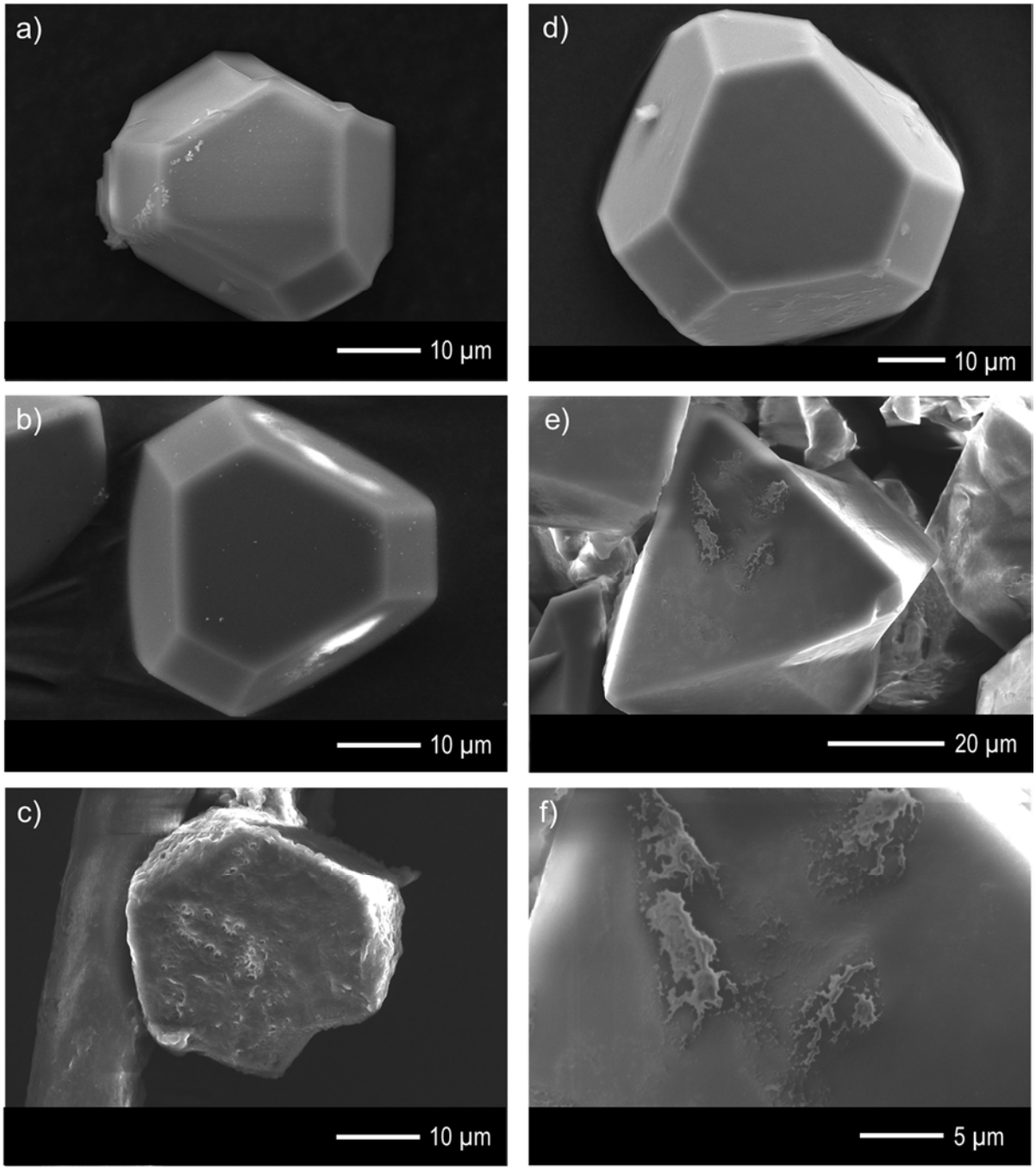

Figure **4.A.13**: SEM images of post-catalysis samples including; a) **Pd·2**$_{\textbf{core}}$, b) **Pd·2**$_{\textbf{core-shell-1}}$ (1st cycle), c) **Pd·2**$_{\textbf{core-shell-1}}$ (3rd cycle), d) **Pd·2**$_{\textbf{core-shell-3}}$ (3 h), and e-f) **Pd·2**$_{\textbf{rev-core-shell}}$.

4.13.12. GC-FID analysis of ***Pd·2$_{core\text{-}shell\text{-}1}$***

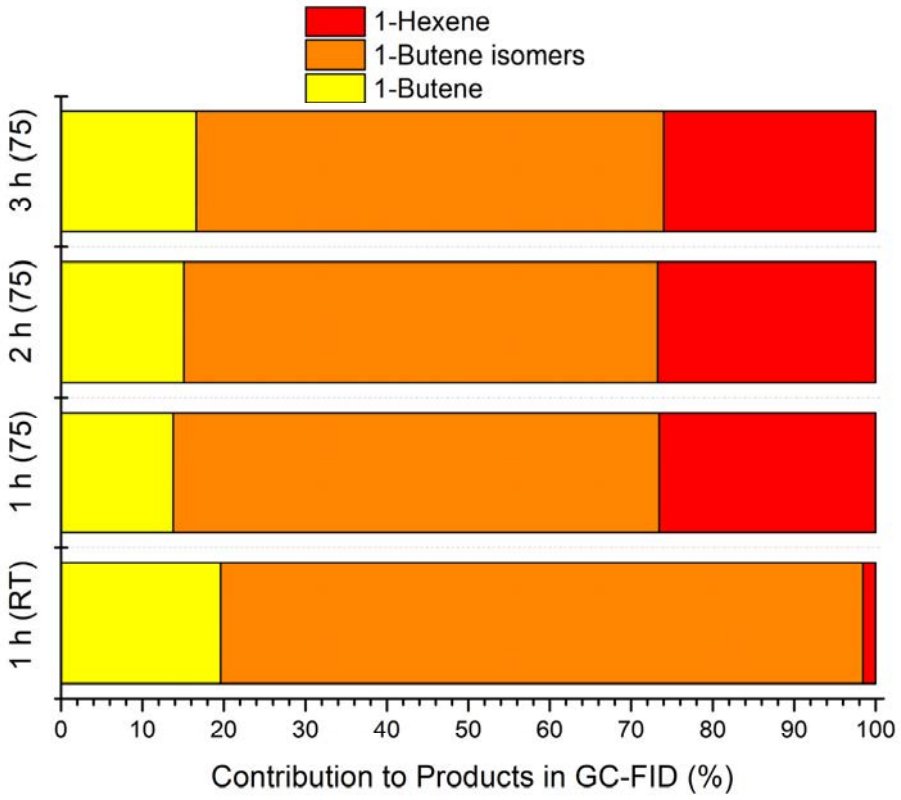

Figure **4.A.14**: GC-FID analysis of gas mixture at varied time points of the ethylene oligomerisation reaction catalysed by **Pd·2$_{core\text{-}shell\text{-}3}$**, showing the contribution of products (%) of 1-butene, 1-butene isomers and 1-hexene.

4.13.13. Sorption analysis of post-catalysis samples

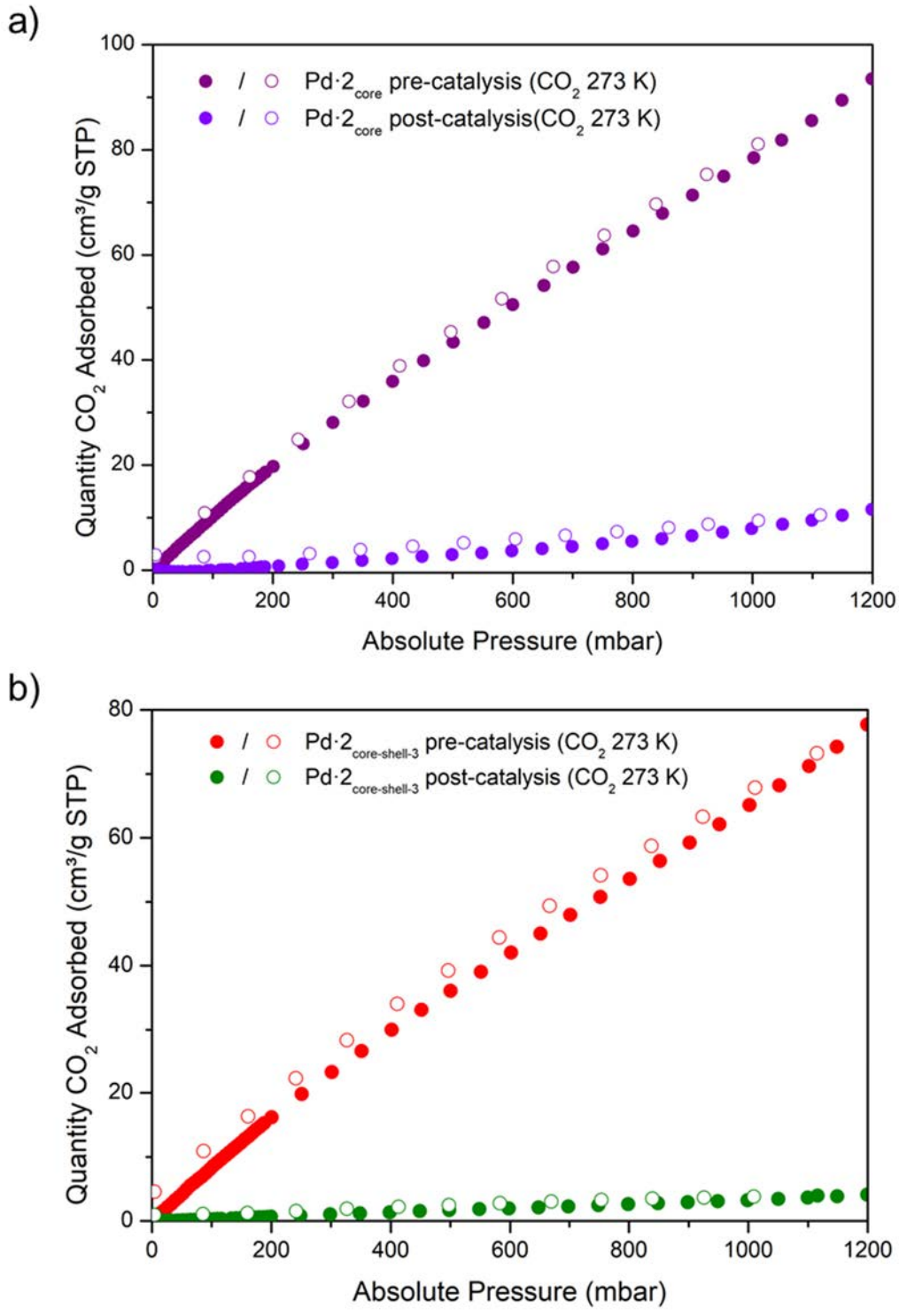

Figure **4.A.15**: CO_2 273 K isotherms of a) **Pd·2$_{core}$** and b) **Pd·2$_{core\text{-}shell\text{-}3}$** both pre- and post-catalysis.

4.13.14. RGA reaction profile for ***Pd·2*** $_{\textbf{rev-core-shell}}$

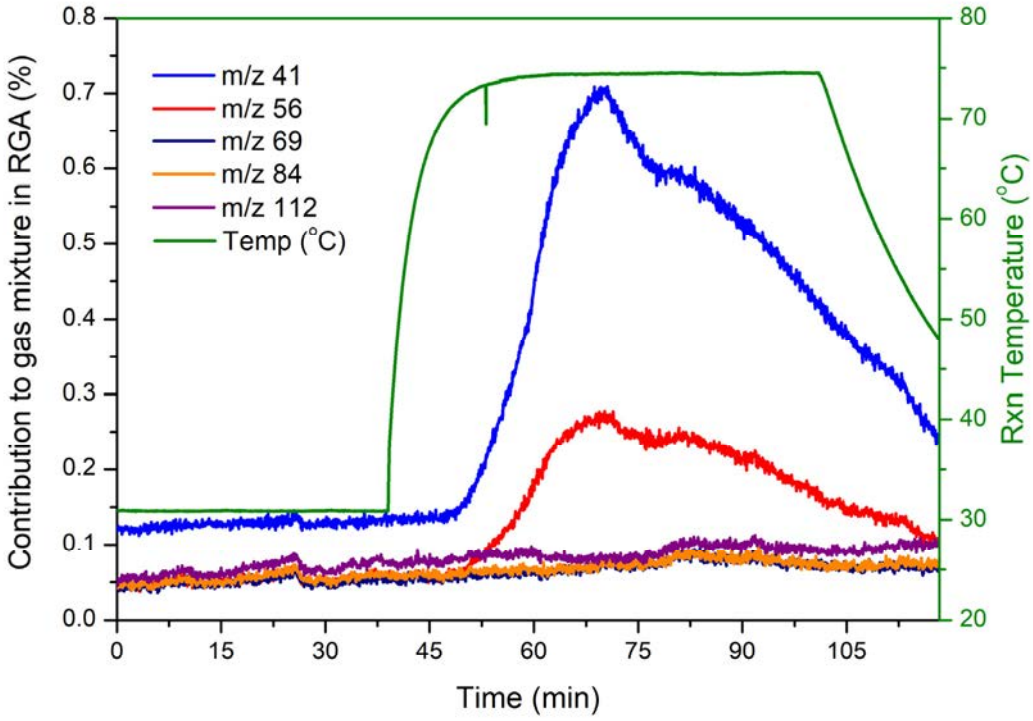

Figure **4.A.16**: Reaction profile of ethylene oligomerisation catalysed by **Pd·2** $_{\textbf{rev-core-shell}}$ (50 ml/min, 6 bar back pressure) on the flow reactor. The reaction profile is displayed as the contribution to the total pressure in the RGA (%) for 1-butene (m/z 41 and 56), 1-hexene (m/z 69 and 84) and 1-octene (m/z 112).

4.13.15. Surface Passivation through Polymer Coating

Attempts were made to passivate the surface of **Pd·1** with a polymer coating, in order to minimise catalyst deactivation during the catalysis of ethylene oligomerisation. Tao Li *et. al.* were able to synthesise UiO-66@polymer composites with coating thickness's of 13-59 nm and demonstrated increased stabilisation of the MOF to unfavourable conditions (strong acid/base).[1] The polymer coatings reportedly minimised the diffusion of aggressive chemicals to the MOF core, thereby prolonging the stability of the framework. We adopted this methodology because it showed promise in slowing diffusion of guest molecules, which might slow the formation of long chain oligomers which deactivated **Pd·1** during catalysis. The polymer coatings trailed included polymethyl acrylate, polystyrene, and polyimide. Polymer coated samples of 1 μm UiO-67-bpydc$_{0.5}$bpdc$_{0.5}$ with polymethyl acrylate (PMA) and polystyrene (PS), and polymer coating methods with polyimide (PI) were provided from our collaborator Tao Li *et. al.*[1]

Samples of polymer coated 1 μm UiO-67-bpydc$_{0.5}$bpdc$_{0.5}$ with PMA and PS were metalated with [PdMe(MeCN)]BF$_4$ after surface coating, whereas the PI coated sample could be metalated prior to polymer coating. These samples will be denoted **Pd·1$_{PMA}$**, **Pd·1$_{PS}$**, and **Pd·1$_{PI}$**, for polymer coatings with PMA, PS and PI respectively. All of the polymer coated composites were crystalline via PXRD, matching the pattern of simulated UiO-67-bpydc (see Figure **4.A.17)**. SEM/EDX analysis of **Pd·1$_{PMA}$**, **Pd·1$_{PS}$**, and **Pd·1$_{PI}$** revealed varied catalyst uptakes, with Pd to Zr ratios of 65.8 ± 7.9, 3.1 ± 1.3 and 35.5 ± 0.7 % respectively. It was apparent that the PS coating around the MOF crystals was not able to swell sufficiently to allow [(COD)PdMe(MeCN)]BF$_4$ to access the core MOF and coordinate to the framework. The palladium detected was likely polymer surface associated having not been removed during MeCN washes. Subsequently, **Pd·1$_{PS}$** demonstrated no catalytic activity for the gas oligomerisation of ethylene oligomerisation.

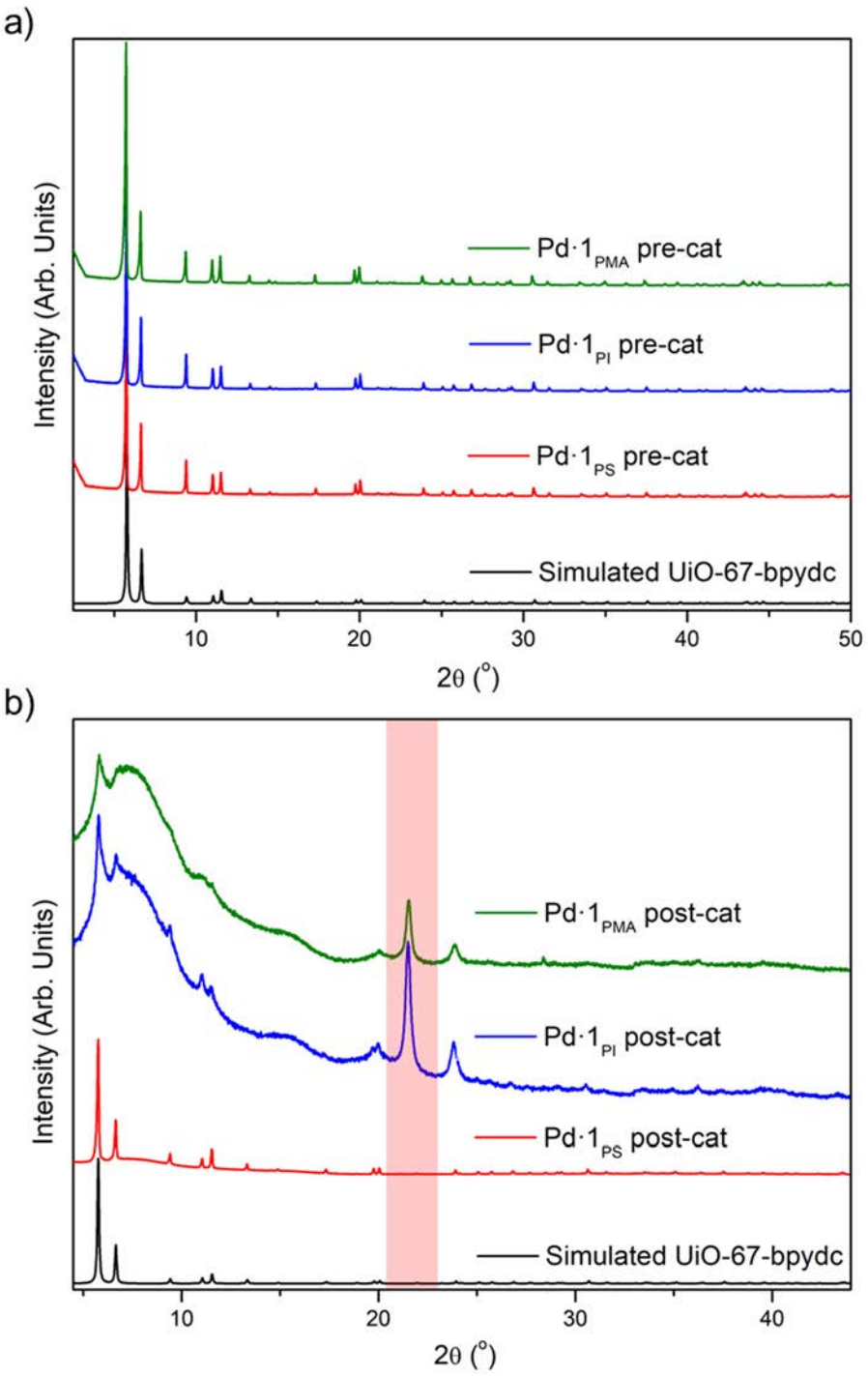

Figure **4.A.17**: PXRD patterns of simulated UiO-67-bpydc (black), **Pd·1$_{PS}$** (red), **Pd·1$_{PI}$** (blue), and **Pd·1$_{PMA}$** (green) a) pre- and b) post-catalysis under flow reaction conditions. Crystalline polyethylene is highlighted with a red shaded box at 21.5 º.

The catalytic activity of the polymer coated samples was analysed under flow conditions, identical to those used for **Pd·1**, for the gas phase catalysis of ethylene oligomerisation. The RGA reaction profiles for **Pd·1$_{PMA}$**, **Pd·1$_{PS}$**, and **Pd·1$_{PI}$** are displayed in Figure **4.A.18**, along with GC-FID analysis of the gas mixture at 1 h into heating at 75 ºC. The

GC-FID data for **Pd·1$_{PS}$** is not shown, as mentioned earlier **Pd·1$_{PS}$** was not catalytically active, hence no oligomers of ethylene were detected via gas chromatography. **Pd·1$_{PMA}$** and **Pd·1$_{PI}$** were shown to be catalytically active, but both were shown to deactivate in a similar fashion to **Pd·1**, with production of m/z 41 (1-butene) decreasing by 65 and 88 % respectively 30 minutes after initial peak activity. There is no significant difference in product distributions between the active polymer coated samples and the non-coated **Pd·1** by gas chromatography. Post-catalysis analysis by PXRD and SEM imaging revealed the presence of crystalline polyethylene and a surface coating of the polymer which charged under the electron beam respectively for **Pd·1$_{PMA}$** and **Pd·1$_{PI}$** (Figures **4.A.17** and **4.A.19**). From this data it is apparent that the polymer coatings of PMA and PI did little to passivate the surface of **Pd·1**, with no significant retention of activity being retained for either **Pd·1$_{PMA}$** or **Pd·1$_{PI}$**.

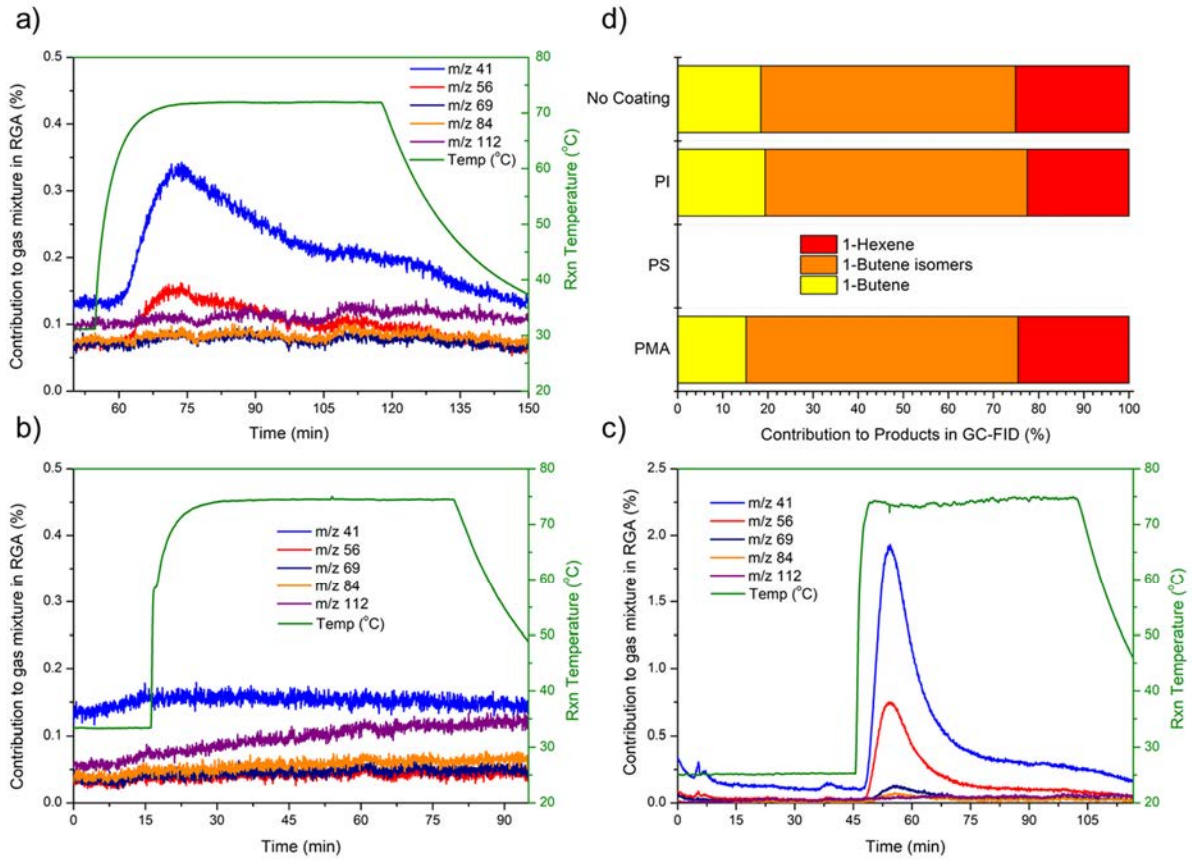

Figure **4.A.18**: Reaction profiles for ethylene oligomerisation displayed as the contribution to the total pressure in the RGA (%) catalysed by a) **Pd·1$_{PMA}$**, b) **Pd·1$_{PS}$**, c) **Pd·1$_{PI}$**, and d) GC-FID product distribution for each catalyst 1 h into the reaction at 75 ºC, including **Pd·1**.

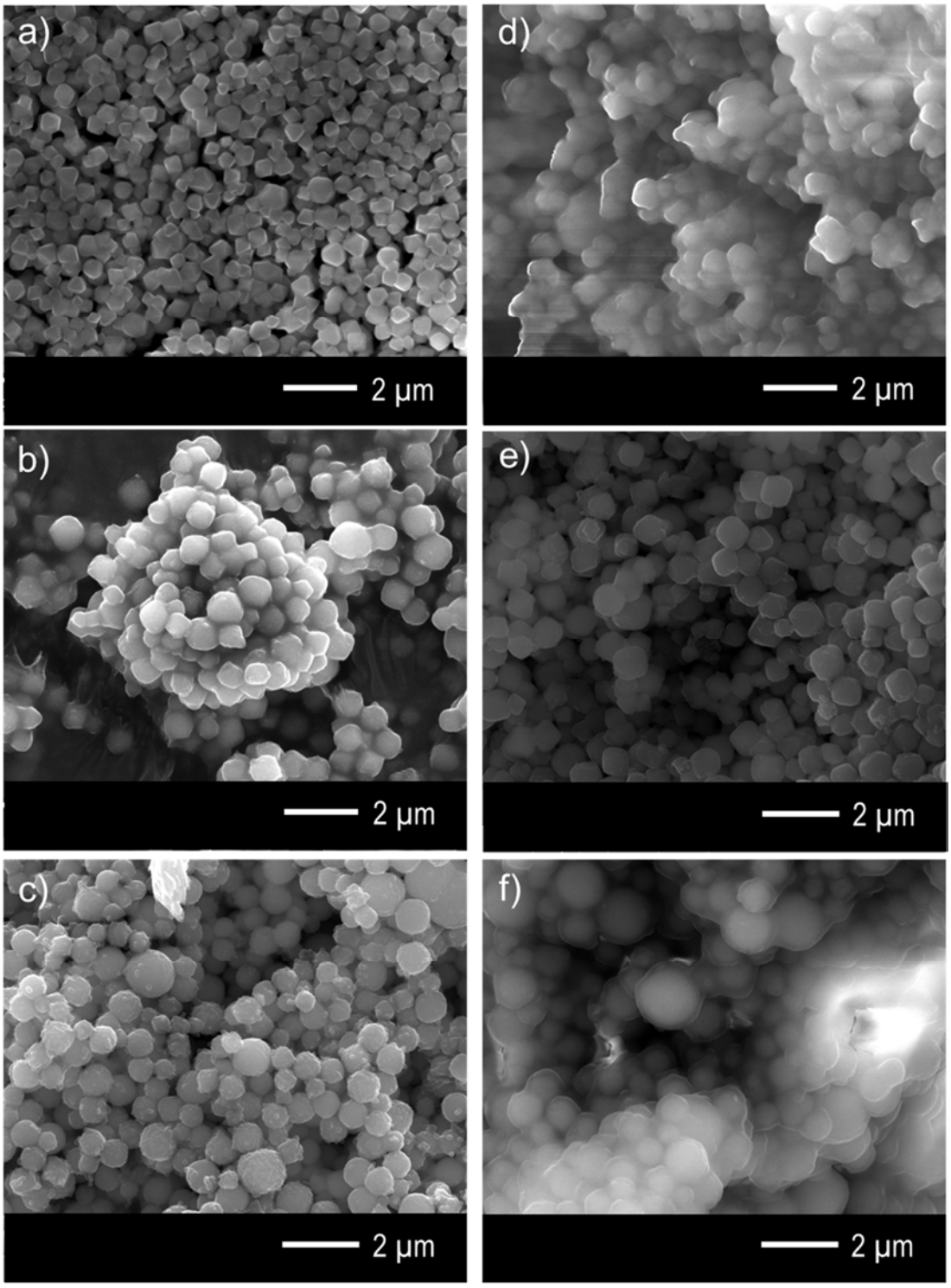

Figure **4.A.19**: SEM images of a)/d) **Pd·1**$_{PMA}$, b)/e) **Pd·1**$_{PS}$ and c)/f) **Pd·1**$_{PI}$ pre-/post-catalysis respectively.

Sorption studies with N_2 (77 K) and CO_2 (195 and 273 K) were done on **Pd·1$_{PMA}$** pre- and post-catalysis to determine whether the porosity was retained despite deactivation from the production of long chain ethylene oligomers (see Figure **4.A.20**). Pre-catalysis **Pd·1$_{PMA}$** exhibits a type 1 N_2 isotherm, with a relatively low BET surface area in comparison to the non-metalated species (reported in Chapter 3), 586.6 ± 2.9 and 2641.2 ± 3.0 m²/g respectively. Post-catalysis **Pd·1$_{PMA}$** was non-porous to N_2 (77 K) or CO_2 (195 and 273 K), and as such no pore-size analysis or BET measurements of surface area could be done. The long chain oligomers produced during catalysis block access to the pores of the framework for **Pd·1$_{PMA}$** which deactivates the catalyst by stopping the diffusion of guest molecules into the framework. The PMA polymer coating was not sufficient to passivate the surface to limit the deactivation, this trend was also observed for **Pd·1$_{PI}$**, but no sorption analysis was done due to the conclusions drawn from **Pd·1$_{PMA}$** post-catalysis sample. Whilst framework stabilisation is possible with polymer coatings, the deactivation of the palladium catalyst is clearly not an issue of stabilisation, rather the location of active sites which likely affects product formation aka long chain oligomers to a larger extent than limiting access to the crystal surface does. As such, further critical analysis of the polymer composites, such as coating thickness, was not investigated.

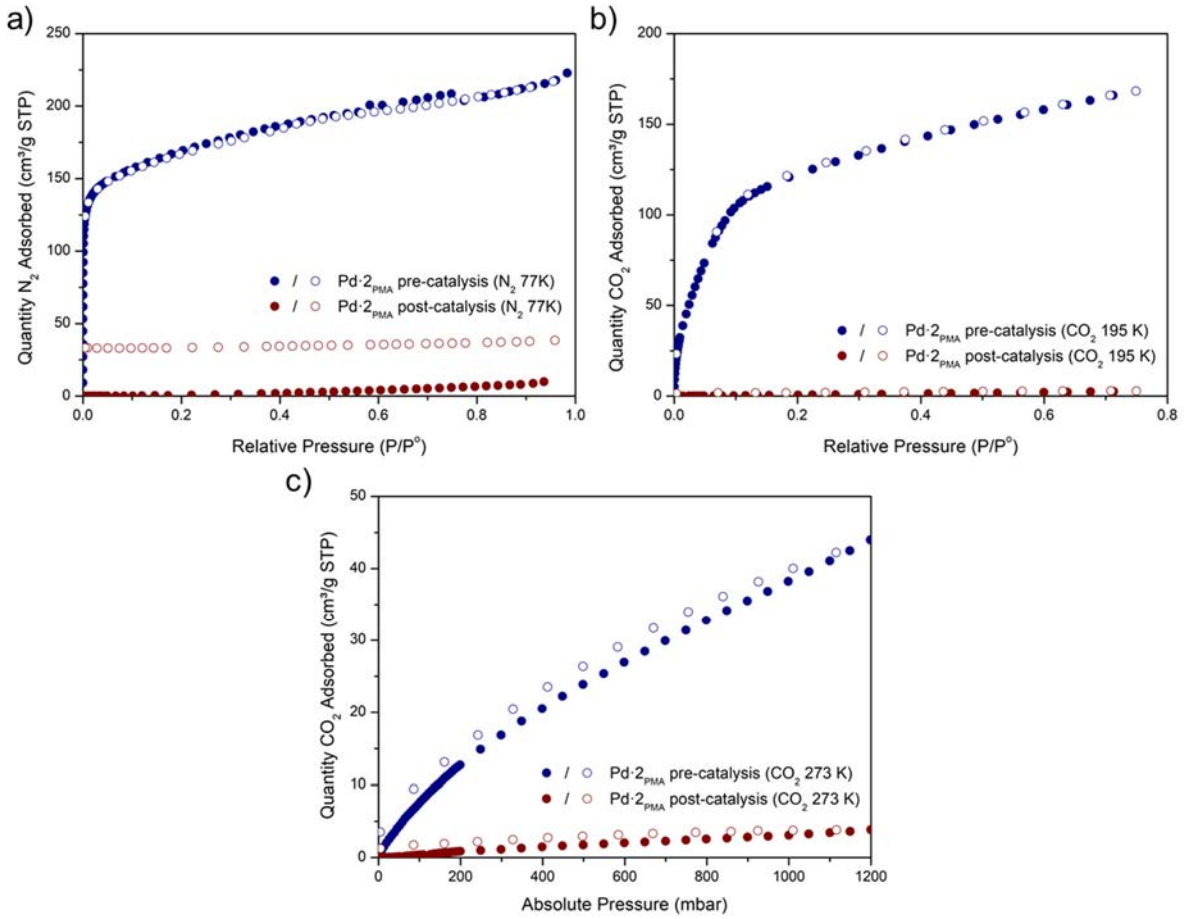

Figure **4.A.20**: a) N_2 77K, b) CO_2 195 K and c) CO_2 273 K isotherms of **Pd·1$_{PMA}$** pre- (blue) and post-catalysis (red), demonstrating a reduction in porosity of **Pd·1$_{PMA}$** post-catalysis.

Appendix 4.13. References

1. He, S.; Wang, H.; Zhang, C.; Zhang, S.; Yu, Y.; Lee, Y.; Li, T., A Generalizable Method for the Construction of MOF@Polymer Functional Composites through Surface-Initiated Atom Transfer Radical Polymerization. *Chem Sci* **2019,** *10* (6), 1816-1822.

Chapter 5.

Towards Reactive Group Isolation in a UiO-67 Derivative

Chapter 5. Towards Reactive Group Isolation in a UiO-67 Derivative

5.1. Introduction

Metal-organic frameworks (MOFs) have the capacity to bind additional metal species via post-synthetic metalation (PSMet), which has emerged as a versatile method of forming materials with isolated and well-defined metal sites.[1-11] Recently, there has been a surge of interest in characterising the coordination environment of catalytically active transition metal species coordinated to MOFs.[12-17] In certain circumstances, entire catalytic cycles can be followed via single-crystal X-ray diffraction (SCXRD), enabling elucidation of the coordination environments of intermediates during catalysis in controlled reaction enviroments.[18] A vast range of catalytic reactions have been reported with MOFs that have undergone PSMet, some of which have been evaluated in Chapters 3 and 4, but rarely are the precursor catalytic metal sites, let alone intermediates formed during catalysis, able to be studied by SCXRD. There are several reasons for the paucity of such studies. SCXRD information can be hard to obtain for MOFs after PSMet due to diminished crystal and data quality arising from low site occupancy of the chelating moiety by the extraneous metal ion and/or significant disorder.[19-23] Successes in this area have arisen from minimising the crystallographic complexity of the system, through either judicious ligand design, or from PSMet induced single-crystal to single-crystal (SC-SC) transformations to lower symmetry structures.[12, 14, 24] The latter of these strategies was observed by Long *et. al.* with UiO-67-bpydc metalated with a range of transition metal complexes (CuCl, $CuCl_2$, $CoCl_2$, $FeBr_2$ and $Cr(CO)_4$).[14] These SC-SC transformations involved a change in space group of the MOF from *Fm-3m* to *Pa-3*, resulting from the ordering of metalated linkers within the framework, which enabled structural characterisation of the resulting metal complexes (see Figure **5.1**).[14]

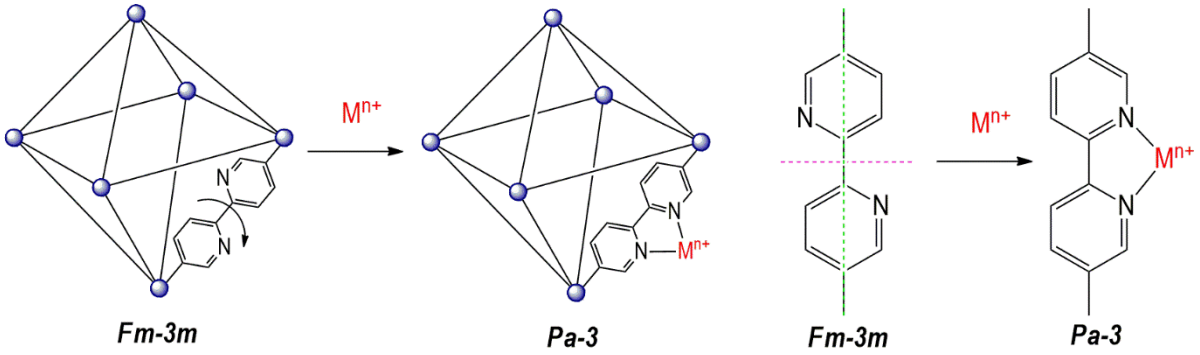

Figure **5.1**: Schematic of a) UiO-67-bpydc metalation demonstrating PSMet induced SC-SC transformation to a lower symmetry space group *Pa-3* from *Fm-3m* and, b) the planes of symmetry for the ligand are indicated by dashed green and purple lines, with an additional mirror plane co-planar with the ligand. When metalated there is a reduction of symmetry associated with the ligand, enabling structural determination of the chelated metal complex .

The work presented in this chapter utilised the strategy outlined by Long *et. al*. to examine PSMet of a Zr-framework isoreticular with UiO-67-bpydc (**1**) and unambiguously define the coordination sphere of inserted transition metal complexes. The isoreticular Zr-framework used was 6,6'-Me_2bpydc-UiO-67 (UiO-67-Me_2bpydc, **1-Me_2**), where Me_2bpydc is 6,6'-dimethyl-(2,2'-bipyridine)-5,5'-dicarboxylic acid.[25] Li *et at.* reported the synthesis of the ligand Me_2bpydc and the corresponding UiO-67 variant. The ligand engineering of **1-Me_2** was shown to increase the rate of a Suzuki-Miyaura cross coupling reaction with a 110 fold increase in activity when metalated with $PdCl_2$ in comparison to $PdCl_2$@UiO-67-bpydc.[25] Li *et. at.* were able to demonstrate that the stereo-electronic properties of metal-binding linker moieties are critical to the activity of MOF-tethered single-site organometallic catalysts. However, as is typical for most MOF catalysts, there was limited structural characterisation (SCXRD) of the coordination environment of the active catalyst by Li *et. at.* in their initial and follow up papers, with the majority of work being performed on sub-micron crystals.[26] As such, **1-Me_2** offers a chance to investigate the impact of sterics and electronics on PSMet induced SC-SC transformations in UiO-67 materials and further to examine their influence on the added metal complex (reactivity etc.).

Investigating UiO-67 derivatives via SCXRD necessitates the synthesis of large pristine crystals, with minimal ligand defects and high occupancy of extraneous metals for PSMet species. It is challenging to synthesise large Zr-MOFs crystals (> 10 μm), as discussed in Chapter 3, with most requiring the addition of monotopic modulators.[27-29] Yang *et. al.* reported conditions to synthesise larger Zr-MOF crystals which were adopted to synthesise UiO-67-

bpdc and UiO-67-bpydc crystals ≥ 40 μm in size, as discussed in Chapter 4.[30] However, the use of modulators such as TFA results in a significant number of ligand defects (14 %) for **1**, which lowers the ligand occupancy of the framework and makes the crystals unsuitable for collecting high quality diffraction data.[31] Through the advent of crystal engineering techniques such as linker exchange and crystal healing, these ligand defects can be minimised post-synthetically, affording crystals which have high ligand occupancy and are better suited to SCXRD. Using these strategies, pristine large single crystals of **1-Me$_2$** were prepared to allow examination of the coordination chemistry of PSMet materials.

The overall objective of Chapter 5 is to follow post-synthetic SC-SC transformations of **1-Me$_2$** upon PSMet in order to ascertain whether this material is well suited to matrix isolation and structural characterisation of reactive species, including azides and nitrenes. The synthesis and subsequent characterisation of **1-Me$_2$** crystals suitable for SCXRD will be investigated in the first half of this chapter, with the second half focusing on PSMet and the characterisation of metalated species via SCXRD.

5.2. Synthesis and Characterisation of SCXRD Suitable Crystals

Large **1-Me$_2$** crystals were synthesised from $ZrCl_4$ and Me_2bpydc in DMF using TFA as a modulator, see Chapter 4. The first reaction simply involved replacing H_2bpydc with an equi-molar amount of Me_2bpydc, which resulted in the synthesis of large yellowish crystals after 7 days, see experimental section **5.7** and schematic in Figure **5.2** for detailed synthesis conditions. Single crystals formed on the sides of the vials and were subsequently collected, separated from the microcrystalline material at the bottom of the reaction vials via careful pipetting, washed with DMF (4 × 10 ml) and then stored in DMF until needed. The single crystals were analysed via PXRD (post-MeCN solvent exchange, see Figure **5.2**), which confirmed the framework topology was isostructural to **1**, with the as-synthesised powder pattern closely matching the simulated pattern of **1**.

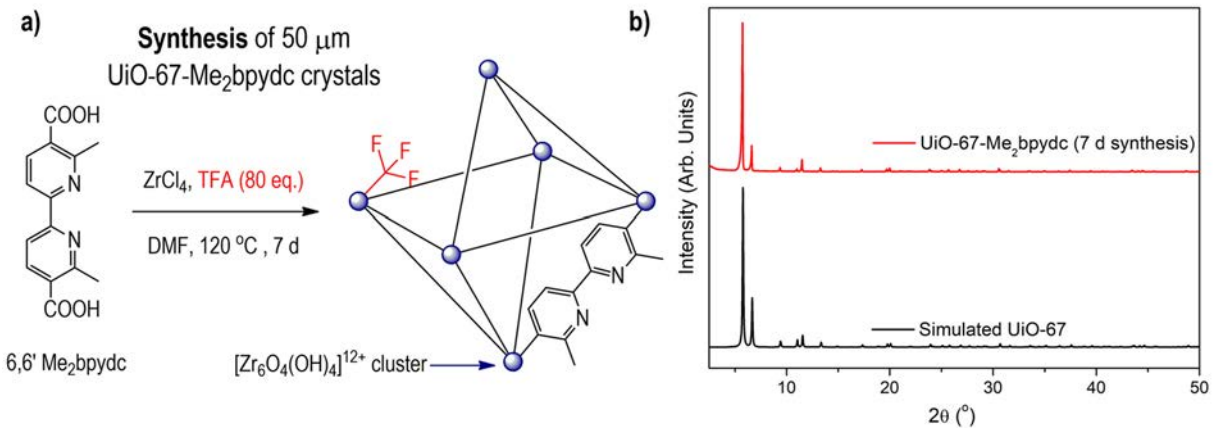

Figure **5.2**: a) Schematic representation of the synthesis of large **1-Me$_2$** crystals, with a cartoon representation of the MOF structure showing three key features; the zirconium-oxo cluster $[Zr_6O_6(OH)_4]^{12+}$, the Me_2bpydc ligand coordinated to two different clusters and a trifluoroacetate (TFA) coordinating to one cluster causing a ligand defect. b) PXRD patterns of simulated UiO-67 (black) and UiO-67-Me_2bpydc (**1-Me$_2$**, red) synthesised from conditions outlined in a) (post-MeCN solvent exchange).

The crystal size and morphology of the single **1-Me$_2$** crystals were investigated via SEM, as shown in Figure **5.3**. The average diameter of the single crystals was 65.4 ± 2.4 μm and the crystals had a similar morphology to **1** synthesised under the same conditions (see Appendix **5.9.1**, Figure **5.A.1**). The single crystals have a truncated octahedral morphology, as discussed in Chapter 4; the TFA modulator appears to attenuate crystal growth at the vertices causing the truncation of the crystals. This is due to preferential coordination to the terminating chemical environment at the [100] Miller plane of the vertices rather than the [111] Miller plane of the crystal faces. Additionally, the single crystals have no noticeable surface defects, were not intergrown and could be easily selected/viewed via optical microscopy, making them ideal for SCXRD analysis (see Figure **5.3**).

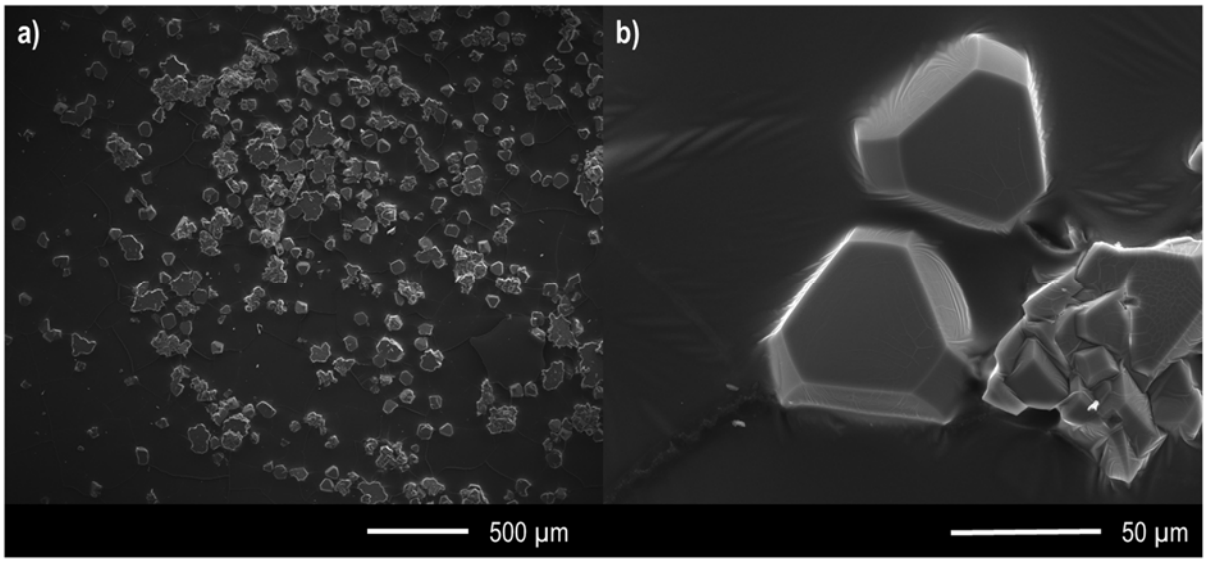

Figure **5.3**: SEM images of UiO-67-Me$_2$bpydc a) an area view and b) a close up of two crystals showing the truncated octahedral morphology.

Whilst the crystals of **1-Me$_2$** appear ideal for SCXRD studies, the conditions utilised for their synthesis are prone to introducing ligand defects. Modulators such as TFA have been shown to introduce a significant number of missing ligand defects in UiO-67 framework materials, as discussed in Chapter 4.[32-33] Missing ligand defects reduce the ligand occupancy in the crystalline lattice, making structural analysis via SCXRD challenging.[34-35] Defect analysis and subsequent mitigation is therefore critical prior to SCXRD studies. Defect analysis of **1-Me$_2$** single crystals was performed via ^{1}H and ^{19}F NMR spectroscopy following previously discussed framework digestion protocols with DMSO$_{d6}$/DCl, (see experimental section **5.7**). Me$_2$bpydc and TFA were observed in the digested as-synthesised crystals by ^{1}H and ^{19}F NMR spectroscopy respectively (see Figure **5.4**). Following previously discussed procedures, defect analysis was performed by firstly exchanging TFA with benzoic acid, which can be quantified by ^{1}H NMR spectroscopy (see experimental section **5.7**). Upon exchange with benzoic acid, there are no peaks in the ^{19}F NMR for TFA, indicating full exchange by benzoic acid. Quantitative defect analysis of the benzoic acid exchanged sample revealed the presence of 14% ligand defects in **1-Me$_2$**, comparable to the proportion of ligand defects observed in **1** (14%), synthesised under similar conditions (see Appendix **4.1** for calculations, Tables **4.1** and **5.A.1**).

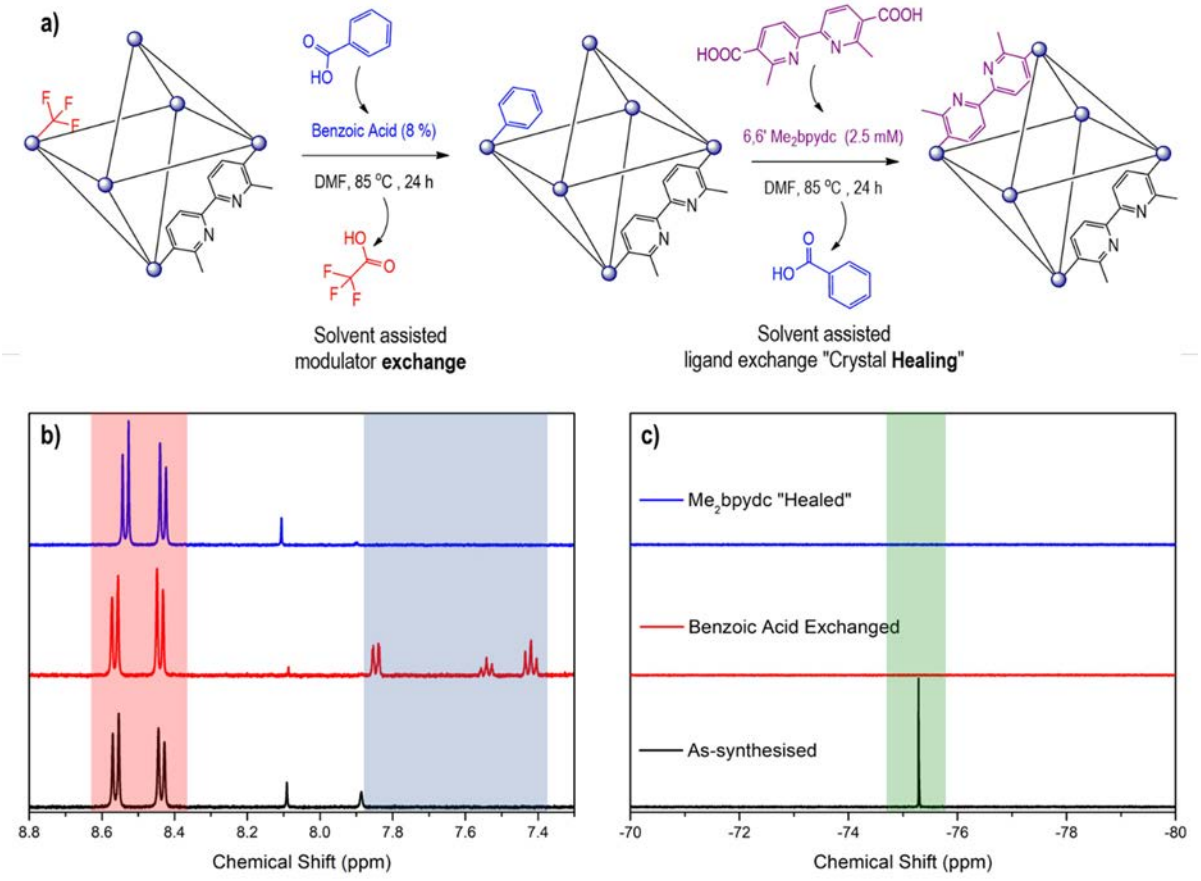

Figure **5.4**: a) Schematic of modulator exchange and "healing" protocols for **1-Me$_2$** to minimise ligand defects and stacked b) ^{1}H and c) ^{19}F NMR of as-synthesised, benzoic acid exchanged and "healed" MOF demonstrating the extent of modulator exchange and removal during exchange and "healing" processes'. H$_2$bpydc, benzoic acid and trifluoroacetic acid NMR chemical shifts are highlighted by red, blue, and green shaded regions respectively.

The ligand defects in **1-Me$_2$** were removed using solvent assisted ligand exchange (SALE) to reintroduce Me$_2$bpydc back into the framework to displace the coordinated benzoic acid modulators, as described in Chapter 4 and in Figure **5.4**.[32] The modulator exchange and "healing" processes were followed by ^{1}H and ^{19}F NMR spectroscopy of washed and digested samples of **1-Me$_2$**, as shown in Figure **5.4**. Exchanging TFA with excess benzoic acid removed TFA from the MOF, and the subsequent incorporation of the ligand results in a material absent of any modulators, quantified in Table **5.A.1**. The benzoic acid exchanged and Me$_2$bpydc "healed" materials were found to be isomorphous by PXRD, matching the powder pattern of as-synthesised **1-Me$_2$** (see Appendix **5.9.2**, Figure **5.A.2**). The NMR spectroscopy data suggests that the ligand defects within the framework have been healed, but for confirmation

surface area analysis of the materials at each step in the modulator exchange and healing process was completed.

N_2 77 K adsorption isotherms for as-synthesised, BA-exchanged and healed single crystal samples of **1-Me$_2$** were collected post-activation from acetonitrile (see experimental section **5.7.4**). The N_2 77 K isotherms for all samples exhibited Type 1 characteristics with high uptake at low pressure, indicating that all of the samples are microporous (see Figure **5.5**).[36] The total uptake of N_2 increased slightly going from the as-synthesised, BA-exchanged and healed samples of **1-Me$_2$**, with corresponding BET surface areas of 2061 ± 7, 2073 ± 3 and 2269 ± 4 m^2/g (see Figure **5.5**). Additionally, the pore size distribution (calculated via DFT N_2 model) in Figure **5.5** shows a subtle shift decrease in the average pore size with each step in the modulator exchange and healing processes. These results suggest that Me$_2$bpydc has been successfully incorporated into the framework of the single crystals at the sites of missing ligand defects, increasing ligand occupancy and thereby increasing the internal surface area and decreasing the average pore size. Additionally, these results mirror ligand re-incorporation results for UiO-67-bpdc and UiO-67-bpydc, as seen in Chapter 4, indicating that for the UiO-67 series the quality of as-synthesised crystals (i.e. ligand occupancy and defect removal) can be improved through aforementioned post-synthetic procedures. The Me$_2$bpydc healed single crystals of **1-Me$_2$** meet the aforementioned criteria for SCXRD analysis due to large average crystal size and high ligand occupancy.

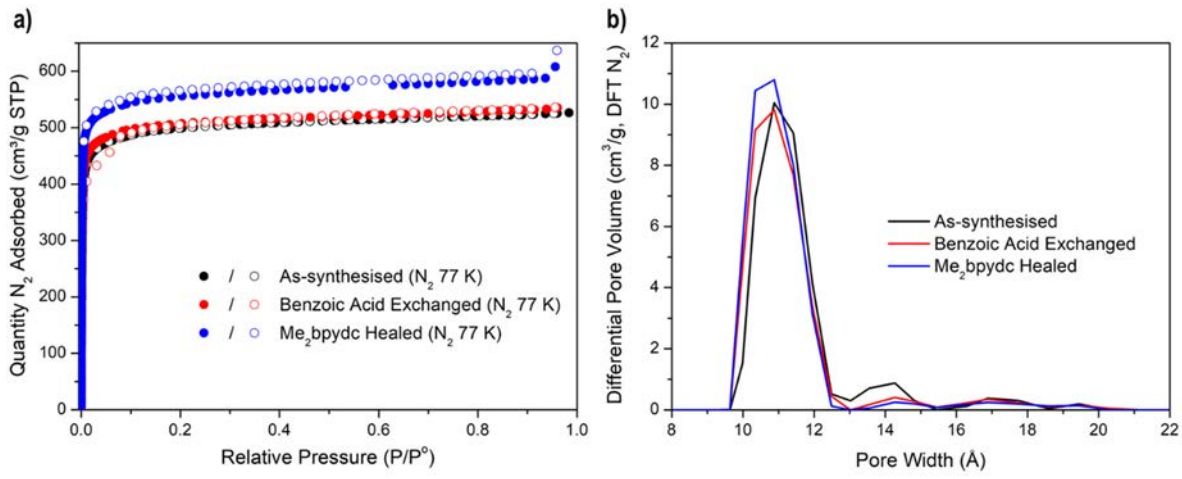

Figure **5.5**: a) 77 K N_2 adsorption isotherms and b) pore-size distributions of **1-Me$_2$** as-synthesised (black), benzoic acid exchanged (red) and healed with Me$_2$bpydc (blue).

5.3. Crystal Structure of UiO-67-Me$_2$bpydc

Structure solution through X-ray crystallography can enable unambiguous structural determination of ordered motifs in crystalline matrices.[37] Single crystals **1-Me$_2$** post-Me$_2$bpydc healing were analysed via SCXRD. **1-Me$_2$** crystallises in the cubic space group *Fm-3*, consisting of a face-centred cubic array of $Zr_6O_4(OH)_4$ clusters bridged by the linear Me$_2$bpydc linkers generating the *fcu* topology (see Figure **5.6**). The asymmetric unit contains half of the Me$_2$bpydc ligand disordered over two positions (refined at 50% occupancy), one zirconium (IV) centre and one oxygen which occupies a special position with a split occupancy between μ_3-O and μ_3-OH groups, see Figure **5.A.5**. The formula for **1-Me$_2$** as refined is $Zr_6O_4(OH)_4$(Me$_2$bpydc)$_6$. **1-Me$_2$** is isostructural with other UiO-67 variants, which crystallise in the cubic space group, *Fm-3m*.[38-39]

Structural refinement of **1-Me$_2$** was complicated by disorder of solvent molecules within the pores of the framework and ligand disorder. The pores of the framework contained badly disordered solvent molecules (CH_3CN) and consequently the associated electron density was removed using the SQUEEZE routine of Platon prior to final structural refinement. The ligand disorder observed is due to the rotatable C-C bond between pyridine rings in the ligand but restricted by the connectivity of the framework and the conjugation of the carboxypyridyl moiety. Due to the disorder of the ligand, it was refined over two positions with each ring restrained using the FLAT command. Chemically sensible refinement of the methyl groups was difficult, which were restrained using DFIX commands. There are two mirror planes associated with the ligand, one is co-planar with the ligand and the other is orthogonal to the ligand, bisecting the C-C bond between the pyridine rings. The position of methyl group assigned to one half of the ligand was refined to be out of plane with respect to the pyridine ring and the co-planar mirror plane, hence two methyl groups are observed for the ligand when the full structure is generated from the asymmetric unit using symmetry elements. It is noteworthy that the methyl groups in Me$_2$bpydc align in a para orientation, minimising steric hindrance within the structure (see Figure **5.6**).

The structure of **1-Me$_2$** is similar to all UiO-67 variants, containing the same network topology and zirconium nodes. Each zirconium node in the structure is constructed from six eight coordinate Zr(IV) atoms, each coordinated by eight O atoms in a square-antiprismatic geometry. One square face of the zirconium-oxygen square-antiprism consists of alternating μ_3-O and μ_3-OH groups, whilst the second square face consists of oxygens supplied by bridging the carboxylic acid groups of the ligand. The resulting Zr-oxo cluster, as shown in Figure **5.4**,

is a 12 coordinate SBU with the formula $Zr_6O_4(OH)_4(CO_2)_{12}$ (where CO_2 represents a coordinating carboxylic acid group). Due to the 12 coordinate nature of the Zr-oxo cluster, each node is connected to 12 half ligands, as such the empirical formula features six full ligands (see above). The Zr-oxo nodes are interconnected by the ligand, Me_2bpydc, forming a network with an octahedral cage which is capped at each face by a tetrahedral cage. The methyl substituents point into both the tetrahedral and octahedral cages of the framework, with one half of the pointing into the tetrahedral cage and other into the octahedral cage due to the anti-orientation of the ligand. This feature reduces the pore size of **1-Me$_2$** relative to **1**, which was also observed for the isoreticular UiO-67 framework featuring a similar methyl substituted ligand, 3,3′-dimethylbiphenyl-4,4′-dicarboxylic acid (Me_2bdc).[40]

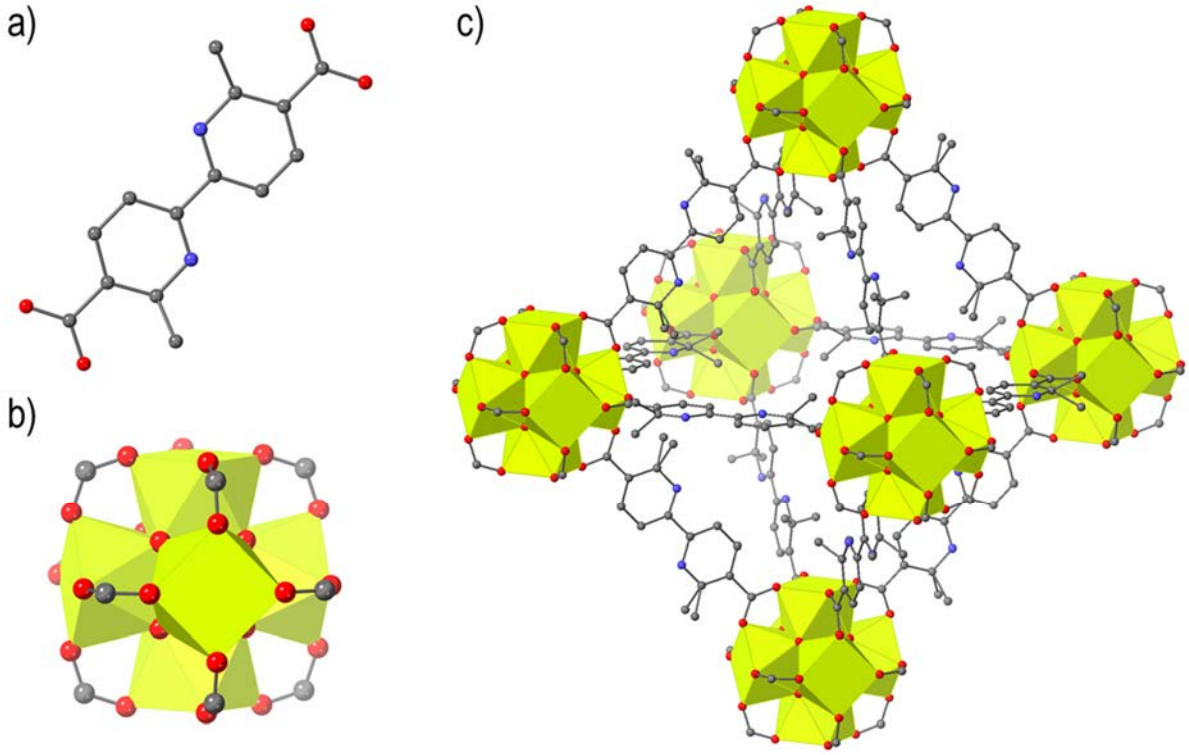

Figure **5.6**: Structure of a) Me_2bpydc^{2-} ligands, b) the octahedral $Zr_6O_4(OH)_6$ inorganic nodes and c) a portion of the crystal structure of **1-Me$_2$** as determined by analysis of single-crystal X-ray diffraction data. The Me_2bpydc^{2-} ligand was modelled as being disordered over two positions but is represented here in one of the possible orientations. Zr, O, N and C atoms are represented by yellow coordination polyhedral, red, blue, and grey spheres respectively; H atoms were omitted for clarity.

5.4. Post-synthetic Metalation of UiO-67-Me$_2$bpydc

1-Me$_2$ has slightly smaller triangular pore apertures than **1**, 7.7 and 8.3 Å respectively,[38] and the chelating moiety Me$_2$bpydc is more electron donating than bpydc; therefore, it is likely that the conditions for metalation will differ. Additionally, the methyl substituents of Me$_2$bpydc provides additional steric bulk in plane with the bipyridine chelating site, which may limit the types of metal complexes that can coordinate to the framework. As such, a broad range of transition metal complexes, with different geometries and coordinated ligands, were examined under a variety of synthetic conditions for the metalation of **1-Me$_2$**, see Table **5.1**. Metal halides and nitrates were initially investigated because it was expected that the relatively small, solvated metal species would be able to easily diffuse into the pores of the framework.[14] Additionally, the reaction with bulkier and potentially catalytically active species were also investigated, including [RhCODCl]$_2$ and Pd(COD)Cl$_2$, as summarised in Table **5.1**.

The solvent stability of **1-Me$_2$** was first assessed by exposing the crystals to the metalation solvents (MeCN, MeCN/EtOH and MeCN/DMF) at 65 ºC for 7 days. The samples were exchanged with distilled MeCN four times and their crystallinity was analysed via PXRD (see Appendix **5.9.4** Figure **5.A.3**). **1-Me$_2$** demonstrated no reduction in crystallinity upon solvation in MeCN, MeCN/EtOH or MeCN/DMF, hence post-synthetic metalation in using these solvent systems was attempted. Post-synthetic metalation was attempted by treating batches of single crystals of **1-Me$_2$** with metal salt solutions (solvents: MeCN, MeCN/EtOH and MeCN/DMF) at varied temperatures (65-80 ºC) for 2-14 days (see experimental section **5.7.3**). Following the reaction, the crystals were washed with distilled acetonitrile four times and analysed via SEM/EDX to ascertain metalation. Similar to **1**, **1-Me$_2$** has a 1:1 ratio of ligand to Zr, hence full occupation of bipyridine sites would be denoted by a 1:1 ratio of Zr : M^{n+} via EDX, this data was summarised in Table **5.1**.[14, 25]

Several interesting trends arose upon analysis of PSMet **1-Me$_2$** samples via SEM/EDX. Small metal halides, including $CoCl_2 \cdot 6(H_2O)$ and $ZnCl_2 \cdot 4(H_2O)$, demonstrated the highest occupancies, with increasing reaction times resulting in greater than 100% occupancy, possibly resulting from the further coordination of metal halides within the pores, as has been recently reported by Gonzalez *et al*.[41] Gonzalez *et. al.* were able to demonstrate the growth of metal halide sheets within the pores of **1**, with $CoCl_2 \cdot 6(H_2O)$, $NiCl_2 \cdot 6(H_2O)$, $FeCl_2 \cdot 4(H_2O)$ and $NiBr_2 \cdot 3(H_2O)$, when using excess metal salt relative to bipyridine moieties in the framework and extended reaction times (>1 month).[41] Subsequently, PSMet with $NiCl_2$ was also examined; $NiCl_2 \cdot 6(H_2O)$ was not particularly soluble in MeCN, hence alternate solvent

conditions were tested, with the highest metal uptake occurring in MeCN/EtOH, producing pale pink crystals. Additionally, high occupancies of metal nitrates could be also be achieved with longer reaction times for $Co(NO_3)_2 \cdot 6(H_2O)$ and $Cu(NO_3)_2 \cdot 6(H_2O)$, 128% occupancy for both samples. PSMet with potentially catalytically active species was more challenging. The square planar palladium complexes required more forcing conditions (higher temperature) than other complexes, which increased the metal occupancies in the framework to approximately 100% for $PdCl_2$ and $Pd(MeCN)_2Cl_2$. **1-Me$_2$** demonstrated limited uptake of the bulky cyclo-octadiene complexes $Pd(COD)Cl_2$ or $[RhCODCl]_2$, due to reduced space within the pores from the methyl substituents of Me_2bpydc which point into the pores of the framework. Unlike **1**, **1-Me$_2$** did not coordinate rhodium complexes readily, due to either the increased steric bulk or the more electron donating nature of Me_2bpydc relative to bpydc, which would favour more electron deficient complexes.

All of the metalated species which had high levels of PSMet (100% within error) were examined via SCXRD to see if structural ordering arose, as was observed for PSMet UiO-67.[14] For these examples where structural determination was possible, the coordination environment of the coordinated metal was determined. Although many iterations of **1-Me$_2$**$\cdot M^{n+}$ (UiO-67-Me_2bpydc metalated with a transition metal denoted M^{n+}) were examined via SCXRD, only two structures could be solved, with the other samples being either ambigous, weakly diffracting and/or suffering from signifcant amounts of disorder of the ligand and/or chelating site. Single crystal structures were obtained for **1-Me$_2$** metalated with $CoCl_2$ and $ZnCl_2$ (**1-Me$_2$**$\cdot CoCl_2$ and **1-Me$_2$**$\cdot ZnCl_2$ respectively).

Table **5.1**: Summary of metalation conditions attempted with **1-Me$_2$**, with the EDX Zr:M^{n+} ratio displayed as the percent occupancy of chelating sites in the framework.

Metal Salt	Typical coordination geometry (CSD)[a]	Solvent	Temp (°C)	Time (d)	Crystal Colour	Zr : M^{n+} (SEM/EDX)
$CoCl_2 \cdot 6(H_2O)$	Td[42]	MeCN	65	2 7 14	Blue	92.9 ± 3.4 100.0 ± 5.0 146.6 ± 5.9
$ZnCl_2 \cdot 4(H_2O)$	Td[43-44]	MeCN	65	7 14	Colourless	114.7 ± 7.8 112.3 ± 3.6
$NiCl_2 \cdot 6(H_2O)$	Td,[45] Oh[46]	DMF MeCN/DMF MeCN/EtOH	65	7	Green Green Pale pink	77.8 ± 12.2 28.2 ± 6.1 106.7 ± 9.2
$FeCl_2 \cdot 4(H_2O)$	Td/Oh[47]	MeCN MeCN/EtOH	65	7 14	Red/Orange	170.3 ± 12.4 113.3 ± 3.3
$CuCl_2 \cdot 6(H_2O)$	Td/Sp[14]	MeCN	65	7 14	Yellow	113.0 ± 4.6 88.3 ± 5.0
$CdCl_2 \cdot (H_2O)$	Td[48]	MeCN	65	7	Colourless	85.9 ± 3.0
$MnCl_2 \cdot 4(H_2O)$	Oh[49-50]	MeCN	65	7	Colourless	71.1 ± 8.1
$PdCl_2$	Sp[51]	MeCN	65 80	2	Red	61.2 ± 0.7 106.9 ± 1.6
$Co(NO_3)_2 \cdot 6(H_2O)$	D_{5h}[52]	MeCN	65	7 14	Pale pink	102.0 ± 2.1 128.0 ± 13.1
$Zn(NO_3)_2 \cdot 6(H_2O)$	Oh[53]	MeCN	65	2	Colourless	85.2 ± 7.7
$Cu(NO_3)_2 \cdot 6(H_2O)$	Oh[54]	MeCN	65	2 7 14	Green	58.5 ± 9.1 104.9 ± 7.5 128.0 ± 13.1
$[RhCOCl]_2$	-	MeCN	65	2	Light red	72.5 ± 5.25
$[Rh(COD)Cl]_2$	-	MeCN	65	2	Light orange	25.6 ± 1.4
$Pd(COD)Cl_2$	Sp[51]	MeCN	65 80	2	Light orange	26.0 ± 0.8 30.4 ± 1.2
$Pd(MeCN)_2Cl_2$	Sp[51]	MeCN	65 80	2	Red	48.4 ± 1.7 105.2 ± 4.3

[a]CSD = Cambridge Structural Database, used to determine typical coordination environments of the transition metal complexes with either a 2,2'-bipyridyl or 6,6'dimethyl-2,2'bipyridyl moiety, when no structures were reported this was denoted by a dash (-). Sp = Square planar, Td = Tetrahedral, Oh = Octahedral, D_{5h} = Pentagonal bipyramidal.

1-Me$_2$·$CoCl_2$ and **1-Me$_2$**·$ZnCl_2$ under go SC-SC transformations upon PSMet from **1-Me$_2$**; both structures were solved in the primitive cubic space group *Pa-3*. Both structures are comprised of a cubic array of $Zr_6O_4(OH)_4$ clusters bridged by Me_2bpydc linkers, which are bent to accommodate the chelation of $CoCl_2$/$ZnCl_2$ at the bipyridine site of the linker. The asymetric units contain one Me_2bpydc ligand, one cobalt/zinc (II) centre, two chloride atoms, one zirconium (IV) centre, one oxygen with a split occupancy (μ_3-O/μ_3-OH, 38.8/61.1%) and another oxygen on a special position with split occupancy (μ_3-O/μ_3-OH, 83.3/16.6%), see Appendix **5.9.5**, Figures **5.A.6** and **5.A.7**. The formulas of **1-Me$_2$**·$CoCl_2$ and **1-Me$_2$**·$ZnCl_2$ as refined are $Zr_6O_4(OH)_4(Me_2bpydc)_6(CoCl_2)_6$ and $Zr_6O_4(OH)_4(Me_2bpydc)_6(ZnCl_2)_6$ respectively. There was electron density detected in the pores of both the frameworks, but the solvent acetonitrile molecules could not be assigned due to disorder. As such, the electron density associated with the non-structural acetonitrile molecules was removed using the SQUEEZE routine of Platon prior to final structure refinement of both **1-Me$_2$**·$CoCl_2$ and **1-Me$_2$**·$ZnCl_2$.

As noted, analysis of **1-Me$_2$**·$CoCl_2$ and **1-Me$_2$**·$ZnCl_2$ revealed a decrease in the local site symmetry of the framework *Fm-3* to *Pa-3* upon PSMet. This shift mirrors the change in symmetry which arises from metalating UiO-67-bpydc, which lowers in symmetry from *Fm-3m* to *Pa-3*.[14] The metalated 6,6'-dimethyl-2,2-bipyridine entities are crystallographically ordered, enabling structural determination of the coordination environments of metal complexes within the framework. The lowering of symmetry arises from the ordering of the metalated ligands, a simplified comparison of **1-Me$_2$** and **1-Me$_2$**·$CoCl_2$ is shown in Figure **5.7**. The non-metalated framework exhibits mirror symmetry along the diagonals of its unit cell and face-centring translations that relate the zirconium clusters at the ends of each linker. In the metalated structure, that mirror symmetry is removed by the ordering of the ligands, while the face centring is lost as the clusters at the ends of each linker are tilted in opposite directions. The 6,6'-dimethyl-2,2-bipyridine unit distorts in order to chelate the metal, and it has been postulated that such distortions of 2,2-bipyridine ligands serves to facilitate better orbital overlap with the metal (see Figure **5.7**).[14] The Zr-oxo clusters consequently rotate slightly to accommodate the arching of the ligand and accordingly the ligands around each cluster become orientated to conform to the direction of cluster rotation. These changes from the parent framework **1-Me$_2$** facilitate structure determination of the metal-ligand complexes because they go from a site with two mirror planes in *Fm-3* to a site with no symmetry in *Pa-*

3. This is the second known reporting of this phenomenon in a MOF, the first being by Gonzalez *et al*.,[14] albeit in a closely related MOF.

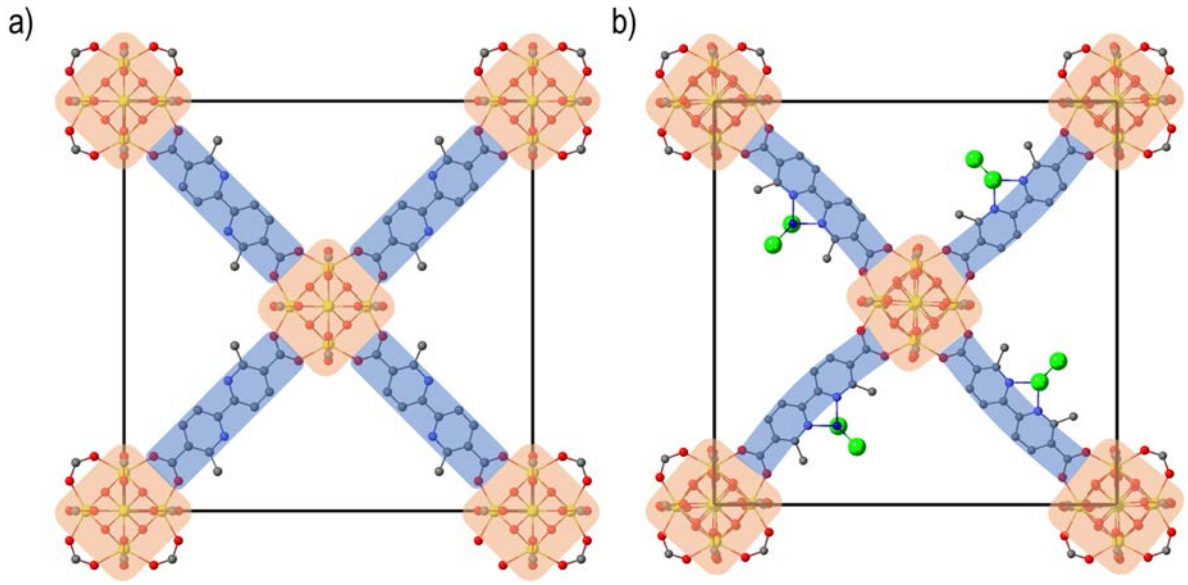

Figure **5.7**: Comparison of the structures of a) **1-Me$_2$** and b) **1-Me$_2$**·$CoCl_2$ viewed along the [100] direction; the unit cell edges are shown as black lines, with Zr-oxo nodes and linkers highlighted in red and blue respectively.

The structure of **1-Me$_2$**·$CoCl_2$ was reasonably well ordered, which enabled measurement of the interatomic distances and angles for Co(Me$_2$bpydc)Cl_2 units, (different representations of the crystal structure are shown in Figure **5.8**). The Co(II) centres are four coordinate, arranged in a distorted tetrahedral geometry. The Co-N distances of 2.022(10) and 2.040(9) Å, Co-Cl bond distances of 2.214(5) and 2.231(6) Å and N-Co-N and Cl-Co-Cl bond angles of 82.5(4) and 118.3(2)º in the complex match closely to analogous molecular complex Co(Me$_2$bpy)Cl_2 (Me$_2$bpy = 6,6'dimethyl-2,2'bipyridine).[42, 55] The distorted tetrahedral geometry of Co(Me$_2$bpydc)Cl_2 units arises from the steric repulsion between chloride ligands and the methyl groups from Me$_2$bpydc, forcing the Cl-Co-Cl plane to be perpendicular to the N-Co-N plane. This geometry has been observed for the equilavent discrete Co(Me$_2$bpy)Cl_2 complex.[42, 55] The pyridine rings are rotated 24.55 and 161.55º out of plane with the O-C-O plane the carboylic acid groups on either side of Me$_2$bpydc. In comparison, the pyridine rings in the parent framework both lie in plane with the carboxylic acid groups, with torsional angles of 0º.

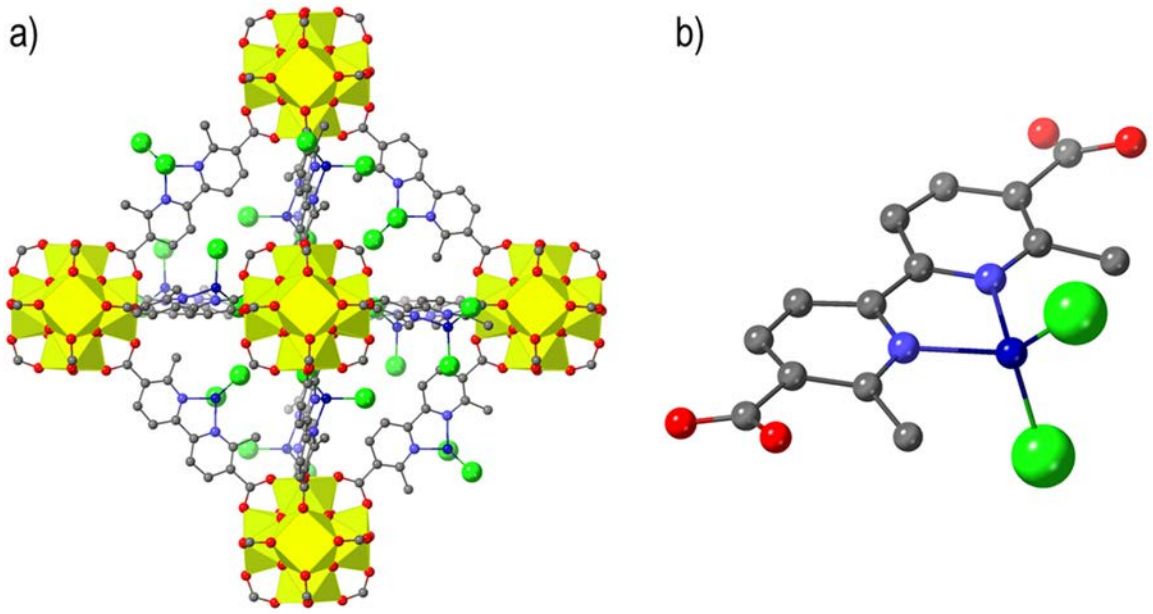

Figure **5.8**: a) A representation of a portion of the crystal structure of **1-Me$_2$**·$CoCl_2$ viewed along the a-axis and b) the structure of the 6,6'-dimethyl-2,2'-bipyridine metal entity in **1-Me$_2$**·$CoCl_2$, with Zr(IV), O, N, C, Co(II) and Cl atoms represented by yellow polyhedra and red, light blue, grey, dark blue and green spheres.

The ordering of Co(Me$_2$bpydc)Cl_2 units in **1-Me$_2$**·$CoCl_2$ results in some interesting packing effects within the octahedral and tetrahedral pores of the framework. In the octahedral pore, the interatomic distance between two chorides pointing into the centre of the pore associated with two different $CoCl_2$ moieties is 5.46 Å. In two of the octahedral pore windows there are three $CoCl_2$ moieties arranged in the aforementioned alignment, and consequently the interatomic distace across the octahedral pore is 10.89 Å (Cl-Cl). In the other octahedral pore windows $CoCl_2$ moieties are rotated relative to one another, so as to point into the tetrahedral pores with inter atomic Cl-Cl distances of 5.98 Å. As a result, for each octahedral pore there are six chloride atoms pointed towards the centre of the pore, and each tetrahedral pore contains three chloride atoms pointed towards the centre of that pore.

Similar to **1-Me$_2$**·$CoCl_2$, metalation of the bipyridine site in **1-Me$_2$**·$ZnCl_2$ allows for crystallographic determination of the Zn coordination environment (see Figure **5.9**). The Zn(Me$_2$bpydc)Cl_2 units adopt a distorted tetrahedral geometry, with the Zn(II) centres being four coordinate, chelated by N-donors of Me$_2$bpydc and coordinated to two Cl^- ligands. The Cl-Zn-Cl plane is rotated perpendicular to the N-Zn-N plane, arising from steric repulsion from the methyl groups of the chelating ligand. The Zn-N distances of 2.050(9) an 2.059(10) Å and Zn-Cl distances of 2.203(4) and 2.245(5) Å and N-Zn-N and Cl-Zn-Cl bond angles of 81.3(4)

and 120.25(17)º in the complex are consitent with analogous molecular complexes $Zn(Me_2bpy)Cl_2$ and $Zn(bpy)Cl_2$ (bpy = 2,2'bipyridine).[43-44] The $Zn(Me_2bpydc)Cl_2$ units are rotated 24.22 and 160.70º out of plane with the O-C-O plane the carboylic acid groups on either side of Me_2bpydc in a similar manner to the $Co(Me_2bpydc)Cl_2$ units in **1-Me$_2$**·$CoCl_2$. There is residual electron density close to the Zn(II) centre, however, which may indicate an alternate arrangement of the $Zn(Me_2bpydc)Cl_2$ moiety or a possible five coordinate geometry for a portion of the Zn(II) sites. Unfortunately, the low occupancy of this component in comparision to the major $Zn(Me_2bpydc)Cl_2$ moiety prevented a sensible model from being developed and refined.

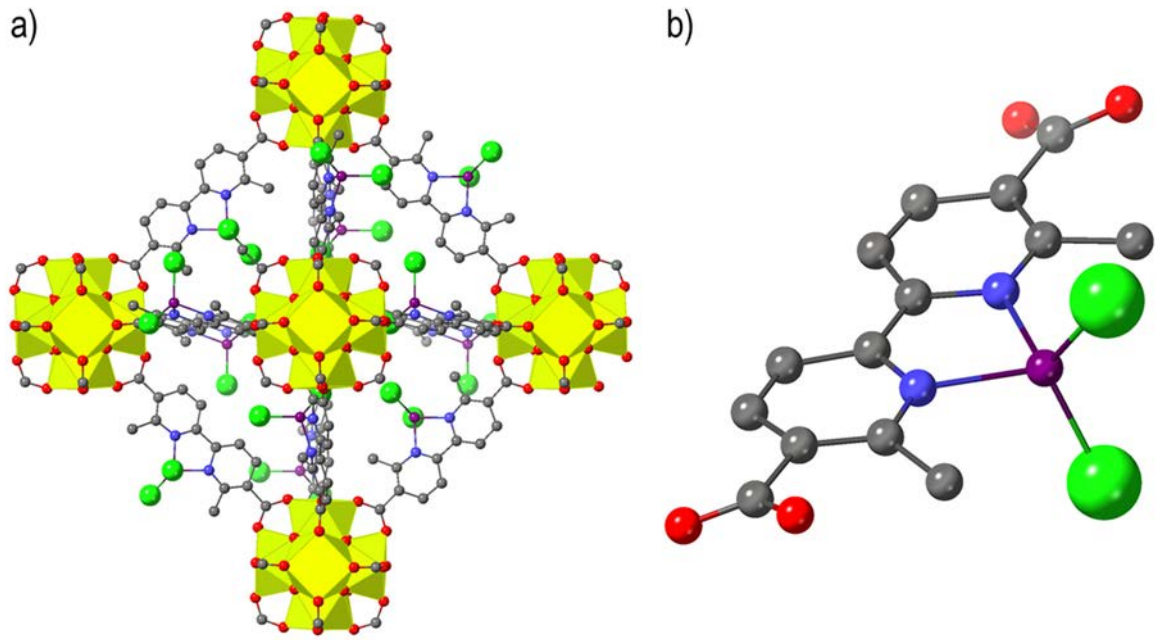

Figure **5.9**: a) A representation of a portion of the crystal structure of **1-Me$_2$**·$ZnCl_2$ viewed along the a-axis and b) the structure of the 6,6'-dimethyl-2,2'-bipyridine metal entity in **1-Me$_2$**·$ZnCl_2$, with Zr(IV), O, N, C, Zn(II) and Cl atoms represented by yellow polyhedra and red, light blue, grey, purple and green spheres.

Structural determination of the metal coordination environments in **1-Me$_2$**·$CoCl_2$ and **1-Me$_2$**·$ZnCl_2$ was made possible due to the ordering of ligands within the structure, causing a symmetry transition from a face-centred cubic to a primative cubic space group; but this was not the case for **1-Me$_2$** metalated with other transition metals. In UiO-67-bpydc this symmetry transition upon metalation corresponds to a contraction of the unit cell from a = 26.520(2) Å to 26.255(4) – 26.020(5) Å depending on the transition metal.[14] The unit cell contraction for **1-Me$_2$** is almost non-existent reducing from a = 26.615(3) Å to a = 26.597(3) and 26.609(3) Å

for **1-Me$_2$**·$CoCl_2$ and **1-Me$_2$**·$ZnCl_2$ respectively, suggesting that there is limited space within the pores for a large unitcell contraction. The atomic coordinates of $Zr_6O_4(OH)_4$ nodes of **1-Me$_2$**·$CoCl_2$ and **1-Me$_2$**·$ZnCl_2$ are not perturbed significantly from the non-metalated framework, meaning that when collecting SCXRD data the positions of high electron density within the frameworks are very similar. This similarity is highlighted by the near identical powder diffraction patterns of **1-Me$_2$**, **1-Me$_2$**·$CoCl_2$ and **1-Me$_2$**·$ZnCl_2$ in the low angle 2θ region, see Figure **5.A.4**.

All of the SCXRD experiments were conducted at the Australian Synchrotron on the quantitatively metalated samples. Unfortunately, due to the strong diffraction of the Zr-oxo node and the lack of distinct structural differences (minimal unit-cell contraction) between the metalated and non-metalated frameworks, the assignment of the correct, lower symmetry during crystal screening routines and auto-processing did not occur. This precluded direct structure solution in the expected lower symmetry space groups, as seen for **1-Me$_2$**·$CoCl_2$ and **1-Me$_2$**·$ZnCl_2$. As such, attempts were made to re-process the raw diffraction images collected from SCXRD experiments at the Australian Synchrotron, in order to increase the data redundancy and so enable structure solution in the expected lower symmetry space groups. Unfortunately, due to the current detectors in use on both the MX1 and MX2 beamlines, there is no current way to process the raw diffraction image files without proprietary software, which was inaccessible in the timeframe of this project. These methodology problems were further exacerbated by poor crystal quality, lower than 100 % occupation of the bipyridine moieties and lack of ordering of 6,6'-dimethyl-2,2'-bipyridine complexes within the framework. As such, all further analysis focuses on the two structures which could be solved, **1-Me$_2$**·$CoCl_2$ and **1-Me$_2$**·$ZnCl_2$.

The distortions observed for **1-Me$_2$**·$CoCl_2$ and **1-Me$_2$**·$ZnCl_2$ suggested that the complexes could be susceptible to leaching, which could occur in steps where the crystals are washed or undergo further reactions. As such, a leaching study was undertaken with **1-Me$_2$**·$CoCl_2$ in MeCN in order to investigate whether the Co(II) ion could be displaced during simple manipulations like washing the crystals. Additionally, a structurally flexible MOF, also metalated with $CoCl_2$, was investigated under the same conditions to provide a point of reference. The flexible framework utilised was a Mn(II) based framework (**Mn-MOF-1**) with a flexible bis(pyrazolyl)methane ligand bis(4-(4′-carboxyphenyl)-3,5-dimethyl-pyrazolyl)methane, which chelates metals at its bis-pyrazolyl moieties.[12, 16] Both materials were metalated with $CoCl_2·6(H_2O)$, solvent exchanged four times and left to soak in MeCN

(**1-Me$_2$**·$CoCl_2$ and **MnMOF-1**·$CoCl_2$) and in MeOH (**MnMOF-1**·$CoCl_2$). Aliquots of the crystalline samples were examined each day for a week via SEM/EDX (post solvent exchange ×4 to remove metal from the pores, see Figure **5.10**). Since the leaching studies were done in organic solvents ICP-MS and AAS could not be used to analysed the metal concentrations in solution accurately, and the study could not be performed under aqueous conditions because the UiO-67 series of MOFs are not sufficiently water stable.

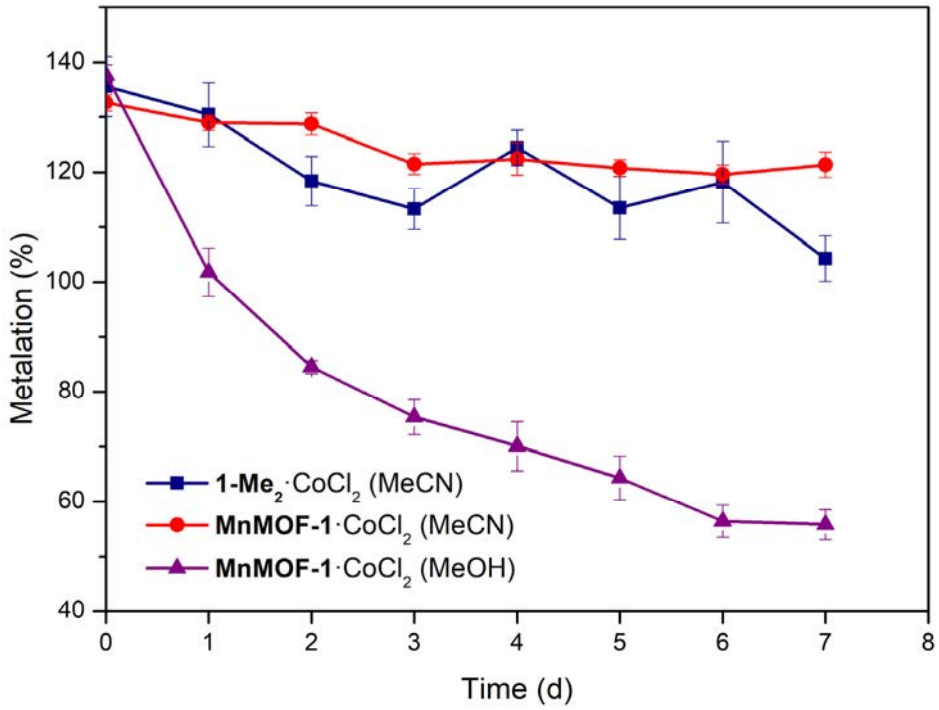

Figure **5.10**: Leaching of $CoCl_2$ from **1-Me$_2$**·$CoCl_2$ in MeCN and **MnMOF-1**·$CoCl_2$ in MeOH and MeCN.

1-Me$_2$·$CoCl_2$ and **MnMOF-1**·$CoCl_2$ in MeCN show minimal loss of $CoCl_2$ by SEM/EDX, decreasing by 31 and 11% from their starting occupancies respectively after 7 days in MeCN. All three samples had greater than 100% metalation initially, determined by EDX comparing Co to Zr or Mn for **1-Me$_2$**·$CoCl_2$ and **MnMOF-1**·$CoCl_2$ respectively. As previously discussed, **1-Me$_2$**·$CoCl_2$ has a 1:1 of Zr to Me_2bpydc so 100% occupation is observed as a 1:1 ratio of Co:Zr, whereas **MnMOF-1** has a 3:1 ratio of Mn to vacant chelating sites hence 100% occupation is represented by a 3:1 ratio of Mn:Co.[12, 16] Greater than 100% metalation is indicative of excess metal salt in the pores of the framework, if the coordinated $CoCl_2$ is bound tightly to the chelating sites, the metalation should overtime trend towards 100% and not below this value. This trend was observed for **1-Me$_2$**·$CoCl_2$ after 7 days in MeCN, **MnMOF-1**·$CoCl_2$ in MeCN decreased by a much smaller amount, but this could be due to the presence of a

solvated octahedral Co(II) complex which can be retained in the pores of the framework, as reported by Huxley *et al.*[16] Interestingly, when soaked in MeOH there is significant leaching of Co(II) for **MnMOF-1**·$CoCl_2$ with Co metalation reducing to 55% after 7 days. Note, UiO-67 frameworks are not particularly stable to polar protic solvents, hence leaching studies were not conducted in MeOH for **1-Me$_2$**·$CoCl_2$. These results highlight the need to characterise the stabilty of each metalated MOFs sample/solvent combinatons prior to their use for post-synthetic modifications. Indeed, due to the relative stability of **1-Me$_2$**·$CoCl_2$ in acetonitrile, the chemistry of the Co(II) centre within **1-Me$_2$**·$CoCl_2$ was further investigated by reaction with NaN_3.

5.5. Post-synthetic reactions with 1-Me$_2$·CoCl$_2$

Obtaining crystallographic information of reactive species can be challenging as these species are often short-lived. One such type of short-lived species are metal nitrides, which are highly reactive as potential intermediates in C-H activation reactions.[56-58] Metal nitrides/nitrenoids are metal complexes which feature metal-ligand multiple bonds between a metal and a nitrene, with the M-N multiple bonds and hence reactivity being dictated by the d-electron count of the metal complexes.[58-59] The nitrene ligands of metal nitrides/nitrenoids are highly reactive, especially when complexed to late group transition metals, acting as either electrophiles or nucleophiles depending on the transition metal complex and its oxidation state.[60] As such, there has been a lot of interest in isolating molecular metal nitrides/nitrenoids and studying the photochemistry involved in synthesising them from their azide counterparts via SCXRD.[59, 61-63] Metal nitrides/nitrenoids can be synthesized from the photolysis of metal azide complexes forming N_2 as a by-product; however, their high reactivity usually results in reaction with nearby solvent and or ligand moieties making characterization challenging.[59, 61-63] Powers *et al*. were able to characterize a reactive lattice confined Ru_2 nitride by photocrystallography, directly observing the reactive M-L multiply bonded nitrene and the evolved nitrogen post-photolysis.[59] Additionally, the matrix isolation of an metal nitrenoid formed from the photolysis of an organic azide adduct coordinated to a bulky Rh_2 complex has been shown by Powers *et al*.[63] Isolating species such as these in porous crystalline supports, like MOFs, could enable the characterization of reactive metal nitride species via SCXRD.

MOFs have been used previously to isolate unstable molecular catalysts within MOFs via PSMet and through post-synthetic reactions with the site isolated metal. Zhang *et. al*. were able to coordinate $CoCl_2$ within a Zr-MOF containing 2,2'-bipyridyl moieties and conduct post-synthetic modifications enabling access to the active catalyst (bpy)Co(THF)$_2$ which can be

used for hydrogenation reactions.[64] No direct crystal structures were obtained of the active catalyst in this study due to disorder and incomplete occupation of the chelating site; however, confirmation of the structure was obtained via EXAFS (extended X-ray absorption fine structure).[64] Considering the interest in this area and that **1-Me$_2$**·$CoCl_2$ contains site isolated $CoCl_2$ species in a crystallographically accessible site, post-synthetic reactions with **1-Me$_2$**·$CoCl_2$ were investigated.

Metal azides are commonly encountered in inorganic chemistry, being widely used as sources of N_2 release in airbags of automobiles and as explosives.[65-67] Cobalt has been shown to form stable azide complexes,[68-71] with several examples being stabilised with bipyridine ligands.[72-74] A common method of forming a cobalt azide complexes is to react $CoCl_2 \cdot 6H_2O$ with a methanolic solution of sodium azide (NaN_3).[74] The first step in the isolation of a nitride complex of cobalt(II) in **1-Me$_2$** is to from a stable cobalt azide complex post-synthetically from **1-Me$_2$**·$CoCl_2$; the proposed strategy is outlined in Figure **5.11**.

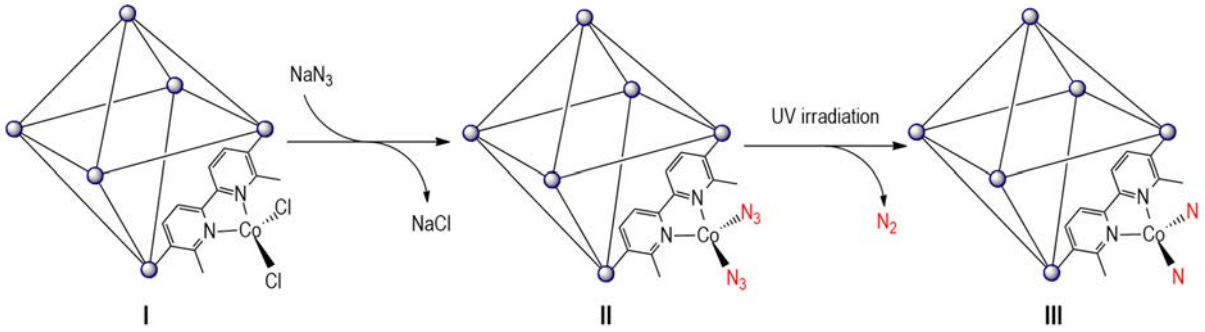

Figure **5.11**: Proposed synthesis of a cobalt azide complex (II) through anion exchange of **1-Me$_2$**·$CoCl_2$ (I) with NaN_3 and proposed photolysis of II to form a reactive cobalt nitride complex (III).

UiO-67 frameworks are not particularly stable to polar protic solvents such as MeOH, hence a range of different solvent conditions were examined for the reaction between NaN_3 and **1-Me$_2$**·$CoCl_2$. Since **1-Me$_2$** is stable in MeCN and a 1:1 MeCN/EtOH mixture (see Appendix **5.9**, Figure **5.A.3**) and minimal leaching was observed for **1-Me$_2$**·$CoCl_2$ in MeCN over 7 days, azide incorporation was tested in EtOH, EtOH/MeCN and MeCN. Additionally, as NaN_3 is not particularly soluble in non-polar protic solvents the presence of EtOH was necessary to adequately solubilise NaN_3. The anion exchange reaction was monitored by IR spectroscopy, to determine whether a Co-azide complex had formed, and via SEM/EDX to determine whether anion exchange of N_3^- for Cl^- had occurred. Initial testing involved slow diffusion of NaN_3 into **1-Me$_2$**·$CoCl_2$ in each of the solvents for three days, see experimental

section **5.7** for further details. There was a distinct colour change for crystals **1-Me$_2$**·$CoCl_2$, from dark blue to green/yellow in EtOH/MeCN and EtOH after 3 days of anion exchange with NaN_3, but no colour change in MeCN. IR spectroscopy revealed the successful incorporation of N_3^- into **1-Me$_2$**·$CoCl_2$ in EtOH and EtOH/MeCN, from the strong azide antisymmetric stretch at 2066 cm^{-1} indicating the presence of monodentate azide complexed to Co in **1-Me$_2$**·$CoCl_2$ (see Figure **5.12**).[75-76] There was no observable azide antisymmetric stretch when anion exchange was attempted in MeCN, which was either due to the poor solubility of NaN_3 in MeCN or that a polar protic solvent was necessary to facilitate the anion exchange. The azide-chloride exchange was checked after 14 d in EtOH/MeCN and a slightly diminished azide band was detected via IR spectroscopy (see Figure **5.12**), indicating the potential leaching of Co(II). As IR spectroscopy of the anion exchanged samples only provides a qualitative measure of Co-azide formation, the samples were analysed via SEM/EDX.

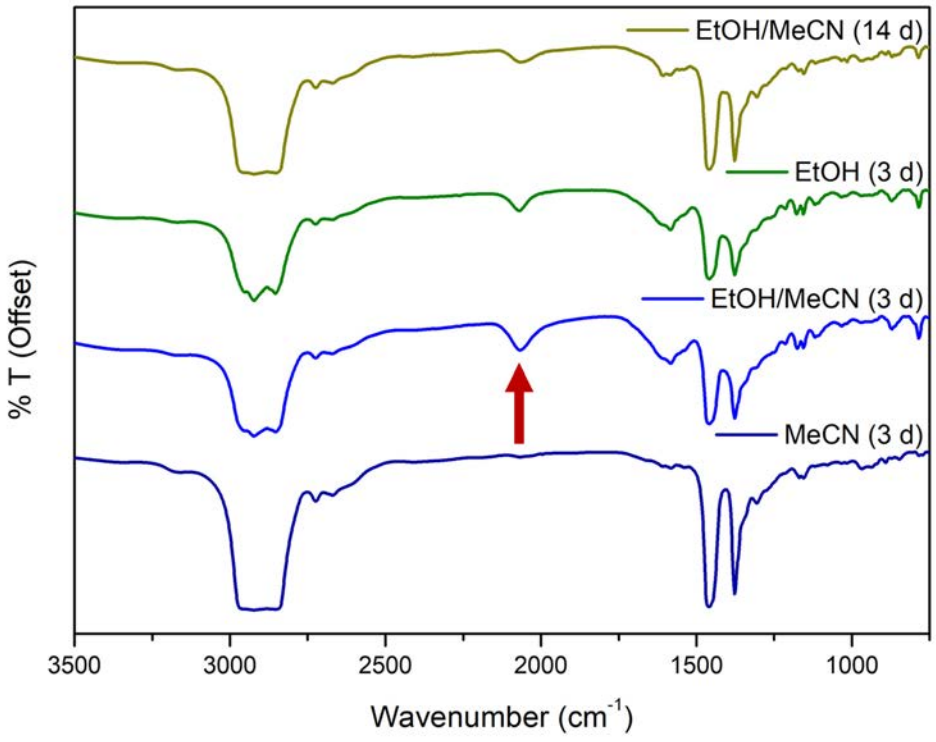

Figure **5.12**: IR spectra of dried samples of **1-Me$_2$**·$CoCl_2$ after anion exchange with NaN_3 in MeCN (3 d, royal blue), EtOH/MeCN (3 and 14 d, blue and gold) and EtOH (3 d, green), with the presence of an azide stretch at 2066 cm^{-1} indicated by the red arrow.

SEM/EDX enabled direct quantification of chloride; if exchange has occurred it is expected that the amount of Cl^- would decrease relative to both Co and Zr. Furthermore, the Co:Zr ratio should show that the Co(II) centre is not being displaced from the MOF. The previously mentioned samples were examined via SEM/EDX along with samples solvated in EtOH, MeOH and MeCN/EtOH for 7 days with NaN_3 (see Figure **5.13**). These additional samples were examined due to the poor solubility of NaN_3 in MeCN, being more easily solubilised in polar protic solvents, facilitating potentially faster anion exchange despite framework instability to such solvents. All of the samples are compared against **1-Me$_2$**·$CoCl_2$ which has Co:Zr and Cl:Co occupancies of 100 ± 5 and 194 ± 8% and accounts for one $CoCl_2$ moiety per ligand/Zr atom in the framework, as expected from SCXRD data. In MeCN, anion exchange does not occur readily, with minimal reduction in Cl:Co ratio, supporting the IR spectroscopy results discussed previously. In MeCN/EtOH anion exchange was successful but slow, with significant Cl presence even after 14 d. Additionally, there was some cobalt leaching observed in MeCN/EtOH, but this was somewhat sample dependent as each of the samples was prepared separately and the 7 d experiments were conducted with a different batch of **1-Me$_2$**·$CoCl_2$ crystals. Three days of anion exchange in MeCN/EtOH produced a sample with an approximate a Zr:Co:Cl ratio of 1.00:1.12:1.26 which could correspond to an "averaged" tetrahedral Co(Me$_2$bpydc)(N_3)Cl complex. Indeed, anion exchange was most successful in EtOH and MeOH after 7 days, with almost all of the Cl removed from the framework, although this also corresponded to a significant amount of leaching of Co with Co:Zr ratios of 51 ± 3 and 35 ± 7% respectively. On the basis of these results, EtOH and MeOH are not ideal solvent systems for anion exchange with **1-Me$_2$**·$CoCl_2$, despite sucessful Cl exchange, because loss of the metal centre would hinder structure determination via SCXRD.

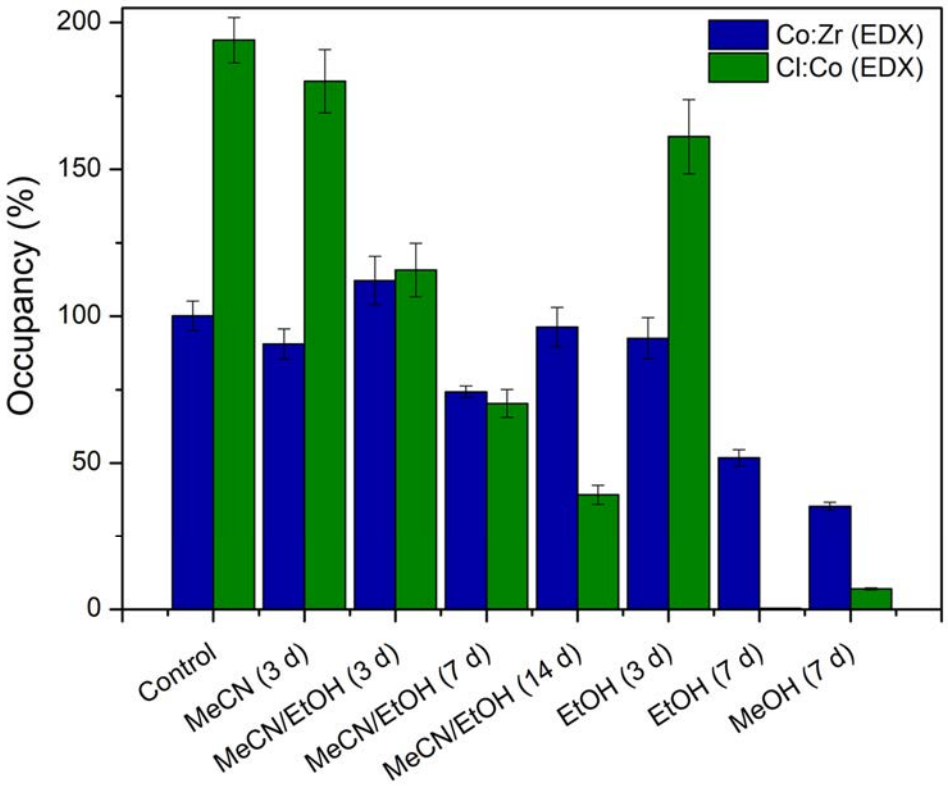

Figure **5.13**: SEM/EDX analysis of anion exchange of **1-Me$_2$**·$CoCl_2$ with NaN_3 in different solvent systems (MeCN, EtOH, MeOH and MeCN/EtOH) for varied time scales (3, 7 and 14 d), the Co:Zr and Cl:Co ratios are plotted as percentage occupancy (ratio × 100) in blue and green respectively.

SCXRD analysis was attempted with samples of **1-Me$_2$**·$CoCl_2$ post-anion exchange with NaN_3, but the data could not be solved. As previously discussed, the challenges associated with data collection and structure solution of samples of **1-Me$_2$**·$CoCl_2$ after PSMet are exacerbated by lower than 100% metalation and ligand disorder at the site of metalation. During anion exchange it is possible for both incomplete anion exchange and cobalt leaching from the framework, as discussed previously see Figure **5.13**, which increases the disorder of the complex and lowers the metal complex occupancy. Unfortunately, without a structure of **1-Me$_2$**·$CoCl_2$ post anion exchange no further progress could be made towards isolating a reactive cobalt-nitride complex within **1-Me$_2$**. The studies described herein further highlights the challenges associated with structure solution of metal complexes in highly symmetric frameworks.

5.6. Summary

In summary, a series of post-synthetically metalated analogues of **1-Me$_2$** have been synthesised and analysed via SCXRD, confirming that **1-Me$_2$** has the capability for matrix isolation of metal complexes. To achieve this, large single defect free X-ray quality crystals of **1-Me$_2$** were synthesised following previously established crystal engineering techniques of modulator use and crystal healing (see Chapter 4). SC-SC transformations were observed upon PSMet of **1-Me$_2$** with both $CoCl_2$ and $ZnCl_2$ (separately), corresponding to a drop in local site-symmetry of the framework *Fm-3* to *Pa-3*, resulting from the ordering of metalated ligand moieties throughout the framework. As such, the lower symmetry enabled structural characterisation of the metal complexes chelated to the ligand, establishing the credentials of **1-Me$_2$** as a suitable framework for the matrix isolation and characterisation of metal complexes. Post synthetic anion exchange with NaN_3 was attempted with **1-Me$_2$**·$CoCl_2$ to attempt structure determination of a reactive cobalt-nitride complex; but, due to incomplete anion exchange and low metal occupancy, no structures were obtained.

To overcome some of these challenges, alternate methods of azide anion exchange could be employed, utilising organic azide anions in non-protic solvents, as it was identified that the alcohol solvents used in the anion exchange reactions resulted in leaching of cobalt from the 2,2'bipyridine site.[77] The organic azide trimethylsilyl azide (TMS-N_3) is soluble in THF, and hence Co-N_3 could be formed in the MOF via the elimination of TMS-Cl potentially without the leaching of cobalt from the framework. Additionally, once the installation and characterisation of a site isolated Co-N_3 complex has been achieved, further chemistry can be attempted including photolysis, click chemistry with alkynes, or Schiff-base reactions.

5.7. Experimental

5.7.1. Materials and Measurements

Unless otherwise stated, all chemicals were obtained from commercial sources and used as received. MeCN was distilled over CaH_2 under N_2 and degassed with Ar prior to use. NMR spectra were recorded on a Varian 500 MHz spectrometer at 23 ºC using a 5 mm probe. MOF samples (5 mg) were digested in DCl/d_6-DMSO (2 drops of DCl/ 600 µl d_6-DMSO) at 85 °C, stirred at 500 rpm for 30 min – 1 h, or until fully dissolved, prior to NMR analysis. Infrared spectra were collected were collected on a Perkin-Elmer Spectrum 100 using a UATR sampling accessory. with dry samples loaded on NaCl disks in Paratone-N oil. Powder X-ray diffraction data were collected on a Bruker Advanced D8 diffractometer (capillary stage) using Cu Kα radiation (λ = 1.54056 Å, 40 kW/ 40 mA, 2θ = 2 – 52.94°, Phi rotation = 20 rotation/min at 1 sec exposure per step, with 5001 steps using 0.5 mm glass capillaries). Scanning Electron Microscope (SEM) images were collected on a Phillips XL30 scanning electron microscope in secondary electron mode, (spot size 3 and 10 KeV). Some SEM images were collected on a Quanta450 scanning electron microscope with the same settings as the XL-30. Electron Dispersive X-ray Analysis was collected with an Oxford Instruments Ultim Max 170 EDX attachment on the Phillips XL30/Quanta 450 (spot size 4, 15 KeV). Samples for SEM analysis were dry loaded onto adhesive carbon tabs on aluminium stubs and carbon coated (5 nm) prior to analysis.

5.7.2. Single Crystal X-ray Diffraction Data

Single crystals were mounted in Paratone-N oil on a nylon loop. Single crystal X-ray data for **1-Me$_2$**, **1-Me$_2$**·$CoCl_2$ and **1-Me$_2$**·$ZnCl_2$ were collected at 100(2) K on the MX1 beamline of the Australian Synchrotron using the BluIce software interface, λ = 0.7108 Å. Data sets were solved by direct methods using SHELXS-2018/3.[77-79] Data sets were then refined by full-matrix least squares on F^2 by SHELXL-2018/3,[78-80] interfaced through the program X-Seed.[78-80] Unless otherwise stated, all non-hydrogen atoms were refined anisotropically and hydrogen atoms were placed at geometrically idealised positions. All three structures have a solvent accessible void which contained a number of diffuse electron density peaks that could not be adequately identified and refined as a solvent. The SQUEEZE routine of PLATON was applied to the collected data,[81-83] which gave new HKL files and resulted in an improvement in the GOF.

1-Me$_2$

The dataset was solved with SHELXS and refined using SHELXL interfaced through X-Seed.[78-80] Disorder of the oxygen atom in the zirconium-oxo cluster was accommodated by modelling two distinct oxygen atoms, O2 and O2B. The occupancy was set at 50% for O2 and O2B respectively. The EADP command was used to restrain constrain the anisotropic displacement parameter of O2 to be equal to O2B. The EXYZ command was used to restrain the atomic coordinates of O2 to be equal to O2B. DFIX constraints were used to enforce chemically reasonable bond lengths for O3 relative to Zr1. Rotational disorder of the methyl-pyridyl ligand (Me$_2$bpydc) was accommodated by modelling the methyl-pyridyl ligand over two positions. The occupancies of the two rings were set at 25% respectively, accounting for a plane of symmetry within the asymmetric unit, co-planar with one orientation of the ligand. DFIX commands were used to enforce chemical reasonable bond lengths for the methyl groups (C9 and C9B relative to C4 and C6B respectively). A FLAT command was used to enforce planarity of the two orientations of the methyl-pyridyl ring. Hydrogen atoms were incorporated at calculated positions. The SIMU command was used to enable anisotropic refinement of carbon and nitrogen atoms in the structure. In order to subtract the contribution from the disordered acetonitrile solvent, the SQUEEZE routine available in Platon was applied to the data, which gave a new HKL file.[81-83] The number of located electrons is 3801, which equates to approximately 48 MeCN molecules per unit cell and 2 per asymmetric unit.

1-Me$_2$·*CoCl$_2$*

The dataset was solved with SHELXS and refined using SHELXL interfaced through X-Seed.[78-80] Disorder of the two oxygen atoms in the zirconium-oxo cluster was accommodated by modelling two distinct oxygen atoms for each site; O1 and O1B and, O2 and O2B. The occupancies were set at 38.8 and 61.1% for O1 and O1B respectively and 16.6 and 83.3% for O2 and O2B respectively which lie on a special position. The EADP command was used to restrain constrain the anisotropic displacement parameter of O1 and O2 to be equal to O1B and O2B respectively. DFIX constraints were used to enforce chemically reasonable bond lengths for O1 and O2 relative to Zr1. The SIMU command was used to enable anisotropic refinement of oxygen atoms in the structure and was also paired with the ISOR command for O1 and O2 enabling their anisotropic refinement. In order to subtract the contribution from the disordered acetonitrile solvent, the SQUEEZE routine available in Platon was applied to the data, which

gave a new HKL file.[81-82] The number of located electrons is 4019, which equates to approximately 48 MeCN molecules per unit cell and 8 per asymmetric unit.

***1*-Me_2·$ZnCl_2$**

The dataset was solved with SHELXS and refined using SHELXL interfaced through X-Seed.[78-80] Disorder of the two oxygen atoms in the zirconium-oxo cluster was accommodated by modelling two distinct oxygen atoms for each site; O1 and O1B and, O2 and O2B. The occupancies were set at 38.8 and 61.1% for O1 and O1B respectively and 16.6 and 83.3% for O2 and O2B respectively which lie on a special position. The EADP command was used to restrain constrain the anisotropic displacement parameter of O1 and O2 to be equal to O1B and O2B respectively. DFIX constraints were used to enforce chemically reasonable bond lengths for O1, O1B, O2 and O2B relative to Zr1. The SIMU command was used to enable anisotropic refinement of oxygen atoms in the structure and was also paired with the ISOR command for O1 and O2 enabling their anisotropic refinement. In order to subtract the contribution from the disordered acetonitrile solvent, the SQUEEZE routine available in Platon was applied to the data, which gave a new HKL file.[81-83] The number of located electrons is 3753, which equates to approximately 42 MeCN molecules per unit cell and 7 per asymmetric unit.

5.7.3. Synthetic Methods

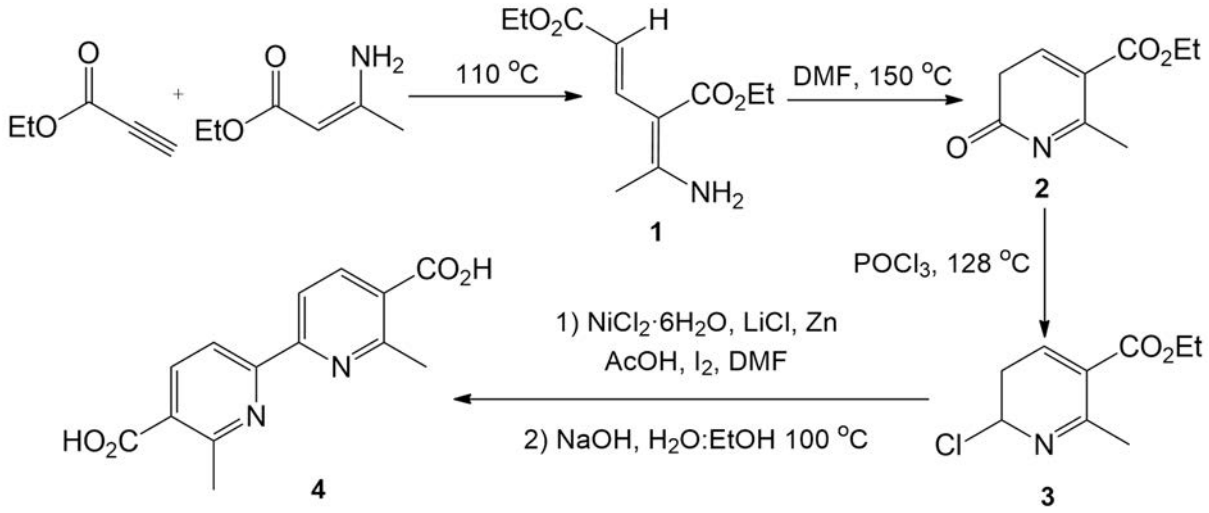

Schematic **5.1**: Stepwise synthesis of 6,6'-dimethyl-[2,2'bipyridine]-5,5'-dicarboxylic acid.

*Diethyl (2E, 4Z)-4-(1-aminoethylidene)pent-2-enedioate (**1**)*

1 was prepared according to literature procedures with minor modifications.[25] Ethyl-3-amino crotonate (5.00 g, 38.46 mmol, 1.00 eq.) and ethyl propionate (3.91 ml, 38.46 mmol, 1.00 eq.) were added to a 50 ml round-bottom flask. The mixture was heated at 108 ºC under an atmosphere of N_2 for 4 h. The red solution was cooled to room temperature where the resulting yellow/orange solid was recrystallised from MeOH. In order to maximise the yield, the solid was dissolved in a minimum amount of boiling MeOH, then the solution was left to cool to RT and then subsequently cooled at 3 ºC overnight. The resultant yellow solid was collected via vacuum filtration to give diethyl (2E, 4Z)-4-(1-aminoethylidene)pent-2-enedioate **1** (4.35 g, 19.11 mmol, 50 % yield). Characterisation data was consistent with previous reports.[25] ^{1}H NMR (500 MHz, $CDCl_3$): δ = 1.29 (t, J = 7.0 Hz, 3H), 1.38 (t, J = 7.0 Hz, 3H), 2.28 (s, 3H), 4.20 (q, J = 7.0, 2 H), 4.27 (q, J = 7.0, 2 H), 6.17 (d, J = 15.6 Hz, 1H), 7.66 (d, J = 15.6 Hz, 1H).

*Ethyl-2-methyl-6-oxo-5,6-dihydropyridine-3-carboxylate (**2**)*

2 was prepared according to literature procedures with minor modifications.[25] A mixture of diethyl (2E, 4Z)-4-(1-aminoethylidene)pent-2-enedioate **1** (4.31 g, 18.9 mmol, 1.00 eq.) and DMF (10 ml) were heated at reflux for 24 h under an atmosphere of N_2. The solution was cooled to room temperature slowly and was further cooled to 3 ºC overnight to maximise the recovery of the precipitate. The resultant solid was collected via vacuum filtration and washed with ice cold ether (3×) and dried to give ethyl-2-methyl-6-oxo-5,6-dihydropyridine-3-carboxylate **2** as plate like crystals (1.97 g, 10.9 mmol, 58 % yield). ^{1}H NMR data was consistent with previous reports.[25] ^{1}H NMR (500 MHz, $CDCl_3$): δ = 1.37 (t, J = 7.0 Hz, 3H), 2.75 (s, 3H), 4.34 (q, J = 7.0 Hz, 2H), 6.43 (d, J = 9.6 Hz, 1H), 8.05 (d, J = 9.6 Hz, 1H), 12.87 (br, s, 1H).

*Ethyl-6-chloro-2-methylnicotinate (**3**)*

3 was prepared according to literature procedures with minor modifications.[25] A mixture of ethyl-2-methyl-6-oxo-5,6-dihydropyridine-3-carboxylate **2** (1.97 g, 10.9 mmol, 1.00 eq.) and phosphorous oxychloride (4.74 ml, 50.77 mmol, 4.66 eq.) was heated at 128 ºC for 4 h. The reaction was then cooled to room temperature, poured over ice water, made basic with NaOH (8 M) and extracted three times with EtOAc (100 ml). The combined organic extracts were washed with brine, dried over $MgSO_4$, and concentrated under reduced pressure to give Ethyl-6-chloro-2-methylnicotinate **3** (1.77 g, 9.87 mmol, 91 % yield. ^{1}H NMR data was

consistent with previous reports.[25] ^{1}H NMR (500 MHz, $CDCl_3$): δ = 1.41 (t, J = 7.2 Hz, 3 H), 2.83 (s, 3H), 4.40 (q, J = 7.2 Hz, 2H), 7.42 (d, J = 8.0 Hz, 1H), 8.16 (d, J = 8.0 Hz, 1H).

*6,6'-dimethyl-[2,2'bipyridine]-5,5'-dicarboxylic acid (Me_2bpydc, **4**)*

Me_2bpydc **4** was prepared according to literature procedures with minor modifications.[25] A solution of $NiCl_2 \cdot 6H_2O$ (0.23 g, 0.98 mmol, 0.10 eq.) in DMF (59 ml) in a 100 ml round-bottom flask was stirred and heated at 40 ºC. Ethyl-6-chloro-2-methylnicotinate **3** (1.77 g, 9.87 mmol, 1.00 eq.), anhydrous LiCl (0.42 g, 9.87 mmol, 1.00 eq.) and zinc dust (0.77 g, 11.84 mmol, 1.20 eq.) were added to the stirring solution. When the temperature of the solution rose to 50 ºC, a grain of iodine and two drops of acetic acid (glacial) were added. The solution was stirred at 60 ºC for 36 h and then cooled to room temperature. 10 % HCl (12.5 ml) was added to the solution, the resulting mixture was made basic with aqueous ammonia (25 %) and extracted with DCM. The organic layers were combined, washed with brine, dried over Na_2SO_4 and concentrated under reduced pressure, then purified via flash chromatography over Celite. The purified methyl-protected **4** was added to a round bottom and deprotected with KOH (2 g, 35.56 mmol, >10 eq.), water (50 ml) and EtOH (50 ml) at reflux for 16 h. The reaction mixture was cooled to room temperature and then made acidic (pH 2 - 3) with 1 M HCl. The precipitate was collected via vacuum filtration and washed three times with ice cold ether (10 - 15 ml) and dried to give 6,6'-dimethyl-[2,2'bipyridine]-5,5'-dicarboxylic acid **4** as a sand coloured powder (0.67 g, 2.45 mmol, 50 % yield). ^{1}H NMR data was consistent with previous reports.[25] ^{1}H NMR (500 MHz, *d*$_6$-DMSO): δ = 2.82 (s, 6H), 8.35 (q, J = 8.2 Hz, 4H) and 13.31 (br s, 2H).

*UiO-67-Me_2bpydc (**1-Me_2**):*

$ZrCl_4$ (63.54 mg, 0.273 mmol), Me_2bpydc **4** (74.22 mg, 0.277 mmol) and trifluoroacetic acid (1.66 ml, 21.69 mmol, 80 equivalents) were dissolved in DMF (10 ml) 20 ml Teflon capped Wheaton vial) and sonicated for 1 h until fully dissolved. The solution was heated in an oven for 7 days at 120 ºC. The resulting crystals on the sides of the container were collected and washed DMF (4×10 ml) and MeCN (4×10 ml) resulting in pure single crystals of **1-Me_2**.

Ligand Modulator Exchange (benzoic acid):

Single crystals of **1-Me$_2$** (10-30 mg dried from distilled MeCN) were dispersed in a solution of benzoic acid (8%, 0.65 M, 20 ml) in DMF in a 20 ml screw capped (Teflon cap) Wheaton vial. The solution was heated in an oven at 85 ºC overnight without agitation. The solution was cooled to room temperature and then the MOF crystals were solvent exchanged with DMF (10 ml × 5). Prior to NMR analysis samples were solvent exchanged with distilled MeCN (10 ml × 5) then dried under vacuum in a desiccator.

Healing Protocol with Me$_2$bpydc:

Modulator exchanged single crystals of **1-Me$_2$** (10-30 mg) were soaked in a solution of H$_2$bpydc (2.5 mM, 20 ml) in DMF in a 20 ml screw capped (Teflon cap) Wheaton vial. The solution was heated in an oven at 85 ºC overnight without agitation. The solution was cooled to room temperature and then the MOF crystals were solvent exchanged with DMF (10 ml × 5). Prior to NMR analysis samples were solvent exchanged with distilled MeCN (10 ml × 5) then dried under vacuum in a desiccator.

***1-Me$_2$** metalation with transition metals for SCXRD analysis:*

Samples of **1-Me$_2$** were metalated with the transition metal complexes (as summarised in Table **5.1**), by placing solvent exchanged single healed crystals of **1-Me$_2$** into small vials with the appropriate solvent. The transition metal salt of choice was then added in excess and the mixture was held at the appropriate temperature for 2 – 14 d, cooled to room temperature and then solvent exchanged with the metalation solvent until the solution is colourless (4 – 7 times). The solvent exchanged crystals were analysed via SEM/EDX and SCXRD, with the metalation conditions and SEM/EDX data summarised in Table **5.1**.

Leaching Study:

Single crystal samples of **1-Me$_2$**·$CoCl_2$ and **MnMOF-1**·$CoCl_2$ were placed in 20 ml Teflon capped Wheaton vial solvated 15 ml of solvent, distilled MeCN for **1-Me$_2$**·$CoCl_2$ and distilled MeCN or MeOH for **MnMOF-1**·$CoCl_2$. Aliquots of each solvated sample were taken at T = 0 – 7 d and were solvent exchanged 3 times. The solvent exchanged samples were dried and analysed via SEM/EDX to determine the Co content relative to Zr, summarised in Figure **5.10**.

*Anion exchange with **1-Me$_2$**·CoCl$_2$ with NaN$_3$:*

For each anion exchange reaction, a small quantity of **1-Me$_2$**·$CoCl_2$ and NaN_3 were placed in two separate 2 ml glass vials (without caps), both vials were placed in a 20 ml Teflon capped Wheaton vial and then submersed in a the relevant solvent system (EtOH, MeOH, MeCN and MeCN/EtOH). The larger vial was sealed in the absence of light and the anion exchange was monitored by taking aliquots of the samples after 3 – 14 d of exchange, solvent exchanging the single crystals 4 times and analysing the Co, Zr and Cl content via SEM/EDX.

5.7.4. Gas Adsorption Analysis

Activation Protocol:

In a typical activation procedure, crystals of UiO-67-Me_2bpydc were solvent exchanged with DMF (× 5) over a 1-day period and the distilled MeCN (× 5) over a 1-day period. The samples were then dried in a desiccator for 1 h then transferred into sorption analysis tubes. The samples were then dried under a vacuum at 150 ºC for 3 h to yield activated samples.

Gas Adsorption Measurements:

Gas adsorption isotherms were measured using volumetric methods on a micromeritics 3-Flex analyser (Micromeritics Instrument Corporation, Norcross, GA, USA) at 77 K (using a cryo-cooler circulator). Brunauer-Emmett-Teller (BET) surface areas were calculated using experimental points at relative pressure of P/P_0 = 0.05-0.25. Pore size distributions were calculated from N_2 using DFT modelling software on a Micromeritics 3-Flex analyser. UHP grade (99.999 %) N_2 was used for all measurements.

5.8. References

1. Evans, J. D.; Sumby, C. J.; Doonan, C. J., Post-Synthetic Metalation of Metal–Organic Frameworks. *Chem Soc Rev* **2014,** *43* (16), 5933-5951.

2. Juan-Alcañiz, J.; Gascon, J.; Kapteijn, F., Metal–Organic Frameworks as Scaffolds for the Encapsulation of Active Species: State of the Art and Future Perspectives. *J Mater Chem* **2012,** *22* (20), 10102-10118.

3. Genna, D. T.; Wong-Foy, A. G.; Matzger, A. J.; Sanford, M. S., Heterogenization of Homogeneous Catalysts in Metal–Organic Frameworks via Cation Exchange. *J Am Chem Soc* **2013,** *135* (29), 10586-10589.

4. Meilikhov, M.; Yusenko, K.; Esken, D.; Turner, S.; Van Tendeloo, G.; Fischer, R. A., Metals@MOFs – Loading MOFs with Metal Nanoparticles for Hybrid Functions. *Eur J Inorg Chem* **2010,** *2010* (24), 3701-3714.

5. Dau, P. V.; Cohen, S. M., Cyclometalated Metal–Organic Frameworks as Stable and Reusable Heterogeneous Catalysts for Allylic N-Alkylation of Amines. *Chem Commun* **2013,** *49* (55), 6128-6130.

6. Fei, H.; Cohen, S. M., A Robust, Catalytic Metal–Organic Framework With Open 2,2′-Bipyridine Sites. *Chem Commun* **2014,** *50* (37), 4810-4812.

7. Manna, K.; Zhang, T.; Lin, W., Postsynthetic Metalation of Bipyridyl-Containing Metal–Organic Frameworks for Highly Efficient Catalytic Organic Transformations. *J Am Chem Soc* **2014,** *136* (18), 6566-6569.

8. Falkowski, J. M.; Sawano, T.; Zhang, T.; Tsun, G.; Chen, Y.; Lockard, J. V.; Lin, W., Privileged Phosphine-Based Metal–Organic Frameworks for Broad-Scope Asymmetric Catalysis. *J Am Chem Soc* **2014,** *136* (14), 5213-5216.

9. Manna, K.; Zhang, T.; Carboni, M.; Abney, C. W.; Lin, W., Salicylaldimine-Based Metal–Organic Framework Enabling Highly Active Olefin Hydrogenation with Iron and Cobalt Catalysts. *J Am Chem Soc* **2014,** *136* (38), 13182-13185.

10. Valvekens, P.; Bloch, E. D.; Long, J. R.; Ameloot, R.; De Vos, D. E., Counteranion Effects on the Catalytic Activity of Copper Salts Immobilized on the 2,2′-Bipyridine-Functionalized Metal–Organic Framework MOF-253. *Catal Today* **2015,** *246*, 55-59.

11. Capon, P. K.; Burgun, A.; Coghlan, C. J.; Crees, R. S.; Doonan, C. J.; Sumby, C. J., Hydrogen Adsorption in Azolium and Metalated N-heterocyclic Carbene Containing MOFs. *CrystEngComm* **2016,** *18* (37), 7003-7010.

12. Bloch, W. M.; Burgun, A.; Coghlan, C. J.; Lee, R.; Coote, M. L.; Doonan, C. J.; Sumby, C. J., Capturing Snapshots of Post-Synthetic Metallation Chemistry in Metal–Organic Frameworks. *Nat Chem* **2014,** *6*, 906.

13. Bloch, W. M.; Champness, N. R.; Doonan, C. J., X-ray Crystallography in Open-Framework Materials. *Angew Chem Int Ed* **2015,** *54* (44), 12860-12867.

14. Gonzalez, M. I.; Bloch, E. D.; Mason, J. A.; Teat, S. J.; Long, J. R., Single-Crystal-to-Single-Crystal Metalation of a Metal-Organic Framework: a Route Toward Structurally Well-Defined Catalysts. *Inorg Chem* **2015,** *54* (6), 2995-3005.

15. Bloch, W. M.; Burgun, A.; Doonan, C. J.; Sumby, C. J., Probing Post-Synthetic Metallation in Metal–Organic Frameworks: Insights from X-ray Crystallography. *Chem Commun* **2015,** *51* (25), 5486-5489.

16. Huxley, M. T.; Coghlan, C. J.; Bloch, W. M.; Burgun, A.; Doonan, C. J.; Sumby, C. J., X-ray Crystallographic Insights into Post-Synthetic Metalation Products in a Metal-Organic Framework. *Philos Trans A Math Phys Eng Sci* **2017,** *375* (2084).

17. Huxley, M. T.; Young, R. J.; Bloch, W. M.; Champness, N. R.; Sumby, C. J.; Doonan, C. J., Isomer Interconversion Studied through Single-Crystal to Single-Crystal Transformations in a Metal–Organic Framework Matrix. *Organometallics* **2019,** *38* (18), 3412-3418.

18. Burgun, A.; Coghlan, C. J.; Huang, D. M.; Chen, W.; Horike, S.; Kitagawa, S.; Alvino, J. F.; Metha, G. F.; Sumby, C. J.; Doonan, C. J., Mapping-Out Catalytic Processes in a Metal–Organic Framework with Single-Crystal X-ray Crystallography. *Angew Chem* **2017,** *129* (29), 8532-8536.

19. Cohen, S. M., Postsynthetic Methods for the Functionalization of Metal–Organic Frameworks. *Chem Rev* **2012,** *112* (2), 970-1000.

20. Jacobs, T.; Clowes, R.; Cooper, A. I.; Hardie, M. J., A Chiral, Self-Catenating and Porous Metal–Organic Framework and its Post-Synthetic Metal Uptake. *Angew Chem Int Ed* **2012,** *51* (21), 5192-5195.

21. Øien-Ødegaard, S.; Shearer, G. C.; Wragg, D. S.; Lillerud, K. P., Pitfalls in Metal–Organic Framework Crystallography: Towards more Accurate Crystal Structures. *Chem Soc Rev* **2017,** *46* (16), 4867-4876.

22. Wang, C.; deKrafft, K. E.; Lin, W., Pt Nanoparticles@Photoactive Metal–Organic Frameworks: Efficient Hydrogen Evolution via Synergistic Photoexcitation and Electron Injection. *J Am Chem Soc* **2012,** *134* (17), 7211-7214.

23. Dau, P. V.; Kim, M.; Cohen, S. M., Site-Selective Cyclometalation of a Metal–Organic Framework. *Chem Sci* **2013,** *4* (2), 601-605.

24. Gonzalez, M.; Oktawiec, J.; Long, J. R., Ethylene Oligomerization in Metal–Organic Frameworks Bearing Nickel(II) 2,2′-Bipyridine Complexes. *Faraday Discuss* **2017**.

25. Li, X.; Van Zeeland, R.; Maligal-Ganesh, R. V.; Pei, Y.; Power, G.; Stanley, L.; Huang, W., Impact of Linker Engineering on the Catalytic Activity of Metal–Organic Frameworks Containing Pd(II)–Bipyridine Complexes. *ACS Catalysis* **2016,** *6* (9), 6324-6328.

26. Li, X.; Zhang, B.; Van Zeeland, R.; Tang, L.; Pei, Y.; Qi, Z.; Goh, T. W.; Stanley, L. M.; Huang, W., Unveiling the Effects of Linker Substitution in Suzuki Coupling with Palladium Nanoparticles in Metal–Organic Frameworks. *Catal Lett* **2018,** *148* (3), 940-945.

27. Shan, B.; James, J. B.; Armstrong, M. R.; Close, E. C.; Letham, P. A.; Nikkhah, K.; Lin, Y. S.; Mu, B., Influences of Deprotonation and Modulation on Nucleation and Growth of UiO-66: Intergrowth and Orientation. *J of Phys Chem C* **2018,** *122* (4), 2200-2206.

28. DeStefano, M. R.; Islamoglu, T.; Garibay, S. J.; Hupp, J. T.; Farha, O. K., Room-Temperature Synthesis of UiO-66 and Thermal Modulation of Densities of Defect Sites. *Chem Mater* **2017,** *29* (3), 1357-1361.

29. Guo, H.; Zhu, Y.; Wang, S.; Su, S.; Zhou, L.; Zhang, H., Combining Coordination Modulation with Acid–Base Adjustment for the Control over Size of Metal–Organic Frameworks. *Chem Mater* **2012,** *24* (3), 444-450.

30. Yang, X.; Yuan, S.; Zou, L.; Drake, H.; Zhang, Y.; Qin, J.; Alsalme, A.; Zhou, H.-C., One-Step Synthesis of Hybrid Core–Shell Metal–Organic Frameworks. *Angew Chem Int Ed* **2018,** *57* (15), 3927-3932.

31. Hoshino, M.; Khutia, A.; Xing, H.; Inokuma, Y.; Fujita, M., The Crystalline Sponge Method Updated. *IUCrJ* **2016,** *3* (Pt 2), 139-51.

32. Gutov, O. V.; Gonzalez Hevia, M.; Escudero-Adan, E. C.; Shafir, A., Metal-Organic Framework (MOF) Defects under Control: Insights into the Missing Linker Sites and Their Implication in the Reactivity of Zirconium-Based Frameworks. *Inorg Chem* **2015,** *54* (17), 8396-400.

33. Fang, Z.; Bueken, B.; De Vos, D. E.; Fischer, R. A., Defect-Engineered Metal-Organic Frameworks. *Angew Chem Int Ed Engl* **2015,** *54* (25), 7234-54.

34. Cliffe, M. J.; Wan, W.; Zou, X.; Chater, P. A.; Kleppe, A. K.; Tucker, M. G.; Wilhelm, H.; Funnell, N. P.; Coudert, F.-X.; Goodwin, A. L., Correlated Defect Nanoregions in a Metal–Organic Framework. *Nat Commun* **2014,** *5* (1), 4176.

35. Inokuma, Y.; Yoshioka, S.; Ariyoshi, J.; Arai, T.; Hitora, Y.; Takada, K.; Matsunaga, S.; Rissanen, K.; Fujita, M., X-ray Analysis on the Nanogram to Microgram Scale using Porous Complexes. *Nature* **2013,** *495* (7442), 461-466.

36. Zhang, Y.; Xiao, H.; Zhou, X.; Wang, X.; Li, Z., Selective Adsorption Performances of UiO-67 for Separation of Light Hydrocarbons C1, C2, and C3. *Ind Engg Chem Res* **2017,** *56* (30), 8689-8696.

37. Bragg, W. H.; Bragg, W. L., *X rays and Crystal Structure*. G. Bell: London, 1915.

38. Cavka, J. H.; Jakobsen, S.; Olsbye, U.; Guillou, N.; Lamberti, C.; Bordiga, S.; Lillerud, K. P., A New Zirconium Inorganic Building Brick Forming Metal Organic Frameworks with Exceptional Stability. *J Am Chem Soc* **2008,** *130* (42), 13850-13851.

39. Wong, Y.-L.; Diao, Y.; He, J.; Zeller, M.; Xu, Z., A Thiol-Functionalized UiO-67-Type Porous Single Crystal: Filling in the Synthetic Gap. *Inorg Chem* **2019,** *58* (2), 1462-1468.

40. Øien-Ødegaard, S.; Bouchevreau, B.; Hylland, K.; Wu, L.; Blom, R.; Grande, C.; Olsbye, U.; Tilset, M.; Lillerud, K. P., UiO-67-type Metal–Organic Frameworks with Enhanced Water Stability and Methane Adsorption Capacity. *Inorg Chem* **2016,** *55* (5), 1986-1991.

41. Gonzalez, M. I.; Turkiewicz, A. B.; Darago, L. E.; Oktawiec, J.; Bustillo, K.; Grandjean, F.; Long, G. J.; Long, J. R., Confinement of Atomically Defined Metal Halide Sheets in a Metal–Organic Framework. *Nature* **2020,** *557*, (7788), 64-68.

42. Akbarzadeh Torbati, N.; Rezvani, A. R.; Safari, N.; Saravani, H.; Amani, V., Dichlorido(6,6'-Dimethyl-2,2'-Bipyridine-Kappan,N')Cobalt(II). *Acta Cryst E* **2010,** *66* (Pt 10), m1284.

43. Eom, G. H.; Park, H. M.; Hyun, M. Y.; Jang, S. P.; Kim, C.; Lee, J. H.; Lee, S. J.; Kim, S.-J.; Kim, Y., Anion Effects on the Crystal Structures of ZnII Complexes Containing 2,2′-Bipyridine: their Photoluminescence and Catalytic Activities. *Polyhedron* **2011,** *30* (9), 1555-1564.

44. Alizadeh, R.; Kalateh, K.; Ebadi, A.; Ahmadi, R.; Amani, V., Dichlorido(6,6'-Dimethyl-2,2'-Bipyridine-Kappan,N')Zinc(II). *Acta Crystal E* **2009,** *65* (Pt 10), m1250.

45. Marshall, W. J.; Grushin, V. V., Activation of Chlorobenzene with Ni(0) N,N-chelates — A Remarkably Profound Effect of a Minuscule Change in Ligand Structure. *Can J Chem* **2005,** *83* (6-7), 640-645.

46. Rogan, J.; Poleti, D.; Karanović, L.; Jagličić, Z., Synthesis, Magnetic, Thermal and Structural Properties of Co(II), Ni(II) and Cu(II) Complexes Containing Isophthalato Ligands. *J Mol Struct* **2011,** *985* (2), 371-379.

47. Avdeeva, V. V.; Vologzhanina, A. V.; Goeva, L. V.; Malinina, E. A.; Kuznetsov, N. T., Boron Cluster Anions $[B_nH_n]^{2-}$ (n = 10, 12) in Reactions of Iron(II) and Iron(III) Complexation with 2, 2′-Bipyridyl and 1, 10-Phenanthroline. *Z Anorg Allg Chem* **2014,** *640* (11), 2149-2160.

48. Alizadeh, R.; Mohammadi Eshlaghi, P.; Amani, V., Dichlorido(6,6'-Dimethyl-2,2'-Bipyridine-Kappan,N')Cadmium(II). *Acta Cryst E* **2010,** *66* (Pt 8), m1024.

49. Philouze, C.; Henry, M.; Auger, N.; Vignier, D.; Lance, M.; Nierlich, M.; Girerd, J.-J., Experimental and Theoretical Investigations of Condensation and Disproportionation of Mn(bpy)Cl3(H2O) in Aqueous Solution. *Inorg Chem* **1999,** *38* (1), 4-11.

50. Danica, Č.; Alena, M.; Jan, M., Structure of Cis-Dichlorobis(1,10-Phenanthroline)Manganese(II) and Cis-Dichlorobis(2,2′-Bipyridine)Manganese(II). *Acta Chim Slov* **2014,** *7* (1), 15-19.

51. Canty, A.; Skelton, B.; Traill, P.; White, A., Structural Chemistry of the Platinum Group-Metals: MCl_2(bpy) (M = Pd, Pt, bpy = 2,2'-Bipyridine). *Aust J Chem* **1992,** *45* (2), 417-422.

52. Wang, J.; Cui, H.-H.; Zhang, Y.-Q.; Chen, L.; Chen, X.-T., Magnetic Anisotropy and Slow Magnetic Relaxation of Seven-Coordinate Cobalt(II)–Nitrate Complexes. *Polyhedron* **2018,** *154*, 148-155.

53. Nasser Ostad, S.; Abedi, A.; Amani, V.; Karimi, P.; Heydarnezhad, S., Influence of Methyl Group Position in Bipyridine Ligand on Structure and Luminescence of Related Zinc(II) Nitrate Complexes. *J Iran Chem Soc* **2016,** *13* (8), 1417-1427.

54. Liu, F. Y.; Zhang, M. H.; Kou, J. F., (2,2'-Bi-pyridine-kappa(2) N,N')bis-(nitrato-kappa(2) O,O')copper(II). *Acta Cryst E* **2013,** *69* (Pt 11), m609.

55. Baker, G. L.; Fronzek, F. R.; Kiefer, G. E.; Marston, C. R.; Modenbach, C. L.; Newkome, G. R.; Puckett, W. E.; Watkins, S. F., Dichloro(6,6'-dimethyl-2,2'bipyridyl)cobalt(II) Hemibenzene Solvate. *Acta Cryst.* **1988,** *C44*, 1668-1669.

56. Berry, J. F., Terminal Nitrido and Imido Complexes of the Late Transition Metals. *Comments Inorg Chem* **2009,** *30* (1-2), 28-66.

57. Grant, L. N.; Pinter, B.; Kurogi, T.; Carroll, M. E.; Wu, G.; Manor, B. C.; Carroll, P. J.; Mindiola, D. J., Molecular Titanium Nitrides: Nucleophiles Unleashed. *Chem Sci* **2017,** *8* (2), 1209-1224.

58. Kono, M.; Harada, S.; Nemoto, T., Rhodium-Catalyzed Stereospecific C−H Amination for the Construction of Spiroaminal Cores: Reactivity Difference between Nitrenoid and Carbenoid Species against Amide Functionality. *Chem Eur* **2017,** *23* (31), 7428-7432.

59. Das, A.; Reibenspies, J. H.; Chen, Y.-S.; Powers, D. C., Direct Characterization of a Reactive Lattice-Confined Ru_2 Nitride by Photocrystallography. *J Am Chem Soc* **2017,** *139* (8), 2912-2915.

60. Abbenseth, J.; Bete, S. C.; Finger, M.; Volkmann, C.; Würtele, C.; Schneider, S., Four- and Five-Coordinate Osmium(IV) Nitrides and Imides: Circumventing the “Nitrido Wall”. *Organometallics* **2018,** *37* (5), 802-811.

61. Thomson, R. K.; Cantat, T.; Scott, B. L.; Morris, D. E.; Batista, E. R.; Kiplinger, J. L., Uranium Azide Photolysis Results in C-H Bond Activation and Provides Evidence for a Terminal Uranium Nitride. *Nat Chem* **2010,** *2* (9), 723-9.

62. Carsch, K. M.; DiMucci, I. M.; Iovan, D. A.; Li, A.; Zheng, S.-L.; Titus, C. J.; Lee, S. J.; Irwin, K. D.; Nordlund, D.; Lancaster, K. M.; Betley, T. A., Synthesis of a Copper-Supported Triplet Nitrene Complex Pertinent to Copper-Catalyzed Amination. *Science* **2019,** *365* (6458), 1138-1143.

63. Das, A.; Chen, Y.-S.; Reibenspies, J. H.; Powers, D. C., Characterization of a Reactive Rh_2 Nitrenoid by Crystalline Matrix Isolation. *J Am Chem Soc* **2019,** *141* (41), 16232-16236.

64. Zhang, T.; Manna, K.; Lin, W., Metal-Organic Frameworks Stabilize Solution-Inaccessible Cobalt Catalysts for Highly Efficient Broad-Scope Organic Transformations. *J Am Chem Soc* **2016,** *138* (9), 3241-9.

65. Betterton, E. A., Environmental Fate of Sodium Azide Derived from Automobile Airbags. *Crit Rev Environ Sci Technol* **2003,** *33* (4), 423-458.

66. Wang, Q.; Feng, X.; Wang, S.; Song, N.; Chen, Y.; Tong, W.; Han, Y.; Yang, L.; Wang, B., Metal-Organic Framework Templated Synthesis of Copper Azide as the Primary Explosive with Low Electrostatic Sensitivity and Excellent Initiation Ability. *Adv Mater* **2016,** *28* (28), 5837-5843.

67. Šima, J., Photochemistry of Azide-Moiety Containing Inorganic Compounds. *Coord Chem Rev* **2006,** *250* (17), 2325-2334.

68. Meghdadi, S.; Mereiter, K.; Amirnasr, M.; Fadaee, F.; Amiri, A., Synthesis, crystal structure, and electrochemistry of [Co{(Me-sal)$_2$dien}(N_3)] and [Co{(Me-sal)$_2$dpt}(N_3)]. *J Coord Chem* **2009,** *62* (5), 734-744.

69. Wang, X.-T.; Wang, Z.-M.; Gao, S., Honeycomb Layer of Cobalt(II) Azide Hydrazine Showing Weak Ferromagnetism. *Inorg Chem* **2007,** *46* (25), 10452-10454.

70. Grant, L. N.; Carroll, M. E.; Carroll, P. J.; Mindiola, D. J., An Unusual Cobalt Azide Adduct That Produces a Nitrene Species for Carbon–Hydrogen Insertion Chemistry. *Inorg Chem* **2016,** *55* (16), 7997-8002.

71. Zhao, J.-P.; Zhao, C.; Song, W.-C.; Wang, L.; Xie, Y.; Li, J.-R.; Bu, X.-H., 4-Substituent Pyridine Directed Cobalt(Ii) Azides: Solvothermal Synthesis, Structure, and Magnetic Properties. *Dalton Trans* **2015,** *44* (22), 10289-10296.

72. Hong-Ji, C., Synthesis and Structural Characterization of Bis(2, 2′-bpy)bis(azide)cobalt(III) nitrate dihydrate. *Jiegou Huaxue* **2002,** *21*.

73. Zhang, F.; Xie, C.-Z.; Wang, X.-Q.; Shen, G.-Q.; Shen, D.-Z., Diazidobis(2,2′-bipyridine)cobalt(III) perchlorate. *Acta Cryst E* **2007,** *63* (10), m2615-m2616.

74. Nath, J. K.; Baruah, J. B., Azide Containing Bipyridine Complexes of Cobalt(III). *Polyhedron* **2012,** *36* (1), 1-5.

75. Ghosh, K.; Banerjee, A.; Bauzá, A.; Frontera, A.; Chattopadhyay, S., One Pot Synthesis of Two Cobalt(Iii) Schiff Base Complexes with Chelating Pyridyltetrazolate and Exploration of their Bio-Relevant Catalytic Activities. *RSC Adv* **2018,** *8* (49), 28216-28237.

76. Schmid, P.; Maier, M.; Pfeiffer, H.; Belz, A.; Henry, L.; Friedrich, A.; Schönfeld, F.; Edkins, K.; Schatzschneider, U., Catalyst-Free Room-Temperature iClick Reaction of Molybdenum(Ii) and Tungsten(Ii) Azide Complexes with Electron-Poor Alkynes: Structural Preferences and Kinetic Studies. *Dalton Trans* **2017,** *46* (39), 13386-13396.

77. He, J.; Waggoner, N. W.; Dunning, S. G.; Steiner, A.; Lynch, V. M.; Humphrey, S. M., A PCP Pincer Ligand for Coordination Polymers with Versatile Chemical Reactivity: Selective Activation of CO2 Gas over CO Gas in the Solid State. *Angew Chem Int Ed* **2016,** *55* (40), 12351-12355.

78. Sheldrick, G. M., *Acta Cryst.* **2015,** *C71*, 3.

79. Sheldrick, G. M., Univserity of Gottingen: 2014.

80. Sheldrick, G. M., *Acta Cryst* **2008,** *A64*, 112.

81. Spek, A. L., checkCIF Validation ALERTS: What They Mean and How to Respond. *Acta Cryst E* **2020,** *76* (Pt 1), 1-11.

82. Spek, A. L., PLATON SQUEEZE: a Tool for the Calculation of the Disordered Solvent Contribution to the Calculated Structure Factors. *Acta Cryst C* **2015,** *71* (Pt 1), 9-18.

83. Van Der Sluis, P., Spek, A. L., BYPASS: an Effective Method for the Refinement of Crystal Structures Containing Disordered Solvent Regions. *Acta Cryst* **1990,** *A46*, 194-201.

5.9. Appendix

5.9.1. Crystal Size Analysis of Single UiO-67-Me$_2$bpydc crystals

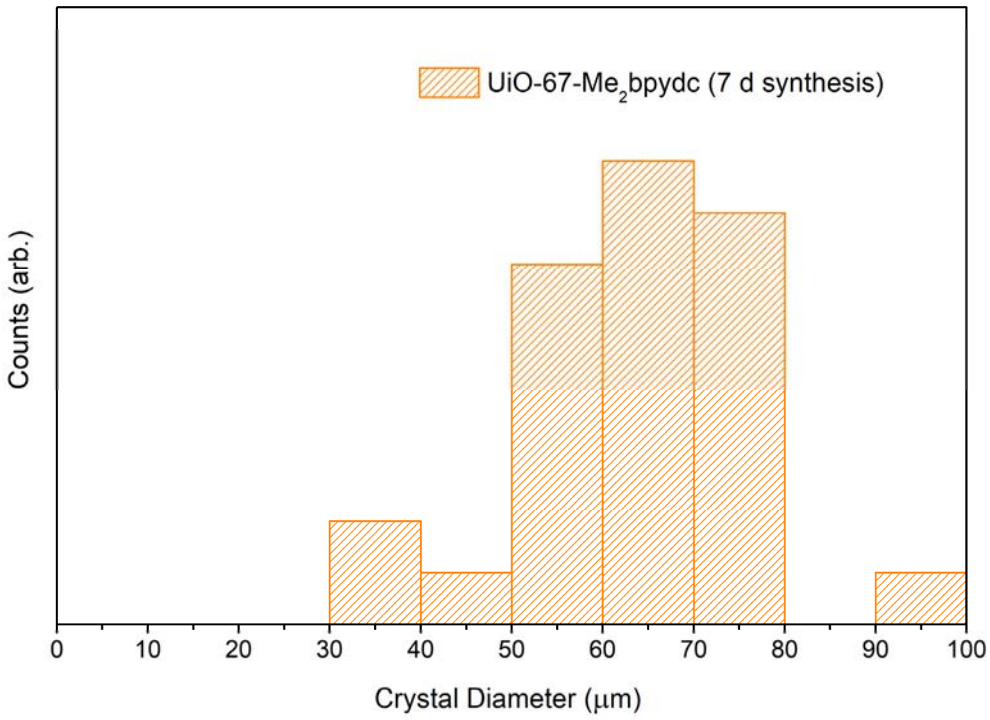

Figure **5.A.1**: Particle size distribution data for UiO-67-Me$_2$bpydc single crystals.

5.9.2. Modulator Exchange and Healing of UiO-67-Me$_2$bpydc

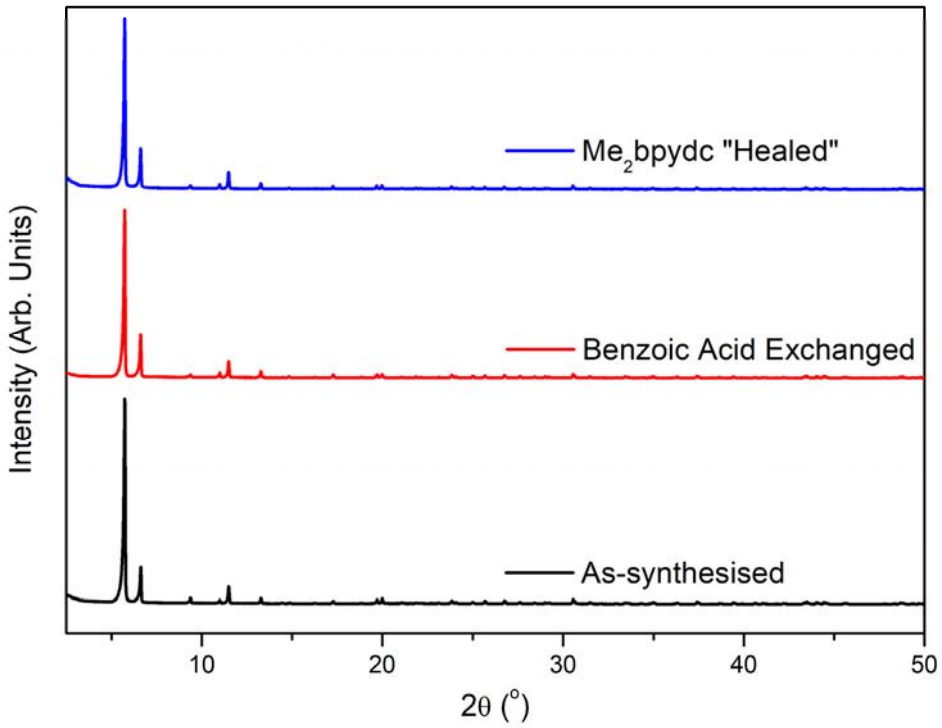

Figure **5.A.2**: PXRD patterns of UiO-67-Me$_2$bpydc, as-synthesised (black), benzoic acid exchanged (red) and ligand defect healed with Me$_2$bpydc (blue).

Table **5.A.1**: Defect analysis of benzoic acid (BA) exchanged samples of as-synthesised and healed UiO-67-Me$_2$bpydc from ^{1}H NMR data.

Sample	Acid:Me$_2$bpydc (by integration)	#Acid molecules in formula	#Me$_2$bpydc molecules in formula	Me$_2$bpydc:Zr	% Ligand defects
BA exchanged	0.32	1.66	5.16	0.86	14
BA exchanged + Me$_2$bpydc healed	0.00	0.00	6.00	1.00	0

5.9.3. Crystallographic information for UiO-67-Me$_2$bpydc

Table **5.A.2**: Crystallographic data for **1-Me$_2$**, **1-Me$_2$**·$CoCl_2$, and **1-Me$_2$**·$ZnCl_2$.

Compound	**1-Me$_2$**	**1-Me$_2$·CoCl$_2$**	**1-Me$_2$·ZnCl$_2$**
Empirical formula	$C_{84}H_{64}N_{12}O_{32}Zr_6$	$C_{84}H_{64}N_{12}O_{32}Zr_6Co_6Cl_{12}$	$C_{84}H_{64}N_{12}O_{32}Zr_6Zn_6Cl_{12}$
Formula weight (g/mol)	2300.79	3079.77	3118.41
Crystal system	Cubic	Cubic	Cubic
Space group	*Fm-3*	*Pa-3*	*Pa-3*
***a* = *b* = *c* (Å)**	26.615(3)	26.597(3)	26.609(3)
α = ß = γ (°)	90	90	90
Volume (Å^3)	18853	18815	18841(7)
Z	4	4	4
Density (calc.) (mg/m^3)	0.813	1.087	1.099
Absorption coefficient (mm^{-1})	0.363	1.048	1.282
Temperature (K)	100 (2)	100 (2)	100 (2)
$\theta_{min} - \theta_{max}$ (°)	1.325 to 32.225	1.326 to 32.238	1.325 to 32.222
Reflections measured	2696	10689	10467
Reflections collected	2767	10114	9427
[R(int)]	0.061	0.109	0.165
Restraints/Parameters	227/105	25/236	27/236
Largest peak/Deepest hole (e·Å^{-3})	1.412/-1.382	4.267/-2.727	16.340/-3.930
Goodness-of-fit on F^2	1.058	1.115	2.712
R_1 [I>2σ(*I*)]	0.0416	0.1828	0.2086
***w*R$_2$ (all data)**	0.1005	0.4034	0.5818

5.9.4. Metalation of UiO-67-Me$_2$bpydc

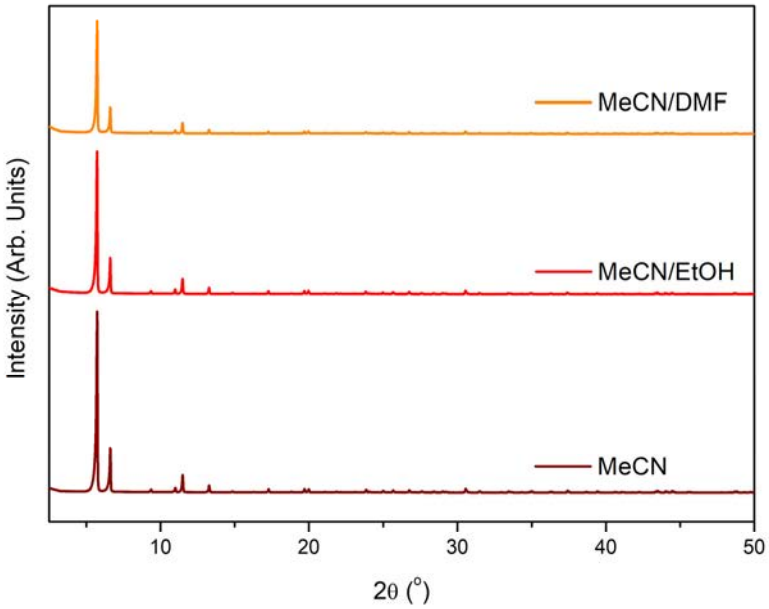

Figure **5.A.3**: PXRD patterns of single crystals of UiO-67-Me$_2$bpydc solvated in MeCN (dark red), MeCN/EtOH (red) and MeCN/DMF (orange) for 7 d at 65 ºC to simulate metalation conditions.

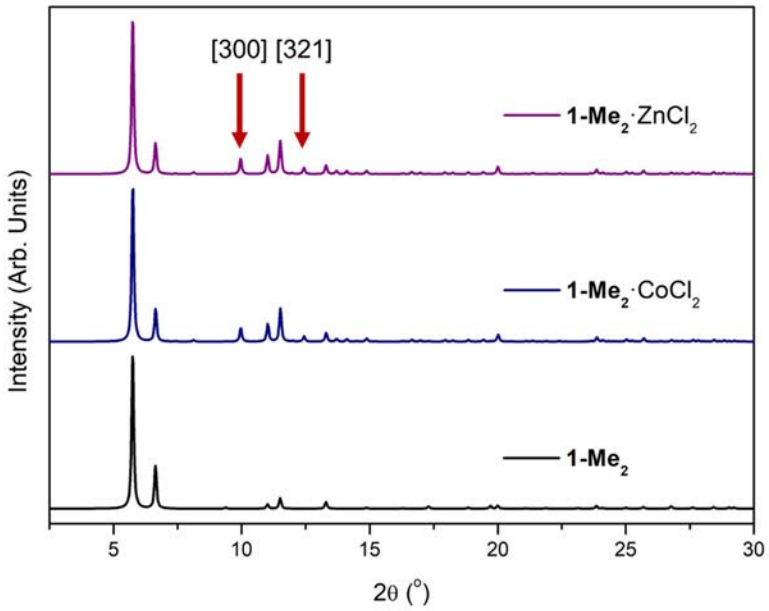

Figure **5.A.4**: PXRD patterns of **1-Me$_2$**, **1-Me$_2$**·CoCl$_2$ and **1-Me$_2$**·ZnCl$_2$ simulated from their respective crystal structures. The major differences in the patterns include the presence of new diffraction peaks at 10.12 and 12.62 º for **1-Me$_2$**·CoCl$_2$ and **1-Me$_2$**·ZnCl$_2$ corresponding to hkl planes of [300] and [321] respectively.

5.9.4. *Asymmetric Units of* ***1-Me₂***, ***1-Me₂***·$CoCl_2$, *and* ***1-Me₂***·$ZnCl_2$

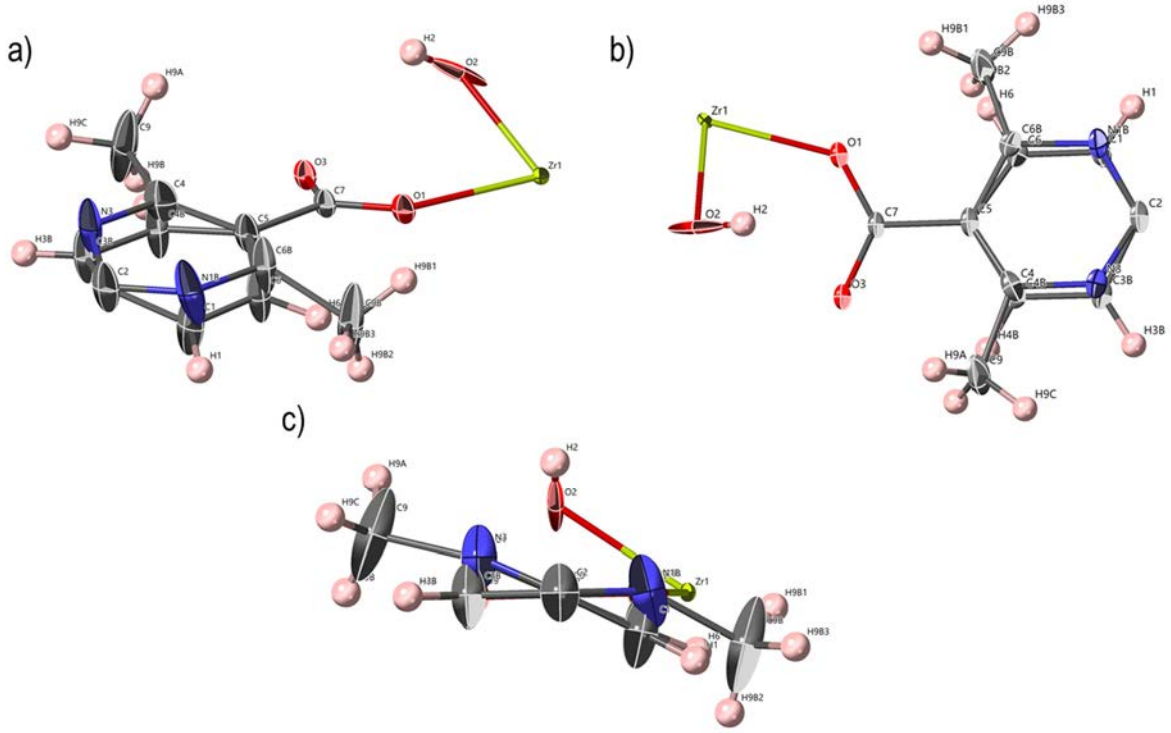

Figure **5.A.5**: Asymmetric unit of **1-Me₂** shown in three orientations (a), (b) and (c) with all non-hydrogen atoms represented by ellipsoids at the 50% probability level (Zr, yellow; O, red; C, grey; N, light blue; H, pink). The ligand was disordered over two positions, with the atoms in each ring refined at 25% occupancy because there is a mirror plane co-planar with one orientation of the ligand. The O atoms (O2 and O2B) are disordered with a half occupancy factor, accounting for the split occupancy between μ_3-O and μ_3-OH groups.

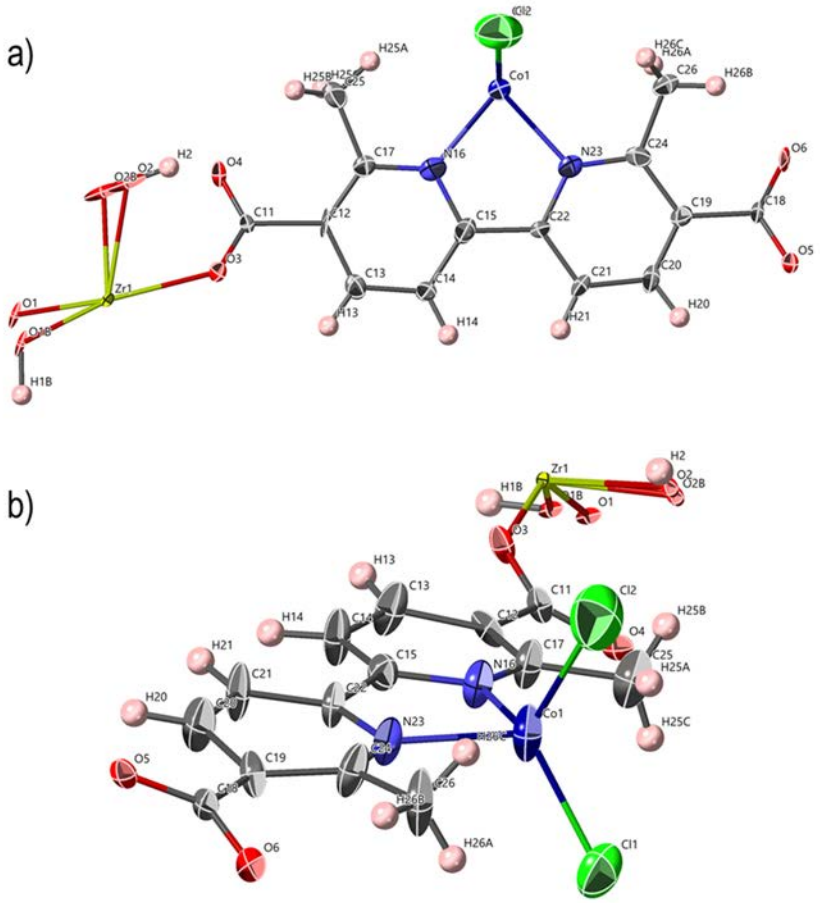

Figure **5.A.6**: Asymmetric unit of **1-Me$_2$**·$CoCl_2$ represented in a (a) top down manner and (b) off angle with respect to the plane of the ligand, with all non-hydrogen atoms represented by ellipsoids at the 50% probability level (Zr, yellow; O, red; C, grey; N, light blue; H, pink; Co, dark blue; Cl, green). The O atoms in the Zr-oxo cluster are disordered over two positions, O1 and O1B were refined with occupancies of 38.8 and 61.1% respectively, where as O2 and O2B lie on a special position and were refined with occupancies of 16.6 and 83.3% to account for the split occupancy between μ_3-O and μ_3-OH groups.

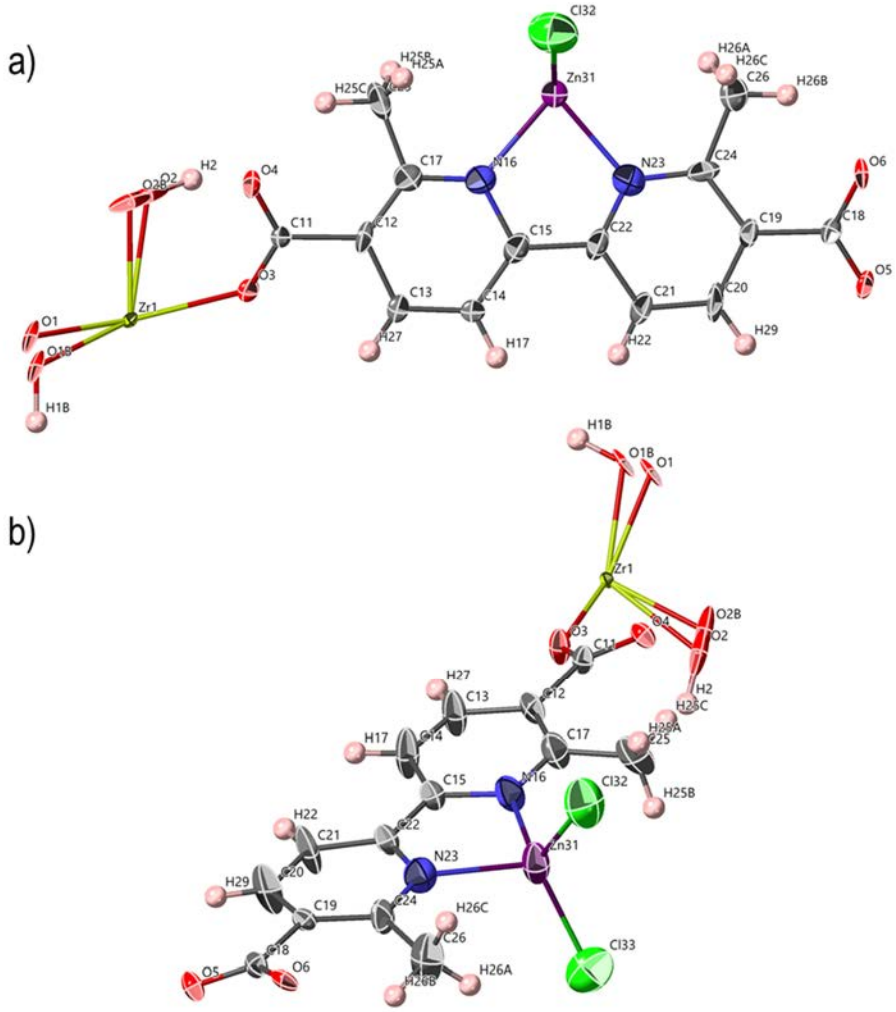

Figure **5.A.7**: Asymmetric unit of **1-Me$_2$**·$ZnCl_2$ represented in a (a) top down manner and (b) off angle with respect to the plane of the ligand, with all non-hydrogen atoms represented by ellipsoids at the 50% probability level (Zr, yellow; O, red; C, grey; N, light blue; H, pink; Zn, purple; Cl, green). The O atoms in the Zr-oxo cluster are disordered over two positions, O1 and O1B were refined with occupancies of 38.8 and 61.1% respectively, where as O2 and O2B lie on a special position and were refined with occupancies of 16.6 and 83.3% to account for the split occupancy between μ_3-O and μ_3-OH groups.

Chapter 6.

Conclusions and Future Outlook

Chapter 6. Conclusions and Future Outlook

6.1. Conclusions

A view of the impact of manipulation of crystal size, morphology, and surface chemistry on the properties of MOFs has been canvassed. This body of work shows that systematic analysis of MOF nanoscale structuralisation is essential prior to their integration within high precision devices and/or the fabrication of MOF-containing composites. The capabilities of these materials in the field of heterogeneous catalysis has been introduced. This work highlighted that whilst MOFs can catalyse a wide range of reactions, there is a limited understanding about which active sites are primarily being accessed (internal vs external) and how this reactivity can be manipulated through nanoscale structuralisation. In summary, this thesis describes a detailed investigation of how nanoscale structuralisation impacts heterogeneous MOF catalysis for several systems.

The effect of crystal size and morphology on exterior surface catalysis was first investigated with ZIF-8. Results presented in Chapter 2 show that improved activity for the transesterification of hexanol and vinylacetate can be achieved by exposing more surface active sites via crystal size reduction. However, increasing the amount of external surface area (which is inversely proportional to particle size) also exposed the framework to more rapid surface degradation and the leaching of Zn^{2+}/2-mIM under reaction conditions. In this circumstance particle size was shown to directly impact the surface stability of ZIF-8 crystals under transesterification and Knoevenagel reaction conditions. Whilst this work did not yield conclusive results as to the impact of crystal size and morphology on surface catalysis with ZIF-8, it did however highlight that MOFs are susceptible to nanoscale structural changes during solution phase catalysis. Thus, an important finding of this study is that such effects must be carefully considered when assessing the catalytic performance of MOFs. Furthermore, it emphasises the importance of understanding nanoscale structuralisation effects on MOF catalyst stability as well as activity.

The modular synthesis of MOFs facilitates control over crystal size, via coordination modulation and allows for active sites to be dispersed throughout the framework. The site isolation of homogeneous catalysts within MOFs makes them intriguing materials for heterogeneous catalysis. Chapters 3 and 4 focussed on elucidating crystal size and active site localisation effects on the activity and selectivity of gas phase catalysis with the stable, yet chemically mutable, UiO-67-bpydc framework. These chapters featured the heterogenization of molecular catalysts employed for ethylene hydroformylation/hydrogenation and

oligomerisation, $[RhCOD(acetone)_2]BF_4$ and $[PdMe(MeCN)]BF_4$ respectively. In Chapter 3 it was shown that the selectivity of the heterogenized catalyst within the framework was crystal size dependent. The 100 nm, 1 μm, and 10 μm catalysts displayed a selectivity of 24.5, 28.1, and 57.3% for hydroformylation over hydrogenation, respectively. This phenomenon was attributed to the increased prevalence of pore confinement effects with decreasing surface/volume ratios (increasing particle size). However, further experimentation is necessary to confirm this hypothesis. Due to the presence of active sites throughout the framework, there was no definitive way to deconvolute internal and external catalysis in this study. To confirm this hypothesis the synthesis and catalytic reactivity of surface passivated frameworks will be required.

Chapter 4 detailed the further investigation of internal catalysis through surface passivation. Core-shell UiO-67-bpydc⊂UiO-67-bpdc catalysts for gas phase ethylene oligomerisation were synthesized via slow-diffusion SALE. In this work attempts were made to synthesize a composite material where all of the active sites were localised at the interior of the MOF crystals, whilst the exterior would consist of the same framework but with a ligand which could not chelate molecular catalysts and would not alter the diffusion of guests. However, this elegant approach was complicated by the similar pKa/steric bulk of the core and shell ligands, which resulted in the formation of diffuse core-shell architectures, as characterised by NMR and SEM/EDX. A highlight of this study is that it described the first reported of single site isolation of the homogeneous palladium catalyst $[PdMe(MeCN)]BF_4$ within a MOF via PSMet, requiring no activating agent prior to catalysis. Whilst the core-shell boundary was not well defined, the dilution of surface active sites prolonged catalyst activity (when loaded with the palladium catalyst) for ethylene oligomerisation, relative to samples where active sites were dispersed throughout the framework and localised exclusively at the exterior. Nevertheless, catalyst deactivation was observed for all samples due to pore blockage and surface coating from the production of long chain non-volatile oligomers. This work was hindered by the poor definition of the core-shell boundary and catalyst choice. However, insight was gained into how the active sites location can be controlled through crystal engineering techniques and how that can impact catalysis with MOFs. Further investigation of MOF surface modification is necessary to aid the study of internal and external catalysis with MOFs.

Site isolation of molecular catalysts and reactive species within crystalline MOF scaffolds facilitates the development of heterogeneous catalysts as reactions can be monitored

via SCXRD. In order to characterise such species, large single crystals of the UiO-67-Me_2bpydc were synthesised (20-50 μm). Through a process of modulator exchange and crystal healing (also utilised in Chapter 4), ligand defects were removed resulting in X-ray quality crystals. These crystals were impregnated with a range of transition metal catalysts/precursors to reactive species via PSMet, and then analysed via SCXRD. Single-crystal to single crystal transformations were observed upon PSMet with only $CoCl_2$ and $ZnCl_2$ (separately), corresponding to a shift from high to low symmetry *Fm-3* to *Pa-3*, resulting from the ordering of metalated ligand moieties throughout the framework. The limited number of crystal structures obtained in this work stemmed from low occupation of the chelating site and disorder around the ligand. This study highlighted some of the challenges associated with extracting crystallographic information from high symmetry MOF structures which rely on ordering throughout the crystal to transition to a lower symmetry group. There was an attempt to extend the chemistry of site isolated $CoCl_2$ moieties through anion exchange with NaN_3, in order to probe the structure of reactive cobalt complexes such as cobalt-nitrides. However, incomplete anion exchange and low metal occupancy meant that no crystal structures of the metal azides could be obtained. These preliminary experiments established that UiO-67-Me_2bpydc can be used as a crystalline matrix to characterise certain tetrahedral metal complexes, but more work is required before this system can be adapted to a broader range of transition metals/reactive intermediates.

6.2. Future Outlook

The work presented in this thesis emphasises the need to understand the influences of nanoscale structuralisation on MOF catalysis and the challenges in doing so in a systematic manner. Unexpected effects, such as the surface instability of ZIF-8 to reaction conditions in the liquid phase, have complicated such investigations and future experiments would aim to build upon this work, simplifying the studies in order to minimise these additional impacts. Analysing catalysis with ZIF-8 could be improved by conducting such experiments in the gas phase, thereby minimising any solvent or reagent mediated Zn^{2+}/2-mIM leaching. This would likely necessitate using smaller more volatile reagents which could diffuse throughout the framework and hence subsequent studies would need to be informed by the considerations described in Chapters 3 and 4.

Investigating the impact of active site location within a framework is paramount to further our understanding of how MOF catalysis can be tuned through nanoscale structuralisation. The work outlined in Chapters 3 and 4 is a good starting point for future

studies, but further deconvolution of internal and external catalysis in necessary to better understand these processes. Gas phase hydroformylation of ethylene/longer alkenes is the most interesting reaction studied in this thesis for such an investigation, as multiple reactions occur (hydroformylation, hydrogenation and isomerisation) that may be influenced by active site localisation. In order to study the catalyst activity/selectivity in relation to active site location, synthetic methods to control active site location to the exterior/interior of the crystal must be further developed. Within our research group this has been recently achieved through epitaxial growth of a UiO-67 framework with a bulky ligand on the surface of 1 µm crystals of UiO-67-bpydc, extending the work described by Luo *et al.*,[1] forming a well-defined core-shell boundary. Conducting catalytic studies on samples with well-defined core-shell boundaries would enable a more systematic investigation of pore confinement effects on the kinetic control of reaction selectivity (hydrogenation vs hydroformylation) and linear vs branched product formation (when using longer alkenes). This would improve our understanding of MOF catalysis and may enable us to tune the activity/selectivity of MOF catalysts through nanoscale structuralisation rather than through design of new MOF architectures. Additionally, this understanding may make the integration of MOF catalysts in existing technologies would be one step closer to being realised.

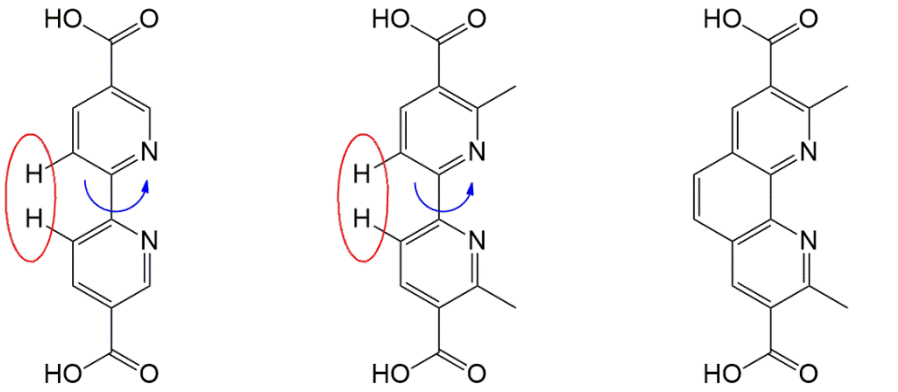

Figure **6.1**: Representations of *cis*-bpydc, *cis*-Me2bpydc and 1,10-phenanthroline-3,8-dicarboxylic acid ligands, demonstrating the hydrogen interactions in the cis conformation (circled in red).

The challenges surrounding both the site isolation reactive species within a MOFs and their subsequent characterisation have been detailed in Chapter 5. The dominant issues with this work were the subtle nature of the structural ordering to lower symmetry space groups and

disorder surrounding the site of metalation. The disorder could be reduced by using a ligand with fewer rotatable bonds such as one based around a 1,10-phenanthroline core, which would minimise steric destabilisation related to H to H interactions that arise in the cis conformations of Me_2bpydc and bpydc, see Figure **6.1**.[2] However, the acute angle of bidentate coordination (< 90°) of the bipyridine/phenanthroline ligands to metal centres may not be suitable for the desired wide range of coordination environments, thereby limiting the range of complexes that can be isolated. Alternate ligand design strategies must therefore be implemented to balance the diametrically opposite requirements of increased flexibility at the coordinating moiety with ligand rigidity for permanent porosity. Ideally, the work initiated in Chapter 5 could then be extended to follow the progress of reactive species isolated within isostructural Zr-frameworks, namely the catalytic cycles of reactions discussed in this thesis; hydroformylation with $[RhCOD(acetone)_2]BF_4$ and, ethylene oligomerisation with $[PdMe(MeCN)]BF_4$. Such studies would broaden our understanding of heterogeneous catalysis within Zr-frameworks and may enable us to design better scaffolds to isolate reactive species within MOFs.

6.3. References

1. Luo, T.-Y.; Liu, C.; Gan, X. Y.; Muldoon, P. F.; Diemler, N. A.; Millstone, J. E.; Rosi, N. L., Multivariate Stratified Metal-Organic Frameworks: Diversification Using Domain Building Blocks. *J Am Chem Soc* **2019,** *141* (5), 2161-2168.

2. Hancock, R. D.; Nikolayenko, I. V., Do Nonbonded H--H Interactions in Phenanthrene Stabilize it Relative to Anthracene? A Possible Resolution to this Question and its Implications for Ligands such as 2,2′-Bipyridyl. *J Phys Chem A* **2012,** *116* (33), 8572-8583.

Publications

Linder-Patton, O. M.; de Prinse, T. J.; Furukawa, S.; Bell, S. G.; Sumida, K.; Doonan, C. J.; Sumby, C. J., Influence of Nanoscale Structuralisation on the Catalytic Performance of ZIF-8: a Cautionary Surface Catalysis Study. *CrystEngComm* **2018,** *20* (34), 4926-4934.

Linder-Patton, O. M.; Rogers, B. T.; Sumida, K., Impact of Higher-Order Structuralization on the Adsorptive Properties of Metal–Organic Frameworks. *Chem Asian J* **2018,** *13* (16), 1979-1991.

Riccò, R.; **Linder-Patton, O. M**.; Sumida, K.; Styles, M. J.; Liang, K.; Amenitsch, H.; Doonan, C. J.; Falcaro, P., Conversion of Copper Carbonate into a Metal–Organic Framework. *Chem Mater* **2018,** *30* (16), 5630-5638.

Peralta, R.; Huxley, M.; Young, R.; **Linder-Patton, O. M**.; Evans, J. D.; Doonan, C. J.; Sumby, C. J., MOF Matrix Isolation: Cooperative Conformational Mobility Enables Reliable Single Crystal Transformations. *Faraday Discuss* **2020**. (Accepted).